Vol. 24. No 1, 2022

ISSN 1507-2711
Cena: 25 zł

EKSPLOATACJA I NIEZAWODNOŚĆ
MAINTENANCE AND RELIABILITY

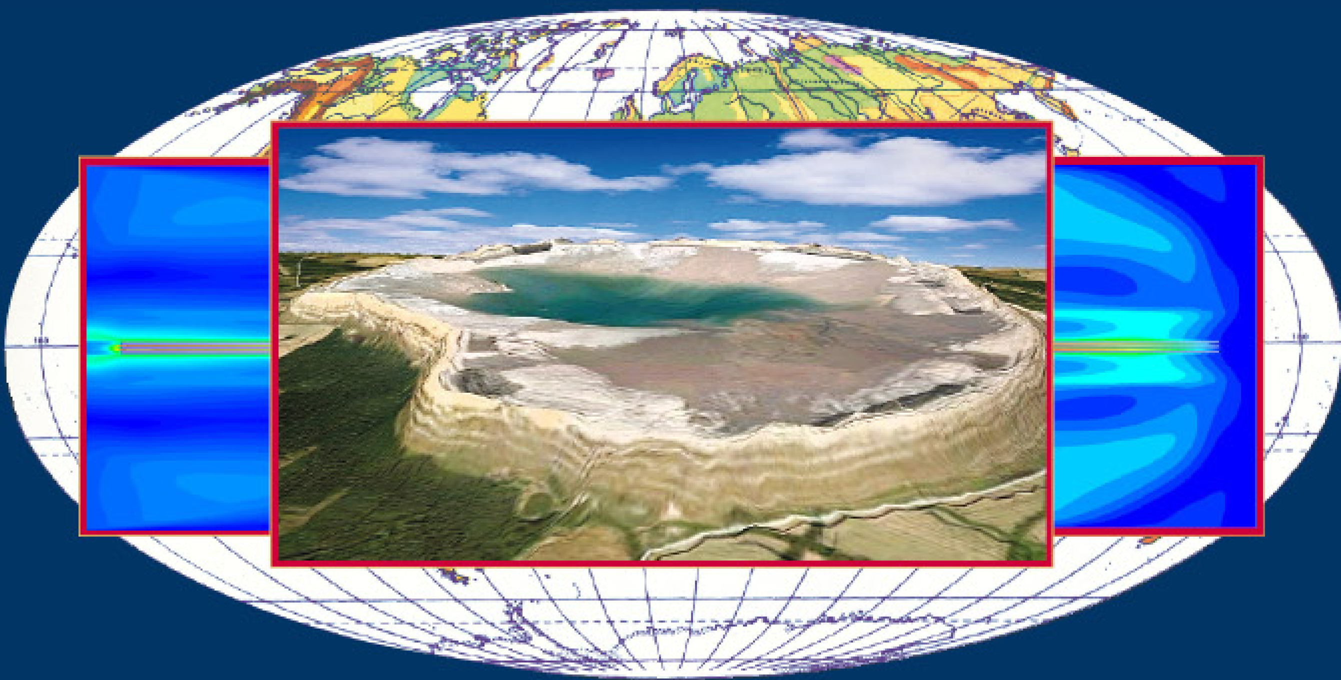

Polskie Naukowo Techniczne Towarzystwo Eksploatacyjne
Warszawa

Polish Maintenance Society
Warsaw

Indexed by:

The Journal is indexed and abstracted in the Journal Citation Reports (JCR Science Edition), Scopus, Science Citation Index Expanded (SciSearch®) and Index Copernicus International.

The Quarterly appears on the list of journals credited with a high impact factor by the Polish Ministry of Science and Higher Education and is indexed in the Polish Technical Journal Contents database – BAZTECH and the database of the Digital Library Federation.

Task *„Implementation of procedures ensuring the originality of scientific papers published in the quarterly „Eksploatacja i Niezawodność – Maintenance and Reliability"* financed under contract 532/P-DUN/2018 from the funds of the Minister of Science and Higher Education for science dissemination activities.

All the scientific articles have received two positive reviews from independent reviewers.
Our 2020 Impact Factor is 2.176

Editorial staff:	Dariusz Mazurkiewicz, PhD, DSc (Eng), Associate Professor (Editor-in-Chief, Secretary of the Editorial Board) Anna Borucka, Ph.D., D.Sc., Eng. – Deputy Editor-in-Chief Tomasz Klepka, PhD, DSc (Eng), Associate Professor (Deputy Editor-in-Chief) Magdalena Krolopp, MSc (Editorial secretary) Andrzej Koma (Typesetting and text makeup) Krzysztof Olszewski, PhD (Eng) (Webmaster)
Publisher:	Polish Maintenance Society, Warsaw
Scientific patronage:	Polish Academy of Sciences Branch in Lublin
Address for correspondence:	"Eksploatacja i Niezawodność" – Editorial Office ul. Nadbystrzycka 36, 20-618 Lublin, Poland e-mail: office@ein.org.pl http://www.ein.org.pl/
Circulation:	550 copies

Table Of Contents

EKSPLOATACJA I NIEZAWODNOŚĆ
MAINTENANCE AND RELIABILITY

Eksploatacja i Niezawodnosc – Maintenance and Reliability

Volume 24 (2022), Issue 1

journal homepage: http://www.ein.org.pl

Article citation info:
Chiou K-C, Chen K-S. Lifetime performance evaluation model based on quick response thinking. Eksploatacja i Niezawodnosc – Maintenance and Reliability 2022; 24 (1): 1–6, http://doi.org/10.17531/ein.2022.1.1.

Lifetime performance evaluation model based on quick response thinking

Indexed by:
Web of Science Group

Kuo-Ching Chiou [a], Kuen-Suan Chen [b,c,d,*]

[a] Chaoyang University of Technology, Department of Finance, Taichung 41349, Taiwan, R. O. C.
[b] National Chin-Yi University of Technology, Department of Industrial Engineering and Management, Taichung 411030, Taiwan, R. O. C.
[c] Asia University, Institute of Innovation and Circular Economy, Asia University, Taichung 41354, Taiwan,R. O. C.
[d] Chaoyang University of Technology, Department of Business Administration, Chaoyang University of Technology, Taichung 41349, Taiwan, R. O. C.

Highlights

- This study explored the lifetime of products based on type II censoring.
- Adopted right censoring to find the bester estimator of the lifetime index.
- The 1-α confidence interval and UMP test model of lifetime index were found.
- A numerical example was demonstrated the application of the proposed model.
- Under above methods, the products can take market share earlier.

Abstract

In practice, lifetime performance index CL has been a method commonly applied to the evaluation of quality performance. L is the upper or lower limit of the specification. The product lifetime distribution is mostly abnormal distribution. This study explored that the lifetime of commodities comes from exponential distribution. Complete data collection is the primary goal of analysis. However, the censoring type is one of the most commonly used methods due to considerations of manpower and material cost or the timeliness of product launch. This study adopted Type-II right censoring to find out the uniformly minimum variance unbiased (UMVU) estimator of the lifetime performance index CL and its probability density function. Afterward this study obtained the 100×(1-α)% confidence interval of the lifetime performance index CL as well as created the uniformly most powerful (UMP) test and the power of the test for the product lifetime performance index. Last, this study came up with a numerical example to demonstrate the suggested method as well as the application of the model.

Keywords

lifetime performance index, Type-II right censoring, *UMVU* estimators, *UMP* test.

1. Introduction

A number of studies related to process quality have pointed out that enhancing process quality can increase product lifetime as well as reduce the rate of process scrap and rework. Not only can it raise the value of the product, but it also can contribute to the sustainable development of enterprises in the face of challenges to global warming [7, 10, 17]. Numerous studies have stated that under the thinking of circular economy and sharing economy, good product quality, high availability, and long lifetime can not only reduce operating costs but also improve operating efficiency, thereby enhancing users' satisfaction and willingness [18, 20, 24]. Obviously, improving quality and lifetime for a product can increase its value and industrial competitiveness.

Regarding product quality, quite a few quality control engineers and experts in statistics have been dedicated to their studies on process capability indicators in terms of evaluation, analysis, and improvement [3, 31, 34-35]. In addition, Six Sigma is also a method commonly adopted in the industry to improve process quality [15, 21-22, 25]. Subsequently, many scholars discussed the relation between the abovementioned process capability indicators and the Six-Sigma quality level widely used in the industry, and then they proposed the Six-Sigma quality index, hoping to apply the process capability index to the model of Six-Sigma quality management [6, 29].

Concerning the product lifetime performance, Tong et al. [28] came up with a lifetime performance index on the basis of the larger-the-better process capability index. Under the assumption of exponentially complete data, the proposed lifetime performance index is presented as follows:

$$C_L = \frac{\lambda - L}{\lambda} = 1 - \frac{L}{\lambda}, \tag{1}$$

where L refers to the minimum required time unit of the lifetime for each electronic product. According to the research of Chen et al. [5], there is a one-to-one mathematical relation between the lifetime performance index C_L and the rate of failure. When the average lifetime value of λ is larger, the rate of failure becomes relatively smaller. Then, some scholars also have invested in related research to explore

(*) Corresponding author.
E-mail addresses: K-C. Chiou (ORCID: 0000-0003-2617-5856): kcchiou@cyut.edu.tw, K-S. Chen (ORCID: 0000-0002-1091-639): kuensuan.chen@gmail.com

the product lifetime performance. The above-mentioned studies all used complete sample data with a sample size of n to make statistical inferences. However, in the experiment on product lifetime performance and reliability, data collection is subject to time constraints or another factor (like money, material resources, machine or experimental difficulties), so that the experimenter is usually unable to view the data of quality for each tested product. Therefore, the censored sample is considered as one of the methods [11, 16]. There are three censoring types: Type-I censoring, Type-II censoring, and random censoring (also known as Type-III censoring) [14, 19].

In right censoring, the observations are $Y_1, Y_2, Y_3, \ldots, Y_n$, as follows:

$$Y_i = \begin{cases} T_i\ ,\ T_i \geq C_i \\ C_i\ ,\ T_i \leq C_i\ , \end{cases} \quad i = 1, 2, 3, \ldots, n, \tag{2}$$

where T_i represents time of failure, and C_i is censoring time associated with T_i.

Right censoring refers to dividing the obtained data into two parts: one is T, time of failure for the product lifetime, and the other is C, censoring time. If T of the experimented product lifetime is greater than C, then T is regarded as the censored observation, denoted by T^+. As to the censored observation T^+, the corresponding C is used as the imputation value of T for the product lifetime, and the imputation value is called censored data [19]. Type-I censoring and Type-II censoring are applied to engineering (censoring time is a fixed value), while random censoring are applied to medical science, like experimental studies using animals or experiments done in clinical research (censoring time is a random variable) [19].

Based on right censored data, point and interval prediction of the censoring number of failures is discovered by means of a simulation study under indeterminate survival times and censoring status [13]. Parameters of the exponential distribution are estimated by means of complete samples of Type -I censoring, Type-II censoring, and random censoring [2, 4, 30, 36]. The Type-II progressive censoring scheme has been widely adopted to analyze lifetime data for highly reliable products. For example, construct interval estimators and hypothesis testing of the lifetime performance index based on progressive type II right-censored data. And the potentiality of the model is analyzed by a numerical example [1, 8, 16]. The fuzzy statistical estimator of the lifetime performance index is then utilized to develop a new fuzzy statistical hypothesis testing procedure [33]. Finally, by Monte Carlo power simulation, the objectives assess the behavior of the lifetime performance index [1, 32].

Therefore, this study applies the Type-II right censoring data. In Type-II right censoring, only the lifetimes of the first r components are censored, whereas the lifetimes of the remaining (n-r) components are uncensored or missing.

In Type-II right censoring, the observations are $Y_1, Y_2, Y_3, \ldots, Y_n$, displayed as follows:

$$Y_i = \begin{cases} T_i\ ,\ T_i \leq T_{(r)} \\ T_{(r)}\ ,\ T_i > T_{(r)}\ , \end{cases} \quad i = 1, 2, 3, \ldots, n, \tag{3}$$

where $T_{(r)}$ is the order statistic of failure times $T_1, T_2, T_3, \ldots, T_n$, and r is the number of uncensored data, $r \leq n$.

In this paper, the product lifetime T comes from the exponential distribution with the mean λ, which is the probability density function (*p.d.f.*) of T as follows:

$$f_T(t) = \frac{1}{\lambda} exp\left(-\frac{t}{\lambda}\right),\ t > 0\ . \tag{4}$$

Then, the survival function is:

$$S_T(t) = p\left(T > t\right) = 1 - F_T(t) = exp\left(-\frac{t}{\lambda}\right),\ t > 0\ , \tag{5}$$

where $F_T(t)$ is the cumulative distribution function of T.

With the exponentially complete data, the lifetime performance index which Tong et al. [28] suggested is denoted as Eq. (1). Based on the above, the graphic scheme of methods as following (Fig.1).

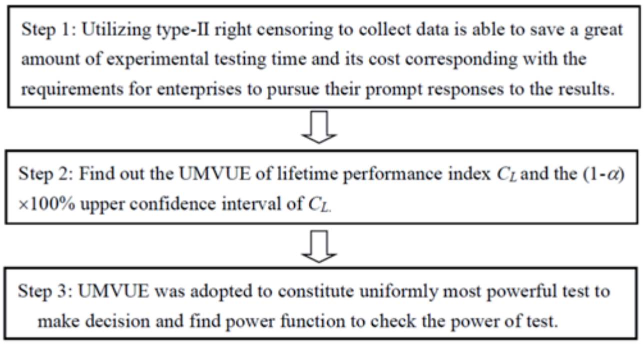

Fig. 1. The graphic scheme of methods

In fact, the statistic testing method the study proposed is equipped with more advantages shown as follows than others:

1. Find the uniformly minimum-variance unbiased estimator (UMVUE) of the lifetime performance index.
2. Derive the uniformly most powerful (UMP) test.
3. Utilizing type-II right censoring is able to save a great amount of experimental testing time and its cost corresponding with the requirements for enterprises to pursue their prompt responses to the results; moreover, the technique is more likely to assist enterprises to efficiently make sensible decision in a short time.

In this paper, the other sections are arranged as follows. In Section 2, we discover the uniformly minimum-variance unbiased estimator (UMVUE) of the lifetime performance index. Next, in Section 3, we demonstrate the (1-α) ×100% upper confidence of the performance index. Furthermore, the uniformly most powerful (UMP) test of the lifetime performance index is developed in Section 4. Also, a numerical example is employed to describe the efficacy of the suggested method in Section 5. Finally, we make conclusions in Section 6.

2. Estimation of lifetime performance index and uniformly minimum variance unbiased estimator

Let $Y_1, Y_2, Y_3, \ldots, Y_n$ be the observed data with sample size n under Type-II right censoring as follows [32]:

$$Y_i = \begin{cases} T_i\ ,\ \ T_i \leq T_{(r)}\ (uncensored\ data) \\ T_{(r)},\ \ T_i > T_{(r)}\ (censored\ data) \end{cases} \quad , i=1, 2, 3, \ldots, n, \tag{6}$$

where the order statistic $T_{(r)}$ is the time of censoring. Failure time T follows the exponential distribution with the mean λ. We figure out the estimator of λ under Type-II censoring. By Eq. (4) and the maximum likelihood method, we find the unbiased estimator of λ as follows [19]:

$$\hat{\lambda} = \frac{\sum_{i=1}^{n} Y_i}{r}\ , \tag{7}$$

where:

$$\sum_{i=1}^{n} Y_i = \sum_{i=1}^{r} T_{(i)} + (n-r)T_{(r)} . \tag{8}$$

When r=n (complete data), the estimator $\hat{\lambda}$ is equal to $\overline{T}$. By Eq. (1), the unbiased estimator of C_L is expressed below:

$$\hat{C}_L = 1 - \left(\frac{r-1}{r}\right)\frac{L}{\hat{\lambda}} = 1 - \frac{(r-1)L}{\sum_{i=1}^{n} Y_i} . \tag{9}$$

Furthermore:

$$\lim_{r\to\infty} E\left[\left(\hat{C}_L - C_L\right)^2\right] = \lim_{r\to\infty} Var\left(\hat{C}_L\right) = \lim_{r\to\infty} \frac{(1-C_L)^2}{r-2} = 0 . \tag{10}$$

According to the Lehmann-Scheffé theorem, $\hat{C}_L$ is the uniformly minimum-variance unbiased estimator (UMVUE) of C_L . To compare with Lee et al., their study proposed that the estimator $\hat{C}_L$ is not unbiased of C_L , an asymptotically unbiased estimator [16]. Hence, the findings from the estimator in Eq. (9) indicated that it was better than the results of Lee et al. [16].

3. Find the (1-α) ×100% upper confidence of performance index

According to Miller [19], the failure time T follows the exponential distribution with the mean λ. Let $X = \frac{2\sum_{i=1}^{n} Y_i}{\lambda}$, then we get X to follow the chi-square distribution with degree 2r (i.e. $X \sim \chi^2_{2r}$). Let $W = \hat{C}_L$, the cumulative distribution function of W is denoted by:

$$\begin{aligned} F_W(w) &= P(W \le w) \\ &= P\left(\frac{2(r-1)(1-C_L)}{1-W} \ge \frac{2(r-1)(1-C_L)}{1-w}\right) \\ &= P\left(X \ge \frac{2(r-1)(1-C_L)}{1-w}\right) \\ &= 1 - P\left(X \le \frac{2(r-1)(1-C_L)}{1-w}\right). \end{aligned} \tag{11}$$

By the fundamental theorem of calculus (part 1), we get the probability density function of W as follows:

$$f_W(w) = \frac{1}{\Gamma(r)}\left((r-1)(1-C_L)\right)^r (1-w)^{-(r+1)} \exp\left(-\frac{(r-1)(1-C_L)}{(1-w)}\right),\ w<1 \tag{12}$$

Furthermore, we can derive the level of (1-α)×100% upper confidence limit of C_L as follows:

$$1-\alpha = P\left(X \ge \chi^2_{\alpha,2r}\right) = P\left(\frac{2(r-1)}{1-W}(1-C_L) \ge \chi^2_{2r,\alpha}\right). \tag{13}$$

Therefore:

$$P\left(C_L \le 1 - \frac{(1-\hat{C}_L)}{2(r-1)}\chi^2_{\alpha,2r}\right) = 1-\alpha , \tag{14}$$

and the (1-α) ×100% upper confidence limit of C_L is:

$$UC_L = 1 - \frac{(1-\hat{C}_L)}{2(r-1)}\chi^2_{\alpha,2r} = 1 - \frac{(r-1)L}{2(r-1)\sum_{i=1}^{n} Y_i}\chi^2_{\alpha,2r} , \tag{15}$$

where $\chi^2_{\alpha;2r}$ is the upper α quintile of χ^2_{2r} .

4. Uniformly most powerful test

To know whether C_L is larger than or equal to c, it is necessary to take into account the null hypothesis: $H_0 : C_L \ge c$ (showing that the product lifetime performance is good) versus the alternative hypothesis: $H_1 : C_L < c$ (showing that the product lifetime performance is poor) at a desired level of significance α. Significance α represents the probability indicating that the product lifetime performance is satisfying but denied, so it can be called the producer risk. Then, the uniformly most powerful (UMP) test is defined by:

$$\phi(Z) = \begin{cases} 1, \text{ if } \hat{C}_L < c_0 \ (\textit{reject } H_0 \textit{ region}) \\ 0, \text{ otherwise} \end{cases} , \tag{16}$$

where c_0 is the critical value determined by Eq. (17):

$$\mathrm{E}\left[\phi(Z)\middle|\hat{C}_L = c\right] = p\left\{C_L < c_0 \middle| C_L = c\right\} = p\left\{X < \chi^2_{\alpha;2r} \middle| C_L = c\right\} = \alpha, \tag{17}$$

where $\chi^2_{\alpha;2r}$ is the upper α quintile of χ^2_{2r} . Based on Eq. (12) and Eq. (17), we derive Eq. (18) and Eq. (19) as follows:

$$\chi^2_{\alpha;2r} = \frac{1-C_L}{1-C_0}\cdot 2(r-1) \tag{18}$$

and:

$$c_0 = 1 - \frac{2(r-1)(1-c)}{\chi^2_{\alpha;2r}} . \tag{19}$$

As a matter of fact, the power of the test is critical in learning the probability that the test correctly rejects the null hypothesis H_0 as the alternative hypothesis H_1 is true. Based on Eq. (17), Eq. (18), and Eq. (19), the power of the test for C_L is given by Eq. (20) below.

$$p\left\{C_L < c_0 \middle| C_L = c_1,\ c_1 \in H_1\right\} = 1-\beta , \tag{20}$$

where β is the Type-II error of $C_L = c_1,\ c_1 \in H_1$. By Eq. (12) and Eq. (20), we get Eq. (21) as follows:

$$\pi(c_1) = p\left\{\frac{1-C_L}{1-\hat{C}_L}\cdot 2(r-1) < \frac{1-C_L}{1-c_0}\cdot 2(r-1) \middle| C_L = c_1,\ c_1 \in H_1\right\} = 1-\beta . \tag{21}$$

Similarly, based on Eq. (12) and Eq. (21), we have:

$$\frac{1-c_1}{1-c_0}\cdot 2(r-1) = \chi^2_{1-\beta;2r} . \tag{22}$$

Based on the null hypothesis H_0 ($C_L \ge c$) versus alternative hypothesis H_1 ($C_L < c$), Figure 1 shows the power curve for $c = 0.7$

and $r = 60, 80, 100$ (bottom-up in the plot) with $n = 100$. According to Figure 2, the greater the power function $\pi(c_1)$ with the value of c_1 ($c_1 \in H_1$), the greater the power. Also, when the power function $\pi(c_1)$ is fixed at c_1 ($c_1 \in H_1$), the greater the value of r (i.e. the number of uncensored data is greater), the greater the power. That is, the larger the number of uncensored data, the stronger the power, which meets the more the original data, the better the quality of the analysis.

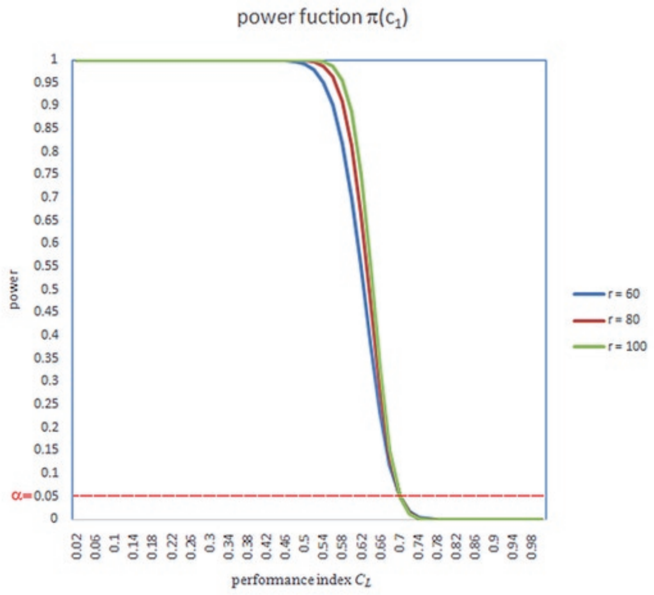

Fig. 2. Power curve for c = 0.7 and r = 60, 80, 100 (bottom-up in the plot) with n = 100

When product lifetime (T) follows the exponential distribution with the mean λ, the estimate of $\hat{C}_L$, the confidence interval for C_L, and the uniformly most powerful test are discovered as stated above. The steps of the statistical testing method are listed below:

Step 1: Collect the sample size n, $Y_1, Y_2, \ldots, Y_{100}$ under Type-II right censoring, as shown in Eq. (3).

Step 2: Given the value L, we can find the estimate of $\hat{C}_L$ by Eq. (7) and Eq. (9).

Step 3: By Eq. (15), we get the level of $(1-\alpha)\times 100\%$ upper confidence interval for C_L.

Step 4: We construct hypotheses as follows:

null hypothesis $H_0 : C_L \geq c$ (the product lifetime perform ance is good)

versus

alternative hypothesis $H_1 : C_L < c$ (the product lifetime performance is poor)

5. Numerical example

In this section, a numerical example is adopted to elaborate the above four steps stated in Section 4, assuming that the lifetime of an electronic product follows an exponential distribution ($\lambda = 1$) as well as assuming that sample size $n = 100$. By Type-II censoring, $r = 80$ is given. The four steps are listed as follows:

Step 1: Collect the sample data $T_1, T_2, \ldots, T_{100}$ from an exponential distribution with the mean ($\lambda = 1$). Given the number of uncensored data $r = 80$, we can find the order statistic $T_{(80)} = 1.6377$, and then we can collect Type-II right censored data $Y_1, Y_2, \ldots, Y_{100}$ by Eq. (3).

Step 2: Given the ratio $L/\lambda = 0.35$ (i.e. $L<\lambda$) and then $C_L = 0.65$ by Eq. (1), we can find $\sum_{i=1}^{100} Y_i = 830392$ by Eq. (3) and the estimate of $\hat{C}_L = 0.6644$ by Eq. (9).

Step 3: Given the confidence level of 95% by Eq. (15), we can get that the upper confidence interval for C_L is $(-\infty, 0.7201]$.

Step 4: We give the level of significance ($\alpha = 0.05$) and the value of requirement ($c = 0.7$). Then, the hypotheses are expressed as follows:

null hypothesis $H_0 : C_L \geq 0.7$ (the product lifetime performance is good)

versus

alternative hypothesis $H_1 : C_L < 0.7$ (the product lifetime performance is poor).

By Eq. (17) and Eq. (19), the reject H_0 region is $\{\hat{C}_L < 0.6402\}$. Since $\hat{C}_L = 0.6644$, obviously, H_0 is not rejected, concluding that the product lifetime performance is good. Obviously, type-II right censoring method the study adopted allowed investigators to make the best of eighty samples out of one hundred valid ones to conduct the survey, which saved twenty percent of experimental testing time and its cost. Therefore, the result was totally correspondent with the needs of pursuing enterprises' requirements for prompt responses and efficiently making wise decision in no time [12, 27].

6. Conclusions

The process capability index C_L is a common method used to practically evaluate the lifetime performance index of the product. However, in the product development process, when taking time and labor costs into consideration, collecting data in the form of censoring is one of the methods to improve the defect. This study took the research and development of the electronic product manufacturing process as an example and adopted Type-II right censoring to collect data. When the data collection is incomplete, the missing data values are replaced by the experiment termination time $T_{(r)}$. This study not only derived the uniformly minimum-variance unbiased estimator (UMVVUE) $\hat{C}_L$ of the process capability index C_L and its probability density function but also derived the $(1-\alpha)$ 100% upper confidence interval of C_L. Assuming that the period of warranty was L unit time, this study created the uniformly most powerful (UMP) test for the lifetime performance index of the product and obtained the power of the test for C_L. From the graph of the power function, it is learned that the greater the number of uncensored data r, the greater the power. When other conditions remain unchanged, the complete data ($r = n$) has the greatest power. For the convenience of manufacturers, this paper then established a testing process and at the same time proposed a numerical case. According to the testing process to perform the best statistical testing model, the proposed method and the applications of the model were explained in this paper.

According to reliable life tests, apart from type-II right censoring, type-I right censoring [9, 23] and type-III right censoring [26] are also widely utilized to collect data. Thus, for the purpose of offering more relevant references to even more enterprises, the study suggests that three different right censoring types to be further investigated and analyzed in the future study.

References

1. Alsaedi BSO, Abd El-Raouf MM, Hafez EH, Almaspoor Z, Alamri OA, Alanazi K A, Khosa SK. Decision-Making for the Lifetime Performance Index. Computational Intelligence and Neuroscience 2021: 3005067, https://doi.org/10.1155/2021/3005067.
2. Bedbur S, Mies F. Confidence bands for exponential distribution functions under progressive type-II censoring. Journal of statistical computation and simulation 2021: 1-21, https://doi.org/10.1080/00949655.2021.1931211.
3. Borgoni R, Zappa D. Model-based process capability indices: The dry-etching semiconductor case study. Quality and Reliability Engineering International 2020; 36(7): 2309-2321, http://doi.org/10.1002/qre.2698.
4. Celik N, Guloksuz CT. A new lifetime distribution. Eksploatacja i Niezawodnosc – Maintenance and Reliability 2017; 19 (4): 634-639, http://doi.org/10.17531/ein.2017.4.18.
5. Chen KS, Chiou KC, Yu CM. Lifetime performance index of electronic products. Microelectronics Reliability 2020; 113: 113941, https://doi.org/10.1016/j.microrel.2020.113941.
6. Chen KS, Huang CF, Chang TC. A mathematical programming model for constructing the confidence interval of process capability index Cpm in evaluating process performance: An example of five-way pipe. Journal of the Chinese Institute of Engineers, Transactions of the Chinese Institute of Engineers, Series A 2017; 40(2): 126-133, https://doi.org/10.1080/02533839.2017.1294996.
7. Chen KS, Wang CH, Tan KH. Developing a fuzzy green supplier selection model using Six Sigma quality indices. International Journal of Production Economics 2019; 212: 1-7, https://doi.org/10.1016/j.ijpe.2019.02.005.
8. Dey S, Sharma VK, Anis MZ, Yadav B. Assessing lifetime performance index of Weibull distributed products using progressive type II right censored samples. International Journal of System Assurance Engineering and Management 2017; 8(2): 318-333, https://doi.org/10.1007/s13198-016-0437-z.
9. EL-Helbawy AA, AL-Dayian GR, Rezk HR. Bayesian approach for constant-stress accelerated life testing for Kumaraswamy Weibull distribution with censoring. Pakistan Journal of Statistics and Operation Research 2016; 12 (3): 407-428, https://doi.org/10.18187/pjsor.v12i3.1171.
10. Ershadi MJ, Qhanadi Taghizadeh O, Hadji Molana SM. Selection and performance estimation of green lean six sigma projects: A hybrid approach of technology readiness level, data envelopment analysis, and ANFIS. Environmental Science and Pollution Research 2021; 28(23): 29394-29411, https://doi.org/10.1007/s11356-021-12595-5.
11. Hon CW, Wu JW, Cheng CH. Computational procedure of performance assessment of lifetime index of businesses for the pareto lifetime model with the right type II censored sample. Applied Mathematics and Computation 2007; 184(2): 336-350, https://doi.org/10.1016/j.amc.2006.05.199.
12. Kirkos, E. Airbnb listings' performance: Determinants and predictive models. European Journal of Tourism Research 2022; 30: 3012.
13. Lee BL, Crunk SM, Khan M, Fairley WB. Prediction for a Future Number of Failures Based on Right Censored Data with Indeterminate Survival Times and Censoring Status. International Journal of Applied Science and Engineering 2018; 15(1): 47-57, https://doi.org/10.6703/IJASE.201802_15(1).047.
14. Lee ET. Statistical Methods for Survival Data Analysis (2nd ed). New York: John Wiley and Sons, 1992.
15. Lee JY, McFadden KL, Lee MK, Gowen CR. U. S. hospital culture profiles for better performance in patient safety, patient satisfaction, six sigma, and lean implementation. International Journal of Production Economics 2021; 234: 108047, https://doi.org/10.1016/j.ijpe.2021.108047.
16. Lee WC, Wub JW, Hong CW. Assessing the lifetime performance index of products with the exponential distribution under progressively type II right censored samples. Journal of computational and applied mathematics 2009; 231 (2): 648-656, https://doi.org/10.1016/j.cam.2009.04.018.
17. Lo W, Yang CM, Lai KK, Li SY, Chen CH. Developing a novel fuzzy evaluation model by one-sided specification capability indices. Mathematics 2021; 9(10): 1076, https://doi.org/10.3390/math9101076.
18. Martinsen K, Assuad CSA, Kito T, Matsumoto M, Reddy V, Guldbrandsen-Dahl. S. Closed loop tolerance engineering modelling and maturity assessment in a circular economy perspective. Sustainable Production, Life Cycle Engineering and Management 2021: 297-308, https://doi.org/10.1007/978-981-15-6779-7_21.
19. Miller RG. Survival Analysis. New York: John Wiley and Sons, 1981.
20. Mutlu HT, Yildiz MS. Determination of the optimal warranty policy and period from the manufacturer's/seller's perspective. Communications in Statistics: Simulation and Computation 2021, https://doi.org/10.1080/03610918.2021.1941110.
21. Niveditha A, Joghee R. Six sigma quality evaluation of life test data based on weibull distribution. International Journal of Quality and Reliability Management 2021; 38(4): 1005-1022, https://doi.org/10.1108/IJQRM-01-2020-0014.
22. Qayyum S, Ullah F, Al-Turjman F, Mojtahedi M. Managing smart cities through six sigma DMADICV method: A review-based conceptual framework. Sustainable Cities and Society 2021; 72: 103022, https://doi.org/10.1016/j.scs.2021.103022.
23. Ramadan SZ, Ramadan KZ. Bayesian simple step-stress acceleration life testing plan under progressive type-I right censoring for exponential life distribution. Modern Applied Science 2012; 6 (3): 91-99, https://doi.org/10.5539/mas.v6n3p91.
24. Salmasnia A, Baratian M, Ghazanfari M, Fallah-Ghadi H. Optimisation of two-dimensional warranty region under preventive maintenance over product lifetime by considering both manufacture and consumer's point of views. International Journal of Quality Engineering and Technology 2021; 8(3): 306-323, https://doi.org/10.1504/IJQET.2021.116754.
25. Sarpiri MN, Gandomani TJ. A case study of using the hybrid model of scrum and six sigma in software development. International Journal of Electrical and Computer Engineering 2021; 11(6): 5342-5350, https://doi.org/10.11591/ijece.v11i6.pp5342-5350.
26. Shen A, Guo J, Wang Z, Zhang Q. Sensitivity analysis of objective Bayesian evaluation under random right censoring and Weibull distribution. Systems Engineering and Electronics 2017; 39(8): 1891-1897, https://doi.org/10.3969/j.issn.1001-506X.2017.08.32.
27. Sutagundar A, Sangulagi P. Fog computing based information classification in sensor cloud-agent approach. Expert Systems with Applications 2021; 182: 115232, https://doi.org/10.1016/j.eswa.2021.115232.
28. Tong LI, Chen KS, Chen HT. Statistical testing for assessing the performance of lifetime index of electronic components with exponential distribution. International Journal of Quality & Reliability Management 2002; 19(7): 812-824, https://doi.org/10.1108/02656710210434757.
29. Wang CC, Chen KS, Wang CH, Chang PH. Application of 6-sigma design system to developing an improvement model for multi-process

multi-characteristic product quality. Proceedings of the Institution of Mechanical Engineers Part B – Journal of Engineering Manufacture 2011; 225(7): 1205-1216, https://doi.org/10.1177/2041297510393464.
30. Wang FK, Bizuneh B, Cheng XB. New control charts for monitoring the Weibull percentiles under complete data and Type-II censoring. Quality and Reliability Engineering International 2018; 34 (3): 403-416, https://doi.org/10.1002/qre.2261.
31. Wang S, Chiang JY, Tsai TR, Qin Y. Robust process capability indices and statistical inference based on model selection. Computers and Industrial Engineering 2021; 156: 107265, https://doi.org/10.1016/j.cie.2021.107265.
32. Wu CC, Chen LC, Chen YJ. Statistical Inferences for the Lifetime Performance Index of the Products with the Gompertz Distribution under Censored Samples. Communications in Statistics: Simulation and Computation 2016, 45(4): 1318-1336, https://doi.org/10.1080/03610918.2013.827710.
33. Wu JW, Hong CW. The assessment of quality performance of lifetime index of exponential products with fuzzy data under progressively type ii right censored sample. ICIC Express Letters, Part B: Applications 2018; 9(11): 1101-1107, https://doi.org/10.24507/icicelb.09.11.1101.
34. Yu CM, Chen KS, Lai KK, Hsu CH. Fuzzy Supplier Selection Method Based on Smaller-The-Better Quality Characteristic. Applied Science 2020; 10: 3635, https://doi.org/10.3390/app10113635.
35. Yu CM, Lai KK, Chen KS, Chang TC. Process-quality evaluation for wire bonding with multiple gold wires. IEEE Access 2020; 8: 106075-106082, https://doi.org/10.1109/ACCESS.2020.2998463.
36. Zhu T, Yan Z, Peng X A. Weibull failure model to the study of the hierarchical Bayesian reliability. Eksploatacja i Niezawodnosc – Maintenance and Reliability 2016, 18 (4): 501-506, http://dx.doi.org/10.17531/ein.2016.4.4.

Eksploatacja i Niezawodnosc – Maintenance and Reliability
Volume 24 (2022), Issue 1
journal homepage: http://www.ein.org.pl

Article citation info:
Szumska EM, Pawełczyk M, Jurecki R. Total Cost of Ownership analysis and energy efficiency of electric, hybrid and conventional urban buses. Eksploatacja i Niezawodnosc – Maintenance and Reliability 2022; 24 (1): 7–14, http://doi.org/10.17531/ein.2022.1.2.

Indexed by: Web of Science Group

Total Cost of Ownership analysis and energy efficiency of electric, hybrid and conventional urban buses

Emilia M. Szumska[a], Marek Pawełczyk[b], Rafał Jurecki[a]

[a] Kielce University of Technology, Faculty of Mechatronics and Mechanical Engineering, al. Tysiąclecia Państwa Polskiego 7, 25-314 Kielce, Poland
[b] Kielce University of Technology, Faculty of Management and Computer Modeling, al. Tysiąclecia Państwa Polskiego 7, 25-314 Kielce, Poland

Highlights

- We have described a modelling framework for some urban bus routes in Kielce, Poland.
- We have defined assumptions for the conducted TCO analysis.
- We have presented some results of the TCO analysis for different types of urban buses.
- We have determined two factors that have a significant impact on TCO values.
- In our opinion, electric buses represent the highest TCO values among urban buses.

Abstract

From an economic perspective, the purchase cost of an electric bus is greater than that of a conventional one. This results from the additional components of the bus drivetrain and the costly charging infrastructure. However, it should be noted that electric bus ensures greener and more sustainable public transport. The presented study focuses on the economic and energy efficiency analysis of city buses with different types of driving system evaluated for selected urban and suburban routes. The routes differ in terms of the number of journeys per day, elevation, the daily distance travelled, and the daily operating time. The results demonstrate that driving conditions can affect economic efficiency. The Total Cost of Ownership (TCO) method used in the study shows that electric buses represent the highest TCO values among the vehicles taken into account. However, for the TCO calculated for electric and hybrid buses, fuel (energy) costs have a much lower share than for the TCO of conventional buses.

Keywords

public transport, electric bus, Total Cost of Ownership.

1. Introduction

Currently, the largest part of the fleet of Polish companies operating urban public transport have buses equipped with conventional diesel propulsion systems. Positive information is the growing year-by-year share of buses powered by alternative fuels or equipped with alternative drives.

The increase in the number of low-emission vehicles is associated with the increasing level of ecological awareness of the society. Lowering noise levels, environmental protection, and air quality are the main reasons why Polish cities are trying to replace conventional buses with low-emission vehicles. Adopted more than two years ago, the Responsible Development Strategy [20] assumes the dissemination of transport based on electric buses and other vehicles using electric drive trains. The Ministry of Development has assumed that by 2021 1,000 electric urban buses will be in operation on Polish roads. With the help of EU funds and Polish government programs, city carriers can count on cofinancing for the purchase of alternative powered vehicles.

Rising fuel prices are another issue. In the global economy, oil plays a key role in the economic system [13]. Transport is particularly dependent on oil. The fuel market is sensitive to any economic and political changes. Oil prices depend on political, economic, social, technical, climatic, and military factors. Large fluctuations in the fuel market occur during armed conflicts, especially in areas extracting crude oil [21, 29].

It is also worth emphasizing that vehicles with alternative drives show lower energy consumption, which significantly reduces operating costs. These factors make hybrid (HEV) and electric (EV) vehicles more and more competitive compared to conventional vehicles. One of the barriers to increasing the market share of this type of vehicles is still high purchase costs.

The diversity of alternative powertrain technologies increases the challenges in decision making, so it is necessary to study in detail the different configurations of city buses. This is especially important when estimating the profitability of city buses, taking into account operating schedules and route planning. Compared to passenger cars, the energy indicators that characterize the fuel consumption of city buses for the period of their operation are much higher.

The aim of this work was an analyse of the economic efficiency of city buses with different types of drive system for selected urban and suburban lines, using the Total Cost of Ownership (TCO) method. The

E-mail addresses: EM. Szumska (ORCID: 0000-0001-6024-6748): eszumska@tu.kielce.pl, M. Pawełczyk (ORCID: 0000-0002-8668-6343): m.pawelczyk@tu.kielce.pl, R. Jurecki (ORCID: 0000-0003-0105-1283): rjurecki@tu.kielce.pl

value of owning and operating costs for city buses depends largely on the type of propulsion system. Electrically powered vehicles require batteries to be replaced during the lifetime of the bus. Operators who decide to purchase low-emission vehicles should take into account the costs of additional infrastructure, and this applies to electric buses. Often this involves adapting bus depots or bus stops to install battery charging devices. TCO makes it possible to estimate the total costs of a vehicle related to its purchase, use and decommissioning. The aim of this paper was to estimate the amount of the following costs: purchase cost of the vehicle, cost of fuel consumption, cost of repairs, cost of battery replacement, cost of charging infrastructure during the lifetime of the vehicle. In this study, an analysis of the costs associated with the ownership of urban buses with conventional, hybrid and electric drive systems was conducted.

The presented paper is organized as follows. Section 2 describes the general description of the Total Cost of Ownership concept. Section 3 illustrates the modelling framework, presenting the selected routes, vehicles, and simulation program. Section 4 provides the TCO model. Section 5 discusses the results. Section 6 concludes and highlights shortcomings of the study.

2. Total Cost of Ownership (TCO)

Total Cost of Ownership - TCO (Total Cost of Ownership) is the sum of all vehicle costs from its purchase phase, through usage, to its disposal. The TCO analysis allows for the assessment of direct and indirect purchase costs. It gives the opportunity to determine the amount of costs associated with the use and possession of the purchased means of transport. In the literature, the main cost categories that make up a vehicle's TCO are: purchase cost, fuel (energy) cost, repair, and maintenance costs.

In the work [37] it was suggested that the total cost of vehicle use consists of: One-Time Cost (e.g. purchase cost, registration cost) and recurring costs (e.g. fuel, repair, insurance costs). According to the authors of [15], the TCO analysis of a vehicle can be carried out in two categories: consumer-oriented research and society-oriented research. The first group takes into account the costs distinguished by consumers and compares various technologies of vehicle propulsion systems. For society-oriented TCOs, consumer costs include the external costs of using a vehicle, such as air pollution, noise, accidents, congestion, climate change, and environmental impact.

In many analyses and studies, the total cost of using vehicles is extended to include factors relevant to the author. For example, in [37] it was shown that as many as 34 different factors influence the TCO level of a vehicle with an electric drive system. Among them there were identified the main groups of costs associated with the production of the vehicle and batteries, operating costs, costs associated with charging, taxes and fees. These costs were distinguished on the basis of available scientific articles and articles, opinions of specialists and employees of the automotive industry, and on the basis of the results of the consumer survey.

The article [10] presents the TCO analysis carried out for passenger cars with electric and conventional hybrid drives. The authors have shown that consumer preferences have a significant impact on the purchase of an electric vehicle. According to the results of the analysis, buyers (consumers) are mainly guided by the purchase price of the vehicle.

For example, work [1] presents a comprehensive TCO model, in which special attention has been paid to the costs of using a vehicle with a hybrid plug-in drive system. The maintenance cost of the vehicle includes the insurance cost, the annual cost of registration, the fuel cost, the repair cost, the value of the redemption and the cost of the loan. The authors emphasized that the value of TCO is significantly influenced by vehicle type, annual mileage, and changes in fuel prices. The authors of the articles [17, 3] drawn similar conclusions. A TCO analysis was carried out for various types of passenger car (small, medium, large) and three assumed annual mileage values. Furthermore, in the TCO cost analysis of hybrid and electric vehicles presented in [17], the resale value of the battery for its next use (so-called second life, for example, as an energy storage device) was taken into account.

The article [40] presents the TCO values for various types of passenger cars (small, medium and large). The Monte Carlo method was used to estimate the TCO in 2025. Based on the results obtained, it was found that "small" electric cars in 2025 will have a lower TCO level than conventional cars of the same class.

Owners of new vehicles usually use them for an average of 5 to 8 years. Then they resell the vehicle. According to [9], the vehicle's resale price is influenced, among others, by mechanical reliability, durability, user feedback, and social trends. In the works [28, 9], the costs of the total use of vehicles with conventional and alternative drives were compared. The analyses assume that the car has a lifetime of 5 years and the TCO includes the resale value of the vehicle. The authors developed a model on the basis of which it was found that the resale price of a vehicle depends on its mileage. On the basis of the results, hybrid and electric vehicles have higher resale prices than conventional vehicles, in addition to lower fuel costs.

Vehicle use conditions have a significant impact on the total cost of their use. The article [11] provides an analysis of the TCO level for light duty vehicles (LDV) with conventional and alternative drives. The results presented show that the values of the total cost of ownership values of electric and hybrid vehicles are lower in urban driving conditions and higher when the share of driving on highways is high.

The geographical region may also affect the TCO level. Fuel price level, average annual mileage, taxes and insurance prices, as well as climatic conditions, as well as road condition depend on the country or region [33]. The impact of the factors mentioned above on the TCO values of vehicles with various types of propulsion system was confirmed in the paper [2]. Based on the TCO analyzes carried out for 14 cities in the United States, electric vehicles have been shown to have the highest TCO levels. Government subsidies are a key factor in the increase in the number of electric and hybrid vehicles on the vehicle market. In the article [31], an analysis of the cost of using passenger cars was carried out for 11 Chinese cities.

In the paper [25], the TCO level for passenger cars with hybrid, electric, and plug-in hybrid cars was estimated in the years 2000-2015 for the UK, the US, and Japan. Using the regression model, the relationship between the TCO value and the market share of hybrid and electric vehicles was determined. The authors conclude that the increase in the market share of alternative powered vehicles is affected by a reduction in the TCO value through government subsidies (Japan). Similarly, the authors of the work [18] state how the cost of TCO for conventional and electric passenger cars is calculated in eight European countries. The authors analysed the impact of taxes and fees on the TCO level of a vehicle. As in previous publications, the authors emphasize that government subsidies can increase the number of electric vehicles.

In addition to economic factors, in the analysis of the total cost of ownership, many studies also consider the ecological aspects of various types of propulsion systems in vehicles. For example, the analysis of operating costs presented in [12] takes into account the emission costs of 44 vehicles available on the market with 6 different hybrid propulsion configurations. Based on the results, driving conditions have a significant impact on the level of total cost of ownership. Hybrids tested show the lowest costs in urban driving conditions, while the highest on highways. The paper [35] presents the analysis of TCO costs, including emission costs for passenger cars with conventional (gasoline, diesel) and alternative (HEV, HEV, plug-in HEV, EV, LPG) cars.

The paper [14] presents the analysis of operating costs, including the cost of emissions of conventional and alternative heavy-duty vehicles (HEV, EV, CNG). Fuel consumption, energy, and emissions values were estimated for six routes in the British Columbia (Canada) region.

In the literature, one work can be found in which the value of the total cost of use includes social costs. Among the factors that influence social costs, the following are mainly distinguished: emissions costs, costs of climate change, costs of accidents, costs of noise, and costs of congestion. The article [9] presents the analysis of total cost of use, taking into account the social costs of passenger cars with conventional propulsion (Diesel, gasoline) and equipped with engines fueled with natural gas (LPG, CNG). Social costs include the cost of the harmful effects of air pollution and greenhouse gas emissions on the human body. In [30], the TCO values were estimated taking into account the social costs of 66 passenger cars with conventional and alternative drives. As a result of the analyses, the average TCO value was estimated for each of the types of propulsion system available on the market. The total cost of ownership values presented in [5] include the social costs of using the vehicle. The authors also examined the impact of driving behavior on the TCO level. Based on the results of the aforementioned works, electric vehicles are characterized by the lowest social costs. They show the lowest emission values and have the lowest noise level.

In many works, the level of TCO cost was considered as the one taking into account technical aspects, such as the capacity of the fuel tank and the distance that the vehicle runs using only an electric motor, among other [24, 38]. The paper [16] presents the TCO analysis of LDV category vehicles with different types of propulsion system (ICE, BEV, HEV, FCEV and FC-R) taking into account the impact of range of electric vehicles. Electric vehicles and vehicles equipped with fuel cells show significantly higher TCO values. The authors predict that this may change only after 2030, when the cost of lithium ion cell and battery production decreases and the range of this type of vehicle increases.

In the literature, TCO cost analyses can be found mainly for passenger cars. The authors focus on comparing vehicles equipped with conventional and alternative drives. Few publications on the evaluation of economic benefits and the TCO estimate for city buses are available. These works as a rule present a comparison of the TCO cost level for buses with different types of propulsion system, including [23, 36, 8].

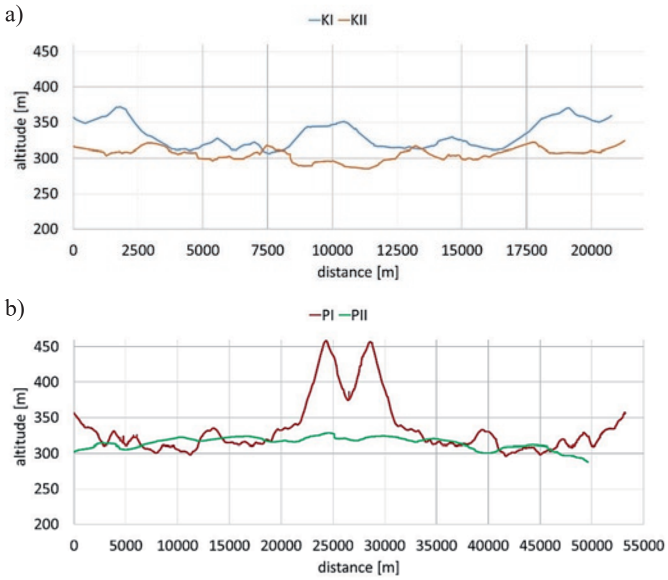

Fig.1. Vertical shape of terrain for a) urban and b) suburban routes

Table 1. Driving cycle parameters

cycle		time [h]	length [km]	average speed [km / h]	average acceleration [m / s^2]
urban	KI	1,35	21,90	15,95	0,55
	KII	1,27	20.81	16,44	0,54
suburban	PI	2,19	49.61	26,62	0,58
	PII	2,08	53.19	23,64	0,4

3. Modelling framework

3.1. Routes

Routes regularly served by public transport vehicles in Kielce, Poland, have been used for analyses. The routes run through the city centre. The route chosen as the first cycle (KI) reflects the bus route 13, which runs more or less latitudinal, from the east to the west of the city, in a relatively flat area. For the second urban cycle (KII), the bus route No. 30 was used, which runs longitudinally from the northern to the southern part of the city in the highland area. The maximum gradient of the route is 4%.

Lines No. 41 (PI) and No. 43 (PII) were used to develop suburban cycles. These lines are characterized by similar length and similar travel time, while they differ in vertical profile. Differences in the height of the terrain along bus route No. 41 reach 160 meters, while for route No. 43 - only 60 m.

The urban KI cycle lasts 4568 s, its length is 20.25 km, and the average speed is 15.95 km / h. The KII cycle is about 700 m shorter and has a higher average speed of 16.44 km / h. The PI suburban cycle is about 4 km shorter than the PII and has a higher average speed. The duration of both cycles is similar. Selected driving cycle parameters are presented in Table 1.

The speed profiles of the selected driving cycles are presented in Fig. 2.

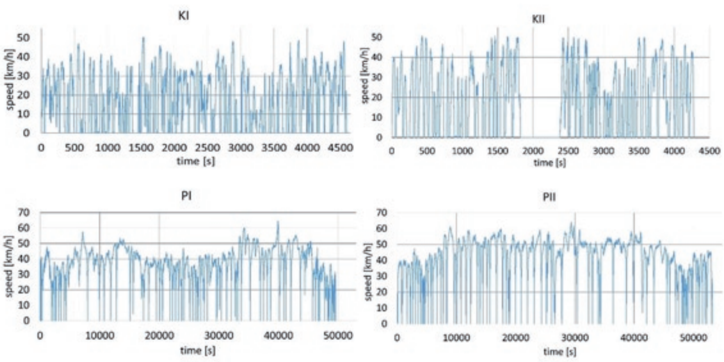

Fig. 2. Speed profiles of driving cycles

3.2. Vehicles

A city bus with a length of 12 meters, a frontal area equal to 7.24 m2, a rolling resistance coefficient equal to 0.001, and an aerodynamic drag coefficient of 0.6 was chosen for the simulation tests. Simulations were carried out for the following propulsion system options: conventional, series hybrid (SHEV), parallel hybrid (PHEV) and electric with a battery of 200 kWh (EV 200 kWh) and 300 kWh (EV 200 kWh) energy capacity. Other vehicle technical specifications are presented in Table 2.

Lithium ion batteries were assumed to be used in vehicles. The initial battery state of charge (SoC) in hybrids was 70% and in electric buses was 100%.

3.3. Ways to charge electric vehicles

Buses with an electric drive system have a limited range, usually 100-150 km. This determines the need for the appropriate selection of

Table 2. Data describing the configuration of bus propulsion systems

	Diesel	EV 200 kWh	EV 200 kWh	SHEV	PHEV
combustion engine power [kW]	205	-	-	140	190
electric motor power [kW]	-	200	170	150	40
battery energy capacity [kWh]	-	300	200	9,4	1,8

the strategy and the battery charging method so that the vehicle can properly implement the assumed timetable. The energy charging of electric buses can be performed in the depot or using fast charging devices at stops or bus termini. Currently, the following methods for charging electric bus batteries are distinguished:

- charging via plug connector,
- charging using a pantograph,
- wireless (inductive) charging.

Two of the above-mentioned methods are widely used in Poland: charging with a plug connector and with a pantograph. The battery charging system using a plug connector (similar to obvious plug-in) is similar to charging systems for electric passenger cars. It is about supplying electricity using a cable with a plug, DC or AC. When charging with alternating current, it is necessary to use a rectifier installed in the vehicle, which results in an increase in the weight of the bus and a reduction in the passenger space. The charging method using a plug-in connector is carried out mainly in depots during a night stopover due to the long charging time.

Charging electric bus batteries using a pantograph is currently the most popular method. Unlike the previous charging method, the use of a pantograph allows the battery to be recharged at bus stops and loops (bus termini). Depending on the configuration of the system, the pantograph can be pulled out of the charging station ('Off-board Top-down Pantograph') or from the vehicle ('Off-board Bottom-up Pantograph'). After stopping at a designated place, the bus is connected to the charging station using a pantograph. Charging is carried out with a direct voltage of up to 750V at a current of up to 1000A. The pantograph charging method allows for quick charging of the bus battery; however, it requires appropriate and expensive infrastructure [6, 32].

Plug-in chargers usually allow buses to charge with a power of 100-150 kW. It takes several hours to fully charge the battery. For pantograph chargers, it is possible to charge at night with a power of 50-150 kW, as well as to recharge the battery at stops and loops with a power of 150-600 kW. High charging power allows batteries to be recharged in a short time [34].

3.4. Vehicle Modelling and Simulation Software - ADVISOR

ADVISOR software (ADvanced Vehicle SImulatOR) software was used for simulations. Their results have been presented in the paper. The software is an overlay on the Matlab / Simulink environment. ADVISOR is a popular tool for simulating vehicles with various drive configurations. It was developed by the American National Renewable Energy Laboratory (NREL). The software contains embedded vehicle models (LDV, HDV) with conventional, serial, and parallel hybrid drives, electric vehicles, and vehicles equipped with hydrogen cells. Using extensive libraries, the user develops the vehicle model using drop-down menus in the dialog box. In the first step, the type of vehicle, the type of drive, and the individual elements of the drive system can be selected. The user can specify the parameters of the power train, its efficiency, and mass. In the next step, the driving cycle can be chosen. With the assumed propulsion configuration and the specified driving cycle, the program enables the evaluation of the drive characteristics and execution of the energy flow analysis for the developed vehicle. The program also allows modification of models by entering files with vehicle data, characteristics and parameters of the propulsion system modules and the storage tank, or design and implementation of the user's own model. It is also possible to modify the built-in or add developed by the user driving cycle by implementing files with data describing speed as a function of time, road gradient as a function of road distance covered, etc. [19, 39].

ADVISOR is a widely used tool for assessing the energy of vehicles equipped with an alternative drive train. Examples of using the ADVISOR program in city bus modeling and simulation tests can be found, eg, in works [22, 4, 26].

4. Cost analysis

4.1. TCO model

The total cost of ownership in relation to the route covered by the vehicle can be described in the following form:

$$C_{TCO} = \sum_{n=1}^{N} \left(C_p + \sum_{i=1}^{I} \left(C_f + C_m \right) + C_b + C_i \right) \tag{1}$$

where: C_{TCO} - the total cost of ownership, C_p - the cost of vehicle purchase, C_f - the cost of fuel consumption, Cm - the cost of maintenance and operation, C_b - the cost of battery replacement, Ci - the cost of infrastructure, i (1,2,..., I) - vehicle age, n (1,2,..., N) - number of vehicles.

The first component of the TCO is the cost of vehicle purchase (C_P). Companies providing public transport services decide on the selection of the transport means supplier based on the tender results. Therefore, city bus manufacturers always adapt the offer to the individual buyer's expectations. The cost of purchasing C_p can be calculated as follows:

$$C_P = \sum_{n=1}^{N} P_a \tag{2}$$

where: P_a - purchase price of the bus.

The TCO cost includes the fuel costs (C_f) for conventional or hybrid buses and, in the case of an electric vehicle, the electric energy purchase costs. The fuel cost (C_f) can be calculated using the formula:

$$C_f = \sum_{n=1}^{N} \left(\frac{f_c}{100} \cdot P_f \cdot D \right) \tag{3}$$

where: f_c - average fuel consumption (energy) [dm^3 / 100km, kWh / 100km], P_f - price per unit of measure [euro / dm^3, PLN / kWh], D - annual mileage [km].

Another component of the total cost of ownership (TCO) is the cost of vehicle maintenance and operation (Cm), which includes insurance costs, periodic inspection costs, costs of replacement of tires and working fluids, as well as the costs of repairs required and costs of removing defects.

Current operational experience shows that the energy storage device has a much shorter service life than the bus life. It was assumed that the battery pack should be replaced every 6 years; therefore, the battery will need to be replaced twice during the life of the bus. The cost of the battery replacement C_b is as follows:

$$C_b = \sum_{n=1}^{N}\sum_{j=1}^{J}(P_b \cdot B) \quad (4)$$

where:
P_b – is the battery replacement price [euro / kWh], B - battery capacity [kWh], j (1,2,..., J) - the number of battery replacements during vehicle life.

Buses equipped with an electric drive system require special infrastructure to be launched. It is a set of battery charging stations. The cost of the infrastructure - C_i can be calculated as follows:

$$C_i = L \cdot P_C \quad (5)$$

where: L - number of charging stations on a given bus line, P_C – total cost of installation of the charging station [euro].

4.2. Data used for cost analysis

The analysis has assumed that the useful life of the bus is 15 years, the price of diesel oil is 1.17 euros / dm^3, and the price of electricity is 0.15 euros / kWh (Polish Chamber of Liquid Fuels, 2020). The prices of fuels, electric energy and the cost of replacing batteries in EV and HEV vehicles mentioned above were treated as fixed. In Table 3 data from vehicles taken for analysis are presented. Repair and operating costs are based on [41]. The battery replacement cost was taken from [7].

In the paper, two main methods of charging electric bus batteries were considered: fast charging using a pantograph located on the loops and slow charging using a plug-in, used mainly in depots. Table 4 presents the prices of the chargers taken from [41].

Table 3. Vehicle data for TCO analysis

	Diesel	EV	SHEV (9,4 kWh)	PHEV (1,8 kWh)
purchase cost [euro]	214 300	595 300	357 100	357 100
maintenance and operation costs [euro/year]	3 500	3 000	3 600	3 600
cost of battery replacement [euro]	-	215 000	6 700	13 000

The driving cycles presented in the previous section reflect the currently implemented public transport routes in Kielce (Poland). Table 5 shows the daily parameters of selected urban and suburban bus routes. Data were taken from the Urban Mobility Plan for City Kielce [27].

Table. 4. Prices of pantograph chargers used for calculations

	charging power [kW]	cost [PLN]
Plug-in charger	150	12 000
Pantograph charger	150	72 000
	300	85 000
	450	95 000
	600	120 000

5. Results

5.1. Energy consumption

Fig. 3 shows the energy consumption values obtained for the analyzed vehicles after completing the routes once.

Table. 5. Daily operation parameters on selected bus route

cycle	daily work time [h]	weekly distance [km]	number of trips per week	number of buses on the route per day
KI	21.15	951.75	87	3
KII	15.56	956.97	82	4
PI	10.95	256.9	6	1
PII	18.72	500.13	9	1

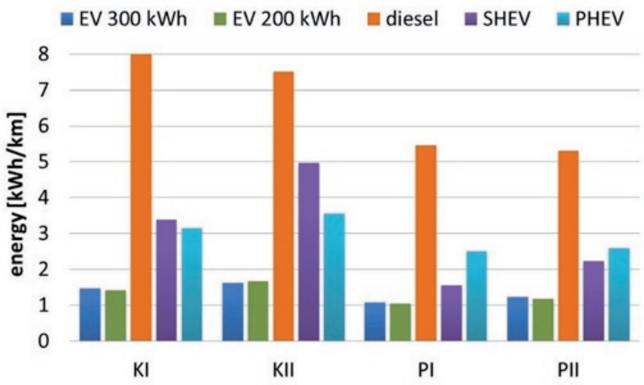

Fig. 3. Energy consumption

The highest energy consumption values obtained for the vehicles analyzed were observed for urban cycles. This is especially evident for buses with conventional and hybrid propulsion systems. For the KI urban cycle, the vehicle with a classic powertrain recorded about 35% lower energy consumption in suburban cycles. Compared to the KI cycle, electric buses showed a 27% lower energy consumption in the PI suburban cycle and a 16% lower energy consumption in the PII cycle. The bus with parallel hybrid drive compared to the KI cycle noted a lower energy consumption by about 20% in suburban cycles. In relation to the KI cycle, a vehicle with a serial hybrid drive recorded a lower energy consumption of 54% in the PI cycle and 34% in the PII cycle, respectively.

For cycles with a varied route profile (KII and PII), the electric and hybrid buses that were analyzed, the higher level of energy consumption was obtained. Vehicles with electric and hybrid powertrains can recover some of the kinetic energy during braking. Fig.4 presents the energy regenerated in the cycle per 1 km of the route.

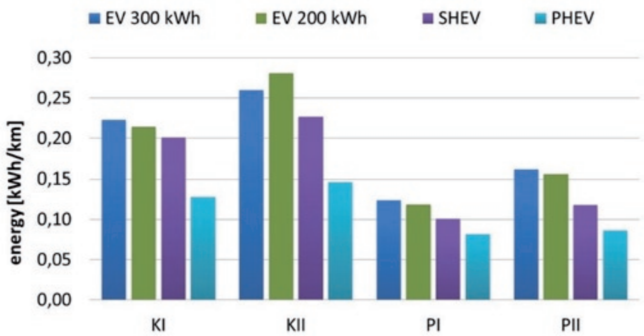

Fig. 4. Regenerated energy level

The highest values of recovered energy were obtained for urban cycles. It can be explained by short driving distances and, thus, the need for frequent accelerations and braking. Higher levels of recovered energy were achieved on routes with a varied route profile.

Fig. 5 shows the percentage share of energy taken from the electric bus battery after one cycle. The initial battery state of charge (SoC) has been assumed to be 100%.

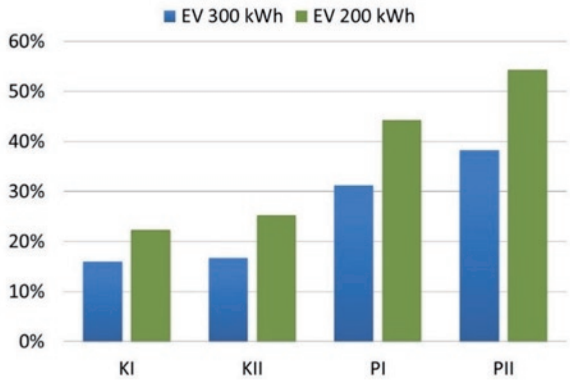

Fig. 5. Percentage share of energy taken from the battery

An electric bus equipped with a 300 kWh onboard battery consumes 16% of the energy available during a city cycle. For suburban cycles, the level of energy spent from the battery is 31% for the PI cycle and 38% of the energy stored in the battery pack for the PII cycle.

For the electric bus with the 200 kWh battery, for a single KI cycle about 22% of the stored energy must be used and for the KII cycle - 25%, respectively. This bus consumes about half of the energy available in the battery to perform one suburban cycle.

For the routes analyzed, electric buses are not able to meet the assumed daily working time (Table 5) without recharging the battery. The possible solution may be installation of the pantograph chargers with high charging power: 150, 300, 450, or 600 kW at the termini. In the presented study, the percentage of energy that can be stored when charging during 5 min 10 min, and 15 min stops between courses has been estimated (Fig. 6).

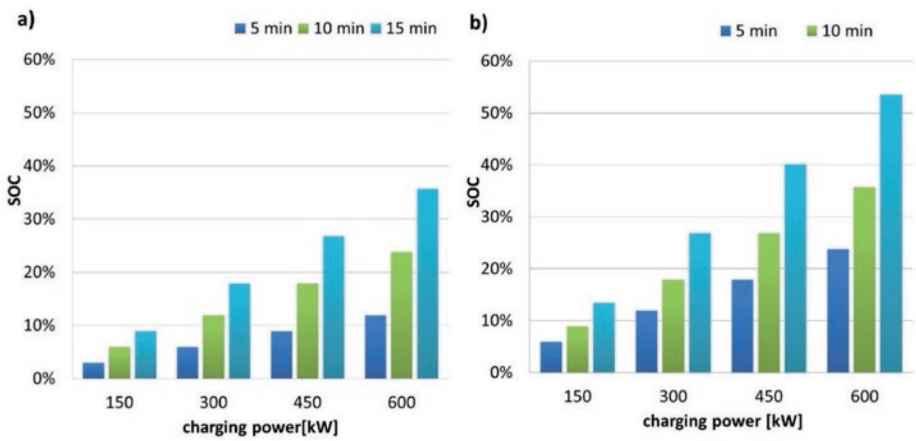

Fig. 6. Percentage of energy stored in the battery during charging of the battery with an energy capacity of a) 300 kWh, b) 200 kWh

The selection of the appropriate charging power depends on the range of the vehicle, the daily schedule, and the length of the routes. It can be seen in the figure above that using the 150 kW charger during 15 minutes of bus inactivity can charge 9% of the 300 kWh battery and 13% of the 200 kWh battery. This is not sufficient for the considered driving cycles.

For the KI and KII urban cycle routes, usage of the 450 kW charger is to be used, which should allow 300 kWh battery charge by 18% and a 200 kWh battery charge by 27% within 10 minutes. For the PI suburban route, the daily number of routes is small and the average sum of break time is 30 minutes. On this route, it is possible to use a 300 kW charger. For the PII route, three courses are scheduled in the morning and three at the traffic peak in the afternoon. This requires the installation of a 600 kW charger.

5.2. TCO analysis

The total cost of ownership (TCO) values for vehicles taken into account for urban and suburban cycles are presented in Fig. 7.

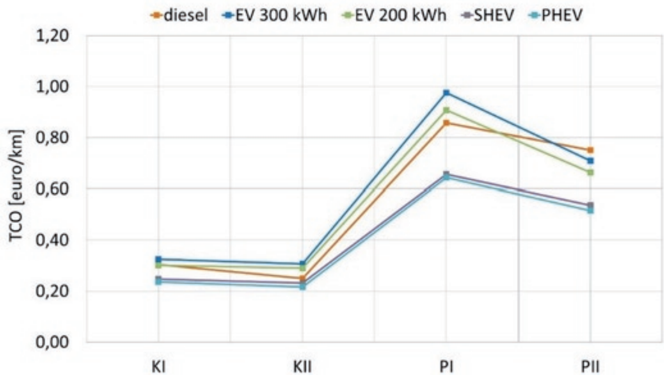

Fig. 7. Summary of Total Cost of Ownership (TCO) on selected bus routes

The total cost of ownership significantly depends on the route (R). For urban routes, the TCO values obtained for hybrid and conventional vehicles are similar. In urban cycles, the TCO values calculated for electric buses are nearly 50% higher compared to buses with standard power trains.

The vertical profile of the route is also an important issue. For the urban KII and suburban PI cycles, the route profile was varied, which significantly influenced the fuel (energy) consumption, and thus the TCO values of the analyzed vehicles increased. For hybrid buses, lower fuel consumption values were obtained compared to conventional vehicles. Therefore, hybrids work well on routes with varying terrain. For the urban cycle KI, the TCO values obtained for hybrids were similar to the TCO level of conventional vehicles, and in the PII cycle, the TCO was lower for hybrids by approximately 25%.

Furthermore, the number of courses performed during the week has a significant impact on the value of TCO. The purchase costs and infrastructure installation costs are incurred on a one-off basis and therefore they are not dependent on mileage. The more courses, the lower the influence of the fixed costs listed above is. This is especially visible in the case of the PI route, which is operated by only one vehicle and runs only six courses a week.

Purchase costs represent the highest share in the TCO of buses with electric and hybrid drives (Fig.8). Depending on the route, its share is 50-74% TCO. However, for electric and hybrid buses, fuel (energy) costs have a much lower share. For electric buses, this share is 4-18% TCO, and for hybrids, 15-40% TCO, respectively. Fuel costs have the largest share of the TCO of conventional vehicles.

6. Conclusions

The purpose of this study was to analyze the total ownership cost of city buses with different types of propulsion system and for selected urban and suburban cycles. On the basis of the results, it can be seen that the route and the daily courses have a significant impact on the TCO values. These two factors significantly affect the total cost of

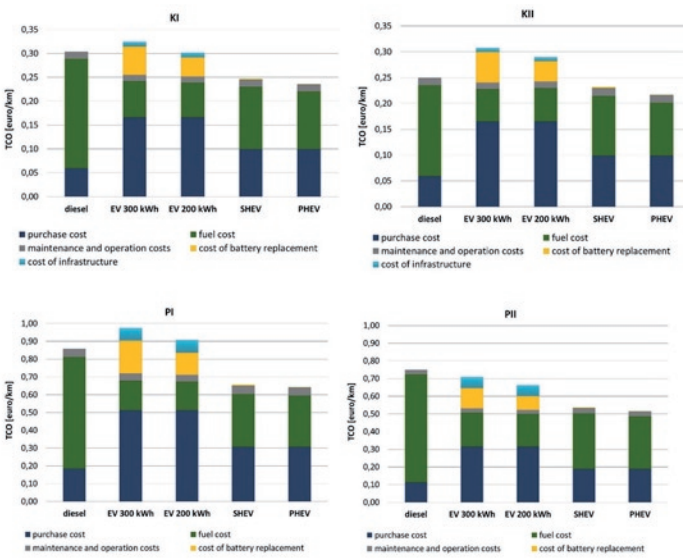

Fig. 8. TCO structure for the analyzed bus routes

ownership of the vehicle regardless of the type of propulsion system.

In addition, it was shown that the costs of owning and operating a city bus depend on the type of drive train. The TCO method allowed the assessment of the values of the individual cost components comprising vehicle purchase and operating costs. The test results show that electric buses represent the highest TCO values among the vehicles taken into account. Compared to standard buses, the TCO values obtained for electric buses in urban cycles are about twice as high. Currently, only hybrid buses can compete with conventional buses. They are characterized by a lower level of fuel consumption and similar values of the total cost of ownership.

Many authors of the works mentioned in the first part of the paper expect that vehicles equipped with electric propulsion systems will become competitive for vehicles with standard buses in a few years. This will be the result of the lower prices of lithium-ion batteries and the rising fuel prices. Currently, the only chance to increase the share of electric buses in the fleets of Polish municipal public transport companies is the total or partial financing of their purchase using government or local government subsidies.

References

1. Al-Alawi, BM, Bradley TH. Total cost of ownership, payback, and consumer preference modeling of plug-in hybrid electric vehicles. Applied Energy 2013; 103: 488-506, https://doi.org/10.1016/j.apenergy.2012.10.009.
2. Breetz HL, Salon D. Do electric vehicles need subsidies? Ownership costs for conventional, hybrid, and electric vehicles in 14 U.S. cities. Energy Policy 2018; 120: 238-249, https://doi.org/10.1016/j.enpol.2018.05.038.
3. Bubeck S, Tomaschek J, Fahl U. Perspectives of electric mobility: Total cost of ownership of electric vehicles in Germany. Transport Policy 2016; 50: 63-77, https://doi.org/10.1016/j.tranpol.2016.05.012.
4. Chen, D, Li X, Chen L, Yang L, Tian F, Xu D. Research on simulation of the hybrid electric vehicle based on software ADVISOR. Sensors & Transducers 2014; 171: 68-77, http://www.sensorsportal.com/HTML/DIGEST/P_2085.htm.
5. De Clerck Q, Van Lier T, Messagie M, Macharis C, Van Mierlo J, Vanhaverbeke L. Total Cost for Society: A persona-based analysis of electric and conventional vehicles. Transportation Research Part D: Transport and Environment 2018; 64: 90-110, https://doi.org/10.1016/j.trd.2018.02.017.
6. Dobrzycki A, Filipiak M, Jajczyk J. Zasilanie układów ładowania akumulatorów autobusów elektrycznych. Poznań University of Technology Academic Journals. Electrical Engineering 2017; 92: 25-35, https://doi.org/10.21008/j.1897-0737.2017.92.0002.
7. Dybalski J. MPK Tarnów has tested the electric bus and lists the vehicle's disadvantages (in Polish). Transport Publiczny 2018, available at: https://www.transport-publiczny.pl/wiadomosci/mpk-tarnow-przetestowalo-elektrobus-i-wylicza-wady-takiego-pojazdu-59229.html.
8. Gerbec M, Samuel RO, Kontić D. Cost benefit analysis of three different urban bus drive systems using real driving data. Transportation Research Part D: Transport and Environment 2015; 41: 433-444, https://doi.org/10.1016/j.trd.2015.10.015.
9. Gilmore EA, Lave LB. Comparing resale prices and total cost of ownership for gasoline, hybrid and diesel passenger cars and trucks. Transport Policy 2013; 27: 200-208, https://doi.org/10.1016/j.tranpol.2012.12.007.
10. Hagman J, Ritzén S, Stier JJ, Susilo Y. Total cost of ownership and its potential implications for battery electric vehicle diffusion. Research in Transportation Business & Management 2016; 18: 11-17, https://doi.org/10.1016/j.rtbm.2016.01.003.
11. Harvey DLD. Cost and energy performance of advanced light duty vehicles: Implications for standards and subsidies. Energy Policy 2018; 114: 1-12, https://doi.org/10.1016/j.enpol.2017.11.063.
12. Hutchinson T, Burgess S, Herrmann G. Current hybrid-electric powertrain architectures: Applying empirical design data to life cycle assessment and whole-life cost analysis. Applied Energy 2014; 119: 314-329, https://doi.org/10.1016/j.apenergy.2014.01.009.
13. International Energy Agency - World Energy Balances and Statistics. 2019; https://www.iea.org/.
14. Lajevardi SM, Axsen J, Crawford C. Comparing alternative heavy-duty drivetrains based on GHG emissions, ownership and abatement costs: Simulations of freight routes in British Columbia. Transportation Research Part D: Transport and Environment 2019; 76: 19-55, https://doi.org/10.1016/j.trd.2019.08.031.
15. Lebeau K, Lebeau P, Macharis C, Van Mierlo J. How expensive are electric vehicles? A total cost of ownership analysis. World Electric Vehicle Journal 2013; 6(4): 996-1007, http://doi.org/10.3390/wevj6040996.
16. Le Duigou A, Smatti A. On the comparison and the complementarity of batteries and fuel cells for electric driving. International Journal of Hydrogen Energy 2014; 39(31): 17873-17883, http://doi.org/10.1016/j.ijhydene.2014.08.077.
17. Letmathe P, Suares M. A consumer-oriented total cost of ownership model for different vehicle types in Germany. Transportation Research Part D: Transport and Environment 2017; 57: 314-335, https://doi.org/10.1016/j.trd.2017.09.007.
18. Lévay ZP, Drossinos Y, Thiel C. The effect of fiscal incentives on market penetration of electric vehicles: A pairwise comparison of total cost of ownership. Energy Policy 2017; 105: 524-533, https://doi.org/10.1016/j.enpol.2017.02.054.
19. Markel T, Brooker A, Hendricks T, Johnson V, Kelly K, Kramer B, O'Keefe M, Sprik S, Wipke K. ADVISOR: a systems analysis tool for advanced vehicle modeling. Journal of Power Sources 2002; 110: 255–266, https://doi.org/10.1016/S0378-7753(02)00189-1.
20. Ministry of Development Funds and Regional Policy - The SRD Strategy for Responsible Development for the period up to 2020 (including

the perspective up to 2030), 2017. https://www.gov.pl/documents/33377/436740/SOR_2017_streszczenie_en.pdf.
21. Mollick VA, Sakaki H. Exchange rates, oil prices and world stock returns. Resources Policy 2019; 61: 585-602, https://doi.org/10.2139/ssrn.3127547.
22. Nicolaides D, Cebon D, Miles J. An Urban Charging Infrastructure for Electric Road Freight Operations: A Case Study for Cambridge UK. IEEE Systems Journal 2019; 13(2): 2057-2068, http://doi.org/10.1109/JSYST.2018.2864693.
23. Nurhadi L, Borén S, Ny H. A Sensitivity Analysis of Total Cost of Ownership for Electric Public Bus Transport Systems in Swedish Medium Sized Cities. Transportation Research Procedia 2014; 3: 818-827, https://doi.org/10.1016/j.trpro.2014.10.058.
24. Offer GJ, Contestabile M, Howey DA, Clague R, Brandon NP. Technoeconomic and behavioural analysis of battery electric, hydrogen fuel cell and hybrid vehicles in a future sustainable road transport system in the UK. Energy Policy 2011; 39: 1939–1950, https://doi.org/10.1016/j.enpol.2011.01.006.
25. Palmer K, Tate JE, Wadud Z, Nellthorp J. Total cost of ownership and market share for hybrid and electric vehicles in the UK, US and Japan. Applied Energy 2018; 209: 108-119, https://doi.org/10.1016/j.apenergy.2017.10.089.
26. Pawełczyk M, Szumska E. Evaluation of the efficiency of hybrid drive applications in urban transport system on the example of a medium size city. 13th International Conference Modern Electrified Transport – MET'2017, MATEC Web of Conferences 2018, 180: 03004, http://doi.org/10.1051/matecconf/201818003004.
27. Plan on Urban Mobility for City Kielce; ZTM - Kielce Municipal Transport Authority. Polish Chamber of Liquid Fuels: Fuel prices report, available at http://www.paliwa.pl/strona-startowa/aktualnosci.
28. Propfe B, Redelbach M, Santini DJ, Friedrich H. Cost analysis of Plug-in Hybrid Electric Vehicles including Maintenance & Repair Costs and Resale Values. World Electric Vehicle Journal 2012; 5(4): 886-895, https://doi.org/10.3390/wevj5040886.
29. Qadan M, Idilbi-Bayaa Y. Risk appetite and oil prices. Energy Economics 2020; 85: 104595, https://doi.org/10.1016/j.eneco.2019.104595.
30. Rusich A, Danielis R. Total cost of ownership, social lifecycle cost and energy consumption of various automotive technologies in Italy. Research in Transportation Economics 2015; 50: 3-16, http://doi.org/10.1016/j.retrec.2015.06.002.
31. Saxena S, Phadke A, Gopal A. Understanding the fuel savings potential from deploying hybrid cars in China. Applied Energy 2014; 113: 1127-1133. https://doi.org/10.1016/j.apenergy.2013.08.057.
32. Sidorski F. - Work characteristics of charging stations for electric buses. Przegląd Elektrotechniczny 2018; 94: (10), 95-98.
33. Skrúcaný T, Kendra M, Stopka, O, Milojević, S, Figlus, T, Csiszár C. Impact of the Electric Mobility Implementation on the Greenhouse Gases Production in Central European Countries. Sustainability 2019; 11(18): 4948, https://doi.org/10.3390/su11184948.
34. Suarez C, Martinez W. - Fast and Ultra-Fast Charging for Battery Electric Vehicles – A Review. 2019 IEEE Energy Conversion Congress and Exposition (ECCE), Baltimore, MD, USA, 2019; 569-575, https://doi.org/10.1109/ECCE.2019.8912594.
35. Szumska E, Jurecki R, Pawełczyk M. Assessment of Total Costs of Ownership for Midsize Passenger Cars with Conventional and Alternative Drive Trains. Communications - Scientific Letters of the University of Zilina 2019; 21(3): 21-27, https://doi.org/10.26552/com.C.2019.3.21-27.
36. Szumska E, Pawełczyk M. TCO comparison for city buses equipped with hybrid and conventional propulsion drive. Prace Naukowe Politechniki Warszawskiej. Transport 2017; 118: 277-285.
37. Van Velzen A, Annema JA, Van de Kaa G, Van Wee B. Proposing a more comprehensive future total cost of ownership estimation framework for electric vehicles. Energy Policy 2019; 129: 1034-1046, https://doi.org/10.1016/j.enpol.2019.02.071.
38. Van Vliet O, Kruithof T, Turkenburg WC, Faaij APC. Techno-economic comparison of series hybrid, plug-in hybrid, fuel cell and regular cars. Journal of Power Sources 2010; 195: 6570–6585, https://doi.org/10.1016/j.jpowsour.2010.04.077.
39. Wipke KB, Cuddy MR, Burch SD. Advisor 2.1: a user-friendly advanced powertrain simulation using a combined backward/forward approach', IEEE Transaction on Vehicular Technology 1999; 48 (6): 751–1761.
40. Wu G, Inderbitzin A, Bening C. Total cost of ownership of electric vehicles compared to conventional vehicles: A probabilistic analysis and projection across market segments. Energy Policy 2015; 80: 196-214, https://doi.org/10.1016/j.enpol.2015.02.004.
41. Wyszomirski O, Wołek M, Jagiełło A, Koniak M, Bartłomiejczyk M, Grzelec K, Gromadzki M. - Electromobility in public transport (in Polish). Polish Development Fund (PFR) 2018.

Eksploatacja i Niezawodnosc – Maintenance and Reliability
Volume 24 (2022), Issue 1
journal homepage: http://www.ein.org.pl

Article citation info:
Zhang C, Zhang Y, Dui H, Wang S, Tomovic MM. Importance measure-based maintenance strategy considering maintenance costs. Eksploatacja i Niezawodnosc – Maintenance and Reliability 2022; 24 (1): 15–24, http://doi.org/10.17531/ein.2022.1.3.

Importance measure-based maintenance strategy considering maintenance costs

Indexed by: Web of Science Group

Chao Zhang[a,b,c], Yadong Zhang[a,c], Hongyan Dui[d], Shaoping Wang[a,c,*], Mileta M. Tomovic[e]

[a] Beihang University, School of Automation Science and Electrical Engineering, Beijing 100191, China
[b] Beihang University, Research Institute for Frontier Science, Beijing 100191, China
[c] Beihang University, Ningbo Institute of Technology, Ningbo 315800, China
[d] Zhengzhou University School of Management Engineering, , Zhengzhou 450001, China
[e] Old Dominion University, Engineering Technology Department, Norfolk, VA 23529, USA

Highlights

- A new maintenance priority is proposed to guide the preventive maintenance of components.
- A joint importance is applied into the opportunistic maintenance of components.
- Characteristics of the maintenance model in series-parallel systems are analyzed.
- Maintenance strategies of components in 2H2E architecture are discussed.
- The effectiveness of two proposed models are verified with the 2H2E architecture.

Abstract

Maintenance is an important way to ensure the best performance of repairable systems. This paper considers how to reduce system maintenance cost while ensuring consistent system performance. Due to budget constraints, preventive maintenance (PM) can be done on only some of the system components. Also, different selections of components to be maintained can have markedly different effects on system performance. On the basis of the above issues, this paper proposes an importance-based maintenance priority (IBMP) model to guide the selection of PM components. Then the model is extended to find the degree of correlation between two components to be maintained and a joint importance-based maintenance priority (JIBMP) model to guide the selection of opportunistic maintenance (OM) components is proposed. Also, optimization strategies under various conditions are proposed. Finally, a case of 2H2E architecture is used to demonstrate the proposed method. The results show that generators in the 2E layout have the highest maintenance priority, which further explains the difference in the importance of each component in PM.

Keywords

system reliability, importance measure, maintenance cost, preventive maintenance, opportunistic maintenance.

1. Introduction

Maintenance occupies a very important proportion in the whole life cycle of various systems. A good maintenance strategy can improve the reliability of the system and reduce the cost of system maintenance. To achieve the maintenance objective, it is necessary to identify some important components of the system. However, in actual systems, the system structure could be complex, and how to determine the maintenance priority of components and reduce the system maintenance cost while improving the reliability of the system become very important.

Importance measure is an important method to evaluate the influence of components on the performance of the whole system in the field of reliability, and it is widely used in repairable systems [17, 26, 27, 28]. In 1969, Birnbaum [2] firstly proposed an importance measure theory and established its theoretical framework. The Birnbaum importance measure evaluates the relationship between component reliability and system reliability. Griffith et al. [9] explained the effects of component performance improvements on system performance based on the Birnbaum importance measure. Wu and Chan [21] defined a new utility importance that overcomes some drawbacks of Griffith importance measure. In addition, Wu et al. [23] proposed a component maintenance priority importance measure to identify the order of preventive maintenance components. Based on the importance of multi-state components, Si et al. [18] proposed an integrated importance measure to identify the components which have the greatest impact on system performance. Dui et al. [7] extended the integrated importance measure and proposed a joint integrated importance measure to maximize the gain of the system performance. In order to allocate limited maintenance resources to important components in repairable systems and improve the overall reliability of the system, some scholars consider combining importance measure with preventive maintenance and opportunistic maintenance to guide the maintenance of components. Zhang et al. [29] introduced the importance measure theory into the opportunistic maintenance strategy to provide guidance for the maintenance of the heave compensation system and retard the degradation of the expected performance of the

(*) Corresponding author.
E-mail addresses: C. Zhang (ORCID: 0000-0001-9054-5132): czhangstar@gmail.com, Y. Zhang (ORCID: 0000-0003-0133-9009): zyd2019@buaa.edu.cn, H. Dui: duihongyan@zzu.edu.cn, S. Wang (ORCID: 0000-0002-8102-3436): shaopingwang@vip.sina.com, MM. Tomovic: mtomovic@odu.edu

system. Babishin et al. [3] proposed an aperiodic strategy of joint optimization of maintenance and inspection, which provides a promising approach for system maintenance. In addition, some scholars have proposed reliability models to identify weak links of the system under specific circumstances, so as to guide component maintenance and improve system reliability. Xing et al. [24] proposed a combinatorial reliability model of correlation system probabilistic competitions and random failure propagation time to optimize the function dependence of components. Gao et al. [10] proposed a reliability model related to the failure process and the degradation impact to consider the dependency relationship between the soft and hard failure process. Sun et al. [19] proposed a dynamic linear model for fault prediction and predictive maintenance of aircraft air conditioning systems. Legát et al. [11] proposed a method to determine the optimal interval of preventive periodic maintenance and studied the relationship between preventive maintenance interval and reliability function.

In the process of maintenance, system maintenance cost restricts the number of maintenance components and the determination of maintenance degree. Considering the importance of cost-effectiveness in maintenance, Wu and Coolen [22] extended Birnbaum importance measure from the perspective of cost and proposed a cost-based importance measure. Dui et al. [8] proposed a cost-based integrated importance measure to identify components or component groups that can be used for preventive maintenance. Minwoo et al. [14] conducted a systematic analysis and assessment of the direct operating costs of wide-body airliners and identified the most cost-effective aircraft types that could be helpful to airline operators and policy makers. Tan et al. [20] proposed a maintenance strategy to effectively reduce the maintenance cost of the hemodialysis machine and ensure the high availability of the equipment. Andrzejczak et al. [1] conducted a simple fault random model for the cost of vehicle corrective maintenance, and applied the model to identify the damaged components of the vehicle. In recent years, Bayesian networks have been widely used in the reliability research of multi-level complex systems. In terms of component fault diagnosis, Cai et al. [4-6] used Bayesian network to analyze the reliability of components, which can play a guiding role in the follow-up preventive maintenance of components. In addition, it is inevitable to encounter some irresistible factors to restrict the system maintenance and reliability improvement. Considering the impact of random shocks, Zhao et al. [30] analyzed the reliability in a random shock environment and provided the optimal task termination strategy for the system. Qiu et al. [16] proposed a mission abort strategy for internal system failures and external shocks to improve the survivability of critical systems. Peng et al. [15] proposed a hybrid incomplete maintenance model with random adjustment, and studied a sequential preventive maintenance strategy with periodicity leisure interval. Moreover, Levitin et al. [12, 13] conducted a series of studies on the mission abort policy of systems.

Although the above researches made outstanding contributions, traditional importance measure-based methods seldom consider the change rate of system maintenance cost caused by the state transition of system components. In this paper, we propose an importance-based maintenance priority (IBMP) model and a joint importance-based maintenance priority (JIBMP) model to perform cost-based maintenance decision analyses. We use the model to sort the important components and determine the maintenance cost level of system in different states, which could reduce the expected maintenance cost of the system while improving the performance of the system. Thus, the models can provide theoretical guidance for the maintenance of components in the system.

The rest of this article is organized as follows. In Section 2, IBMP and JIBMP models are proposed to guide the selection of components in preventive maintenance and opportunistic maintenance, and then the features of JIBMP in series-parallel systems are discussed. In Section 3, the IBMP model and the JIBMP model are applied to the aircraft 2H2E architecture to help identify the important components of the system, and the combination of system components in each state is listed. In Section 4, the application of the model in 2H2E architecture is simulated, and the results show that the model is effective. Then we analyze the maintenance optimization strategy of the 2H2E architecture under the condition of a limited budget and determine the number of components that can be maintained under various budget constraints. Finally, the conclusions are drawn in Section 5.

2. Proposed maintenance model

In this section, we first introduce the expected maintenance cost of the system. Then the definitions of IBMP and JIBMP are proposed in Sections 2.1 and 2.2. The features of JIBMP in a series-parallel system are discussed in Section 2.3. The number of PM components is discussed in Section 2.4.

Assuming that a multistate system has n components and M states, where State 0 is the system's complete failure state and State M is the system's perfect state. States from state 1 to state M-1 are the intermediate state of the system, in which some components of the system fail and the system performance deteriorates but the system can continue to operate. Then, the expected maintenance cost of the system at time t is defined as:

$$C(X(t)) = \sum_{j=0}^{M-1} c_j \Pr[\Phi(X(t)) = j] = \sum_{j=0}^{M-1} c_j \Pr[\Phi(X_1(t), X_2(t), \ldots, X_n(t)) = j], \tag{1}$$

where c_j is the failure maintenance cost when the system is in state j. Let $\{0 \le c_{M-1} \le c_{M-2} \le \cdots \le c_0\}$ be the corresponding failure maintenance cost levels. The function $\Phi(X(t))$ is the structural function of the system related to the state of each component. $\Pr[\Phi(X(t)) = j]$ is a system probability function and could also be written as $f_j(R_1(t), R_2(t), \ldots, R_n(t))$.

2.1. Definition of importance-based maintenance priority

IBMP determines how to make maintenance choices for components when a system's performance degrades; different choices of components can lead to marked differences in system expected maintenance cost. When component i changes from state m to state 0, the IBMP value of component i is defined as:

$$I_i^{IBMP}(t) = P_{i,m} \cdot \lambda_{m,0}^i \cdot \sum_{j=0}^{M-1} c_j \{\Pr[\Phi(0_i, X(t)) = j] - \Pr[\Phi(m_i, X(t)) = j]\}, \tag{2}$$

where $P_{i,m}$ is the probability that component i is in state m, $\lambda_{m,0}^i$ is the transition rate of component i from state m to state 0. State 0 is the failure state of the component. $\Pr[\Phi(0_i, X(t)) = j]$ is the probability that component i is in a failure state and the rest of components are in state j at time t. $\Pr[\Phi(m_i, X(t)) = j]$ is the probability that component i is in state m and the rest of components are in state j at time t. For each component we consider two states, the perfect state and the failure state. So the probability that the component is in state m is the probability that the component is in perfect state, and we can express that in terms of the reliability of the component. The transition rate of the component from state m to state 0 is the transition rate of the component from perfect state to failure state, which can be expressed by the failure rate of the component. Therefore, the IBMP value of component i can also be expressed as:

$$I_i^{IBMP}(t) = R_i(t) \cdot \lambda_i(t) \cdot \sum_{j=0}^{M-1} c_j \{\Pr[\Phi(0_i, X(t)) = j] - \Pr[\Phi(1_i, X(t)) = j]\}, \tag{3}$$

$I_i^{IBMP}(t)$ is the contribution of component i from perfect state to failure state to the change rate of system expected maintenance cost.

When the component $I_i^{IBMP}(t)$ value is large, it means that component i contributes the most to the rate of change in system expected maintenance cost. We know that the component failure maintenance cost is much higher than the component preventive maintenance cost. So in order to prevent component failure from increasing the change rate of system expected maintenance cost, we should give priority to the maintenance of those components with large IBMP values.

Next, we give the relation between the change rate of the expected maintenance cost of the system and the IBMP value of each component:

$$\frac{dC(X(t))}{dt}=\frac{d[\sum_{j=0}^{M-1}c_j f_j(R_1(t),R_2(t),\ldots,R_n(t))]}{dt}=\sum_{j=0}^{M-1}c_j\sum_{i=1}^{n}\frac{dR_i(t)}{dt}\frac{\partial f_j(R_1(t),R_2(t),\ldots,R_n(t))}{\partial R_i(t)}$$
$$=\sum_{j=0}^{M-1}c_j\sum_{i=1}^{n}\frac{dR_i(t)}{dt}\frac{\partial \Pr[\Phi(X(t))=j]}{\partial R_i(t)}=\sum_{i=1}^{n}\sum_{j=0}^{M-1}c_j\frac{dR_i(t)}{dt}\frac{\partial \Pr[\Phi(X(t))=j]}{\partial R_i(t)}$$

$$\begin{aligned}\Pr[\Phi(X(t))=j]&=\Pr[X_i(t)=0]\cdot\Pr[0_i,X(t)=j]+\Pr[X_i(t)=1]\cdot\Pr[1_i,X(t)=j]\\&=(1-R_i(t))\cdot\Pr[0_i,X(t)=j]+R_i(t)\cdot\Pr[1_i,X(t)=j]\end{aligned},$$

and $\lambda_i(t)=-\dfrac{dR_i(t)/dt}{R_i(t)}$, so we can get:

$$\frac{dC(X(t))}{dt}=\sum_{i=1}^{n}\sum_{j=0}^{M-1}c_jR_i(t)\lambda_i(t)\{\Pr[\Phi(0_i,X(t))=j]-\Pr[\Phi(1_i,X(t))=j]\}=\sum_{i=1}^{n}I_i^{IBMP}(t) \tag{4}$$

Eq. (4) shows the relation between the change rate of the expected maintenance cost of the system and the IBMP value of each component. From the formula, we can know that the change rate of expected maintenance cost of the system at time t is equal to the sum of the IBMP values of n components at time t. Therefore, the IBMP value of component i is the contribution of component i to the change rate of the expected maintenance cost of system at time t.

IBMP is a PM model, so it is performed by the size of each component's IBMP value at a given time. Next we will introduce the JIBMP model. JIBMP model is an opportunistic maintenance (OM) model. It means that when a component in the system fails and needs to be shut down for maintenance, this component needs to be repaired; at the same time, PM of several other components should be performed in order to reduce the expected maintenance cost of the system as much as possible while improving the reliability of the system. The JIBMP model is derived from the IBMP model.

2.2. Derivation of joint importance-based maintenance priority

When component k suffers performance degradation that leads to failure, the expected maintenance cost of the system $C(X(t))$ becomes $C(0_k,X(t))$. According to Eq. (4) in the IBMP model, when component k fails, the relationship between the change rate of the expected maintenance cost of the system and the IBMP value of each component can be expressed as:

$$\frac{dC(0_k,X(t))}{dt}=\sum_{i=1,i\neq k}^{n}\sum_{j=0}^{M-1}c_jR_i(t)\lambda_i(t)\{\Pr[\Phi(0_k,0_i,X(t))=j]-\Pr[\Phi(0_k,1_i,X(t))=j]\}. \tag{5}$$

Therefore, according to Eq. (4) and Eq. (5), when component k is in a failure state, the IBMP value of component i can be expressed as:

$$I_i^{IBMP}(t)_{X_k(t)=0}=\sum_{j=0}^{M-1}c_jR_i(t)\lambda_i(t)\{\Pr[\Phi(0_k,0_i,X(t))=j]-\Pr[\Phi(0_k,1_i,X(t))=j]\}. \tag{6}$$

Here, $I_i^{IBMP}(t)_{X_k(t)=0}$ is the contribution of component i to the change rate of the expected maintenance cost of the system when component k is in a failure state. Similarly, when component k is in a perfect state, it can be seen from Eq. (5) that the relationship between the change rate of system expected maintenance cost and the IBMP value of each component can be expressed as:

$$\frac{dC(1_k,X(t))}{dt}=\sum_{i=1,i\neq k}^{n}\sum_{j=0}^{M-1}c_jR_i(t)\lambda_i(t)\{\Pr[\Phi(1_k,0_i,X(t))=j]-\Pr[\Phi(1_k,1_i,X(t))=j]\}. \tag{7}$$

So in the same way when component k is in a perfect state, the IBMP value of component i can be expressed as:

$$I_i^{IBMP}(t)_{X_k(t)=1}=\sum_{j=0}^{M-1}c_jR_i(t)\lambda_i(t)\{\Pr[\Phi(1_k,0_i,X(t))=j]-\Pr[\Phi(1_k,1_i,X(t))=j]\}. \tag{8}$$

$I_i^{IBMP}(t)_{X_k(t)=1}$ is the contribution of component i to the change rate of the expected maintenance cost of the system when component k is in a perfect state.

JIBMP is an OM model. It means that when there is a key component failure in the system, the system needs to be shut down for maintenance. In this downtime maintenance for some other potentially malfunctioning components can be performed. So when component k is in the maintenance state, the JIBMP value of component i is defined as:

$$I_i^{IBMP}(t)_{X_k(t)}=I_i^{IBMP}(t)_{X_k(t)=0}-I_i^{IBMP}(t)_{X_k(t)=1}. \tag{9}$$

$I_i^{IBMP}(t)_{X_k(t)}$ is the contribution of component i to the change rate of the expected maintenance cost of the system when component k is in the maintenance state. Therefore, if component k is under maintenance, component i with the highest JIBMP value should have the highest maintenance priority, because if component i fails, component i will contribute the most to the change rate of the expected maintenance cost of the system, so in order to avoid the failure of component i leading to an increase in the change rate of the expected maintenance cost of the system, component i should be maintained first. If component maintenance is carried out in accordance with the JIBMP model, the system performance can be improved while at the same time the growth rate of the expected maintenance cost of the system can be reduced.

Next we demonstrate the relationship between the change rate of the expected maintenance cost of the system and the JIBMP value of each component.

When component k is under maintenance, the change rate of the expected maintenance cost of the system can be expressed as:

$$\frac{dC(0_k,X(t))-dC(1_k,X(t))}{dt}=\frac{dC(0_k,X(t))}{dt}-\frac{dC(1_k,X(t))}{dt}.$$

Substituting Eq. (6) into Eq. (5), we can get:

$$\frac{dC(0_k,X(t))}{dt}=\sum_{i=1,i\neq k}^{n}I_i^{IBMP}(t)_{X_k(t)=0}.$$

In the same way, substituting Eq. (8) into (7) we have:

$\dfrac{dC(1_k,X(t))}{dt}=\sum_{i=1,i\neq k}^{n}I_i^{IBMP}(t)_{X_k(t)=1}$. Then,

$$\frac{dC(0_k,X(t))}{dt}-\frac{dC(1_k,X(t))}{dt}=\sum_{i=1,i\neq k}^{n}(I_i^{IBMP}(t)_{X_k(t)=0}-I_i^{IBMP}(t)_{X_k(t)=1})=\sum_{i=1,i\neq k}^{n}I_i^{IBMP}(t)_{X_k(t)}.$$

Therefore, the change rate of the expected maintenance cost of the system at time t is the sum of JIBMP values of the n-1 components at time t after removing the failure component k, so the JIBMP value of component i at time t is the contribution of component i to the change rate of the expected maintenance cost of the system. We should give priority to the maintenance of component i to prevent the failure of component i from increasing the change rate of the expected maintenance cost of the system. Thus, when using the JIBMP model to guide OM, it can improve system performance while reducing the expected maintenance cost of the system as much as possible.

2.3. Features of series-parallel system of JIBMP

In the following sections, we will discuss some characteristics of the JIBMP model in multi-state series-parallel systems. When state transition occurs after one components fails, the JIBMP illustrates the importance change of each of the rest components. The JIBMP can also be used to determine the component which induces the lowest change rate of system maintenance costs and has the highest preventive maintenance priority in remaining components.

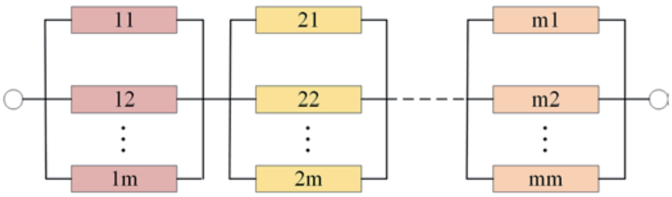

Fig. 1. Series-parallel system model

Assume that a system consists of n components. From Eq. (6), we can know that when component k is in a failure state, the JIBMP of component i from state p to state q ($p<q$) is expressed as:

$$I_i^{IBMP}(t)_{X_k(t)=0} = \sum_{j=0}^{M-1} c_j R_i(t)\lambda_i(t)\{\Pr[\Phi(0_k,p_i,X(t))=j]-\Pr[\Phi(0_k,q_i,X(t))=j]\}.$$

This equation can also be written as:

$$I_i^{IBMP}(t)_{X_k(t)=0} = \sum_{j=0}^{M-1}(c_j-c_{j+1})R_i(t)\lambda_i(t)\{\Pr[\Phi(0_k,p_i,X(t))\le j]-\Pr[\Phi(0_k,q_i,X(t))\le j]\}. \tag{10}$$

where $\Pr(\Phi(0_k,p_i,X(t))\le j)$ means the probability that the state of other components is lower than system state j when the component k is in the fault state and the component i is in state p. Similarly, $\Pr(\Phi(0_k,q_i,X(t))\le j)$ means the probability that the state of other components is lower than system state j when the component k is in the fault state and the component i is in state q. Simplifying Eq. (10):

$$\begin{aligned} I_i^{IBMP}(t)_{X_k(t)=0} &= \sum_{j=0}^{M-1}(c_j-c_{j+1})R_i(t)\lambda_i(t)\{\Pr[\Phi(0_k,p_i,X(t))\le j]-\Pr[\Phi(0_k,q_i,X(t))\le j]\} \\ &= \sum_{j=0}^{M-1}(c_j-c_{j+1})R_i(t)\lambda_i(t)[(1-\Pr(\Phi(0_k,p_i,X(t))>j))-(1-\Pr(\Phi(0_k,q_i,X(t))>j))] \\ &= \sum_{j=0}^{M-1}(c_j-c_{j+1})R_i(t)\lambda_i(t)[\Pr(\Phi(0_k,q_i,X(t))>j)-\Pr(\Phi(0_k,p_i,X(t))>j)] \end{aligned}$$

and:

$$\begin{aligned} &\sum_{j=0}^{M-1}(c_j-c_{j+1})\Pr(\Phi(0_k,q_i,X(t))>j) \\ &= \sum_{j=0}^{q-1}(c_j-c_{j+1})\Pr(\Phi(0_k,q_i,X(t))>j)+\sum_{j=q}^{M-1}(c_j-c_{j+1})\Pr(\Phi(0_k,q_i,X(t))>j) \end{aligned}$$

we know that during the operation of the system without intervention, components will degrade from a perfect state to a failed state, so the system state will gradually decrease; therefore:

$$\begin{aligned} &\Pr(\Phi(0_k,q_i,X(t))>j)=0,\ j=q,q+1,\ldots,M-1, \\ &\Pr(\Phi(0_k,p_i,X(t))>j)=0,\ j=p,p+1,\ldots,M-1. \end{aligned}$$

So we have:

$$\sum_{j=0}^{M-1}(c_j-c_{j+1})\Pr(\Phi(0_k,q_i,X(t))>j)=\sum_{j=0}^{q-1}(c_j-c_{j+1})\Pr(\Phi(0_k,q_i,X(t))>j).$$

In the same way, we have:

$$\begin{aligned} &\sum_{j=0}^{M-1}(c_j-c_{j+1})\Pr(\Phi(0_k,p_i,X(t))>j) \\ &= \sum_{j=0}^{p-1}(c_j-c_{j+1})\Pr(\Phi(0_k,p_i,X(t))>j)+\sum_{j=p}^{M-1}(c_j-c_{j+1})\Pr(\Phi(0_k,p_i,X(t))>j) \\ &= \sum_{j=0}^{p-1}(c_j-c_{j+1})\Pr(\Phi(0_k,p_i,X(t))>j) \end{aligned}.$$

Therefore, the $I_i^{IBMP}(t)_{X_k(t)=0}$ of component i in a multistate series-parallel system can be expressed as:

$$I_i^{IBMP}(t)_{X_k(t)=0}=R_i\cdot\lambda_i\cdot[\sum_{j=0}^{q-1}(c_j-c_{j+1})\Pr(\Phi(0_k,q_i,X(t))>j)-\sum_{j=0}^{p-1}(c_j-c_{j+1})\Pr(\Phi(0_k,p_i,X(t))>j)].$$

Similarly, when component k is in a perfect state, the $I_i^{IBMP}(t)_{X_k(t)=1}$ of component i from state p to state q can be expressed as:

$$I_i^{IBMP}(t)_{X_k(t)=1}=R_i\cdot\lambda_i\cdot[\sum_{j=0}^{q-1}(c_j-c_{j+1})\Pr(\Phi(1_k,q_i,X(t))>j)-\sum_{j=0}^{p-1}(c_j-c_{j+1})\Pr(\Phi(1_k,p_i,X(t))>j)].$$

From Eq. (9) and the analysis above, we know that $I_i^{IBMP}(t)_{X_k(t)}$ in a multistate series-parallel system can be expressed as:

$$\begin{aligned} I_i^{IBMP}(t)_{X_k(t)} &= I_i^{IBMP}(t)_{X_k(t)=0}-I_i^{IBMP}(t)_{X_k(t)=1} \\ &= R_i\cdot\lambda_i\cdot[\sum_{j=0}^{q-1}(c_j-c_{j+1})\Pr(\Phi(0_k,q_i,X(t))>j)+\sum_{j=0}^{p-1}(c_j-c_{j+1})\Pr(\Phi(1_k,p_i,X(t))>j) \\ &-\sum_{j=0}^{p-1}(c_j-c_{j+1})\Pr(\Phi(0_k,p_i,X(t))>j)-\sum_{j=0}^{q-1}(c_j-c_{j+1})\Pr(\Phi(1_k,q_i,X(t))>j)] \end{aligned}. \tag{11}$$

2.4. Discussion on the number of preventive maintenance components

When we do PM, after determining the maintenance budget C, we should determine which maintenance components have priority and the total number of components to be maintained. From the above analysis, we know that the maintenance strategy can be expressed as:

$$\max_{d_i}\sum I_i^{IBMP}(t)\cdot d_i, \tag{12}$$

and the limitation function of maintenance cost is $\sum c_i d_i \le C$, where c_i is the cost of component i in PM, d_i is a variable that determines whether component i needs to be maintained, $d_i\in\{0,1\}$, and C is the total cost of the budget. When decisions are made on maintenance optimization, we know that there are 2^n combinations. The number of PM components can be expressed as $\sum d_i$. When a component has a maximum IBMP value, it should be maintained first. When the component with the highest change rate of the expected maintenance cost of the system is maintained first, the maximum increase in system cost per unit time due to failure of that component is reduced. However, the maintenance cost of each component is different. When the PM budget is fixed, components with the maximum IBMP value may not be maintained first because the maintenance cost exceeds the budget. Therefore, the number of component maintenance in various time periods should be taken into account in combination with the above analysis.

3. Case study for 2H2E architecture

Hydraulic energy systems are crucial in ensuring flight security. State-of-the-art Airbus A380 airplane uses a dual-architecture hydraulic energy system. This is a hybrid flight control actuator power distribution system that combines a distributed electric actuator used as a backup system with a conventional telex hydraulic servo control for active control, forming four independent main flight control systems. Two of the systems are hydraulically powered and the other two are electrically powered. Therefore, this architecture is also known as the 2H2E architectural layout. 2H is the pump source of the traditional hydraulic power actuating system, consisting of eight engine-driven pumps (EDPs) and four AC electric motor pumps (EMPs). They provide hydraulic power for the aircraft's main flight control, landing gear, front-wheel turning, and other related systems. 2E is an electrically powered, distributed, electro-hydraulic actuator system, which consists of electro-hydraulic actuators and backup electro-hydraulic actuators. Each of the four systems can be individually controlled, bringing the independence, redundancy and reliability of the A380 hydraulic energy system to a new level.

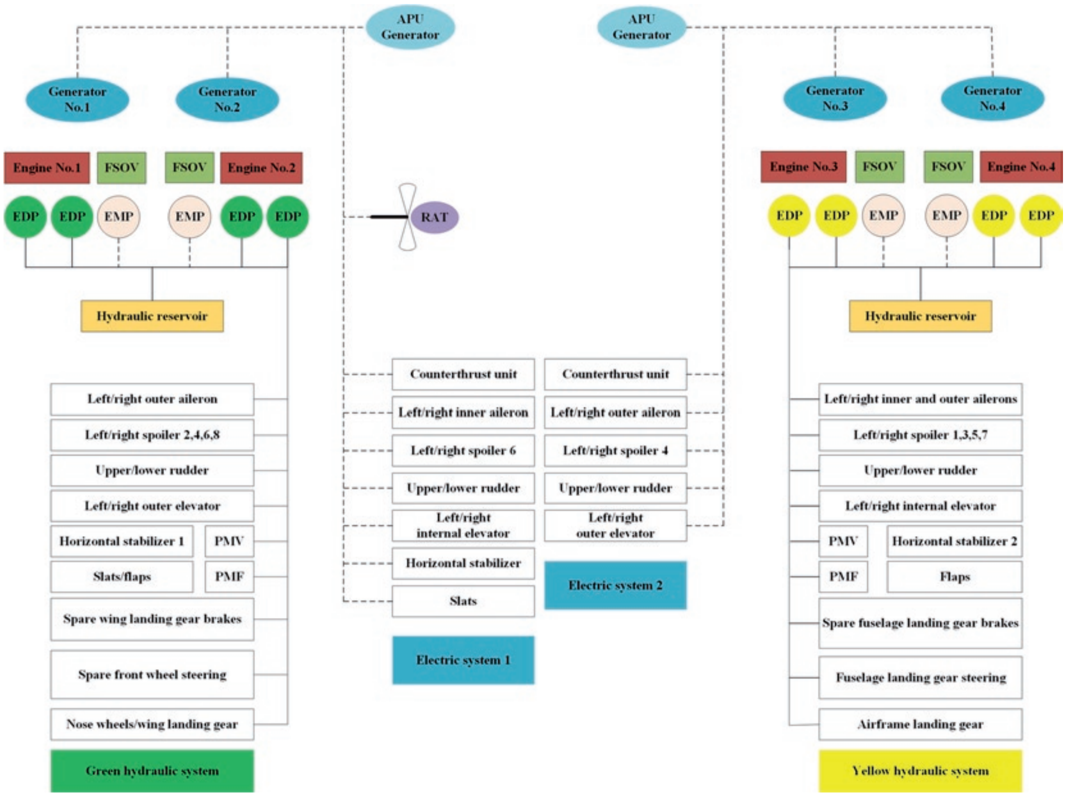

Fig. 2. Configuration diagram of a two-hydraulically-powered and two-electrically-powered architecture used by Airbus A380 airplane

A configuration diagram of the 2H2E architecture used in the A380 is shown in Fig. 2 the main components include four engines, eight EDPs, four EMPs, four fuel shut-off valves (FSOVs), four generators, two auxiliary power unit (APU) generators, two hydraulic reservoirs, and one ram air turbine (RAT). Based on statistics, some components do not fail often, including engines, FSOVs, and RAT. However, EDPs, generators, EMPs, and hydraulic reservoirs run most of the time that an aircraft is in flight, and hence may become vulnerable components. Failure of any of these components may result in system performance degradation or failure [31]. Therefore, to ensure flight safety, we must do PM on important components. But due to maintenance cost, PM cannot be done on all components, so maintenance must be prioritized based on the requirements of each component.

Table 1 lists 29 important components that play an important role in the safety of an A380 airplane. There is redundancy in some important components, and when one of the components fails, the backup components still function but the system performance will inevitably degrade. If the backup component fails, the system fails.

Table 1. Major components in the 2H2E architecture of an A380 airplane

Code	Component	Code	Component
X1	Engine No.1	X16	APU generator No.2
X2	Electric motor pump No.1	X17	Electric motor pump No.2
X3	Engine-driven pump No.1	X18	Engine No.3
X4	Engine-driven pump No.2	X19	Engine-driven pump No.5
X5	Generator No.1	X20	Engine-driven pump No.6
X6	Hydraulic reservoir No.1	X21	Generator No.3
X7	APU generator No.1	X22	Electric motor pump No.3
X8	Fuel shut-off valve No.1	X23	Fuel shut-off valve No.3
X9	Ram air turbine	X24	Engine No.4
X10	Engine No.2	X25	Generator No.4
X11	Engine-driven pump No.3	X26	Engine-driven pump No.7
X12	Engine-driven pump No.4	X27	Engine-driven pump No.8
X13	Generator No.2	X28	Electric motor pump No.4
X14	Hydraulic reservoir No.2	X29	Fuel shut-off valve No.4
X15	Fuel shut-off valve No.2		

The Weibull distribution is a widely used statistical distribution, especially in the life analysis of mechanical components [25]. On the basis of engineering practice, we assumed that all of the above 29 important components follow the Weibull distribution $W(\theta,\gamma,t)$ with the parameters shown in Table 2.

By the properties of the Weibull distribution, the reliability function of component is $R(t)=\exp[-(\frac{t}{\theta})^{\gamma}]$ and the failure rate function is $\lambda(t)$, which is given by $\lambda(t)=\frac{\gamma}{\theta}\cdot(\frac{t}{\theta})^{\gamma-1}$. Of the above 29 compo-

Table 3. System states and corresponding state maintenance cost in descending order of maintenance cost. j is the system state and cj is the failure maintenance cost.

j	System state						c_j
0	Complete failure state						1
1	X5/X7/X13	X2/X17	X3/X4/X11/X12	X8/X15	X9	X6	0.95
2	X5/X7/X13	X2/X17	X3/X4/X11/X12	X8/X15	X9	–	0.90
3	X5/X7/X13	X2/X17	X3/X4/X11/X12	X8/X15	–	X6	0.87
4-5	X5/X7/X13	X2/X17	X3/X4/X11/X12	–	X9	X6	0.85
6-9	X5/X7/X13	X2/X17	–	X8/X15	X9	X6	0.83
10-11	X5/X7/X13	–	X3/X4/X11/X12	X8/X15	X9	X6	0.80
12	X5/X7/X13	X2/X17	X3/X4/X11/X12	X8/X15	–	–	0.77
13-15	–	X2/X17	X3/X4/X11/X12	X8/X15	X9	X6	0.75
16-17	X5/X7/X13	X2/X17	X3/X4/X11/X12	–	X9	–	0.75
18-21	X5/X7/X13	X2/X17	–	X8/X15	X9	–	0.73
22-23	X5/X7/X13	X2/X17	X3/X4/X11/X12	–	–	X6	0.72
24-25	X5/X7/X13	–	X3/X4/X11/X12	X8/X15	X9	–	0.70
26-29	X5/X7/X13	X2/X17	–	X8/X15	–	X6	0.70
30-37	X5/X7/X13	X2/X17	–	–	X9	X6	0.68
38-39	X5/X7/X13	–	X3/X4/X11/X12	X8/X15	–	X6	0.67
40-42	–	X2/X17	X3/X4/X11/X12	X8/X15	X9	–	0.65
43-46	X5/X7/X13	–	X3/X4/X11/X12	–	X9	X6	0.65
47-54	X5/X7/X13	–	–	X8/X15	X9	X6	0.63
55-57	–	X2/X17	X3/X4/X11/X12	X8/X15	–	X6	0.62
58-59	X5/X7/X13	X2/X17	X3/X4/X11/X12	–	–	–	0.62
60-65	–	X2/X17	X3/X4/X11/X12	–	X9	X6	0.60
66-69	X5/X7/X13	X2/X17	–	X8/X15	–	–	0.60
70-81	–	X2/X17	–	X8/X15	X9	X6	0.58
82-89	X5/X7/X13	X2/X17	–	–	X9	–	0.58
90-95	–	–	X3/X4/X11/X12	X8/X15	–	X6	0.58
96-97	X5/X7/X13	–	X3/X4/X11/X12	X8/X15	–	–	0.57
98-103	–	–	X3/X4/X11/X12	X8/X15	X9	X6	0.55
104-107	X5/X7/X13	–	X3/X4/X11/X12	–	X9	–	0.55
108-115	X5/X7/X13	X2/X17	–	–	–	X6	0.55
116-123	X5/X7/X13	–	–	X8/X15	X9	–	0.53
124-127	–	X2/X17	X3/X4/X11/X12	X8/X15	–	–	0.52
128-131	X5/X7/X13	–	X3/X4/X11/X12	–	–	X6	0.52
132-137	–	X2/X17	X3/X4/X11/X12	–	X9	–	0.50
138-145	X5/X7/X13	–	–	X8/X15	–	X6	0.50
146-157	–	X2/X17	–	X8/X15	X9	–	0.48
158-173	X5/X7/X13	–	–	–	X9	X6	0.48
174-179	–	X2/X17	X3/X4/X11/X12	–	–	X6	0.47
180-185	–	–	X3/X4/X11/X12	X8/X15	X9	–	0.45
186-197	–	X2/X17	–	X8/X15	–	X6	0.45
198-205	X5/X7/X13	X2/X17	–	–	–	–	0.45
206-229	–	X2/X17	–	–	X9	X6	0.43
230-233	X5/X7/X13	–	X3/X4/X11/X12	–	–	–	0.42
234-245	–	–	X3/X4/X11/X12	–	X9	X6	0.40
246-253	X5/X7/X13	–	–	X8/X15	–	–	0.40
254-277	–	–	–	X8/X15	X9	X6	0.38
278-293	X5/X7/X13	–	–	–	X9	–	0.38
294-299	–	X2/X17	X3/X4/X11/X12	–	–	–	0.37
300-311	–	X2/X17	–	X8/X15	–	–	0.35
312-327	X5/X7/X13	–	–	–	–	X6	0.35
328-351	–	X2/X17	–	–	X9	–	0.33
352-357	–	–	X3/X4/X11/X12	X8/X15	–	–	0.32
358-369	–	–	X3/X4/X11/X12	–	X9	–	0.30
370-393	–	X2/X17	–	–	–	X6	0.30
394-417	–	–	–	X8/X15	X9	–	0.28
418-429	–	–	X3/X4/X11/X12	–	–	X6	0.27
430-453	–	–	–	X8/X15	–	X6	0.25
454-469	X5/X7/X13	–	–	–	–	–	0.25
470-517	–	–	–	–	X9	X6	0.23
518-541	–	X2/X17	–	–	–	–	0.20
542-553	–	–	X3/X4/X11/X12	–	–	–	0.17
554-577	–	–	–	X8/X15	–	–	0.15
578-625	–	–	–	–	X9	–	0.13
626-649	–	–	–	–	–	X6	0.10
650	Perfect state						0

Table 2. *Parameters of component failure times. θ is a scale parameter and γ is a shape parameter*

No.	Component	Codes	θ	γ
1	Engine	X1, X10, X18, X24	20000	1.95
2	Electric motor pump	X2, X17, X22, X28	14000	2.13
3	Engine-driven pump	X3, X4, X11, X12, X19, X20, X26, X27	16000	2.43
4	Fuel shut-off valve	X8, X15, X23, X29	32000	2.24
5	Generator	X5, X13, X21, X25	14000	1.68
6	Hydraulic reservoir	X6, X14	30000	1.21
7	APU generator	X7, X16	18000	1.79
8	Ram air turbine	X9	10000	1.46

nents, there are a total of 8 types of components, which include engines X1, X10, X18, X24; generators X5, X13, X21, X25; EDPs X3, X4, X11, X12, X19, X20, X26, X27; EMPs X2, X17, X22, X28; FSOVs X8, X15, X23, X29; APU generators X7, X16; RAT X9; and hydraulic reservoirs X6, X14. Considering the common cause failure of the redundant components of the aircraft, we only analyze and discuss the energy components of one hydraulic system and one electrical system in the 2H2E structure layout.

Based on the above analysis, we listed a combination of all the failed-component situations. Components that may fail comprise various states of the hydraulic energy system. These states are shown in Table 3. Each column indicates that there is a type of component failure in the system, and the "/" in each column means "or". States 1 to 649 are the intermediate states; they represent system performance degradation but no failure. State 0 is the complete failure state, which represents that the system has failed. State 650 is the perfect state. The components in each state represent that failure has occurred. Therefore, c_j represents the combination of failure maintenance cost for components in each state. For the failure maintenance cost c_j of each state, we did normalization processing.

4. Results analysis

In this section, we simulated the above model. The reliability and failure rate of the model follow the Weibull distribution of two parameters, i.e. the scale parameter θ and the shape parameter γ. Fig. 3 shows the plot of the IBMP values of each component over time. Fig. 4 shows the JIBMP values for each component at 3,000 h. Fig. 5 shows the JIBMP values at 6,000 h. Then we analyzed the simulation results. On this basis, we analyzed the maintenance optimization strategy of a hydraulic energy system under the condition of a limited budget and determined the number of PM components under various budget constraints.

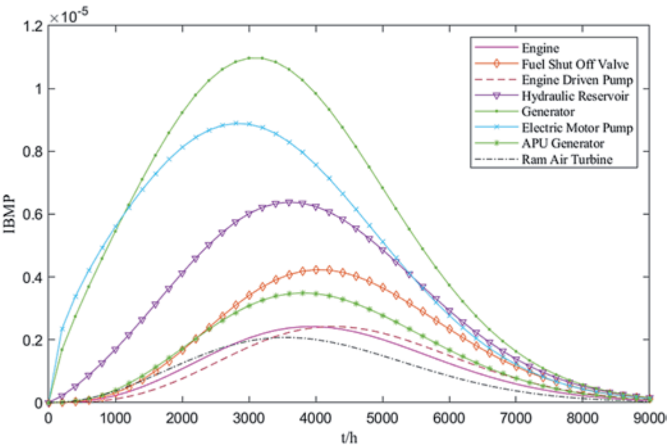

Fig. 3. Change in importance-based maintenance priority over time for various components

Fig. 3 shows the change in IBMP values over time. Their changing trend is affected by their reliability, failure rate and state transfer of each component at time *t*. Since the changing trend and degradation rate of the reliability and failure rate of each component are not the same, the probability of state transition of each component of the system is constantly changing due to their joint action. As can be seen from Fig. 3 the IBMP value of each component is zero at the beginning. This is because each component is in a perfect state at the beginning, so the contribution of each component to the change rate of the expected maintenance cost of the system is zero. With the operation of components, the performance of each component of the system degrades faster, so the expected maintenance cost of each component increases faster. Hence the contribution of each component to the change rate of the expected maintenance cost of the system increases, and the IBMP value increases. In the later period, components run for a long time, which makes all components unreliable. Therefore, the expected maintenance cost tends to be the largest, so the contribution of each component to the change rate of the expected maintenance cost of the system tends to zero.

From Fig. 3 we can see that the IBMP value of the generator is the highest. On one hand, generators are relatively important and responsible for the entire electrical system of the aircraft. On the other hand, generators have a higher failure rate compared with other components. We can also see from Fig. 3 that the hydraulic reservoir also has a high maintenance priority. That is because on one hand the redundancy of the hydraulic reservoir is low in the aircraft hydraulic energy system, and on the other hand, when the hydraulic reservoir fails, the entire hydraulic system starts to malfunction, leading to a hydraulic actuator failure, which affects the safety of the aircraft. Fig. 3 shows that the engine has a relatively low IBMP value because the failure rate of the engine is extremely low, and it has high redundancy. Therefore, although it plays an extremely important role in the operation of the aircraft, it has a very low maintenance priority. By sorting the IBMP values at a certain moment, the maintenance priority of each component can be determined, and the maintenance strategy of each component can be carried out based on this order.

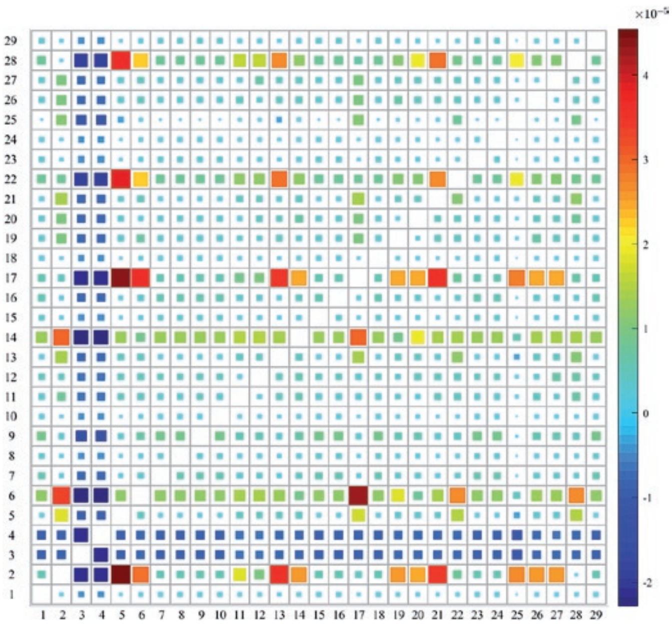

Fig. 4. Components of joint importance-based maintenance priority values at 3,000 h. Sizes and colors of squares represent levels of JIBMP values.

Fig. 4 shows the JIBMP interrelationship of each component at 3,000 h, and Fig. 5 at 6,000 h. The size and color of each grid cell

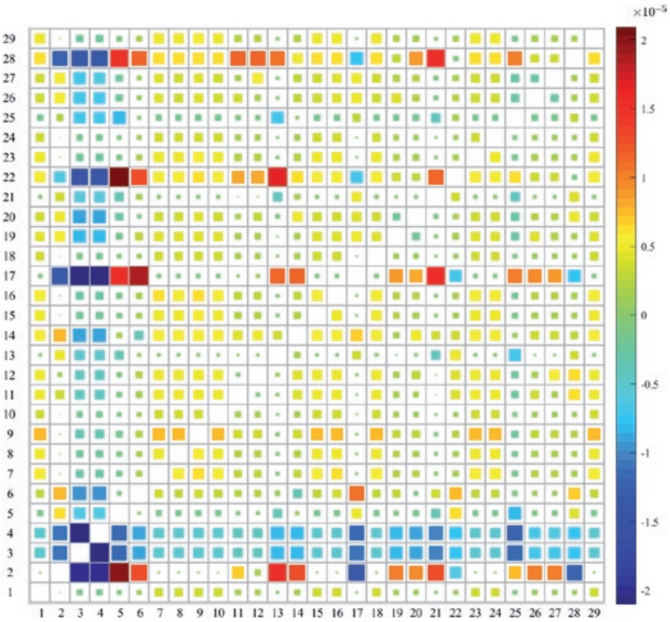

Fig. 5. Components of joint importance-based maintenance priority values at 6,000 h. Sizes and colors of squares represent levels of JIBMP values.

represent the level of JIBMP values between the components. From Fig. 4, we can see that when the hydraulic energy system has run for 3,000 h, the JIBMP values of components 5 and 2, and 5 and 17, are the highest. Combined with Table 1, it shows that when the generator X5 is under maintenance, the maintenance priority should be given to the EMPs X2 and X17. Components 6 and 17 have relatively large JIBMP values, indicating that when EMP X17 is under maintenance, hydraulic reservoir X6 is the best choice for PM, and vice versa. Fig. 5 shows that the JIBMP interrelationships of components 5 and 2, 6 and 17, and 5 and 22 are similar to those in Fig. 4. Also, JIBMP values between some components are negative, indicating that the maintenance sequence of these components has a negative effect on reducing the rate of change of system expected maintenance cost. Next we use the IBMP model to discuss components maintenance strategy.

Table 4 lists the sequence of the IBMP value of each component at 3,000 and 6,000 h. We can see that the sequences of IBMP values are different for the two durations. At 3,000 h, the top three values in the PM sequence are generator, EMP, and hydraulic reservoir. However, at 6,000 h, the top three are generator, hydraulic reservoir, and EMP. This is because the reliability and failure rate of components change over time, which leads to changes in the change rate of system maintenance costs. Therefore, according to the IBMP value, we can determine the best PM sequence, which can effectively guide the selection of PM components on a limited budget.

Table 4. Values of the importance-based maintenance priority at 3,000 h and 6,000 h

	Value at 3,000 h		Value at 6,000 h	
Component	IBMP ($\times 10^{-5}$)	Order	IBMP ($\times 10^{-5}$)	Order
Engine	0.206	6	0.125	7
Electric motor pump	0.886	2	0.278	3
Ram air turbine	0.196	7	0.085	8
Fuel shut-off valve	0.341	4	0.234	4
Generator	1.097	1	0.374	1
Hydraulic reservoir	0.602	3	0.293	2
APU generator	0.309	5	0.167	5
Engine-driven pump	0.178	8	0.150	6

From the analysis in Section 2.4, we can know that the maintenance strategy can be expressed as $\max_{d_i} \sum I_i^{IBMP}(t) \cdot d_i$, and the constraint function of maintenance cost is $\sum c_i d_i \le C$. There are 29 important components in the aircraft hydraulic energy system, so d_i has 2^{29} cases. The IBMP value of each component changes with time, so the maintenance strategy also changes. The maintenance cost for each component is listed in Table 5.

The maintenance strategy according to the rank of IBMP value and the constraint function of the maintenance budgets are shown in Table 6. We set two maintenance periods of 3,000 h and 6,000 h. When the total maintenance budget is within \$30,000, priority should be given to the maintenance of generators and EMPs. When the total maintenance budget is within \$70,000, the best choice is to add hydraulic reservoirs and FSOVs for maintenance. When the total maintenance budget is within \$100,000, we need to add APU generators to the PM.

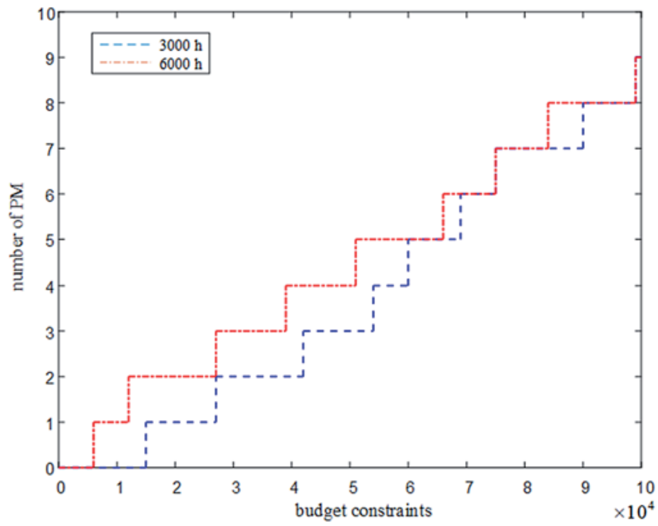

Fig. 6. Number of PM instances for various budget constraints

Fig. 6 shows the relation between budget constraints and the number of PM instances. The number of components available for PM gradually increases with increases in the budget. However, because the IBMP values for each component change over time, the two curves for the number of PM components do not overlap. As can be seen from Fig. 6, when the budget is less than \$30,000, two or three components should be considered for PM. When the budget is within \$70,000, six components should be considered for PM. When the budget is under \$100,000, nine components should be considered for PM. The sequence of PM for components under various budget constraints can be seen in Table 6.

5. Conclusions and future work

In this paper, two maintenance measures are proposed to guide cost-based maintenance for the priority issue of component maintenance. The proposed methods are applied to aircraft 2H2E architecture, and the following conclusions are drawn: a) Preventive maintenance (PM) priority of different components changes over time, and importance-based maintenance priority (IBMP) value increases first and then decreases over time, indicating that the expected change rate of maintenance cost of components increases with the decrease of component reliability until the maintenance cost tends to the maximum and the maintenance cost change rate tends to zero; b) When a key component of the system fails, the expected change rate of maintenance cost of the system is different for the opportunistic maintenance (OM) of different components

Table 5. Maintenance cost in US dollars for each component

Component	Maintenance cost	Component	Maintenance cost
Engine	30,000	Generator	15,000
Electric motor pump	12,000	Hydraulic reservoir	6,000
Engine-driven pump	10,000	APU generator	15,000
Fuel shut-off valve	9,000	Ram air turbine	8,000

Table 6. Maintenance strategy for different budgets at different operation durations

	30,000 dollars	70,000 dollars	100,000 dollars
3,000 h	Generator No. 1	Generator No. 1	Generator No. 1
	Electric motor pump No. 1	Generator No. 2	Generator No. 2
		Electric motor pump No. 1	Electric motor pump No. 1
		Electric motor pump No. 2	Electric motor pump No. 2
		Hydraulic reservoir No. 1	Hydraulic reservoir No. 1
		Fuel shut-off valve No. 1	Hydraulic reservoir No. 2
			Fuel shut-off valve No. 1
			Fuel shut-off valve No. 2
			APU generator No. 1
6,000 h	Generator No. 2	Generator No. 3	Generator No. 3
	Hydraulic reservoir No. 1	Generator No. 4	Generator No. 4
	Hydraulic reservoir No. 2	Hydraulic reservoir No. 2	Hydraulic reservoir No. 1
		Electric motor pump No. 3	Hydraulic reservoir No. 2
		Electric motor pump No. 4	Electric motor pump No. 3
		Fuel shut-off valve No. 2	Electric motor pump No. 4
			Fuel shut-off valve No. 3
			Fuel shut-off valve No. 4
			APU generator No. 2

at different time periods, and the joint importance-based maintenance priority (JIBMP) values of different components are significantly different; c) After determining the planned expenditure cost of the airline for regular maintenance of the aircraft, i.e. the budgeted cost, with the increase of the budgeted cost, the number of components which need to be maintained is gradually increasing. With the change of maintenance time, the components which need to be maintained are also changing.

Future work will combine IBMP and JIBMP models proposed with component resilience measures to conduct joint maintenance decision analysis for key components at different stages of the system.

Acknowledgments

The authors gratefully express their appreciation for the financial supports from the National Key R&D Program of China (Grant No.2019YFB2004504), the Aviation Science Foundation (Grant No. 201902051001) and National Natural Science Foundation of China (Grant No. 51875015, 51620105010).

References

1. Andrzejczak K, Mlynczak M, Selech J. Poisson-distributed failures in the predicting of the cost of corrective maintenance. Eksploatacja i Niezawodnosc – Maintenance and Reliability 2018; 20: 602-609, http://doi.org/10.17531/ein.2018.4.11.
2. Birnbaum ZW. On the importance of different components in a multi-component system. New York: Academic Press 1969: 581-592.
3. Babishin V, Hajipour Y, Taghipour S. Optimisation of Non-Periodic Inspection and Maintenance for Multicomponent Systems. Eksploatacja i Niezawodnosc – Maintenance and Reliability 2018; 20: 327-342, http://doi.org/10.17531/ein.2018.2.20.
4. Cai B, Huang L, Xie M. Bayesian networks in fault diagnosis. IEEE Transactions on Industrial Informatics 2017; 13: 2227–2240, http://doi.org/10.1109/TII.2017.2695583.
5. Cai B, Kong X, Liu Y, et al. Application of Bayesian networks in Reliability Evaluation. IEEE Transactions on Industrial Informatics 2019; 15: 2146-2157, http://doi.org/10.1109/TII.2018.2858281.
6. Cai B, Liu Y, Liu Z, et al. Bayesian Networks for Reliability Engineering. Singapore: Springer 2019: 187-196.
7. Dui H, Li S, Xing L, et al. System performance-based joint importance analysis guided maintenance for repairable systems. Reliability Engineering & System Safety 2019; 186: 162-175, http://doi.org/ 10.1016/j.ress.2019.02.021.
8. Dui H, Si S, Yam R. A cost-based integrated importance measure of system components for preventive maintenance. Reliability Engineering & System Safety 2017; 168: 98-104, https://doi.org/10.1016/j.ress.2017.05.025.
9. Griffith W.S. Multistate Reliability Models. Journal of Applied Probability 1980; 17: 735–744, https://doi.org/10.2307/3212967.
10. Gao H, Cui L, Qiu Q. Reliability modeling for degradation-shock dependence systems with multiple species of shocks. Reliability Engineering & System Safety 2019; 185: 133-143, https://doi.org/ 10.1016/j.ress.2018.12.011.
11. Legát V, Mošna F, Aleš Z, et al. Preventive maintenance models – higher operational reliability. Eksploatacja i Niezawodnosc – Maintenance and Reliability 2017; 19: 134-141, http://doi.org/10.17531/ein.2017.1.19.
12. Levitin G, Xing L, Dai Y. Mission Abort Policy for Systems with Observable States of Standby Components. Risk Analysis 2020; 40: 1900-1912, http://doi.org/10.1111/risa.13532.
13. Levitin G, Finkelstein M, Dai Y. State-based mission abort policies for multistate systems. Reliability Engineering & System Safety 2020; 204: 107122, https://doi.org/10.1016/j.ress.2020.107122.
14. Lee M, Li L, Song W. Analysis of direct operating cost of wide-body passenger aircraft: A parametric study based on Hong Kong. Chinese Journal of Aeronautics 2019; 32: 1222-1243, https://doi.org/10.1016/j.cja.2019.03.011.
15. Peng W, Liu Y, Zhang X, et al. Sequential preventive maintenance policies with consideration of random adjustment-reduction features. Eksploatacja i Niezawodnosc – Maintenance and Reliability 2015; 17: 306-313, http:// doi.org/10.17531/ein.2015.2.19.
16. Qiu Q, Cui L. Optimal mission abort policy for systems subject to random shocks based on virtual age process. Reliability Engineering &

System Safety 2019; 189: 11-20, http:// doi.org/10.1016/j.ress.2019.04.010.
17. Si S, Zhao J, Cai Z, et al. Recent advances in system reliability optimization driven by importance measures. Frontiers of Engineering Management 2020; 7: 335-358, http:// doi.org/10.1007/s42524-020-0112-6.
18. Si S, Dui H, Zhao X, et al. Integrated importance measure of component states based on loss of system performance. IEEE Transactions on Reliability 2012; 61:192–202, http:// doi.org/ 10.1109/TR.2011.2182394.
19. Sun J, Wang F, Ning S. Aircraft air conditioning system health state estimation and prediction for predictive maintenance. Chinese Journal of Aeronautics 2020; 33: 947-955, https://doi.org/10.1016/j.cja.2019.03.039.
20. Tan C, Narula U, Lai L, et al. Optimal maintenance strategy on medical instruments used for haemodialysis process. Eksploatacja i Niezawodnosc – Maintenance and Reliability 2019; 21: 318–328, https://doi.org/10.17531/ein.2019.2.17.
21. Wu S, Chan L. Performance utility-analysis of multi-state systems. IEEE Transactions on Reliability 2003; 52: 14-21, https://doi.org/10.1109/TR.2002.805783.
22. Wu S, Coolen F. A cost-based importance measure for system components: An extension of the Birnbaum importance. European Journal of Operational Research 2013; 225: 189-195, https://doi.org/10.1016/j.ejor.2012.09.034.
23. Wu S, Chen Y, Wu Q, et al. Linking component importance to optimisation of preventive maintenance policy. Reliability Engineering & System Safety 2016;146: 26-32, https://dx.doi.org/ 10.1016/j.ress.2015.10.008.
24. Xing L, Zhao G, Wang Y, et al. Reliability modeling of correlated competitions and dependent components with random failure propagation time. Quality and Reliability Engineering International 2020; 36: 947-964, https://doi.org/10.1002/qre.2609.
25. Yuan F. Parameter estimation for bivariate Weibull distribution using generalized moment method for reliability evaluation. Quality and Reliability Engineering International 2018; 34: 631-640, https://doi.org/10.1002/qre.2276.
26. Zhai Q, Yang J, Xie M, et al. Generalized moment-independent importance measures based on Minkowski distance. European Journal of Operational Research 2014; 239: 449–455, https://doi.org/10.1016/j.ejor.2014.05.021.
27. Zhu X, Fu Y, Yuan T, et al. Birnbaum importance based heuristics for multi-type component assignment problems. Reliability Engineering & System Safety 2017; 165: 209–221, https://doi.org/10.1016/j.ress.2017.04.018.
28. Zheng Z, Cui L, Hawkes A. A study on a single-unit Markov repairable system with repair time omission. IEEE Transactions on Reliability 2006; 55: 182–188, https://doi.org/10.1109/TR.2006.874933.
29. Zhang C, Qian Y, Dui H, et al. Opportunistic maintenance strategy of a Heave Compensation System for expected performance degradation. Eksploatacja i Niezawodnosc – Maintenance and Reliability 2021; 23: 512-521, http://doi.org/10.17531/ein.2021.3.12.
30. Zhao X, Wang S, Wang X, et al. Multi-state balanced systems in a shock environment. Reliability Engineering & System Safety 2020; 193: 106592, http://doi.org/10.1016/j.ress.2019.106592.
31. Zhao X, Huang X, Sun J. Reliability modeling and maintenance optimization for the two-unit system with preset self-repairing mechanism. Proceedings of the Institution of Mechanical Engineers 2020; 234: 221-234, http://doi.org/10.1177/1748006X19890739.

Eksploatacja i Niezawodnosc – Maintenance and Reliability
Volume 24 (2022), Issue 1
journal homepage: http://www.ein.org.pl
Article citation info:
Karpenko M, Prentkovskis O, Šukevičius Š. Research on high-pressure hose with repairing fitting and influence on energy parameter of the hydraulic drive. Eksploatacja i Niezawodnosc – Maintenance and Reliability 2022; 24 (1): 25–32, http://doi.org/10.17531/ein.2022.1.4.

Research on high-pressure hose with repairing fitting and influence on energy parameter of the hydraulic drive

Indexed by: Web of Science Group

Mykola Karpenko[a], Olegas Prentkovskis[a], Šarūnas Šukevičius[a]

[a]Vilnius Gediminas Technical University, Department of Mobile Machinery and Railway Transport, Plytinės st. 27, LT-10105, Vilnius, Lithuania

Highlights

- High-pressure hoses and junctions failure influence to flow parameters were analyzed.
- Comparative analysis between non-repaired and repaired high-pressure hoses were performed.
- Numerical simulations (CFD) and experimental measurement applied in the research.
- Pressure drops and flow coefficients at non-repaired and after maintenance hose was obtained.
- Research find the insignificant power losses in repaired hose compared to standard hose.

Abstract

Reliability and maintenance analysis of transport machines hydraulic drives, basically focused to power units: pumps, cylinders etc., without taking in to account junction elements. Therefore, this paper proposes a research analysis on high-pressure hoses and junctions during technical maintenance. Comparative analysis of fluid behavior and energy efficiency inside non-repaired and repaired high-pressure hoses is presented in this research. Theoretical and experimental research results for hydraulic processes inside high-pressure hose is based on the numerical simulations using Navier–Stokes equations and experimental measurement of fluid flow pressure inside high-pressure hoses. Research of fluid flow dynamics in the hydraulic system was made with main assumptions: system flow rate in the range from 5 to 100 l/min, diameter of the hoses and repairing fitting are 3/8". The pressure drops, power losses, flow coefficients at non-repaired and after maintenance hose was obtained as a result. Simulation results were verified by running physical experiments to measure the pressure losses.

Keywords

high-pressure hose, fitting, maintenance, energy, pipeline, fluid flow, numerical modeling, hydraulic system, CFD.

1. Introduction

Due to the wide use of hydraulic drives in machines and mechanisms in various technical area from the transport engineering [3, 16, 17] to aviation engineering [32] and even in industrial sectors [6, 25], there is an objective need for monitoring the technical condition of its elements. Modern hydraulic drive of any mobile machine or industrial system are complex, branch and usually considering from a lot different hydraulic elements (pumps, valves, throttles, cylinders and etc.). For connection all hydraulic elements to one system - using a special object which is high-pressure hose. High-pressure hoses is metal or flexible composite pipelines [5, 26, 43] designed to transmit hydraulic forces and working fluid between units of hydraulic drive. The wall of high-pressure hoses is multilayer, consisting of rubber and reinforcing layers. The number of reinforcing layers depends on the required characteristics of high-pressure hose and can vary from one to seven layers. However, according to [22, 34], the most common in the hydraulic drive of a transport-technological machine is the high-pressure hoses with one and two metal reinforcing layers (Fig.1a).

The composite pipelines and high-pressure hoses is being used as the main components for hydraulic systems, especially in strong vibration environments. These exploitation conditions may cause composite pipe fatigue or even long-term damage [30]. In the research [31] pointed that from a total of 106 flexible pipe failure or damage incidents 20% of flexible pipes were found to have experienced some form of damage or failure. 2/3 cases occurred during long-term using and 1/3 cases during normal period of operation, from this 20% amount. 32 failures requires replace flexible pipes, rest amount can be repaired, from these total 106 cases. Hose defects and malfunctions were extensively studied and discussed by specialists and researchers. According to [10 and 21], there are two main types of to the high pressure hoses damage, that produce failure:

A) External damage. Caused by environmental influences and loads or friction of a high pressure hose against a surface shown at Fig 1b.
B) Internal damage (damage to the inner layers, shown at Fig. 1c). Caused by high pressures by fluid pulsation inside the hose, by non-compliance with frequency characteristics or other factors (e.g. aggressive oil, flexural vibrations of hose, etc.).

External damage of high-pressure hoses is easily diagnosed by visual inspection, but internal damage diagnosed without special tests

E-mail addresses: M. Karpenko (ORCID: 0000-0002-1915-5219): mykola.karpenko@vilniustech.lt, O. Prentkovskis (ORCID: 0000-0003-0910-591X): olegas.prentkovskis@vilniustech.lt, Š. Šukevičius (ORCID: 0000-0002-1393-1731): sarunas.sukevicius@vilniustech.lt

Fig. 1. Views of high pressure hose: a) high-pressure hose with two metal braid; b) external damage of high-pressure hose; c) result from internal damages of high-pressure hose

is impossible, until the hoses are not braked. Failure of hydraulic hoses is a critical problem, factors associated with hoses failure are material characteristics [38], hose geometry [11], environmental conditions [10], internal or external loadings [27], and manufacturing flaws [8]. The interaction of these factors is very complex to analyses. The high-pressure hose with external and internal damages could be operated for some time, but dynamic flow parameters and reliability of hydraulic system will be reduced. Damage to the external or internal layer of the high-pressure hose will not only effect on the energy and reliable parameters of the hydraulic system, but can lead to accidentally lead to the break of the high-pressure hose during exploitation. The volumetric surface defects of high-pressure hose appear because of corrosion or erosion-corrosion processes in the reinforcing layer and these areas considerably decreasing the high-pressure hose strength. [28]. It is important to find out the cause of the external defects and understand the destruction process in order to reduce the risk of injury, equipment failure, energy loses or environmental disaster. The sooner the fact of damage is established and the high-pressure hose is technically serviced or replaced, the lower the risk of failure of the entire hydraulic drive and energy losses, the more reliable the system [29].

Therefore, it is very important, to study fretting fatigue and failure mechanism of hoses and fittings after maintenance to improve the reliability of hydraulic hoses system in a future [44]. The evaluation of maintenance costs of pipelines system should not only take in to account the present repair cost hydraulic system, but also the value of future maintenance cost using this repaired system, according to the [37]. That is why, after repair high-pressure hose and installation back to the hydraulic drive system there is a need to study the influence of the repair performance to the fluid dynamic inside the hose, as well as to the reliability and energy parameters.

2. Repair of damaged high-pressure hose

Repair of damaged high-pressure hoses or it's segments is a complicated operation which require to remove hose from the hydraulic drive. Therefore repair actions are performed only in case of defect that and in special zones during machine maintenance [5]. Usually, if high-pressure hose is relatively short, it is replaced with the new one. In case if high-pressure hose is longer than one meter and have an external damages, it can be repaired and installed back (economically better solution) [13]. One way decrease maintenance cost is to apply repairing fitting (hose junction) in the area of high-pressure hose defect instead of replacing hose with the new hose. This technique involves that the damaged segments can be cutted off and hose repaired with a hose junction, scheme of high-pressure hose repairing with a repair fitting is showed in Fig. 2. The main idea of the reinforcement techniques is to transfer hoop stress [33], caused by the internal fluid pressure, from the defected area and cutted ends of the high-pressure hose to the steel sleeves and repair fitting.

The repaired hose should withstand not only internal fluid pressure but also external interference, such as environment loads, friction and heat transfer. This is because wide part of high-pressure hose external damage are the result of damage due hose friction with other surfaces or environment influences [39]. As a result, the fluid behaviour and it influence on energy consumption inside the repaired hose with repair fitting is required determination and compared with the fluid behaviour in the non-repair hose, since, the sudden cross-section changes hoses influence on pressure and energy parameters of the hydraulic system [19]. Unfortunately, during reviewing of similar researches on high-pressure hoses the mention problematic doesn't was found. The current research is proposes a model for investigation fluid behaviour

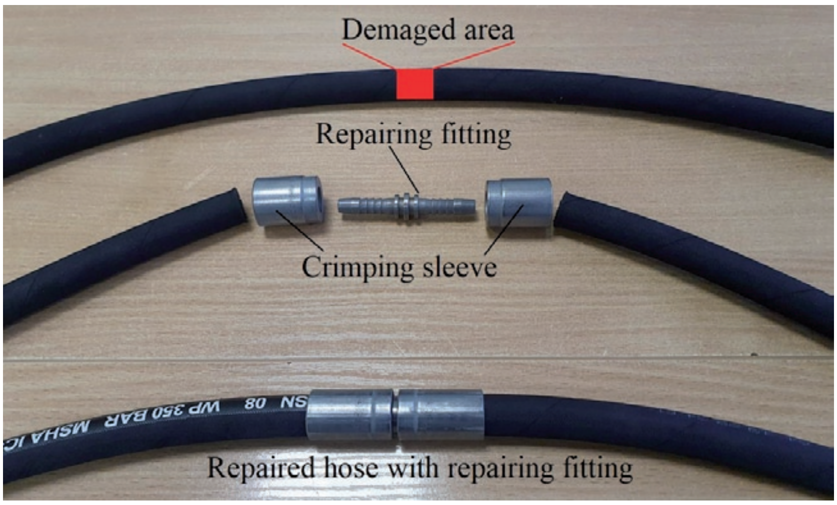

Fig. 2 Scheme of high-pressure hose repairing with a repairing fitting (hose junction)

inside repaired high-pressure hoses and it influences on energy parameter of hydraulic drive after maintenances.

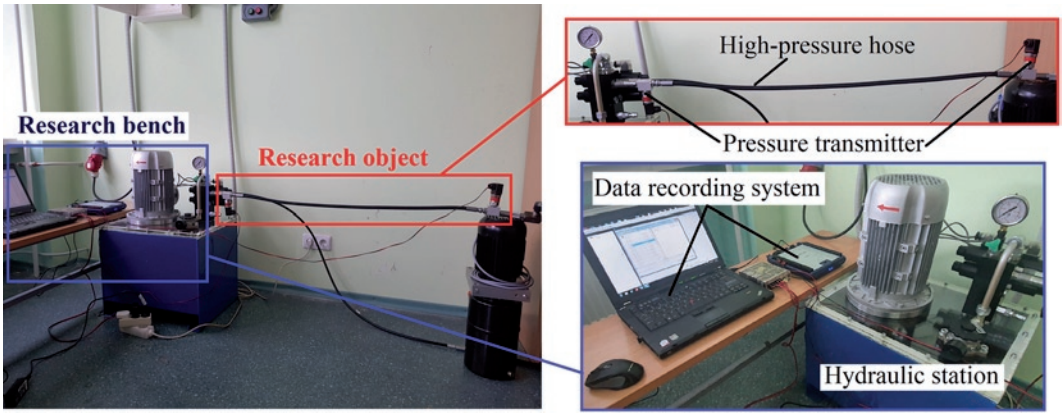

Fig. 4. An experimental bench for measuring of pressure drop inside a high-pressure hoses

3. Research objects

In presented research, for comparing analysis between flow characteristics inside repaired and non-repaired high-pressure hoses was used two metal braid reinforced hydraulic hose (2SN) according to European Standard [9] and repairing fitting connector (hose junction) according to International Standard [15]. The high-pressure hose with conditional passage 06 DASH (which is equal to the diameters 3/8" or 9.5 mm) and the same size hose junction for repairing is accepted for research. Parameters of used high-pressure hoses and hose junction in the research is presented in Table 1.

Table 1. Physical and geometrical parameters of the research objects

Research object	Inner diameter	Outer diameter	Max working pressure	Weight
High-pressure hose	3/8" or 9.5 mm	19 mm	350 bar	0.63 kg/m
Repair fitting	6.5 mm	3/8" or 9.5 mm	not indicated	0.04 kg

For numerical simulation, the cross-section of the 3D model of high-pressure hose with repair fitting is created. The cut in the connection of repair fitting (hose junction) and high-pressure hose is shown in Fig. 3.

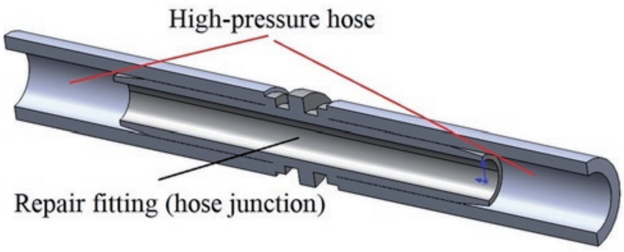

Fig. 3. View of cut in the connection of the repair fitting and high-pressure hose

The main issue in high-pressure hose with repair fitting connection is changes in the size and configuration of the cross-section area of the flow stream inside hydraulic line. The length of high-pressure hoses, used in the current research is 1 meter. Presented high-pressure hose and hose junction are International Certificate and are used in the most mobile machinery, vehicle and aviation hydraulic drives.

4. Pre-experimental part of the research

Pre-experimental part was conducted towards establishing the evidence of proposed research direction. The pre-experimental part of the current research included the measurement and analysis of pressure drop inside a high-pressure hose and high-pressure hose with repair fitting. The obtained results from the pre-experimental measurements is used for boundary conditions of numerical simulation model.

The experimental bench for the pre-experimental research is shown in Fig. 4. The main parameters in the research bench: fluid pressure ~ 2.5 MPa; flow rate ~ 50 l/min; high-pressure hose is 3/8"(9.5 mm); length of hoses is 1 meter; hose fittings connection standard and repairing fitting size – 06 DASH. The pre-experimental test performed via Multiple Measurement Design and based on One-Sample Statistical Method with Estimating Uncertainty in Repeated Measurements of data processing by [42].

From obtained measurement, after excluding a pressure drops on hydraulic tee fitting and hose connections, the actual fluid pressure on inlet and outlet of high-pressure hoses and high-pressure hose with repairing fitting is presented in Fig. 5.

Four measurements, for each high-pressure hose type, to eliminate data distortion (error between measurements) have been provided and is shown in Table 2.

Table 2. Percentage error between measurements

№ of fluid pressure measurement	Error value at high-pressure hose, %	Error value at at high-pressure hose with repairing fitting, %
1st measurement	1.04	1.28
2nd measurement	0.98	1.19
3rd measurement	1.14	1.31
4th measurement	1.09	1.07

The nominal fluid pressure different between inlet and outlet of high-pressure hoses is ~ $0.108 \cdot 10^6$ Pa for non-repaired high-pressure hose; ~ $0.151 \cdot 10^6$ Pa for repaired hoses was obtained. According to measuring and by graph can be pointed the installation of repair fitting inside high-pressure hose lead to incise the pressure losses inside a hydraulic drive system.

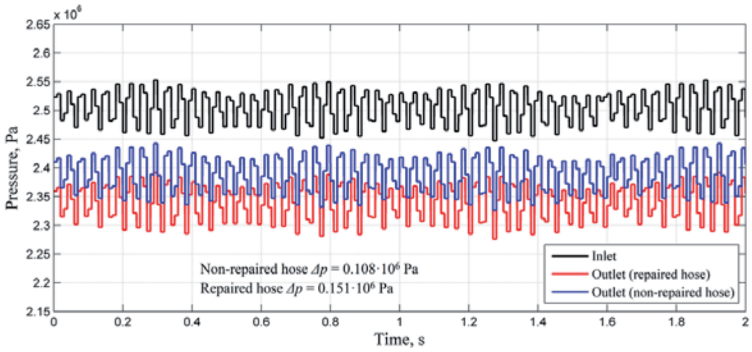

Fig. 5. The fluid pressure inside high-pressure hoses

5. Numerical modelling of fluid flow inside high-pressure hoses

Fluid movement is considered in 3D. Velocity (u, v, w) with a pressure depends on coordinates (x, y, z) and time (t). The dynamics of the fluid flow is governed by Navier–Stokes equations and is represented by the conservation of momentum. Thus, from mass conservation, the divergence of the velocity field is equal to zero ($\nabla u = 0$) [36, 41]. Movement and continuity equations for a viscous, compressible fluid in the research high-pressure hoses have the following form [12, 40]:

$$\begin{cases} \frac{\partial(\rho u)}{\partial t}+\frac{\partial(\rho u^2)}{\partial x}+\frac{\partial(\rho uv)}{\partial y}+\frac{\partial(\rho uw)}{\partial z}=-\frac{\partial p}{\partial x}+\frac{1}{\mathrm{Re}}\left[\frac{\partial\tau_{xx}}{\partial x}+\frac{\partial\tau_{xy}}{\partial y}+\frac{\partial\tau_{xz}}{\partial z}\right], \\ \frac{\partial(\rho v)}{\partial t}+\frac{\partial(\rho uv)}{\partial x}+\frac{\partial(\rho v^2)}{\partial y}+\frac{\partial(\rho vw)}{\partial z}=-\frac{\partial p}{\partial y}+\frac{1}{\mathrm{Re}}\left[\frac{\partial\tau_{xy}}{\partial x}+\frac{\partial\tau_{yy}}{\partial y}+\frac{\partial\tau_{yz}}{\partial z}\right], \\ \frac{\partial(\rho w)}{\partial t}+\frac{\partial(\rho uw)}{\partial x}+\frac{\partial(\rho vw)}{\partial y}+\frac{\partial(\rho w^2)}{\partial z}=-\frac{\partial p}{\partial z}+\frac{1}{\mathrm{Re}}\left[\frac{\partial\tau_{xz}}{\partial x}+\frac{\partial\tau_{yz}}{\partial y}+\frac{\partial\tau_{zz}}{\partial z}\right], \end{cases} \tag{1}$$

$$\frac{\partial\rho}{\partial t}+\frac{\partial(\rho u)}{\partial x}+\frac{\partial(\rho v)}{\partial y}+\frac{\partial(\rho w)}{\partial z}=0\,. \tag{2}$$

Computations of fluid flow inside high-pressure hoses were carried out employing commercial CFD software Ansys® Fluent®. The Standard k–ε turbulence model was selected to analyse fluid flow. For the application of the Standard k–ε turbulence model, the following transport equations for turbulent kinetic energy (k) and turbulent dissipation (ε) are implemented by [18, 21]:

$$\frac{\partial}{\partial t}(\rho k)+\frac{\partial}{\partial x_i}(\rho k u_i)=\frac{\partial}{\partial x_j}\left[\left(\mu+\frac{\mu_t}{\sigma_k}\right)\frac{\partial k}{\partial x_j}\right]+2\mu_t E_{ij}E_{ij}-\rho\varepsilon, \tag{3}$$

$$\frac{\partial}{\partial t}(\rho \varepsilon)+\frac{\partial}{\partial x_i}(\rho \varepsilon u_i)=\frac{\partial}{\partial x_j}\left[\left(\mu+\frac{\mu_t}{\sigma_\varepsilon}\right)\frac{\partial \varepsilon}{\partial x_j}\right]+C_{1\varepsilon}\frac{\varepsilon}{k}(2\mu_t E_{ij}E_{ij})-C_{2\varepsilon}\rho\frac{\varepsilon^2}{k}.$$

$$\mu_t=\rho C_\mu k^2/\varepsilon. \tag{4}$$

$C_{1\varepsilon}$, $C_{2\varepsilon}$, C_μ, σ_k, σ_ε – constants for Standard k-ε turbulence model (Table 3).

Multiphase simulation involves homogenous material, i.e. standard mineral hydraulic oil Hydraux HLP 46, that conforms to the DIN 51524-2:2016 [14]. The specification of oil, used in simulations, are shown in Table 4.

Table 3. Constants for Standard k–ε turbulence model

$C_{1\varepsilon}$	$C_{2\varepsilon}$	C_μ	σ_k	σ_ε
1.44	1.92	0.09	1.00	1.30

Table 4. Oil (HLP 46) specification used in numerical simulation

Properties	Value
Molar mass	300 kg/kmol
Density	874 kg/m^3
Kinematic viscosity	46 mm^2/s
Specific heat capacity	1966 J/kg·K
Ref temperature	40 C°
Reference pressure	$1\cdot10^5$ N/mm^2
Thermal conductivity	0.292 W/m·K

In the Fig. 6 shows the applied boundary conditions used to solve the compressible Navier–Stokes equations with a Standard k–ε turbulence model for fluid flow simulation inside high-pressure hoses.

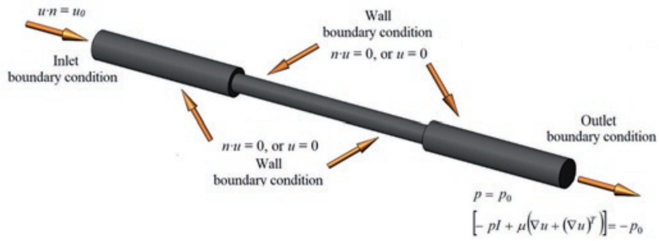

Fig. 6. Boundary conditions of the fluid flow for Ansys® Fluent® simulation

The inlet boundary and specified by a velocity vector what is normal to the inlet:

$$u{\cdot}n = u_0. \tag{5}$$

In the figure above and equation *n* is a unit vector that has a direction perpendicular to a boundary or normal to a boundary. For the outlet, certain pressure in the outlet/pressure boundary condition is imposed:

$$\begin{gathered} p=p_0 \\ \left[-pI+\mu\left(\nabla u+(\nabla u)^T\right)\right]=-p_0. \end{gathered} \tag{6}$$

The wall boundary condition states that due to fluid flow, the velocity of fluid near the wall is equal to zero:

$$n{\cdot}u = 0. \tag{7}$$

The numerical simulation of fluid flow inside high-pressure hoses was developed employing the Ansys® Workbench®. The numerical code was based on the Finite Volumes Method. The investigation area covered a 3D volume closed from all sides and divided into tetrahedrons. The dependent pressure, velocity and turbulent kinetic energy variables as well as volume fraction were calculated for each node of flow-element according to [2]. The mesh refined near changes in the cross-section area and around restrictive objects, according to [23], in order to obtain more accurate to experimental measurements. Close to the walls, boundary layers maximally affect velocity gradients in the normal direction to the wall. Thus, ten inflation layers were created with an expansion factor of 1.2…1.6 depending on changes in diameter. The mesh independence study was performed according to [19].

Ansys® Fluent® simulation was performed to established pressure drop (*Δp*) in research objects fluid flow and taken at a rate from 5 to 100 *l/min*. The *Re* number for both case is provided in the chart of Fig. 7. The total pressure profile of fluid inside repaired and non-repaired hoses are displayed in Fig.8. The additional results of numerical simulation are provided in Fig. 9.

According to Reynolds number chart, the turbulence of fluid flow inside repaired hose started at the flow rate (in the inlet of hose) of

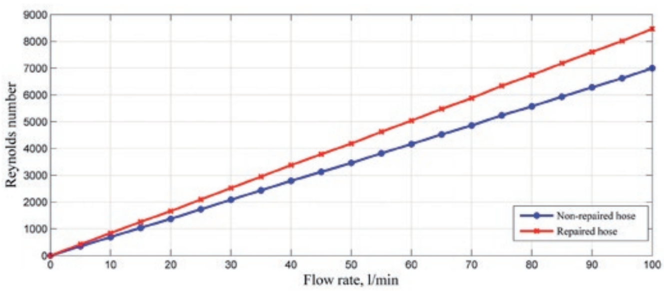

Fig. 7. The diagram of depending Re number from flow rate

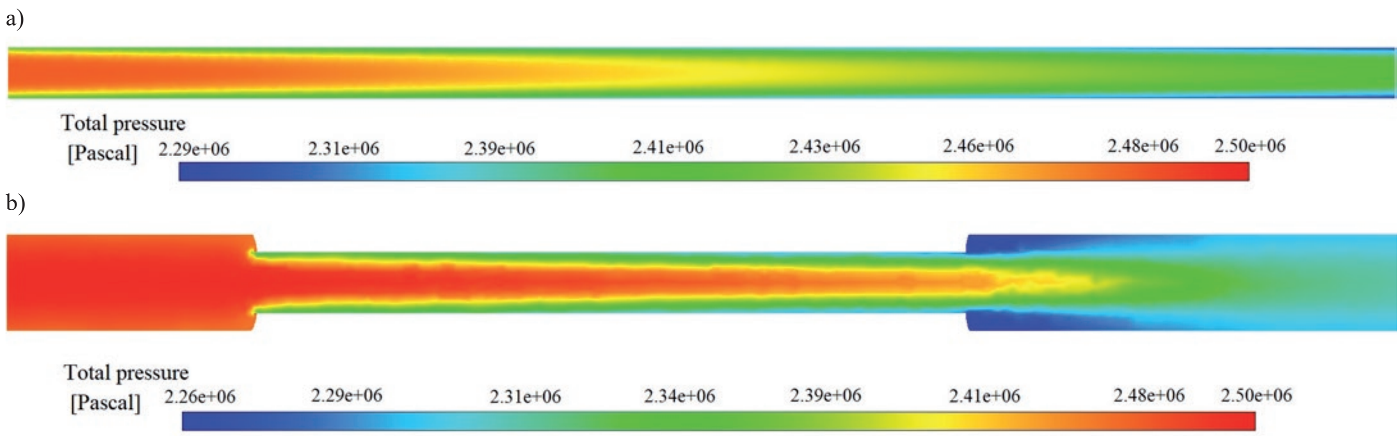

Fig. 8. Total fluid pressure inside high-pressure hoses: a) non-repaired hoses; b) repaired hose

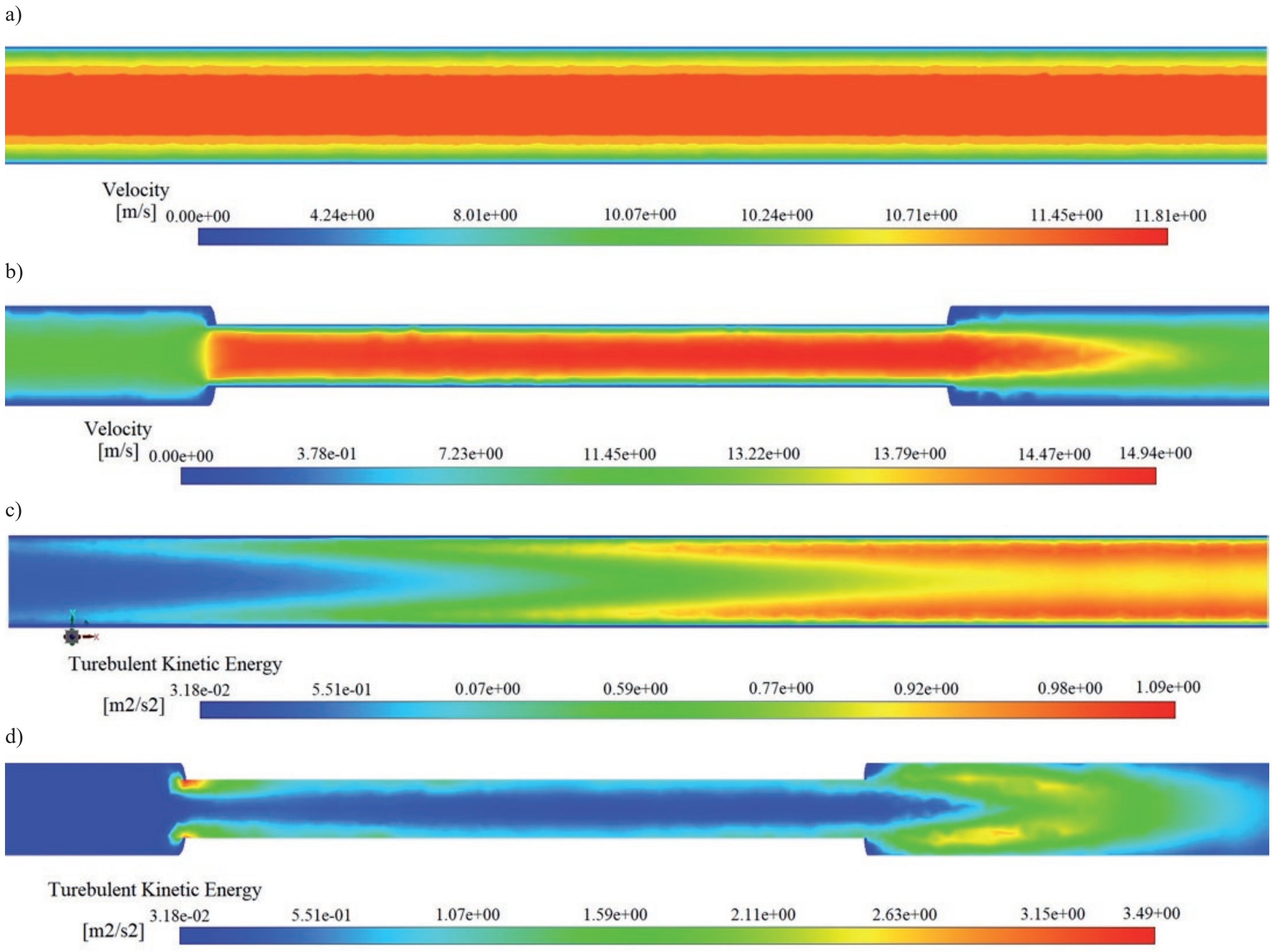

Fig. 9. Additional results from the fluent simulation: a) velocity inside non-repaired hose; b) velocity inside repaired hose; c) turbulence kinetic energy inside non-repaired hose; d) turbulence kinetic energy inside repaired hose

approximately 28 l/min, and that for non-repaired hose – at a flow rate of 34 l/min, which confirms that the installation of repairing fitting, during maintenance, significant influenced on fluid flow inside a high-pressure hoses.

All above introduced results were taken from Ansys® Fluent® simulation where in inlet upload velocity was 11.764 m/s, which corresponded to the flow rate of 50 l/min in the inlet of hoses.

The flow coefficient (μ) is a relative measure of high-pressure hose efficiency at an allowed fluid flow. The coefficient describes the relationship between pressure drop (Δp) across the orifice and the corresponding flow rate:

$$\mu = \frac{Q}{A\sqrt{\frac{1}{1-b^4}}\sqrt{2\Delta p / \rho}} \tag{8}$$

where $b = d/D$, where b – cross section diameter of fluid flow, m; D – diameter of the high-pressure hose, m; d – diameter of repairing fitting, m; Q – flow rate, m^3/s; A – average cross-section area of hose before and after repairing, m^2; Δp – pressure drop, Pa; ρ – fluid density, kg/m^3.

For repaired and non-repaired high-pressure hoses the funded flows coefficient is shown in Fig. 10.

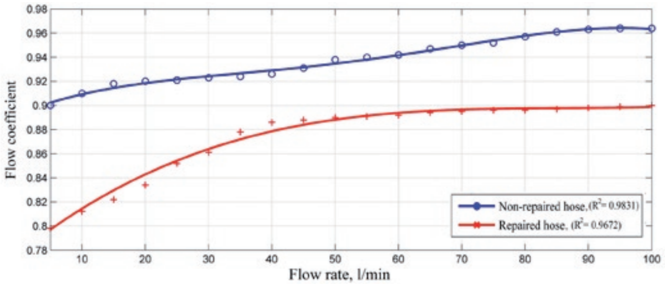

Fig. 10. Flow coefficient at a different flow rate for repaired and non-repaired hoses

The research demonstrated that non-repaired hose performed in the most efficient way (flow coefficient ranged from 0.91 to 0.962) than repaired hose (from 0.798 to 0.903). The difference between changes in the cross-section areas had a significant impact on flow characteristics. Changes in the cross-section areas of repaired hose were higher than those in standard hose. Difference between flow coefficients, which made ~ 14% at the beginning of the chart (laminar processes) is observed. However, in terms of the turbulence of flow processes, the two type of hoses have the more close flow characteristics. The difference in the flow coefficient, because of flow turbulence, between repaired and non-repaired hoses was ~ 9%. This proves that changes in the cross-section areas inside investigated hoses had more influence on laminar flow`s processes than on flow's turbulence.

According to proposed numerical model of the determination hydrodynamic processes inside repaired and non-repaired high-pressure hoses the pressure losses, as well as flow coefficients can be established. The obtained results will help for evaluation the power losses on different flow rate inside investigated hoses.

6. Analysis of the energy efficiency

According to [7] and [24] researches – the less pressure drops exist in a system, the less power cost of hydraulic units can be obtained. According to achieved results of pressure losses from numerical modelling, power losses at each type of hoses were calculated by different flow rates. Power losses (N_l) are calculated using equation:

$$N_l = \frac{1}{\eta_p \eta_d} Q_i \Delta p_i \,, \tag{9}$$

where Δp_i – hydraulic loses at the *i-th* hydraulic hose of the system; η_p – overall efficiency of hydraulic pump; η_d – efficiency of the pump-motor drive; Q_i – flow rate at the *i-th* hydraulic hose of the system.

a) b)

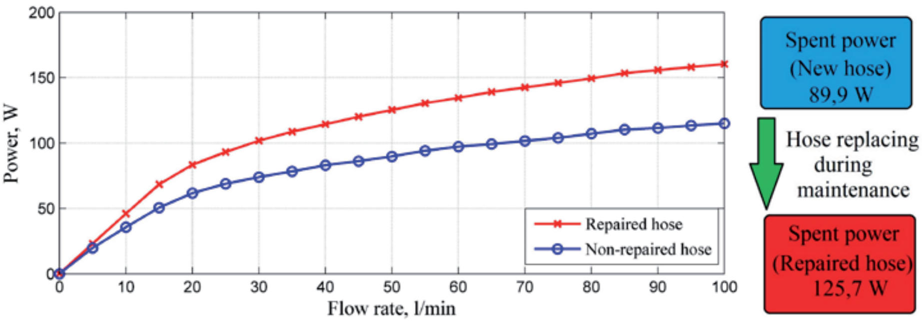

Fig. 11. Energy graphs: a) graph of power losses using repaired and non-repaired high-pressure hoses; b) the energy flow chart when high-pressure hose during maintenance is repaired

Power losses by using repaired and non-repaired hoses for hydraulic drive is presented in Fig. 11a (by one meter of each high-pressure hose).

Research on power losses in repaired hoses demonstrate insignificant power losses (from 22.98 W to 160.34 W at flow rate from 5 l/min to 100 l/min) compared to non-repaired hose (ranged from 7.85 W to 131.42 W). Although the pressure losses for one repaired hoses are not significant, but in modern transport vehicles hydraulic drive can be over than 100 high-pressure hoses. Even if 10% from all hoses of the system will be repaired that significantly effects on theresistance and loss in all hydraulic system.

The analysis of the investigated high-pressure hoses energy efficiency and its influence on the hydraulic system is presented on example by applied parameters of hydraulic system by experimental measuring and validated fluent model, by flow rate – 50 l/min (middle range). The energy flow charts (Fig. 11b) is applicable for illustration energy transformation visually and quantitatively during replacing damaged high-pressure hose by repaired hose with junction fitting. The obtained results showed that the better options for energy saving in the hydraulic drive could be reached using non-repaired hose (spent power – 89.9 W), compared to repaired hose (spent power – 125.7 W), on length one meter. The difference on spent power 35.8 W (28.4%) compered to whole hydraulic power is a not significant, but taking in an account the sum of all repaired hoses in the system and time of machinery operation during the year, from the economical side the changes of damages hoses on a new can be more rational than repairing hose during a maintenance. For future research, it will be useful to investigate the compact versions of high-pressure hoses after repairing with expand experimental setup and numerical simulation taking in account a temperature analysis and hoses vibration, since installation of repairing fitting influence on hose mechanical behaviour.

7. Conclusion

In the present research, by experimental measuring's and numerical simulation, compared a repaired high-pressure hose and non-repaired hose. As a result of the research, pressure drops at different fluid flow rates (from 5 to 100 l/min), hence flow coefficients was determined. Was found that non-repaired hose performed in the most efficient way (flow coefficient ranged from 0.91 to 0.962) than repaired hose (flow coefficient ranged from 0.798 to 0.903).

The difference between changes in the cross-section areas had a significant impact on flow characteristics. Changes in the cross-section areas of repaired hose were higher than those in non-repaired hose. Difference between flow coefficients, which made around 14% at the laminar processes and around 9% at turbulent processes is observed. The results was identified that turbulence started in repaired hoses at a range of 28 l/min, which explained a significant jump in the flow coefficient. As for the non-repaired hose turbulent processes started following 34 l/min, because changes in the hydraulic diameter hardly occurred in the case of the straight pipeline.

By the proposed numerical model of the determination hydrodynamic processes inside repaired and non-repaired high-pressure hoses the pressure losses was established, what held to evaluate the power losses on different flow rate inside investigated hoses. Research on power losses in repaired hoses demonstrated insignificant power losses from 22.98 W to 160.34 W, compared to non-repaired hose, ranged from 7.85 W to 131.42 W.

In final it was disclosed that repairing of the hose with a junction fitting lead to achieve an increase of power losses and decrease hydraulic drive efficiency by replacing a high-pressure hoses on repaired hose, during machinery hydraulic drive maintenance.

References

1. ANSYS Fluent Theory Guide, 2013. ANSYS, Inc., 275 Technology Drive Canonsburg, PA 15317.
2. Biluš I, Škerget L, Predin A, Hriberšek M. Experimental and numerical analyses of the cavitational flows around a hydrofoil. Strojniški vestnik - Journal of Mechanical Engineering 2005; 51(2): 103-118.
3. Bogdevičius P, Prentkovskis O, Bogdevičius M. Transmission with cardan joint parametre influence to centrifugal pump characteristics. Mokslas – Lietuvos Ateitis / Science – Future of Lithuania 2017; 9(5): 559-564, https://doi.org/10.3846/mla.2017.1073.
4. Budinski M. Failure analysis of a rubber hose in anhydrous ammonia service. Case Studies in Engineering Failure Analysis 2013; 1(2): 156-164, https://doi.org/10.1016/j.csefa.2013.04.009.
5. Cho J. Anisotropic large deformation and fatigue damage of rubber-fabric braid layered composite hose. Procedia Engineering 2017; 173: 1169-1176. https://doi.org/10.1016/j.proeng.2016.12.097.
6. Doerfler P, Sick M, Coutu A. Flow-induced pulsation and vibration in hydroelectric machinery. Engineer's guidebook for planning design and troubleshooting, Springer-Verlag 2013: 242, https://doi.org/10.1007/978-1-4471-4252-2.
7. Domagała Z, Kędzia K, Stosiak M. The use of innovative solutions improving selected energy or environmental indices of hydrostatic drives. IOP Conference Series. Materials Science and Engineering 2019; 679(1): 12, https://doi.org/10.1088/1757-899X/679/1/012016.
8. Drumond G, Pasqualino I, Ferreira da Costa M. Study of an alternative material to manufacture layered hydraulic hoses. Polymer Testing 2016; 53: 29-39, https://doi.org/10.1016/j.polymertesting.2016.05.003.
9. European standard. EN 853 2SN:2015. Rubber hoses and hose assemblies. Wire braid reinforced hydraulic type. Specification 2015; 17.
10. Fedorko G, Molnar V, Dovicab M, Tothb T, Fabianova J. Failure analysis of irreversible changes in the construction of the damaged rubber hoses. Engineering Failure Analysis 2015; 58(1): 31–43, https://doi.org/10.1016/j.engfailanal.2015.08.042.
11. Firoozabad E, Jeon B, Choi H, Kim N, Failure criterion for steel pipe elbows under cyclic loading. Engineering Failure Analysis 2016; 66: 515-525, https://doi.org/10.1016/j.engfailanal.2016.05.012.
12. Foias C, Manley O, Rosa R, Temam R. Navier-Stokes equations and turbulence (Encyclopedia of Mathematics and its Applications). Cambridge: Cambridge University Press 2001; 347, https://doi.org/10.1017/CBO9780511546754.
13. Gates Corporation. A Guide to Preventive Maintenance & Safety for Hydraulic Hose & Couplings. Printed in Denver, USA by Tomkins Company 2009; 76, http://www.marshall-equipement.com/Library/SafeHydraulics.pdf.
14. German Institute for Standardisation. DIN 51524-2:2016. Pressure Fluids – Hydraulic Oils – Part 2: HLP Hydraulic Oils, Minimum Requirements. Specification 2016; 11.
15. International Organization for Standardization. ISO 8434-1:2018. Metallic tube connections for fluid power and general use — Part 1: 24° cone connectors. Specification 2018; 51.
16. Karpenko M, Bogdevičius M. Review of energy-saving technologies in modern hydraulic drives. Science – Future of Lithuania - Mokslas – Lietuvos Ateitis 2017; 9(5): 553–558, https://doi.org/10.3846/mla.2017.1074.
17. Karpenko M, Bogdevičius M. Investigation of hydrodynamic processes in the system – "Pipeline-Fittings". TRANSBALTICA XI: Transportation Science and Technology. TRANSBALTICA 2020; 331-340. Lecture Notes in Intelligent Transportation and Infrastructure. Springer, Cham, https://doi.org/10.1007/978-3-030-38666-5_35.
18. Karpenko M, Bogdevičius M. Investigation into the hydrodynamic processes of fitting connections for determining pressure losses of transport hydraulic drive. Transport 2020; 35(1): 108-120, https://doi.org/10.3846/transport.2020.12335.
19. Kubrak M, Malesińska A, Kodura A, Urbanowicz K, Stosiak M. Hydraulic transients in viscoelastic pipeline system with sudden cross-section changes. Energies 2021; 14(14): 4071, https://doi.org/10.3390/en14144071.
20. Kwak S, Choi N. Micro-damage formation of a rubber hose assembly for automotive hydraulic brakes under a durability test. Engineering Failure Analysis 2009; 16: 1262-1269, https://doi.org/10.1016/j.engfailanal.2008.08.009.
21. Launder B, Spalding D. Lectures in mathematical models of turbulence. Academic Press, London, England 1972; 16, https://doi.org/10.1002/zamm.19730530619.
22. Lee G, Kim H, Park J, Jin H, Lee Y, Kim J. An experimental study and finite element analysis for finding leakage path in high pressure hose assembly. International Journal of Precision Engineering and Manufacturing 2011; 12: 537–542, https://doi.org/10.1007/s12541-011-0067-y.
23. Lisowski E, Panek M. CFD modeling method of vanes working in the vane pump. Eksploatacja i Niezawodnosc - Maintenance and Reliability 2004; 2: 36-41.
24. Liu H, Zhang X, Quan L, Zhang H. Research on energy consumption of injection molding machine driven by five different types of electro-hydraulic power units. Journal of Cleaner Production 2020: 242: 1–11, https://doi.org/10.1016/j.jclepro.2019.118355.
25. Lu X, Huang M. Novel multi-level modeling method for complex forging processes on hydraulic press machines. The International Journal of Advanced Manufacturing Technology 2015; 79: 1869–1880, https://doi.org/10.1007/s00170-015-6970-0.
26. Lubecki M, Stosiak M, Bocian M, Urbanowicz K. Analysis of selected dynamic properties of the composite hydraulic microhose. Engineering Failure Analysis 2021; 125: 1-9, https://doi.org/10.1016/j.engfailanal.2021.105431.
27. Luczko, J., Czerwiński, A. 2014. Parametric vibrations of pipes induced by pulsating flows in hydraulic systems, Journal of Theoretical and Applied Mechanics, 52 (3): 719–730.
28. Mazurkiewicz L, Malachowski J, Damaziak K, Tomaszewski, M. Evaluation of the response of fibre reinforced composite repair of steel pipeline subjected to puncture from excavator tooth. Composite Structures 2018; 202: 1126–1135, https://doi.org/10.1016/j.compstruct.2018.05.065.
29. Mikota G. Modal analysis of hydraulic pipelines. Journal of Sound and Vibration 2013; 332(16): 3794 – 3805, https://doi.org/10.1016/j.jsv.2013.02.021.
30. Miller S. Systematic techniques of hose failure mode analysis. SAE Transactions 1991; 100: 687–703, http://www.jstor.org/stable/44632066.
31. Obrien P, Meldrum E, Overton C, Picksley J, Anderson K, Ian M. Outcomes from the SureFlex joint industry project - an international

initiative on flexible pipe integrity assurance. Paper presented at the Offshore Technology Conference, Houston, Texas, USA, May 2011, https://doi.org/10.4043/21524-MS.
32. Parvaresh A, Mardani M. Model predictive control of a hydraulic actuator in torque applying system of a mechanically closed-loop test rig for the helicopter gearbox. Aviation 2019; 23(4): 143-153, https://doi.org/10.3846/aviation.2019.11869.
33. Pavloušková Z, Klakurková L, Man O, Čelko L, Švejcar J. Assessment of the cause of cracking of hydraulic hose clamps. Engineering Failure Analysis 2015; 56: 14-19, https://doi.org/10.1016/j.engfailanal.2015.05.014.
34. Pelevin L, Machyshyn G, Bogdevičius M, Karpenko M. Assessment of application high pressure hoses using mathematical model calculation load distribution between the metal braid. Mining, constructional, road and melioration machines: AllUkrainian collection of scientific works 2016; 88: 64-70.
35. Pierce S, Evans J. Failure analysis of a metal bellows flexible hose subjected to multiple pressure cycles. Engineering Failure Analysis 2012; 22: 11-20, https://doi.org/10.1016/j.engfailanal.2011.12.005.
36. Santos F, Brito A, de Castro A, Almeida M, da Cunha Lima A, Zebende G, da Cunha Lima I. Detection of the persistency of the blockages symmetry on the multi-scale cross-correlations of the velocity fields in internal turbulent flows in pipelines. Physica A: Statistical Mechanics and its Applications 2018; 509(1): 294–301, https://doi.org/10.1016/j.physa.2018.06.009.
37. Romaniuk M. Optimization of maintenance costs of a pipeline for a V-shaped hazard rate of malfunction intensities. Eksploatacja i Niezawodnosc – Maintenance and Reliability 2018; 20 (1): 46–56, https://doi.org/10.17531/ein.2018.1.7.
38. Tawancy H, Al-Hadhrami L. Failure analysis of a welded outlet manifold pipe in a primary steam reformer by improper selection of materials. Engineering Failure Analysis 2009; 16(3): 816-824, https://doi.org/10.1016/j.engfailanal.2008.07.001.
39. Taylor C, Thompson J, Handewith H, Thimons E. Hose safety during high-pressure water-jet cutting. Information Circular by USA Bureau of Mines Information, Pittsburgh 1987; 9.
40. Urbanowicz K, Stosiak M, Towarnicki K, Bergant A. Theoretical and experimental investigations of transient flow in oil-hydraulic small-diameter pipe system. Engineering Failure Analysis 2021; 128: 105607, https://doi.org/10.1016/j.engfailanal.2021.105607.
41. Urbanowicz K, Bergant A, Kodura A, Kubrak M, Malesińska A, Bury P, Stosiak M. Modeling transient pipe flow in plastic pipes with modified discrete bubble cavitation model. Energies 2021; 14(20):6756, https://doi.org/10.3390/en14206756.
42. Vardeman S, Jobe M. Statistical methods for quality assurance: basics, measurement, control, capability and improvement. Part of the Springer Texts in Statistics book series (STS) Springer–Verlag, New York 2016: 437, https://doi.org/10.1007/978-0-387-79106-7.
43. Wei Q, Huailiang Z, Wenqian S, Wei L. Stress response of the hydraulic composite pipe subjected to random vibration. Composite Structures 2021; 255: 1-8, https://doi.org/10.1016/j.compstruct.2020.112958.
44. Yangyang Y, Mengjiang C. Sealing failure and fretting fatigue behavior of fittings induced by pipeline vibration. International Journal of Fatigue 2020; 136: 105602, https://doi.org/10.1016/j.ijfatigue.2020.105602.

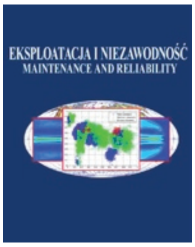

Eksploatacja i Niezawodnosc – Maintenance and Reliability

Volume 24 (2022), Issue 1

journal homepage: http://www.ein.org.pl

Article citation info:
Antunes Rodrigues J, Torres Farinha J, Mendes M, Mateus R, Marques Cardoso A. Short and long forecast to implement predictive maintenance in a pulp industry. Eksploatacja i Niezawodnosc – Maintenance and Reliability 2022; 24 (1): 33–41, http://doi.org/10.17531/ein.2022.1.5.

Indexed by: Web of Science Group

Short and long forecast to implement predictive maintenance in a pulp industry

João Antunes Rodrigues[a,b]*, José Torres Farinha[c,d], Mateus Mendes[c,e]*, Ricardo Mateus[b], António Marques Cardoso[a]

[a] CISE—Electromechatronic Systems Research Centre, University of Beira Interior, Calçada Fonte do Lameiro,62001-001 Covilhã, Portugal
[b] EIGeS - Research Centre in Industrial Engineering, Management and Sustainability, Lusófona University, Campo Grande, 376, 1749-024 Lisboa, Portugal
[c] Polytechnic of Coimbra – ISEC, Quinta da Nora, 3030-199 Coimbra, Portugal
[d] University of Coimbra, CEMMPRE - Centre for Mechanical Engineering, Materials and Processes, 3030-788 Coimbra, Portugal
[e] University of Coimbra, ISR - Institute of Systems and Robotics, 3004-531 Coimbra, Portugal

Highlights

- This article presents a predictive model for a wood chip pump system.
- The Ishikawa diagram and the FMECA analysis were used to identify possible causes of system failures.
- Development of an algorithm for predicting the values of equipment sensors in the short and long term.
- The prediction made through Neural Networks had a mean absolute percentage error in all variables lower than 10%.

Abstract

Predictive maintenance is very important for effective prevention of failures in an industry. The present paper describes a case study where a wood chip pump system was analyzed, and a predictive model was proposed. An Ishikawa diagram and FMECA are used to identify possible causes for system failure. The Chip Wood has several sensors installed to monitor the working conditions and system state. The authors propose a variation of exponential smoothing technique for short time forecasting and an artificial neural network for long time forecasting. The algorithms were integrated into a dashboard for online condition monitoring, where the users are alerted when a variable is determined or predicted to get out of the expected range. Experimental results show prediction errors in general less than 10 %. The proposed technique may be of help in monitoring and maintenance of the asset, aiming at greater availability.

Keywords

predictive maintenance, condition based maintenance, time series, artificial neural networks, forecasting.

1. Introduction

As technology evolves, industrial processes are forced to adapt. That is currently the case with Industry 4.0, which may require process changes in all areas, including tracking products[2], monitoring and predicting production [36], quality control [37], or condition-based maintenance [4], among other uses of sensor networks and algorithms.

Due to this fact, there is a need for maintenance departments to reorganize, integrate new sensors, and process collected data for better performance. Machine learning can be beneficial in quality management and control, reducing maintenance costs, and improving the overall manufacturing process. That can make a key difference in modern industries.

This article presents a case study, where data analysis is performed and a predictive system is developed for a wood chip pump system, operating in an industrial paper company. This asset had frequent failures on an axis. The pump shaft and its entire fastening system had a much shorter life cycle than recommended by the manufacturer. The shaft opened cracks quickly. The analysis aimed to determine the cause of failure, as well as other potential failures.

To identify all possible causes of malfunction, Ishikawa Diagram, and Failure Mode, Effects, and Criticality Analysis (FMECA) were used. After identification of the actual cause, sensors were installed for monitoring key condition variables of the system's equipment to improve its reliability.

A global analysis of the data collected from the sensors installed in each equipment, including their minimum and maximum expected values, is presented. The variables' behaviour is studied, including graphical analysis for visualization, and forecast algorithms based on time series and Artificial Neural Networks (ANN) are applied.

A short term prediction model, with a gap of 5 days, was implemented, based on the common technique of exponential smoothing. A long term prediction model, with a gap of 3 months, was implemented, based on artificial neural networks. The short term gap of 5

(*) Corresponding author.

E-mail addresses: J. Antunes Rodrigues (ORCID: 0000-0002-8210-5468): p5942@ulusofona.pt, J. Torres Farinha (ORCID: 0000-0002-9694-8079): tfarinha@isec.pt, M. Mendes (ORCID: 0000-0003-4313-7966): mmendes@isec.pt, R. Mateus (ORCID: 0000-0003-3630-6426): p5768@ulusofona.pt, A. Marques Cardoso (ORCID: 0000-0001-8737-6999): ajmc@ubi.pt

days is adequate for the company to prepare small interventions. The long term gap allows the company to adequately prepare and schedule maintenance interventions, thereby avoiding loss of production and optimizing downtime. The duration of the gaps was decided so that a competitive advantage is achieved by reducing maintenance downtime and increasing production time.

A dashboard was developed, in which some alerts are displayed through semaphores, along with some quantitative and graphical information.

The system is designed to avoid unexpected failures and to reduce costs as much as possible, which are two of the main objectives of a good maintenance policy [22].

The present paper describes a case study where different diagnostic and prediction tools are combined to improve maintenance performance and maximize equipment availability. The fault diagnosis methodology as well as the prediction method proposed can be adapted and applied to other equipment. Fault diagnosis methods are suitable for any type of equipment, while the machine learning methods can be applied to any dataset with adaptations and proper training.

The paper is organized as follows. Section 2 presents related work and the theoretical framework. Section 3 describes the chip pump system and its diagnosis. Section 4 presents the system's condition monitoring variables. Section 5 is about the condition variables global analysis. Section 6 presents the approach about short time forecast. Section 7 proposes the approach of long- time forecast. Finally, section 8 draws some conclusions and proposes future work.

2. Background

2.1. Predictive Maintenance and Diagnosis

Predictive maintenance aims to maximize the system's availability, based on the identification of the weakest components of this physical asset [29].

According to the European Standard EN 13306:2017, a failure is the loss of the ability of an item to perform a required function after its failure, which may be complete or partial [38].

Predictive maintenance currently uses a lot of hardware to collect and store data and software to analyse it. Farinha (2018) presents an overview of the subject [9]. The purpose of predictive maintenance is to enable proactive scheduling of corrective work and thus avoiding unexpected equipment failures [33].

Maintenance optimization is a priority, due to the great trend in simulation-based optimization [28]. Currently, the best maintenance plans are tirelessly sought to minimize the overall cost of maintenance or to maximize the production and availability of assets [31]. Maintenance costs can reach 50% of production costs, which reinforces the importance of improving this area [1][26].

Predictive maintenance has evolved since visual inspection, which was its first method. Currently, with the advance of sensors and computer power, several advanced signal processing techniques are used based on pattern recognition, classification, clustering, and prediction algorithms [25].

According to FMECA reliability theory process, several types of failure mode, reasons, effects, and criticality of assets can be determined [16].

After detecting all possible failures through the Ishikawa Diagram and subsequent FMECA analysis, the main objective of predictive maintenance is to avoid the same failures by predicting them in advance.

2.2. Industry 4.0 in Industrial Maintenance

As hardware prices decrease and computing power increases, the Internet of Things (IoT) is increasingly more present in the industry [12][6]. That is a key factor to make processes predictable, simpler, controllable, and efficient, thus reducing equipment manufacturing and maintenance costs as much as possible [35].

Industry 4.0 is a result of the technological revolution, thus helping predictive maintenance [19][34]. In such a globalized and competitive market, it is necessary to make decisions about people and equipment all the time. Predictive maintenance decisions of this kind, in general, depend on massive amounts of data [7][30]. Predicting with low error the need to perform maintenance operations on the assets at a certain future point in the medium and long term is one of the main challenges in this field [14].

Due to the importance that IoT has acquired in recent years in industry and maintenance, a new concept applied specifically to the industrial sector has emerged, which is Industrial Internet of Things (IIoT).

To have an accurate forecast, it is imperative to have timely calibration and certification of industrial sensors. This is indispensable because, without the support of metrology based on measurement quality, there could be evaluation errors and discrepant data, which can result in prediction errors, poor forecasting, risks, large costs, and, consequently, loss of confidence from the market [23].

According to Hashemian, condition-based maintenance techniques for equipment and industrial processes are divided into three categories. The first category uses signals from existing process sensors, such as resistance temperature detectors and thermocouples, to help verify the performance of assets [13]. The second category depends on signals from test sensors that are installed on the equipment. The third category involves injecting a test signal into the equipment. The present work falls into the second type, as it depends on sensor signals that are installed in the equipment to measure the operational parameters.

2.3. Other Related Work

In this section some works are presented, whose aim is to predict the values of sensors installed in equipment, stressing the important of this research field for predictive maintenance using Artificial Intelligence (AI).

Kanawaday *et al.* took advantage of the machine data generated by various sensors by applying different data analysis algorithms to obtain information that help in making decisions [17]. The data captured by the sensors were always accompanied by the date and time, both of which are vital parameters for predictive modelling. The same authors used the Auto Regressive Integrated Moving Average (ARIMA) forecast in the sensor database of a longitudinal cutting machine [11][10][8].

Short-term forecasting work in maintenance has also been carried out by other authors. However, it should be noted that those studies are only focused on short-term forecasting, which shows a clear limitation in the area of long-term forecasting. An example of this type of study is the work presented below.

Kolocas *et al*. presented a predictive maintenance methodology to predict possible equipment failures of an industrial equipment in real time, using data from process sensors of operation periods. The alert period for the failure of the asset is forecasted in short-term, since a forecast gap was defined around 5-10 minutes before the incident occurred [20].

The following review section demonstrates a promising avenue of research in the use of neural networks in the area of predictive maintenance.

Tian [32] developed an Artificial Neural Network (ANN) based method designed to achieve more accurate remaining life prediction of equipment subject to condition monitoring. The proposed ANN method is validated using vibration monitoring data collected from pump bearings. The ANN model has as input to the network the age of the equipment and current condition measurement values and inspection performed. The network gives a percentage of the asset's life as an output.

Rafiee *et al*. [27] used a 2-layer perceptron neural network to detect gear and bearing failures and identify gearboxes using a new feature vector updated by the standard deviation of wavelet packet coefficients of vibration signals. Synchronization of vibration signals used cubic Hermite interpolation by parts.

Heidarbeigi *et al*. [15] developed a neural network built to predict gearbox failures. In this project a backpropagation learning algorithm and a multilayer network were used. The network has three classification outputs, which are: worn, broken teeth of gear, and faultless condition. The ideal Multilayer Perceptron Neural Network (MLP) selected for classification exhibited a 489-10-3 layer structure and had 87% accuracy. The model shown works based on vibration differences, so it can be used in other applications.

Karpenko [18] developed a neural network pattern classifier to diagnose and identify failures in an actuator of a Fisher-Rosemount 667 industrial process valve. The network is trained with experimental data obtained from the asset. The test results show that the resulting multilayer feedforward network can detect and identify various types of failure.

Wang [33] presents an artificial intelligence algorithm based on neural networks to identify failures in diesel engine lubrication pumps using vibration data. The algorithm has been tested on more than fifty lube pumps which have proven its effectiveness.

The studies mentioned above show that neural networks using monitoring data such as vibration and temperature can detect and even anticipate failures. That is useful in the diagnosis of faults with high reliability, as well as foreseeing potential failures and preventing them from happening. The research carried out also shows that there is gap in a long-term forecasts, specially predicting with 3 months advance. Nonetheless, this should be a research goal, because industries often need several weeks to prepare and carry out complex maintenance operations with minimum downtime.

3. Chip Pump System: Problem and Diagnosis

The chip pump system is depicted in Figure 1. It comprises three chip pumps, each one fed by one asynchronous motor through a mechanical connection. The inputs of the system are wood chips and liquor. The final product is a mixture of them.

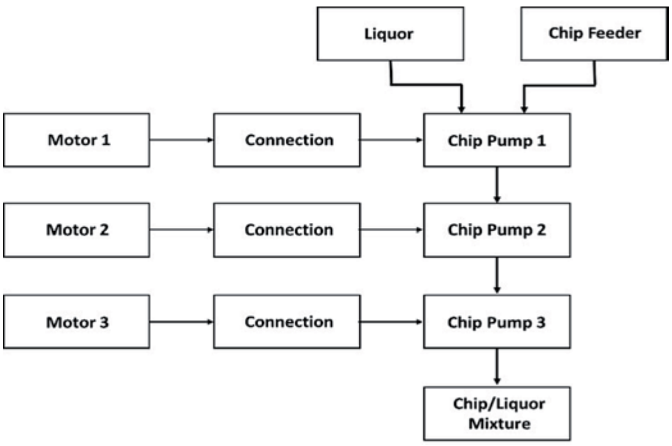

Fig. 1. Chip Pump System

The company found that the shaft of the chip pump 3 depicted in Figure 1 had shorter life services than expected. Frequent failures on that chip pump had led to cracks in the shaft, damaging its fixation cones.

Pressure is an important parameter in diagnosis, and active diagnosis is a proposal for future work to be developed after this manuscript. After several measurements, it was concluded that the pressure exerted by the mixture at the output of the chip pump increases, as shown in Figure 2.

Ishikawa diagrams allow to carry out an exhaustive diagnosis of the potential causes of equipment defects [5]. Figure 3 shows the Ishikawa diagram carried out for the fissure or breakage of the shaft and cone of the chip pump 3.

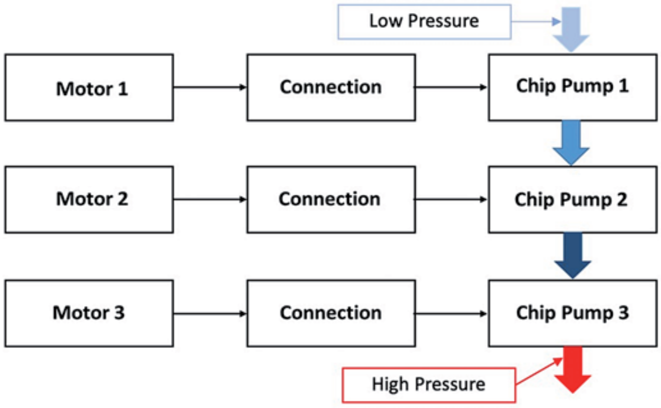

Fig. 2. Pressure increases throughout the system

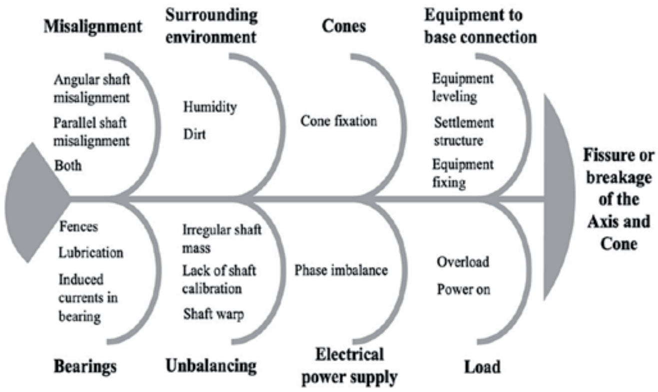

Fig. 3. Ishikawa diagram about fissure or breakage of the shaft and cone

The previous root-cause approach was complemented by a FMECA following the guidelines given by the IEC 60812:2018 [24].

FMECA allows the identification of the main possible problems in the asset. This type of analysis can be developed through a hierarchy of potential failures, complemented by a list of recommendations for avoiding them through maintenance techniques.

Through FMECA it is possible: to develop a working method; to evaluate modes of failure and their impact, to organize them; to identify the points of failure and verify the integrity of the system; to resolve failures faster; and, finally, to define criteria for tests and verifications that must be included in the preventive maintenance plan. A failure analysis can be used to understand the asset's failure mechanism. FMECA includes Failure Mode and Effect Analysis (FMEA) and the Criticality Analysis (CA) [3], [21].

The main problem was identified as the "fissure or breakage of shaft and cone", according to the FMECA matrix illustrated in Figure 4.

Based on the Ishikawa diagram and the FMECA analysis, and subsequent vibration analysis, it was possible to conclude that the actual cause of the defects was the poor seating of the chip pump machine, which was causing excessive vibration, cracking the shaft and consequently damaging the cones.

4. Chip Pump System Monitoring

Following the correction of the problem, the company decided to install a monitoring system over the key variables identified in the Ishikawa and FMECA analysis.

The system has the following sensors to monitor its condition: accelerometers; temperature sensors in roller bearings, in oil circuits, and in motor windings; load sensors; pressure sensors; flow meters; and rotation meters. Sensor readings are recorded every minute.

Figure 5 gives a global vision of the variables that are continuously monitored.

Equipament	Chip Pump				Prepared by		Team Company					
Team	Company				Date		2021					
Equipment Module	Function	Failure Mode	Failure Effect	Severity	Potential Cause of Failure	Occurrence	Preventive Action	Detection Action	Detection	RPN	Recommended Actions	Responsible and Deadline
Chip Pump (412-306)	Mechanical Traction / Mechanical Transmission	Crack or breakage of shaft and cone	Stop system for Chip Pump (412-306) and production system		**Misalignment**							
				2	Angular shaft misalignment	1	Angular alignment	Vibration Analysis	3	6	Perform alignment	
				2	Angular shaft misalignment	1	Angular alignment	Vibration Analysis	3	6	Perform alignment	x
				3	Angular and parallel shaft misalignment	2	Angular and parallel alignment	Vibration Analysis	3	18	Perform alignment	
					Imbalance							
				3	Irregular shaft mass	1	Regulate the mass	Vibration Analysis	4	12	Replacement	
				3	Lack of shaft calibration	1	Calibration	Vibration Analysis	3	9	Perform calibration	
				3	Wash Shaft	1	Replacement	Vibration Analysis	3	9	Replacement	
					Cones							
				4	Cone fixing	1	Fix the cone	Vibration Analysis	3	12	Perform predictive inspection	
					Connecting the equipment to the base							
				4	Leveling of equipment	2	Leveling the equipment	Vibration analysis and leveling check	3	24	Inspect settlement	
				4	Equipment laying structure	4	Fix the equipment	Visual displacement of the equipment	1	16	Inspect settlement	
				4	Fixing the equipment	4	Fix the equipment	Visual displacement of the equipment	1	16	Using standard screws	
					Environment							
				2	Humidity	1	Correct infiltrations	Existence of fungi	1	2	Perform isolation	
				2	Dirtiness	1	Check the cleaning of the equipment	Existence of dirt	1	2	Perform a clean-up	
					Bearings							
				2	Seals	4	Leak control or replacement	Leak checking	1	8	Perform lubrication	
				2	Lubrication	1	Lubricate bearings	Excessive friction in bearings	2	4	Perform lubrication	
				2	Induced currents in bearing	1	Improve housing insulation	Measurement of the current in the rotor	4	8	Improve housing insulation	
					Electric Power							
					Engine windings temperature		Download load	Temperature Measurement of windings			Do not exceed the recommended load	
				3	Phase imbalance	2	Balance phases	Phase measurement	1	6	Systemic phase control	
					Load							
				4	Overload	4	Respect the maximum recommended load	Analysis of Vibrations, Temperature and Electric Currents of the Motor	3	48	Follow the equipment standard	
				4	Start	4	Start at the proper speed in sequence and in conjunction with the start-up of the previous pumps	Tachometers / Voltimeters and Amperimeters	4	64	Follow the manufacturer's procedures	

Fig. 4. FMECA analysis of fissure or breakage of shaft and cone

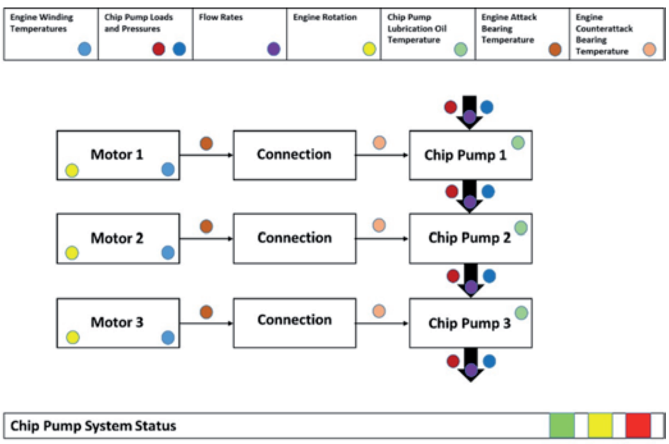

Fig. 5. Global vision of the variables that are continuously monitored

A more sophisticated algorithm to determine the relationship between predicted variables and the possibility of asset failure is out of the scope of the current project. That is a work to be developed in the future, in a separate project. The goal of the present project is just to monitor the equipment status and to predict future values. A short time prediction is performed, to anticipate future values five days in advance. A long-time prediction is performed, for three months in advance.

Relying on the forecast results, the company can anticipate malfunctions when peaks or ebbs in the predicted parameters are detected. By preventing and anticipating these failures, the company reduces its operating and maintenance costs.

5. Condition variable global analysis

The first analysis made on the condition monitoring variables was about their average and amplitude. The average, minimum and maximum values, and the time when the two latter occurred, were analyzed for all variables: vibration; temperature of attack and counterattack bearings, oil, and motor windings; load; pressure; flow; and rotation velocity.

This section presents statistics of temperature and pressure values for the three chip pumps from May 2017 to August 2019 (Tables 1-4). Pressure increases significantly throughout the system, as the mixture increases density.

Table 2 presents a comparison of engine winding temperatures from May 2017 to August 2019.

6. Short Time forecast

The short time forecast is based on an Exponential Smoothing self-adaptive, model according to Formula (1).

$$S_{t+1} = \alpha_t \times X_t + (1 - \alpha_t) S_t \qquad (1)$$

Table 1. Analysis of Pressures before and after each Chip Pump

	Pressure before chip pump 1			Pressure after chip pump 1			Pressure after chip pump 2			Pressure after chip pump 3		
Year	**Average value (kPa)**	**Max. value (kPa)**	**Max. value date**	**Average value (kPa)**	**Max. value (kPa)**	**Max. value date**	**Average value (kPa)**	**Max. value (kPa)**	**Max. value date**	**Average value (kPa)**	**Max. value (kPa)**	**Max. value date**
2017	-	-	-	357.67	1031.45	2017-12-05 11:01	678.12	1492.63	2017-08-09 12:22	1007.29	1201.84	2019-06-17 16:47
2018	46.57	160.16	2018-12-12 21:51	357.19	565.89	2018-02-04 02:50	685.23	1547.28	2018-11-16 12:14	995.44	1187.94	2018-06-26 11:22
2019	48.31	162.68	2019-01-23 08:03	361.64	558.97	2019-07-18 12:32	676.26	909.47	2019-06-05 11:29	1023.69	1244.60	2019-07-22 11:54

Table 2. Chip pump lubricating oil temperature

	Chip pump 1 lubricating oil temperature			Chip pump 2 lubricating oil temperature			Chip pump 3 lubricating oil temperature		
Year	**Average value (°C)**	**Max. value (°C)**	**Max. value date**	**Average value (°C)**	**Max. value (°C)**	**Max. value date**	**Average value (°C)**	**Max. value (°C)**	**Max. value date**
2017	36.1	43.11	2017-11-03 21:26	37.47	51.42	2017-01-16 13:26	36.56	44.56	2017-11.03 21:26
2018	-	-	-	42.54	108.19	2018-09-28 15:44	42.71	64.87	2018-10-04 12:43
2019	54.18	61.72	2019-07-26 13:18 2019-07-06 13:19	54.07	62.5	2019-07-26 13:15	54.28	62.23	2019-03-24 12:22

Table 3. Temperature analysis of the drive pump bearing for the chip pump

	Temperature analysis of the drive pump bearing for the chip pump 1			Temperature analysis of the drive pump bearing for the chip pump 2			Temperature analysis of the drive pump bearing for the chip pump 3		
Year	**Average Value (ºC)**	**Max. Value (ºC)**	**Max. Value Date**	**Average Value (ºC)**	**Max. Value (ºC)**	**Max. Value Date**	**Average Value (ºC)**	**Max. Value (ºC)**	**Max. Value Date**
2017	53.58	76.87	2017-08-03 13:06	58.99	83.36	2017-10-01 16:48	68.53	95.58	2017-10-27 15:03
2018	63.75	94.62	2018-08-03 18:28	71.69	93.29	2018-08-03 18:31	72.16	105.78	2018-09-25 14:06
2019	62.02	89.37	2019-05-30 15:14	64.33	95.71	2019-05-12 17:33	68.46	105.32	2019-07-09 18:57

Table 4. Temperature analysis of the counterattack bearing to the chip pump motor

	Temperature analysis of the counterattack bearing for the chip pump 1			Temperature analysis of the counterattack bearing for the chip pump 2			Temperature analysis of the counterattack bearing for the chip pump 3		
Year	**Average Value (ºC)**	**Max. Value (ºC)**	**Max. Value Date**	**Average Value (ºC)**	**Max. Value (ºC)**	**Max. Value Date**	**Average Value (ºC)**	**Max. Value (ºC)**	**Max. Value Date**
2017	27.36	46.22	2017-06-20 12:12	27.71	53.90	2017-06-20 12:12	24.45	57.38	2017-06-20 14:22
2018	27.83	55.95	2018-10-03 15:02	27.93	58.86	2018-10-03 15:08	25.60	56.68	2018-10-03 15:04
2019	27.98	48.32	2019-07-11 13:49	28.78	50.77	2019-07-11 14:08	26.70	53.67	2019-07-11 14:00

where:

S_{t+1} is the expected value for time t+1

α_t is the the Auto Adaptive Smoothing Coefficient for time t ($0 \le \alpha_t \le 1$)

X_t is the variable value at time t

S_t is the expected value for time t

The Auto Adaptive Smoothing Coefficient α_t is calculated through Formula (2):

$$\alpha_{t+1} = Min(1, k_t) \quad (2)$$

where:

$$E_t = X_t - S_t \quad (3)$$

and:

$$k_t = \left|\frac{A_t}{M_t}\right|, \text{ if } M_t > 0, \text{ 0 otherwise} \quad (4)$$

$$A_t = \beta \times E_t + (1-\beta) \times A_{t-1}, \ 0 \le \beta \le 1 \quad (5)$$

$$M_t = \beta \times |E_t| + (1-\beta) \times M_{t-1}, \ 0 \le \beta \le 1 \quad (6)$$

E_t is the forecast error for time t. β is a parameter of the algorithm – a larger value will result in faster response of the filter.

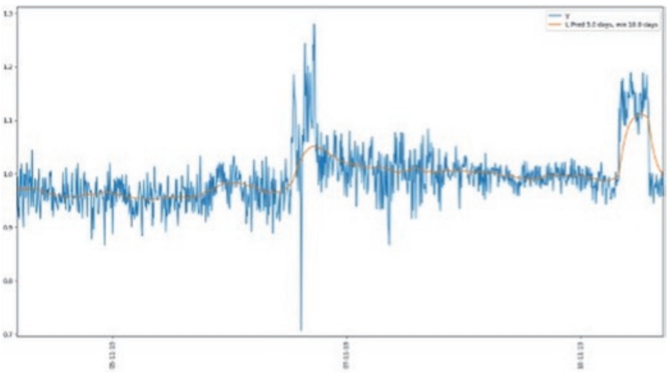

Fig. 6. Result of the short time prediction algorithm for variable Vibration

The short-term algorithm was implemented in Python. Figure 6 shows an example of the output produced by the short time prediction algorithm for vibration, with a $\beta = 0.4$. As the plot shows, the prediction follows the trends of the signal very closely. Since it is smoothed, the prediction is much more stable and immune to short spikes. For vibration, the Mean Squared Error (MSE) is 0.068 and the Mean Average Percentage Error (MAPE) is 5.61%. For pressure, the MSE is 990.64 and the MAPE is 1.36%. For the U, V, W motor winding temperatures, the MSE are 0.18, 0.21, 0.18 and the MAPE are 0.39, 0.41 and 0.36 %, respectively. For flow, MSE is 322.5, MAPE is 0.45. For the temperature of the attack roller bearing, MSE is 0.30, and MAPE is 0.59 %. For the counterattack roller bearing, the errors are 3.14 and 5.76 %. For velocity and temperature oil temperature, MSE are 254.07 and 0.15m and MAPE are 0.37% and 0.29%.

7. Long Time Forecast

To forecast the parameters, a dataset provided by the company was used. The dataset contains sensor data from 2017 to 2020, with a sampling period of 1 minute, as stated above.

The dataset was divided into two parts, 80% for training and 20% for testing. Each training iteration takes between six hours and eight hours on a computer with Intel Xeon E5-2680v2 CPU.

The code used was developed by the authors in Python, using the the ScyPy Sk-learn Library. Several mode tests were carried out and based on the results the best parameters were chosen.

It was ensured that there were no overfitting problems, as graphs were developed about the network's learning history, having presented a converging curve. The final Neural Network has two hidden layers (140-2).

7.1. Dataset, filter, smoothing and normalization

The dataset was composed of 11 variables: Vibration, Pressure, Velocity, U Winding temperature, V Winding temperature, W Winding temperature, Oil temperature, Flow, Temperature of Attack Roller Bearing, Temperature of Counterattack Bearing and Load. It should be noted that the load will not have a forecast, as it is only used as an input to the neural network.

Missing data in the dataset were filled with last known value for that variable, *i.e.* all missing or null values are replaced.

Then a median filter was applied using a sliding window with the previously defined window width (*w*, in samples). Finally, the data of all variables under study were normalized using the python Standard-Scaller library. The normalization interval used was [0, 1].

7.2. Input vector creation

To create the input vector for the neural network, a sliding window of width *wn* is applied. The following diagram illustrates the application of the window to the time series *u*.

u[n - ...]	u[n-*wn*-2]	u[n-*wn*-1]	u[n-wn]	...	u[n-1]	u[n]
			W[*wn*]	...	*W*[2]	*W*[1]

Fig. 7. A sliding window W, with size wn, is applied to the time series u, so that wn samples of the sequence u are selected to create the input to the neural network

Applying the sliding window *W* to sequence *u*, *wn* samples, from *u[n]* to *u[n-wn],* are selected to create the input vector to the neural network.

Once the *wn* samples are selected, a signature *Sn* of the window is calculated to feed as input to the neural network.

The signature *Sn* comprises the mean value of the window (m_w), the Standard Deviation (std_w), the median (med_w) of the *wn* samples, and the Power Spectrum Density (psd_w), as represented in (7). Experiments with other vectors were performed, but for succinctness the results are not presented in the paper.

$$Sn(n) = [m_w, std_w, med_w, psd_w] \quad (7)$$

Once the sequence of signatures of each window is created, a transformed dataset is constructed, with the structure represented in Figure 8.

Sn[n - ...]	Sn[n-5]	Sn[n-4]	Sn[n-3]	Sn[n-2]	Sn[n-1]	Sn[n]

Fig. 8. Representation of the transformed dataset, containing the signatures of each window wn

To train the model to predict future values, a time gap *g*, in samples, is applied to create the desired output vector. The vector is introduced, so that the predicted value *p* for time *n*+*g* is a function of *Sn[n],* as shown in (8).

$$p[n+g] = f(Sn[n]) \quad (8)$$

Figure 9 schematically shows the correspondence between signature *Sn* in the dataset and the predicted value *p*, where *Sn[n]* is used to predict *p[n-g]*. In the figure, *g=3*. In the experiments, *g* was the number of samples in 90 days.

wn[n - ...]	wn[n-5]	wn[n-4]	wn[n-3]	wn[n-2]	wn[n-1]	wn[n]
p[n - ...]	p[n-5]	p[n-4]	p[n-3]	p[n-2]	p[n-1]	p[n]

Fig. 9. Representation of the prediction model, where the signature of the signal at time n-3 is used to predict the value at time n

The machine learning model used to make the predictions was an Artificial Neural Network, namely the MLPRegressor of the Sklearn library. The neural network after several training procedures, achieved good results. Figures 10-12 show the original signal and the prediction for different values. Those results were obtained using a multilayer neural network with two hidden layers, with 200 and 10 neurons, respectively, using the ReLU activation function. The sliding window applied on the data comprised 7 days of data.

For better stability of the values predicted, they were smoothed using median filter with window size 20.

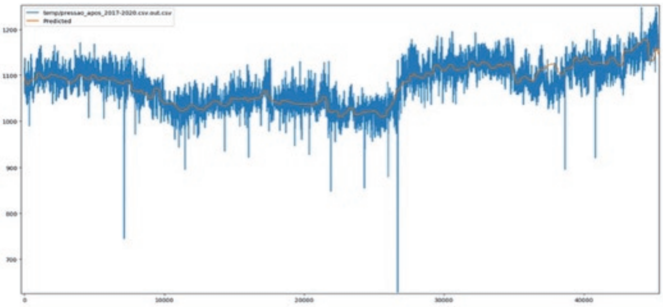

Fig. 10. Results of prediction for temperature. The signal is in blue, the prediction in orange

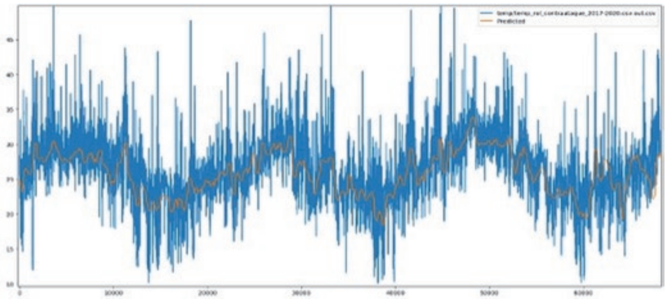

Fig. 11. Results of prediction for counterattack bearing temperature

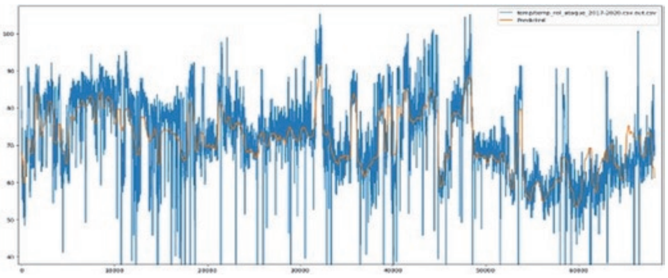

Fig. 12. Results of prediction for attack bearing temperature

To better understand the efficiency of the neural network, Table 5 shows the Mean Absolute Percentage Errors and the Mean Squared Errors for all the predicted variables.

Table 5 shows that it is possible to predict the status of the equipment in advance, with errors on average less than 10 %.

Table 5. MAPE and MSE of the 3-month forecast of all variables.

VARIABLE	MAPE	MSE
Vibration	9.47	0.19
Pressure	1.59	507.08
Velocity	1.32	847.25
Winding temperature U	4.26	25.93
Winding temperature V	4.32	28.13
Winding temperature W	4.47	29.89
Oil	5.34	31.75
Flow	3.35	5652.65
Temperature Attack	6.63	39.16
Temperature Against Attack	9.72	10.13

7.3. User end interface

The end user interface was implemented through semaphores, quantitative values, and graphs, aiming to give, in an intuitive way for the user, a global vision of the system behaviour.

In this colour system, red is for the anomaly, yellow for lookout, and green for good working. This choice of colours was chosen to be like the traffic light system used on roads, making it easy to interpret and assimilate by everyone.

Through this system, it is easy, quick, and simple for the operator to know in which state of operation the equipment is, which can also contribute to prevent serious failures or malfunctions (when it is yellow or red).

The limits for green, yellow, and red were proposed by the company technicians, based on previous experience and manufacturer's information.

8. Conclusion

Failures in industrial plants can cause huge losses, or even endanger people and property. A case study of chip pumps has been described, where a dataset of approximately three years of sensory data and factory inspections were used to diagnose problems and develop a model to predict future behaviour. FMECA analysis identified that the last of three chip pumps was subjected to huge strain. Such effort was justified by the fact that it must transport its load vertically, while the predecessor chip pumps do it horizontally.

The same chip pump has deficiencies in its settlement which exponentially increase its vibration. Such vibration associated with a greater Strain effort make the shaft of the chip pump to suffer more stress than recommended, hence its useful life is doomed to be much shorter than required.

The forecast of sensor values to three months offers a great advantage for decision-making in equipment maintenance management. The temporal dimension of the forecast is totally innovative since, in the review of the state of the art, only short/medium-term forecasts were found.

Prediction made through Neural Networks proved to be valid for this type of problem. The Mean Absolute Percentage Error in all variables was below 10%.

Given the results achieved, this work offers the industry concerned the possibility of making more informed scheduled maintenance stops. This contributes very positively to increase the availability of assets as well as to reduce costs, as it reduces unexpected breakdowns. One limitation of the approach is that it relies on past sensory data. Changes in one or more key variables, for example due to differences in parts, environment, or other changes, can result in more uncertain predictions.

This methodology can be applied to other equipment by training the neural networks with appropriate data, although there is no guarantee that the same results can be achieved in another asset. The results can be better or worse, depending on the type of patterns present in the data.

This problem may be subject to future work. Other future work includes the study of more variables, as well as other machine learning models.

Funding

The research leading to these results has received funding from the European Union's Horizon 2020 research and innovation programme under the Marie Sklodowvska-Curie grant agreement 871284 project SSHARE and the European Regional Development Fund (ERDF) through the Operational Programme for Competitiveness and Internationalization (COMPETE 2020), under Project POCI-01-0145-FEDER-029494, and by National Funds through the FCT—Portuguese Foundation for Science and Technology, under Projects PTDC/EEI-EEE/29494/2017, UIDB/04131/2020, and UIDP/04131/2020.

Acknowledgments

This research is sponsored by FEDER funds through the program COMPETE — Programa Operacional Factores de Competitividade—and by national funds through FCT—Fundação para a Ciência e a Tecnologia—under the project UIDB/00285/2020. This work was produced with the support of INCD funded by FCT and FEDER under the project 01/SAICT/2016 nº 022153.

Abbreviations

The following abbreviations are used in this manuscript:

AI	Artificial Intelligence
ANN	Artificial Neuronal Networks
ARIMA	Auto Regressive Integrated Moving Average
FMEA	Failure Mode and Effect Analysis
FMECA	Failure Mode, Effects and Criticality Analysis
MAPE	Mean Absolute Percentage Error
MLP	Multilayer Perceptron
MSE	Mean Squared Error
NN	Neuronal Networks
WS	Windows Size
IoT	Internet of Things
IIoT	Industrial Internet of Things

References

1. Balduíno M, Torres Farinha J, Marques Cardoso A. Production Optimization versus Asset Availability – a Review. WSEAS Transactions on Systems and Control 2020; 15: 320–332, https://doi.org/10.37394/23203.2020.15.33.
2. Barata J. A Systematic Approach to Design Product Traceability in Industry 4.0: Insights from the Ceramic Industry. [https://www.researchgate.net/publication/319998541_A_Systematic_Approach_to_Design_Product_Traceability_in_Industry_40_Insights_from_the_Ceramic_Industry]
3. Berger R, Benbow D, Ahmad Elshennawy, Walker H. The Certified Quality Engineer Handbook, Second Edition. Faculty and Staff Books 2006.
4. Cachada A, Barbosa J, Leitño P et al. Maintenance 4.0: Intelligent and Predictive Maintenance System Architecture. 2018 IEEE 23rd International Conference on Emerging Technologies and Factory Automation (ETFA), 2018; 1: 139–146, https://doi.org/10.1109/ETFA.2018.8502489.
5. Cahyana R. A preliminary investigation of information system using Ishikawa diagram and sectoral statistics. IOP Conference Series: Materials Science and Engineering 2018; 434: 012050, https://doi.org/10.1088/1757-899X/434/1/012050.
6. Compare M, Baraldi P, Zio E. Challenges to IoT-Enabled Predictive Maintenance for Industry 4.0. IEEE Internet of Things Journal 2020; 7(5): 4585–4597, https://doi.org/10.1109/JIOT.2019.2957029.
7. Daily J, Peterson J. Predictive Maintenance: How Big Data Analysis Can Improve Maintenance. In Richter K, Walther J (eds): Supply Chain Integration Challenges in Commercial Aerospace, Cham, Springer International Publishing: 2017: 267–278, https://doi.org/10.1007/978-3-319-46155-7_18.
8. Efthymiou K, Papakostas N, Mourtzis D, Chryssolouris G. On a Predictive Maintenance Platform for Production Systems. Procedia CIRP 2012; 3: 221–226, https://doi.org/10.1016/j.procir.2012.07.039.
9. Farinha J M T. Asset Maintenance Engineering Methodologies. 1st edition. Boca Raton, FL, CRC Press: 2018.
10. Fernandes M, Canito A, Corchado J M, Marreiros G. Fault Detection Mechanism of a Predictive Maintenance System Based on Autoregressive Integrated Moving Average Models. In Herrera F, Matsui K, Rodríguez-González S (eds): Distributed Computing and Artificial Intelligence, 16th International Conference, Cham, Springer International Publishing: 2020: 171–180, https://doi.org/10.1007/978-3-030-23887-2_20.
11. Francis F, Mohan M. ARIMA Model based Real Time Trend Analysis for Predictive Maintenance. 2019 3rd International conference on Electronics, Communication and Aerospace Technology (ICECA), 2019: 735–739, https://doi.org/10.1109/ICECA.2019.8822191.
12. Gbadamosi A-Q, Oyedele L O, Delgado J M D et al. IoT for predictive assets monitoring and maintenance: An implementation strategy for the UK rail industry. Automation in Construction 2021; 122: 103486, https://doi.org/10.1016/j.autcon.2020.103486.
13. Hashemian H M. State-of-the-Art Predictive Maintenance Techniques. IEEE Transactions on Instrumentation and Measurement 2011; 60(1): 226–236, https://doi.org/10.1109/TIM.2010.2047662.
14. Hegedűs C, Kosztyán Z T. 46 The consideration of measurement uncertainty and maintenance related decisions. Problems of Management in the 21stcentury 2011; 1: 46-59.
15. Heidarbeigi K, Ahmadi H, Omid M, Tabatabaeefar A. Evolving an Artificial Neural Network Classifier for Condition Monitoring of Massey Ferguson Tractor Gearbox. International Journal of Applied Engineering Research 2010; 5: 2097–2107.
16. Jun L, Huibin X. Reliability Analysis of Aircraft Equipment Based on FMECA Method. Physics Procedia 2012; 25: 1816–1822, https://doi.org/10.1016/j.phpro.2012.03.316.
17. Kanawaday A, Sane A. Machine learning for predictive maintenance of industrial machines using IoT sensor data. 2017 8th IEEE International Conference on Software Engineering and Service Science (ICSESS), 2017: 87–90, https://doi.org/10.1109/ICSESS.2017.8342870.
18. Karpenko M, Sepehri N. Neural network classifiers applied to condition monitoring of a pneumatic process valve actuator. Engineering Applications of Artificial Intelligence 2002; 15(3): 273–283, https://doi.org/10.1016/S0952-1976(02)00068-4.
19. Kiangala K S, Wang Z. Initiating predictive maintenance for a conveyor motor in a bottling plant using industry 4.0 concepts. The International Journal of Advanced Manufacturing Technology 2018; 97(9): 3251–3271, https://doi.org/10.1007/s00170-018-2093-8.

20. Kolokas N, Vafeiadis T, Ioannidis D, Tzovaras D. Forecasting faults of industrial equipment using machine learning classifiers. 2018 Innovations in Intelligent Systems and Applications (INISTA), 2018: 1–6, https://doi.org/10.1109/INISTA.2018.8466309.
21. Lipol L S, Haq J. Risk analysis method: FMEA/FMECA in the organizations. International Journal of Basic & Applied Sciences IJBAS-IJENS 2011; 11(05): 9.
22. Lu B, Durocher D B, Stemper P. Predictive maintenance techniques. IEEE Industry Applications Magazine 2009; 15(6): 52–60, https://doi.org/10.1109/MIAS.2009.934444.
23. Martins A B, Torres Farinha J, Marques Cardoso A. Calibration and Certification of Industrial Sensors – a Global Review. WSEAS Transactions on Systems and Control 2020; 15: 394–416, https://doi.org/10.37394/23203.2020.15.41.
24. Organisation internationale de normalisation, Commission électrotechnique internationale, Association française de normalisation. International Standart - Failure modes and effects analysis (FMEA and FMECA) - EC 60812:2018. 2018.
25. Paolanti M, Romeo L, Felicetti A et al. Machine Learning approach for Predictive Maintenance in Industry 4.0. 2018 14th IEEE/ASME International Conference on Mechatronic and Embedded Systems and Applications (MESA), 2018: 1–6, https://doi.org/10.1109/MESA.2018.8449150.
26. Parida A, Kumar U. Maintenance Productivity and Performance Measurement. In Ben-Daya M, Duffuaa SO, Raouf A et al. (eds): Handbook of Maintenance Management and Engineering, London, Springer: 2009: 17–41, https://doi.org/10.1007/978-1-84882-472-0_2.
27. Rafiee J, Arvani F, Harifi A, Sadeghi M H. Intelligent condition monitoring of a gearbox using artificial neural network. Mechanical Systems and Signal Processing 2007; 21(4): 1746–1754, https://doi.org/10.1016/j.ymssp.2006.08.005.
28. Rahmati S H A, Ahmadi A, Govindan K. A novel integrated condition-based maintenance and stochastic flexible job shop scheduling problem: simulation-based optimization approach. Annals of Operations Research 2018; 269(1): 583–621, https://doi.org/10.1007/s10479-017-2594-0.
29. Ran Y, Zhou X, Lin P et al. A Survey of Predictive Maintenance: Systems, Purposes and Approaches. arXiv:1912.07383 [cs, eess] 2019.
30. Sajid S, Haleem A, Bahl S et al. Data science applications for predictive maintenance and materials science in context to Industry 4.0. Materials Today: Proceedings 2021; 45: 4898–4905, https://doi.org/10.1016/j.matpr.2021.01.357.
31. Sheu D D, Kuo J Y. A model for preventive maintenance operations and forecasting. Journal of Intelligent Manufacturing 2006; 17(4): 441–451, https://doi.org/10.1007/s10845-005-0017-6.
32. Tian Z. An artificial neural network method for remaining useful life prediction of equipment subject to condition monitoring. Journal of Intelligent Manufacturing 2012; 23(2): 227–237, https://doi.org/10.1007/s10845-009-0356-9.
33. Wang J, Li C, Han S et al. Predictive maintenance based on event-log analysis: A case study. IBM Journal of Research and Development 2017; 61(1): 11:121-11:132, https://doi.org/10.1147/JRD.2017.2648298.
34. Yan J, Meng Y, Lu L, Li L. Industrial Big Data in an Industry 4.0 Environment: Challenges, Schemes, and Applications for Predictive Maintenance. IEEE Access 2017; 5: 23484–23491, https://doi.org/10.1109/ACCESS.2017.2765544.
35. Yeh R H, Kao K-C, Chang W L. Preventive-maintenance policy for leased products under various maintenance costs. Expert Systems with Applications 2011; 38(4): 3558–3562, https://doi.org/10.1016/j.eswa.2010.08.144.
36. Uygun Y. Industry 4.0: Principles, Effects and Challenges – Nova Science Publishers: 2020 https://books.google.pt/books/about/Industry_4_0.html?id=pkExzgEACAAJ&redir_esc=y
37. J. Imaging | Free Full-Text | Real-Time Quality Control of Heat Sealed Bottles Using Thermal Images and Artificial Neural Network | HTML. [https://www.mdpi.com/2313-433X/7/2/24/htm].
38. EN 13306:2017 - Maintenance - Maintenance terminology. [https://standards.iteh.ai/catalog/standards/cen/5af77559-ca38-483a-9310-823e8c517ee7/en-13306-2017].

Eksploatacja i Niezawodnosc – Maintenance and Reliability
Volume 24 (2022), Issue 1
journal homepage: http://www.ein.org.pl
Article citation info:
Wang W, Liu S, Wang J, Lu G. A calibration-based method for interval reliability analysis of the multi-manipulator system. Eksploatacja i Niezawodnosc – Maintenance and Reliability 2022; 24 (1): 42–52, http://doi.org/10.17531/ein.2022.1.6.

A calibration-based method for interval reliability analysis of the multi-manipulator system

Indexed by: Web of Science Group

Wei Wang[a,d], Shuangyao Liu[b], Jin Wang[c,d,*], Guodong Lu[c,d]

[a]Zhejiang Sci-Tech University, Faculty of Mechanical Engineering & Automation, Hangzhou, China, 310018
[b]Zhejiang Institute of Mechanical & Electrical Engineering, Hangzhou, China, 310053
[c]Zhejiang University, Engineering Research Center for Design Engineering and Digital Twin of Zhejiang Province, School of Mechanical Engineering, Hangzhou, China, 310027
[d]Zhejiang University, School of Mechanical Engineering, State Key Laboratory of Fluid Power and Mechatronic Systems, Hangzhou, China, 310027

Highlights

- Numerical evaluation of reliability for multi-manipulators system from the new perspective of kinematics.
- Efficient conversion from the series system to the parallel system via the base frame calibration.
- Significant improvement of reliability based on the establishing connections among all the manipulators.

Abstract

The multiple manipulators can construct a special multi-agent system with the distinction that the type can be serial or parallel according to their cooperative way. We proposed a comprehensive method to handle the problem of reliability estimation. The wide and narrow bound method are applied to calculate the interval reliability respectively when multiple manipulators work as the series system. Aims to decrease the system complexity and enhance the dynamic adjustment capability, the base frame calibration technique is presented to convert the series system to a parallel one, naturally the reliability can be improved significantly. A system composed by three manipulators is utilized as an example to illustrate the feasibility of the proposed method.

Keywords

multiple manipulators, series/parallel system, reliability estimation, base frame.

1. Introduction

Manipulators have a wide range of applications in industry because of their high efficiency, accuracy and easy operation. They are often used in the field of transportation, gripping and assembling etc. in which end-effector of the manipulator is designed to move from one point to another with the same position and orientation repetitively[1,4].In practice, errors that originated from manufacturing and assembling process of the manipulator cannot be eliminated. The main uncertainties include joint clearance, dimensional deviations, material deformation et al. which can finally result in the erratic shocks, vibration and deterioration of motion capability over its service life [9, 13,22]. Therefore, analyzing the behavior of a manipulator with consideration of parameter uncertainties and evaluating the reliability appropriately can be significant issues.

To calculate the reliability of a manipulator with reference to a particular point during a repetitive work. Rao and Bhatti [20] proposed a probabilistic method to measure the extent of influence caused by the joint clearance on the repeatability of the two-link manipulator. The instability of the behavior from the aspect of dynamics and kinematics are both analyzed. Kim et al. [12] focused on the analysis of impact caused by joint clearance, all the variables were treated as normally distributed and then the first order reliability method (FORM) was applied. With integration of the second order Taylor expansion and an entropy-based optimization approach, Wang et al. [27] analyzed the reliability of a manipulator when confronted with arbitrarily distributed joint clearance.

Though the reproducibility of a manipulator outperforms its ability to reach an expected position [18], there are a lot of demands in which the motion should be controlled in the entire trajectory instead of only a few points, such as tasks of welding, sculpture, spraying etc. [4,29,31]. Pandey and Zhang[17]proposed a fractional moment estimation method, the drawback lies in that two layers of optimization process are required, which makes it complicated. Zhao et al. [30] developed an approximated approach to study the motion reliability of a parallel mechanism during a circle trajectory movement, in their work, the first passage method, Lie group and Lie algebra were utilized to describe the variables with time-variant character. Other popular methods like FOSM (first order second moment method) and MCS (Monte Carlo simulation) are also widely used [26].

The researches mentioned-above exhibit an obvious feature in common that only one failure mode is needed to be concerned. When the multi-agent system consists of many subsystems, the numerical

(*) Corresponding author.
E-mail addresses: W. Wang (ORCID: 0000-0003-3681-7955): wangw@zstu.edu.cn, S.Liu (ORCID: 0000-0002-0870-1587): liushuangyao@zime.edu.cn, J. Wang (ORCID:0000-0003-3106-021X): dwjcom@zju.edu.cn, G. Lu: lugd@zju.edu.cn

evaluation for such a sophisticated system can be a big challenge [11]. In the context of the system reliability analysis. Cornell [5] proposed the first order bound method (also called the wide bound method) to compute the failure probability of the series/parallel system, an interval instead of an exact value was firstly used to measure the stability and safety. However, the range of the result was too wide to satisfy the requirement of accuracy in practical applications. Later on, given the correlation and dependence of failure between the paired subsystems, Ditlevsen[7] developed the second order bound method (also called narrow bound method), the precision of result can be much better enhanced compared to that of the wide bound method. Through introducing a truncation technique to limit the possible value of random variables, Qiu et al.[19] analyzed the truss system and figured out the interval of failure probability. Safaei et al. [21] studied the redundant system mixed by the series and parallel subsystems, in order to reduce the cost caused by the sudden breaking down of machines and keep the manufacturing cellular with high reliability and production efficiency, they established a multi-objective optimization model. Aims at making a better trade-off between calculation accuracy and efficiency, Bichon et al.[3] put forward a surrogate model-based method to handle the problem of reliability analysis of a large system with multiple failure modes. Xie et al. [28] defined a time-domain series system for the gear train that has typical features of time-dependent multiple configuration, then proposed a reliability modeling technique to measure the system reliability. Some improved approaches with the foundation of the bound method have been also proposed to handle the problem of their unique structural systems[23,32].

As well known, with the rapid development of modern equipment technology, the cooperative system made up of several manipulators exhibits the dominant advantages compared to the single manipulator. The reasons can also stem from the fact that the multi-manipulator system has many outstanding abilities, for instance, the wider working space, greater caring capacity, better suitability to manufacture the large-size and complex components etc.[15,24]. Naturally, the research on the multi-manipulator system has drawn intensive attention. In order to realize that the leading manipulator can be followed fast and accurately by the other one. Liu et al.[16] proposed an adaptive impedance control algorithm for two cooperative manipulators. A simple task was planned to demonstrate feasibility of the method in their simulation and experiment. To ensure the qualified transportation of objects, Aldo et al. [2] designed a predefined-time controller with utilization of the hybrid/position sliding model control algorithm. All the subsystems including cooperative manipulators, tools and objects were supposed to be rigid. Korayem et al.[14] put forward an optimal control method based on the state-dependent Riccati equation, which was used to strengthen the capability of dual-arms to carry the heavy loads. Dohmann and Sandra[8] divided the transportation task into two subtasks including object trajectory tracking and grasp maintenance, then they proposed a distributed impedance control scheme to increase the two-manipulators system flexibility and efficiency of reaction to disturbance.

As described in previous, we can note that great progress has been made since so many efforts have been devoted to this area. Both the theory and practical applications are abundant in the reliability analysis of a single manipulator as well as the control scheme developing for multi-agent system. From another perspective, if the single manipulator is regarded as a subsystem, hence the manipulators can constitute a kind of special multi-agent system with the distinction that the type and configurations may be varied. The existing research maybe insufficient in terms of the reliability analysis for a multi-manipulator system. Some aspects can be still improved and they are listed as follows.

(1) *Immutable type of the multi-agent system*. In the open literature, the categories of a multi-agent system mainly include the series, parallel and hybrid system [7,18,32]. The failure mode is decided ever since the structure design process has been completed. Therefore, the system type only can belong to one of the three modes and is unchangeable. Whereas cooperative manipulators may differ quite a lot, they can carry out the task together by a cooperative way with the assistant of machine vision, contact force controller etc. [2,4] or just by an independent way with the movement along its own pre-planned path[1]. The failure mode varies with their cooperation way and the type can be even transformed from the series to the parallel, articles in this field are rather limited.

(2) *Insufficient analysis of the kinematic reliability.* Most current approaches aim to develop a kind of control scheme to grasp the rigid object based on the complicated dynamic model [8,16,24], instead of trying to evaluate the reliability numerically. From the perspective of dynamics, the system stability is measured by the changes of the joint torque and the path tracking error. However, since there is the probability of failure both in kinematics and dynamics for a single manipulator[12,17,19,24], it is reasonable to believe that the multi-manipulator system maybe also failed to meet the demand in the kinematics over the execution of tasks from the perspective of probability theory, no matter how robust and excellent the controller is. So the kinematic reliability analysis of the multi-manipulator system can provide a new insight and become an important issue.

Given all, we proposed a novel method that can analyze the reliability of multi-manipulator system comprehensively for the first time. The wide and narrow bound method are applied to obtain the reliability interval that is rigorously limited by the lower and upper bound respectively.

The type of such a special multi-agent system depends on the way that how the single component is connected and cooperated. When each manipulator is just designed to move along its own trajectory planned beforehand independently and no connection is available for the internal communication, multiple manipulators can be treated as a series system. The mission will be failed as long as any one of the manipulators breaks down or becomes unreliable in kinematics. Since the negative influence caused by the failed manipulator can be expanded and propagated through the closed chain of internal force into the rest of the components, due to the lack of the dynamic adjustment capability, the other manipulators may deviate from their desired positions simultaneously.

In order to construct the connections among the multiple manipulators, an efficient base frame calibration method is introduced to figure out the relative position between any pair of cooperative manipulators. Similar to the leader-follower scheme, all the manipulators that play the role of a follower can have the flexibility to track the position of the leader. Furthermore, the actual position of the leading manipulator can be treated as the desired position which means the leader's behavior can be always acceptable and reliable in kinematics with the failure probability dropping to zero. In this situation, the failure mode of the multi-manipulator system can be identical to that of a parallel system, under the condition that all single components are defected, the system can be failed. The significant contributions in our work mainly include three aspects: 1) numerical evaluation of the multi-manipulator system reliability from the novel view of kinematics for the first time, 2) efficient conversion from the series system to a parallel system via the base frame calibration and 3) remarkable optimization of the reliability.

Remainder of this paper is organized as follows: section 2 presents the probabilistic failure model of the manipulator, section 3 describes the details about the proposed method that mainly include the computation and conversion process for the series /parallel system with multi-manipulator. Simulation is conducted in section 4 followed by discussion in section 5. Conclusions are summarized in the last section.

2. Probabilistic modeling of a manipulator

2.1. Forward kinematic with random variables

The common used manipulator is constructed a several of linkages, as shown in Fig.1 (a).

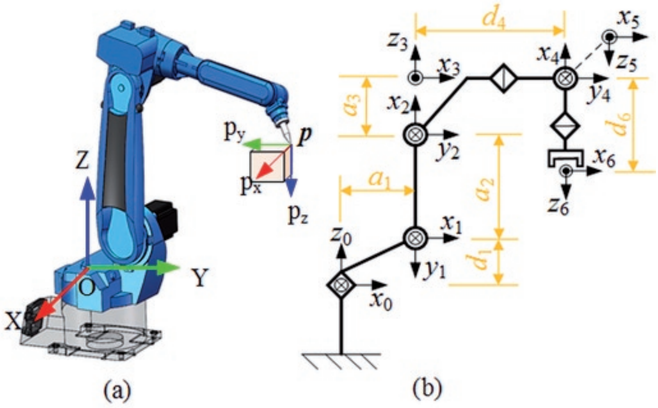

Fig. 1 a schematic diagram of a single manipulator

The relative position between a pair of adjacent joints can be described by a homogeneous matrix, written as[6]:

$$A_i^{i-1} = \begin{bmatrix} Cos\theta_i & -Sin\theta_i Cos\alpha_i & Sin\theta_i Sin\alpha_i & a_i Cos\theta_i \\ Sin\theta_i & Cos\theta_i Cos\alpha_i & -Cos\theta_i Sin\alpha_i & a_i Sin\theta_i \\ 0 & Sin\alpha_i & Cos\alpha_i & d_i \\ 0 & 0 & 0 & 1 \end{bmatrix} \quad (1)$$

where $(a_i, d_i, \alpha_i, \theta_i)$ are the D-H parameters of the ith link.

The position and orientation of the end-effector can be obtained through a series of transformation from the base frame to the final one, the whole D-H coordinates of such a manipulator is drawn in Fig.1 (b), formulated as:

$$T = \prod_{i=1}^{n} A_i^{i-1} = \begin{bmatrix} \boldsymbol{Rot} & \boldsymbol{Pos} \\ 0 & 1 \end{bmatrix} \quad (2)$$

where $\boldsymbol{Rot}$ denotes the orientation matrix, $\boldsymbol{Pos} = \left[p_x, p_y, p_z \right]$ represents the position of the end-effector and n is the total number of degree of freedoms.

The kinematics is studied based on the 6-DOFs manipulator, the corresponding structure parameters are listed in Table 1.

Table 1. The standard D-H parameters

No.	$a_i\,(mm)$	$d_i\,(mm)$	$\alpha_i\,(°)$	$\theta_i\,(°)$	Initial angle (°)
1	40	330	−90	θ_1	0
2	315	0	0	θ_2	−90
3	70	0	−90	θ_3	0
4	0	310	90	θ_4	0
5	0	0	−90	θ_5	90
6	0	70	0	θ_6	0

As presented in section 1, due to the unavoidable errors that originated from defects of manufacturing, assembling and material deformation etc., the manipulator can be seriously affected by those uncertainties. In this work, the dimensional deviations and joint clearances are mainly concerned and they are treated as variables because of the random nature [23], which are listed in Table 2.

Table 2. Distribution of the random variables

variable	distribution	μ (mm)	σ(mm)
a_1	normal	40	0.04
a_2	normal	315	0.32
a_3	normal	70	0.07
d_1	normal	330	0.33
d_4	normal	310	0.31
d_6	normal	70	0.07

Under the influence of the joint clearance, the actual angle of ith link θ_i can be modeled as:

$$\theta_i = \tilde{\theta}_i + \zeta \quad (3)$$

where $\tilde{\theta}_i$ is the desired value of θ_i and ζ is a small normally distributed variable with its $\mu_\zeta = 0$ and $\sigma_\zeta = 0.5°$.

With consideration of the impact caused by dimensional deviations and joint clearance, the forward kinematic model is:

$$\mathrm{T} = f\left(\boldsymbol{X}\right) \quad (4)$$

where $\boldsymbol{X}$ represents the vector of the random variables (including dimensional parameters $\boldsymbol{a,d}$ and joint angle $\boldsymbol{\theta}$).

2.2. Failure probability of a manipulator

Due to the effect of joint clearance and link dimension deviations, the actual position of the end-effector may deviate from the desired position, the possible location with reference to the ideal position can be plotted in Fig.2.

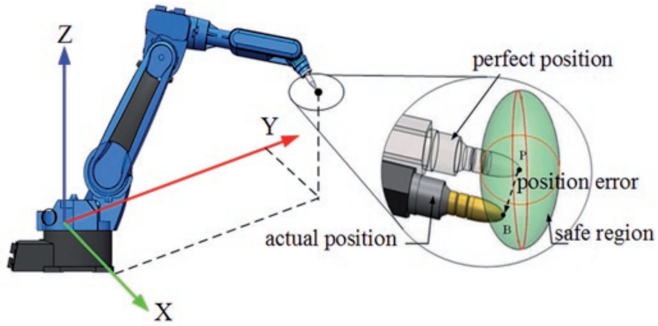

Fig. 2 the relative position between actual and desired location

This deviation is defined as the position error ε, thus [12]:

$$\varepsilon\left(\mathbf{X}\right) = \sqrt{\left(x_d - p_x\right)^2 + \left(y_d - p_y\right)^2 + \left(z_d - p_z\right)^2} \quad (5)$$

where $\left(x_d, y_d, z_d\right)$ denote the desired position and $\left(p_x, p_y, p_z\right)$ represent the actual position.

The unaccepted performance of a manipulator means the end-effector falls outside a permissible region under the influence of random variables, suppose the size of such a safe area is δ, the performance function can be expressed as:

$$\rho = g(X) = \delta - (X) \tag{6}$$

FOSM can provide a convenient way to evaluate the reliability for a system with the normally distributed output. As it linearizes the performance function $g(X)$ with the first order Taylor expansion at the mean value of variables $\boldsymbol{\mu}_{\mathbf{X}}$, we have [23]:

$$\rho \approx g(\mu_{\mathbf{X}}) + \sum \frac{\partial g(\mu_{\mathbf{X}})}{\partial \mathbf{X}}(\mathbf{X} - \mu_{\mathbf{X}}) \tag{7}$$

Define the reliability index β as:

$$\beta = {}^{\mu_\rho}\!\big/_{\sigma_\rho} \tag{8}$$

where μ_ρ and σ_ρ are the mean value and the standard deviation of ρ.

So the probability of failure defined in Eq. (6) can be computed by:

$$P_f = 1 - \varnothing(\beta) \tag{9}$$

where $\varnothing(\cdot)$ is the standard cumulative distribution function of a Gaussian variable.

3. Interval reliability estimation of the system with multiple manipulators

Though the kinematic reliability analysis of the multi-manipulator system can be extended from the single manipulator with much similarity, the dependent component can introduce mutual impact on the each other and finally result in multiple potential failure modes instead of only one, which makes it rather complicated. A practical attempt is to work out an appropriate interval of failure probability in theoretic [5]. For brevity, the *i*th manipulator is denoted as R_i for a multi-agent system with a number of *m*.

3.1. Reliability analysis of the series system

When every component is isolated to each other and is controlled independently to move along its own trajectory, in which the relative position between any cooperative manipulators cannot be obtained, the object is hold and remains relative static to all the end-effectors by the contact force provided by the manipulators. Because of the error originated from the failed one, the others can be negatively influenced by the disturbance propagated via the closed-chain of internal force, therefore, the task is terminated and failed. Such the number of *m* manipulators can be regarded as a series system, the failure mode can be shown in Fig. 3.

Define the failure event for *i*th manipulator as E_i, the reliable event can be denoted as $\bar{E}_i$, the failure probability of the series system can be formulated by[20]:

$$P(E) = P(E_1 \cup E_2 \cdots \cup E_m) \tag{10}$$

If the failure event is independent, we can have:

$$P(E) = 1 - \prod_{i=1}^{m} P(\bar{E}_i) \tag{11}$$

In practice, the single manipulator can hardly avoid to bring about the impact on the others since all they touch the same object, which means the assumption of independent component is spurious. Suppose the correlation coefficient between the failure modes of *i*th and

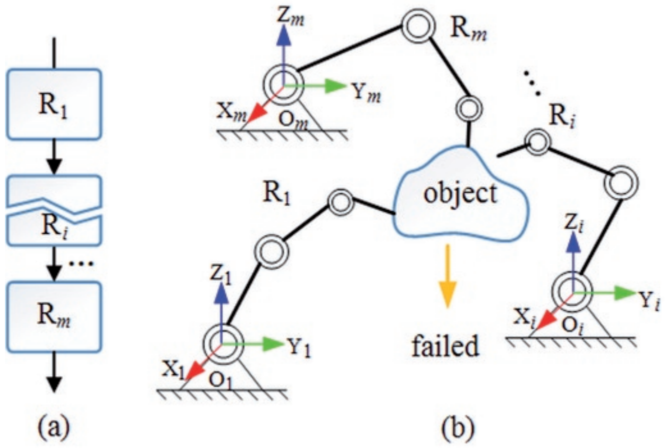

Fig. 3. the series system with multiple manipulators

*j*th manipulator is $\rho_{ij}\,(1 \le i, j \le m)$ which can be easily deduced that the index is positive (ρ_{ij}>0).

According to the conditional probability law, we can obtain:

$$P(E_iE_j) = P(E_i)P(E_j|E_i) \tag{12}$$

$P(E_j|E_i) \ge P(E_j)$ because of (ρ_{ij}>0), therefore, we have $P(E_iE_j) \ge P(E_i)P(E_j)$,which leads to the following result:

$$P(E) \le 1 - \prod_{i=1}^{m} P(\bar{E}_i) \tag{13}$$

Due to $P(E_i) \in [0,1]$, we can derive the lower bound as:

$$P(E) \ge \max\{P(E_1), P(E_2), \cdots, P(E_m)\} \tag{14}$$

The wide reliability interval for the series multi-manipulator system can be formulated by:

$$\max_{1 \le i \le m}(P_{fi}) \le P(E)_W \le 1 - \prod_{i=1}^{m} P(\bar{E}_i) \tag{15}$$

The narrow bound theory is frequently applied because of its outstanding trade-off between accuracy and efficiency[7]. To acquire a more precise result of the reliability interval, Eq. (10)can be represented as:

$$\begin{aligned} P(E) = {} & \sum_{i=1}^{m} P(E_i) - \sum_{1 \le i \le j \le m}^{m} P(E_iE_j) + \\ & \sum_{1 \le i \le j \le k \le m}^{m} P(E_iE_jE_k) + \cdots + (-1)^{m-1} P(E_1E_2 \cdots E_m) \end{aligned} \tag{16}$$

Since $P(E_i) \ge P(E_iE_j) \ge P(E_iE_j \cdots E_m)\,(1 \le i \ne j \le m)$, the lower bound of the narrow reliability interval is:

$$P(E)_N \ge P(E_1) + \sum_{i=2}^{m} \max\left\{P(E_i) - \sum_{j=1}^{i-1} P(E_iE_j), 0\right\} \tag{17}$$

Furthermore,
$P(E_1E_3) + P(E_2E_3) - P(E_1E_2E_3) = P[(E_1E_3) \cup (E_2E_3)]$ and

$P\left[(E_1E_3)\cup(E_2E_3)\right]\geq \max\left\{P(E_1E_3),P(E_2E_3)\right\}$, so the upper bound for the narrow reliability interval is:

$$P(E)_N \leq \sum_{i=1}^{m} P_{\mathrm{f}\,i} - \sum_{i=2}^{m} \max^{i<j} P_{\mathrm{f}\,i,j} \tag{18}$$

where $P_{\mathrm{f}\,i,j}$ denotes the joint failure probability that the ith and jth manipulator can fail simultaneously.

3.2. Base frame calibration

The lack of communications among the components makes the multiple manipulators become the series system and result in the poor dynamic adjustment capability, the behavior of all the manipulators have to be acceptable to ensure the system safety. In order to overcome this defect and enhance the system reliability. A feasible way is to figure out the relative position for the cooperative manipulators which can be realized by the base frame calibration [10].

The projection-based method is a simple but quite efficient calibration approach for manipulators under the typical installation, the requirement of only two points and straightforward calculation process make it attractive when compared with the matrix-equation methods[25].

As shown in Fig. 4. The calibration procedure can be briefly described as follows:

Step1 Select one point in two manipulators' common working space and denote as P_1.

Step2 Drive manipulators and make their measuring tips touch the calibration block respectively.

Step3 Record down the coordinate values.

Step4 Repeat step1 to step3 once more in another point denoted as P_2.

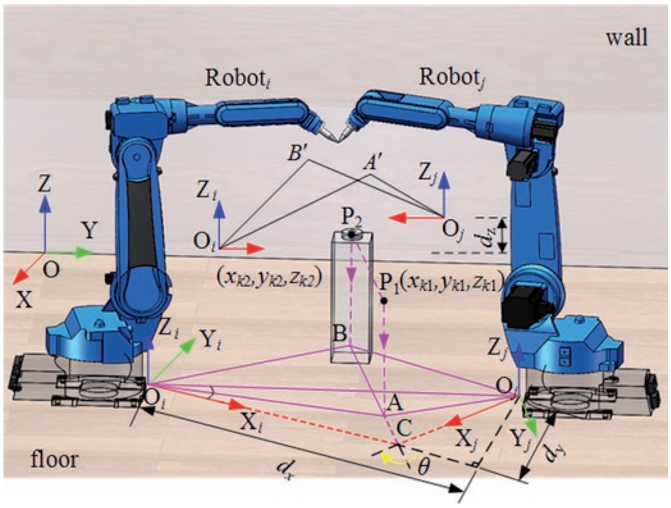

Fig. 4. Two floor-mounted manipulators

As we can see from the Fig. 4, the transformation from O_i-$X_iY_iZ_i$ to O_j-$X_jY_jZ_j$ can be obtained by the rotation around axis-Z_i and translation along the axis-X_i,Y_i and Z_i .${}^{i}T_j = [dx, dy, dz]$ and θ are represented as the translation vector and rotation angle respectively. The rotation matrix can be formulated as[6]:

$$Rot(\theta,Z)=\begin{bmatrix} cos\theta & -sin\theta & 0 \\ sin\theta & cos\theta & 0 \\ 0 & 0 & 1 \end{bmatrix} \tag{18}$$

where Rot (θ, Z) means a rotation matrix with angle θ around axis-Z.

The coordinate values of P_1 and P_2 relative to its own base frame are denoted as $P_{k1}\left(x_{k1}, y_{k1}, z_{k1}\right)$ and $P_{k2}\left(x_{k2}, y_{k2}, y_{k2}\right)$(k=i,j). The relative position between two base frames in X-Y plane and Y-Z plane are obtained by the projection, when cooperative manipulators shake hands with each other at P_1 and P_2.

The translation parameters dx and dy can be computed by:

$$\begin{cases} d_x = \left|O_iO_j\right| \times cos\angle O_jO_iC \\ d_y = \left|O_iO_j\right| \times sin\angle O_jO_iC \end{cases} \tag{20}$$

In a similar way, the rotation angle θ can be computed by:

$$\theta = \angle ACO_j + \angle ACO_i \tag{21}$$

As for the parameter d_z that measures the distance between two base frames along axis-Z_i. The topological structure is projected into Y-Z plane (wall) in the world frame. The formulation can be written as:

$$d_z = \frac{\left(z_{i1} - z_{j1}\right) + \left(z_{i2} - z_{j2}\right)}{2} \tag{22}$$

For a better illustration of the calibration procedure, more specific details about the computation of middle parameters can be found in appendix A.

Since all the paired manipulators are calibrated, the whole system can be naturally calibrated according to the coordinate transformation theory.

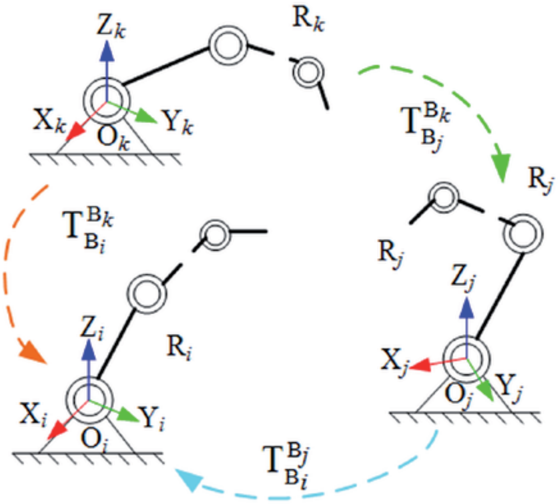

Fig. 5. Coordinate transformation for the multi-manipulator system

The relative transformation among base frames of the manipulators is plotted in Fig. 5, if the transformation matrix $T_{B_i}^{B_j}$ and $T_{B_j}^{B_k}$ have been calibrated by the projection-based method, then the $T_{B_i}^{B_k}$ can be determined by the following Eq. (23), formulated as:

$$T_{B_i}^{B_k} = T_{B_i}^{B_j} \cdot T_{B_j}^{B_k} \tag{23}$$

For the multi-agent system consists of m manipulators, we just need to calibrate m-1 times and the relative transformation matrix among all the manipulators can be computed.

3.3. Reliability analysis of the parallel system converted from a series system

Since the connections among the manipulators have been set up by the base frame calibration, the movement of each manipulator can be coordinated rather than independent. We use the leader-follower scheme to describe the role that each manipulator can play in the system. One of the manipulators is designed as the leader and the others become follower that can adjust themselves' position dynamically and timely according to the leader's position. One of the manipulators' failure cannot result in the final mission failure, therefore, the series system can be converted into a parallel system, as shown in Fig. 6.

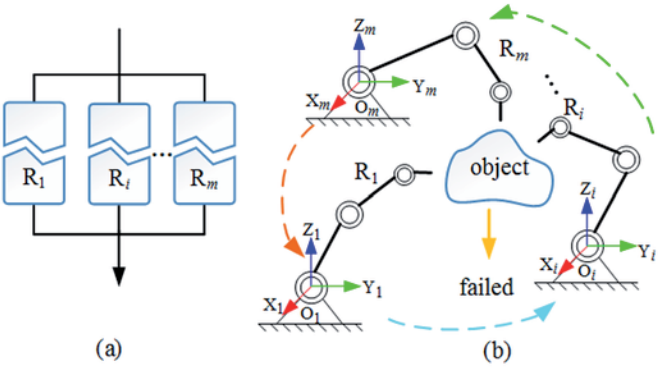

Fig. 6. The parallel system with multiple manipulators

The failure of a parallel system can be modeled as:

$$P(E)=P(E_1 \cap E_2 \cdots \cap E_m) \tag{24}$$

According to Eq. (12), the above equation can be rewritten as:

$$P(E)=P(E_1)P(E_2|E_1)\cdots P(E_m|E_1E_2\cdots E_{m-1}) \tag{25}$$

Similarly, because of $\rho_{ij}>0$, $P(E_i|E_1E_2\cdots E_{i-1})\geq P(E_i)$,the wide bound of the probability of failure is:

$$\prod_{i=1}^{m} P_{\mathrm{f}\,i} \leq P(E)_W \leq \min(P_{\mathrm{f}\,1},P_{\mathrm{f}\,2},\cdots,P_{\mathrm{f}\,m}) \tag{26}$$

Since $P(E_1E_2\cdots E_m)\leq P(E_iE_j)(1\leq i\neq j\leq m)$,the narrow bound of the probability of failure is:

$$\prod_{i=1}^{m} P_{\mathrm{f}\,i} \leq P(E)_N \leq \min_{1\leq i<j\leq m} P_{\mathrm{f}\,ij} \tag{27}$$

Based on Eq.(9), we can derive that P_{fi} is $\varnothing(-\beta_i)$. The P_{fij} of two manipulators can be calculated by [5]:

$$P_{\mathrm{f}\,ij}=\int_{-\infty}^{-\beta_i}\int_{-\infty}^{-\beta_j}\frac{1}{2\pi\sqrt{1-\rho_{ij}^2}}\exp\left\{\frac{2\rho_{ij}\beta_i\beta_j-\beta_i^2-\beta_j^2}{2\left(1-\rho_{ij}^2\right)}\right\}d\beta_j d\beta_i \tag{28}$$

mhere the Matlab functions *intergral* and *prod* are utilized to figure out the P_{fij}.

4. Numerical example

To better illustrate the problem, a handing system consists of three 6-DOFs manipulators, as shown in Fig. 7, is used as an example.

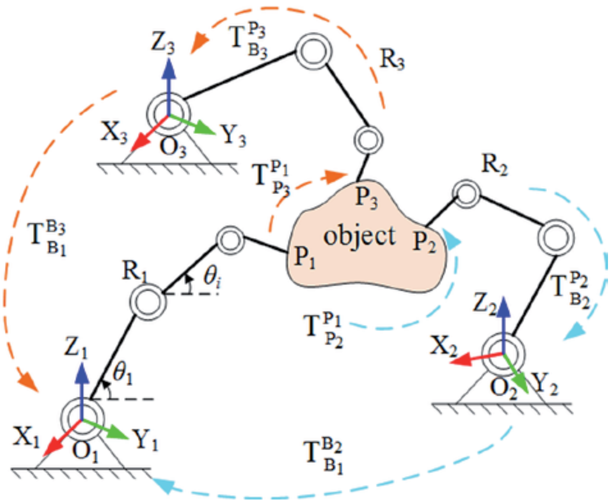

Fig. 7. The three-manipulators system

Each manipulator forms its own configuration and the corresponding desired joint angles are $\bar{\theta}_{R1}$= [6.17°, 22.25°, 5.62°, 2.31°, 46.12°, 21.68°], $\bar{\theta}_{R2}$ = [−18.78°, 12.22°, −162.57°, 113.46°, −113.72°, −138.07°] and $\bar{\theta}_{R3}$= [75.52°, −37.28°, 122.43°, 75.88°, −121.79°, 28.46°] respectively, the radius of the permissible region is δ=2.5mm,the correlation coefficients are ρ_{12}=ρ_{23}=ρ_{13}=0.8. The distributions of all random variables are normal. For simplicity, the homogeneous matrix with the size of 4×4 is represented by T=[p_x,p_y,p_z,α,β,γ], in which α,β and γ denotes the series of rotation angles around axis-X, axis-Y, and axis-Z respectively, they can also be called as the RPY angle [6].

With utilization of $\boldsymbol{\mu}_\mathbf{x}$ and $\boldsymbol{\sigma}_\mathbf{x}$ listed in Table 2, the FOSM presented in section 2.2 can be adopted to compute $\boldsymbol{\mu}_\rho$ and $\boldsymbol{\sigma}_\rho$ of the performance function ρ= g($\boldsymbol{X}$) for the three manipulators. They are $\boldsymbol{\mu}_\rho$ = [1.8652, 1.9326, 1.8956] and $\boldsymbol{\mu}_\rho$= [0.6103, 0.6186, 0.6293]. The point in which the manipulator's end-effector contact with the object is P_i (i=1,2,3), assume that the relative position between P_1 and P_2 is T_{p1}^{p2} = [17.36, 22.28, ,21.32, 8.27°, 5.15°, 5.26°], P_1 and P_3 is T_{p1}^{p3} = [29.55,27.42, 28.73, 5.85°, 6.38°, 9.11°],the tool frames are given as Tol_i = [0,0, 20, 0°, 0°, 0°] (i=1,2,3).

4.1. The P_f of the series system

As the relative position is unknown and no information can be transmitted among the three manipulators. They have to move along their own trajectory that have been planned beforehand. Every manipulator can't adjust the position with reference to the others' automatically.

According to Eq.(8), the reliability index can be obtained and they are β = $\boldsymbol{\mu}_\rho/\boldsymbol{\sigma}_\rho$= [3.0564, 3.1241, 3.0124]. Then, we can figure out the failure probability of the three manipulators, they are $P_{f1}=1.120\times10^{-3}$, $P_{f2}=0.8917\times10^{-3}$ and $P_{f3}=1.2959\times10^{-3}$ respectively. Through Eq.(28), the joint probability of failure can be calculated as P_{f12}=2.6255×10^{-4}, P_{f13}=3.2606×10^{-4} and $P_{f2\,3}$=2.8413×10^{-4}.

Based on Eq.(15), the wide interval of $P(E)_W$ for the series system can be estimated as:

$$\begin{cases} P(E)_W \geq \max(P_{f1},P_{f2},P_{f3}) \\ P(E)_W \leq 1-(1-P_{f1})(1-P_{f2})(1-P_{f3}) \end{cases} \tag{29}$$

Therefore, we can finally compute the result which is presented as follows:

$$1.2959\times10^{-3}\leq P(E)_W\leq 3.3042\times10^{-3}.$$

As mentioned above, because of the positive correlation relationship among the manipulators, a more accurate estimation process can be carried out and the corresponding narrow bound of the failure probability for the series system can be obtained.

The part $\sum_{i=2}^{m}\max\left\{P(E_i)-\sum_{j=1}^{i-1}P(E_iE_j),0\right\}$ can be equivalent to $\max\{P_{f2}-P_{f12},0\}+\max\{P_{f3}-P_{f13}\text{-}P_{f23},0\}$, so we can have the lower bound that is 2.4350×10^{-3}. By the same way, according to Eq.(18), we can calculate the upper bound that is 2.7192×10^{-3}. At the end, the narrow interval value of failure probability for the series manipulator is:

$$2.4350\times10^{-3}\le P(E)_N\le 2.7192\times10^{-3}.$$

4.3. Base frame calibration

As shown in Fig. 7, each manipulator has its own coordinate $O_i-X_iY_iZ_i\,(i=1,2,3)$ attached on the base. The aim of the base frame calibration is to figure out the transformation matrix T_{B1}^{B2}, T_{B1}^{B3} and T_{B2}^{B3}.

For example, relative to the base frame $O_1-X_1Y_1Z_1$, the two calibration points Pnt_1 and Pnt_2 are recorded as $P_{11}(x_{11},y_{11},z_{11})$ and $P_{12}(x_{12},y_{12},z_{12})$ respectively. In a similar way, relative to base frame $O_2-X_2Y_2Z_2$, the corresponding values are $P_{21}(x_{21},y_{21},z_{21})$ and $P_{22}(x_{22},y_{22},z_{22})$. The data are listed in Table 3.

Table 3. Calibration points for base frame1 and base frame2

point	X(mm)	Y(mm)	Z(mm)
$Pnt1$	$x_{11}=393.44$	$y_{11}=95.84$	$z_{11}=591.07$
	$x_{21}=136.80$	$y_{21}=-168.35$	$z_{21}=588.15$
$Pnt2$	$x_{12}=99.06$	$y_{12}=398.79$	$z_{12}=598.17$
	$x_{22}=79.31$	$y_{22}=-586.84$	$z_{22}=595.25$

According to the computation process detailed in Table 6, we can get the translation parameters (d_x = 610.33, d_y = 100.00, and d_z = 2.92) and rotation angle (θ=−128.0°). So the transformation matrix from O_1-$X_1Y_1Z_1$ to O_2-$X_2Y_2Z_2$ can be represents as T_{B1}^{B2} = [610.33, 100. 00, 2.92, 0°, 0°, −128°]. More specific computation details can be found in appendix A.

By the same way, to figure out T_{B1}^{B3}, another two calibration points ($Pnt1'$ and $Pnt2'$) are selected, they are listed as follows.

Table 4. Calibration points for base frame1 and base frame3

point	X(mm)	Y(mm)	Z(mm)
$Pnt1'$	$x_{11}=67.35$	$y_{11}=113.54$	$z_{11}=578.24$
	$x_{31}=410.46$	$y_{31}=149.57$	$z_{31}=576.68$
$Pnt2'$	$x_{12}=35.59$	$y_{12}=265.81$	$z_{12}=585.25$
	$x_{32}=378.70$	$y_{32}=301.84$	$z_{32}=583.69$

Naturally, through repetition of the calibration process, we can obtain the T_{B1}^{B3} = [95.12, 331.62, 1.56, 0°, 0°, −112°]. Based on the Eq. (23), $T_{B2}^{B3}=\left(T_{B1}^{B2}\right)^{-1}\cdot T_{B1}^{B3}$ = [134.68, −548.59, −1.36, 0°, 0°, 16°].

4.3. The P_f of the parallel system

Since the relative position between any couple of manipulators has been computed. The three manipulators can be converted as a parallel system. The manipulator R_1 is regarded as the leader and the rest R_2 and R_3 are followers. The expected angles of R_1 are $\bar{\theta}_{R1}$, under the influence of joint clearance that is normally distributed. The actual angles may be different from the desired values, and they are $\bar{\theta}_{R1}$ = [4.12°, 21.80°, 8.01°, 3.98°, 48.75°, 22.57°]. Therefore, through forward kinematic model formulated as Eq.(2) We can compute the actual location T_{B1}^{P1} = [168.95, 30.88, 511.40, 172.86°, −78.55°, 11.76°]. To keep contact with the object simultaneously, R_2 and R_3 are desired to arrive the position that is computed according to the leader R_1 position, the formulation is:

$$\begin{cases} T_{B_2}^{P_2}=\left(T_{B_1}^{B_2}\right)^{-1}\cdot T_{B_1}^{P_1}\cdot\left(T_{P_2}^{P_1}\right)^{-1} \\ T_{B_3}^{P_3}=\left(T_{B_1}^{B_3}\right)^{-1}\cdot T_{B_1}^{P_1}\cdot\left(T_{P_3}^{P_1}\right)^{-1} \end{cases} \tag{30}$$

Thus we can have T_{B2}^{P2} = [168.95, −150.34, 521.36, 96.29°, 46.10°, −80.19°] and T_{B3}^{P3} = [134.22, 377.37, 536.01, 94.60°, 28.04°, −81.92°].

By the invers kinematic, we can further obtain the actual joint angles for the followers R_2 and R_3 that are the result of the dynamic adjustment process, the equation can be written as:

$$\theta_{Ri}=f^{-1}\left[\left(T_{B_1}^{B_i}\right)^{-1}\cdot T_{B_1}^{P_1}\cdot\left(T_{P_i}^{P_1}\right)^{-1}\cdot\left(Tol_i\right)^{-1}\right]\ (i=2,3) \tag{31}$$

They are θ_{R2} = [−20.02°, 15.03°, −165.24°, 116.21°, −111.31°, −140.02°] and θ_{R3} = [74.36°, −36.19°, 119.73°, 178.68°,−121.43°, 29.18°] respectively.

The actual location of the leading manipulator R_1 can be regarded as its ideal values since it is the benchmark to the followers. The possible system failure can be only from the failure of the followers R_2 and R_3. The new reliability index for R_2 and R_3 are computed again by the FOSM, they are β = [3.1534, 3.0426]. The actual failure probability are P'_{f2} = 0.8068×10^{-3} and P'_{f3} = 1.1727×10^{-3} respectively. The joint failure probability is P'_{f23} = 2.5329×10^{-4}. According to Eq.(26), the wide interval of the parallel manipulators system can be obtained as:

$$9.4621\times10^{-7}\le P(E)'_W\le 8.0685\times10^{-4}$$

According to Eq.(27), the narrow interval with much more accuracy can be obtained as:

$$9.4621\times10^{-7}\le P(E)'_N\le 2.5329\times10^{-4}$$

To provide a straightforward insight to the result, the lower bound and upper bound for the interval of failure probability in the series system computed by different methods are plotted in Fig. 8(a), as for the parallel system, the results can be drawn in Fig. 8(b).

For measuring the extent of optimization numerically when we use the narrow bound method to overcome the defect of the unsatisfied accuracy existing in the wide bound method. The following equation is presented, written as:

$$\eta=\frac{\left(P_{f\_upp}^{W}-P_{f\_low}^{W}\right)-\left(P_{f\_upp}^{N}-P_{f\_low}^{N}\right)}{\left(P_{f\_upp}^{W}-P_{f\_low}^{W}\right)}\times100\% \tag{32}$$

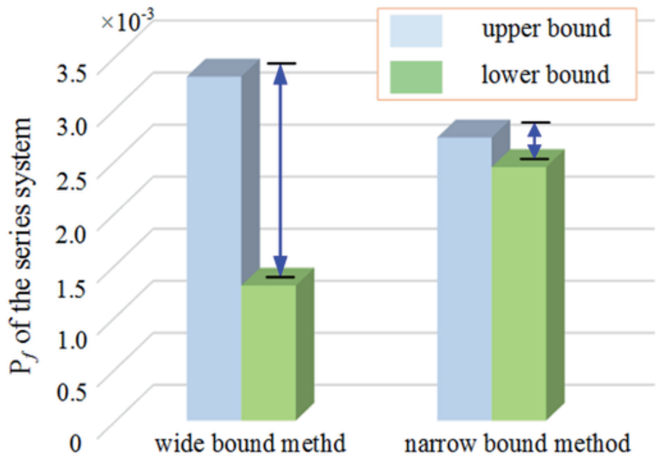

(a) P_f of the serial multi-manipulator system

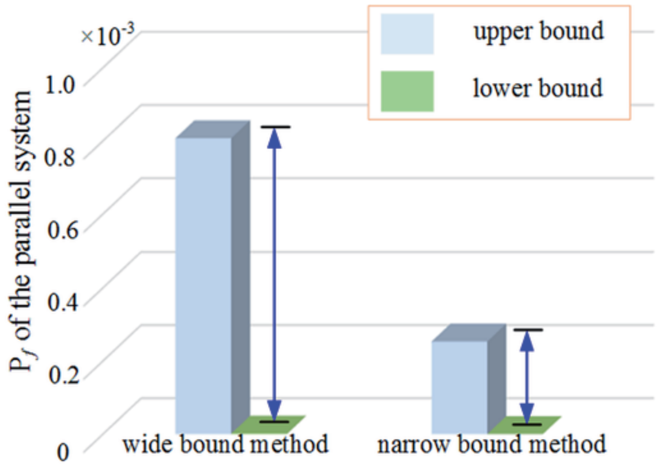

(b) P_f of the parallel multi-manipulator system

Fig. 8. Failure probability interval of different system

where the superscripts W and N denote the wide bound and narrow bound method respectively, the subscripts *upp* and *low* represent the upper bound and lower bound of the failure probability interval respectively.

Other things equal, when the system type of multiple manipulators is mainly concerned, the percentage of reliability enhancement realized by conversion from the series into the parallel system can be evaluated by the equation, given as:

$$\lambda=\frac{\left(P^{s}_{f\_upp}-P^{s}_{f\_low}\right)-\left(P^{p}_{f\_upp}-P^{p}_{f\_low}\right)}{\left(P^{s}_{f\_upp}-P^{s}_{f\_low}\right)}\times 100\% \qquad (33)$$

where the superscripts S and P denote the series and parallel system respectively.

So we can further obtain the optimization result listed in the Table 5.

Table 5. Percentage of optimization

system type	method	interval length	η	λ
series	wide bound	0.201×10^{-2}	–	–
	narrow bound	0.284×10^{-3}	85.86%	–
parallel	wide bound	0.806×10^{-3}	–	59.86%
	narrow bound	0.253×10^{-3}	68.61%	10.92%

It can be easily observed from Fig. 8 that the upper bound (maximum value) computed by the narrow bound method is much smaller than that of the wide bound method while the lower bound (minimum value) is contrary. In the series system, the interval length of failure probability are 0.201×10^{-2} (wide bound method) and 0.284×10^{-3} (narrow bound method) respectively. The narrower interval means the higher approximation accuracy. The optimization percentage provided by the narrow bound method is 85.86%, as for the parallel system, the value can be 68.61%.

Another significant feature can be also found in Table 5, is that the failure probability for the parallel system is much lower than that of the series system when the same approximate method is applied. It demonstrates the parallel system can outperform the series system. For example, the interval length of failure probability obtained by the wide bound method for the series and parallel system are 0.201×10^{-2} and 0.806×10^{-3} respectively, the reliability can be ameliorated by nearly 60%, and the result is about 10.92% when the narrow bound method is applied.

The whole process for the reliability analysis of multi-manipulators can be summarized in the flow chart drawn in Fig. 9 , in which the series system is converted into the parallel system based on the calibration technique and failure probability is calculated by use of the wide bound method and narrow bound method respectively.

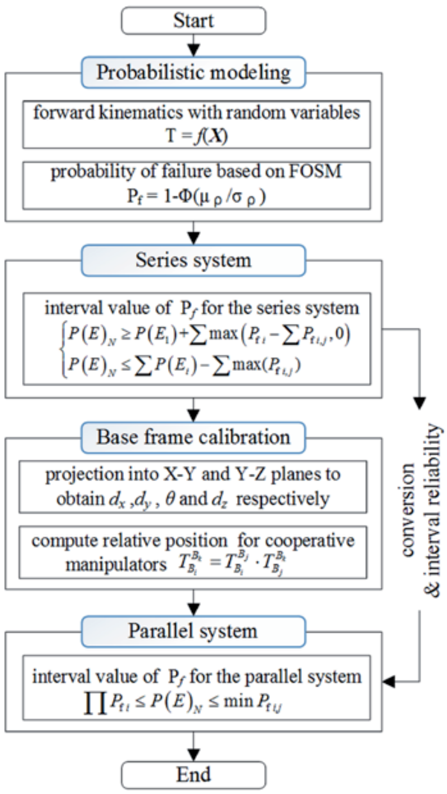

Fig. 9. Procedure for reliability analysis of multi-manipulators

5. Discussion

A deep insight is provided to better understand the problem of interval reliability estimation of the multi-manipulator system. Three aspects are focused and the corresponding specific details are given as follows.

1) Failure probability in kinematics

Unlike the dynamic analysis for multi-manipulators, of which the major objective is to develop a control algorithm to ensure the tracking error of the joint torque and position in working space can be converged close to zero. The reliability analysis in kinematics mainly focuses on the computation of probability that the multiple manipulators' positional error can satisfy the requirement together. Since there is the possibility for a single manipulator to fail both in kinematics and dynamics, it is rational to infer the multi-manipulator system can also have the failure possibility from the perspective of probability theory. No matter how robust and intelligent the control algorithm can be designed, there are always some uncertainties originated from parameters that are either ignored by us or modeled inappropriately, let alone the impact caused by the suddenly random disturbance. Therefore, both the model and control strategy are far away perfect to guarantee that the multi-manipulator system can never be failed over the service life. Similar to the study of the single manipulator, the failure probability analysis is essential and can be another important aspect to evaluate the performance of multi-manipulator system.

2) Approximate accuracy enhancement

As we can see from the Fig. 8, the approximate result can be quite different when the wide and narrow bound method are used respectively. The wide bound method lays the foundation that it is more practical to introduce the upper and lower bounds to construct an interval of the failure probability, rather than to compute a precise value which is almost impossible to obtain. However, in terms of the multi-manipulator system, the internal forces formed by the closed-chain configuration make each component dependent, the impact caused by the others on the manipulator itself is significant and therefore cannot be ignored. With this consideration, the narrow bound method further computed the joint failure probability of paired manipulators having the correlation relationship. That is the reason why the length of the interval reliability can be much shorter and the computation accuracy can be significantly increased.

3) Influence of the system type

When no connections are available, each manipulator just moves along its own trajectory independently. Actually, the errors originated from the failed manipulator can be propagated and even expanded through the closed –chain of internal force and finally bring about the negative influence on the others. The unintelligent cooperative way in the series system limits the ability of component to react to the disturbance. The base frame calibration is used to figure out the relative position, which can construct the relationship among the manipulators for the information transmission. The leader-follower scheme is applied to assign the role that each manipulator needs to play, the leading manipulator's movement is treated as the benchmark for the rest of manipulators to follow, which means the leader's actual behavior is always acceptable and safe during the transportation process. From this point of view, the series system composed by m manipulators can be converted into a parallel system consists of m-1 components, the failure may be only from the followers. In summary, the parallel system can perform more reliably than the series system mainly because of two folds: a) reduction of the number of components decreased the complexity of the system and b) strengthening in dynamic adjustment capability of each manipulator makes the parallel system more robust and reliable.

6. Conclusion

The purpose of our work is to analyze the reliability of a multi-manipulator system from the novel perspective of kinematics which is quite different from the traditional dynamic analysis. Some conclusions are made as follows.

(1) **Interval reliability estimation is suitable for the multi-manipulator system.** Since the manipulators are effected mutually by each other, which can bring about highly nonlinear, time-variant and even random parameter uncertainties, acquiring a precise value of the reliability becomes difficult. Therefore, working out the appropriate upper and lower bounds to construct an interval of failure probability is practical and economic. With consideration of the joint failure probability, the narrow bound method can provide the much more satisfied result for both the series and parallel system, of which the accuracy can be enhanced by 85.86% and 68.61% when compared to that of the wide bound method.

(2) **Base frame calibration can convert the series system to the parallel system efficiently.** Since only two different points are required to figure out the relative position and the computation process is quite simple, connections among the manipulators can be established efficiently through the base frame calibration, each manipulator is out of isolation and can acquire the dynamic adjustment capability. Therefore, the conversion from the series system to a parallel system can be realized.

(3) **The parallel multi-manipulator system can behave more stably and reliably compared with the serial mode.** Because of the outstanding dynamic adjustment capability and decrease of the complexity of the parallel system, the reliability can be much ameliorated when compared to the series system. The percentage of optimization can be nearly 59.86% and 10.92% for the wide bound and narrow bound method respectively.

Appendix A

Because of the importance of system type conversion, to better illustrate the base frame calibration procedure, the computation of the transformation from $O_1 - X_1Y_1Z_1$ to $O_2 - X_2Y_2Z_2$ is detailed with much more specific. The geometric relationship projected into the X-Y plane can be drawn in Fig. 10.

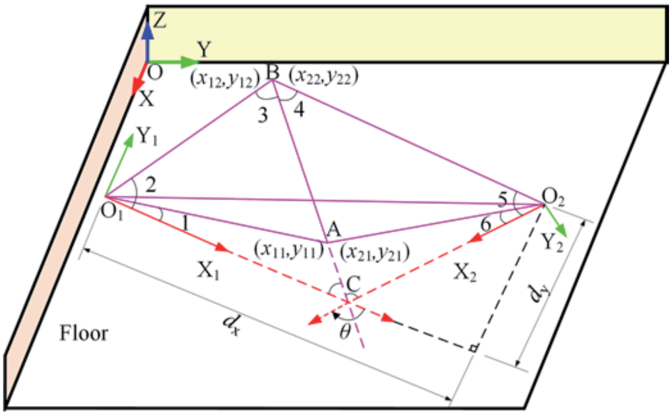

Fig. 10. Projection into the X-Y plane

The formulas for all the parameter calculation are listed in Table 6. For simplicity, the arctangent and arccosine functions are denoted as *atan* and *arcos* respectively.

Table 6. Geometric parameters in the calculating process

parameter	formula	result
$\lvert AO_1\rvert$	$\sqrt{x_{11}^2+y_{11}^2}$	404.9438
$\lvert BO_1\rvert$	$\sqrt{x_{12}^2+y_{12}^2}$	410.9163
$\angle 1$	$atan2(y_{11},x_{11})$	13.6905°
$\angle 2$	$atan2(y_{12},x_{12})$	76.049°
$\angle BO_1A$	$\angle 2-\angle 1$	62.3593°

$\lvert AB\rvert$	$\sqrt{\lvert AO_1\rvert^2+\lvert BO_1\rvert^2-2\times\lvert AO_1\rvert\times\lvert BO_1\rvert\times cos\left(\angle AO_1B\right)}$	422.4207
$\angle 3$	$arcos\left(\dfrac{\lvert BO_1\rvert^2+\lvert AB\rvert^2-\lvert AO_1\rvert^2}{2\times\lvert BO_1\rvert\times\lvert AB\rvert}\right)$	58.1273°
$\lvert AO_2\rvert$	$\sqrt{x_{21}^2+y_{21}^2}$	216.9311
$\lvert BO_2\rvert$	$\sqrt{x_{22}^2+y_{22}^2}$	592.1767
$\angle 4$	$arcos\left(\dfrac{\lvert BO_2\rvert^2+\lvert AB\rvert^2-\lvert AO_2\rvert^2}{2\times\lvert BO_2\rvert\times\lvert AB\rvert}\right)$	15.5199°
$\angle O_1BO_2$	$\angle ABO_1+\angle ABO_2$	73.6472°
$\lvert O_1O_2\rvert$	$\sqrt{\lvert BO_1\rvert^2+\lvert BO_2\rvert^2-2\times\lvert BO_1\rvert\times\lvert BO_2\rvert\times cos\left(\angle O_1BO_2\right)}$	618.4680
$\angle 5$	$\lvert atan2\left(y_{22},x_{22}\right)\rvert$	82.3030°
$\angle BCO_2$	$180°-\left(\angle 4+\angle 5\right)$	82.1771°
$\angle BCO_1$	$180-\left(\angle 2+\angle 3\right)$	45.8229°
$\boldsymbol{\theta}$	$\angle BCO_1+\angle BCO_2$	**128.00°**
$\angle BO_1O_2$	$arcos\left(\dfrac{\lvert BO_1\rvert^2+\lvert O_1O_2\rvert^2-\lvert BO_2\rvert^2}{2\times\lvert BO_1\rvert\times\lvert O_1O_2\rvert}\right)$	66.7448°
$\angle CO_1O_2$	$\angle 2-\angle AO_1O_2$	9.3050°
$\boldsymbol{d_x}$	$\lvert O_1O_2\rvert\times cos\angle CO_1O_2$	**610.33**
$\boldsymbol{d_y}$	$\lvert O_1O_2\rvert\times sin\angle CO_1O_2$	100.00
$\boldsymbol{d_z}$	$\left[\left(z_{11}-z_{21}\right)+\left(z_{12}-z_{22}\right)\right]/2$	2.92

Acknowledgement

This work was supported in part by Natural Science Foundation of Zhejiang Province (No.LQ22E050022),the National Natural Science Foundation of China (No.52175032,51775492),the Key R&D Program of Zhejiang Province (No.2020C01025,2020C01026) and the Science Foundation of Zhejiang Sci-Tech University(ZSTU) (No.21022095-Y).

References

1. Abdul RS, Norsinnira ZA and Khan MR. Kinematics Analysis and Trajectory Validation of Two Cooperative Manipulators Handling a Flexible Beam,2019 7th International Conference on Mechatronics Engineering (ICOM), Putrajaya, Malaysia, 2019, 1-6, http://doi.org/10.1109/ICOM47790.2019.8952048.
2. Aldo J, Muoz-V, Juan D, et al. Predefined-time control of cooperative manipulators. International Journal of Robust and Nonlinear Control 2020; 16(8): 1–12, https://doi.org/10.1002/rnc.5171.
3. Bichon BJ,Mcfarland JM and Mahadevan S. Efficient surrogate models for reliability analysis of systems with multiple failure modes. Reliability Engineering & System Safety 2011; 96(10): 1386-1395, http://dx.doi.org/10.1016/j.ress.2011.05.008.
4. Carlos G and Rosario D. Development of Trajectories Through the Kalman Algorithm and Application to an Industrial Robot in the Automotive Industry. IEEE Access 2019; 7(1): 23570-23578, https://doi.org/10.1109/ACCESS.2019.2899370.
5. Cornell CA. Bounds on reliability of structural systems. American Society of Civil Engineers Proceedings, Journal of the Structural Division 1967; 93(1): 171–200.
6. Craig JJ. Introduction to robotics. Addison-Wesley 2010: 2187-2195.
7. Ditlevsen O. Narrow Reliability Bounds for Structural Systems. Journal of Structural Mechanics 1979; 7(4): 453-472, https://doi.org/10.1080/03601217908905329.
8. Dohmann PBG ,Hirche S.Distributed Control for Cooperative Manipulation With Event-Triggered Communication. IEEE Transactions on Robotics 2020; 36(4): 1038-1052, https://doi.org/10.1109/TRO.2020.2973096.
9. Gallant M , Gosselin C . Singularities of a planar 3-RPR parallel manipulator with joint clearance. Robotica 2018; 36(7): 1-12, https://doi.org/10.1017/S0263574718000279.
10. Gan YH, Dai XZ, Base frame calibration for coordinated industrial robots. Robotics & Autonomous Systems 2011; 59(8): 563-570, https://doi.org/10.1016/j.robot.2011.04.003.
11. Hohenbichler M , Rackwitz R. First-order concepts in system reliability. Structural Safety 1983; 1(3): 177-188, https://doi.org/10.1016/0167-4730(82)90024-8.
12. Kim J, Song WJ and Kang BS. Stochastic approach to kinematic reliability of open-loop mechanism with dimensional tolerance. Applied Mathematical Modelling 2010; 34(5): 1225-1237, https://doi.org/10.1016/j.apm.2009.08.009.
13. Kluz R, Kubit A, Sęp J, Trzepiecinski T. Effect of temperature variation on repeatability positioning of a robot when assembling parts with cylindrical surfaces. Eksploatacja i Niezawodnosc – Maintenance and Reliability 2018; 20 (4): 503–513, https://doi.org/10.17531/ein.2018.4.1.
14. Korayem AH , Nekoo SR and Korayem M H . Optimal sliding mode control design based on the state-dependent Riccati equation for cooperative manipulators to increase dynamic load carrying capacity. Robotica 2019; 37(2):321-337, https://doi.org/10.1017/S0263574718001030.
15. Liang X, Wang H , Liu Y H, et al. Adaptive Task-Space Cooperative Tracking Control of Networked Robotic Manipulators Without Task-Space Velocity Measurements. IEEE Transactions on Cybernetics 2016; 46(10): 2386-2398.
16. Liu XY, Zhang P, Du G L. Hybrid adaptive impedance-leader-follower control for multi-arm coordination manipulators. Industrial Robot 2016; 43 (1): 112–120, https://doi.org/10.1108/IR-05-2015-0093.
17. Pandey MD and Zhang X. System reliability analysis of the robotic manipulator with random joint clearances. Mechanism & Machine Theory 2012; 58(3): 137-152, https://doi.org/10.1016/j.mechmachtheory.2012.08.009.
18. Płaczek M and Piszczek Ł. Testing of an industrial robot's accuracy and repeatability in off and online environment. Eksploatacja i

Niezawodnosc - Maintenance and Reliability 2018; 20(3): 455–464, https://doi.org/10.17531/ein.2018.3.15.
19. Qiu ZP , Yang D , Elishakoff I. Probabilistic interval reliability of structural systems. International Journal of Solids & Structures 2008; 45(10): 2850-2860, https://doi.org/10.1016/j.ijsolstr.2008.01.005.
20. Rao SS and Bhatti PK. Probabilistic approach to manipulator kinematics and dynamics. Reliability Engineering & System Safety 2001; 72(1): 47-58, https://doi.org/10.1016/S0951-8320(00)00106-X.
21. Safaei N, Tavakkoli MR, Sassani F. A series—parallel redundant reliability system for cellular manufacturing design. Proceedings of the Institution of Mechanical Engineers, Part O: Journal of Risk and Reliability 2009; 223(3): 233-250, https://doi.org/10.1243/1748006XJRR212.
22. Selçuk E. Experimental investigation of flexible connection and clearance joint effects on the vibration responses of mechanisms. Mechanism & Machine Theory 2018; 121(6): 515-529, https://doi.org/121:515-529.10.1016/j.mechmachtheory.2017.11.014.
23. Temraz NSY . Availability and reliability of a parallel system under imperfect repair and replacement: analysis and cost optimization]. International Journal of System Assurance Engineering and Management 2019; 10(5): 1002-1009, https://doi.org/10.1007/s13198-019-00829-2.
24. Thummaros R, Gang T. An adaptive actuator failure compensation scheme for a cooperative manipulator system. Robotica 2016; 34(7): 1529-1552, https://doi.org/10.1017/S0263574714002434.
25. Wang J, Wang W, et al. A Plane Projection Based Method for Base Frame Calibration of Cooperative Manipulators. IEEE Transactions on Industrial Informatics 2019; 15(3): 1688-1697, https://doi.org/10.1109/TII.2018.2878248.
26. Wang J , Zhang J, Fand Du XP. Hybrid dimension reduction for mechanism reliability analysis with random joint clearances. Mechanism & Machine Theory 2011; 46(10): 1396-1410, https://doi.org/10.1016/j.mechmachtheory.2011.05.008.
27. Wei W, Jin W, Jian H F, et al. A moment-matching based method for the analysis of manipulator's repeatability of positioning with arbitrarily distributed joint clearances. Eksploatacja i Niezawodnosc - Maintenance and Reliability 2019; 21 (1):10–20, https://doi.org/10.17531/ein.2019.1.2.
28. Xie L , Wu N and Qian W. Time domain series system definition and gear set reliability modeling. Reliability Engineering & System Safety 2016; 155(11): 97-104, https://doi.org/10.1016/j.ress.2016.06.009.
29. Zaeh MF and Roesch O. Improvement of the machining accuracy of milling robots. Production Engineering 2014; 8(6): 737-744, https://doi.org/10.1007/s11740-014-0558-7.
30. Zhao Q, Guo J and Hong J. Time-dependent system kinematic reliability analysis for planar parallel manipulators. Mechanism and Machine Theory 2020; 152(6): 1-22, https://doi.org/10.1016/j.mechmachtheory.2020.103939.
31. Zhao X, Ma M, Li B, et al. Structural Design and Analysis of 3-DOF Manipulator for Spraying Operation. 2019 IEEE International Conference on Mechatronics and Automation (ICMA), Tianjin, China, 2019: 572-577, https://doi.org/10.1109/ICMA.2019.8816606.
32. Zhang Z, Jiang C, Ruan XX, et al. A novel evidence theory model dealing with correlated variables and the corresponding structural reliability analysis method. Structural & Multidisciplinary Optimization 2017; 57: 1749–1764, https://doi.org/10.1007/s00158-017-1843-9.

Eksploatacja i Niezawodnosc – Maintenance and Reliability
Volume 24 (2022), Issue 1
journal homepage: http://www.ein.org.pl

Article citation info:
Albaghdadi AM, Baharom M, Sulaiman S. Hybrid methodology using balancing optimization and vibration analysis to suppress vibrations in a double crank-rocker engine. Eksploatacja i Niezawodnosc – Maintenance and Reliability 2022; 24 (1): 53–61, http://doi.org/10.17531/ein.2022.1.7.

Hybrid methodology using balancing optimization and vibration analysis to suppress vibrations in a double crank-rocker engine

Indexed by: Web of Science Group

Anwr M. Albaghdadi[a,]*, Masri Baharom[a], Shaharin Sulaiman[a]

[a] Universiti Teknologi Petronas (UTP), Department of Mechanical Engineering, 32610 Bandar Seri Iskandar, Perak, Malaysia

Highlights

- A combination of balancing and vibration analysis is introduced for engine evaluation.
- Variable speed balancing optimization was conducted for reliable results within speed range.
- Vibration analysis was performed in frequency and time domain for comparison and verification.
- Vibration analysis operates as a monitoring tool for engine balancing process outcome.

Abstract

This study aims to present mathematical modelling to evaluate and analyze double crank-rocker engine performance. The study suggests the use of two methods to reduce system vibration through balancing optimization and vibrational analysis. The combination of both methods acts as a verification method; besides it can be used as a tool for further system design enhancement and condition monitoring. The derived mathematical model is then used for balancing optimization to identify system shaking forces and moments, while variable speed is considered as an added parameter to evolve the optimization process. This factor shows better enhancement in reducing system shaking forces and moments compared to constant speed balancing method. Next, the system characteristics were concluded in terms of mode shapes and natural frequencies using modal and frequency response analysis, which give clear clue for secure system operational ground. Finally, the reduction in system vibrations was translated into engine's centre of mass velocity, which evaluates balancing process effectiveness and indicate if further enhancement should be conducted.

Keywords

balancing optimization, vibration analysis, double crank rocker engine, mathematical modelling, and simulation.

1. Introduction

Internal combustion engines are still the most dominant engines in today's transportation and power generation aspects. Therefore, development and condition monitoring of these engines are crucial to achieve better efficiency, higher safety, and more reliable for users. Vibrations resulted from these engines are considered as one of the biggest issues that degrade overall performance. Hence, vibration reduction is a key factor to elevate these machines productivity level and to monitor their endurance during desired working period. Vibration monitoring and analysis is one of the best tools that enable researchers and engineers to understand various problems accompanied by these engines[20].

Recently, the crank-rocker engine was introduced as a newly invented engine, where high-performance outcome was achieved due to its unique configuration [13]. However, as any new engine, this engine is still under continuous enhancement process to receive better outcome in terms of thermal and mechanical performances. This new configuration is found to have a vibration problem which might lead to degradation of engine overall performance. In this particular case, vibration was mainly caused by mechanism unbalance which led to system high shaking forces and moments. To overcome vibration issue, proper dynamic study and balancing must be done, then a system performance study would prove the efficiency of this process. Therefore, in his research, Mohammed et.al. [12] proposed a method to reduce resulting forces caused by system unbalance. This study succeeded in eliminating all shaking forces by adding counterweights to both crank and rocker linkages. but, shaking moments are naturally accompanying counterweights added as a trade-off when using such method [4]. Hence, the need for new methods to eliminate both shaking forces and shaking moments are required, and some of these methods were discussed previously in [2]. The suggested configuration is using a duplicate crank-rocker mechanism arrangement to counter the inertial forces caused by this mechanism. Based on previous studies, a reliable vibration investigation is needed to investigate the outcome from balancing process and validate the suggested method. Hence, in this study, a vibrational study is introduced to explore the transmitted vibration levels from this mechanism configuration to the engine block during operating conditions.

The purpose of recognizing the vibration problem and identifying all excitations forces, is to create a proper tool that can be utilized to analyse and troubleshoot these machines. Delvecchio et. al. [6] introduced literature on different methods used to analyze and perform a condition monitoring tool that can be used practically on internal combustion engines. Different fault conditions caused by engine vi-

(*) Corresponding author.
E-mail addresses: AM. Albaghdadi (ORCID: 0000-0003-2680-419X): al.bghdady@gmail.com, M. Baharom (ORCID: 0000-0001-9437-9186): masrib@utp.edu.my, S. Sulaiman (ORCID: 0000-0001-8819-6703): shaharin@utp.edu.my

brations were identified then diagnostic techniques and applications were discussed accordingly. In their study, Hmida et. al. [8] discussed some factors that cause engine vibrations such as combustion pressure, inertial and torsional forces, misalignment and engine main structure, etc. with the emphasis on problems accompanying cyclic variations and misfiring in engine. The authors suggested a mathematical model to analyze the effects of misfiring on crankshaft vibrations. Likewise, Liu et. al. [10] introduced piston slap of a reciprocating engine as the biggest source of vibration. In their simulation, he noticed the importance of including the torsional forces of single-cylinder reciprocating system analysis to estimate the overall vibration.

As for measuring and identifying internal combustion engine excitation forces and their impact, Zhao et. al. [23] identified and measured the excitation forces of 2-cylinder diesel engine besides combustion pressure which are cylinder slap, bearing load and inertial forces. The author claimed that the acquired data can be used effectively to model this engine, and to be used to eliminate non-combustion excitation forces. Zhao et. al. [22] suggested an inverse method to find these forces from the measured velocity of engine mounting points. This method was found to be effective to reconstruct the exact values of forces and moments values. A similar approach was proposed by [19] using the interpolation method to establish engine excitation forces.

Generally, vibration could be suppressed practically by eliminating the source causing these vibrations, such applying balancing [7] or alignment [1] to rectify equipment problems. Another method is by isolating the vibratory element from the rest of the system by applying isolators such as mechanical shock dampeners, mechanical or hydraulic absorbers, or both depending on design aspects [17]. Another classification of vibration reduction methods are also presented as passive, semi-active and active methods[3]. Wang et. al. [18] presented three methods to isolate the vibrations of a vehicle during engine start-stop operation. All three methods concluded that increasing mounting damping coefficient is more efficient to reduce these vibrations. Similarly, Ooi et. al. [14] perform an optimization process to determine engine mounts stiffness and location. The optimized values show less force transmission from engine block to the ground compared to original engine configuration. Similar work for vibration isolation and control in high speed, heavy-duty engines was introduced in [21], also by using active mount system in [9]. In their research, Sleesongsom et. al. [16], introduced a new design method through part shape design optimization to overcome vibrations on a single-cylinder engine. This process resulted an optimal design of the shape of the moving part which is considered practical to control parts vibration amplitudes. More approaches and techniques were introduced in [11] for vibration reduction in the application of internal combustion engine.

Usually, the balancing process is used to overcome shaking forces and moments of specific mechanism configuration, but when this mechanism is integrated into a mechanical system, vibration might still present due to parameters interference such as system masses, stiffness and damping of different elements. In practice, Tuning and testing the system vibrations after performing balancing might take a lot of effort and time. Therefore, this paper intends to introduce a combined study on balancing optimization and vibration analysis for double crank-rocker (DCR) engine design enhancement and as a future troubleshooting tool. The advised model is desired to introduce a basic tool to identify pre- and post-balanced engine excitation forces, analyze the system and predict engine performance. The construction of this paper goes through 6 DOF mathematical modelling of this engine model, which leads to the identification of the excitation forces caused by shaking forces and moments resulted from this mechanism operation. Next, the method of conducting balancing optimization is proposed, followed by modal and vibrational analysis of this system. The results and discussion are presented by performing a comparison between virtual engine model dynamic response and simulation results of this engine model, with verification.

2. Methodology and mathematical model

2.1. Six DOF DCR engine dynamic model

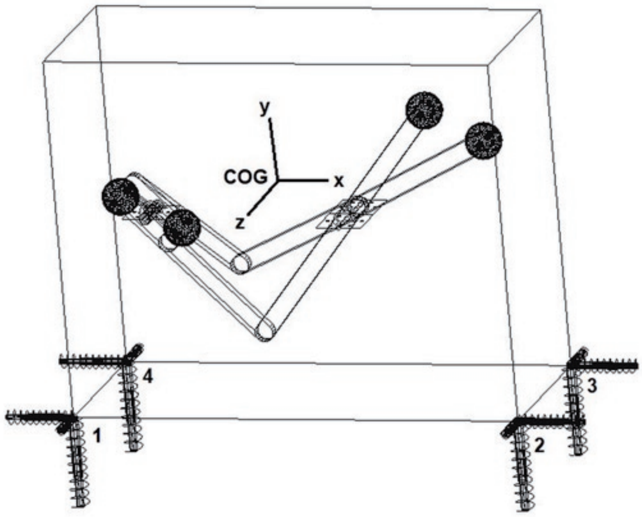

Fig. 1. DCR mechanism and engine block

In this section, the equation of motion of DCR engine model is constructed, as illustrated in Figure (1). This engine block is considered to have six degrees of freedom, also is treated as a rigid body. The engine model is attached to the ground via twelve dampers fixed into four points and oriented in three directions, namely X, Y and Z. The equation of motion for this engine can be described as:

$$M\ddot{X}(t)+C\dot{X}(t)+KX(t)=F(t) \tag{1}$$

where M, C and K represent engine block mass, damping and stiffness of each spring, introduced by 6x6 matrices. X, $\dot{X}$, and $\ddot{X}$ are displacement, velocity, and acceleration of the system respectively. $F(t)$ is the excitation forces applied on the system. The matrix of engine mass M can be represented by:

$$M=\begin{bmatrix} m & 0 & 0 & 0 & 0 & 0 \\ 0 & m & 0 & 0 & 0 & 0 \\ 0 & 0 & m & 0 & 0 & 0 \\ 0 & 0 & 0 & I_{xx} & -I_{xy} & -I_{xz} \\ 0 & 0 & 0 & -I_{xy} & I_{yy} & -I_{yz} \\ 0 & 0 & 0 & -I_{xz} & -I_{yz} & I_{zz} \end{bmatrix} \tag{2}$$

Where x, y, and z are the centre of gravity (COG) location of engine mass and coincide with system global coordinate position. Additionally, engine block moments of inertia with respect to the origin of the global coordinate system are referred by I_{xx}, I_{yy} and I_{zz} . Matrices of the stiffness and damping, are introduced by:

$$k_i=\begin{bmatrix} k_{ix} & 0 & 0 \\ 0 & k_{iy} & 0 \\ 0 & 0 & k_{iz} \end{bmatrix} \tag{3}$$

$$c_i=\begin{bmatrix} c_{ix} & 0 & 0 \\ 0 & c_{iy} & 0 \\ 0 & 0 & c_{iz} \end{bmatrix} \tag{4}$$

where k_i, and c_i represents each individual mounting i, stiffness and damping position corresponding to local location $(ix, iy, and\, iz)$, where i =1, 2,3 and 4. To transfer both matrices from the local to the global coordinate position, a $3x3$ transformation matrix A is needed. This matrix is identified using the Euler angle matrix [14], which is represented by:

$$[A]=\begin{bmatrix}\cos\alpha\cos\gamma & -\sin\alpha\cos\beta+\cos\alpha\sin\gamma\sin\beta & \sin\alpha\sin\beta+\cos\alpha\sin\gamma\cos\beta \\ \sin\alpha\cos\gamma & \cos\alpha\cos\beta+\sin\alpha\sin\gamma\sin\beta & -\cos\alpha\sin\beta+\sin\alpha\sin\gamma\cos\beta \\ -\sin\gamma & \cos\gamma\sin\beta & \cos\gamma\cos\beta\end{bmatrix} \tag{5}$$

where $\alpha, \beta\ and\ \gamma$ are rotation angles about the X-, Y- and Z-axes respectively. Hence, the transformed matrices of stiffness and damping can be calculated by:

$$k = A^{-1}\, k_i\, A \tag{6}$$

and:

$$c = A^{-1}\, c_i\, A \tag{7}$$

where k and c are the coefficient stiffness and damping matrices in the global coordinates. As for the excitation forces, it can be formulated by $6x1$ vector as follows:

$$F=\begin{Bmatrix}F_x\\F_y\\F_z\\T_x\\T_y\\T_z\end{Bmatrix} \tag{8}$$

where F represents shaking forces component in the relevant coordinate, and T is the shaking moment component about the corresponding axis. More details on identifying the excitation forces are discussed in the next section. The displacement vector is composed of 6x1 matrix as follows:

$$X=\begin{Bmatrix}\partial_x\\\partial_y\\\partial_z\\\theta_x\\\theta_y\\\theta_z\end{Bmatrix} \tag{9}$$

where ∂ and θ represent COG transitional and angular displacement vector of engine respectively corresponding to the relevant axis.

2.2. Excitation forces identification

Forces generated during internal combustion engine operation result from many reasons such as combustion pressure, engine internal parts friction, interconnection with other equipment, and speed fluctuation. In this section, forces produced by DCR parts inertial forces are highlighted to investigate the suggested mechanism stability and to make sure this engine can be elevated to the next design level. Previously, several studies were conducted to perform balancing on this mechanism [2], the advised model has shown a significant reduction in both shaking forces and moments. When this mechanism is desired to be integrated into the developed engine assembly, a vibrational analysis would help to identify engine design parameters such as corresponding masses, dampers, and stiffness characteristics. Furthermore, it is desirable to tune the whole system vibrations, identify safe operating conditions and avoid any probable damages which might occur during engine lifespan.

The transmitted forces due to mechanism inertial forces to the supporting engine bearings can be calculated using virtual work method which was illustrated in precedent studies. The generated forces are measured on joints connecting engine mechanism and engine block, which represents bearing housing in practice. The force-measurements corresponding to their axes of action are theoretically represented by:

$$\bar{F}_x = F_{C2x} + F_{R1x} - (F_{C1x} + F_{R2x}) \tag{10}$$

$$\bar{F}_y = F_{C1y} + F_{R2y} - \left(F_{R1y} + F_{C2y}\right) \tag{11}$$

$$\bar{F}_Z = F_{C1z} + F_{R2z} - \left(F_{R1z} + F_{C2z}\right) \tag{12}$$

$$\bar{F} = \Sigma\left(\bar{F}_x^{\,2} + \bar{F}_y^{\,2} + \bar{F}_z^{\,2}\right)^{\frac{1}{2}} \tag{13}$$

where $\bar{F}$ is the summation of generated forces $\bar{F}_x$, $\bar{F}_y$, and $\bar{F}_z$, on the linking joints with respect to X_i, Y_i and Z_i coordinates. These forces are generated from the crank shaking forces F_C and rocker forces F_R for the same coordinate system, where two pairs of crank linkages $C_{1,2}$ and rocker linkages $R_{1,2}$ are involved. Similarly, the exerted moments of this mechanism about relevant axes are illustrated by:

$$\bar{T}_x = \frac{P_1}{2}\times\left(F_{R1y} + F_{R2y} - F_{C1y} - F_{C2y}\right) \tag{14}$$

$$\bar{T}_y = \frac{P_1}{2}\times\left(F_{C1x} + F_{C2x} - F_{R1x} - F_{R2x}\right) \tag{15}$$

$$\bar{T}_z = \frac{P_2}{2}\times\left(F_{C1y} - F_{C2y} + F_{R1y} - F_{R2y}\right) \tag{16}$$

$$\bar{T} = \Sigma\left(\bar{T}_x^{\,2} + \bar{T}_y^{\,2} + \bar{T}_z^{\,2}\right)^{\frac{1}{2}} \tag{17}$$

where $\bar{T}$ is the total moment of shaking moments $\bar{T}_x$, $\bar{T}_y$, and $\bar{T}_z$, caused by parts inertial forces about relevant axes. P_1 is the space between both linkages, and P_2 is the distance between fixed joints. The resulting forces and moments are calculated in the local coordinate system and need to be transferred to the global coordinate system using the transformation matrix A used in (7) as follows:

$$F = [A]^{-1} * \begin{bmatrix}\bar{F}\\\bar{T}\end{bmatrix} \tag{18}$$

The above matrix is expected to have a periodic but non-harmonic time wave-form of the acting forces, owing to the interaction between double mechanism arrangement.

2.3. Frequency response function and modal analysis

If we consider a system under multiple excitation forces as input and multiple outputs, an analysis of a multi-degree of freedom MDOF system response can be translated using analysis of a group of single degree of freedom (SDOF). The conceptual representation for this solution is illustrated in Figure (2). This indicates that implementing a superposition approach can correlate final output response to related input forces.

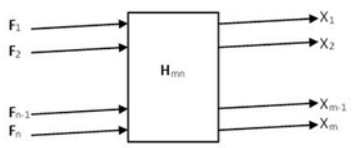

$$X_1 = H_{11} \times F_1 + H_{12} \times F_2 + \cdots + H_{1n} \times F_n$$
$$X_2 = H_{21} \times F_1 + H_{22} \times F_2 + \cdots + H_{2n} \times F_n$$
$$\vdots$$
$$X_m = H_{m1} \times F_1 + H_{m2} \times F_2 + \cdots + H_{mn} \times F_n$$

Fig. 2. Response representation of a system for multiple inputs and multiple outputs

Hence, each individual SDOF can be described in terms of natural frequency ω_n and damping ratio ξ, where both can be found by:

$$\omega_n = \sqrt{\frac{k}{m}} \tag{19}$$

$$\xi = \frac{c}{2\sqrt{km}} \tag{20}$$

The solution for the dynamic equation can be assumed to be:

$$F(t) = F_0 e^{i\omega t} \tag{21}$$

$$X(t) = X_0 e^{i\omega t} \tag{22}$$

where ω is the excitation frequency, F_0 and X_0 are the force and displacement amplitudes respectively at the respective frequency. The corresponding derivative to displacement give us velocity and acceleration equation as follows:

$$\dot{X}(t) = i\omega X_0 e^{i\omega t} \tag{23}$$

$$\ddot{X}(t) = -\omega^2 X_0 e^{i\omega t} \tag{24}$$

Apply equations (19)-(21) to the solution to SDOF system dynamic equation represented in (1) gives us displacement response as follows:

$$X = \frac{\delta}{\sqrt{\left(1-r^2\right)^2 + \left(2\xi r\right)^2}} \tag{25}$$

$$\varnothing = \tan^{-1} \frac{2\xi r}{1-r^2} \tag{26}$$

It can be noticed that the response is complex where X is the amplitude and $\varnothing$ is the response lag of the excitation frequency. The terms δ and r, are the static displacement and excitation frequency of natural frequency ratio respectively and are identified by:

$$\delta = \frac{F_0}{k} \tag{27}$$

$$r = \frac{\omega}{\omega_n} \tag{28}$$

Moreover, when considering the relation between outputs to inputs in frequency domain, the magnitude H_ω is calculated using the frequency response function (FRF) represented by:

$$H_\omega = \frac{Output}{Input} = \frac{X_\omega}{F_\omega} \tag{29}$$

Practically, to determine FRF of such system measurements, the procedure is performed by utilizing the spectra of output vibration response to the input force amplitudes. This can be achieved easily using Fast Fourier Transform (FFT) method.

In this study, the flow of the vibration analysis is performed through these steps:

- Identify system dynamic governing equations to correlate inputs to the outputs.
- Introduce modal analysis to identify system natural frequencies and corresponding shape modes.
- Find the response of the system according to the applied system forces.

Representation of FRF and system response usually can be introduced using one of three measurements, namely receptance identified by displacement X, mobility identified by velocity $\dot{X}$, or inertance defined by acceleration $\ddot{X}$, where each is in relation to the input excitation forces F. In this paper, the adopted measurement of the output response is to find system mobility, and this is justified since the frequency range is in the middle range i.e., 10 to 1000 Hz as per ISO 10816. This measurement handling is considered a good practice when dealing with applications such as rotating equipments and internal combustion engine [5].

2.4. Balancing optimization method

This part introduces balancing method conducted to determine the counterweights to be attached to the DCR mechanism to reduce resulting shaking forces and shaking moments. The basic steps considered to perform this optimization are firstly using mechanism kinematics and dynamics analysis to identify system constraints, then to decide on the design variables, and lastly to implement the objective function from equations derived in the previous section.

Usually, mechanism balancing studies are conducted at a constant speed (CS) when performing optimization of working mechanism, and seldom researches were observed to conduct variable speed (VS) balancing for less vibration values [15]. In this study, it is desired to include variable speed as a crucial factor to perform balancing optimization, which is more adequate and reasonable for implementing this mechanism in internal combustion engine applications. This enhanced approach is expected to present better engine stability within engine working speed range. This engine is desired to work under variable speed from 0 to 5000 rpm, and frequency range will be taken from 0 to 100 Hz for this study analysis. The DCR engine configurations are stated in Table (1).

It is suggested to use counterweights to balance this engine mechanism for simplicity, so four counterweights are attached to the crank and rocker linkages, and their masses are taken as design variables μ_j for (j= 1 to 4). The objective function (*of*) is introduced using both equations (10) and (14) to achieve the minimum shaking forces and moments resulting during mechanism operation. The optimization function can be written as:

$$of : \text{minimize}\left(\sigma_1 \bar{F} + \sigma_2 \bar{T}\right) \tag{30}$$

where σ_1 and σ_2 are weight factors, assigned the values of (0.5, 0,5) respectively. The proposed method is conducted first when engine is experiencing speed variation (*VS)* during the optimization. The speed

Table 1. DCR engine model configuration

Parameter	values
Engine mass m	30.5 (kg)
Center of gravity, COG location	$[0, 0, 0]^T$ (mm)
Moment of inertia $[I_{xx}, I_{yy}, I_{zz}, I_{xy}, I_{yz}, I_{zx}]$	[1.2, 0.88, 0.64, 0, 0, 0] E+08 (Kg.mm^2)
Mount stiffness, k	1900 (newton/mm)
Mount Damping, c	0.1 (newton-sec/mm)
Crank Length $C_{1,2}$	141.4 (mm)
Connecting Rod Length, CR	282.8 (mm)
Rocker length, $R_{1,2}$	640.3 (mm)
Space between linkages, P_1	100 (mm)
Distance between fixation joints, P_1	450 (mm)

during simulation time t is governed by the following conditional equation:

$$VS = \begin{cases} Max\,rpm \times t & if\ time < t \\ Max\,rpm & if\ time \geq t \end{cases} \quad (31)$$

Then, another optimization is conducted when the engine is running at constant speed CS, (i.e., 2000 rpm), and the maximum speed is 5000 rpm. The outcome results are compared corresponding to the reduction that occurred in the RMS values of system shaking forces and moments. Counterweight (μ_j) masses before and after this optimization operation are listed in Table (2).

3. Results and discussion

In this section, three main subsections are introduced to illustrate the outcomes resulting from the proposed modelling and simulation methods. The first section presents balancing results, where the shaking forces and moments values outcomes are presented and conclude the effectiveness of the utilized balancing method discussed in section 2.4.

Table 2. Counterweights values

Counter-weight (μ)	Lower limit (Kg)	Initial value (Kg)	Upper limit (Kg)	Optimized value (Kg)	
				VS Balancing	CS Balancing
1	0.01	2	10	2.269	0.01
2	0.01	2	10	2.237	1.32
3	0.01	2	10	0.795	0.876
4	0.01	2	10	0.575	0.902

Then, a modal study is presented where the natural frequencies and corresponding modal shapes of DCR system are established. This will give us an indication of safe operational frequencies and help in further system enhancement. The last part correlates balancing optimized results to perform system mobility response, where engine's COG velocity components are measured and analysed. A comparison between dynamic virtual model and simulation is conducted for results verification.

3.1. Balancing results

The balancing method illustrated in section 2.4 was conducted using the objective function described in equation (16), where the simulation is carried out under two cases: first for variable rotational speed VS of DCR mechanism from 0 to 5000 rpm, and second under constant speed CS of 2000 rpm. The counterweights μ_j are obtained for each case as stated in Table (3), and the results are individually used to perform system dynamic analysis to show the difference between both outcomes

VS balancing optimization method shows better results than CS balancing optimization method in terms of reducing forces and moments exerted by DCR mechanism. The RMS results from both balancing simulations along with percentage difference between both values are listed in Table (3). The difference in percentage was calculated using the following correlation:

$$Diff\ \% = \frac{CS\ RMS - VS\ RMS}{CS\ RMS} \times 100 \quad (32)$$

Table 3. Shaking forces and moments values with respect to VS and CS balancing method

Simulation rotation speed		Fx (Newton)	Fy (Newton)	Fz (Newton)	Tx (Newton-mm)	Ty (Newton-mm)	Tz (Newton-mm)
0-5000 rpm	CS Balancing (RMS)	1.87E+03	1.95E+03	7.50E-13	8.80E+05	1.30E+06	1.30E+06
	VS Balancing (RMS)	3.24E+02	5.55E+02	4.10E-13	7.50E+05	1.10E+06	2.50E+05
	Diff. %	82.70	71.53	45.33	14.77	15.38	80.77
2000 rpm	CS Balancing (RMS)	6.66E+02	7.09E+02	2.60E-13	3.20E+05	4.40E+05	4.60E+05
	VS Balancing (RMS)	1.16E+02	2.54E+02	1.50E-13	2.70E+05	3.80E+05	8.78E+04
	Diff. %	82.57	64.12	42.31	15.63	13.64	80.92

Table 4. VS and CS simulation results using configurations by VS balancing method

	Engine speed CS @ 2000 rpm				Engine speed VS 0 to 5000 rpm		
	Balanced	Unbalanced	Reduction %		Balanced	Unbalanced	Reduction %
Fx	1.16E+02	2.36E+03	95.09		3.24E+02	6.66E+03	95.14
Fy	2.54E+02	1.59E+03	83.97		5.55E+02	4.40E+03	87.38
Fz	1.40E-13	3.20E-12	95.63		4.13E-13	9.08E-12	95.45
Tx	2.70E+05	4.30E+05	37.21		7.58E+05	1.22E+06	37.87
Ty	3.70E+05	5.90E+05	37.29		1.06E+06	1.68E+06	36.90
Tz	8.78E+04	3.13E+06	97.20		2.46E+05	8.80E+06	97.20

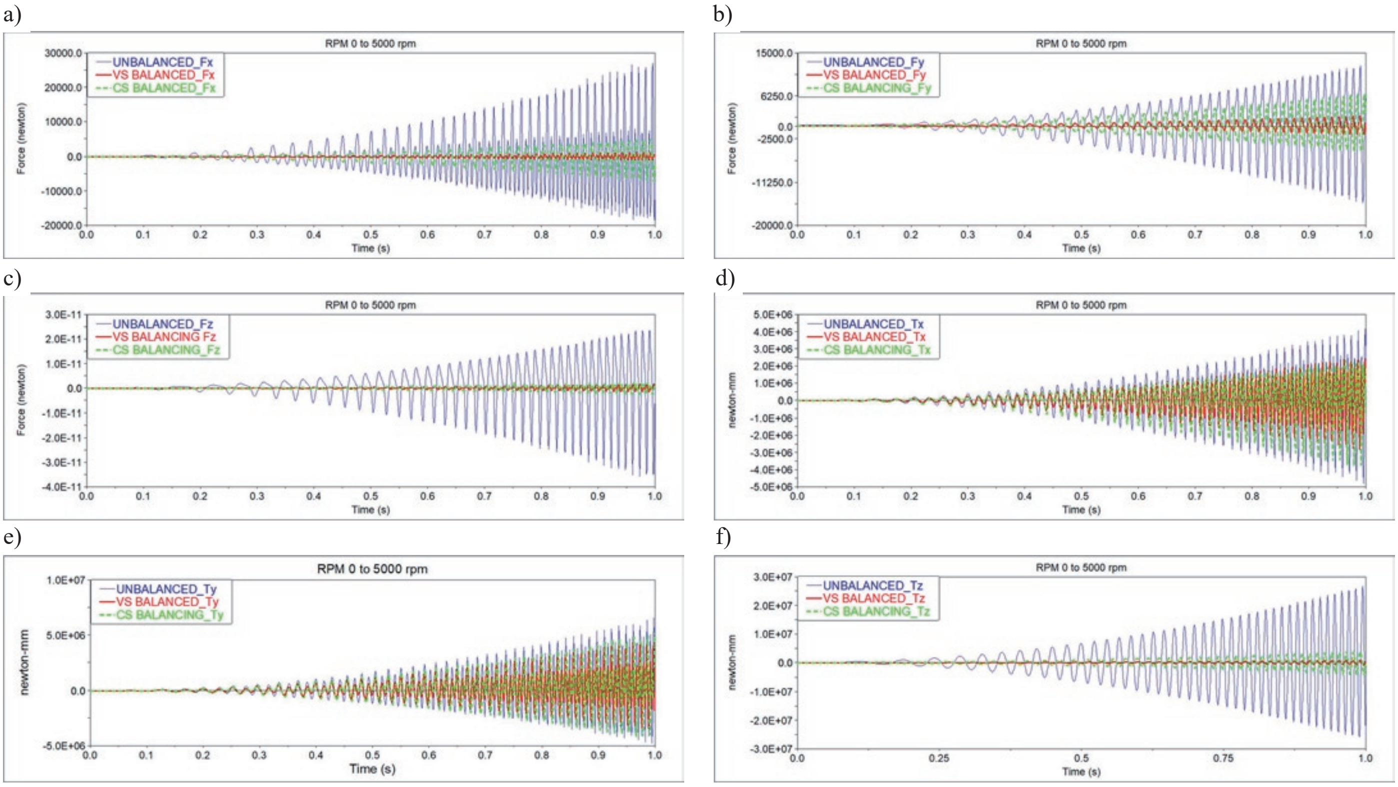

Fig. 3. Engine shaking forces and moments simulation results at variable rotational speed (i.e., 0-5000 rpm), a) Fx, b) Fy, c) Fz, d) Tx, e) Ty, and f) Tz

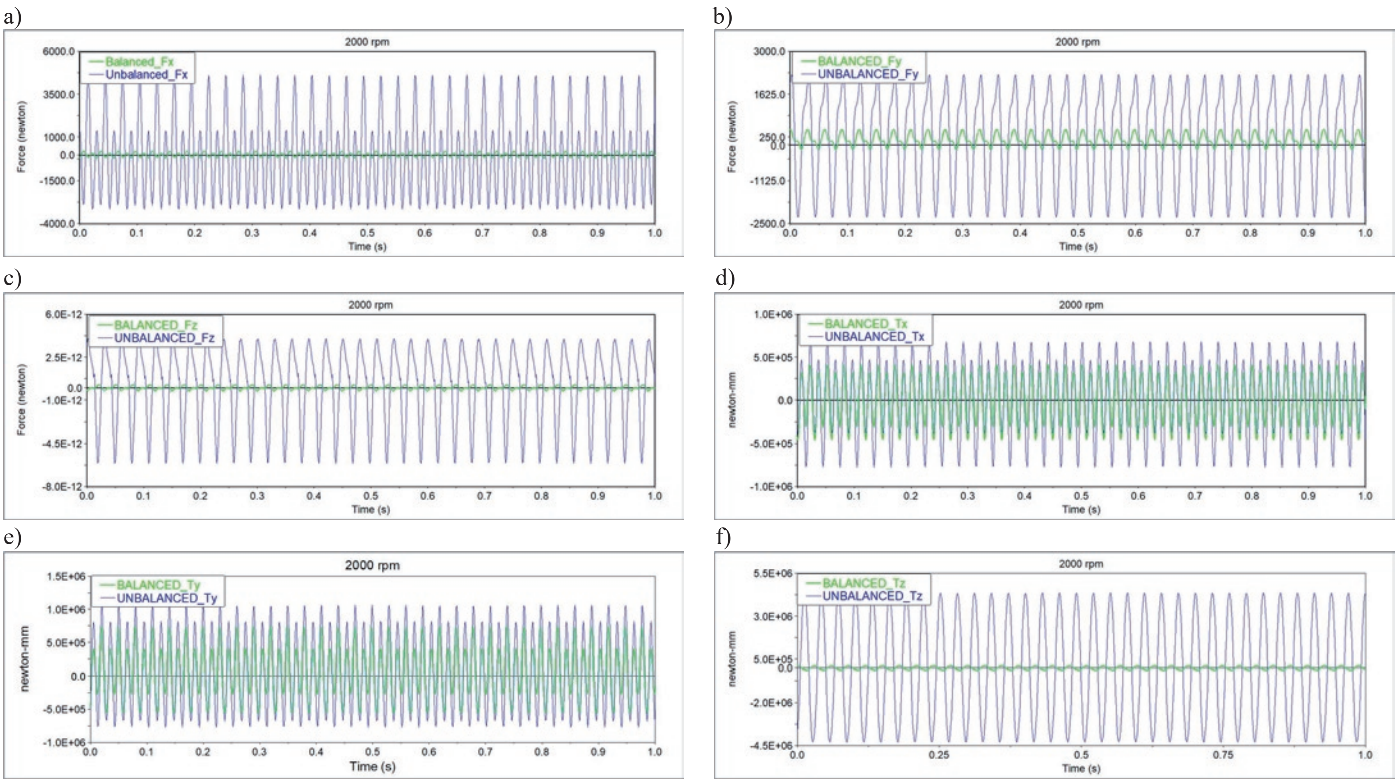

Fig. 4. Engine shaking forces and moments simulation results at constant rotational speed (i.e., 2000 rpm), a) Fx, b) Fy, c) Fz, d) Tx, e) Ty, and f) Tz

For better illustration, Figure (3) illustrates the reduction of system vibrations when simulating the engine under variable speed during simulation time using equation (17). Similarly, Figure (4) represents the outcome of this method if used during constant rotation speed (i.e., 2000 rpm). Table (4) lists the RMS values for vibration results when engine is operated under VS and CS, then compare these results to the unbalanced condition to show reduction percentage. The results of VS balancing method shaking forces and moments are then implemented next in the analysis for further system investigation through vibrational analysis.

3.2. Modal modes and frequency response function analysis

Before carrying out the proposed method to system frequency response analysis, system modal parameters namely natural frequen-

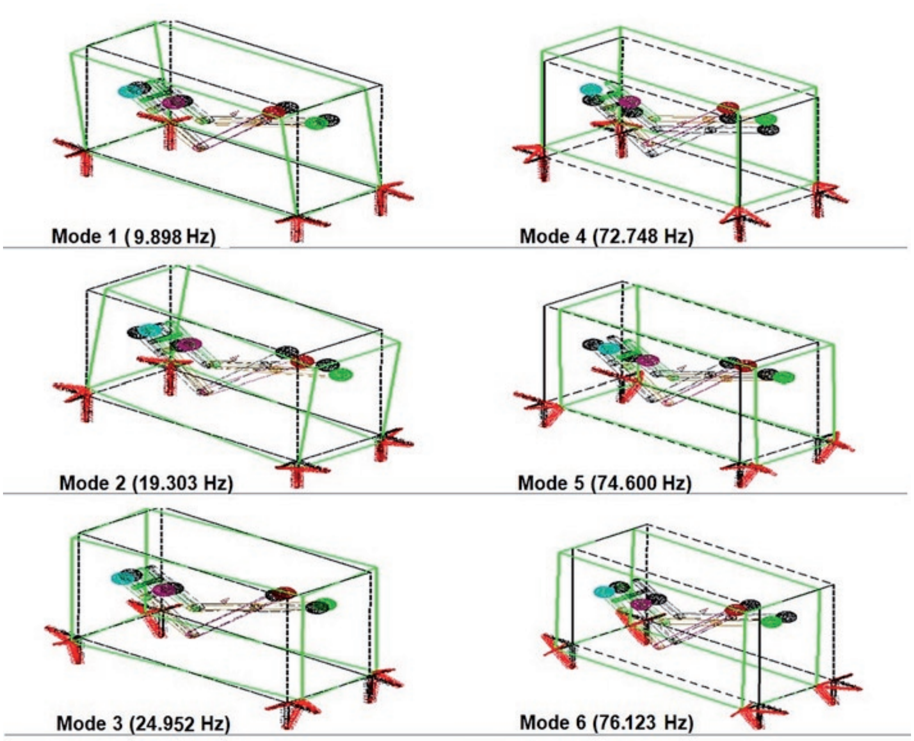

Fig. 5. DCR engine six mode of shapes and corresponding natural frequencies, (dashed lines-original position and solid line- engine mode).

a)
b)

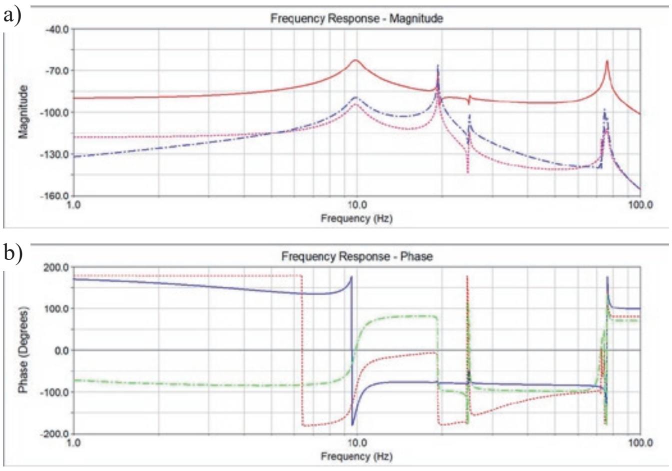

Fig. 6. Model mobility frequency response a) Magnitude and b) Phase

c)

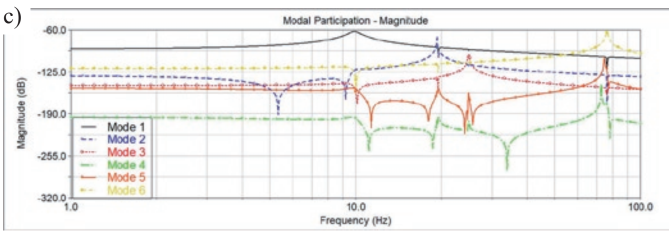

Fig. 7. Individual mode participation for mobility response Υx

cies and mode shapes are obtained for better visualization and data verification. This test also enables the created model to predict system performance better in case of any modification in the system construction. The modal analysis results using FEM describe DCR frame system free vibration analysis, where a harmonic sinusoidal force of (10 Newton) was applied to excite this system. The mode shapes corresponding to 6-DOF natural frequencies are shown in Figure (5). The illustration presents DCR engine frame mode shapes at their corresponding frequencies in green line, compared to the original position represented by dashed line. Six shapes plying harmonic forces on this 6 DOF-system, which gives an indication of system behaviour when experiencing one of these operational frequencies.

Since frequency response function has the advantage to include the effects of modes outside the measurement range and the collected data can be set to the desired range of working frequency, the frequency response of DCR mechanism was performed. For result comparison, frequency response for mobility magnitude and phase in decibels are illustrated in Figure (6).

In Figure (6), mobility response in three directions Υx, Υy, and Υz are illustrated in magnitude and phase. System mobility at operational range from 0 to 100 Hz is predicted to indicate critical frequencies that cause higher vibrational values. It can be noted that the frequency recorded for peak responses shows close values to frequencies resulting from modal analysis.

Modes' participation magnitudes are also illustrated in Figure (7), where mobility response Υx is presented. This shows how each mode contributes to the overall peak frequencies, where six modes are contributing to the mobility response Υx. Since all modes are participating to a certain degree to determine system response, it can be noticed that frequency response of all mobility outputs is resulted due to this contribution. For better illustration, Table (5) shows a list of frequency values from both modal and FRF analysis.

3.3. Engine response verification

Due to the change in operating conditions, the relation between system velocity response and excitations are proportional. The reduction of input forces is crucial to improve the engine response and to reduce the vibration levels. Figure (8) shows the effect of VS force balancing method illustrated earlier on system velocity response. The resultant forces on the DCR engine block from both CS and VS are reduced and the velocities as well. This gives us indications of how much vibrations can be controlled using this method and how much this system needs to be further enhanced. The simulation speed in this analysis is conducted at 0 to 5000 rpm variable speed, then steady-state after t=1 with 5000 rpm. The velocity components Υx, Υy, and Υz show less response by about 80%, 93%, and 22% respectively. Both Υx, and Υy shows high reduction in values which is convenient since both are dominant if compared to Υz, which shows less velocity amplitudes.

Table 5. System Natural Frequencies

Frequency Hz	1	2	3	4	5	6
Modal analysis	9.898	19.303	24.952	72.748	74.600	76.123
FRF	9.908	19.319	25.003	72.778	74.473	76.207

The response resulting from VS optimization was verified by comparing between virtual model operated at 2000 rpm and Simulation analysis, see Figure (9). The outcome results for velocity components show almost identical values, where the difference in values for Υx was about 2.91%, for Υy was about 4.78%, and for Υz was about 0.26%. This shows the consistency between proper balancing optimization using VS balancing method and vibration response for DCR engine.

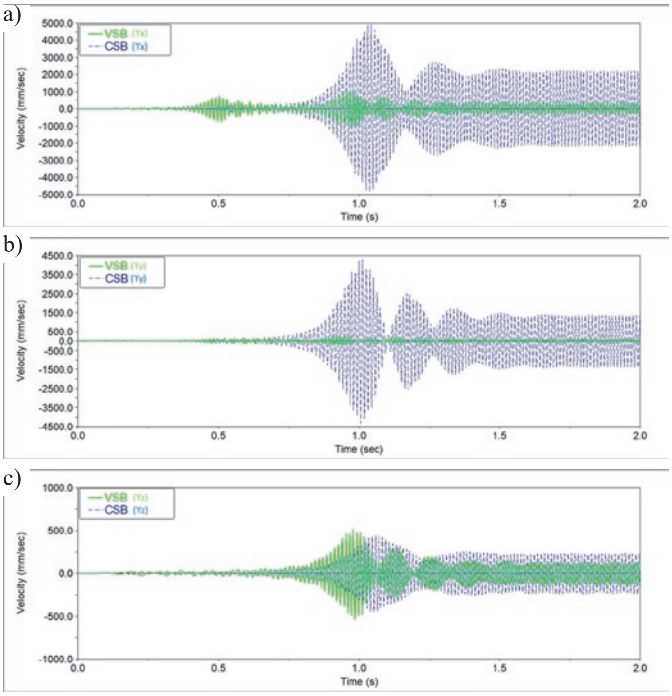

Fig. 8. Velocity response comparison between VS and CS balancing method a) Υx, b) Υy, and c) Υz

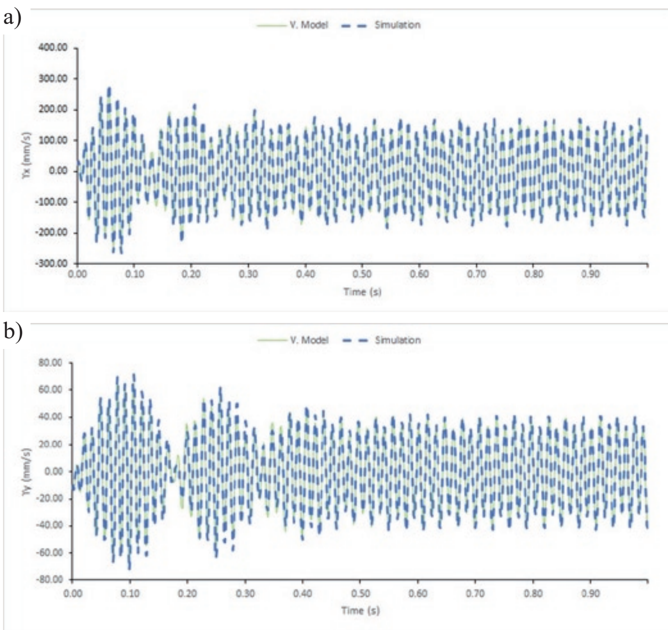

Fig. 9. Velocity response comparison between virtual model and simulation analysis a) Υx, b) Υy, and c) Υz

FFT results for velocity component is introduced in Figure (10) to identify velocity amplitudes corresponding to their frequencies. It is observed that each component is having single or multiple frequencies where it coincides with system natural frequencies identified earlier or coincides with excitation forces frequencies which are in this case having 33.33 and 66.66 Hz, respectively. Moreover, beat phenomena can be identified for Υx and Υy in this case owing to the closeness between the forces excitation frequency and system natural frequency values. Another result can be illustrated in figure (11), where resonance occurred in one or more of the velocity components (e.g., Υx), when the system is excited close enough to the system natural frequency (i.e., 75 Hz). This demonstration shows that if operational frequency matches or gets close to one of the natural frequencies, the system will experience higher vibration levels, which should be considered during design and operations.

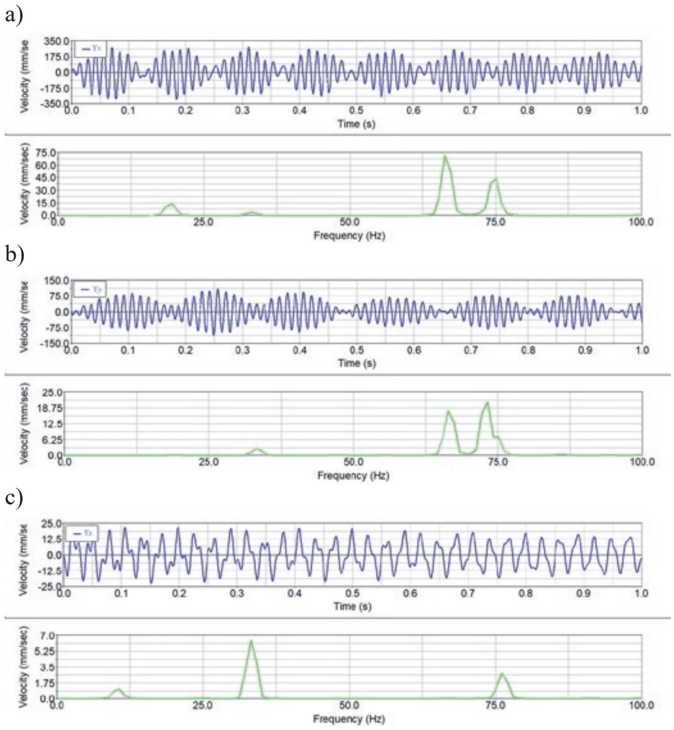

Fig. 10. Velocity response in time domain and FFT a) Υx, b) Υy, and c) Υz

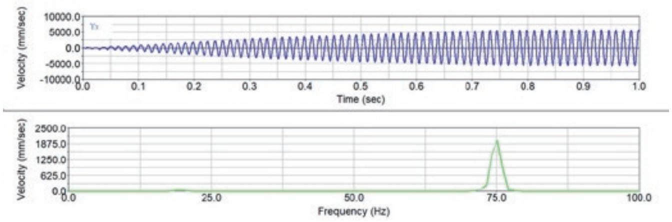

Fig. 11. Velocity response Υx when system experiences resonance

4. Conclusion

In this study, a combination of two methods were suggested for DCR engine vibration control and monitoring; these are mechanism balancing optimization and vibrational analysis. The mathematics for system dynamics and vibration response were illustrated according to the desired sequence, where system excitation forces determination is presented and correlated to the equation of motion for vibrational analysis. Then, a balancing method was suggested using engine rotation speed variations to reduce the forces and moments caused by the DCR configuration. This method has been found to be effective because forces and moments were reduced to a marginal level, the shaking forces Fx, Fy and Fz, were reduced by 82%, 71% and 45% respectively when compared to CS balancing. Similarly, shaking moments Tx, Ty and Tz were reduced by 14%, 15% and 80% using VS balancing method.

For further verification, a vibrational study was constructed to evaluate DCR system characteristics and response. The characteristics were determined by performing a modal and frequency response analysis. The results give us basic indications about this system by identifying the system natural frequency and frequency response function, which enable us to understand safe frequency zones of balanced engine operation. Both modal and FRF give close results for system natural frequencies, where six mode shapes presented corresponding to 6 DOF.

Lastly, an analysis in time domain was conducted where the velocity response of engine COG was measured and compared to show the effect of the utilized balancing method. VS balancing method results in better velocity response when compared to common balancing method using fixed rotational speed. The results when using

VS balancing show that the velocity components Υx, Υy, and Υz show less response by about 80%, 93%, and 22% respectively when compared to CS balancing. Upon implementing the effect of the optimized parameters to verify engine velocity response when running under 2000 rpm, the results show that the virtual model response was almost identical to the simulation response, the maximum difference in results between both methods was about 4% in the case of velocity component Υz.

It can be noticed that this model can be further improved to achieve better results in terms of structure design and maintenance development. Further studies can be done considering design factors such mounting design or by including other external excitations such as combustion pressure and internal parts friction.

References

1. Al-attab IIEKA, Zainal ZA. Alignment and Vibration Responses of High-Speed Alternator Couplings on Micro Gas Turbine. Arabian Journal for Science and Engineering 2020, https://doi.org/10.1007/s13369-020-04389-7.
2. Albaghdadi AM, Baharom MB, Sulaiman SA. Tri-planar balancing optimization of a double crank rocker mechanism for shaking forces and shaking moments reduction. Proceedings of the Estonian Academy of Sciences 2021; 70(3): 286-296, https://doi.org/10.3176/proc.2021.3.07.
3. Białas K, Buchacz A. Active reduction of vibration of mechatronic systems. Eksploatacja i Niezawodnosc - Maintenance and Reliability 2015; 17(4): 528-534, https://doi.org/10.17531/ein.2015.4.7.
4. Briot S, Arakelian V. Complete shaking force and shaking moment balancing of in-line four-bar linkages by adding a class-two RRR or RRP Assur group. Mechanism and Machine Theory 2012; 57: 13-26, https://doi.org/10.1016/j.mechmachtheory.2012.06.004.
5. Castilla-Gutiérrez J, Fortes J C, Pulido-Calvo I. Analysis, evaluation and monitoring of the characteristic frequencies of pneumatic drive unit and its bearing through their corresponding frequency spectra and spectral density. Eksploatacja i Niezawodnosc - Maintenance and Reliability 2019; 21(4): 585-591, https://doi.org/10.17531/ein.2019.4.7.
6. Delvecchio S, Bonfiglio P, Pompoli F. Vibro-acoustic condition monitoring of Internal Combustion Engines: A critical review of existing techniques. Mechanical Systems and Signal Processing 2018; 99: 661-683, https://doi.org/10.1016/j.ymssp.2017.06.033.
7. Guan N, Wang A, Gu Y et al. A novel coaxial balance mechanism for reciprocating piston engines. Applied Sciences 2021, https://doi.org/10.3390/app11125647.
8. Hmida A, Hammami A, Chaari F et al. Effects of misfire on the dynamic behavior of gasoline Engine Crankshafts. Engineering Failure Analysis 2021; 121: 105149, https://doi.org/10.1016/j.engfailanal.2020.105149.
9. Hong D, Kim B. Vibration reduction against modulated excitation using multichannel NLMS algorithm for a structure with three active paths between plates. Journal of Mechanical Science and Technology 2019; 33(10): 4673-4680, https://doi.org/10.1007/s12206-019-0910-0.
10. Liu S, Li W, Shuai Z, Chen M. Vibration analysis of a single-cylinder reciprocating compressor considering the coupling effects of torsional vibration. Shock and Vibration 2019, https://doi.org/10.1155/2019/3904595.
11. Mahdisoozani H, Mohsenizadeh M, Bahiraei M et al. Performance enhancement of internal combustion engines through vibration control: State of the art and challenges. Applied Sciences 2019, https://doi.org/10.3390/app9030406.
12. Mohammed SEE, Baharom MBB, Aziz ARA. Estimation of counterweight for shaking force balancing of a crank-rocker mechanism. Applied Mechanics and Materials 2014; 663: 135-140, https://doi.org/10.4028/www.scientific.net/AMM.663.135.
13. Mohammed SE, Baharom MB, Aziz ARA. Performance and combustion characteristics of a novel crank-rocker engine. Journal of Mechanical Science and Technology 2017; 31(7): 3563-3571, https://doi.org/10.1007/s12206-017-0643-x.
14. Ooi LE, Ripin ZM. Optimization of an engine mounting system with consideration of frequency-dependent stiffness and loss factor. JVC/Journal of Vibration and Control 2016; 22(10): 2406-2419, https://doi.org/10.1177/1077546314547532.
15. Peplow A, Isavand J, Kasaei A et al. A speed-variant balancing method for flexible rotary machines based on acoustic responses. Sustainability 2021; 13(13): 1-19, https://doi.org/10.3390/su13137237.
16. Sleesongsom S, Bureerat S. Vibration suppression of a single-cylinder engine by means of multi-objective evolutionary optimisation. Sustainability 2018; 10(6): 2067, https://doi.org/10.3390/su10062067.
17. Stone R, Ball J K. Automotive Engineering Fundamentals. Warrendale, SAE International: 2004, https://doi.org/10.4271/R-199.
18. Wang D, Jiang M, He K et al. Study on vibration suppression method of vehicle with engine start-stop and automatic start-stop. Mechanical Systems and Signal Processing 2020; 142: 106783, https://doi.org/10.1016/j.ymssp.2020.106783.
19. Xu C, Cao F. Engine Excitation Force Identification on the Basis of Discrete Spectrum Correction. Mathematical Problems in Engineering 2015, https://doi.org/10.1155/2015/175257.
20. Xu Y, Huang B, Yun Y et al. Model based IAS analysis for fault detection and diagnosis of IC engine powertrains. Energies 2020, https://doi.org/10.3390/en13030565.
21. Zhang B, Zhan H, Gu Y. A general approach to tune the vibration properties of the mounting system in the high-speed and heavy-duty engine. JVC/Journal of Vibration and Control 2016; 22(1): 247-257, https://doi.org/10.1177/1077546314528963.
22. Zhao X, Cheng Y, Wang L, Ji S. Real time identification of the internal combustion engine combustion parameters based on the vibration velocity signal. Journal of Sound and Vibration 2017; 390: 205-217, https://doi.org/10.1016/j.jsv.2016.11.013.
23. Zhao X, Yang Z, Pan B et al. Analysis of excitation source characteristics and their contribution in a 2-cylinder diesel engine. Measurement 2021; 176: 109195, https://doi.org/10.1016/j.measurement.2021.109195.

Eksploatacja i Niezawodnosc – Maintenance and Reliability
Volume 24 (2022), Issue 1
journal homepage: http://www.ein.org.pl
Article citation info:
Kang J, Lu Y, Zhao B, Luo H, Meng J, Zhang Y. Remaining useful life prediction of cylinder liner based on nonlinear degradation model. Eksploatacja i Niezawodnosc – Maintenance and Reliability 2022; 24 (1): 62–69, http://doi.org/10.17531/ein.2022.1.8.

Remaining useful life prediction of cylinder liner based on nonlinear degradation model

Indexed by: Web of Science Group

Jianxiong Kang[a,b], Yanjun Lu[a,b,*], Bin Zhao[a,b], Hongbo Luo[a,b], Jiacheng Meng[a,b], Yongfang Zhang[b,c,*]

[a] Xi'an University of Technology, School of Mechanical and Precision Instrument Engineering, Xi'an 710048, PR China
[b] Xi'an Jiaotong University, State Key Laboratory for Manufacturing Systems Engineering, Xi'an 710049, PR China
[c] Xi'an University of Technology, School of Printing, Packaging Engineering and Digital Media Technology, Xi'an 710054, PR China

Highlights

- A nonlinear degradation model is established to predict the RUL.
- The off-line and on-liner data are used to estimate the unknow parameters adaptively.
- The proposed model has a high evaluation accuracy

Abstract

In order to effectively monitor the wear and predict the life of cylinder liner, a nonlinear degradation model with multi-source uncertainty based on Wiener process is established to evaluate the remaining useful life (RUL) of cylinder liner wear. Due to complex service performance of cylinder liner, the uncertainty of operational environment and working conditions of cylinder liner wear are considered into the model by a random function. The probability density function (PDF) formula of RUL is derived, and the maximum likelihood estimation method is adopted to estimate the unknown parameters of PDF. Considering the evaluated parameters as the initial values, the model parameters are updated adaptively, and an adaptive PDF is obtained. Furthermore, the proposed model is compared with two classical degradation models. The results show that the proposed model has a good performance for predicting the life, and the error is within 5%. The method can provide a reference for condition monitoring of cylinder liner wear.

Keywords

remaining useful life, cylinder liner wear, nonlinear degradation, maximum likelihood estimation, adaptive PDF.

1. Introduction

Failure analysis methods are widely used in aviation, navigation, wind power and other industries. To prevent sudden failure of components, a hybrid approach with the fusion of model-based and data-driven approaches was proposed, and the nonlinear degradations of dynamical system components was analyzed [17]. In order to investigate the effects of stiffness degradation of fiber reinforced polymer (FRP) on reliability and failure, the relationship between stiffness degradation and strength degradation was established, and a probability model of stiffness degradation of FRP was presented [6]. Aim to control the operation risk of the internal combustion engines (ICEs), the diagnosis [20, 29], repair and replacement [23] technologies were used to assess service status. Piston ring-cylinder liner (PRCL) system is the core component of ICEs, and it determines the power conversion efficiency of the system. The cylinder liner plays an important role in PRCL, and the wear of cylinder liner greatly impacts on the safe operation and long life of the system. Prognostics and health management (PHM) is an important method to monitor operational condition of cylinder liner wear. Therefore, to ensure high-efficiency and safe operation of the system, the degradation performance of cylinder liner needs to be evaluated, and RUL needs to be predicted based on degradation data.

Cylinder liner wear occurs during the operational process inevitably, and it is related to the tribological characteristics [5], dynamic characteristics [1] and operation conditions of PRCL system [2]. It is difficult to acquire a large number of data sets because that the wear changes randomly and slowly. It increases the difficulty of life assessment of cylinder liner. In recent years, many works have been done to reveal the mechanism of cylinder liner wear. The friction and wear characteristics of PRCL at top dead center (TDC) were investigated by numerical method, and the oil and lubrication types, surface coatings were considered into the testing [32]. The wear behaviors of cylinder liners and piston rings were investigated in a linear reciprocating tribometer, and the wear of cylinder liners of different material was compared in boundary lubrication [26]. Synchronously, the friction and wear of honing cylinder liner were discussed based on experiment analysis [12]. The above literatures analyzed the cylinder liner wear from different factors, and the results provide a reference for wear evaluation. However, the models cannot be used in the PHM. Currently, the vibration, acoustic and wear signal are used to diagnose, monitor and predict the condition of ICEs. To monitor the scuffing fault of

(*) Corresponding author.
E-mail addresses: J. Kang (ORCID: 0000-0002-6359-223X): Jianxiong_Kang@163.com, Y. Lu (ORCID: 0000-0002-3974-7705): yanjunlu@xaut.edu.cn, B. Zhao (ORCID: 0000-0002-1924-6508): 2190221137@stu.xaut.edu.cn, H. Luo (ORCID: 0000-0003-1647-8773): 1190211020@stu.xaut.edu.cn, J. Meng (ORCID: 0000-0001-7469-4234): 2200221225@stu.xaut.edu.cn, Y. Zhang (ORCID: 0000-0001-9509-7834): zhangyf@xaut.edu.cn

cylinder liner, the vibration and acoustic emission analysis were applied, the influence of emissions on scuffing fault was analyzed [19]. The failures of timing device piston and supply pump in transport utility vehicles were evaluated, and the remedial actions to avoid the failure of the system were suggested [3]. The wavelet transform and neural network were applied to extract feature and recognize the fault automatically, and the method was applied to diagnose the wear of the hydraulic cylinder [11]. Based on evidential reasoning (ER) rule, a multi-model fusion system was proposed to diagnose the wear faults of diesel engine [29]. RUL prediction is an effective way to prevent accidents, and it is conducive to monitor the operational condition of the system. A method was presented to predict the wear of piston/cylinder pair, the load-bearing and lubrication parameters were considered into the model, and the model was validated by the experiments [14]. RUL of an aviation hydraulic pump was predicted by using the numerical approach [15], and the Monte Carlo method was used to simulate the wear debris features. Considering the effects of loading sequence, a new generic framework for fatigue life prediction under the multi-level cyclic (MLC) loading is developed, the method can calculate fatigue life of materials under any MLC loading [7].

The artificial intelligence (AI) is widely used to predict RUL [4, 27], whereas the machine learning methods need adequate training data. It is difficult to obtain adequate data for long-life equipment, but the machine learning model relies too much on training data. Therefore, the stochastic models (Wiener process, Gamma process and Inverse Gaussian process) are used to describe the degradation process and predict RUL, and the empirical knowledge and dynamic information are fused into the degradation model. In the earlier study, linear Wiener process was adopted to deal with the degradation process. Nevertheless, the degradation process of equipment is usually nonlinear. It is necessary to extend the linear Wiener process to nonlinear Wiener process. Therefore, a nonlinear model was established [21], and the variable threshold was used to characterize the nonlinear characteristics of the degradation process. The nonlinear Wiener process model is widely applied due to its better performance [33]. Considering the impact of degradation rate on RUL, a novel RUL prediction method was developed under time-varying temperature condition, and a stochastic degradation rate model based on Arrhenius temperature model was proposed [28]. A system reliability model with phase-type distribution considering the variation of the degradation rate was established [16]. Similarly, the degradation states of different parameters were estimated by information of operating modes of the system [18]. A degradation model was presented to address the stochastic processes with random initial degradation [22]. However, the historical degradation data was not considered into most models. In order to consider the historical data, a degradation model with an adaptive drift was proposed, and the nonlinear characteristics of temporal uncertainty, time-varying degradation and item-to-item variability were considered into the model [31]. To consider hidden states, a nonlinear-drifted Brownian motion model under multiple hidden states was established, and the model was applied to predict RUL of rechargeable batteries [24]. For reducing the prognostic uncertainty, a right-time prediction method was proposed, and hidden Markov model and proportional hazard model were used to map the degradation path [9]. An adaptive predictive maintenance model was developed to support the regular inspection, repair and replacement of the system [10]. Based on nonlinear-drift-driven Wiener process model, the multi-source uncertainties were built by an age-dependent state-space model for the RUL estimation of degrading systems [30].

It can be seen from the above analysis that the degradation model based on Wiener process is widely used in PHM of equipment. Nonetheless, there are few applications in cylinder liner wear. Furthermore, the service process of cylinder liner has the characteristics of multi-source uncertainty during the operational conditions. Most of the existing models focus on one or a few service conditions. In order to predict RUL of cylinder liner more accurately, an adaptive nonlinear degradation with multi-source uncertainty model based on Wiener process is proposed. Different from the existing degradation models, the proposed model considers the adaptive process and stochastic effects of drift coefficient, and the Bayesian method is used to update the model parameters. On this basis, RUL of the cylinder liner wear is predicted, and the comparison of the proposed model with two classical degradation model is conducted.

2. Model description

2.1. Basic degradation model

Let $X(t_k)$ denotes the degradation process of cylinder liner wear at time t_k. The general Wiener process model with constant drift coefficient can be expressed as [25]:

$$X(t_k) = X(0) + \mu t_k + \sigma B(t_k) \tag{1}$$

where $X(0)$ is the degradation parameter at the initial time, it is usually assumed to 0. μ is the drift coefficient, σ is the diffusion coefficient, and $\sigma>0$. $B(t)$ is the standard Brownian motion. In this model, the increments are assumed to be independent of each other and followed a normal distribution: $(X(t_k)-X(t_{k-1}))\sim N(\mu(t_k-t_{k-1}), \sigma^2(t_k-t_{k-1}))$. To express conveniently, the model is marked as Model 1.

If the degradation data $X(t_k)$ exceeds the failure threshold W, the equipment is considered to be failure. The degradation process can be shown in Figure 1. Based on the concept of the first passage time (FPT), the lifetime of the equipment is defined as:

$$T=\inf\{t : X(t_k) \geq W\} \tag{2}$$

It is known that the lifetime T follows an inverse Gaussian distribution, PDF and cumulative distribution function (CDF) are formulated as:

$$f_T(t_k) = \frac{W}{\sqrt{2\pi\sigma^2 t_k^3}} \exp\left(-\frac{(W-\mu t_k)^2}{2\sigma^2 t_k}\right) \tag{3}$$

$$F_T(t_k) = \Phi\left(\frac{\mu t_k - W}{\sqrt{\sigma^2 t_k}}\right) + \exp\left(-\frac{2\mu W}{\sigma^2}\right) \cdot \Phi\left(-\frac{\mu t_k + W}{\sqrt{\sigma^2 t_k}}\right) \tag{4}$$

where $\Phi(\cdot)$ is the standard normal CDF. Based on the above analysis, RUL can be predicted.

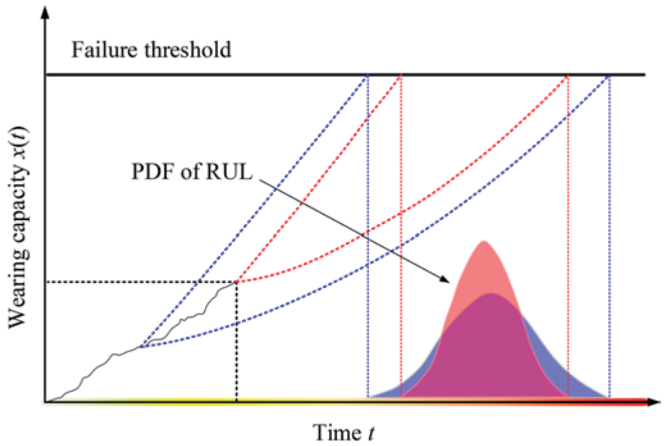

Fig. 1. Diagram of degradation process

2.2. Degradation model with individual influence

The influence of individual differences on RUL is not considered into the Model 1, and the drift coefficient is defined as a fixed constant. However, the degradation rate changes with time going on. To describe the influence of changes on degradation process, the Model 2 is proposed, and it can be expressed as:

$$X(t_k) = X(0) + \lambda t_k + \sigma B(t_k) \tag{5}$$

where λ is the drift coefficient, it defined as the random function to describe the heterogeneity among the different individuals, and it is assumed to follow the normal distribution with parameters λ_α and λ_σ.

The lifetime of equipment is defined as the formula (2). In order to derive PDF of RUL of the Model 2, the following Lemma is used.

Lemma 1 if $\alpha \sim N(\mu_\alpha, \sigma_\alpha^2)$, and $A, B \in R$, $C \in R^+$, then [21]:

$$\begin{aligned} &E_\alpha\left[(A-\alpha)\exp\left(-\frac{(B-\alpha)^2}{2C}\right)\right] = \sqrt{\frac{C}{\sigma_\alpha^2 + C}} \\ &\times\left(A - \frac{\sigma_\alpha^2 B + \mu_\alpha C}{\sigma_\alpha^2 + C}\right) \times \exp\left(-\frac{(B-\mu_\alpha)^2}{2(\sigma_\alpha^2 + C)}\right) \end{aligned} \tag{6}$$

According to the Lemma 1, PDF of RUL for Model 2 can be given as:

$$f_{L_k}(l_k) = \frac{W - x_k}{\sqrt{2\pi l_k^3(\lambda_\sigma^2 l_k + \sigma^2)}} \exp\left\{-\frac{(W - x_k - \lambda_\alpha l_k)^2}{2l_k(\lambda_\sigma^2 l_k + \sigma^2)}\right\} \tag{7}$$

2.3. The proposed nonlinear model

The degradation rates of individuals are variable for the same batch of products, and the multi-source uncertainties of products in degradation process are usually caused by environmental factors and operating conditions. To describe the degradation process in this case, the nonlinear degradation model is proposed. It is given as:

$$X(t_k) = X(0) + \alpha\int_0^{t_k} \mu(\tau)d\tau + \sigma B(t_k) \tag{8}$$

where α is the drift coefficient, and it is assumed to follow the normal distribution with mean μ_α and variance σ_α^2, which can be written as $\alpha \sim N(\mu_\alpha, \sigma_\alpha^2)$. $\mu(\tau)$ is the nonlinear function, σ is the diffusion coefficient. It is marked as Model 3.

Due to the characteristics of the wear, the exponential function is used to model the process of the wear. It can be expressed as follows:

$$\mu(\tau) = b \cdot \exp(b\tau) \tag{9}$$

In order to derive PDF of RUL, the following Lemma is given.

Lemma 2: For the degradation process $\{X(t_k), t_k \geq 0\}$ given by Eq. (8), if $\mu(\tau)$ is a continuous function at time t_k in $[0, \infty]$, PDF of the T of $X(t_k)$ can be approximated as follows:

$$f_{T|\Theta}(t_k|\Theta) \cong \frac{1}{\sqrt{2\pi t_k}}\left(\frac{S_B(t_k)}{t_k} + \frac{\alpha}{\sigma}\mu(\tau)\right)\exp\left(-\frac{S_B(t_k)^2}{2t_k}\right) \tag{10}$$

where $S_B(t_k) = (W - \alpha\int_0^{t_k}\mu(\tau)d\tau)/\sigma$, $\boldsymbol{\Theta}$ is the unknown vector, and the proof of formula (10) can be referred to literature [21].

Based on the Lemma 1 and 2, when the degradation status x_k is given at t_k, the PDF of RUL for Model 3 can be written as:

$$\begin{aligned} f_{L_k}(l_k) &= \int f_{L_K}(l_k|\alpha)p(\alpha)d\alpha \\ &= \frac{1}{\sigma\sqrt{2\pi l_k^3}} E_\alpha\left[\begin{matrix}(W - x_k - \alpha\varphi(l_k)) \\ \times\exp\left(-\dfrac{(W - x_k - \alpha\cdot\xi(l_k))^2}{2\sigma^2 l_k}\right)\end{matrix}\right] \\ &= \frac{1}{\sqrt{2\pi l_k^2(\sigma_\alpha^2\cdot\xi(l_k)^2 + \sigma^2 l_k)}}\exp\left(-\frac{(W - x_k - \mu_\alpha\cdot\xi(l_k))^2}{2(\sigma_\alpha^2\cdot\xi(l_k)^2 + \sigma^2 l_k)}\right) \\ &\times\left[W - x_k - \varphi(l_k)\frac{(W - x_k)\cdot\sigma_\alpha^2\cdot\xi(l_k) + \mu_\alpha\cdot\sigma^2 l_k}{\sigma_\alpha^2\cdot\xi(l_k)^2 + \sigma^2 l_k}\right] \end{aligned} \tag{11}$$

where $\xi(l_k) = \exp(b(l_k + t_k)) - \exp(bt_k)$; $\varphi(l_k) = (1 - bl_k)\exp(b(l_k + t_k)) - \exp(bt_k)$.

By using Eq. (11), the PDF of RUL at time t_k can be obtained.

3. Parameter estimation

3.1. Off-line parameters estimation

In this section, the unknown parameters of PDF are evaluated. Let $\boldsymbol{\Theta} = (\mu_\alpha, \sigma_\alpha^2, \sigma, b)'$ expressed the unknown parameter vector. To obtain the maximum likelihood value of $\boldsymbol{\Theta}$, the ith system is monitored at the time series $t_{i,1}, t_{i,2}, t_{i,3}, \ldots t_{i,j}$. In this case, the Eq. (5) can be given by:

$$X_i(t_{i,j}) = \alpha\left[\exp(bt_{i,j}) - 1\right] + \sigma B(t_{i,j}) \tag{12}$$

where $i = 1, 2, 3, \ldots N$, N is the independent testing system. $j = 1, 2, 3, \ldots M_i$, M_i is the number of degradation data for each system.

Let's define the function $\kappa_i(t_{i,j}) = \exp(bt_{i,j}) - 1$, $\boldsymbol{T}_i = (T_{i,1}, T_{i,2}, T_{i,3}, \cdots T_{i,j})'$, where $T_{i,j} = \kappa_i(t_{i,j})$, $\boldsymbol{X}_i = (x_i(t_{i,1}), x_i(t_{i,2}), x_i(t_{i,3}), \cdots x_i(t_{i,j}))'$. According to the characteristics of mutual independence of the standard Brownian motion, $\boldsymbol{X}_i$ obeys the multi-dimensional normal distribution. Its mean and variance can be expressed as:

$$\mu_i = \mu_\alpha \boldsymbol{T}_i, \quad \Delta = \Omega_i + \sigma_\alpha^2 \boldsymbol{T}_i \boldsymbol{T}_i' \tag{13}$$

In the Eq. (13), the $\boldsymbol{\Omega}_i$ is written as:

$$\Omega_i = \sigma^2\begin{bmatrix} t_{i,1} & t_{i,1} & \cdots & t_{i,1} \\ t_{i,1} & t_{i,2} & \cdots & t_{i,2} \\ \vdots & \vdots & \ddots & \vdots \\ t_{i,1} & t_{i,2} & \cdots & t_{i,j} \end{bmatrix} \tag{14}$$

The degradation processes of the individual device are independent each other. Once the degradation data $\boldsymbol{X}_i$ is given, the log-likelihood function of the $\boldsymbol{\Theta}$ can be expressed as:

$$\begin{aligned} \ell(\Theta|\boldsymbol{X}_i) &= -\frac{1}{2}\sum_{i=1}^N M_i\ln(2\pi) - \frac{1}{2}\sum_{i=1}^N \ln|\Delta| \\ &- \frac{1}{2}\sum_{i=1}^N (\boldsymbol{X}_i - \mu_\alpha\boldsymbol{T}_i)'\Delta^{-1}(\boldsymbol{X}_i - \mu_\alpha\boldsymbol{T}_i) \end{aligned} \tag{15}$$

$$|\Delta| = |\Omega_i|(1 + \sigma_\alpha^2 \boldsymbol{T}_i'\Omega_i^{-1}\boldsymbol{T}_i) \tag{16}$$

$$\Delta^{-1} = \Omega_i^{-1} - \frac{\sigma_\alpha^2}{1 + \sigma_\alpha^2\boldsymbol{T}_i'\Omega_i^{-1}\boldsymbol{T}_i}\Omega_i^{-1}\boldsymbol{T}_i\boldsymbol{T}_i'\Omega_i^{-1} \tag{17}$$

The first-order partial derivatives of μ_α and σ_α of the Eq. (15) are written as:

$$\frac{\partial \ell(\Theta|\boldsymbol{X}_i)}{\partial \mu_\alpha} = \sum_{i=1}^N \boldsymbol{T}_i' \Delta^{-1}\boldsymbol{X}_i - \mu_\alpha \sum_{i=1}^N \boldsymbol{T}_i' \Delta^{-1}\boldsymbol{T}_i \tag{18}$$

$$\begin{aligned}\frac{\partial \ell(\Theta|\boldsymbol{X}_i)}{\partial \sigma_\alpha} &= \sum_{i=1}^N \frac{\sigma_\alpha \boldsymbol{T}_i' \Delta^{-1}\boldsymbol{T}_i}{1+\sigma_\alpha^2 \boldsymbol{T}_i' \Delta^{-1}\boldsymbol{T}_i} \\ &+ \frac{\sigma_\alpha \sum_{i=1}^N (\boldsymbol{X}_i - \mu_\alpha \boldsymbol{T}_i)\Omega_i^{-1}\boldsymbol{T}_i\boldsymbol{T}_i'\Omega_i^{-1}(\boldsymbol{X}_i - \mu_\alpha \boldsymbol{T}_i)}{(1+\sigma_\alpha^2 \boldsymbol{T}_i'\Omega_i^{-1}\boldsymbol{T}_i)^2}\end{aligned} \tag{19}$$

Let Eq. (18) equal zero, the maximum likelihood estimation of μ_α can be estimated by:

$$\hat{\mu}_\alpha = \frac{\sum_{i=1}^N \boldsymbol{T}_i' \Delta^{-1}\boldsymbol{X}_i}{\sum_{i=1}^N \boldsymbol{T}_i' \Delta^{-1}\boldsymbol{T}_i} \tag{20}$$

The profile log-likelihood function of σ_α, σ and b can be written as:

$$\begin{aligned}\ell(\sigma_\alpha,\sigma,b|\boldsymbol{X}_i,\hat{\mu}_\alpha) &= -\frac{1}{2}\sum_{i=1}^N M_i \ln(2\pi) - \frac{1}{2}\sum_{i=1}^N \ln|\Delta| \\ &-\frac{1}{2}\left(\begin{array}{l}\left\{\sum_{i=1}^N \boldsymbol{X}_i'\Omega_i^{-1}\boldsymbol{X}_i - 2\dfrac{\sum_{i=1}^N \boldsymbol{T}_i'\Delta^{-1}\boldsymbol{X}_i}{\sum_{i=1}^N \boldsymbol{T}_i'\Delta^{-1}T_i}\sum_{i=1}^N \boldsymbol{T}_i'\Delta^{-1}\boldsymbol{X}_i\right. \\ +\left(\dfrac{\sum_{i=1}^N \boldsymbol{T}_i'\Delta^{-1}\boldsymbol{X}_i}{\sum_{i=1}^N \boldsymbol{T}_i'\Delta^{-1}T_i}\right)^2\sum_{i=1}^N \boldsymbol{T}_i'\Delta^{-1}\boldsymbol{T}\end{array}\right)\end{aligned} \tag{21}$$

Based on the above analysis, the maximum likelihood estimation of σ_α, σ and b can be obtained using the three-dimensional search method by maximizing Eq. (21), and then substituting the σ_α, σ and b into Eq. (20), the μ_α can be obtained.

3.2. On-line parameter update

In order to predict RUL more accurately, the on-line parameter estimation method based on the off-line parameters is proposed. The historical degradation data and real-time data are considered to update the drift coefficient using the Bayesian method. The posterior distribution of α at time t_k can be expressed as:

$$\begin{aligned}p(\alpha|\boldsymbol{X}_{1:k}) &= \frac{p(\boldsymbol{X}_{1:k}|\alpha)p(\alpha)}{p(\boldsymbol{X}_{1:k})} \\ &= \frac{p(x_k|\boldsymbol{X}_{1:k-1},\alpha)p(\alpha|\boldsymbol{X}_{1:k-1})p(\boldsymbol{X}_{1:k-1})}{p(\boldsymbol{X}_{1:k})} \\ &= \frac{p(x_k|\boldsymbol{X}_{1:k-1},\alpha)p(\alpha|\boldsymbol{X}_{1:k-1})}{p(x_k|\boldsymbol{X}_{1:k-1})} \\ &\propto p(x_k|\boldsymbol{X}_{1:k-1},\alpha)p(\alpha|\boldsymbol{X}_{1:k-1})\end{aligned} \tag{22}$$

where $p(\alpha|\boldsymbol{X}_{1:k-1})$ denotes the posterior distribution of α at time t_{k-1} with parameters $(\mu_{\alpha,k-1}, \sigma_{\alpha,k-1})$.

According to the characteristics of Wiener process, $(x_k|\boldsymbol{X}_{1:k-1}, \alpha)$ follows normal distribution, and PDF can be expressed as:

$$\begin{aligned}p(x_k|X_{1:k-1},\alpha) &= \frac{1}{\sqrt{2\pi\sigma^2(t_k-t_{k-1})}} \\ &\times\exp\left(-\frac{(x_k-x_{k-1}-\alpha(t_k-t_{k-1}))^2}{2\sigma^2(t_k-t_{k-1})}\right)\end{aligned} \tag{23}$$

In this situation, the Eq. (22) can be expressed as:

$$\begin{aligned}&p(\alpha|\boldsymbol{X}_{1:k}) \propto p(x_k|\boldsymbol{X}_{1:k-1},\alpha)p(\alpha|\boldsymbol{X}_{1:k-1}) \\ &\propto \exp\left(-\frac{(x_k-x_{k-1}-\alpha(t_k-t_{k-1}))^2}{2\sigma^2(t_k-t_{k-1})}\right)\cdot\exp\left(-\frac{(\alpha-\mu_{\alpha,k-1})^2}{2\sigma_{\alpha,k-1}^2}\right) \\ &\propto \exp\left\{\frac{1}{2\sigma^2(t_k-t_{k-1})\sigma_{\alpha,k-1}^2}\cdot\begin{bmatrix}(x_k-x_{k-1}-\alpha(t_k-t_{k-1}))^2 \\ \times\sigma_{\alpha,k-1}^2+(\alpha-\mu_{\alpha,k-1})^2 \\ \times\sigma^2(t_k-t_{k-1})\end{bmatrix}\right\} \\ &\propto \exp\left(-\frac{(\alpha-\mu_{\alpha,k})^2}{2\sigma_{\alpha,k}^2}\right)\end{aligned} \tag{24}$$

From the Eq. (24), the following equation can be obtained:

$$\mu_{\alpha,k} = \frac{\sigma^2\mu_{\alpha,k-1}}{\sigma_{\alpha,k-1}^2(t_k-t_{k-1})+\sigma^2} + \frac{\sigma_{\alpha,k-1}^2(x_k-x_{k-1})}{\sigma_{\alpha,k-1}^2(t_k-t_{k-1})+\sigma^2} \tag{25}$$

$$\sigma_{\alpha,k} = \sqrt{\frac{\sigma^2\sigma_{\alpha,k-1}^2}{\sigma_{\alpha,k-1}^2(t_k-t_{k-1})+\sigma^2}} \tag{26}$$

It can be seen that the $\mu_{\alpha,k}$ and $\sigma_{\alpha,k}$ are dependent on the parameters $\mu_{\alpha,k-1}$, $\sigma_{\alpha,k-1}$ and the current degradation data x_k. In this case, the historical data is introduced into the model to estimate the drift parameters adaptively. The off-line estimated results of the μ_α, σ_α are regarded as the prior distribution parameters at the initial time.

PDF of RUL of adaptive model at time t_k is:

$$\begin{aligned}f_{L_k|\Theta}(l_k|\Theta) &= \frac{1}{\sqrt{2\pi l_k^2(\sigma_{\alpha,k}^2\cdot\xi(l_k)^2+\sigma^2 l_k)}} \\ &\times\exp\left(-\frac{(W-x_k-\mu_{\alpha,k}\cdot\xi(l_k))^2}{2(\sigma_{\alpha k}^2\cdot\xi(l_k)^2+\sigma^2 l_k)}\right) \\ &\times\left[W-x_k-\varphi(l_k)\cdot\frac{(W-x_k)\cdot\sigma_{\alpha,k}^2\cdot\xi(l_k)+\mu_{\alpha,k}\cdot\sigma^2 l_k}{\sigma_{\alpha,k}^2\cdot\xi(l_k)^2+\sigma^2 l_k}\right]\end{aligned} \tag{27}$$

4. RUL prediction

4.1. Data description

As shown in Figure 2, the TDC of cylinder liner is sharply worn due to the soot particles, wear particles and thermal load. In order to monitor the health status, the wear of cylinder liner at TDC is measured to evaluate the operational status. In this section, the wear data were collected from cylinder liners of two 8-cylinder SULZER RTA 58 single acting two-stroke diesel engines from January 1999 to August 2006 [8]. The diesel engines were equipped on three identical ships of the Grimaldi Group, and they worked on the same routes during the whole year. The load, environment and operational conditions were almost the same. Because the caliper sensitivity is 0.05 mm, the measured values are rounded to the nearest multiple of 0.05. The wear paths are shown in Figure 3. It can be seen that the wear rates change randomly, and the paths of the wear are different during monitoring time. In order to facilitate the comparison of the established model, the average wear path is used to verify the model. The interpolation method is used to obtain the average wear of cylinder liner at the same time interval, and the detailed expression can be found in reference [8].

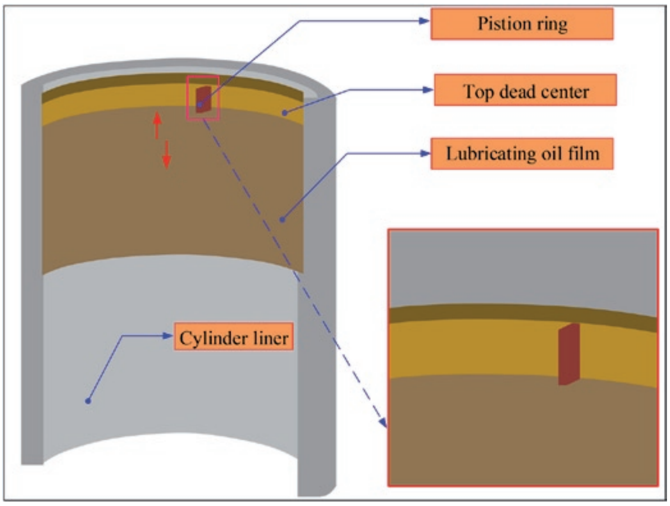

Fig. 2. The wear diagram of the cylinder liner

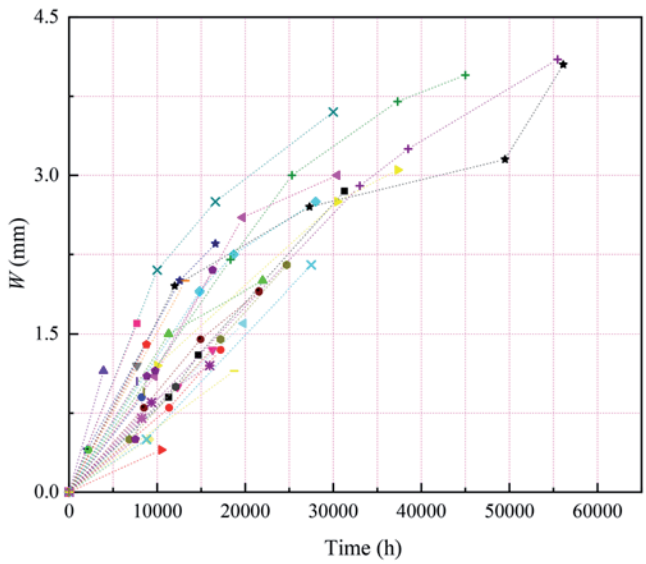

Fig. 3. Wear path of the cylinder liners [13]

4.2. Results and discussion

In this section, the three different RUL models are used to evaluate the health status of cylinder liner. Based on the collected data, the parameters of the models are evaluated by proposed method, and the estimated parameters are shown in Table 1. The evaluating performance of three RUL models can be compared and analyzed once the unknown parameters are obtained. To verify the accuracy of the models, four monitoring data at different operational time are chosen to evaluate RUL, and the maximum value of wear is 4 mm, the failure time is set as 55000 h. The selected monitoring data are t=12000 h, x=1.95 mm; t=27300 h, x=2.70 mm; t=49500 h, x=3.15 mm; t=52000 h, x=3.50 mm, respectively. The cylinder liner wear degradation paths of three models are described at 12000 h, as shown in Figure 4. Comparing the estimated wear path with the average wear path, it can be seen that the degradation path of Model 3 is closer to the average wear path, which can indirectly illustrate the superiority of Model 3.

To illustrate the evaluation performance in more detail, the PDFs of RUL for three models are analyzed at four different operation time. As shown in Figure 5, it can be seen from Figure 5(a) to (c) that the PDFs become narrow with time increases. The narrowing rates of PDF from Model 1 to Model 3 increase. It indicates that the uncertainty of the model decreases with the increase of collecting data. Comparing with Figures 5(a) and (b), the PDF curve of Figure 5(c) is more compact around the RUL. It means that the uncertainty is considered in the Model 3 to estimate the RUL. Based on the above analysis, it can be clearly derived that the random characteristics of models are gradually reduced, and the evaluation results are more accurate. The Model 3 has a better performance in the evaluation of RUL.

Table 1. Estimated results of unknown parameters by different models

Model	parameters	values
1	μ	1.0163×10^{-4}
	σ	5.200×10^{-3}
2	λ_α	1.0133×10^{-4}
	λ_σ	0.0005
	σ	0.0051
3	μ_a	0.0160
	σ_a	0.0011
	σ	0.0034
	b	0.0001

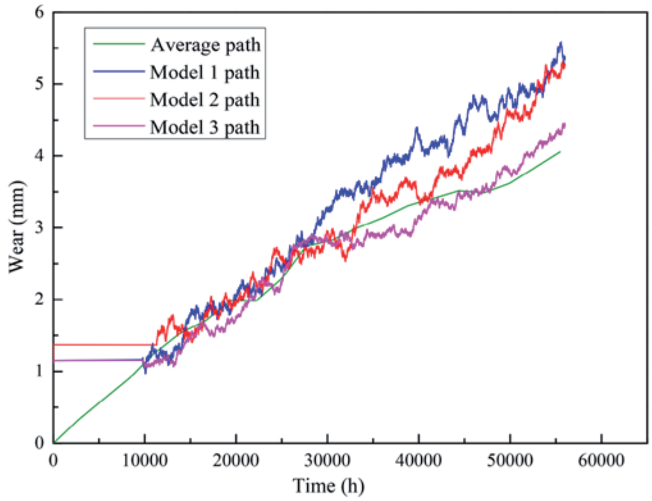

Fig. 4. Evaluated wear path

To further illustrate the evaluation performance of three models, the estimated useful lifetimes at different moments are compared, as shown in Figure 6. It can be seen that when the monitoring time away from the target value, the prediction accuracy of Model 1 and Model 2 is very low. When the monitoring time close to the target value, the prediction result exceeds the actual life. In this case, the prediction can lead to monitoring delays and accidents. For Model 3, the prediction accuracy is more accurate when the monitoring time is closer to the target value. It can effectively predict the life of equipment and prevent accidents. This is mainly because that more influencing factors are added sequentially from Model 1 to Model 3, which makes the evaluation model more perfect and effectively reduces the impact of uncertainty on the evaluation performance. According to the calculation formula of percentage error, the percentage errors of evaluated results are listed in Table 2. The calculation formula can be expressed as:

$$percentage\ errors=\frac{|ES-TA|}{TA}\times100\% \tag{28}$$

where ES is the evaluated value, TA is the target value.

Based on the Model 3, an adaptive nonlinear degradation model of cylinder liner wear is established. The evaluated parameters of Model 3 are used as initial values to update the evaluation parameters by Bayesian theory. Figure 7 is the wear paths of adaptive model at different time. It can be seen from Figure 7 that the predicted wear

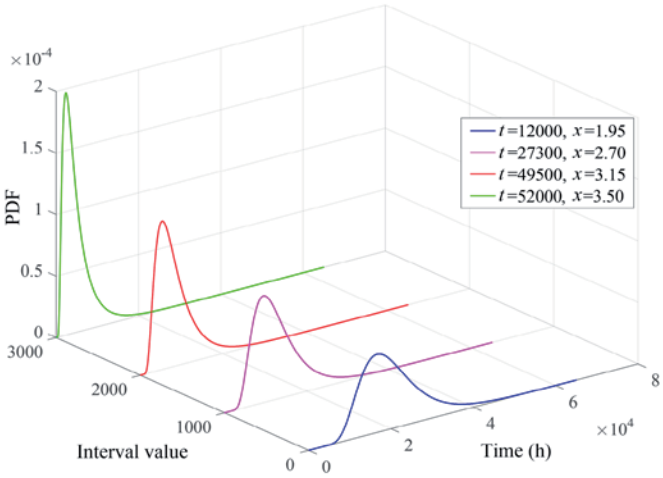

(a) Model 1

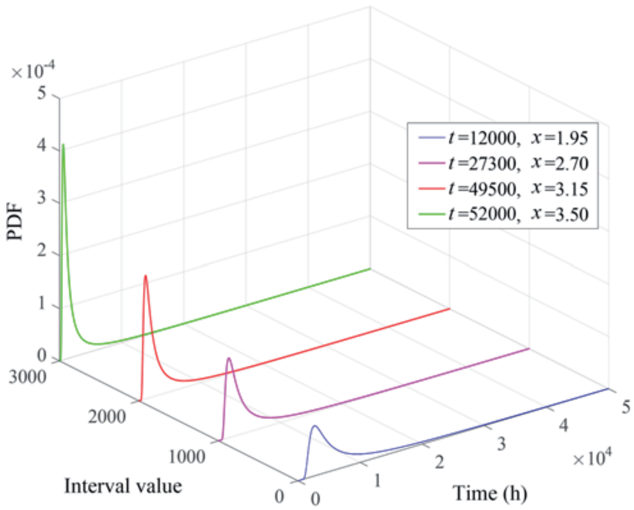

(b) Model 2

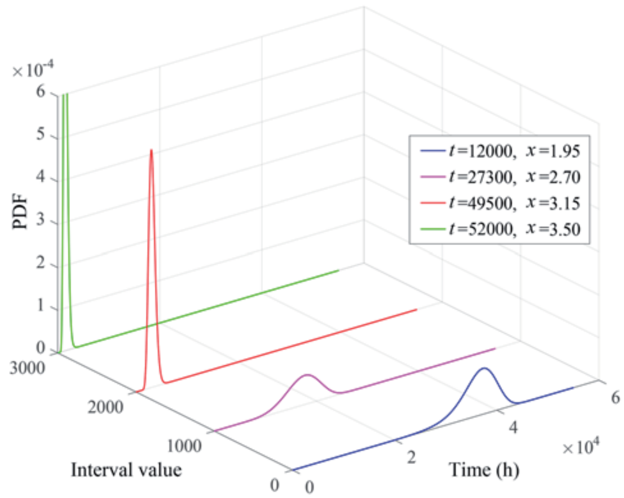

(c) Model 3

Fig. 5. PDFs of RUL for three models at different time

paths are roughly consistent with the average wear path. However, the initial value has an influence on prediction of wear path, and the adaptive model can effectively reduce the influence of the initial value on the system.

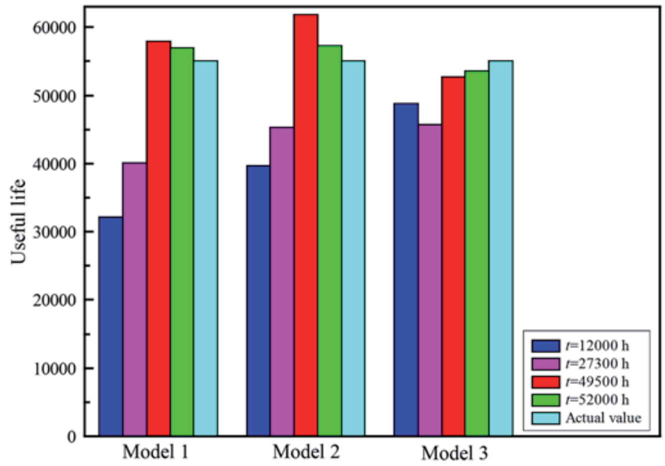

Fig. 6. Estimated useful life at different time

Table 2. Percentage error of estimating lifetime

t	Model 1	Model 2	Model 3
27300 h	26.7%	17.7%	16.9%
49500 h	5.2%	11.9%	4.2%
52000 h	3.5%	7.8%	2.5%

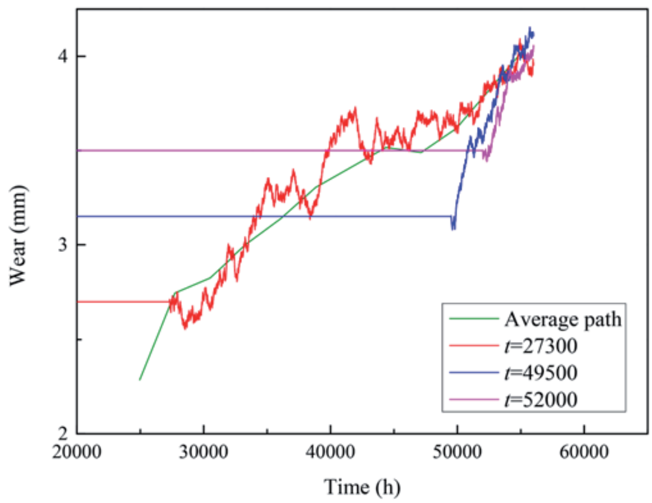

Fig. 7. Wear path under adaptive model

Figure 8 shows PDFs of RUL of adaptive model at different time. Comparing with the Figure 5, the change of the PDF is relatively small in Figure 8. It means that the adaptive method can effectively reduce the uncertainty of the system. The main reason is that real-time test data is used to update the evaluation parameters adaptively, and it can reduce the errors caused by uncertainty. By comparing the PDF at t=49500 h and t=52000 h, it is shown that the adaptive model is more effective when the time interval is small. To quantitative compare the evaluated performance, the useful lives of adaptive model and Model 3 are analyzed at different time, as shown in Figure 9. It can be seen that the accuracy of adaptive model is more accurate than Model 3, it increases 12.32%, 2.04%, and 1.27% at different evaluation points respectively. The smaller time interval is, the higher prediction accuracy of the adaptive model is acquired. When the parameters are updated adaptively, the prediction results are more accurate. The adaptive model can monitor the cylinder liner wear and health status.

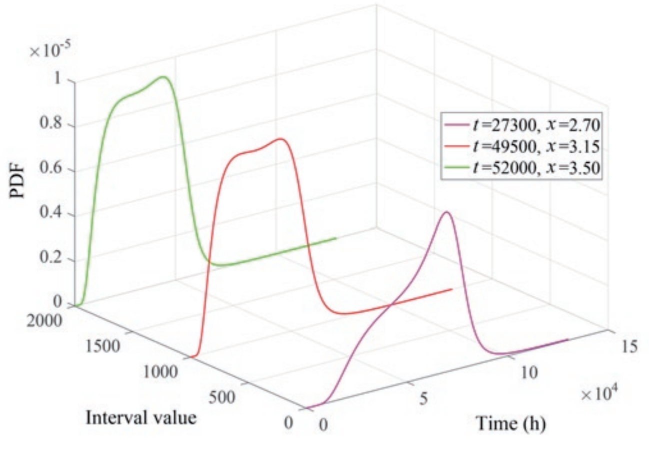

Fig. 8. PDF of adaptive model at different time

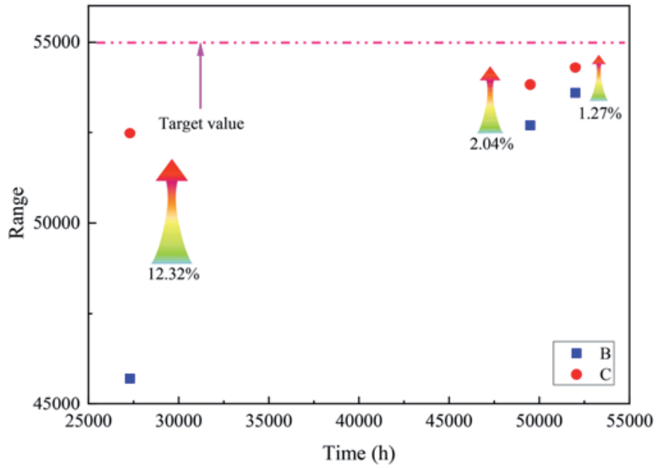

Fig. 9. Estimated useful life at different time for adaptive model

5. Conclusion

The reliability of ICEs is an important indicator of safe operation, and the cylinder liner wear directly affects the reliability of ICEs. In order to improve operation reliability, a nonlinear degradation model of the cylinder liner wear is established in this paper. The different influence factors are considered into the model by a random function, and the variation of wear is characterized as an exponential function. The PDF of RUL of cylinder liner wear is derived, and the unknown parameters are estimated by the maximum likelihood estimation method. An adaptive updating model of RUL is proposed based on the degradation model, and it can implement the prediction of wear life effectively. The main conclusions are as follows:

1) Comparing with the classical stochastic degradation model, the proposed model has a better evaluation performance.
2) The adaptive nonlinear degradation model estimates the operation life more accurately. In addition, the more historical data have, the higher accuracy becomes.
3) An adaptive model can appropriately reduce the influence of random factors on life prediction of the system.
4) The proposed model can provide a reference for monitoring the cylinder liner wear, and reduce the monitoring time as well as save costs.

Acknowledgement

This work is supported by the National Natural Science Foundation of China (Grant Nos. 51775428, 52075438), Key Research and Development Program of Shaanxi Province of China (Grant No. 2020GY-106) and Open Project of State Key Laboratory for Manufacturing Systems Engineering (Grant No. sklms2020010).

References

1. Baker C, Theodossiades S, Rahmani R, Rahnejat H, Fitzsimons B. On the transient three-dimensional tribodynamics of internal combustion engine top compression ring. Journal of Engineering for Gas Turbines and Power 2017; 139(6): 062801, https://doi.org/10.1115/1.4035282.
2. Cousseau T, Serbino E, Rejowski E, Sinatora A. Influence of steadite on the tribological behavior of cylinder liners. Industrial Lubrication and Tribology 2019; 71(2): 324-332, https://doi.org/10.1108/ILT-05-2018-0187.
3. Deulgaonkar V, Joshi K, Jawale P, Bhutada S, Fernandes S. Failure analysis of timing device piston and supply pump vanes in fuel injection system for transport utility vehicles. Journal of Failure Analysis and Prevention 2020; 21(1): 172-178, https://doi.org/10.1007/s11668-020-01052-z.
4. Ellefsen AL, Bjorlykhaug E, Aesoy V, Ushakov S, Zhang HX. Remaining useful life predictions for turbofan engine degradation using semi-supervised deep architecture. Reliability Engineering and System Safety 2019; 183: 240-251, https://doi.org/10.1016/j.ress.2018.11.027.
5. Grabon W, Pawlus P, Wos S, Koszela W, Wieczorowski M. Effects of cylinder liner surface topography on friction and wear of liner-ring system at low temperature. Tribology International 2018; 121: 148-160, https://doi.org/10.1016/j.triboint.2018.01.050.
6. Gao JX, Yuan YP. Probabilistic modeling of stiffness degradation for fiber reinforced polymer under fatigue loading. Engineering Failure Analysis 2020; 116: 104733, https://doi.org/10.1016/j.engfailanal.2020.104733.
7. Gao JX, Yuan YP, Xu RX. A framework for fatigue life prediction of materials under the multi-level cyclic loading. Engineering Failure Analysis 2021; 127: 105496, https://doi.org/10.1016/j.engfailanal.2021.105496.
8. Giorgio M, Guida M, Pulcini G. A state-dependent wear model with an application to marine engine cylinder liners. Technometrics 2010; 52(2): 172-187, https://doi.org/10.1198/TECH.2009.08092.
9. Gao ZY, Li J, Wang RX. Prognostics uncertainty reduction by right-time prediction of remaining useful life based on hidden Markov model and proportional hazard model. Eksploatacja i Niezawodnosc-Maintenance and Reliability 2021; 23 (1): 154–164, http://dx.doi.org/10.17531/ein.2021.1.16.
10. Huynh KT. An adaptive predictive maintenance model for repairable deteriorating systems using inverse Gaussian degradation process. Reliability Engineering and System Safety 2021; 213: 107695, https://doi.org/10.1016/j.ress.2021.107695.
11. Jin Y, Shan C, Wu Y, Xia YM, Zhang YT, Zeng L. Fault diagnosis of hydraulic seal wear and internal leakage using wavelets and wavelet neural network. IEEE Transactions on Instrumentation and Measurement 2019; 68(4): 1026-1034, https://doi.org/10.1109/TIM.2018.2863418.
12. Kim ES, Kim SM, Lee YZ. The effect of plateau honing on the friction and wear of cylinder liners. Wear 2018; 400: 207-212, https://doi.org/10.1016/j.wear.2017.09.028.
13. Kang JX, Lu YJ, Luo HB, Li J, Hou YT, Zhang YF. Wear assessment model for cylinder liner of internal combustion engine under fuzzy uncertainty. Mechanics & Industry 2021; 22: 29, https://doi.org/10.1051/meca/2021028.
14. Lyu F, Zhang JH, Sun GM, Xu B, Pan M, Huang XC, Xu HG. Research on wear prediction of piston/cylinder pair in axial piston pumps. Wear 2020; 456: 203338, https://doi.org/10.1016/j.wear.2020.203338.

15. Li TY, Wang SP, Zio E, Shi J, Ma ZH. A numerical approach for predicting the remaining useful life of an aviation hydraulic pump based on monitoring abrasive debris generation. Mechanical Systems and Signal Processing 2020; 136: 106519, https://doi.org/10.1016/j.ymssp.2019.106519.
16. Lyu H, Wang S, Zhang X, Yang Z, Pecht M. Reliability modeling for dependent competing failure processes with phase-type distribution considering changing degradation rate. Eksploatacja i Niezawodnosc-Maintenance and Reliability 2021; 23 (4): 627-635, http://doi.org/10.17531/ein.2021.4.5.
17. Prakash O, Samantaray AK. Prognosis of dynamical system components with varying degradation patterns using model-data-fusion. Reliability Engineering and System Safety 2021; 213: 107683, https://doi.org/10.1016/j.ress.2021.107683.
18. Prakash O, Samantaray AK, Bhattacharyya R. Adaptive prognosis of hybrid dynamical system for dynamic degradation patterns. IEEE Transactions on Industrial Electronics 2020; 67(7): 5717-5728, https://doi.org/10.1109/TIE.2019.2931489.
19. Ramteke SM, Chelladurai H, Amarnath M. Diagnosis of liner scuffing fault of a diesel engine via vibration and acoustic emission analysis. Journal of Vibration Engineering & Technologies 2020; 1-19, https://doi.org/10.1007/s42417-019-00180-7.
20. Ravikumar KN, Kumar H, Kumar GN, Gangadharan KV. Fault diagnosis of internal combustion engine gearbox using vibration signals based on signal processing techniques. Journal of Quality in Maintenance Engineering 2020; 27(2): 385-412, https://doi.org/10.1108/JQME-11-2019-0109.
21. Si XS, Wang WB, Hu CH, Zhou DH, Pecht MG. Remaining useful life estimation based on a nonlinear diffusion degradation process. IEEE Transactions on Reliability 2012; 61(1): 50-67, https://doi.org/10.1109/TR.2011.2182221.
22. Shen LJ, Wang YD, Zhai QQ, Tang YC. Degradation modeling using stochastic processes with random initial degradation. IEEE Transactions on Reliability 2019; 68(4); 1320-1329, https://doi.org/10.1109/TR.2018.2885133.
23. Wakiru JM, Pintelon L, Muchiri PN, Chemweno PK. A review on lubricant condition monitoring information analysis for maintenance decision support. Mechanical Systems and Signal Processing 2019; 118: 108-132, https://doi.org/10.1016/j.ymssp.2018.08.039.
24. Wang D, Zhao Y, Yang FF, Tsui KL. Nonlinear-drifted Brownian motion with multiple hidden states for remaining useful life prediction of rechargeable batteries. Mechanical Systems and Signal Processing 2017; 93: 531-544, https://doi.org/10.1016/j.ymssp.2017.02.027.
25. Wang H, Ma XB, Zhao Y. An improved Wiener process model with adaptive drift and diffusion for online remaining useful life prediction. Mechanical Systems and Signal Processing 2019; 127: 370-387, https://doi.org/10.1016/j.ymssp.2019.03.019.
26. Wopelka T, Cihak-Bayr U, Lenauer C, Ditroi F, Takacs S, Sequard-Base J, Jech M. Wear of different material pairings for the cylinder liner-piston ring contact. Industrial Lubrication and Tribology 2018; 70(4): 687-699, https://doi.org/10.1108/ILT-07-2017-0218.
27. Wu C, Sun H, Lin S, Gao S. Remaining useful life prediction of bearings with different failure types based on multi-feature and deep convolution transfer learning. Eksploatacja i Niezawodnosc-Maintenance and Reliability 2021; 23 (4): 685–694, http://doi.org/10.17531/ein.2021.4.11.
28. Xu XD, Tang SJ, Yu CQ, Xie J, Han XB, Ouyang MG. Remaining useful life prediction of lithium-ion batteries based on Wiener process under time-varying temperature condition. Reliability Engineering and System Safety 2021; 214: 107675, https://doi.org/10.1016/j.ress.2021.107675.
29. Xu XJ, Zhao ZZ, Xu XB, Yang JB, Chang LL, Yan XP, Wang GD. Machine learning-based wear fault diagnosis for marine diesel engine by fusing multiple data-driven models. Knowledge-Based Systems 2020; 190: 105324, https://doi.org/10.1016/j.knosys.2019.105324.
30. Yu WN, Tu WB, Kim Y, Mechefske C. A nonlinear-drift-driven Wiener process model for remaining useful life estimation considering three sources of variability. Reliability Engineering and System Safety 2021; 212: 107631, https://doi.org/10.1016/j.ress.2021.107631.
31. Yu WN, Shao YM, Xu J, Mechefske C. An adaptive and generalized Wiener process model with a recursive filtering algorithm for remaining useful life estimation. Reliability Engineering and System Safety 2022; 217: 108099, https://doi.org/10.1016/j.ress.2021.108099.
32. Zabala B, Igartua A, Fernandez X, Pestner C, Ofner H, Knaus O, Abramczuk M, Tribotte P, Girot F, Roman E, Nevshupa R. Friction and wear of a piston ring/cylinder liner at the top dead centre: experimental study and modelling. Tribology International 2017; 106: 23-33, https://doi.org/10.1016/j.triboint.2016.10.005.
33. Zhai QQ, Ye ZS. RUL prediction of deteriorating products using an adaptive Wiener process model. IEEE Transactions on Industrial Informatics 2017; 13(6); 2911-2921, https://doi.org/10.1109/TII.2017.2684821.

Eksploatacja i Niezawodnosc – Maintenance and Reliability
Volume 24 (2022), Issue 1
journal homepage: http://www.ein.org.pl
Article citation info:
Nowakowski T, Komorski P. Diagnostics of the drive shaft bearing based on vibrations in the high-frequency range as a part of the vehicle's self-diagnostic system. Eksploatacja i Niezawodnosc – Maintenance and Reliability 2022; 24 (1): 70–79, http://doi.org/10.17531/ein.2022.1.9.

Diagnostics of the drive shaft bearing based on vibrations in the high-frequency range as a part of the vehicle's self-diagnostic system

Indexed by: Web of Science Group

Tomasz Nowakowski [a], Pawel Komorski [a,*]

[a] Poznan University of Technology, Faculty of Civil and Transport Engineering, Institute of Transport, ul. Piotrowo 3, 61-138 Poznań, Poland

Highlights

- Vibration measurements of the drive shaft bearings in selected vehicle during operation.
- Vibration signal processing and analysis in time and frequency domains.
- Selection of the most sensitive diagnostic parameter based on decision trees.
- On-board diagnostic algorithm to assess the technical condition of drive shaft bearings.

Abstract

Currently, one of the trends in the automotive industry is to make vehicles as autonomous as possible. In particular, this concerns the implementation of complex and innovative self-diagnostic systems for cars. This paper proposes a new diagnostic algorithm that evaluates the performance of the drive shaft bearings of a road vehicle during use. The diagnostic parameter was selected based on vibration measurements and machine learning analysis results. The analyses included the use of more than a dozen time domain features of vibration signal in different frequency ranges. Upper limit values and down limit values of the diagnostic parameter were determined, based on which the vehicle user will receive information about impending wear and total bearing damage. Additionally, statistical verification of the developed model and validation of the results were performed.

Keywords

self-diagnostic system, vibration, vehicles, signal processing methods, decision trees.

1. Introduction

An important issue that is part of the scientific field of machine operation is technical diagnostics, which consists in assessing the technical condition of a machine without disassembling it [9, 25]. For this purpose, most often working and/or accompanying processes during the operation of a technical object are used for testing [9, 30, 35]. This type of approach to condition monitoring is particularly used during the operation of various types of road vehicles [29, 32], rail vehicles [11, 26], aircrafts [2, 31] and industrial machinery [6, 18]. Technical components that are particularly susceptible to damage are rotating elements (e.g. bearings, gears, rotors, shafts, etc.). These systems or elements are often exposed to high loads and unfavorable working conditions. In order not to lead to a bad technical condition of the object, their work should be monitored in real time during the operation.

The concept of self-diagnosing vehicles, especially in the automotive industry, is particularly prominent. The origin of OBD systems dates back to the 1970s and 1980s [24]. The essence of OBD systems is the rapid diagnosis of malfunctions that have an adverse effect on the environment. However, the notion of diagnostics may refer to many other factors affecting the technical condition of a vehicle from a broader point of view, i.e. comfort and safety of driving or prediction of repair costs. In the last dozen or so years, the development of this area has been accelerated, and the biggest car corporations outdo each other in terms of developing innovative solutions. The use of various types of sensors (e.g. pressure, temperature, vibrations, etc.), actuators and filters in mechanical systems (e.g. fuel injection, exhaust gas cleaning, etc.), and, most of all, electrical and electronic systems in modern vehicles is not surprising as regards technical condition monitoring and emission testing [17]. One of the many examples of on-board diagnostic systems is the use of noise emissivity to monitor the condition of air-conditioner blower operation using the artificial neural network technique [39]. Another example is the use of pressure change signal as a diagnostic parameter to monitor vehicle tires [32]. The research led to the development of a low cost piezoresistive sensing method based on smart pressure sensor which achieves greater accuracy due to its built-in temperature compensation, filtering and self-calibration capabilities. A recent example of an on-board diagnostic system is a proposal for a tool to monitor the performance of battery systems in electric vehicles (vehicles that are becoming increasingly popular these days) [42]. The system is based on big data statistical methods (machine learning algorithms) using the changes of cell terminal voltages in a battery pack as the main diagnostic parameter. In addition to monitoring vehicle performance, research is also being carried out to analyze driver behavior as one of the main sources of danger on the roads and also the main culprit for some vehicle damage and malfunctions, which may result from improper use and driving style [4]. In conclusion, it is worth noting that the common part of most of the above-mentioned research and

(*) Corresponding author.
E-mail addresses: T. Nowakowski (ORCID: 0000-0001-5415-7052): tomasz.nowakowski@put.poznan.pl, P. Komorski (ORCID: 0000-0003-3213-3855): pawel.komorski@put.poznan.pl

analysis is the use of machine learning algorithms as an effective tool of artificial intelligence in the development of various types of on-board diagnostic systems. Another example of adaptation of machine learning algorithm to the kind and type of malfunction of the throttle control subsystem in a car is the research described in the [29]. On the other hand, the paper [37] presents an extensive literature analysis on the use of artificial intelligence in the diagnostics of various systems/assemblies in a vehicle.

This paper presents a modern approach to monitoring the performance of drive shaft bearings in a road vehicle. Vibration accelerations of a drive shaft bearing in good and bad technical condition were measured. The analyses involved various time domain features of vibration signal over several frequency ranges. Thus, the vibration signal was used as the main diagnostic parameter, using machine learning to develop a new algorithm for diagnosing drive shaft bearings as part of a comprehensive car self-diagnostic system (CSDS). The system is ultimately intended to complement OBD-type systems with information related to predicting operating costs. Permissible and limiting values of the selected diagnostic parameter have been indicated. Additionally, the regression model of the diagnostic parameter as a function of the driving speed has been developed, validated and statistically verified.

2. Related works and other methods

The chapter presents selected methods and tools using the vibration signal as the main diagnostic parameter for monitoring the technical condition of machinery, especially vehicles. In addition, the authors have particularly focused on the description of methods for diagnostics of bearings as an element particularly susceptible to wear.

The paper [35] presents combustion engine valve clearance diagnostics based on vibration signals using machine learning algorithms. Vibration signals were obtained from a triaxial vibration acceleration transducers located on the engine head. The obtained time waveforms of vibration signals were parameterized for the engine working under different loads, with different rotational speeds and valve clearances. A similar approach using the improved variational mode decomposition (VMD) and bispectrum algorithm to analyze the vibration signal is described in the work [5]. The concept of vibration-based diagnostics of internal combustion engines is addressed in work [34]. The most important conclusion of the mentioned works is that it is possible to effectively use vibration signal analysis to evaluate valve clearance in a vehicle internal combustion engine.

Another approach representing the study of vibration signal for detecting sources of excitations in internal combustion engine is the paper [41]. The response signals caused by different excitations are coupled in the time and frequency domains. From the analyzed results, excitations that play a major role in the vibration signal in the context of different phases of engine operation have been identified. This is very useful information for monitoring the correct technical operation of an internal combustion engine. Another approach is presented in [7], where fault detection of diesel engine using vibration signal processing by combining rule-based algorithm and Bayesian networks (BNs) and Back Propagation neural networks (BPNNs) is proposed. The results of the research show the fault diagnosis method has a good diagnostic performance for a wide range of rotation speeds when the training data for BNs and BPNNs are from fixed speeds.

The paper [33] presents the possibility of diagnosing the upper suspension mount of a passenger car based on STFT vibration analysis. The evaluation of the condition is performed from the vehicle position at strictly defined EUSAMA test forces. The developed model allows to estimate the clearance in the mount.

The last example of research where not only vibration signal but mainly acoustic signal was used for machine diagnostics is the work [18]. The processing of vibroacoustic signals was based on the decomposition into several narrow-band spectral components applying different filter bank methods such as empirical mode decomposition, wavelet packet transform and Fourier-based filtering. Then, authors (based on selected measures) estimate the mutual statistical dependence between each component of signal and make the classification of various machine faults. As a result, the methodology is a promising algorithm to implement in condition monitoring of rotating machinery, even using measurements with low signal-to-noise ratio (for example acoustic signal).

Considering the above, the vibroacoustic signal is a very good carrier of machine diagnostic information. It is particularly useful for monitoring the technical condition of bearings, which is confirmed by studies [13, 15, 19, 21, 23, 40]. Analyses of the vibration signal in the frequency domain (e.g., determining the frequencies of characteristic failures of rolling bearing components [13, 21]) are an effective way to detect bearing malfunctions without disassembly. Fourier and Hilbert transforms [21, 40], wavelet transforms [15], and statistical tools in the form of various metrics (e.g., kurtosis, RMS, crest factor, etc.) [19, 23, 38] used in signal decomposition are also known ways to detect rotating element anomalies. The use of decision trees for rolling element bearing diagnostics based on time domain features of vibration signal is also frequently used. This topic is discussed in the works [1, 3, 22, 36]. The obtained results allow effective and fast technical condition diagnosis, but they are not verified in the conditions of real car operation.

Based on the selected literature analysis, the approach to monitoring the technical condition of road vehicle drive shaft bearings via vibration signal analysis was found to be very valid. An important aspect is the possibility to incorporate the low-cost method as one of many components of a comprehensive car self-diagnostic system (CSDS). The idea of diagnosing the technical condition of the vehicle from the position of the vehicle based on vibrations is also known in rail vehicles and presented, for example, in the works [12, 14, 27].

3. Research methodology

3.1. Main concept of the experimental measurements

The main research assumption was to perform vibration measurements of a drive shaft in a road vehicle, based on the assumptions of an active-passive experiment [9] (Figure 1). In the presented experiment, a qualitative assessment of the bearing after vibration tests was performed.

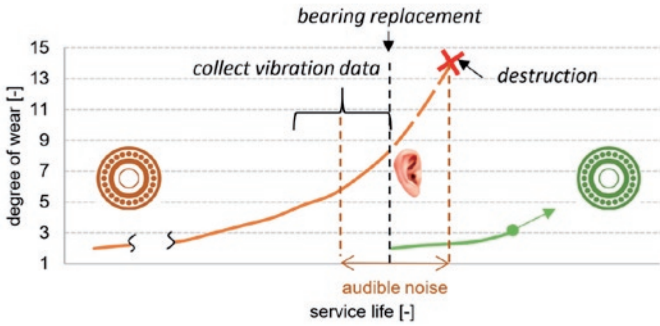

Fig. 1. The idea of the conducted active-passive experiment

The evaluation of the technical condition of the tested bearings was determined organoleptically by the technical team. This method is currently used by the operators. In this case, it is only possible to detect the degree of bearing disturbances in the noise phase, during which audible noise is emitted. This is the only reason why the bearing is currently qualified for replacement. However, detection of the malfunction is difficult at the beginning of this phase due to the relatively low noise level emission, especially in the vehicle interior. Once the malfunction was detected, vibration measurements of the bearing node were recorded under well-defined driving scenarios. The research material collected in this way formed the basis for further analysis to develop assumptions for diagnosing the bearing node, eliminating the previous common approach. The developed method is to be a part of the CSDS – car self-diagnosis system. The user should receive information about bearing malfunctions from the vehicle cockpit.

The measurements were carried out in two test cases. In the first one, the vehicle was equipped with a worn bearing located in the supports of the vehicle drive shaft. In this case, the technical condition of the vehicle can be described as technically efficient and inoperative [25], i.e. the technical condition at the time instant before the bearing failure resulting from normal wear. Next, vibration measurements were conducted after replacing the worn bearing with a new and fully operational one. A total of 90 measurements were conducted, varying with the selected measurement scenarios. Table 1 shows the exact distribution of measurement scenarios, additionally highlighting the measurement data used for analysis and modeling (white background) and validation of results (blue background).

The most important differences concern the driving speeds of the vehicles, which are 40, 60, 80, 90, and 100 km/h, respectively. For each speed, 9 measurement series were carried out for both new and worn bearings. A single measurement was carried out in three vibration transmission axes and lasted for 5 s, during which a constant and unchanged driving speed was maintained.

The tests made use of relations resulting from the basic equations of technical diagnostics with observation of signals according to the implication [9]:

$$S(\Theta) = \Phi[(U(\Theta), E(\Theta), Z(\Theta)] \quad (1)$$

where: $S(\Theta)$ – signal parameters vector, $U(\Theta)$ – state parameters vector, $E(\Theta)$ – control parameters vector, $Z(\Theta)$ – disturbances, Θ – operating ageing measure, Φ – assignment operator.

During the experiment, the authors ensured a constant control vector $E(\Theta)$ comprising the constant driving speed within a given speed range (V_c), single driver driving style (R_s), constant technical condition of the other driving systems (T_s), quality of road surface (R_q), as-new condition of the tire tread (t_t), steady tire pressure (t_p):

$$E(\Theta) = \left[V_c \; R_s \; T_s \; R_q \; t_t \;\; t_p\right] \quad (2)$$

The possible influence of the disturbances $Z(\Theta)$ was minimized (mainly atmospheric conditions). Assuming $E(\Theta)=const.$, $Z(\Theta)=const.$ and $Z(\Theta)=min.$ the following relation was obtained:

$$U(\Theta) = \mathrm{S}(\Theta) \quad (3)$$

This means that in order to assess the technical condition of a system, one needs to know the vector of the parameters of signals generated by this system and the influence on the measured signals will mainly have the change in the technical condition. Measurements were carried out in real traffic conditions, on a straight section of provincial road No. 241 (designated as the main road of accelerated traffic in Poland) with a length of about 3 km. The technical condition of the road is classified as good, characterized by a smooth asphalt surface, without visible and perceptible (while driving) road irregularities that would be an additional disturbance to the research process.

3.2. Research object and location of the measuring point

A Renault Kangoo car was used for the tests, the most important technical data of the vehicle are presented in Table 2.

The target vehicle component that was focused on during the experimental testing was the drive shaft, shown in Figure 2. The shaft is supported in two places (so-called supports), where SKF rolling bearings type 6006 RS were mounted. The outer diameter of the bearing is 55 mm, and the inner diameter is 30 mm.

After the first stage of measurements, the bearings on the supports were replaced in order to regenerate the shaft. The worn bearings were dismantled to perform an organoleptic examination and qualitative evaluation of wear and tear (Figure 3).

Table 1. Main information about measurement data

Bearing technical condition	Measurement series – 5 s each	Vehicle speed [km/h]				
		40	60	80	90	100
Bad	1	✓	✓	✓	✓	✓
	2	✓	✓	✓	✓	✓
	3	✓	✓	✓	✓	✓
	4	✓	✓	✓	✓	✓
	5	✓	✓	✓	✓	✓
	6	✓	✓	✓	✓	✓
	7	✓	✓	✓	✓	✓
	8	✓	✓	✓	✓	✓
	9	✓	✓	✓	✓	✓
Good	1	✓	✓	✓	✓	✓
	2	✓	✓	✓	✓	✓
	3	✓	✓	✓	✓	✓
	4	✓	✓	✓	✓	✓
	5	✓	✓	✓	✓	✓
	6	✓	✓	✓	✓	✓
	7	✓	✓	✓	✓	✓
	8	✓	✓	✓	✓	✓
	9	✓	✓	✓	✓	✓
Total = 90 measurement signals						

Table 2. Main technical data of the research object

Vehicle brand	Renault Kangoo
Combustion engine type	1.9 dCi (direct Common-rail injection)
Drivetrain type	4x4 attached automatically
Power	80 HP (59.66 kW)
Production year	2004
Mileage	300 000 km

Fig. 2. View of the drive shaft and the bearings location

Fig. 3. Wear of the main bearing elements: rolling elements, outer and inner raceways

Based on visual inspection, numerous damages in the form of pitting, scratches and flattening of the major rolling bearing components were found, as shown in Figure 3. The bearing components did not have a characteristic single crack or defect that could be the primary cause of bearing damage. This indicates their general wear from vehicle operation.

3.3. Measuring system and point location

During the measurements, vibration acceleration signals were recorded continuously in three directions with a sampling frequency of 65536 Hz in the frequency range up to 12 kHz. The vibration transducer was placed in the direct mounting area of the support on the differential side of the rear axle, as shown in Figure 4. The transducer was located on a flat surface as close as possible to the test bearing. This mounting arrangement provided a compromise between vibration transmission, measured frequency range, and interference. The measurements were conducted using a Hottinger Brüel & Kjaer triaxial vibration transducer type 4529-B-001 mounted to the vehicle using a dedicated magnet washer (Figure 4).

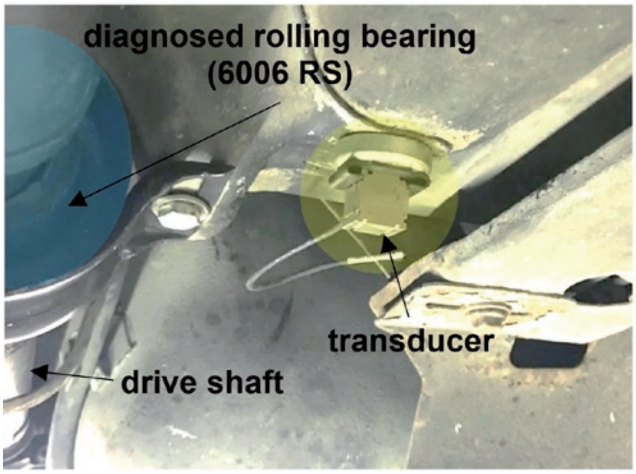

Fig. 4. Measurement point location

A Hottinger Brüel & Kjaer measurement module, type 3050-A-060, was used to acquire the measurement data. The measurement set prepared in this way allowed for individual control of vibration signal acquisition parameters, with synchronous recording and lossless archiving in digital form.

4. Analysis

In order to identify the vibration phenomena in the frequency domain, FFT analyses were performed for the extreme driving speeds. The obtained results were transformed from the time domain to the frequency domain using FFT analysis [28]:

$$X[k] = \sum_{n=0}^{N-1} x[n] e^{-i2\pi kn/N_p} \tag{4}$$

where: *X[k]* - value of the FFT transform for *k*-th frequencies in the signal (amplitude, phase, complex number), N_p – number of signal samples, n – signal sample, x – signal value [m/s^2], k – current frequency (0 Hz to 6.4 kHz).

The analyses were performed with time weighting of Hanning window, with an overlap of 66.7%. Based on the obtained spectra, the main and dominant range of excited frequencies was determined. For this purpose, the effective values of vibration accelerations were calculated considering all measurement directions, as in the equation:

$$E\_RMS_{(f1,f2)} = \sqrt{\frac{1}{3}\sum_{y=1}^{3}\sqrt{\frac{1}{N}\sum_{i=1}^{N-1} a_{P_y i}^2}} \tag{5}$$

where: N – number of signal samples, a_i – i–th signal amplitude of vibration acceleration, P_y – reference of the data to the measuring direction (P_1 – direction X, P_2 – direction Y, P_3 – direction Z), $f1$ -start of the frequency range, $f2$ – end of frequency range,

Figures 5–8 present the example results of case 4.

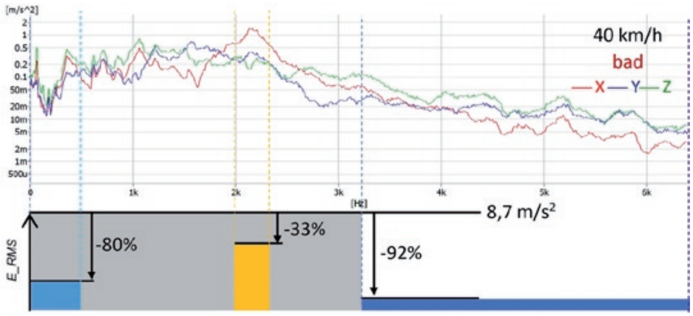

Fig. 5. Vibration acceleration spectrum of a faulty bearing node for case 4 at 40 km/h

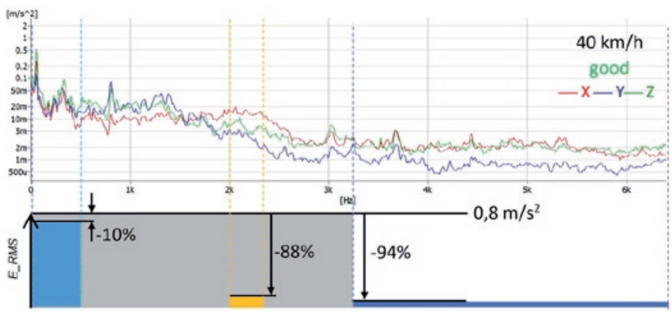

Fig. 6. Vibration acceleration spectrum of an efficient bearing node for case 4 at 40 km/h

The main range of excited frequencies for the bad bearing was in the frequency range up to 3.2 kHz. The calculated *RMS* of vibration acceleration filtered in this range was 8.7 m/s^2. However, the dominant range was the 2-2.4 kHz range, for which the vibration acceleration was 33% lower compared to the main range. The 3.2-6.4 kHz range contained vibration acceleration that was 92% lower. For the good bearing, a different proportion of vibration was observed in the distinguished ranges. The dominant range was the low frequency range up to 500 Hz. This range contained 90% of the vibration acceleration from the main frequency range. In the case of vibration in the range 3.2-6.4 Hz, the vibration contribution was similar to that of the bad bearing. Moreover, in the 2-2.4 kHz range (dominant for the faulty bearing), the total vibration acceleration was 88% lower.

Similar percentage relations of particular frequency ranges between the bad and good case were also observed for the speed of 100 km/h. It should be noted that for the good bearing, the low frequency range up to 500 Hz did not have a dominant contribution to the acceleration in the range up to 3.2 kHz.

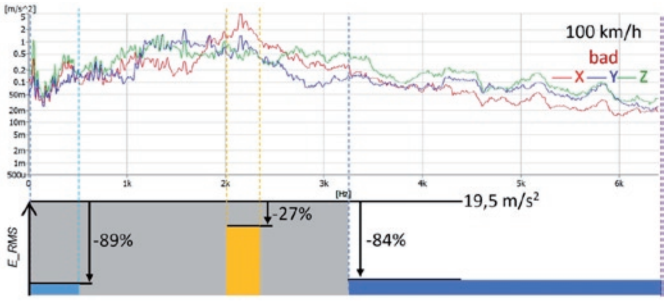

Fig. 7. Vibration acceleration spectrum of a faulty bearing node for case 4 at 100 km/h

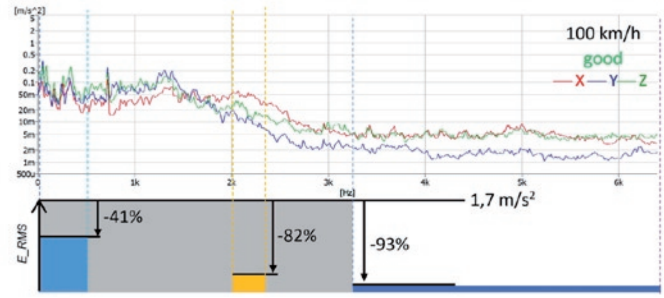

Fig. 8. Vibration acceleration spectrum of an efficient bearing node for case 4 at 100 km/h

In view of the results obtained, time domain features of vibration signal were calculated to develop a diagnostic parameter (also failure symptom). The most popular and proven measures in machine diagnostics were used [9] – root mean square (*RMS*), kurtosis (*K*) and skewness (*S*). The RMS value takes more into account the higher values of the instantaneous amplitude and is one of the most commonly used measures because it is proportional to the process power. Kurtosis, on the other hand, is a measure that is based on the density of the signal distribution, making it a very good parameter for rolling bearing diagnostics [19, 23, 38]. Finally, skewness can most generally be defined as a measure of asymmetry with respect to the mean value, by which it can also be used for machine fault analysis [20]. These measures were calculated according to the following equations [9]:

$$RMS = \sqrt{\frac{1}{N}\sum_{i=1}^{N-1} a_i^2} \tag{6}$$

$$K = \frac{\frac{1}{N}\sum_{i=1}^{N-1}\left(a_i - \bar{a}\right)^4}{\left(\frac{1}{N}\sum_{i=1}^{N-1}\left(a_i - \bar{a}\right)^2\right)^2} \tag{7}$$

$$S = \frac{\frac{1}{N}\sum_{i=1}^{N-1}\left(a_i - \bar{a}\right)^3}{\sigma^3} \tag{8}$$

where: N – number of signal samples, a_i – i-th signal amplitude of vibration acceleration.

The above calculations were preceded by performing a combination of signal filtering. A total of 9 band-pass filters were created, of which 7 were associated with narrow frequency ranges up to 1000 Hz (NFR), and 2 were associated with wide frequency ranges (WFR). A schematic of the calculations along with the developed bandpass filters is shown in Figure 9.

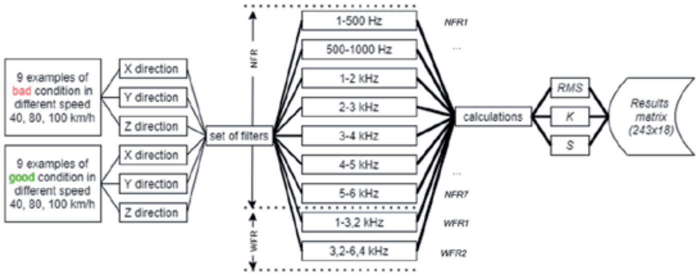

Fig. 9. Procedure for calculating time domain features of vibration acceleration signals

A total of 243 time domain features of vibration signal were obtained for each pass. The results thus obtained provided input to the problem of condition classification using machine learning in the form of decision trees. They are used to determine the affiliation of the results to classes of the qualitative dependent variable based on measurements of explanatory variables - predictors.

Decision tree is a graphical representation of recursive partitioning of a set of observations. This partitioning involved searching the feature space for all possible divisions of the dataset into two parts, so that at each successive step the division that results in the most strongly separated subsets is selected. Binary trees of the CART type were used in this analysis. The criteria for automatically stopping tree growth were based on a minimum number of objects in a leaf equal to 1.

In the analyses presented here, the qualitative dependent variable (categorical variable) classes were assigned a diagnostic condition (good/bad) and individual time domain features of vibration signal were assigned as explanatory variables (continuous variables). The algorithm used in the tree construction divided the classes in a way that minimized the prediction error (the least squares method). Figure 10 shows the division resulting from the decision tree analysis.

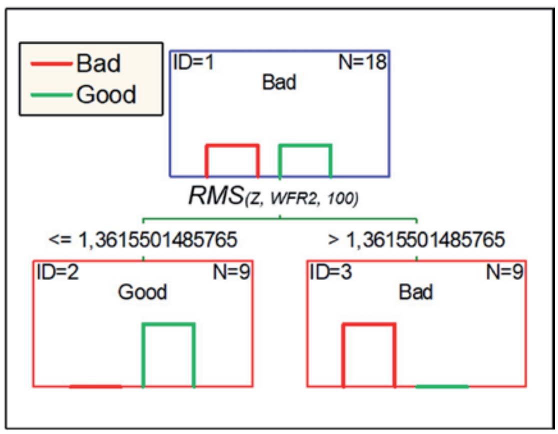

Fig. 10. Decision tree with selected diagnostic parameter

The use of a decision tree allowed the extraction of relevant measures, given the classes adopted. The best distribution of results according to the condition was obtained using the RMS value from the vertical direction Z in the frequency range 3.2-6.4 kHz for the speed of 100 km/h. The value of the measure in the division of observations is 1.36 m/s^2 (D_v) for the damage cases analyzed. Thus, the performed analysis indicates that the differentiation of observations sets is most effective in higher frequency ranges in addition to the previously defined main ranges of dynamic excitations. The relative relationships between the D_v value and the mean values of the diagnostic parameter are shown in Figure 11.

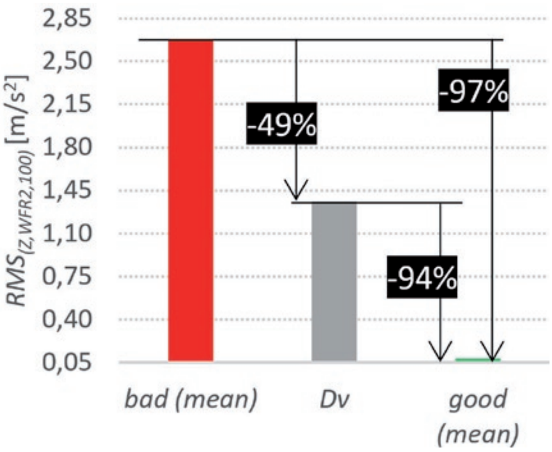

Fig. 11. Relationship between the D_v value and the mean values of the diagnostic parameter

The selected measure $RMS_{(Z,\ WFR2,\ 100)}$ will be used as a diagnostic parameter for the bearings technical condition. Considering only the vertical direction Z is the basis for reducing the applied vibration transducer from triaxial to uniaxial, which will affect the unit cost of the system. The results of $RMS_{(Z,\ WFR2,\ 100)}$ against the background of the studied cases are presented in Figure 12.

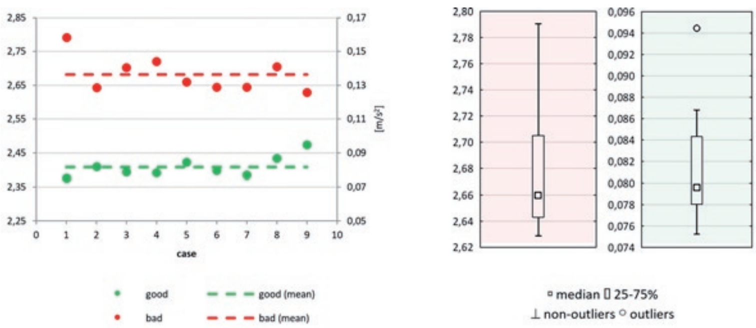

Fig. 12. The value of $RMS_{(Z,\ WFR2,\ 100)}$ parameter for the extreme driving speed cases studied (left) with statistical visualization of the results (right)

The spread of the data for a good bearing is about 0.02 m/s^2, and for a bad bearing it is 10 times larger, i.e. about 0.2 m/s^2. The median parameter for the faulty bearing is 2.66 m/s^2, and for the efficient bearing it is 97% smaller (0.08 m/s^2). Pearson correlation coefficient was calculated between the speed and $RMS_{(Z,\ WFR2,\ 100)}$, according to the equation:

$$r(x,y)=\sum_{i=1}^{N}\frac{(x_i-\bar{x})(y_i-\bar{y})}{\sqrt{\sum_{i=1}^{N}(x_i-\bar{x})^2}\sqrt{\sum_{i=1}^{N}(y_i-\bar{y})^2}} \tag{9}$$

where: N – sample size, x, y – the individual sample points indexed with i, $\bar{x}$, $\bar{y}$ – sample mean.

The resulting Pearson correlation coefficient was $r(V,\ RMS_{(Z,\ WFR2,\ 100)})$=0,98 which shows a strong correlation with driving speed.

For the developed parameter $RMS_{(Z,\ WFR2,\ 100)}$ the authors created models for the assessment of the technical state of the bearings. A total of four different regression models were examined, including the polynomial, gaussian and exponential ones. Figure 13 presents the above-mentioned models.

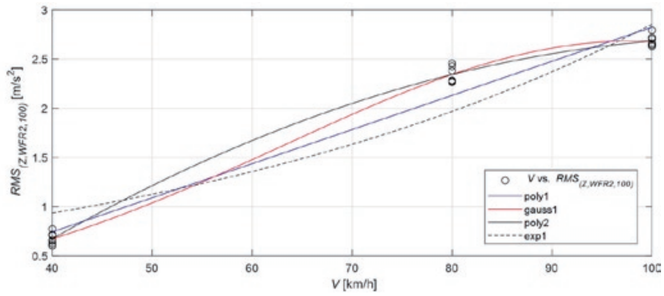

Fig. 13. The developed regression models of the parameter $RMS_{(Z,\ WFR2,\ 100)}$ of a faulty bearing as a function of driving speed.

The equations of the models are shown below:

$$f_{poly1}=-0.03464x-0.64108 \tag{10}$$

$$f_{gauss1}=2.6848e^{-\left(\frac{x-98.35}{49,632}\right)^2} \tag{11}$$

$$f_{poly2}=-0.00041154x^2-0.09108x-2.31107 \tag{12}$$

$$f_{exp1}=1.0312e^{(-0.15948x)} \tag{13}$$

The regression models must be subjected to statistical validation. The models were validated by determining a series of statistical data. First, the fitness level of the models to the actual data was determined. For this reason, a coefficient of determination R^2 was obtained. In order to determine the significance of individual coefficients of regression, the authors proposed the following hypotheses:

$$H_0:\beta_j=0 \tag{14}$$

$$H_1:\beta_j\neq 0 \tag{15}$$

Rejecting H_0 signifies that authors have statistical grounds to state that there exists a correlation between the dependent variable and at least one independent variable. For the testing of the hypotheses related to the determination of the statistical significance of individual coefficients of regression, the authors used a t-Student distribution. In the investigations, the authors adopted a statistical significance on the level of α=0.05. The results of the statistical analysis including root mean square error (RMSE) and coefficient of determination (R^2) of each model have been presented in Table 3.

When analyzing the results in Table 3, the authors have observed that all the models respectively, contained statistically insignificant coefficients, which is why these models were eliminated from further investigations. The authors assumed that they would select a model of regression, for which the coefficient of determination is equal or greater than 0.90, has the lowest *RMSE* value out of all the models and its model coefficients are statistically significant. Such assumptions are met by the models gauss1 and poly2. The obtained coefficients indicate these models can accurately forecast the data. Finally, the authors selected the poly2 model.

Table 3. Statistical analysis results of the models of the parameter $RMS_{(Z,\ WFR2,\ 100)}$

	poly1		gauss1		poly2		exp1	
RMSE	0.171		0.0668		0.0668		0.3	
R^2	0.965		0.995		0.995		0.888	
Estimated coefficient in model (EC)	EC	p-value	EC	p-value	EC	p-value	EC	p-value
1st coefficient	0.03464	1.0686E-19	2.6848	5.9872E-36	-0.00041154	1.6124E-11	0.44513	1.1543E-06
2nd coefficient	-0.64108	1.5056E-06	98.35	7.3189E-32	0.09108	5.604E-16	0.01858	6.2325E-11
3rd coefficient	–	–	49.632	6.5052E-24	-2.31107	3.5702E-14	–	–

5. Validation of the diagnostic parameter model

The validation of the developed model was based on the results for intermediate driving speeds, i.e. 60 km/h and 90 km/h. The measurements were carried out in the same way as for the remaining speeds, by making 9 series. For these speeds, $RMS_{(Z,\ WFR2,\ 100)}$ parameter value was predicted using equation (11). The results as a function of driving speed are shown in Figure 14.

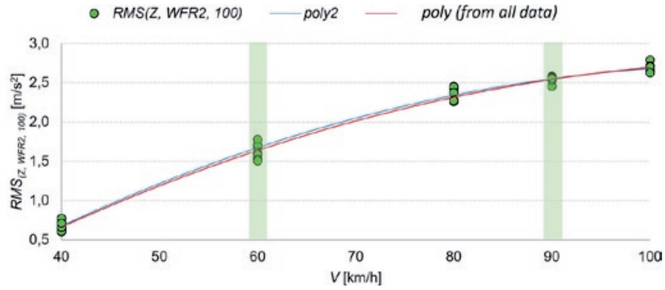

Fig. 14. The value of $RMS_{(Z,\ WFR2,\ 100)}$ parameter as a function of speed together with validation data

For the data obtained, the prediction error (PE) was calculated according to the equation:

$$PE = \frac{\left|x_{a,i} - x_{m,i}\right|}{x_{m,i,j}} \tag{16}$$

where: x_a – the value of $RMS_{(Z,\ WFR2,\ 100)}$ from measurements, x_m – estimated value of $RMS_{(Z,\ WFR2,\ 100)}$ from the model, i – i-th measurement.

The results of the statistical analysis of the prediction error (PE) are shown in Figure 15.

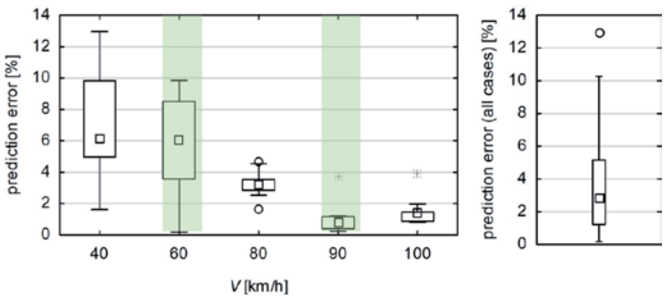

Fig. 15. Prediction error results for individual driving speeds

The largest prediction errors in model validation are for speeds of 60 km/h and in the range of 0.2–9.9%. For the 90 km/h validation speed, the error range was 0.2–1.2% with a single case of extreme observation error of 3.6%. The prediction error range of the model when all data (baseline and validation) were considered in the category of non-outlier observations 0.2–10.3%. Individually, an error of 13.0% defined as an outlier was observed. Figure 16 shows the mean prediction error for a given speed.

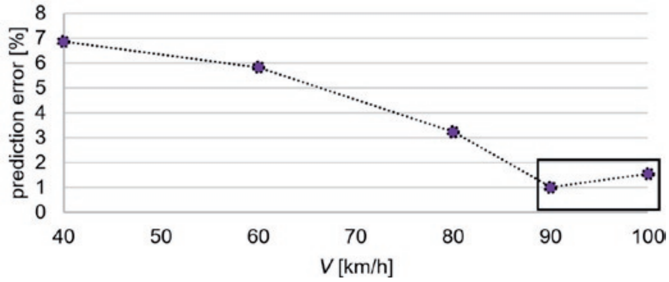

Fig. 16. Mean prediction error as a function of driving speed

As can be seen from the data presented in Figure 16, the mean prediction error is smallest for the two highest driving speeds, being 1-1.6%. The presented results are therefore an additional motivation to carry out diagnostic tests of the bearing condition at 100 km/h.

6. Diagnostic parameter limit value

In the next stage of the work, the evaluation criteria for the developed diagnostic parameter $RMS_{(Z,\ WFR2,\ 100)}$ were established. The number of bearing node conditions W_p was determined based on a three-value condition assessment using the following classes [9, 25]:

$$W_p = \left\{w^1, w_n^1, w^0\right\} \tag{17}$$

where: W_p – set of technical conditions for traction transmission diagnostics, w^1 - class of good technical conditions, w_n^1 - class of average technical conditions (permissible), w^0 – class of bad technical conditions. The w^1 technical condition means that the value of the diagnostic parameter y did not reach and did not exceed the upper limit value Sg. The w^0 technical condition is reached when the value of a diagnostic parameter reaches or exceeds the limit value. In contrast, an unacceptable condition w_n^1 means that the diagnostic parameter has reached or exceeded the down limit value but has not reached the upper limit value. The relationship between the diagnostic parameter and the conditions can be represented as follows:

$$RMS_{(Z,WFR2,100)} \le Sg \rightarrow w^1 \tag{18}$$

$$Sg > RMS_{(Z,WFR2,100)} \ge Sd \rightarrow w_n^1 \tag{19}$$

$$RMS_{(Z,WFR2,100)} \ge Sg \rightarrow w^0 \tag{20}$$

Continued operation of an object that has reached a condition w^0 is not economically, technically and environmentally advisable.

Due to the availability of data related to the damaged bearing, it was decided to use an upper limit value estimation method based on the mean pre-failure value of the symptom. Upper limit value (also breakdown value) (Sg) and down limit value (also alarm value) (Sd) was determined according to equations:

$$Sg = \bar{x}_w - k\sigma \tag{21}$$

$$Sd = Sg - k\sigma \tag{22}$$

where: Sg – upper limit value of diagnostic parameter Sd – down limit value of diagnostic parameter, $\bar{x}_w$ – mean failure value of a diagnostic parameter, k – degradation factor. The factor k=3 was selected *a priori*.

With a large set of pre-failure data, the Cempel method [8], which is a modification of the Neyman-Pearson method [9, 10], is recommended for determining evaluation criteria. In this method, an acceptable level of unnecessary overhauls is assumed when determining the upper limit value A [8, 43]. An erroneous overhaul decision will occur when the diagnostic parameter of an object in a serviceable condition exceeds the value of Sg. The total probability of such an event is equal to the product of the readiness factor $P(z)$ and the probability of exceeding Sg in a good technical condition [9].

The calculated upper limit value and down limit value are respectively Sg=2,52 m/s^2 and Sd=2,37 m/s^2. These are shown against the results obtained in Figure 17. The majority (8/9 cases) of the values of diagnostic parameter $RMS_{(Z,\ WFR2,\ 100)}$ for the bad technical condition of the bearings is above the upper limit value Sg, which indicates the correct classification into the condition w^0 due to the actual technical condition confirmed by the vision tests. When the results of the new bearing are related to the upper limit value, it can be observed that they represent 3.5% of its value.

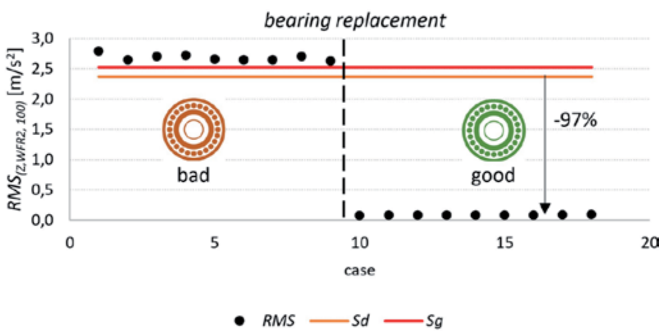

Fig. 17. Upper limit value and down limit value against measurement results

The algorithm for diagnosing the drive shaft is shown in Figure 18.

The diagnostic algorithm assumes first of all monitoring the current driving speed. In the case of detection of reaching the speed of 100 km/h, a five-second measurement of vibration accelerations from the bearing node is triggered. This measurement should be synchronous with the measurement of the driving speed in order to be able to assess the condition of a constant driving speed. The steady speed is met when the speed standard deviation is less than 2 km/h. After meeting the assumed requirements, the value of the diagnostic parameter $RMS_{(Z,\ WFR2,\ 100)}$ is calculated and compared with the evaluation criteria. Exceeding the upper limit value is equivalent to displaying a message to the driver to replace the bearing. If the down limit value is exceeded, the driver is informed of the need to purchase a new bearing for its later replacement. Moreover, the information related to the monitoring of the diagnostic parameter can be used as input data for the maintenance systems of technical objects, taking into account the results of the risk analysis [16].

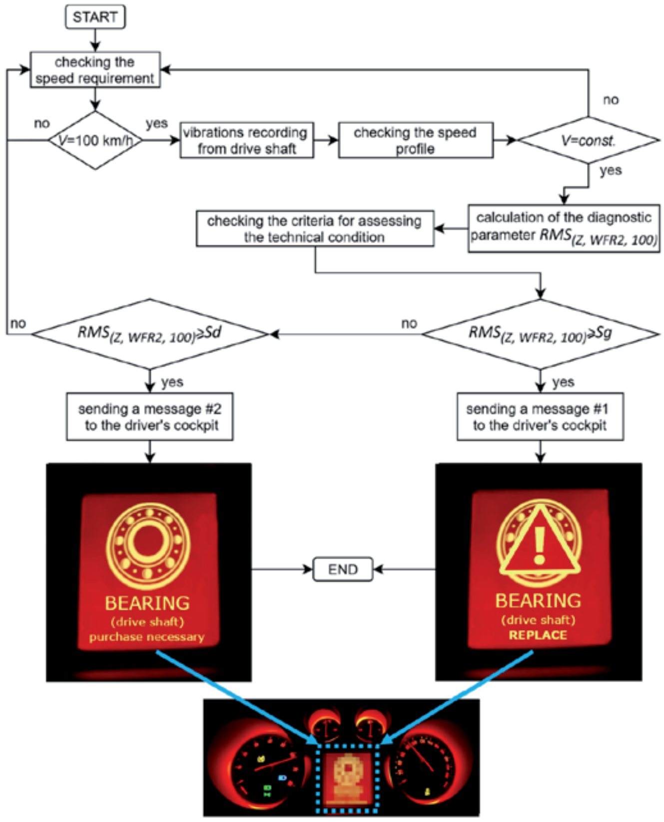

Fig. 18. The algorithm for diagnosing the drive shaft bearing

7. Summary and conclusions

Based on the study, an effective tool was developed to evaluate the technical condition of bearings in the drive shaft support of a passenger car. The use of vibration signal for technical diagnostics of bearings is well known, but most of the work is carried out in steady-state conditions using stationary machines (e.g., production machines). In this case, the distinctive feature of the present work is carrying out experimental tests on a vehicle (based on the assumptions of the active-passive experiment) in real conditions. This makes it possible to effectively implement the developed diagnosis algorithm as a component of a broader, comprehensive car self-diagnostic system called CSDS. The assumptions of the CSDS system are related to the absolution of the concept of OBD systems by diagnosing the key elements from the point of view of driving safety and vehicle service cost planning.

In the presented method, the key issue was to identify the frequency distribution of the vibration acceleration signal. On its basis, a set of filters and time domain features of vibration signal was created to describe vibration phenomena in order to select the most sensitive diagnostic parameter to the change of technical condition. For this purpose, the decision tree algorithm was used to extract relevant measures due to the adopted classes of technical condition. The selected diagnostic parameter is the RMS value measured at 100 km/h in a wide frequency range beyond 3.2 kHz, i.e. outside the main vibration range resulting from the vehicle dynamic phenomena. It is worth noting that for other speeds, it is also possible to adapt the selected diagnostic process. Next, the parameter evaluation criteria were determined by calculating the upper limit values and down limit values. The main purpose of the developed diagnostic algorithm is to inform the user of the vehicle about the necessity of bearing replacement or to alert the driver to impending damage (wear) and the need to plan for the purchase of a new bearing.

In future research directions, the authors will focus on developing a full speed range for the diagnostic process. In addition, the goal is to implement this type of tool into a number of other on-board diagnostic subsystems, which is not associated with high costs, and can bring tangible benefits of quickly responding to impending malfunctions of elements susceptible to wear in a road vehicle.

Acknowledgements

All presented work is partly funded by Statutory Activities fund of the Institute of Transport, PUT (PL) 0416/SBAD/0003.

References

1. Abid F Ben, Sallem M, Braham A. Optimized SWPT and Decision Tree for Incipient Bearing Fault Diagnosis. 2019 19th International Conference on Sciences and Techniques of Automatic Control and Computer Engineering (STA), IEEE: 2019: 231-236, https://doi.org/10.1109/STA.2019.8717197.
2. Ahmed U, Ali F, Jennions I. A review of aircraft auxiliary power unit faults, diagnostics and acoustic measurements. Progress in Aerospace Sciences 2021; 124: 100721, https://doi.org/10.1016/j.paerosci.2021.100721.
3. Amarnath M, Sugumaran V, Kumar H. Exploiting sound signals for fault diagnosis of bearings using decision tree. Measurement 2013; 46(3): 1250-1256, https://doi.org/10.1016/j.measurement.2012.11.011.
4. Andria G, Attivissimo F, Di Nisio A et al. Development of an automotive data acquisition platform for analysis of driving behavior. Measurement: Journal of the International Measurement Confederation 2016; 93: 278-287, https://doi.org/10.1016/j.measurement.2016.07.035.
5. Bi X, Cao S, Zhang D. Diesel Engine Valve Clearance Fault Diagnosis Based on Improved Variational Mode Decomposition and Bispectrum. Energies 2019; 12(4): 661, https://doi.org/10.3390/en12040661.
6. Borucki S, Cichoń A, Majchrzak H, Zmarzły D. Evaluation of the Technical Condition of the Active Part of the High Power Transformer Based on Measurements and Analysis of Vibroacoustic Signals. Archives of Acoustics 2017; 42(2): 313-320, https://doi.org/10.1515/aoa-2017-0033.
7. Cai B, Sun X, Wang J et al. Fault detection and diagnostic method of diesel engine by combining rule-based algorithm and BNs/BPNNs. Journal of Manufacturing Systems 2020; 57: 148-157, https://doi.org/10.1016/j.jmsy.2020.09.001.
8. Cempel C. Limit value in the practice of machine vibration diagnostics. Mechanical Systems and Signal Processing 1990; 4(6): 483-493, https://doi.org/10.1016/0888-3270(90)90047-O.
9. Cempel C. Vibroacoustic condition monitoring (Ellis Horwood Series in Mechanical Engineering). Warsaw, Ellis Horwood: 1993.
10. Cempel C. Vibroacoustical diagnostics of machinery: An outline. Mechanical Systems and Signal Processing 1988; 2(2): 135-151, https://doi.org/10.1016/0888-3270(88)90039-8.
11. Corni I, Symonds N, Wood R J K et al. Real-time on-board condition monitoring of train axle bearings. Stephenson Conference Research for Railways 2015 2015; (17): 477-489.
12. Czechyra B, Firlik B. On-line monitoring system of the technical condition of the infrastructure and running gear of a light rail vehicle (in Polish). Communication Review 2014; 2: 6-10.
13. Donelson J, Dicus R L. Bearing defect detection using on-board accelerometer measurements. ASME/IEEE 2002 Joint Rail Conference, RTD 2002 2002: 95-102, https://doi.org/10.1115/RTD2002-1645.
14. Firlik B, Czechyra B, Chudzikiewicz A. Condition monitoring system for light rail vehicle and track. Key Engineering Materials 2012; 518: 66-75, https://doi.org/10.4028/www.scientific.net/KEM.518.66.
15. Gharesi N, Arefi M M, Ebrahimi Z et al. Analyzing the Vibration Signals for Bearing Defects Diagnosis Using the Combination of SGWT Feature Extraction and SVM. IFAC-PapersOnLine 2018; 51(24): 221-227, https://doi.org/10.1016/j.ifacol.2018.09.581.
16. Gill A. Optimisation of the technical object maintenance system taking account of risk analysis results. Eksploatacja i Niezawodnosc – Maintenance and Reliability 2017; 19(3): 420-431, https://doi.org/10.17531/ein.2017.3.13.
17. 10 Problems Cars Can Diagnose By Themselves. [https://auto.howstuffworks.com/under-the-hood/trends-innovations/10-problems-cars-can-diagnose-themselves.htm].
18. Holguín-Londoño M, Cardona-Morales O, Sierra-Alonso E F et al. Machine Fault Detection Based on Filter Bank Similarity Features Using Acoustic and Vibration Analysis. Mathematical Problems in Engineering 2016, https://doi.org/10.1155/2016/7906834.
19. Immovilli F, Cocconcelli M, Bellini A, Rubini R. Detection of generalized-roughness bearing fault by spectral-kurtosis energy of vibration or current signals. IEEE Transactions on Industrial Electronics 2009; 56(11): 4710-4717, https://doi.org/10.1109/TIE.2009.2025288.
20. Kaul S. Crack diagnostics in beams using wavelets, kurtosis and skewness. Nondestructive Testing and Evaluation 2014; 29(2): 99-122, https://doi.org/10.1080/10589759.2013.854783.
21. Liu H, Li D, Yuan Y et al. Fault diagnosis for a bearing rolling element using improved VMD and HT. Applied Sciences 2019, https://doi.org/10.3390/app9071439.
22. Liu N, Liu B, Xi C. Fault diagnosis method of rolling bearing based on the multiple features of LMD and random forest. IOP Conference Series: Materials Science and Engineering 2020, https://doi.org/10.1088/1757-899X/892/1/012068.
23. Lorenzo F De, Calabro M. Kurtosis : A Statistical Approach to Identify Defect in Roller Bearings. 2nd International Conference on Marine Research and Transportation 2007; 3: 17-24.
24. Merkisz J, Rychter M. Basic proceeding of diagnosis and strategy of decision on OBD II system. AVEC - International Symposium on Advanced Vehicle Control, Hiroshima, 2002.
25. Niziński S, Michalski R. Diagnostics of technical objects (in Polish). Radom (Poland), ITeE: 2002.
26. Nowakowski T, Komorski P, Szymański G M, Tomaszewski F. Wheel-flat detection on trams using envelope analysis with Hilbert transform. Latin American Journal of Solids and Structures 2019, https://doi.org/10.1590/1679-78255010.
27. Nowakowski T, Motyl M, Babiak A. Simplified diagnostics of the drive system in the operation of a rail vehicle. Railway Reports 2019; 2(182): 49-54, https://doi.org/10.36137/1824p.
28. Randall R B, Tech B. Frequency analysis. Brüel & Kjær: 1987.
29. Sankavaram C, Kodali A, Pattipati K R, Singh S. Incremental classifiers for data-driven fault diagnosis applied to automotive systems. IEEE Access 2015; 3: 407-419, https://doi.org/10.1109/ACCESS.2015.2422833.
30. Sawczuk W, Szymański G M. Diagnostics of the railway friction disc brake based on the analysis of the vibration signals in terms of resonant

frequency. Archive of Applied Mechanics 2017; 87(5): 801-815, https://doi.org/10.1007/s00419-016-1202-0.
31. Smith C, Akujuobi C M, Hamory P, Kloesel K. An approach to vibration analysis using wavelets in an application of aircraft health monitoring. Mechanical Systems and Signal Processing 2007; 21(3): 1255-1272, https://doi.org/10.1016/j.ymssp.2006.06.008.
32. Soy H, Toy I. Design and implementation of smart pressure sensor for automotive applications. Measurement: Journal of the International Measurement Confederation 2021, https://doi.org/10.1016/j.measurement.2021.109184.
33. Szymański G M, Josko M, Tomaszewski F, Filipiak R. Application of time-frequency analysis to the evaluation of the condition of car suspension. Mechanical Systems and Signal Processing 2015; 58-59: 298-307, https://doi.org/10.1016/j.ymssp.2014.12.017.
34. Szymański G. Problems in diagnostics of internal combustion engines with the use of resonance vibrations (in Polish). Poznan, Poznan University of Technology: 2013.
35. Szymański G M, Tabaszewski M. Engine valve clearance diagnostics based on vibration signals and machine learning methods. Eksploatacja i Niezawodnosc – Maintenance and Reliability 2020; 22(2): 331-339, https://doi.org/10.17531/ein.2020.2.16.
36. Tabaszewski M. Identification of rolling bearing condition by means of a classification tree. Vibrations in Physical Systems 2019; 30(2): 1-8.
37. Theissler A, Pérez-Velázquez J, Kettelgerdes M, Elger G. Predictive maintenance enabled by machine learning: Use cases and challenges in the automotive industry. Reliability Engineering and System Safety 2021; 215: 107864, https://doi.org/10.1016/j.ress.2021.107864.
38. Wang H, Chen P. Fault diagnosis method based on kurtosis wave and information divergence for rolling element bearings. WSEAS Transactions on Systems 2009; 8(10): 1155-1165.
39. Wu J Da, Liao S Y. A self-adaptive data analysis for fault diagnosis of an automotive air-conditioner blower. Expert Systems with Applications 2011; 38(1): 545-552, https://doi.org/10.1016/j.eswa.2010.06.100.
40. Yu D, Cheng J, Yang Y. Application of EMD method and Hilbert spectrum to the fault diagnosis of roller bearings. Mechanical Systems and Signal Processing 2005; 19(2): 259-270, https://doi.org/10.1016/S0888-3270(03)00099-2.
41. Zhao X, Yang Z, Pan B et al. Analysis of excitation source characteristics and their contribution in a 2-cylinder diesel engine. Measurement: Journal of the International Measurement Confederation 2021; 176(February): 109195, https://doi.org/10.1016/j.measurement.2021.109195.
42. Zhao Y, Liu P, Wang Z et al. Fault and defect diagnosis of battery for electric vehicles based on big data analysis methods. Applied Energy 2017; 207: 354-362, https://doi.org/10.1016/j.apenergy.2017.05.139.
43. Żółtowski B, Łukasiewicz M. Machine vibration diagnostics (in Polish). Bydgoszcz, Scientific Publisher of the Institute of Sustainable Technologies - National Research Institute: 2012.

Eksploatacja i Niezawodnosc – Maintenance and Reliability
Volume 24 (2022), Issue 1
journal homepage: http://www.ein.org.pl
Article citation info:
Lopes H, Silva SP, Machado J. A simulation strategy to determine the mechanical behaviour of cork-rubber composite pads for vibration isolation. Eksploatacja i Niezawodnosc – Maintenance and Reliability 2022; 24 (1): 80–88, http://doi.org/10.17531/ein.2022.1.10.

A simulation strategy to determine the mechanical behaviour of cork-rubber composite pads for vibration isolation

Indexed by:

Helena Lopes [a], Susana P. Silva [b], José Machado [a]

[a] University of Minho, MEtRICs Research Center, Campus of Azurém, 4800-058 Guimarães, Portugal
[b] Amorim Cork Composites, Rua Comendador Américo Ferreira Amorim, 260, 4535-186 Mozelos VFR, Portugal

Highlights

- Use of modelling tools to determine compression behaviour of cork-rubber composites.
- Linear regression models to determine the effect of compound formulation.
- Prediction of the dynamic behaviour of different dimension samples through FEA.
- Comparison between experimental and numerical approaches.

Abstract

The present work aimed to determine the performance of new cork-rubber composites, applying a modelling-based approach. The static and dynamic behaviour under compression of new composite isolation pads was determined using mathematical techniques. Linear regression was used to estimate apparent compression modulus and dynamic stiffness coefficient of compounds samples based on the effect of fillers, cork and other ingredients. Using the results obtained by regression models, finite element analysis (FEA) was applied to determine the behaviour of the same cork-rubber material but considering samples with different dimensions. The majority of the regression models presented R^2 values above 90%. Also, a good agreement was found between the results obtained by the presented approach and previous experimental tests. Based on the developed methodology, the compression behaviour of new cork-rubber compounds can be accessed, improving product development stages.

Keywords

cork-rubber composites, compression, vibration isolation, linear regression, finite element analysis.

1. Introduction

Cork is a natural material obtained from the harvest of *Quercus suber* L. trees and is typically applied in the manufacturing of stoppers for the wine industry. Surplus from the harvest and stoppers production can be introduced in the manufacture of composite materials, like agglomerates and cork-polymer composites, due to cork characteristics like good thermal and acoustic behaviour, high compressibility and recovery characteristics, low Poisson's ratio, impact energy absorption, among others [8, 25, 30]. One example of cork composites is cork-rubber or rubber-cork. The introduction of cork into a rubber mixture improves its compressibility and recovery characteristics as well as the chemical stability of rubber [16, 30].

The manufacture of cork-rubber composites is similar to other rubber-based materials. During mixing stage, cork granules are introduced into a rubber compound with fillers, processing aid ingredients and vulcanizing agents. Several works have been developed to study the effect of rubber compound ingredients on the physical and mechanical properties of vulcanizates, such as the quantity of fillers (carbon black [24], calcium carbonate [5], silica and nanoclay [4], for example), plasticizer [5] and vulcanizing agents and accelerators [4, 5]. Also, several authors have investigated the effect on the rubber properties with the introduction of natural based-materials like bamboo [14], cereal straw [21], mengkuang and wood fibers [29, 31] and also cork powder [12]. Generally, with the increase of fillers quantity and the utilization of smaller particles, an increase in hardness is observed.

In vibration isolation systems, elastomeric materials, like cork-rubber composites, can be applied between structure and potential vibration sources to reduce or avoid vibrations transmission. In order to achieve this requirement, the material must have specific characteristics in terms of static and dynamic performance [15]. One of the first requirements to be met is the capacity to support the structure without exceeding the static deformation allowed of the material, which typically ranges a maximum value between 10 to 15% of the pad thickness in compression, in order to be able to provide efficient dynamic isolation (low stiffness) and avoid the increase of deflection over long periods of time (creep) [15, 27, 28].

An illustrative description of the behaviour of a system composed of a cork-rubber composite subjected to compressive loading is presented in Figure 1. Like other rubbery materials, the mechanical performance of cork-rubber materials is dependent on the sample's hardness and geometry. In terms of quasi-static compression, the increase of hardness usually leads to the increase of Young's modulus (E_0), as accounted by several studies regarding rubber materials [11, 17, 26]. Analytical models describing Young's modulus as a function of a

E-mail addresses: H. Lopes (ORCID: 0000-0002-3315-1134): id7466@alunos.uminho.pt, SP. Silva (ORCID: 0000-0002-2659-1772): susana.silva@amorim.com, J. Machado (ORCID: 0000-0002-4917-2474): jmachado@dem.uminho.pt

single variable hardness have been developed in [11, 26]. The model proposed by Kunz and Studer [17] additionally takes into account the Poisson's ratio of the rubber material.

When rubber materials are subject to static compression between bonded surfaces, the effect of geometry can be described by applying a variable designated by shape factor: ratio between loaded area and total area free to bulge. Several authors have derived and presented mathematical relations between the shape factor and the compression behaviour of rubber blocks [10, 13, 19, 32]. Analytical models differ in terms of material assumptions, such as considering total incompressibility ($\upsilon = 0.5$) [10, 13] or the effect of a smaller Poisson's ratio ($\upsilon < 0.5$) [19, 32]. Also, mathematical models vary according to the block geometry: circular and rectangular cross section blocks as presented in [13, 19]. The performance of these materials is usually described by apparent compression modulus (E_c). Considering the same material, samples with high shape factors present higher stiffness when compared to smaller shape factors.

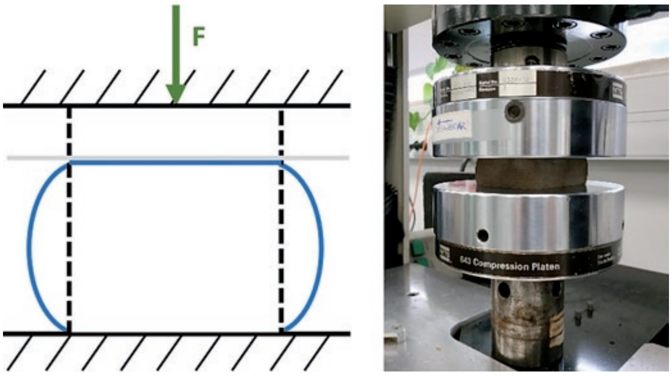

Fig. 1. Compression of cork-rubber composites with frictional contact between surfaces

Another requirement that must be considered when developing a vibration isolation system is its dynamic performance. The dynamic stiffness of cork-rubber composite materials is related to their static behaviour, so it is expected that hardness and shape factor also play a role in the dynamic performance of cork-rubber composites. A measurement for the dynamic performance used is the ratio between dynamic and static stiffness, also known as the dynamic stiffness coefficient (K) [28]. In the case of bearing pads, DIN 53513 [6] is applied to measure the dynamic stiffness of the materials.

In terms of product development, the application of computational resources, namely modelling techniques, in the early stages of a project, can have a positive impact in terms of sustainability and development time. There is a reduction in the number of prototypes developed, industrial tests, raw materials used and project-related costs and time, rather than following a typical trial and error approach.

Besides compound formulation and evaluation of requirements, the application of modelling tools is also present in other aspects like the design and manufacture of rubber products. For example, design of experiments and regression analysis has been used as a method for evaluating mixing [22] and vulcanization related variables [1] and to analyse different design configurations of composite products like conveyor belts [2, 3]. Also, numerical methods have been applied to determine the evolution of the rubber vulcanization process [7] and to assess the behaviour of rubber products under different loading conditions [18].

The goal of this article is to present a modelling approach for the prediction of cork-rubber composites performance, in terms of static and dynamic compression as vibration isolation pads, based on their compound formulation. Variation of fillers and cork granules on a cork-rubber composite was studied using design of experiments. Regression models were derived to predict apparent compression modulus and its relationship with dynamic compression modulus (E_d). The results obtained by regression models, combined with finite element analysis, allow determining the dynamic behaviour of other samples of the same material. To validate the approach, comparisons between experimental and simulation results are presented and discussed.

The present article is structured in the following order: in section 2, the materials and methods applied in this study are described, followed by the presentation of results and discussion in section 3. Finally, the conclusions of this developed study are presented.

2. Materials and methods

To study the influence of compound ingredients on the properties of the cork-rubber composites, a cork-rubber formulation was examined, divided into two groups to be analysed separately: fillers and cork granules. A cork-natural rubber compound formulation with hardness around 60 Shore A was selected as the base formulation of two separate experimental designs focused on finding differences in relation to fillers and cork granules (compound B). The same rubber compound without the addition of cork granules was also considered for this study (compound A).

Regarding fillers study, two variables were analysed: type and quantity of filler. According to the type and origin of the filler used, differences between compounds regarding mechanical properties were expected. In addition to these two parameters, it was also considered a third parameter concerning the effect of the filler activator quantity on the formulation. To analyse this system, a 2^3 factorial design was employed.

Two variables related to cork granules applied in a rubber formulation were also considered in a separate design of experiments. Granulometry and quantity of cork granules were the factors to be analysed through a 2^2 factorial design.

A summary of all cork-rubber composite samples produced in this study is presented in Table 1. In total, eight cork-rubber composites (1A, 1B, …, 1H) were characterized regarding fillers analysis. Related to cork analysis, four cork-rubber composites (2A, 2B, 2C and 2D), and also compound A, were used to determine regression models. For each factorial design, the maximum and minimum values are coded with + and – symbols, respectively. The original quantities of filler and cork granules applied in the base formulation (compound B) are represented by x_f and x_c, respectively. Compound B and other additional compounds (V1, V2, ..., V5) were also produced and characterized to compare with the results given by developed regression models.

2.1. Production of samples

The samples created for the experimental studies were manufactured and evaluated in pilot scale. The production of the cork-rubber samples with dimension 200x200x10 mm was executed following this procedure: weighing of all formulation components, mixture in an internal mixer (Banbury) and in a two-roll open mill, cutting of slab in a square shape of 200x200 mm, placement of the slab inside a mould in a compression moulding press to proceed to vulcanization at 150°C. The vulcanization times were defined based on the optimum cure type determined by Moving Die Rheometer (MDR) and the sample's final thickness.

2.2. Characterization of samples

Five samples with 60×60×10 mm were taken from each vulcanizate, to be use in both static and dynamic compression tests. After a conditioning period of at least 24 h at 23°C @ 50% RH, quasi-static compression tests were performed first. Load-displacement compression curves were obtained from a universal testing machine, with a load cell of 50 kN, until a maximum load level was achieved. Tests were performed at a rate of 5 mm/min and the maximum load applied was around 30 kN. No lubricant or rough surface was applied, it was only considered dry surfaces. For the same sample, three consecutive compression tests were performed, but only the third test was recorded. Due to the linear-like behaviour of the cork-rubber compos-

Table 1. Summary of samples produced, characterized and/or simulated for this study

Compound	Fillers			Cork granules	
	Type	Filler Quantity (phr*)	Activator Quantity (phr)	Type	Quantity (phr)
A	F1	x_f	-	n/a	
B	F1	x_f	-	C1	x_c
Fillers study (1A-1H)	F1 / F2	- / +	- / +	C1	x_c
Cork study (2A-2D)	F1	x_f	-	C1 / C2	- / +
V1	F1	-	x_{aint}	C1	x_c
V2	F1	+	x_{aint}	C1	x_c
V3	F2	-	x_{aint}	C1	x_c
V4	F2	+	x_{aint}	C1	x_c
V5	F1	x_f	-	C2	x_c
V6	F1	x_f	-	C2	x_{cint}

**phr – parts per hundred rubber*

Filler quantity: Level - < x_f < Level +

Cork quantity: Level - < x_c < Level +

Cork granulometry: C1 > C2

x_{aint} : mean activator quantity between levels – and +

x_{cint} : mean cork quantity between levels x_c and +

ites until 10% strain [20], the apparent compression modulus for each sample was calculated by Equation 1:

$$E_c = \frac{\sigma}{0.1} \tag{1}$$

where σ corresponds to the stress at 10% strain in Pa units.

The specimens used in the static compression test were then subjected to a dynamic compression test to evaluate the performance of a mechanical system composed of a mass and the material (acting like a spring-damper system). The tests were performed recurring to a hydraulic universal testing machine. The test procedure consisted of retrieving the resultant signal of displacement when a sample was loaded with a sinusoidal force with a 10% load amplitude at 5 Hz. For each sample, the test was performed six times, with compression stress ranging from 0.5 to 3 MPa, after being pre-conditioned at 5 Hz and a mean stress of 1.8 MPa with 10% load amplitude. Data obtained from the last twenty cycles were retrieved and analysed, calculating parameters like dynamic elastic stiffness (k_d in N/m), dynamic compression modulus and natural frequency of the system (f_n in Hz) when subject to certain stress (Equations 2 to 4).

$$k_d = \frac{F_a}{d_a}\cos\delta \tag{2}$$

$$E_d = \frac{k_d L}{A} \tag{3}$$

$$f_n = \frac{1}{2\pi}\sqrt{\frac{k_d g}{F_m}} \tag{4}$$

where F and d are load (in N) and displacement (in m), δ is the phase shift between load and displacement, a and m are subscripts for the amplitude and mean values of the sinusoidal curves, L (in m) and A (in m^2), are the initial thickness and loaded area of the sample, respectively, and g is the gravitational acceleration (in m/s^2).

Based on the compression tests results, the value of dynamic stiffness coefficient was determined by Equation 5:

$$K = \frac{E_d}{E_c} \tag{5}$$

2.3. Regression models: 60×60×10 mm samples

Due to the amount of data obtained by the application of design of experiments and easiness of implementation compared to other techniques, linear regression was chosen as a first approach method to develop mathematical models. Furthermore, this method has been applied in other works, relating the variation of composition elements with the final properties of rubber products, such as in [4, 5].

Regression models were developed based on the data obtained by the characterization of cork-rubber materials related to fillers and cork granules analysis. Also, compound A results were used as additional data to the latter study. R statistical software was applied to develop all regression models.

After a preliminary study about the main factors, the development of linear regression models was accessed for fillers and cork granules analyses, regarding static and dynamic properties of 60×60×10 mm samples. Independent variables related to filler or cork granules type were treated as dummy variables: value of 0 for type 1 and value of 1 for type 2. The chosen dependent variable related to the static compression performance was the apparent compression modulus (E_c), at 10% strain because, until this point of deformation, all tested materials presented an almost linear behaviour [20]. Concerning dynamic performance, the ratio between dynamic compression modulus and apparent compression modulus at 10% strain, defined as dynamic stiffness coefficient (K), was considered as the dependent variable. In the latter case, it was also considered another additional independent variable: compressive stress imposed during the dynamic test.

In a first approach, the least squares method was applied. To evaluate the prediction capacity of each regression model, coefficient of determination (R^2) and adjusted coefficient of determination (R^2_{adj}) were determined. Several combinations of predictor variables were used to develop regression models. The inclusion of some interaction and quadratic terms was considered in the development of some of the models presented in this work. An example of a model combining main factors, interactions and quadratic terms is presented in Equation 6:

$$y = \beta_0 + \beta_1 x_1 + \beta_2 x_2 + \beta_3 x_1 x_2 + \beta_4 x_1^2 + \beta_5 x_2^2 + \beta_6 x_1^2 x_2 + \beta_7 x_1 x_2^2 \tag{6}$$

where y represents the dependent variable, x_1 and x_2 the dependent variables, and β_0 to β_7 represent the regression model coefficients.

Considering a 95% confidence level, a significant regression model with the highest values of R^2 and R^2_{adj} was selected for each analysis. If the assumption that the residuals are normally and independently distributed with mean zero and constant variance was not met, instead of using the least squares method (function *lm* from R package *stats*), other regression methods were employed. In the case of failure of the assumption of residuals normally distributed, the robust regression method using Huber M-estimator (function *rlm* from R package *MASS*) was applied (more information about robust regression in [9, 23]. If the assumption of homoscedasticity was not verified, the method of weighted least squares (WLS) method was applied (function *lm* from R package *stats*) (more information about WLS in [23]). In this case, due to the existence of replicates, at each combination of predictor variables, the weights corresponded to the inverse of sample's variances of the dependent variable.

Regression models with a coefficient of determination above 90% were used to predict apparent and dynamic compression moduli.

2.4. Simulation of mechanical behaviour of samples with different dimensions

The developed regression models are only applicable to the same sample's geometry, a squared cross section specimen 60×60 mm with 10 mm thickness since all data utilized for its development came from experimental data of these specimens. To evaluate the static and dynamic compression behaviour of other samples, with squared cross-sections but with different dimensions, a procedure including the application of finite element analysis was employed.

Based on the results of apparent compression modulus provided by the regression models developed for 60×60×10 mm samples, estimates of Young's modulus of cork-rubber composites were determined. To do that, the relation between moduli presented in [20] was applied. For other squared cross section samples with different dimensions of the same cork-rubber composite, the apparent compression modulus was determined using the same method, according to its shape factor.

To determine the dynamic properties under compressive loading of squared cross section samples with different dimensions, a methodology presented in Figure 2 was applied. Similarly to the procedure applied for determining static properties, the results of the dynamic stiffness coefficient of 60×60×10 mm sample obtained from the regression model were used to determine an equivalent dynamic Young's modulus $(E_{0_{eq}})$, according to the shape factor of 60×60×10 mm samples and the compression stress level imposed and based on a single degree of freedom model (SDOF). Together with the sample's final thickness obtained through the application of the static compressive load, finite element analysis (using Harmonic Response module of Ansys Workbench) was applied to determine a displacement amplitude value, which allowed the calculation of dynamic compression modulus. Recurring to Equation 2 and 4, dynamic stiffness and natural frequency, correspondent to the dynamic experimental test, were calculated.

The finite element model was composed of a solid block, representing the cork-rubber specimen. A mass point correspondent to the stress level imposed on a cork-rubber specimen during dynamic experimental tests was added to the top surface of the block. A fixed support condition was considered on the opposite surface of the block. The numerical analysis consisted of simulating the application of a sinusoidal load with an amplitude of 10% of the mean applied load, recording as output the displacement amplitude of the system at the value of the exciting frequency used in experimental tests of the standard sample. The 3-D finite element model are presented in Figure 3, respectively.

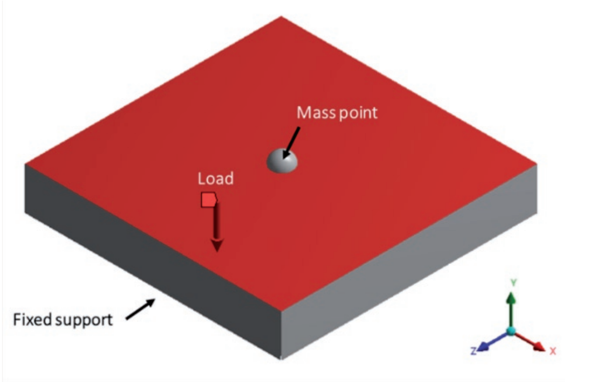

Fig. 3. Dynamic compression of a cork-rubber sample: finite element model.

For this study, the following properties were assumed for cork-rubber materials. All cork-rubber composites presented the same final density: 1000 kg/m^3. Poisson's ratio of compound B was determined through the measurement of lateral deformation when subjected to compressive load. Poisson's ratio of samples with 60×60×30 mm and 60×60×50 mm were determined considering a maximum axial strain of 20%. As the obtained results presented similar results in both transversal directions, the average value was assumed as the Poisson's ratio of a cork-rubber composite, considering isotropic behaviour. Since no significant differences between composite B and other cork-rubber composites were detected, due to small variations on compound formulations, the value obtained for compound B was considered and applied in all simulations: 0.31. Preliminary dynamic mechanical analysis results showed that the loss factor of cork-rubber samples varied from 0.05 to 0.13, depending on amplitude strain (ranging from 0 and 20%) and disturbing frequency (between 5 and 15 Hz). A constant damping ratio (ξ) was considered for all analyses. The damping ratio value was calculated through the average loss factor (η), as presented in Equation 7:

$$\xi = \frac{\eta}{2} = \frac{0.09}{2} = 0.045 \tag{7}$$

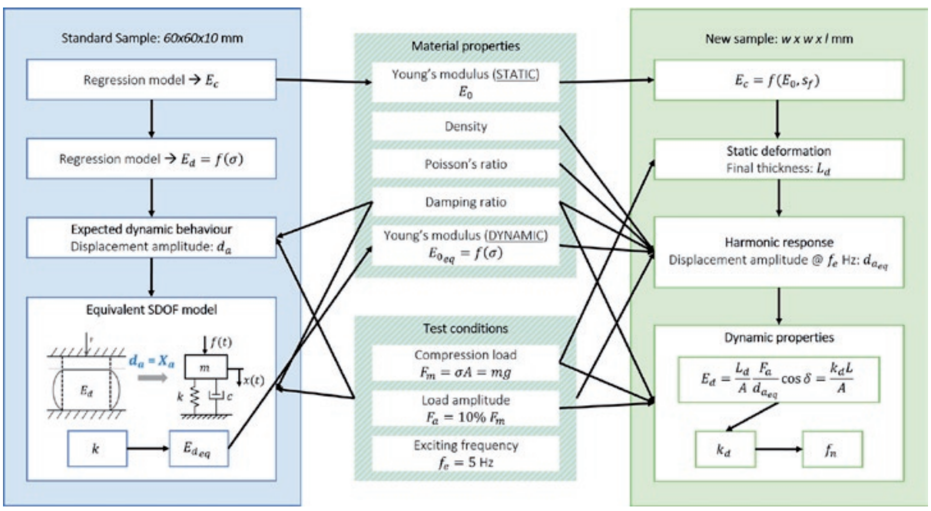

Fig. 2. Methodology to determine the dynamic properties correspondent to the experimental testing of samples with a squared cross section of a cork-rubber composite material

3. Results and Discussion

In this section, results obtained by linear regression and simulation approach are described. For cork-rubber squared cross section samples of 60×60×10 mm, the developed regression models are presented. Based on the results obtained through the application of some of the regression models, predictions about the static and dynamic behaviour of cork-rubber samples with different compound formulations and/or dimensions are reported, as well as their comparison with experimental results related to some materials.

3.1. Development of regression models

Four regression studies were performed to achieve mathematical models able to predict the static and dynamic behaviour of cork-rubber composites, according to fillers and cork granules included in the same rubber formulation.

3.1.1. Fillers

Concerning the fillers study, multiple linear regression models were developed to predict apparent compression modulus (E_c). In a first approach, data from a screening experiment were used considering three independent variables: filler type (t), filler quantity (f) and filler activator quantity (a). Using the least squares method, the model with the best fit presented a R^2 value of 92.36% and a R^2_{adj} of 91.24%. Due to the residuals' lack of normality observed, robust method using Huber M-estimator was applied. The resultant equation is presented in Equation 8. The obtained value of the coefficient of determination R^2 for this model was 91.82%.

$$E_c = 9.583 + 0.582t + 0.159f + 0.613a + 0.484ta - 0.014fa \quad (8)$$

Multiple linear regression was also applied to determine the dynamic stiffness coefficient (K). Besides the three independent variables applied in the static behaviour model, stress applied to the sample was also added during model development, as well as some quadratic terms. Using the least squares method, the best model obtained a R^2 value of 96.23% and R^2_{adj} of 96.08%. Due to the assumption of residuals normality not being fully met, the application of robust regression method using Huber M-estimator was considered. The resultant model given by the application of the robust method is presented in Equation 9. The obtained value of the coefficient of determination R^2 for this model was 96.09%.

$$K = 1.084 + 0.283\sigma - 0.170t + 5.27\times10^{-5} f - 0.024a + 0.046\sigma^2 - 0.002\sigma f + 0.007tf - 0.007ta + 0.001fa \quad (9)$$

3.1.2. Cork granules

For each type of cork granules, a simple linear regression model was determined, in which the independent variable was cork quantity (c), and the dependent variable was the apparent compression modulus of the vulcanizate (E_c). In a first step, least squares method was used. The model of cork-rubber compounds with type C1 cork granules is very limited for the determination of new predictions since the value of R^2 obtained was 48.57%. On other hand, the model for cork-rubber compounds with type C2 granules presented a R^2 of 89.16%. However, the homoscedasticity assumption did not seem to be met based on the model's residuals analysis. To overcome this issue, weighted least squares method was implemented using the same data. The resultant R^2 value for the type C2 model was 93.47%. The models obtained for type C1 and C2 cork granules are presented in Equations 10 and 11, respectively:

$$E_c = 13.293 + 0.041c \quad (10)$$

$$E_c = 13.371 + 0.101c \quad (11)$$

As it is possible to verify through the obtained regression models, the use of cork granules of smaller granulometry and larger quantities increases the static stiffness associated with these compounds.

Regarding the dynamic compression behaviour, multiple linear regression was applied for each type of cork granules. Like in the fillers analysis, another independent variable, the stress imposed on the specimen, was added to the model's development for the prediction of the ratio between dynamic and apparent compression moduli. Some quadratic terms were considered in the two models. Using least squares method, the values of R^2 obtained were 96.90% (R^2_{adj} = 96.72%) and 98.11% (R^2_{adj} = 97.95%) for the models regarding compounds with type C1 and type C2 cork granules, respectively. Due to the lack of residuals normality observed, the model correspondent to the compounds with type C1 cork granules was developed using the robust method with Huber M-estimator. The resultant R^2 value for type C1 robust model was 96.88%. The equations regarding each cork-rubber compound, using type C1 and C2 cork granules, are presented in Equations 12 and 13, respectively:

$$K = 1.508 + 0.205\sigma - 0.084c + 0.062\sigma^2 + 0.004c^2 + 0.005\sigma c \quad (12)$$

$$K = 1.410 + 0.331\sigma - 0.053c + 0.030\sigma^2 + 0.003c^2 - 0.023\sigma c + 4.62\times10^{-4}\sigma c^2 + 0.005\sigma^2 c \quad (13)$$

3.2. Prediction of mechanical behaviour of cork-rubber composite samples

The results related to the application of the previous regression models and simulation approach presented in section 2 are described in the following sections, considering squared cross section samples with 60×60×10 mm or other dimensions.

3.2.1. Static behaviour

3.2.1.1. Samples 60×60×10 mm

To evaluate the performance of previous fillers models, predictions were made about the apparent compression modulus, regarding other cork-rubber composites produced in the same conditions and with the same geometry (60×60×10 mm) as the samples whose data were used to create the regression models. The results obtained by the model presented in Equation 8 and respective error in comparison with experimental results are presented in Table 2.

The regression results obtained for cork-rubber composites with fillers F2 (V3 and V4) are closer to the experimental data when compared with the other cork-rubber compounds produced with fillers F1 (B, V1 and V2). For two of the three cork-rubber compounds with filler type F1, the application of the regression model provided higher values of apparent compression modulus (higher static stiffness) than the results of the experimental samples, exceeding a 10% error.

Due to the high value of R^2, a prediction about the static performance of cork-rubber composites produced with type C2 cork granules

Table 2. Fillers analysis: comparison between experimental and regression model results for apparent compression modulus

Compound	Apparent compression modulus E_c (MPa)		Relative error	Young's modulus E_0 (MPa)**
	Prediction by Equation 8	Experimental*		
B	16.722	14.481 ± 0.829	15.5%	12.962
V1	14.885	12.743 ± 0.224	16.8%	11.538
V2	17.194	16.164 ± 0.404	6.4%	13.327
V3	16.919	17.441 ± 0.596	-3.0%	13.115
V4	19.228	18.828 ± 0.885	2.1%	14.904

** Mean of five samples*

*** Based on Equation 14*

Table 3. Cork granules analysis: experimental and regression model results for apparent compression modulus

Compound (type C2)	Apparent compression modulus E_c (MPa)		Relative error	Young's modulus E_0 (MPa)**
	Prediction by Equation 11	Experimental*		
V5	14.379	15.198 ± 0.150	-5.4%	11.145
V6	14.882	-	-	11.536

* Mean of five samples

** Based on Equation 14

is presented, based on the regression model obtained for the 60×60×10 mm geometry. The static performance of a cork-rubber composite, containing half of the maximum quantity of cork incorporated of all produced composites, was compared with experimental data. The results obtained by the model presented in Equation 11 and respective error in comparison with experimental results are presented in Table 3.

3.2.1.2. Other dimensions

Based on the results obtained in [20] and the shape factor of the samples 60×60×10 mm, estimates of the correspondent Young's modulus (E_0) can be determined for each cork-rubber composite. For a squared cross-section pad with a shape factor of 1.5, the relation between Young's and apparent compression modulus is given by Equation 14. The Young's modulus results are presented in Table 2, corresponding to the results provided by the fillers regression model.

$$E_c = 1.29 E_0 \tag{14}$$

To determine the static behaviour of another squared cross-section sample with different dimensions, the relation between Young's and apparent compression moduli varies according to its shape factor. As an example, the values of apparent compression modulus of samples made from cork-rubber composite material B are presented in Figure 4.

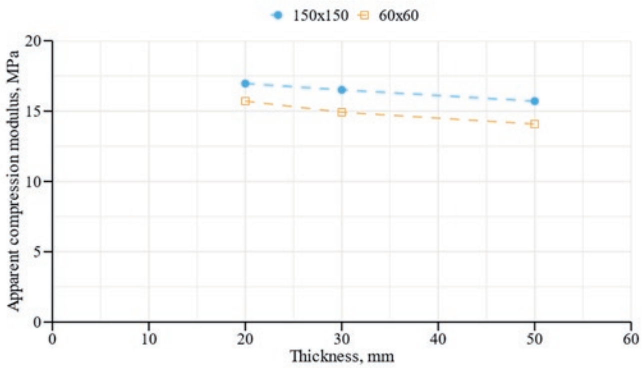

Fig. 4. Simulation results for cork rubber composite B squared cross section samples with different dimensions

Young's modulus results, related to the regression results from the cork granules study, are also presented in Table 3 and were determined based on the relation presented in Equation 14. Using the correspondent relation between Young's and apparent compression moduli, the apparent compression modulus of samples with different dimensions was determined. The results obtained for cork-rubber composites V5 and V6 are presented in Figure 5.

The increase of cross section area subjected to compressive load, increases the sample's apparent compression modulus, comparing samples with equal thicknesses. The decrease of thickness also increases stiffness, concerning equal cross section areas. Regarding squared cross section samples, the shape factor is proportional to the area and inversional proportional to the sample's thickness. Thus, according to the results presented, higher values of apparent compression modulus are obtained for samples with the highest shape factors, and these results are in agreement with the observed mechanical behaviour in experimental and theoretical works regarding the compression of elastomers between bonded or frictional surfaces [10, 13, 19, 32].

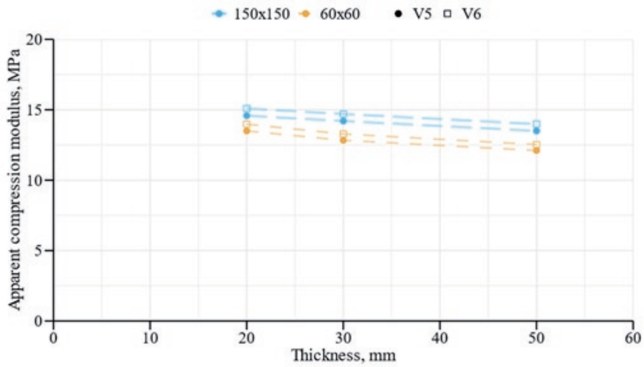

Fig. 5. Simulation results for cork-rubber composites V5 and V6 squared cross-section samples with different dimensions

3.2.2. Dynamic behaviour under compressive load

3.2.2.1. Samples 60×60×10 mm

Before predicting other samples behaviour, a comparison between predicted and experimentally observed dynamic compression behaviour of samples with 60×60×10 mm was performed. Based on the estimates of apparent compression modulus regarding the fillers study, presented in the previous section, and the results of the ratio between compression moduli, obtained by the application of the regression model presented in Equation 9, dynamic compression modulus of these cork-rubber composites under compressive loads were calculated and compared with results from experimental tests. The results for the different compounds are presented in Figures 6 and 7. The maximum error obtained was 7.5%, which demonstrates a good correlation between experimental tests and the results obtained by applying the regression models for all five cork-rubber composites.

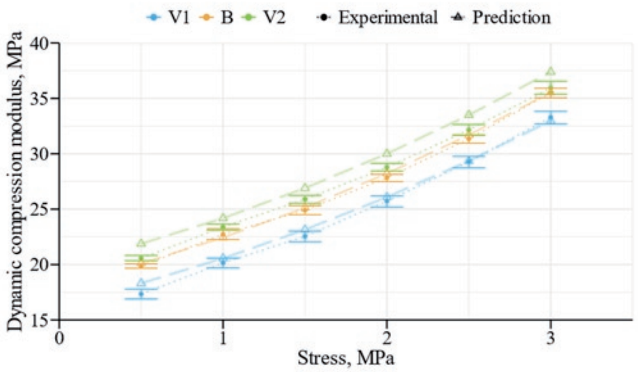

Fig. 6. Simulation results for cork-rubber composites V1, B and V2 squared cross section samples with different dimensions

Regarding the type C2 of cork granules, dynamic compression modulus was determined based on the prediction of apparent compression modulus and regression model presented in Equation 13. A prediction of the dynamic compression behaviour of the two cork-

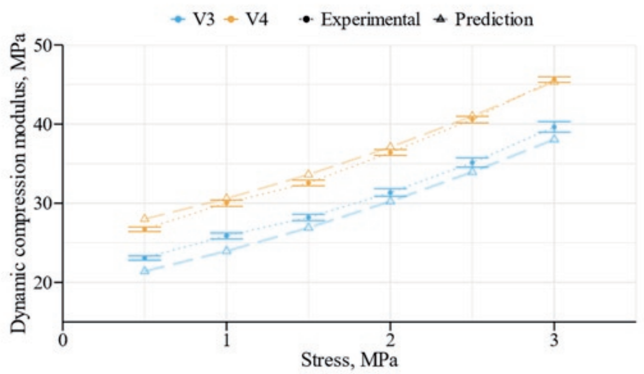

Fig. 7. Simulation results for cork-rubber composites V3 and V4 squared cross section samples with different dimensions

rubber composites 60×60×10 mm samples (V5 and V6), at different stress ranges, is presented in Figure 8.

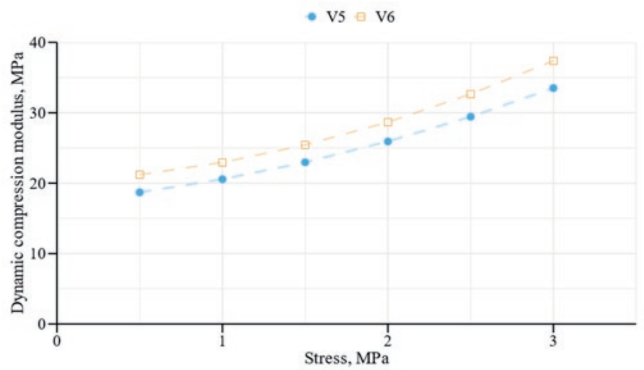

Fig. 8. Results of dynamic compression modulus results based on regression model (Equation 13) for compounds V5 and V6 samples of 60×60×10 mm

3.2.2.2. Other dimensions

Based on the previous results for each 60×60×10 mm cork-rubber compound, obtained by regression models, values of an equivalent Young's modulus were determined, according to the level of stress imposed, and used as input for the application of finite element analysis.

Together with the expected final thickness of a sample submitted to compressive load, finite element analysis was conducted. Based on the output of finite element analysis - displacement amplitude -, the equivalent properties of the experimental dynamic test were determined based on the procedure presented in section 2.4 of the article. The results of natural frequency concerning two of the five different cork-rubber composites samples (V1 and V4), with different cross-section areas and thicknesses, are presented in Figure 9.

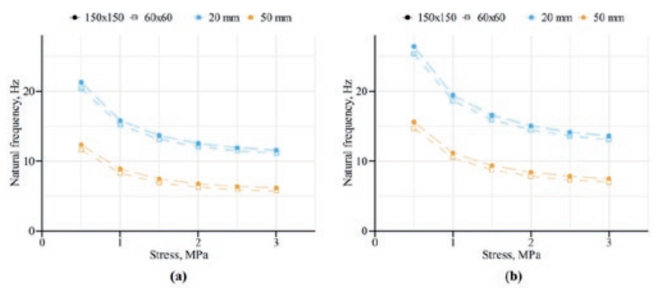

Fig. 9. Simulation results of squared cross section samples with different dimensions: a) cork-rubber composite V1; b) cork-rubber composite V4

Using data related to the cork granules study and applying the same simulation procedure to determine the dynamic behaviour of different dimension samples, the results obtained for cork-rubber composite material V5 and V6 are described in Figure 10.

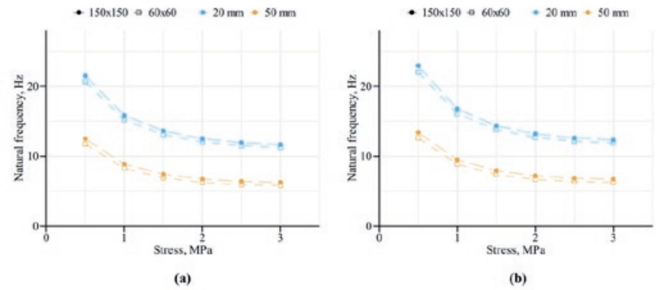

Fig. 10. Simulation results of squared cross section samples with different dimensions: a) cork-rubber composite V5; b) cork-rubber composite V6

Generally, and as expected, higher values of dynamic stiffness are related to the compounds that presented higher values of apparent compression modulus and to samples with higher values of shape factor.

4. Comparative analysis between experimental and simulation approaches

In contrast to what happens following a typical experimental trial and error methodology, where the compounds are fabricated first and then tested throughout several iterations, the systematic approach provided by the application of modelling techniques contributes to a broader understanding of the performance of cork-rubber composites. Also, it contributes to the definition of a more focused plan towards the achievement of specific requirements during product development stages.

The application of the proposed methodology does not fully replace the use of experimental tests since it depends on some of their results (standard sample) to create the regression models relative to the dynamic performance of different cork-rubber compounds. Different formulations need to be dynamically tested. However, with the application of the simulation strategy presented in this study, there is no longer the necessity of materially testing a lot of samples with different dimensions of the same compound in the early stages of product development, since the employed methodology already gives an indication about their expected performance, reducing development time and costs. Although, this does not exclude further experimental tests on the final stages of the product development for validation purposes.

5. Conclusions

A novel approach is presented to predict the static and dynamic performance of cork-rubber composites used as vibration isolation pads. The developed approach uses two modelling techniques for the prediction of material properties: linear regression and finite element analysis.

Based on some data obtained from two experimental designs related to the study of fillers and cork granules in a natural rubber compound, regression models were developed to predict the apparent compression modulus and dynamic stiffness coefficient (ratio between dynamic and apparent compression moduli). Regarding filler models, the independent variables of the models included filler type and quantity, filler activator quantity and, additionally for the dynamic behaviour model, compressive stress imposed on the samples. Using data related to the variation of cork granules quantity, four regression models were determined for static and dynamic compression behaviour, according to the granulometry of cork granules applied in the rubber compound. Most of the regression models presented R^2 values above 90%, except for the case of the regression model for apparent compression modulus concerning compounds with higher size cork granules (R^2 <50%). Regarding the latter result, there could be other variables related to the inclusion of larger cork granules influencing the static behaviour of cork-rubber samples, such as the geometry and porosity of particles and their dispersion on the rubber compound. Another study involving more samples and other variables must be considered in future works to develop a more reliable regression model.

The results obtained by the application of regression models allowed to determine the expected behaviour of new cork-rubber composites, according to their formulation. The application of the developed models is restricted to determine the behaviour of squared cross section samples with 60×60 mm^2 area and 10 mm thickness. A comparison with experimental results of other cork-rubber compounds was carried out and revealed a good approximation with simulation results. Finite element analysis was applied to determine the static and dynamic behaviour of new cork-rubber composites samples with different cross section areas and/or thicknesses, based on the results of the regression models and the dependence of the mechanical behaviour of these elastomers with the sample's shape factor.

Future works may include the application of these methods to other cork-rubber composites formulations, the introduction and analysis of other variables relevant to the final properties, and also the application of these modelling techniques to assess other properties, for example.

Although the methodology and results presented in this article are limited to few formulation variations of a single cork-rubber composite and one type of geometry (blocks with squared cross section area), the application of modelling techniques demonstrated to be a valuable tool during the development of this kind of materials. Potentially, it can decrease the number of iterations during development stages, minimizing resources, energy consumption and saving time.

Acknowledgments

Helena Lopes is supported by scholarship SFRH/BD/136700/2018 financed by Fundação para a Ciência e Tecnologia (FCT-MCTES) and co-funded by European Social Fund through Norte2020 (Programa Operacional Regional Norte). This work has been supported by the FCT within the RD Units Project Scope: UIDP/04077/2020 and UIDB/04077/2020. The authors are also grateful to Amorim Cork Composites for providing all materials and resources for this study.

References

1. Abd Ghani A A, Mohamad N, Abd Razak J et al. Optimization of Hot Press Parameters to Maximize the Physical and Mechanical Properties of Natural Rubber Composites for Elastomeric Mount. Malaysian Journal on Composites Science and Manufacturing 2020; 1(1): 27-37, https://doi.org/10.37934/mjcsm.1.1.2737.
2. Ambriško Ľ, Marasová D, Grendel P. Determination the effect of factors affecting the tensile strength of fabric conveyor belts. Eksploatacja i Niezawodnosc - Maintenance and Reliability 2016; 18(1): 110-116, https://doi.org/10.17531/ein.2016.1.14.
3. Andrejiova M, Grincova A, Marasova D. Analysis of tensile properties of worn fabric conveyor belts with renovated cover and with the different carcass type. Eksploatacja i Niezawodnosc - Maintenance and Reliability 2020; 22(3): 472-481, https://doi.org/10.17531/ein.2020.3.10.
4. Balachandran M, Devanathan S, Muraleekrishnan R, Bhagawan S S. Optimizing properties of nanoclay-nitrile rubber (NBR) composites using Face Centred Central Composite Design. Materials & Design 2012; 35: 854-862, https://doi.org/10.1016/j.matdes.2011.03.077.
5. Correia S L, Palaoro D, Segadães A M. Property Optimisation of EPDM Rubber Composites Using Mathematical and Statistical Strategies. Advances in Materials Science and Engineering 2017; 2017: 1-7, https://doi.org/10.1155/2017/2730830.
6. DIN 53513. Determination of the viscoelastic properties of elastomers on exposure to forced vibration at non-resonant frequencies. 1990.
7. Erfanian M-R, Anbarsooz M, Moghiman M. A three dimensional simulation of a rubber curing process considering variable order of reaction. Applied Mathematical Modelling 2016; 40(19-20): 8592-8604, https://doi.org/10.1016/j.apm.2016.05.024.
8. Fernandes E M, Pires R A, Reis R L. Cork biomass biocomposites. In Jawaid M, Tahir PM, Saba N (eds): Lignocellulosic Fibre and Biomass-Based Composite Materials, Cambridge, Elsevier: 2017: 365-385, https://doi.org/10.1016/B978-0-08-100959-8.00017-2.
9. Fox J, Weisberg S. Robust Regression in R. An R Companion to Applied Regression, 3rd edition. SAGE Publications: 2018.
10. Gent A N, Lindley P B. The Compression of Bonded Rubber Blocks. Proceedings of the Institution of Mechanical Engineers 1959; 173(1): 111-122, https://doi.org/10.1243/PIME_PROC_1959_173_022_02.
11. Gent A N. On the Relation between Indentation Hardness and Young's Modulus. Rubber Chemistry and Technology 1958; 31(4): 896-906, https://doi.org/10.5254/1.3542351.
12. Gul J, Mirza S. Effect of Cork Loading on Mechanical and Thermal Properties of Silica-Ethylene-Propylene-Diene Monomer Composite. Key Engineering Materials 2012; 510-511: 277-283, https://doi.org/10.4028/www.scientific.net/KEM.510-511.277.
13. Horton J M, Tupholme G E, Gover M J C. Axial Loading of Bonded Rubber Blocks. Journal of Applied Mechanics 2002; 69(6): 836-843, https://doi.org/10.1115/1.1507769.
14. Ismail H, Edyham M R, Wirjosentono B. Bamboo fibre filled natural rubber composites: the effects of filler loading and bonding agent. Polymer Testing 2002; 21(2): 139-144, https://doi.org/10.1016/S0142-9418(01)00060-5.
15. Jones D I G. Handbook of Viscoelastic Vibration Damping. Chichester, West Sussex, England, John Wiley & Sons: 2001.
16. Knapic S, Oliveira V, Machado J S, Pereira H. Cork as a building material: a review. European Journal of Wood and Wood Products 2016; 74(6): 775-791, https://doi.org/10.1007/s00107-016-1076-4.
17. Kunz J, Studer M. Determining the Modulus of Elasticity in Compression via the Shore A Hardness. Kunststoffe international 2006; (6): 92-94.
18. Lalo D F, Greco M, Meroniuc M. Numerical Modeling and Experimental Characterization of Elastomeric Pads Bonded in a Conical Spring under Multiaxial Loads and Pre-Compression. Mathematical Problems in Engineering 2019; 2019: 1-14, https://doi.org/10.1155/2019/5182629.
19. Lindley P B. Compression moduli for blocks of soft elastic material bonded to rigid end plates. The Journal of Strain Analysis for Engineering Design 1979; 14(1): 11-16, https://doi.org/10.1243/03093247V141011.
20. Lopes H, Silva S, Machado J. Analysis of the Effect of Shape Factor on Cork-Rubber Composites under Small Strain Compression. Applied Sciences 2020; 10(20): 7177, https://doi.org/10.3390/app10207177.
21. Masłowski M, Miedzianowska J, Strzelec K. The potential application of cereal straw as a bio-filler for elastomer composites. Polymer Bulletin 2020; 77: 2021-2038, https://doi.org/10.1007/s00289-019-02848-2.
22. Mohamad N, Yaakub J, Abd Razak J et al. Effects of epoxidized natural rubber (ENR-50) and processing parameters on the properties of NR/EPDM blends using response surface methodology. Journal of Applied Polymer Science 2014, https://doi.org/10.1002/app.40713.

23. Montgomery D C, Peck E A, Vining G G. Introduction to Linear Regression Analysis. 5th edition. Hoboken, New Jersey, John Wiley & Sons, Inc.: 2012.
24. Mostafa A, Abouel-Kasem A, Bayoumi M R, El-Sebaie M G. Insight into the effect of CB loading on tension, compression, hardness and abrasion properties of SBR and NBR filled compounds. Materials & Design 2009; 30(5): 1785-1791, https://doi.org/10.1016/j.matdes.2008.07.037.
25. Parra C, Sánchez E M, Miñano I et al. Recycled Plastic and Cork Waste for Structural Lightweight Concrete Production. Sustainability 2019; 11(7): 1876, https://doi.org/10.3390/su11071876.
26. Qi H J, Joyce K, Boyce M C. Durometer Hardness and the Stress-Strain Behavior of Elastomeric Materials. Rubber Chemistry and Technology 2003; 76(2): 419-435, https://doi.org/10.5254/1.3547752.
27. Racca R H, Harris C M. Shock and Vibration Isolators and Isolation Systems. In Harris CM, Piersol AG (eds): Harris' Shock and Vibration Handbook, 5th edition. McGraw-Hill: 2002.
28. Rivin E I. Passive Vibration Isolation. New York, ASME Press: 2003, https://doi.org/10.1115/1.80187X.
29. Shao D, Xu M, Cai L, Shi S. Fabrication of Wood-Rubber Composites Using Rubber Compound as a Bonding Agent Instead of Adhesives. Materials 2016; 9(6): 469, https://doi.org/10.3390/ma9060469.
30. Silva S P, Sabino M A, Fernandes E M et al. Cork: properties, capabilities and applications. International Materials Reviews 2005; 50(6): 345-365, https://doi.org/10.1179/174328005X41168.
31. Wan Mohamed W Z, Baharum A, Ahmad I et al. Effects of Fiber Size and Fiber Content on Mechanical and Physical Properties of Mengkuang Reinforced Thermoplastic Natural Rubber Composites. BioResources 2018; 13(2): 2945-2959, https://doi.org/10.15376/biores.13.2.2945-2959.
32. Williams J G, Gamonpilas C. Using the simple compression test to determine Young's modulus, Poisson's ratio and the Coulomb friction coefficient. International Journal of Solids and Structures 2008; 45(16): 4448-4459, https://doi.org/10.1016/j.ijsolstr.2008.03.023.

EKSPLOATACJA I NIEZAWODNOŚĆ
MAINTENANCE AND RELIABILITY

Eksploatacja i Niezawodnosc – Maintenance and Reliability

Volume 24 (2022), Issue 1

journal homepage: http://www.ein.org.pl

Article citation info:
Janutėnienė J, Bogdevičius M, Jankūnas V, Janutėnaitė-Bogdanienė J, Andziulis A, Kurmis M, Drungilas D. Investigation of dynamics and power needs for container unloading from ship process. Eksploatacja i Niezawodnosc – Maintenance and Reliability 2022; 24 (1): 89–99, http://doi.org/10.17531/ein.2022.1.11.

Investigation of dynamics and power needs for container unloading from ship process

Indexed by:
Web of Science Group

Jolanta Janutėnienė[a], Marijonas Bogdevičius[b], Valdas Jankūnas[a], Jūratė Janutėnaitė-Bogdanienė[c,*], Arūnas Andziulis[a], Mindaugas Kurmis[a], Darius Drungilas[a]

[a]Klaipėda University, Faculty of Marine Technologies and Natural Science, Bijunu str. 17, LT-91225 Klaipėda, Lithuania
[b]Vilnius Gediminas Technical University, Faculty of Transport Engineering, Saulėtekio al. 11, LT-10223 Vilnius, Lithuania
[c]Vilnius Gediminas Technical University, Faculty of Fundamental Sciences, Saulėtekio al. 11, LT-10223 Vilnius, Lithuania

Highlights

- A complex mathematical model describes the process of container lifting from a ship.
- The power of frictional forces between oscillating ship and container were analyzed.
- Lifting power needs dependency on mass of container and frictional forces was deduced.
- Results can be applied to safety and efficient handling of containers in green ports.

Abstract

The operational problem of container unloading from the ship is analyzed in this paper. Dynamic “crane-cargo-ship” system was investigated, and a mathematical model was created. In the model, the gap between the container and the ship’s cargo hold, the mass of the cargo, the container’s center of the mass, and the frictional forces that may occur during lifting from the cargo hold were estimated. Numerical analysis of the system was performed. Results of numerical analysis were compared with experimental measurements of containers unloading process in port. Requirement of lifting power was modelled depending on mass of cargo. Additional power needs in case of contact forces between container and wall of the ship’s cargo hold were calculated. Rational lifting conditions could be deduced using a created mathematical model and the reliability of the container and cargo during lifting could be deduced.

Keywords

container unloading, mathematical modelling, numerical analysis, port, ship, ship’s cargo hold.

1. Introduction

Container handling in world ports has increased significantly over the last decade. This has caused both technical and environmental problems in ports, increased the need to automate loading processes, their safety and at the same time reduce energy consumption and pollution. Maritime transport makes up 3% of all CO_2 emissions and various possible solutions on how to reduce it were proposed in paper [4]. A thorough analysis of 150 articles presented by authors shows that one way to address the problem is by evaluating ship efficiency, greenhouse gases (GHG) emissions from shipping, ship design, operations, or performance. Authors of the works [4] divided six main groups (hull design, economy of scale, power and propulsion, speed, alternative sources, weather routing and scheduling) where improvements can lead to reduced (GHG). Another approach to reduce emissions that are generated by maritime transport - green ports. About 85% of all emissions in ports come from container ships and tankers. Ports suffer not only from GHG but also from external costs that are caused by shipping emissions which affect the local population [14]. Although reduced emissions in ports will not have such a major impact on emissions worldwide, it is still a necessary and significant problem that must be addressed [9]. ESPO Green guide was presented in 2021 which provides an extensive database of good green practices in European ports. The aim is to reduce environmental impacts of the port area, greening of the port area, communicating to enhance common understanding, increasing transparency, etc. A guide provides target dates, expected results, and steps that should be taken to achieve the goals.

Container cranes are widely used equipment especially in ports for cargo movement. The main requirements for quay cranes are as follows: the ability to lift the selected maximum load weight; high structural stiffness; high speed; reliable and safe work, etc. Efficiency of container cranes is determined by various parameters, mainly by their speed and energy consumption. A strategy of port (GHG) Emissions Reduction is presented in the article [2]. Authors analyzed 159 academic peer-reviewed studies and provided structured data. The analysis of shipping and land transport (trucks) showed that ports can make a huge impact in reducing total GHG emission and improving energy consumption efficiency [2]. Emission assessment and energy consumption of ports was analyzed in an article [5]. The research showed that efficiency of energy consumption can reach up to 90%. However, there is no single common method for all the ports. Thus, each port

(*) Corresponding author.
E-mail addresses: J. Janutėnienė (ORCID: 0000-0002-5612-4737): jolanta.januteniene@ku.lt, M. Bogdevičius (ORCID: 0000-0003-4947-7638): marijonas.bogdevicius@vilniustech.lt, V. Jankūnas (ORCID: 0000-0003-3077-3568): valdas.jankunas@ku.lt, J. Janutėnaitė-Bogdanienė (ORCID: 0000-0002-1065-7095): j.janutenaite-bogdaniene@vilniustech.lt, A. Andziulis (ORCID: 0000-0002-1735-8901): arunas.andziulis@ku.lt, M. Kurmis (ORCID: 0000-0002-4787-9791): Mindaugas.kurmis@ku.lt, D. Drungilas (ORCID: 0000-0002-7821-3183): darius.drungilas@ku.lt

should perform a thorough economical, technical, and environmental evaluation before implementing energy and pollution reduction measures. GHG reduction can be achieved not only by switching to renewable energy sources, but by saving energy, improving processes so that energy consumption would be more efficient.

A power consumption problem was addressed in previous research where the cargo lowering process of a quay crane was analyzed [8]. Simulation and real experiments have shown that it is possible to ensure a more time efficient and thus energy efficient process. Many risks arise during the container handling procedures performed by the quay cranes and operators. A novel container transportation security and cargo safety assurance method was developed in paper [11]. Such results led to further research and optimization of the cargo lifting process from the ship.

2. Container crane operation and process optimization. A literature review

Port cranes are subjected to various external disturbances which affect operational efficiency. One of such disturbances is the wind and wind loads can lead to large amplitude oscillations of the container or crane itself thus having a negative impact to the whole efficiency of the system. A three-dimensional modeling of container cranes subject to wind loads is presented in the work [3]. Inclination and inextensibility of cables were analyzed in the paper [10]. Main five parameters of crane were taken into account (container mass, frictions at bridge motion, trolley movement handling rope, hydraulic cylinder absorptions) and wind distribution parameters (w_x, w_y, w_φ, and w_θ) were approximated. Novel control algorithm was created, it takes into account fractional-order calculus, sliding mode and adaptive control thus enabling a more precise whole crane control. A similar problem for a 3D overhead crane with simultaneous payload hoisting and wind disturbances was analyzed in the paper [1]. The authors have presented an adaptive command shaping (ACS) technique combined with an integral sliding mode (ISM) control. The ACS is responsible for unwanted payload sway control and hoisting minimization, whereas ISM control is for disturbance compensation. Simulation and experiment with different cable lengths and payload hoisting showed that a combination of ACS and ISM control resulted in significant reduction of payload sway thus ensuring a more accurate precision [1]. When investigating the whole container loading/unloading system, it is important to consider moving load problems as bending stresses are affected by multiple factors such as inertial forces, flexibility of the system, swing angle, etc., especially when bigger mass ratios are taken into consideration [15]. Ship based crane payload motion was investigated in the paper [22]. Stochastic dynamics, stability and control dynamics were separated as the main factors. Coupled simulation of crane operation and ship response in waves is presented in work [6]. Equations of kinematics and dynamics of the system were written. A digital twin of the ship with a crane was created which allows analysis of the dynamics of the full system. Most crane systems exhibit double pendulum characteristics that lead to a difficult control of the whole process. Due to complexity of the analyzed problem, a quadratic programming (QP) based energy-optimal solution with certain constraints for velocity, acceleration and amplitudes of the angle swings was formulated and an energy-optimal trajectory planner was presented with satisfactory results [18]. A research of double pendulum crane system with distributed mass beam showed that by applying sliding mode control allows to stabilize a system [20] and then adding a low-pass filter to the previously developed time optimal anti swing controller could reduce the residual oscillation angle of the distributed mass beams (DMB) [21]. Velocity and displacement control was taken as the basis for the sliding mode control utilizing a low-pass filter to achieve the minimum maximum residual angle.

A different approach to the energy saving problem is to try to recover the energy consumed during the operation of the crane. Operation data of a rubber tire gantry (RTG) crane was collected and energy consumption by various motors analyzed in the paper [16]. For this rectifier energy, hoist energy, gantry energy, losses were calculated, and potentially recoverable energy estimated. The results showed that it is possible to recover about half of the energy consumed during the crane operation. Energy consumption by adding components to a standard query crane that improve cycle times could be saved is presented in paper [17]. Two types of advanced query cranes were presented, and their cycle times calculated. The results showed a significant increase in productivity compared to a common query crane. Power demand can be controlled starting from early stages of crane design thus ensuring reduced dynamic overload values [7]. The analyzed crane is subjected to loads as lifting load, counterweight and weight of the jib and forces acting in ropes during the lift. Energy consumption as a function of the mass of the transported mass was investigated in the article [13]. A mathematical model of a forest crane for the analysis of its operating cycle dynamics is presented in the work [19]. Second-order LaGrange equations are used to derive equations of motion. In the mathematical model, the frictional forces are evaluated. The results of numerical analysis confirm that friction can have a significant impact and could be considered in the initial phase at crane design. Analysis of the lifting mechanism for various lifting cases is presented in paper [12]. The influence of start-up time on machine overloads and energy overloads was determined. Influence of lifting height and lifting weight on the drive overload and energy consumption was presented.

A dynamic system “Crane-Cargo-Ship” is analyzed in this paper. Dynamic model of the crane consists of an electric motor, gearbox and drum, rope system, container, and the spreader of the crane. Mathematical model was created which describes the dynamic process when a container is lifted from the ship’s cargo hold. Parameters such as a gap between container and cargo hold, cargo weight, mass center of containers, frictional forces that may occur during lifting from the cargo hold are taken into a mathematical model. Results of experimental measurements of the container unloading process are used for verification of mathematical models.

Main aim of this paper is to analyze conditions of container unloading from ship when ship oscillates, and friction forces arise between container and ship hold; to deduce unloading duration and power need depending on container masses and friction forces.

Based on the developed mathematical model of the “Crane-Cargo-Ship” system, it is possible to analyze the lifting dynamics and assess the problems of cargo reliability.

Steps of investigation of the “Crane-Cargo-Ship” system are as follows: creation of dynamical model; creation of mathematical model; analysis of experimental measurements of container unloading from the ship; creation of programming code; numerical analysis and comparison with experimental results.

3. Mathematical model of container handling process “Crane-Cargo-Ship”

3.1. Crane transmission mathematical model

Table 1. Symbols and descriptions

Symbol	Units	Description
$r_2 \cdots r_9$	m	Radiuses of gearbox

u_R	m	Gear ratio of transmission
....	rad	Angles of rotation of rotor and gears
φ_{10}	rad	Angle of rotation of drum
$\varphi_{12} \cdots \varphi_{17}$	rad	Angles of rotation of pulleys
M_{eng}	Nm	Torque moment of the asynchronous electric motor
ω_0	Nm	Synchronous angular velocity of motor
c_v, d_v	Nm, 1/s	Parameters of the electric motor
F_{O10XLR}, F_{O10ZRL}	N	Reaction forces in the right and left supports of drum
F_N	N	Normal force in support of drum
k_{SUPP}	N/m	Contact stiffness coefficient
δ_N	m	Penetration shaft of drum
D	-	Coefficient which evaluates hysteresis of contact force
δ_{N_max}	m/s	Maximal values of velocity of penetration
e_{RES}	-	Velocity restitution coefficient
e	m	Eccentricity
$\Delta_{GAP}(t)$	m	Total gap in the drum support
$\Delta_{GAPX}(t), \Delta_{GAPZ}(t)$	m	Gap projection in X and Z axes
$x(t), z(t)$	m	Displacements of drum support in the X and Z directions
A_X, A_Z	m	Amplitudes of support displacements in the X and Z directions
Ω_X, Ω_Z	rad/s	Angular velocities in the X and Z directions
F_{FRICX}, F_{FRICZ}	N	Friction forces in the X and Z axes
F_{p1p2}, F_{p10p09}	N	Forces in the cables (cable between points 1 and 2, and points 9 and 10)
v_{REL}	m/s	Slip velocity of drum shaft in the support
r_{SHAFT}	m	Radius of shaft of drum
$\mu(v_{REL})$	-	Friction coefficient between shaft and support of drum
μ_0, μ_1	-	Static and dynamic friction coefficients
$k_F, \mu_0, \mu_1, \gamma_V$		Parameters to describe friction coefficients
m_{O11}	kg	Total mass of container and spreader
x_C, y_C, z_C	m	Coordinates of mass center of total system „Container-Spreader“
k_{p2p1}		Stiffness coefficient of cable
k_{p7p8}		Stiffness coefficient of cable
E_{cable}	Pa	Modulus of elasticity of cable
A_{cable}	m^2	Cross section area of cable
L_{cable}	m	Length of cable
c_{p2p1}, c_{p7p8}	Ns/m	Damping coefficient of cable
L_{p7p8}	m	Length of cable

k_{SP}	N/m	Contact stiffness between container and ship
$\delta_{X,K}$	m	Penetration of k container corner with ship
$\mu\left(\Delta V_{Y,k}\right),\mu\left(\Delta V_{Z,k}\right)$	m	Friction coefficient of k container corner with ship Y and Z direction
$\Delta V_{Y,k},\Delta V_{Z,k}$	m/s	Slip velocity container corner k in Y and Z directions

The hoist transmission of the crane consists of an asynchronous electric motor, gearbox, and drum (Fig.1 and Fig.2). The dynamic model of drum shaft and support is presented in Fig 3.

Gearbox consists of planetary gear and two-gear join. The gear ratio of transmission is equal:

$$u_R = -\varphi_2 / \varphi_9. \tag{1}$$

Gear ratios of planetary gear, two gear join and total gear ratio are:

$$u_{PL} = 2r_7 / r_2,\ u_G = r_9 / r_8,\ u_R = u_{PL}u_G. \tag{2}$$

The reduction mass inertia of crane hoist transmission is equal:

$$I_{2R} = \left(I_2 u_{PL}^2 + I_3 \left(\frac{r_7}{r_3}\right)^2 u_{PL}^2 + \left(m_1 + m_2 + m_3\right) r_7^2 u_{PL}^2 + \left(I_7 + I_8\right) u_{PL}^2 + I_9 \right) u_G \tag{3}$$

The mathematical model to evaluate the rotation of the transmission elements is:

$$\dot{M}_{eng} + d_v M_{eng} = c_v\left(\omega_0 - \dot{\varphi}_1\right) \tag{4}$$

System of equations of simplified hoist transmission are:

$$I_1\ddot{\varphi}_1 = M_{eng} - k_{12}\left(\varphi_1 + u_R\varphi_{2R}\right) - c_{12}\left(\dot{\varphi}_1 + u_R\dot{\varphi}_{2R}\right) \tag{5}$$

$$I_{2R}\ddot{\varphi}_{2R} = -k_{12}u_R\left(u_R\varphi_{2R} - \varphi_1\right) - c_{12}u_R\left(u_R\dot{\varphi}_{2R} - \dot{\varphi}_{\mathrm{I}}\right) - k_{910}\left(\varphi_{2R} - \varphi_{10}\right) - c_{910}\left(\dot{\varphi}_{2R} - \dot{\varphi}_{\mathrm{I}0}\right) - c_2\dot{\varphi}_{2R} \tag{6}$$

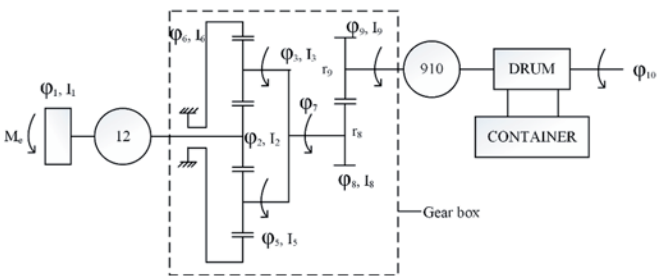

Fig. 1. Hoist transmission of crane

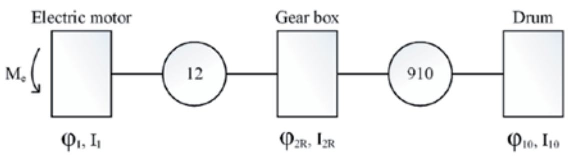

Fig. 2. Simplified hoist transmission of crane

$$m_{O110}\ddot{q}_{O10X} = F_{O10XLR} + F_{O10X} \tag{7}$$

$$m_{O10}\ddot{q}_{O10Z} = F_{O10ZRL} + F_{O10Z}, \tag{8}$$

$$I_{10}\ddot{q}_{10} = -k_{910}\left(\varphi_{10} - \varphi_{2R}\right) - c_{910}\left(\dot{\varphi}_{10} - \dot{\varphi}_{2R}\right) - c_{10}\dot{\varphi}_{10} + M_{\varphi 10} + M_{\varphi 10,FRIC} \tag{9}$$

$$M_{\varphi 10} = r_{10}\left(F_{p2p1} + F_{p10p9}\right) \tag{10}$$

$$F_{O10XRL} = F_{NX} + F_{FRICX} \tag{11}$$

$$F_{NX} = -\left|F_N\right|\cos\left(\alpha\right) \tag{12}$$

$$F_{O10ZRL} = F_{NZ} + F_{FRICZ} \tag{13}$$

$$F_{NZ} = -\left|F_N\right|\sin\left(\alpha\right) \tag{14}$$

$$tg\left(\alpha\right) = q_{O10Z} / q_{O10X} \tag{15}$$

$$F_N = k_{SUPP}\left|\delta_N\right|^n D\left(\dot{\delta}_N\right). \tag{16}$$

$$\delta_N = e - \Delta_{GAP}\left(t\right),\ \dot{\delta}_N = \dot{e} - \dot{\Delta}_{GAP}\left(t\right) \tag{17}$$

$$\mathrm{D}=(1+0.75*(1-\mathrm{e}_{RES}^2))\dot{\delta}_N / \dot{\delta}_{N\_\max} \tag{18}$$

$$e = \sqrt{q_{O10X}^2 + q_{O10Z}^2} \tag{19}$$

The total gap in the drum support, gap projection in X and Z axes:

$$\Delta_{GAP}\left(t\right) = \Delta_{GAPX}\left(t\right)\cos\left(\alpha\right) + \Delta_{GAPZ}\left(t\right)\sin\left(\alpha\right) \tag{20}$$

$$\Delta_{GAPX}\left(t\right) = \Delta_{GAPX0} - \mathrm{x}\left(\mathrm{t}\right) = \Delta_{GAPX0} - \mathrm{A}_X\sin\left(\Omega_X \mathrm{t}\right) \tag{21}$$

$$\Delta_{GAPZ}\left(t\right) = \Delta_{GAPZ0} - \mathrm{z}\left(\mathrm{t}\right) = \Delta_{GAPZ0} - \mathrm{A}_Z\sin\left(\Omega_Z \mathrm{t}\right) \tag{22}$$

$$F_{FRICX} = -F_{FRIC}\sin\left(\alpha\right)sign\left(\mathrm{v}_{REL}\right) \tag{23}$$

$$F_{FRICZ} = -F_{FRIC}\cos\left(\alpha\right)sign\left(\mathrm{v}_{REL}\right) \tag{24}$$

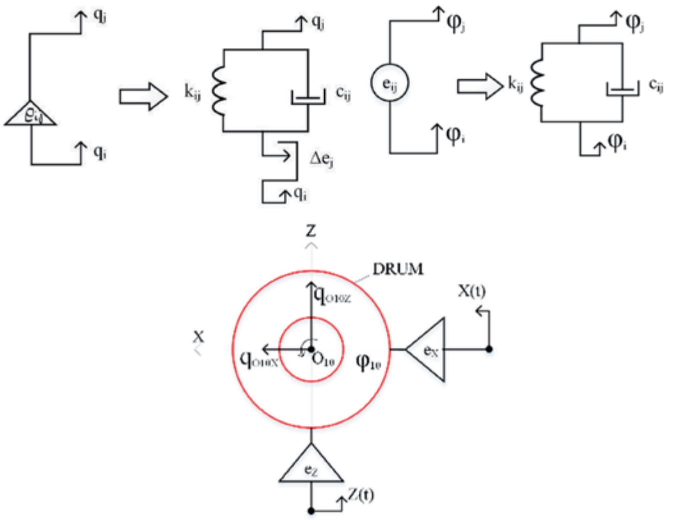

Fig 3. Dynamic model of drum: a) nonlinear model; b) linear model; c) drum and bearing model

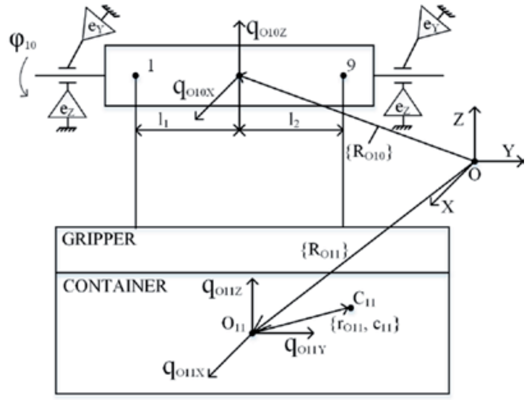

Fig. 4. a) Dynamic model of system "Drum-Container

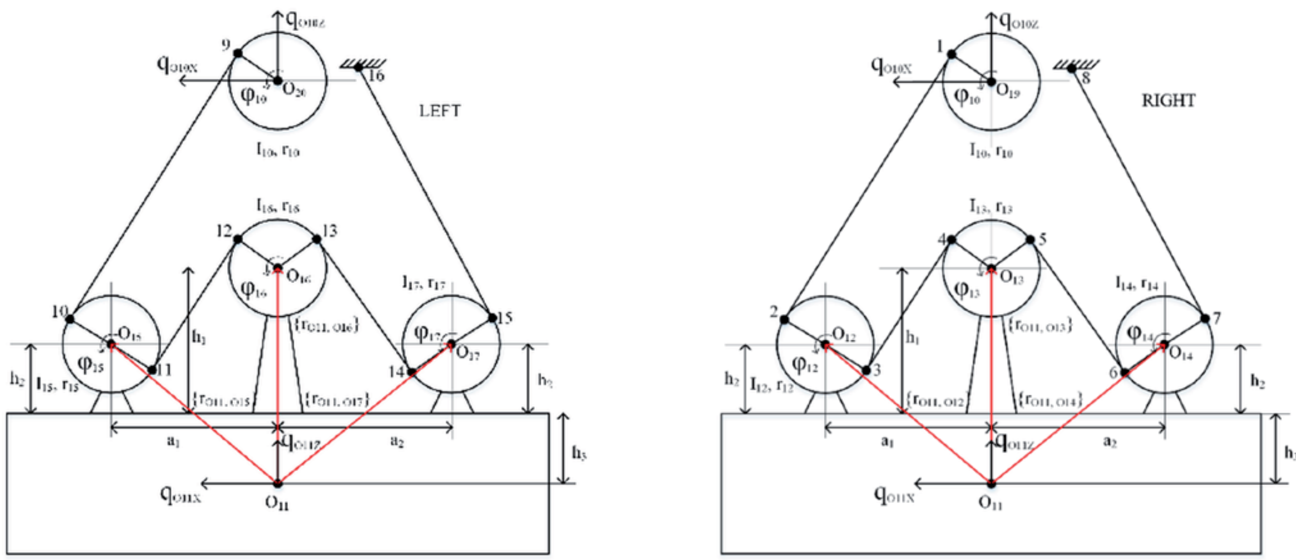

Fig. 4. b) Dynamic model of system "Drum-Container": parts left and right

Here F_{p2p1}, F_{p2p1} is in the cables (cable between points 1 and 2, and points 9 and 10 (Fig. 4 a, 4 b).

If the center of mass of the container does not coincide with its geometric center during loading, the tension forces on the left and right of the ropes are different and the container may rotate about its own axis (Fig.4)

Total friction force is equal:

$$F_{FRIC} = |F_N|\,\mu(v_{REL}) \tag{25}$$

$$v_{REL} = r_{SHAFT}\dot{\varphi}_{10} + \left(\dot{q}_{O10X} - \dot{x}(t)\right)\sin(\alpha) - \left(\dot{q}_{O10Z} - \dot{z}(t)\right)\cos(\alpha) \tag{26}$$

$$\mu(v_{REL}) = \frac{2}{\pi}\arctan\left(k_F|v_{REL}|\right)\left(\mu_1 + (\mu_0 - \mu_1)\exp\left(\gamma_v|v_{REL}|\right)\right) \tag{27}$$

3.2. Mathematical model "System-drum-cargo"

The container can move in the directions of the global axes X, Y, and Z and rotate about the local axes Xo11, Yo11, and Zo11 of the container. The rotation of the vehicle body is estimated using the Cardan's angles $\{\theta_{011}\}^T = [\theta_1, \theta_2, \theta_3]$.

The system of equations for the movement of a container and spreader are equal to:

$$\begin{bmatrix} \left[M_{qo11,qo11}\right] & -\left[A(\theta_{O11})\right]\left[\tilde{S}_{O11,C}\right]\left[G_2\right] \\ -\left[G_2(\theta_{O11})\right]^T\left[\tilde{S}_{O11,C}\right]^T\left[A(\theta_{O11})\right]^T & \left[G_2(\theta_{O11})\right]^T\left[I_{O11}\right]\left[G_2(\theta_{O11})\right] \end{bmatrix}\begin{Bmatrix}\{\ddot{\varphi}_{O11}\} \\ \{\ddot{\theta}_{O11}\}\end{Bmatrix} = \\ = \begin{Bmatrix} -m_{O11}\{a_{O11}\} + \{F_{O11}\} \\ -\{M_{O11,\theta}\} - \left[G_2(\theta_{O11})\right]^T\{M_{O11}\} \end{Bmatrix} \tag{28}$$

here $[M_{qq}] = m_{011}[I]$; $[I]$– identity matrix; m_{011} – total mass of container and spreader; $[I_{011}]$ is a mass inertia tensor:

$$\left[I_{O11}\right] = \int_V \rho\left[\tilde{r}\right]^T\left[\tilde{r}\right]dV. \tag{29}$$

$[A(\theta_{011})]$– rotation matrix; $[\tilde{r}]$ – antisymmetric matrix:

$$[\tilde{r}] = \begin{bmatrix} 0 & -(z+z_C) & (y+y_C) \\ (z+z_C) & 0 & -(x+x_C) \\ -(y+y_C) & (x+x_C) & 0 \end{bmatrix} \quad (30)$$

is generated using vector:

$$\{r\}^T = [x+x_C \quad y+y_C \quad z+z_C] \quad (31)$$

here x_c, y_c, z_c – coordinates of mass center of total system „Container-Spreader“; $\{a_{011}\}$ – acceleration vector:

$$\{a_{O11}\} = [A(\theta_{O11})][\tilde{\varphi}_{O11}]^2 \{S_{O11,C}\} - [A(\theta_{O11})][\tilde{S}_{O11,C}][\dot{G}_2(\theta_{O11})]\{\dot{\theta}_{O11}\} \quad (32)$$

$$\{M_{O11,\theta}\} = [G_2(\theta_{O11})]^T [I_{O11}][\dot{G}_2(\theta_{O11})]\{\dot{\theta}_{O11}\} - [G_2(\theta_{O11})]^T [\tilde{\varphi}_{O11}][I_{O11}]\{\dot{\varphi}_{O11}\} \quad (33)$$

here:

$$[G_2] = \begin{bmatrix} \cos(\theta_2)\cos(\theta_3) & \sin(\theta_3) & 0 \\ -\cos(\theta_2)\sin(\theta_3) & \cos(\theta_3) & 0 \\ \sin(\theta_2) & 0 & 1 \end{bmatrix} \quad (34)$$

$\{\dot{\varphi}_{O11}\}$ – is vector of angular velocity in the body coordinate system

$$\{\dot{\varphi}_{O11}\} = [G_2(\theta_{O11})]\{\dot{\theta}_{O11}\} \quad (35)$$

$$[\tilde{S}_{O11,C}] = \int_V [\tilde{r}]\rho dV, \quad (36)$$

$$\{S_{O11,C}\} = \int_V \{r\}\rho dV. \quad (37)$$

If container is symmetrical body, then:

$$[\tilde{S}_{O11,C}] = 0, \{S_{O11,C}\} = 0. \quad (38)$$

Relation between vector $\{\dot{\varphi}_{O11}\}$ and first derivative of Cardan’s angles vector $\{\dot{\theta}_{O11}\}$ equal to:

$$\{\dot{\varphi}_{O11}\} = [G_2(\theta_{O11})]\{\dot{\theta}_{O11}\}. \quad (39)$$

Vector of coordinates and velocity of point k of container area equal to:

$$\{R\} = \{q_{O11}\} + [A(\theta_{O11})]\{r_k\}, \quad (40)$$

$$\{V_K\} = \{\dot{q}_{O11}\} - [A(\theta_{O11})][\tilde{r}_{O11,K}][G_2(\theta_{O11})]\{\dot{\theta}_{O11}\}. \quad (41)$$

The vector of forces and vector of moments between points 1 and 2 is equal:

$$\{F_{qO11,p2p1}\} = -\frac{F_{p2p1}}{L_{p2p1}}(\{R_{p1}\} - \{R_{p2}\}), \quad (42)$$

$$\{F_{\theta O11,p2p1}\} = -\frac{F_{p2p1}}{L_{p2p1}}([A(\theta_{O11})][\tilde{r}_{O11,2}][G_2(\theta_{O11})])^T (\{R_{p1}\} - \{R_{p2}\}) \quad (43)$$

here:

$$F_{p2p1} = k_{p2p1}\left(\left|\{R_{p1}\} - \{R_{p2}\}\right| - L_{p2p1,0} + r_{12}\varphi_{12} - r_{10}\varphi_{10}\right) \times$$
$$\times c_{p2p1}\left((\{\dot{R}_{p1}\} - \{\dot{R}_{p2}\})^T (\{R_{p1}\} - \{R_{p2}\}) + r_{12}\dot{\varphi}_{12} - r_{10}\dot{\varphi}_{10}\right) \quad (44)$$

$\{R_{p1}\}, \{R_{p1}\}$ – vectors of points 1 and 2.

$$k_{p2p1} = \frac{E_{cable}A_{cable}}{L_{p2p1}} \quad (45)$$

$$L_{p2p1} = \sqrt{(\{R_{p1}\} - \{R_{p2}\})^T (\{R_{p1}\} - \{R_{p2}\})}, \quad (46)$$

$$\{R_{p1}\} = \{R_{O10,19}\} + \{q_{O10}\}, \quad (47)$$

$$\{R_{p2}\} = \{R_{O11,0}\} + \{q_{O11}\} + [A(\theta_{O11})]\{r_{O11,P2}\}, \quad (48)$$

here $[\tilde{r}_{O11,2}]$ – antisymmetric matrix which generates by using vector $\{r_{O11,p2}\}$. This vector is described in the container coordinate system Xo11, Yo11, and Zo11. The vector of forces and vector of moments, between points 9 and 10, are equal:

$$\{F_{qO11,p10p9}\} = -\frac{F_{p10p9}}{L_{p10p9}}(\{R_{p9}\} - \{R_{p10}\}), \quad (49)$$

$$\{F_{\theta O11,p10p9}\} = -\frac{F_{p10p9}}{L_{p10p9}}([A(\theta_{O11})][\tilde{r}_{O11,10}][G_2(\theta_{O11})])^T (\{R_{p9}\} - \{R_{p10}\}), \quad (50)$$

The vector of forces and vector of moments between points 7 and 8, is equal:

$$\{F_{qO11,p7p8}\} = -\frac{F_{p7p8}}{L_{p7p8}}(\{R_{p9}\} - \{R_{p7}\}), \quad (51)$$

$$\{F_{\theta O11,p7p8}\} = -\frac{F_{p7p8}}{L_{p7p8}}([A(\theta_{O11})][\tilde{r}_{O11,7}][G_2(\theta_{O11})])^T (\{R_{p8}\} - \{R_{p7}\}), \quad (52)$$

here:

$$F_{p7p8} = k_{p7p8}\left(\left|\{R_{p8}\} - \{R_{p7}\}\right| - L_{p7p8,0} - r_{14}\varphi_{14}\right) + \quad (53)$$

$$+c_{p2p1}\left((\{\dot{R}_{p1}\} - \{\dot{R}_{p2}\})^T (\{R_{p1}\} - \{R_{p2}\}) - r_{40}\dot{\varphi}_{14}\right), \quad (54)$$

$$k_{p7p8} = \frac{E_{cable}A_{cable}}{L_{p7p8}}, \quad (55)$$

$$L_{p7p8}=\sqrt{\left(\left\{R_{p8}\right\}-\left\{R_{p7}\right\}\right)^T\left(\left\{R_{p8}\right\}-\left\{R_{p7}\right\}\right)}, \qquad (56)$$

Here $\{R_{p7}\}$, $\{R_{p8}\}$ – vectors of points 7 and 8,

$$\left\{R_{p7}\right\}=\left\{R_{O11,0}\right\}+\left\{q_{O11}\right\}+\left[A\left(\theta_{O11}\right)\right]\left\{r_{O11,P7}\right\}, \qquad (57)$$

$\left[\tilde{r}_{O11,7}\right]$ – antisymmetric matrix which generates by using vector $\{r_{O11,p7}\}$. This vector describes the container coordinate system Xo11, Yo11, and Zo11. The system of rotation equations of discs O12,O13 and O14 are equal to:

$$I_{12}\ddot{\varphi}_{12}=-r_{12}F_{P2P1}+k_{34}r_{12}\left(r_{12}\varphi_{12}+r_{13}\varphi_{13}\right)+c_{34}r_{12}\left(r_{12}\dot{\varphi}_{12}+r_{13}\dot{\varphi}_{13}\right)-c_{12}\dot{\varphi}_{12}, \qquad (58)$$

$$I_{13}\ddot{\varphi}_{13}=-k_{34}r_{13}\left(r_{12}\varphi_{12}+r_{13}\varphi_{13}\right)-c_{34}r_{13}\left(r_{12}\dot{\varphi}_{12}+r_{13}\dot{\varphi}_{13}\right)-c_{13}\dot{\varphi}_{13}-$$
$$-k_{56}r_{13}\left(r_{13}\varphi_{13}+r_{14}\varphi_{14}\right)-c_{34}r_{13}\left(r_{13}\dot{\varphi}_{13}+r_{14}\dot{\varphi}_{14}\right), \qquad (59)$$

$$I_{14}\ddot{\varphi}_{14}=r_{14}F_{P7P8}-k_{56}r_{14}\left(r_{13}\varphi_{13}+r_{14}\varphi_{14}\right)+c_{56}r_{14}\left(r_{13}\dot{\varphi}_{13}+r_{14}\dot{\varphi}_{14}\right)-c_{14}\dot{\varphi}_{14}. \qquad (60)$$

The system of rotation equations of discs O15, O16 and O17 are equal:

$$I_{15}\ddot{\varphi}_{15}=-r_{15}F_{P10P9}+k_{1112}r_{15}\left(r_{15}\varphi_{15}+r_{16}\varphi_{16}\right)+c_{1112}r_{15}\left(r_{15}\dot{\varphi}_{15}+r_{16}\dot{\varphi}_{16}-c_{15}\dot{\varphi}_{15}\right) \qquad (61)$$

$$I_{16}\ddot{\varphi}_{16}=-k_{1112}r_{16}\left(r_{15}\varphi_{15}+r_{16}\varphi_{16}\right)+c_{1112}r_{16}\left(r_{15}\dot{\varphi}_{15}+r_{16}\dot{\varphi}_{16}\right)-c_{16}\dot{\varphi}_{16}-$$
$$-k_{1314}r_{16}\left(r_{16}\dot{\varphi}_{16}+r_{17}\dot{\varphi}_{17}\right), \qquad (62)$$

$$I_{17}\ddot{\varphi}_{17}=r_{17}F_{P15P16}-k_{1314}r_{17}\left(r_{16}\varphi_{16}+r_{17}\varphi_{17}\right)+c_{1314}r_{17}\left(r_{16}\dot{\varphi}_{16}+r_{17}\dot{\varphi}_{17}\right)-c_{17}\dot{\varphi}_{17}, \qquad (63)$$

here force F_{P10P9} is described the same as force F_{P2P1} and force F_{P15P16} is described the same as force F_{P7P8}.

The container is unloading from the ship hold in the form of a rectangular parallelepiped. The node *k* global vector coordinates and velocities of rectangular parallelepiped are equal:

$$\left\{R_{SK}\right\}=\left\{R_{OS}\right\}+\left\{R_{OS,K}\right\}+\left\{q_s(t)\right\}, \qquad (64)$$

$$\left\{V_{SK}\right\}=\left\{\dot{q}_s(t)\right\}, \qquad (65)$$

here $\{R_{OS}\}$ - initial vector coordinates of rectangular parallelepiped center; $\{R_{OS,K}\}$ – vector from point OS to angle k of rectangular parallelepiped; $\{q_s(t)\}$ – vector coordinates of rectangular parallelepiped center:

$$\left\{q_S(t)\right\}^T=\left[A_X\sin\left(\Omega_X t\right)A_Y\sin\left(\Omega_X t\right)A_Z\sin\left(\Omega_X t\right)\right]. \qquad (66)$$

The node *k* global vector coordinates and velocities of container corners are equal:

$$\left\{R_K\right\}=\left\{R_{O11,0}\right\}+\left\{q_{O11}\right\}+\left[A\left(\theta_{O11}\right)\right]\left\{r_{O11,K}\right\}, \qquad (67)$$

$$\left\{V_K\right\}=\left\{\dot{q}_{O11}\right\}-\left[A\left(\theta_{O11}\right)\right]\left[\tilde{r}_{O11,K}\right]\left[G_2\left(\theta_{O11}\right)\right]\left\{\dot{\theta}_{O11}\right\}, \qquad (68)$$

Here $\{r_{O11,K}\}$ – vector of coordinates of corner *k*, (*k* = 1, 2, …8). Initial gaps of container corner and ship rectangular parallelepiped corner in the X,Y, Z directions are equal:

$$\left\{\Delta\right\}^T=\left[\Delta_X \quad \Delta_Y \quad \Delta_Z\right]. \qquad (69)$$

Contact forces between container and ship are described in eight angles of container (Fig.5). The normal contact force in the X direction of k container corner with ship rectangular parallelepiped corner k is equal:

$$F_{NX,K}=k_{SC}\left|\delta_{X,K}\right|^n D\left(\dot{\delta}_{X,K}\right), \qquad (70)$$

$$\delta_{X,K}=\begin{cases}X_{SK}-X_K-\Delta_{SCX}, when\ k=1,4,5,8\\ X_K-X_{SK}-\Delta_{SCX}, when\ k=2,3,6,7\end{cases} \qquad (71)$$

$$\dot{\delta}_{X,K}=\begin{cases}V_{SKX}-V_{KX}, when\ k=1,4,5,8\\ V_{KX}-V_{SKX}, when\ k=2,3,6,7\end{cases} \qquad (72)$$

D – coefficient which evaluates hysteresis of contact force:

$$\text{D}=(1+0.75*(1-e_{RES}^2))\dot{\delta}_{NX}/\dot{\delta}_{N\_\max}. \qquad (73)$$

The friction forces in the Y and Z directions are equal:

$$F_{Y,K,FRIC}=-\mu\left(\Delta V_{Y,K}\right)F_{NX,K}sign\left(\Delta V_{Y,K}\right), \qquad (74)$$

$$F_{Z,K,FRIC}=-\mu\left(\Delta V_{Z,K}\right)F_{NX,K}sign\left(\Delta V_{Z,K}\right), \qquad (75)$$

slip velocities are equal:

$$\Delta V_{Y,K}=V_{Y,K}-V_{SY,K}, \Delta V_{Z,K}=V_{Z,K}-V_{SZ,K}. \qquad (76)$$

The total force and moment vector of container corner k with ship is equal:

$$\left\{M_K\right\}=-\left[G_2\left(\theta_{O11}\right)\right]^T\left[\tilde{r}_{O11,K}\right]^T\left[A\left(\theta_{O11}\right)\right]^T\left\{F_K\right\} \qquad (77)$$

The contact forces in the Y and Z axis directions are similarly determined.

4. Experimental results of container loading process

Experimental measurements of the container loading process in the port were done. During the experimental research, the quay crane carried out loading operations. Main parameters of the container unloading process were measured: duration (s), position X, Y, Z (m), velocity (m/s) acceleration (m/s^2). Data was collected using equipment "DL1-MK2 data logger" which was fixed on a spreader of a crane. More than 200 of container unloading processes were measured and statistical analysis of data was performed. More detail information about experimental measurements is presented in the paper [7]. Measurement results of the unloading process were divided into operations

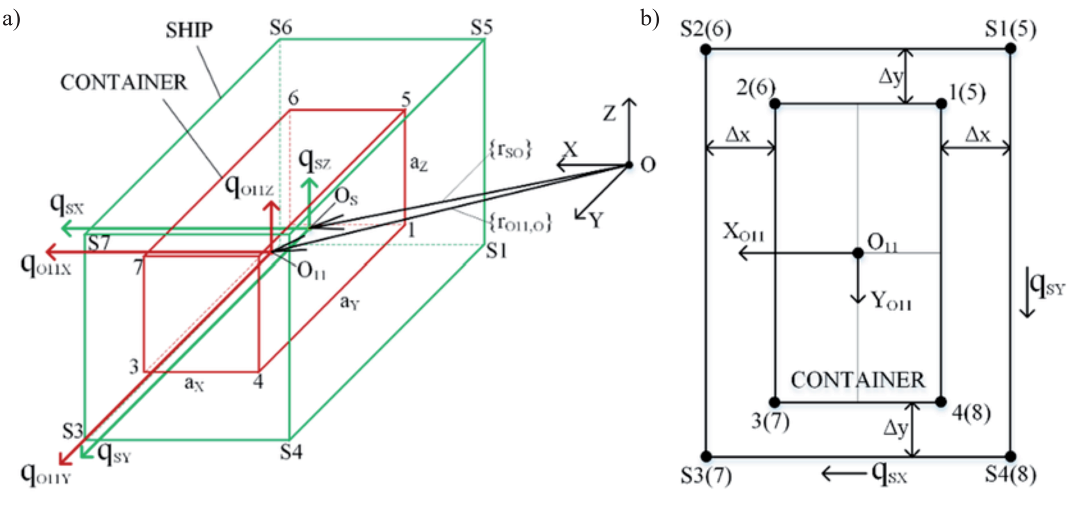

Fig. 5. The container corners and ship rectangular parallelepiped corners: red color–container; green color–ship rectangular parallelepiped

of 7 stages: 1. Start of lifting (hooking); 2. Vertical lifting; 3. Diagonal lifting; 4. Horizontal transportation; 5. Diagonal lowering; 6. Vertical lowering; 7. Placing on (autonomous guided vehicle) AGV.

The data that is relevant for the analysis of unloading containers from the ship: mass of the container, duration of hooking, time of vertical lifting from the ship. The results of the experimental unloading duration are presented in Fig. 6.

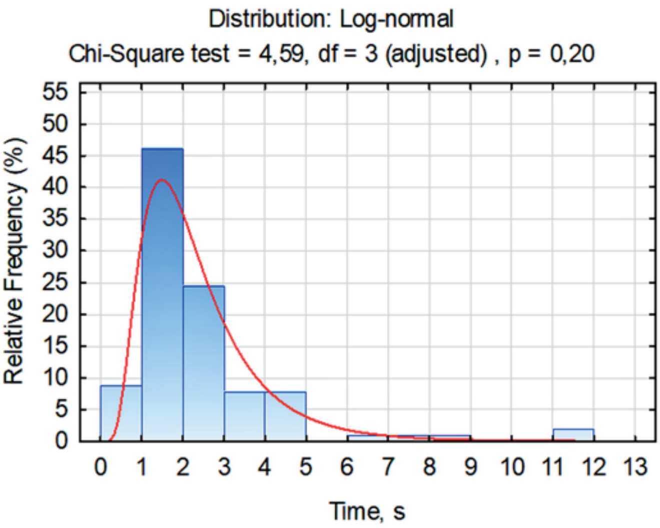

Fig. 6. The duration of hooking the container

The hooking duration of the container on the ship can vary from 0,6 to 12 (s), average is 2,43 (s). Results of the vertical lifting duration from the ship cargo hold are shown in Fig. 7.

The duration of the vertical lifting from the ship depends on the depth at which the container is located; coefficient of correlation is equal r=0,89.

Histogram of container masses is presented in Fig 8. The needs of power for the unloading process depends on the mass of the container, which can vary. Analysis of container masses shows that masses can vary from 2 to 32 tons.

As we can see from the histogram, more than 67 % of container masses are from 25 to 32 tons.

Results of experimental measurements were used to compare the results of mathematical model and numerical analysis with the real data of container unloading from the ship. More results of measurements (acceleration, velocity, displacement) are presented in section 5 Figures 9b, 10b, 11b.

5. Results of numerical analysis

Based on the mathematical model presented in section 2 the computer programming code was created and numerical analysis of container unloading from the ship's cargo hold was performed. Time step for integration of differential equations was 10^{-6} s. The main parameters of the system are given in Table 2.

Numerical analysis was performed when the gap between container and ship's hold wall varies from 10 mm to 50 mm.

Results of numerical modeling are shown in Figures

Table 2. Main parameters used in dynamic model

Symbol	Description [units]	Values
a_1	m	1,0
a_2	m	1,0
b_1	m	0,719
B_2	m	0,719
h_1	m	1,1
h_2	m	0,30
h_3	m	1,0
Length of container	m	6,058
Width of container	m	2,438
Hight of container	m	2,60
Depth of hold	m	10
Parameters of electrical motor:		
I_1	kgm^2	1,811
w_0	rad/s	78,83
c_v	Nm	5093,9
d_v	1/s	405,3
U_R	-	8,0
k_{12}	MNm	0,1636
c_{12}	kNms	10,0
k_{910}	MNm	0,170
c_{910}	kNms	10,0
d_{cable}	m	0,30
E_{cable}	GPa	
c_{cable}	kNs/m	20,0
r_{10}	m	20,0
m_{10}	kg	20
I_{10}	Kgm^2	0,20
$r_{12}=r_{13}=r_{14}=r_{15}=r_{16}=r_{17}$	m	1973,0
$m_{grapper}$	kg	300,0
k_{sc}	GNm^{1,5}	1,50
c_{sc}	Ns/m	1,0
e_{RES}		0,50
n	-	1,5

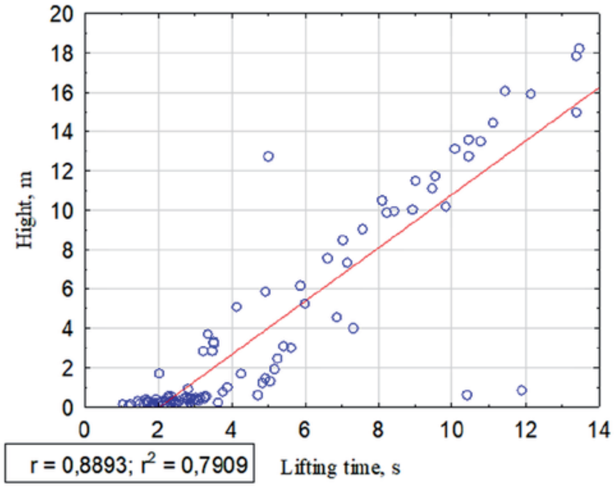

Fig. 7. Relationship between hight and lifting time: experimental measurements

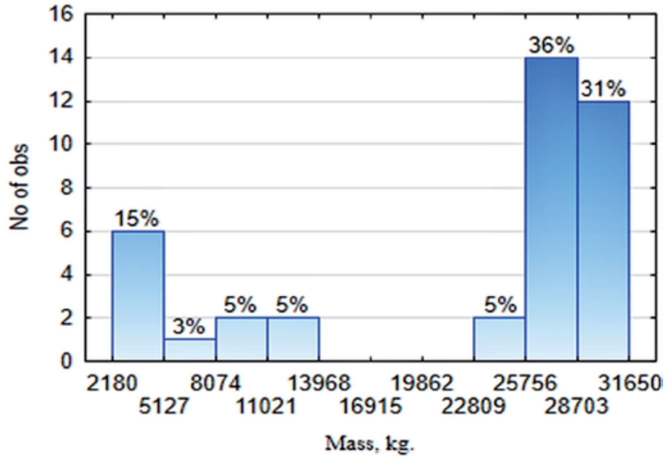

Fig. 8. Container mass distribution

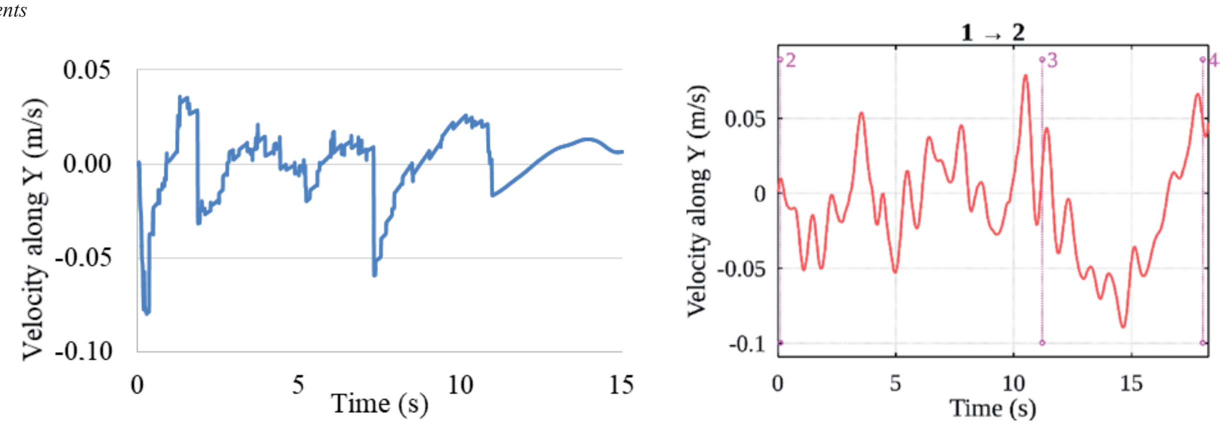

Fig. 9. Cargo movement speed in ship's cargo hold (direction Y): a) mathematical model, b) results of experimental measurements

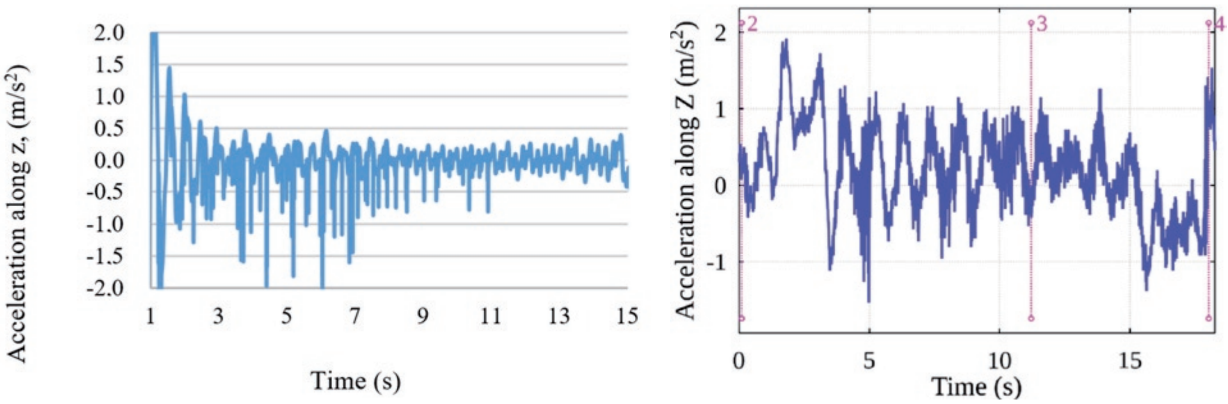

Fig. 10. Lifting acceleration in Z direction: a) mathematical model, b) results of experimental measurements

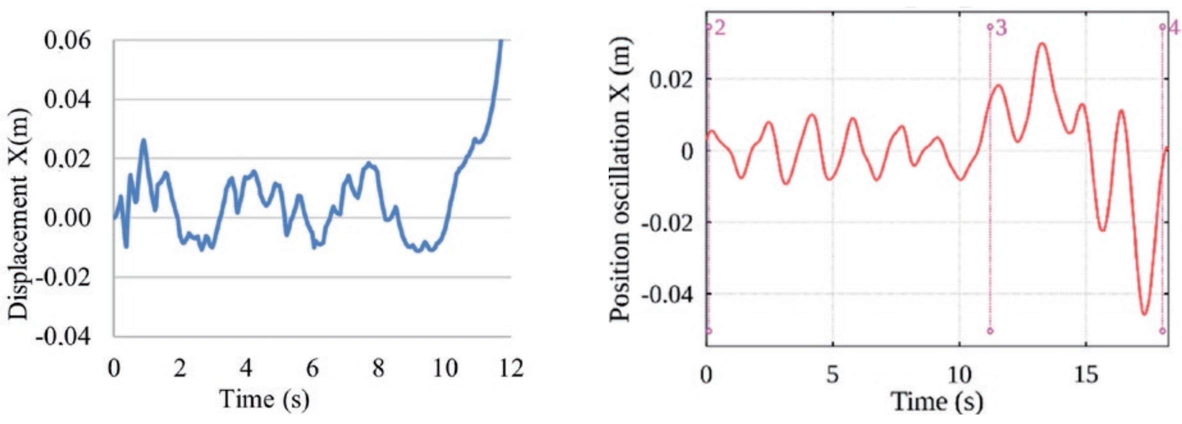

Fig. 11. Container displacements in X direction when loading vertically: a) modelling results, b) results of experimental measurements

9–11, and the obtained results are compared with the results of experimental measurements in case the cargo weight is 28 tons. The velocity of container movement in Y direction is presented in Fig. 9.

As we can see, results of numerical analysis and experimental measurement are very similar i.e., velocity of container movement along Y axis can vary in range ± 0,08 m/s.

The acceleration in Z direction when the lifted cargo weight is 28 tons is presented in Fig. 10.

We can see that acceleration can vary in range from -2 m/s^2 to +2 m/s^2 during experimental measurement and results of numerical analysis.

Container displacements in X direction are shown in Fig. 11. Results show that container displacements in the ship's cargo hold can be approximately +- 0.02m. When the cargo is lifted at about the 11th second, container displacement along the X-axis can increase because it is not limited by ship hold and can move freely. This dependence we can see both during numerical analysis and during the real unloading process.

The power of friction forces when there are oscillations of the ship and contact forces are taken into consideration is presented in Fig. 12.

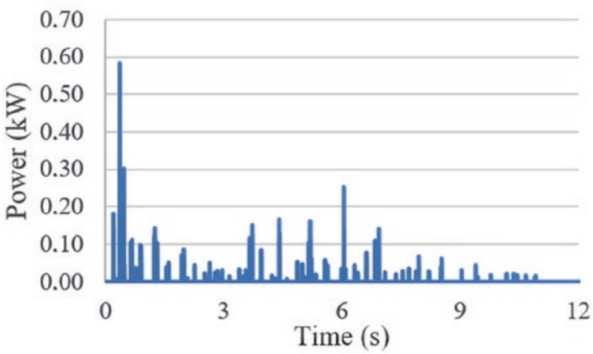

Fig. 12. Power of friction forces

We can see in Fig. 12 if the ship starts to oscillate and cargo comes into contact with the ship's cargo hold wall, then arises the need for additional power.

Mathematical modelling results of power needs of cargo lifting are presented in Fig. 13. We can see dependency power from cargo mass, approximately 220 kW power needed to lift cargo with mass 32 t.

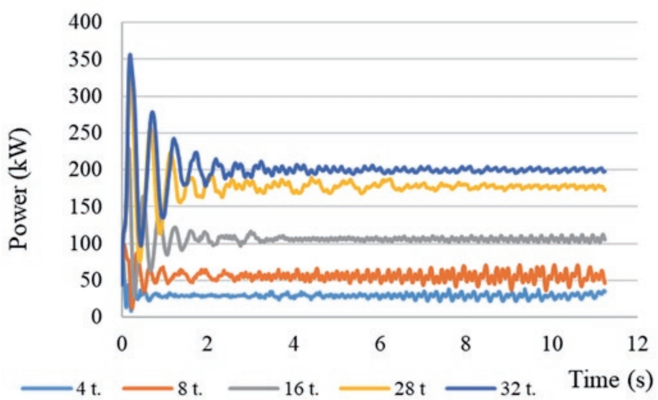

Fig. 13. Lifting power dependency from container mass

Power needs depending on friction forces between container and ship's cargo hold when the ship's oscillating toward X direction was calculated. Results of power of friction forces when the gap is 10 ÷50 mm and frequency of ship oscillation is 0,30 Hz are shown in Table 3.

Table 3. Power of friction forces depending on cargo masses

Cargo mass, tons	Gap, mm	Average power of friction forces, kW
4,0	10	0,433
8,0	10	1,024
24,0	10	1,343
28,0	10	1,506
28,0	30	1,532
28,0	50	2,121

From the given average power of friction force we can see that the power of friction force increases when the cargo mass increases. However, this dependency is nonlinear because the contact forces depend on container mass and mass inertia moments, ship's oscillation, lifting speed, varying rope stiffness, dynamic characteristics of drum bearings.

5. Discussion and conclusions

Mathematical model and programming code were created that allows to determine main parameters of container lifting from ship process: container displacement, velocity, acceleration in X, Y, Z directions during cargo loading process when container movement is limited in the cargo hold in X, Y directions.

Results of experimental measurements of the container unloading process are used for verification of mathematical models and show similar results as numerical analysis.

Mathematical model considers friction forces that occur during the container contact with the ship cargo hold.

Based on real time container loading results it was determined that containers on the ship can be hooked within 0,6 ÷11,5 (s), the average of hooking time being 2,43±1,84 (s).

Experimental measurements of container unloading *in situ* showed that usually container mass is between 24 and 32 tons. Small mass containers (less than 4 tons) make up 15% of all containers. Duration of vertical unloading depends on the weight of the cargo; however, this dependency is not very significant. Mass has a greater impact on energy consumption. Results of modelling show that power consumption during unloading has a nonlinear dependency from cargo mass. The power depends on container mass and 32 tons cargo requires about 220 kW power.

Low oscillations of the ship affect the stability of the container unloading process and power consumption. Contact of container to ship hold can cause frictional forces and increase instantaneous power requirements. The results of mathematical modelling show if the container has a contact with the cargo hold and the ship's oscillation frequency is 0,3Hz, then average power of friction forces increases and is equal to about 2,12 kW.

As we can see from the analysis of frictional power, this power is useless and reduces the energy efficiency of the system. This energy can be saved by controlling the lifting gear using special methods and smart technologies.

Based on results further research of cargo unloading from ships can be continued and rational unloading modes determined to minimize energy consumption and avoid possible cargo damage from contact forces.

Acknowledgements

The authors express gratitude to members of the project No. 01.2.2-LMT-K-718-01-0081: Dr R. Didziokas, Dr A. Senulis, Dr T. Eglynas, Dr. S.Jakovlev, Z Lukosius for valuable insights and collection of data.

Funding

The author(s) disclosed receipt of the following financial support for the research, authorship, and/or publication of this article: This research was funded by the European Regional Development Fund according to the supported activity "Research Projects Implemented by World-class Researcher Groups" under Measure No. 01.2.2-LMT-K-718-01-0081.

References

1. Abdullahi A M, Mohamed Z, Selamat H, Pota H R, Zainal Abidin M S, Fasih S M. Efficient control of a 3D overhead crane with simultaneous payload hoisting and wind disturbance: design, simulation and experiment. Mechanical Systems and Signal Processing 2020; 145: 106893, https://doi.org/10.1016/j.ymssp.2020.106893.
2. Alamoush A S, Ballini F, Ölçer AI. Ports' technical and operational measures to reduce greenhouse gas emission and improve energy efficiency: A review. Marine Pollution Bulletin 2020; 160: 111508, https://doi.org/10.1016/j.marpolbul.2020.111508.
3. Arena A, Casalotti A, Lacarbonara W, Cartmell M P. Dynamics of container cranes: three-dimensional modeling, full-scale experiments, and identification. International Journal of Mechanical Sciences 2015; 93: 8-21, https://doi.org/10.1016/j.ijmecsci.2014.11.024.
4. Bouman E A, Lindstad E, Rialland A I, Strømman A H. State-of-the-art technologies, measures, and potential for reducing GHG emissions from shipping - A review. Transportation Research Part D: Transport and Environment 2017; 52 (A): 408-421, https://doi.org/10.1016/j.trd.2017.03.022.
5. Çağatay I, Lam J S L. A review of energy efficiency in ports: Operational strategies, technologies and energy management systems. Renewable and Sustainable Energy Reviews 2019; 112: 170-182, https://doi.org/10.1016/j.rser.2019.04.069.
6. Chu Y , Li G, Hatledal L I, Holmeset F T, Zhang H. Coupling of dynamic reaction forces of a heavy load crane and ship motion responses in waves. Ships and Offshore structures 2021; 16(1): 58-67, https://doi.org/10.1080/17445302.2021.1907066.
7. Chwastek S. Optimization of crane mechanisms to reduce vibration. Automation in Construction, 2020; 119(1): 103335, https://doi.org/10.1016/j.autcon.2020.103335.
8. Eglynas T, Andziulis A, Bogdevicius M, Januteniene J, Jakovlev S, Jankunas V, Senulis A, Jusis M, Bogdevicius P, Gudas S. Modeling and experimental research of quay crane cargo lowering processes. Advances in Mechanical Engineering 2019; 11(12), https://doi.org/10.1177/1687814019896927.
9. European Sea Ports Organization. ESPO Green Guide 2021 A Manual for European Ports Towards A Green Future 2021.
10. Hoang M C, Hoang Q D, Pham V T, Le A T. Adaptive fractional-order terminal sliding mode control of rubber-tired gantry cranes with uncertainties and unknown disturbances. Mechanical Systems and Signal Processing 2021; 154: 107601, https://doi.org/10.1016/j.ymssp.2020.107601.
11. Jakovlev S, Eglynas T, Voznak M. Application of Neural Network Predictive Control Methods to Solve the Shipping Container Sway Control Problem in Quay Cranes. IEEE Access 2021; PP(99):1-1,https://doi.org/10.1109/ACCESS.2021.3083928.
12. Kosucki A, Malenta P, Stawiński L, Halusia S. Energy consumption and overloads of crane hoisting mechanism with system of reducing operational loads. Eksploatacja i Niezawodnosc - Maintenance and Reliability 2017; 19(4): 508-515, https://doi.org/10.17531/ein.2017.4.3.
13. Kosucki A, Stawiński L, Malenta P, Zaczyński J, Skowrońsk J. Energy consumption and energy efficiency improvement of overhead crane's mechanisms. Eksploatacja i Niezawodnosc - Maintenance and Reliability 2020; 22(2): 323-330, https://doi.org/10.17531/ein.2020.2.15.
14. Merk O. Shipping Emissions in Ports. International Transport Forum, Paris, France 2014; Paper No. 2014-20.
15. Milana G, Banisoleiman K, González A. An investigation into the moving load problem for the lifting boom of a ship unloader. Engineering Structures 2021; 234: 111899, https://doi.org/10.1016/j.engstruct.2021.111899.
16. Papaioannou V, Pietrosanti S, Holderbaum W, Becerra V M, Mayer R. Analysis of energy usage for RTG cranes. Mechanical Systems and Signal Processing 2018; 125: 337-344, https://doi.org/10.1016/j.energy.2017.02.122.
17. Phan-Thi M, Ryu K, Kim K H. Comparing Cycle Times of Advanced Quay Cranes in Container Terminals. Industrial Engineering & Management Systems 2013; 12(4): 359-367, https://doi.org/10.7232/iems.2013.12.4.359.
18. Sun N., Wu Y., He Chen, Fang Y. An energy-optimal solution for transportation control of cranes with double pendulum dynamics: Design and experiments. Mechanical Systems and Signal Processing 2018; 102: 87-101, https://doi.org/10.1016/j.ymssp.2017.09.027.
19. Urbaś A, Szczotka M. The influence of the friction phenomenon on a forest crane operator's level of discomfort. Eksploatacja i Niezawodnosc - Maintenance and Reliability 2019; 21(2): 197-210, https://doi.org/10.17531/ein.2019.2.3.
20. Wu Q, Wang X, Hua L, Xia M. Improved time optimal anti-swing control system based on low-pass filter for double pendulum crane system with distributed mass beam. Mechanical Systems and Signal Processing 2021; 151(9): 107444, https://doi.org/10.1016/j.ymssp.2020.107444.
21. Wu Q, Wang X, Hua L, Xia M. Modelling and nonlinear sliding mode controls of double pendulum cranes considering distributed mass beams, varying roped length and external disturbances. Mechanical Systems and Signal Processing 2021; 158: 107756, https://doi.org/10.1016/j.ymssp.2021.107756.
22. Yurchenko D, Alevras P. Stability, control and reliability of a ship crane payload motion. Probabilistic Engineering Mechanics 2014; 38: 173-179, https://doi.org/10.1016/j.probengmech.2014.10.003.

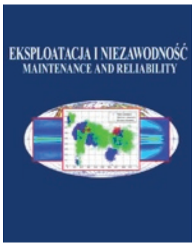

Eksploatacja i Niezawodnosc – Maintenance and Reliability

Volume 24 (2022), Issue 1

journal homepage: http://www.ein.org.pl

Article citation info:
Zhang Z, Feng S, Ding Y, Mei X, Tao Z. Thermal error modeling of spindle and dynamic machining accuracy reliability analysis of CNC machine tools based on IA and LHSMC. Eksploatacja i Niezawodnosc – Maintenance and Reliability 2022; 24 (1): 100–113, http://doi.org/10.17531/ein.2022.1.12.

Thermal error modeling of spindle and dynamic machining accuracy reliability analysis of CNC machine tools based on IA and LHSMC

Indexed by: Web of Science Group

Ziling Zhang[a]*, Shuo Feng[a], Yan Ding[b], Xiao Mei[a], Zhiqiang Tao[c]

[a]Shanghai Maritime University, Logistics Engineering College, Shanghai, 201306, China
[b]Qiqihar Second Machine Tool (Group) Co.Ltd., Heilongjiang, 161005, China
[c]Beijing Union University, College of Robotics, Beijing, 100027, China

Highlights

- A thermal error model of spindle unit is developed based on IA.
- A machining accuracy model considering the thermal error is constructed based on MBS.
- The machining accuracy reliability analysis method is presented based on LHSMC.
- The effectiveness of the method is verified by a four-axis machine tool.

Abstract

Machining accuracy reliability as a key index of CNC machine tools is seriously influenced by the geometric and thermal errors. In the paper, a spindle unit thermal error modeling and machining accuracy reliability analysis method is proposed. By analyzing the heat generation mechanism, a thermal error model was developed to describe the thermal deformation of the electric spindle. Based on the immune algorithm (IA), the heat generation power and the heat transfer coefficient were optimized, and the thermal error was obtained by finite element thermal-mechanical coupling. By adopting the multi-body system theory (MBS), a dynamic machining accuracy model was put forward including the geometric and thermal errors. Based on the Latin hypercube sampling Monte Carlo method (LHSMC), a machining accuracy reliability analysis method was proposed to characterize the machining accuracy reliability considering the geometric and thermal errors. The method was employed to a machine tool, and the experimental results indicate the verification and superiority of the method.

Keywords

electric spindle unit, thermal error, latin hypercube sampling monte carlo method, finite element simulation, machining accuracy reliability.

1. Introduction

CNC machine tools are favored by various enterprises as core equipment owing to their high-speed and high-accuracy characteristics. Machining accuracy reliability is an important criterion, which reflects the capability of machine tools to achieve the desired requirements. The machining accuracy is directly expressed in the dimensional error of the workpiece in the work condition. Geometric and thermal errors are the major contributors to variations in machining accuracy [21, 23]. Among the total error sources, the occupancy rate of thermal error is 40%-75% [14]. The higher machining accuracy reliability of machine tools, the greater their competitiveness, which is a factor that manufacturers need to focus on [4]. Thus, it is crucial to consider the impact of thermal error on the machining accuracy reliability. With the increased requirements for high precision and efficiency in manufacturing technology, the effective prediction of thermal error is becoming increasingly important in studying machining accuracy [30]. Hence, how to characterize the reliability of machining accuracy under the effect of thermal error is critical to evaluate the machining capability of machine tools [18].

The temperature variation of the motor and bearings are the major cause of thermal error [15]. Since it is difficult to be calculated effectively, scientific modeling methods to predict the thermal error are necessary [13]. The thermal error modeling process has the following steps: analyzing the spindle temperature rise field; establishing the connection between the critical region of temperature and thermal deformation field; collecting the critical region temperature to predict the thermal error [24]. Recently, many scholars have devoted themselves to the research of thermal error modeling methods. Zhao et al. calculated the convection heat transfer coefficient on the spindle surface, the temperature and deformation fields of the spindle were derived based on the finite element method and validated experimentally [31]. Hou et al. analyzed the coupled thermal deformation of machine tool components, and a multi-objective genetic algorithm was applied to derive a high robustness thermal error model [6]. By using the improved particle swarm optimization (IPSO) method, Li et al. developed a thermal error model, and the higher modeling efficiency

(*) Corresponding author.

E-mail addresses: Ziling Zhang: zhangziling1119@126.com, Shuo Feng: fengshuojxq@163.com, Yan Ding: ding-4560@163.com, Xiao Mei: xiaomei@shmtu.edu.cn, Zhiqiang Tao: jqrzhiqiang@buu.edu.cn

and accuracy were validated by experiments [11]. Shi et al. introduced a thermal error model by Bayesian neural network, and used fuzzy c-means (FCM) clustering analysis to select the sensitive points of temperature. The model has higher prediction accuracy compared to BP neural network [20]. Uhlmann and Hu established a three-dimensional finite element model to predict the thermal characteristics of electric spindles, quantified the heat transfer process internal to the spindle, and validated it under consideration of complex boundary conditions [22]. Zheng and Chen studied the thermal performance of angular contact bearings, analyzed the heat transfer process of the bearing sub source, and developed a comprehensive thermal grid model to predict the temperature rise of the bearings considering the effect of various factors such as constraints and assembly relationships [33]. To effectively forecast the transient temperature and thermal deformation fields of the spindle unit, Yang et al. developed a coupled thermal-structural model, and compared with the TCP thermal errors obtained by the regression model to validate the feasibility of this model [25].

Most of the above-mentioned thermal error modeling methods were proposed based on empirical formulas, which deviate from the actual situation and decrease predictive performance. In addition, the traditional temperature-thermal error and multivariate-thermal error models did not study the formation mechanism of thermal error of the spindle unit in depth, which leaves room for improvement in the application of these two methods [16]. Hence, how to construct a spindle thermal error model with higher prediction accuracy is an urgent problem.

Meanwhile, geometric and thermal errors are the direct cause of the machining accuracy deviation from the desired requirements [5]. Thus, it is imperative to perform machining accuracy modeling. To this end, there are a lot of efforts made by many researchers to develop modeling methods, such as HTM [10, 7, 26, 5], screw theory [32, 17], D-H method [9], Lagrange method [19], Spearman rank correlation method [3] and so on. Geometric errors can be measured using instruments, the translation geometric errors are determined using a laser interferometer, while the angle errors are determined using a ball-bar [34]. The machining accuracy requires consideration of multiple error sources, which is the key point of this paper's research.

Machining accuracy reliability can effectively indicate the capability of the machine tool to achieve the required machining accuracy [27]. So far, much work has been done by many researchers to characterize the reliability of machines. Cheng et al. developed the reliability and sensitivity model to analyze the machining accuracy of the machine tool based on Monte Carlo method, and verified with a three-axis machine tool [2]. Jiang et al. calculated the reliability of the electric spindle system based on the quasi-Monte Carlo method (QMC), used the Kriging method instead of the QMC method to make the calculation more efficient, and experimentally verified the applicability of the model [8]. Cai et al. developed the machining accuracy reliability and sensitivity models considering multiple failure modes based on the first-order and second-moment (AFOSM) and performed experimental validation [1]. The aforementioned scholars have conducted many works for the reliability of machine tools, which shows that the development of machine tool reliability analysis methods is critical. High accuracy reliability prediction methods can improve the competitiveness of machine tools [12]. Detailed descriptions of this aspect are also provided in this paper.

In the paper, a thermal error modeling of spindle unit and machining accuracy reliability analysis method for CNC machine tools is presented, which has the following advantages:

1. The first advantage is the establishment the thermal error model of the electric spindle based on heat generation mechanism and IA. Besides, the heat generation power and heat transfer coefficient were optimized by IA. This model can reveal the inner mechanism of the thermal error and screen the key factors compared to the current empirical methods and temperature-thermal error neural network methods, which can provide the methodological support for predicting the spindle thermal error.
2. The second advantage is the development of the machining accuracy model by MBS, which considers the comprehensive influence of geometric and thermal errors. This model extends the prediction of machining accuracy from considering a single error source of geometric errors to a multiple error sources of geometric and thermal errors;
3. The third advantage is the proposal of the machining accuracy reliability analysis method by LHSMC, which considers the multiple error sources and the randomness of errors. What's more, the model expands the machining accuracy reliability assessment from the traditional static category to the dynamic category, which is closer to the actual machining process and can provide a valid theoretical guide to analyze the machining accuracy reliability of machine tools.

The other contents are arranged as follows. Section 2 gives a description of the thermal error modeling and machining accuracy modeling process. In Section 3, the machining accuracy reliability model based on LHSMC is established. Then, a four-axis machine tool is utilized to validate this model through experiments, by comparing with AFOSM in Section 4. The conclusion of the paper is given in section 5.

2. Dynamic machining accuracy modeling considering the thermal error of spindle unit

2.1. Heat generation mechanism analysis

As the core of the machine tool, the spindle unit contains many heat generating components. Rotating parts such as bearings and motor inevitably generate heat due to the friction under the high speed rotation. When the heat accumulates, the spindle unit generates the deformation. To decrease the large deformation induced by high temperature rise, the spiral cooling water jackets are placed outside the heat generating components to accelerate the heat dissipation process. When the electric spindle unit is working, the existence of temperature gradients internal to the electric spindle unit drives the heat transfer from the high temperature area to the low temperature area. The components in contact with the air transfer heat to the air in the form of thermal radiation. The heat transfer process between the coolant and the heat generating components carries away most of the heat, as shown in Fig. 1.

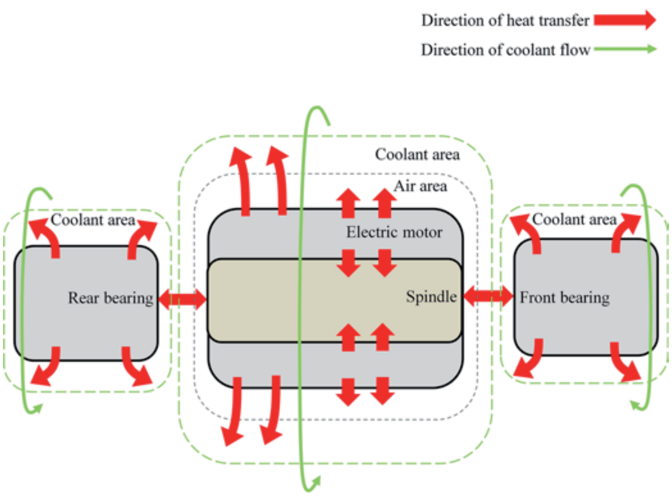

Fig. 1. Heat transfer process of electric spindle unit

It is assumed that the effect of the change in ambient temperature is not considered. According to the law of energy conservation, the relationship between the energy field and the temperature field internal to the spindle unit can be expressed as follows:

$$\begin{aligned} \bar{\Phi}_{total} &= \bar{\Phi}_{pro} + \bar{\Phi}_{thr} - \bar{\Phi}_{dis} = c_{sol} \frac{dT}{dt} \\ and \quad \bar{\Phi}_{thr} &= \bar{\theta} A \frac{dT}{dt} \end{aligned} \tag{1}$$

where $\bar{\Phi}_{pro}$ is the component heat generation power, $\bar{\Phi}_{thr}$ is the heat conduction through the continuous cross section of the spindle unit, $\bar{\Phi}_{dis}$ is the coolant heat exchange power, c_{soL} is the specific heat capacity coefficient, t is the heat transfer time, $\bar{\theta}$ is the thermal conductivity of the spindle unit, and A is the area of the heat exchange surface.

2.2. Thermal error modeling based on IA

Since the electric spindle unit consists of many heat generating components, the process of thermal error modeling can be categorized as following:

1) Front and rear bearing heat generation power modeling

The heat generation power of the bearings operating under the load is expressed as:

$$W_b = 1.047 \times 10^{-4} \omega \cdot (M_v + M_e) \tag{2}$$

where ω is the angular velocity, M_v is the friction torque relevant to the viscous lubrication, and M_e is the friction torque which depends on the applied load.

2) Motor heat generation power modeling

The motor of the electric spindle unit is the driving device, and its heat generation power can be expressed as [29]:

$$\bar{\Phi}_M = \bar{\Phi}_{M1} + \bar{\Phi}_{M2} \tag{3}$$

where $\bar{\Phi}_{M1}$ is the heat generation power of rotor, and $\bar{\Phi}_{M2}$ is the heat generation power of stator.

In Eq. (3), the heat generation power $\bar{\Phi}_M$ can be obtained from the following equation:

$$\begin{cases} \bar{\Phi}_{M1} = \dfrac{Q_1}{V_1} \\ \bar{\Phi}_{M2} = \dfrac{Q_2}{V_2} \end{cases} \tag{4}$$

where Q_1 is the heat generation of rotor, Q_2 is the heat generation of stator, V_1 is the volume of rotor, and V_2 is the volume of stator.

3) Coolant heat transfer coefficient modeling

Coolant is an important medium in the cooling process. The heat transfer process internal to the spindle unit contains three parts: the direct contact heat exchange between the rotating components and the ambient air; the heat exchange between the bearings and the coolant; and the heat exchange between the motor and the coolant. The heat transfer coefficient is expressed as follows:

$$\begin{aligned} h &= Nu \frac{\bar{\theta}}{l_a} \\ and \quad Nu &= 0.133 Re^{2/3} Pr^{1/3} \end{aligned} \tag{5}$$

where Re is the Reynolds value, Pr is the Prandtl value, and l_a is the cross-sectional circumference of the spindle unit.

4) Optimization of heat generation power and heat transfer coefficient

Generally, there is a deviation between the theoretical values and practice values acquired from Eq. (2) to Eq. (5). To narrow the gap between them, the optimal heat generation power and heat transfer coefficient are found based on IA. The iterative optimization process of IA is implemented by the operators, including the operator for evaluating affinity, the operator for evaluating antibody concentration, and the operator for calculating the degree of excitation and so on.

The equation for parameter optimization can be written as:

$$\begin{cases} \hat{U}_{F\_B\_M} = k^U_{F\_B\_M} \times U_{F\_B\_M} + b^U_{F\_B\_M} \\ \hat{h}_{f\_n} = k^h_{f\_n} \times h_{f\_n} + b^h_{f\_n} \end{cases} \tag{6}$$

where $U_{F\_B\_M}$ are the heat generation power of the front bearing, rear bearing and motor, respectively; h_{f_n} are the forced and natural convection heat transfer coefficient, respectively; $k^U_{F\_B\_M}$, $k^h_{f\_n}$ are the proportionality factor of heat generation power and heat transfer coefficient, and $b^U_{F\_B\_M}$, $b^h_{f\_n}$ are the deviation modification factor of heat generation power and heat transfer coefficient.

The vector form of optimized variables can be written as:

$$\begin{aligned} \chi &= [\chi_1, \chi_2, \chi_3, \chi_4, \chi_5, \chi_6, \chi_7, \chi_8, \chi_9, \chi_{10}]^T \\ &= [k^U_F, b^U_F, k^U_B, b^U_B, k^U_M, b^U_M, k^h_f, b^h_f, k^h_n, b^h_n,] \end{aligned} \tag{7}$$

The affinity indicates the binding strength of the immune cells to the antigens, and the antibody affinity function based on the Euclidean distance is expressed as follows:

$$aff(q_i, q_j) = \sqrt{\sum_{k=1}^{r} (q_{i,k} - q_{j.k})^2} \tag{8}$$

where $aff(q_i, q_j)$ is the affinity between antibodies, $q_{i,k}$ and $q_{j.k}$ are the k-th dimension of antibody i and the k-th dimension of antibody j, and r is the number of antibody dimension.

To solve the optimization problem in this paper, Eq. (8) can be transformed into:

$$min\, f(\chi) = min \sqrt{(T_F - T^*_F)^2 + (T_M - T^*_M)^2 + (T_B - T^*_B)^2} \tag{9}$$

where T_F, T_M and T_B are the front bearing, rear bearing and motor simulation temperature, respectively; and $T^*{}_F$, $T^*{}_M$ and $T^*{}_B$ are the front bearing, rear bearing and motor experimental temperature, respectively.

The antibody concentration reflects the quality of antibody population, and the high concentration indicates the presence of many similar individuals which inhibits the global optimization procedure. To guarantee individuals have the characteristics of diversity, the antibody concentration is defined as follows:

$$\begin{aligned} Den(q_i) &= \frac{1}{L} \sum_{j=1}^{L} S(q_i, q_j) \\ and \quad S(q_i, q_j) &= \begin{cases} 1 & aff(q_i, q_j) < \delta_s \\ 0 & aff(q_i, q_j) \geq \delta_s \end{cases} \end{aligned} \tag{10}$$

where L is the population size, $S(q_i, q_j)$ is the similarity between antibodies, and δ_s is the similarity threshold.

The incentive degree is an evaluation indicator for antibodies considering both affinity and concentration, and then the next generation of antibodies is screened. It can be described as:

$$sim(q_i) = a \cdot aff(q_i) - b \cdot Den(q_i) \tag{11}$$

where $sim(q_i)$ is the incentive degree of the antibodies g_i, and a, b are calculation parameters depending on the actual situation.

The cloning process was performed by selecting the antibodies with the high incentives in the antibody population, which is represented as follows:

$$T_C(q_i) = clone(q_i)_m \tag{12}$$

where clone(q_i) is the set consisting of m cloned antibodies identical to q_i, and m is the number of clones.

By updating the antibodies with low incentive degree in the population and replacing them with new antibodies generated randomly, the global search is achieved. The optimization process is shown in Fig. 2, which can be summarized as follows: the basic parameters are set such as the immune algebra G=200, the variation probability P_m=0.7, and the incentive degree factor α =2; the initial range of variation of the variables k and b are set, and the random values of k and b are dynamically generated for the calculation of Eq. (6); the values calculated by Eq. (6) are used in the finite element simulation, the simulated temperature values and the experimental temperature values are used for the calculation of Eq. (7); and the optimal values of k and b are obtained by circular iterations.

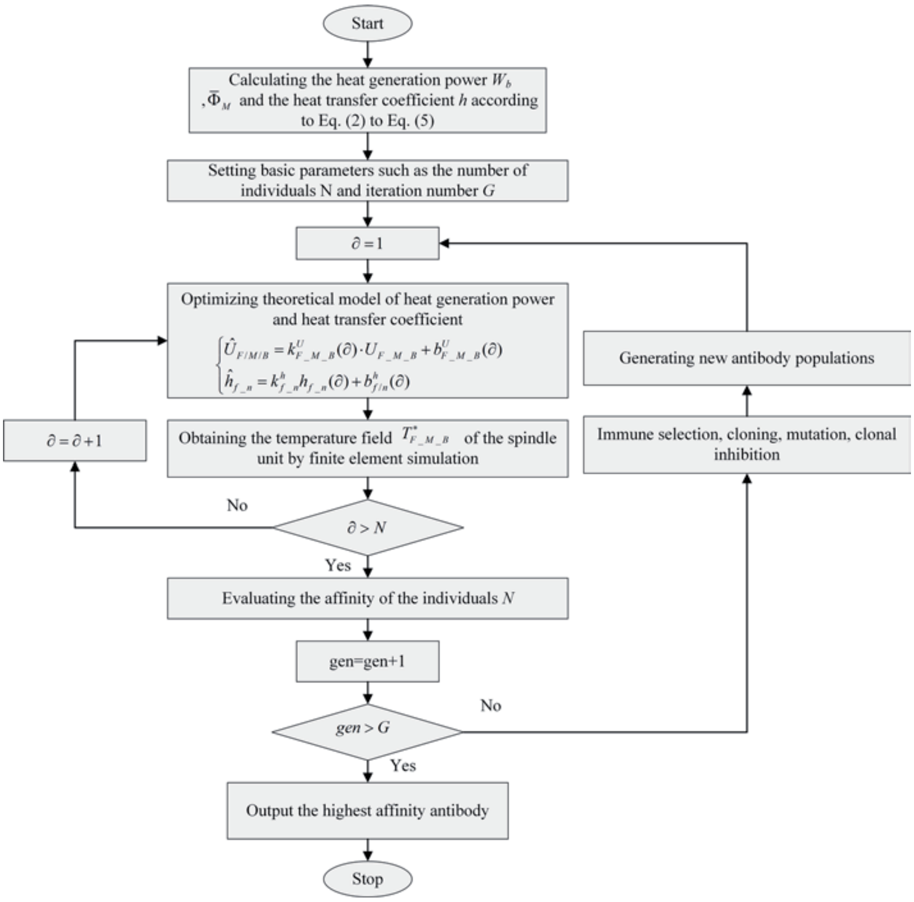

Fig. 2. Optimization process of immune algorithm

5) The finite element simulation of spindle unit

On fluid-solid contact surface, the heat generation and the heat transfer processes of the motor and bearings can be described as:

$$\frac{\partial}{\partial t}\left(\rho_{flu/sol}\vartheta_u\right) + \nabla\cdot\left[\vec{\mu}\left(\rho_{flu/sol}\vartheta_u + p\right)\right] = \nabla\cdot\left[k_{flu/sol}\nabla T + \left(\varsigma\vec{\mu}\right)\right] + Q_v \tag{13}$$

where ϑ_u is the energy carried per unit mass, $k_{flu/sol}$ denotes the thermal conductivity of fluid and solid, $\vec{\mu}$ denotes the vector of velocity, ς is the tensor of stress, $\nabla\cdot\left(\varsigma\vec{\mu}\right)$ is the heat dissipation of the coolant induced by viscous friction, Q_v denotes the heat generation power of the motor and bearings, and $\nabla\cdot\left(k\nabla T\right)$ denotes the heat transfer of solid, coolant and air heat convection.

2.3. Machining accuracy modeling based on MBS

MBS serves as a complete abstraction of complicated mechanical systems, which can abstract the four-axis machine tool to be a system with multiple independent bodies. The machining accuracy model is then established by determining the position relationship between each body. The kinematic model of the four-axis machine tool is shown in Fig. 3. Fig. 3(a) shows the overall structural model of the machine tool. Fig. 3 (b) shows the topological framework of the machine tool. Fig. 3(a) consists of eight typical bodies, represented by D_j (j=1, 2...8). Two branches can be obtained: the bed (D_1) -X-axis moving part (D_2) -Y-axis moving part (D_3) -spindle (D_4)-tool (D_5) branch, and the bed (D_1) -Z-axis moving part (D_6) -B-axis rotating part (D_7) -workpiece (D_8) branch.

The position change relationship between each two adjacent bodies is described by the homogeneous coordinate transformation matrices. The motion of any individual in the machine tool can be decomposed into two sub-motions, namely rotation around the axis and translation along the axis, so six errors are generated. Taking the Z-axis as an explanation, the matrix of error homogeneous transformation is written as follows:

$$\Delta\tilde{K}_{16s} = \begin{pmatrix} 1 & -\Delta\gamma_z & \Delta\beta_z & \Delta x_z \\ \Delta\gamma_z & 1 & -\Delta\alpha_z & \Delta y_z \\ -\Delta\beta_z & \Delta\alpha_z & 1 & \Delta z_z \\ 0 & 0 & 0 & 1 \end{pmatrix}$$

The four-axis machine tool includes X, Y, Z translation axes and B rotation axis. So a total of 30 geometric errors are generated. They are given in Table 1.

The forming point of the tool is in its own coordinate system as:

$$\boldsymbol{H}_t = \begin{bmatrix} H_{tx} & H_{ty} & H_{tz} & 1 \end{bmatrix}^T \tag{14}$$

Similarly, the forming point of the workpiece is in its own coordinate system as:

$$\boldsymbol{H}_w = \begin{bmatrix} H_{wx} & H_{wy} & H_{wz} & 1 \end{bmatrix}^T \tag{15}$$

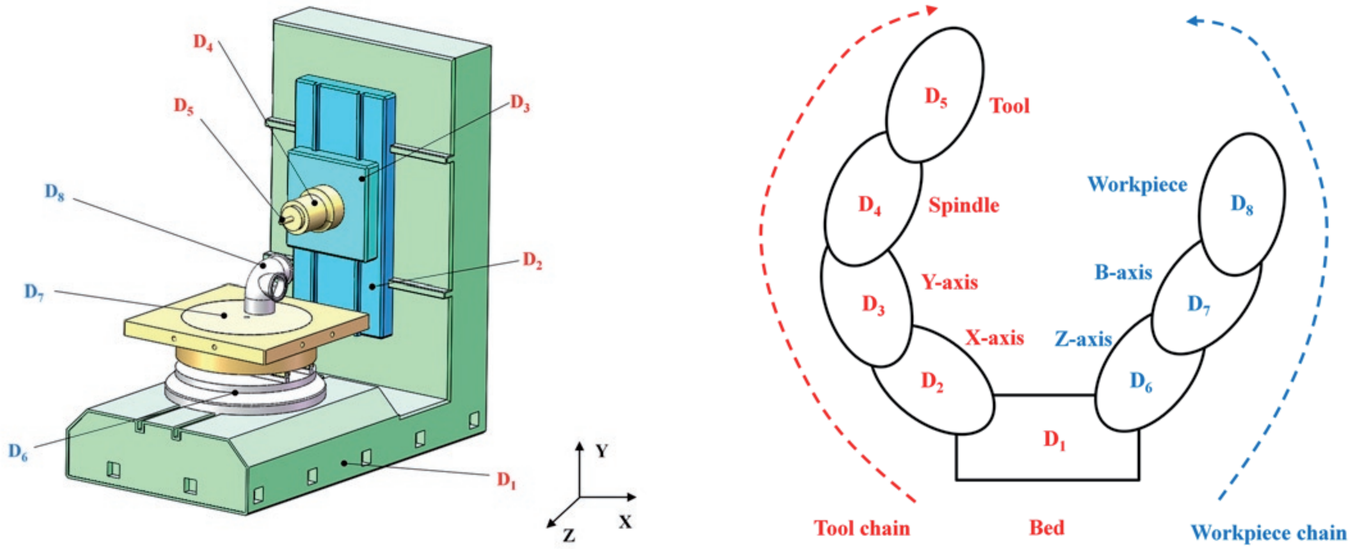

Fig. 3. The structural model and topological structure diagram of a four-axis machine tool platform

Table 1. Explanation of related symbols

Symbol	Definition
Δx_x, Δy_y, Δz_z	Positioning error
Δx_y, Δx_z	Straightness error in *X*-direction
Δy_x, Δy_z	Straightness error in *Y*-direction
Δz_x, Δz_y	Straightness error in *Z*-direction
$\Delta\alpha_x$, $\Delta\beta_y$, $\Delta\gamma_z$	Roll error
$\Delta\beta_x$, $\Delta\alpha_y$, $\Delta\alpha_z$	Pitch error
$\Delta\gamma_x$, $\Delta\gamma_y$, $\Delta\beta_z$	Yaw error
Δx_B, Δy_B, Δz_B	Run-out error in *X*-, *Y*-, *Z*-direction
$\Delta\alpha_B$, $\Delta\beta_B$, $\Delta\gamma_B$	Turning error
S_{XY}, S_{XZ}, S_{YZ}	Perpendicularity error
$\varepsilon\gamma_{yB}$, $\varepsilon\alpha_{xB}$	Parallelism error of *B*-axis in the *XZ, YZ* plane
εz_{yB}	Offset error
$\Delta\varphi_x^T$, $\Delta\varphi_y^T$, $\Delta\varphi_z^T$	Thermal error along the X, Y, Z-direction

Ideally, their forming point coordinates in their own coordinate systems will overlap, so the machining accuracy can be written as:

$$\tilde{K}_{16p}\tilde{K}_{16s}\tilde{K}_{67p}\tilde{K}_{67s}\tilde{K}_{78p}\tilde{K}_{78s}\boldsymbol{H}_w = \tilde{K}_{12p}\tilde{K}_{12s}\tilde{K}_{23p}\tilde{K}_{23s}\tilde{K}_{34p}\tilde{K}_{34s}\tilde{K}_{45p}\tilde{K}_{45s}\boldsymbol{H}_t \tag{16}$$

where p, s are the static state and motion state, and $\tilde{K}_{ijp}$, $\tilde{K}_{ijs}$, $i, j = 1,2,...$ are the homogeneous transformation matrices of static and motion in the ideal state, respectively.

The workpiece forming point in an ideal state can be represented by the tool forming point as:

$$\boldsymbol{H}_t = (\tilde{K}_{12p}\tilde{K}_{12s}\tilde{K}_{23p}\tilde{K}_{23s}\tilde{K}_{34p}\tilde{K}_{34s}\tilde{K}_{45p}\tilde{K}_{45s})^{-1}\tilde{K}_{16p}\tilde{K}_{16s}\tilde{K}_{67p}\tilde{K}_{67s}\tilde{K}_{78p}\tilde{K}_{78s}\boldsymbol{H}_w \tag{17}$$

However, in practice, the geometric and the thermal errors can both affect the machining accuracy. The homogeneous transformation matrices between adjacent bodies are given in Table 2.

In summary, the machining accuracy model in the state of actual machining can be written as:

$$\boldsymbol{E} = \tilde{K}_{16p}\Delta\tilde{K}_{16p}\tilde{K}_{16s}\Delta\tilde{K}_{16s}\tilde{K}_{67p}\Delta\tilde{K}_{67p}\tilde{K}_{67s}\Delta\tilde{K}_{67s}\tilde{K}_{78p}\Delta\tilde{K}_{78p}\tilde{K}_{78s}\Delta\tilde{K}_{78s}\boldsymbol{H}_w - \tilde{K}_{12p}\Delta\tilde{K}_{12p}\tilde{K}_{12s}\Delta\tilde{K}_{12s}\tilde{K}_{23p}\Delta\tilde{K}_{23p}\tilde{K}_{23s}\Delta\tilde{K}_{23s}\tilde{K}_{34p}\Delta\tilde{K}_{34p}\tilde{K}_{34s}\Delta\tilde{K}_{34s}\tilde{K}_{45p}\Delta\tilde{K}_{45p}\tilde{K}_{45s}\Delta\tilde{K}_{45s}\boldsymbol{H}_t \tag{18}$$

where $\Delta\tilde{K}_{ijp}$ and $\Delta\tilde{K}_{ijs}$, $i, j = 1,2,...$ are the homogeneous transformation matrices of the static error and motion error, respectively.

3. Machining accuracy reliability analysis based on LHSMC

3.1. Preliminary

The machining accuracy reliability of the machine tool reflects its ability to achieve a specific function under specified conditions in a predetermined time period [26]. Here, it is regarded as a criterion to evaluate the merits of the four-axis machine tool. Besides, a machining accuracy reliability prediction method is presented based on LHSMC.

The process of LHSMC can be organized as follows: The sample size is determined by Latin hypercube sampling (LHS); the cumulative distribution curve is divided into equal intervals on the cumulative possibility scale [0, 1]; the samples are drawn from each interval of the possibility distribution and used to represent the value of each interval; and the values are used to reconstruct the possibility distribution of the variables.

The steps of drawing K samples $\boldsymbol{v} = (v_{i1}, v_{i2}, ..., v_{in})^T (i = 1,2,...,K)$ from a random vector $\boldsymbol{V} = (V_1, V_2, ..., V_K)^T$ using LHS is as follows:

(1) The range of each random variable $V_j (j = 1,2,...,n)$ is divided into K equal probability intervals, which means that the range [0, 1] of the cumulative distribution function $F_{V_j}(v_j)$ of variable V_j is divided into K non-overlapping subintervals $[0, 1/K], [1/N, 2/K], ..., [1-1/K, 1]$.

(2) One sample is extracted from each of the K subintervals as to variable V_j. Then, only one random number is generated as to each interval, and it is taken as the representative value of the interval. As to the i-th interval, $u_i = (i-1+u)/K$ when the representative value u_i is chosen randomly and the random number u is generated in U

Table 2. Homogeneous transformation matrices of the four-axis CNC machine tool

Adjacent body number	Body ideal static, motion HTMs ($\tilde{K}_{ijp}, \tilde{K}_{ijs}$)	Body static, motion error HTMs ($\Delta\tilde{K}_{ijp}, \Delta\tilde{K}_{ijs}$)
1-2 X-axis	$\tilde{K}_{12p} = \boldsymbol{I}_{4\times4}$	$\Delta\tilde{K}_{12p} = \begin{pmatrix} 1 & -S_{xy} & S_{xz} & 0 \\ S_{xy} & 1 & 0 & 0 \\ -S_{xz} & 0 & 1 & 0 \\ 0 & 0 & 0 & 1 \end{pmatrix}$
	$\tilde{K}_{12s} = \begin{pmatrix} 1 & 0 & 0 & x \\ 0 & 1 & 0 & 0 \\ 0 & 0 & 1 & 0 \\ 0 & 0 & 0 & 1 \end{pmatrix}$	$\Delta\tilde{K}_{12s} = \begin{pmatrix} 1 & -\Delta\gamma_x & \Delta\beta_x & \Delta x_x \\ \Delta\gamma_x & 1 & -\Delta\alpha_x & \Delta y_x \\ -\Delta\beta_x & \Delta\alpha_x & 1 & \Delta z_x \\ 0 & 0 & 0 & 1 \end{pmatrix}$
2-3 Y-axis	$\tilde{K}_{23p} = \boldsymbol{I}_{4\times4}$	$\Delta\tilde{K}_{23p} = \boldsymbol{I}_{4\times4}$
	$\tilde{K}_{23s} = \begin{pmatrix} 1 & 0 & 0 & 0 \\ 0 & 1 & 0 & y \\ 0 & 0 & 1 & 0 \\ 0 & 0 & 0 & 1 \end{pmatrix}$	$\Delta\tilde{K}_{23s} = \begin{pmatrix} 1 & -\Delta\gamma_y & \Delta\beta_y & \Delta x_y \\ \Delta\gamma_y & 1 & -\Delta\alpha_y & \Delta y_y \\ -\Delta\beta_y & \Delta\alpha_y & 1 & \Delta z_y \\ 0 & 0 & 0 & 1 \end{pmatrix}$
1-6 Z-axis	$\tilde{K}_{16p} = \boldsymbol{I}_{4\times4}$	$\Delta\tilde{K}_{16p} = \begin{pmatrix} 1 & 0 & 0 & 0 \\ 0 & 1 & -S_{yz} & 0 \\ 0 & S_{yz} & 1 & 0 \\ 0 & 0 & 0 & 1 \end{pmatrix}$
	$\tilde{K}_{16s} = \begin{pmatrix} 1 & 0 & 0 & 0 \\ 0 & 1 & 0 & 0 \\ 0 & 0 & 1 & z \\ 0 & 0 & 0 & 1 \end{pmatrix}$	$\Delta\tilde{K}_{16s} = \begin{pmatrix} 1 & -\Delta\gamma_z & \Delta\beta_z & \Delta x_z \\ \Delta\gamma_z & 1 & -\Delta\alpha_z & \Delta y_z \\ -\Delta\beta_z & \Delta\alpha_z & 1 & \Delta z_z \\ 0 & 0 & 0 & 1 \end{pmatrix}$
6-7 B-axis	$\tilde{K}_{67p} = \boldsymbol{I}_{4\times4}$	$\Delta\tilde{K}_{67p} = \begin{pmatrix} 1 & -\Delta\gamma_{xB} & 0 & 0 \\ \Delta\gamma_{xB} & 1 & -\Delta\alpha_{zB} & 0 \\ 0 & \Delta\alpha_{zB} & 1 & \Delta z_{yB} \\ 0 & 0 & 0 & 1 \end{pmatrix}$
	$\tilde{K}_{67s} = \begin{pmatrix} \cos B & 0 & \sin B & 0 \\ 0 & 1 & 0 & 0 \\ -\sin B & 0 & \cos B & 0 \\ 0 & 0 & 0 & 1 \end{pmatrix}$	$\Delta\tilde{K}_{67s} = \begin{pmatrix} 1 & -\Delta\gamma_B & \Delta\beta_B & \Delta x_B \\ \Delta\gamma_B & 1 & -\Delta\alpha_B & \Delta y_B \\ -\Delta\beta_B & \Delta\alpha_B & 1 & \Delta z_B \\ 0 & 0 & 0 & 1 \end{pmatrix}$
7-8 Workpiece	$\tilde{K}_{78p} = \begin{pmatrix} 1 & 0 & 0 & x_w \\ 0 & 1 & 0 & y_w \\ 0 & 0 & 1 & z_w \\ 0 & 0 & 0 & 1 \end{pmatrix}$	$\Delta\tilde{K}_{78p} = \boldsymbol{I}_{4\times4}$
	$\tilde{K}_{78s} = \boldsymbol{I}_{4\times4}$	$\Delta\tilde{K}_{78s} = \boldsymbol{I}_{4\times4}$
4-5 Tool	$\tilde{K}_{45p} = \begin{pmatrix} 1 & 0 & 0 & x_t \\ 0 & 1 & 0 & y_t \\ 0 & 0 & 1 & z_t \\ 0 & 0 & 0 & 1 \end{pmatrix}$	$\Delta\tilde{K}_{45p} = \boldsymbol{I}_{4\times4}$
	$\tilde{K}_{45s} = \boldsymbol{I}_{4\times4}$	$\Delta\tilde{K}_{45s} = \boldsymbol{I}_{4\times4}$
3-4 Spindle	$\tilde{K}_{34p} = \boldsymbol{I}_{4\times4}$	$\Delta\tilde{K}_{34p} = \boldsymbol{I}_{4\times4}$
	$\tilde{K}_{34s} = \boldsymbol{I}_{4\times4}$	$\Delta\tilde{K}_{34s} = \begin{pmatrix} 1 & 0 & 0 & \Delta\varphi_x^T \\ 0 & 1 & 0 & \Delta\varphi_y^T \\ 0 & 0 & 1 & \Delta\varphi_z^T \\ 0 & 0 & 0 & 1 \end{pmatrix}$

(0, 1); and $u_i = (i-1/2)/K$ when it is selected at the center of the interval.

(3) The K sample values of variable V_j are randomly sorted according to the ordinal number of the interval to which they belong, and they are placed together in the order of the variables. It is equivalent to constructing a sampling ordinal matrix $\boldsymbol{R} = [r_{ij}]_{K\times n}$ with K rows and n columns. Besides, the variables are in the column order, and each column is a random and unique arrangement of the ordinal numbers $1,2,...,K$, and the K samples of each variable are arranged by numbers in the columns.

The sequential matrix $\boldsymbol{R}$ is randomly generated, and the columns which introduce the statistical correlations affect the simulation results. The Spearman coefficient of the order matrix $\boldsymbol{R}$ is employed to reduce the statistical correlation, described by $\rho_S = [q_{ijs}]_{n\times n}$. The Spearman rank correlation coefficients of the i-th and j-th columns can be obtained by:

$$q_{ijs} = 1 - \frac{6}{K(K^2-1)}\sum_{a=1}^{K}(r_{ai} - r_{aj})^2 \tag{19}$$

where q_{ijs} is a symmetric matrix, and it is equal to the unit matrix $\boldsymbol{I}_n$ in the case of uncorrelated columns. There are no columns with the same sort in $\boldsymbol{R}$, so the matrix ρ_S is positive definite.

The LHSMC reflects the variable distribution characteristics by using the few samples, which can effectively simulate the failure possibility of machine tools.

3.2. Machining accuracy reliability analysis

When a part of the machine structure or the whole exceeds the specified state and cannot operate in accordance with the desired functional requirements, the specified state is a limit state which is critical to judge the structure reliability [28]. To analyze the structure reliability, it is necessary to determine whether it has reached its limit state. This section studied the machining accuracy reliability under the stochastic uncertainty of errors, and the performance function is represented as:

$$\eta = g(\zeta) = (\zeta_1, \zeta_2, ..., \zeta_n) \tag{20}$$

In Eq. (20), $\zeta = (\zeta_1, \zeta_2, ..., \zeta_n)^T$ contains the n basic random variables affecting the machining accuracy reliability, $\eta < 0$ means the structure is in a failure state, and $\eta = 0$ means the structure is in a limit state.

Function η is a continuous random variable, and the failure possibility can be expressed as:

$$p_f = P(\eta \le 0) = \int_{-\infty}^{0} f_\eta(z)dz = F_\eta(0) \tag{21}$$

where $f_\eta(z)$ is the possibility density function of η, and $F_\eta(z)$ is the cumulative distribution function of η.

Also, the failure possibility can be written as:

$$p_f = \int_{\eta\le 0} dF_\zeta(\kappa) = \int_{\eta\le 0} f_\zeta(\kappa)d\kappa = \int ... \int_{\eta\le 0} f_\zeta(\kappa_1, \kappa_2, ..., \kappa_n)d\kappa_1 d\kappa_2 ... d\kappa_n \tag{22}$$

where $f_\zeta(\kappa) = f_\zeta(\kappa_1, \kappa_2, ..., \kappa_n)$ is the joint possibility density function of variable $\zeta = (\zeta_1, \zeta_2, ..., \zeta_n)^T$, and $F_\zeta(\kappa) = F_\zeta(\kappa_1, \kappa_2, ..., \kappa_n)$ is the joint cumulative distribution function of random variable $\zeta = (\zeta_1, \zeta_2, ..., \zeta_n)^T$.

However, the joint possibility density function $f_\zeta(\kappa)$ is hard to obtain. From Eq. (21), p_f is determined by the form of the distribution of the functional function η. Assuming η obeys normal distribution, its mean value and standard deviation are $\bar{\mu}_\eta$ and $\bar{\sigma}_\eta$, which is denoted as $\eta \sim N(\bar{\mu}_\eta, \bar{\sigma}_\eta)$. Then, the possibility density function $f_\eta(z)$ of η is expressed as:

$$f_N(z \mid \bar{\mu}_\eta, \bar{\sigma}_\eta) = \frac{1}{\sqrt{2\pi}\bar{\sigma}_\eta}\exp\left(-\frac{(z-\bar{\mu}_\eta)^2}{2\bar{\sigma}_\eta^2}\right) \tag{23}$$

η is converted to a standard normal distribution variable $K \sim N(0, 1)$ by $K = (\eta - \bar{\mu}_\eta)/\bar{\sigma}_\eta$, and the possibility density function and cumulative distribution function can be expressed as:

$$\begin{cases} \phi(\tilde{k}) = \dfrac{1}{\sqrt{2\pi}}\exp\left(-\dfrac{\tilde{k}^2}{2}\right) \\ \omega(\tilde{k}) = \int_{-\infty}^{k}\varphi(\tilde{k})dk \end{cases} \tag{24}$$

According to Eq. (24), if the variable η is normally distributed, its possibility density and cumulative distribution functions are transformed into:

$$\begin{cases} f_N(z \mid \bar{\mu}_\eta, \bar{\sigma}_\eta) = \dfrac{1}{\bar{\sigma}_\eta}\phi\left(\dfrac{Z-\bar{\mu}_\eta}{\bar{\sigma}_\eta}\right) \\ F_N(z \mid \bar{\mu}_\eta, \bar{\sigma}_\eta) = \omega\left(\dfrac{Z-\bar{\mu}_\eta}{\bar{\sigma}_\eta}\right) \end{cases} \tag{25}$$

Then, the failure possibility can be described by the following equation:

$$p_f = F_N(0 \mid \bar{\mu}_\eta, \bar{\sigma}_\eta) = \omega\left(-\frac{\bar{\mu}_\eta}{\bar{\sigma}_\eta}\right) \tag{26}$$

Up to now, a machining accuracy reliability analysis method for the machine tool based on LHSMC is formed. The proposal procedure of the method is illustrated in Fig. 4.

4. A case demonstration

4.1. Validation of thermal error

The four-axis machine tool is taken as a research example, and its basic parameters are given in Table 3. Through analyzing the heat generation mechanism, the heat generation power and heat transfer coefficient were determined as the characteristic parameters related to the thermal error. Then, they were optimized by IA, and they were employed as the thermal load and boundary conditions of the steady-state thermal analysis of the electric spindle unit in finite element analysis software.

Table 3. Basic parameters of the machine tool

Parameter type	Value
Length×Width×Height	6775mm×4500mm×4370mm
Spindle speed	80-8000r/min
Motor power	22kW
Movable distance in *X*-axis	1400mm

Movable distance in *Y*-axis	1000mm
Movable distance in *Z*-axis	900mm
B-axis rotation	0°-360°

The electric spindle unit is assembled from many parts. Inevitably, there are small features inside the spindle unit. To decrease the complexity of the simulation, the spindle system was simplified by ignoring small chamfers, mounting holes and screw holes. The interference fit between parts is not considered. The bearing balls are regarded as rings for finite element simulation purpose. The simplified spindle unit is shown in Fig. 5(a), and Fig. 5(b) shows the half-section structure of the spindle unit, which shows the internal components and position relationship of the spindle unit. The three-dimensional model of the spindle unit is imported into the analysis software, and its finite element mesh model is obtained by the automatic mesh division method, as shown in Fig. 5(c) and Fig. 5(d). In addition, the material of the spindle unit structure is defined in the material library of analysis software.

The following conditions are set before performing the steady-state thermal temperature field simulation: the material parameters of each component of the electric spindle are set; the environmental and coolant inlet temperature are set at 20°C; the coolant flow rate is set at 5L/min as a constant; the optimized heat generation power is applied to the motor and bearings as the heat source, and the optimized heat transfer coefficient is applied to the heat transfer surface as the boundary condition. The simulation process is in the steady-state thermal analysis module of the analysis software.

The temperature field distribution of spindle unit in the thermal steady state is shown in Fig. 6. Fig. 6(a) shows the temperature field distribution of main components of the spindle unit. The highest temperature and the lowest temperature of the body are 33.09°C and 20.52°C, respectively. The temperature in the middle of the cooling jacket is higher than the two ends, which is related to the direct contact between the cooling jacket and the heat source. Fig. 6(b) shows the temperature distribution of the heat generating parts such as rotor, stator and bearings of the spindle unit. Fig. 6(c) shows the internal temperature distribution of the spindle unit, which implies the internal heat accumulation in the thermal steady state.

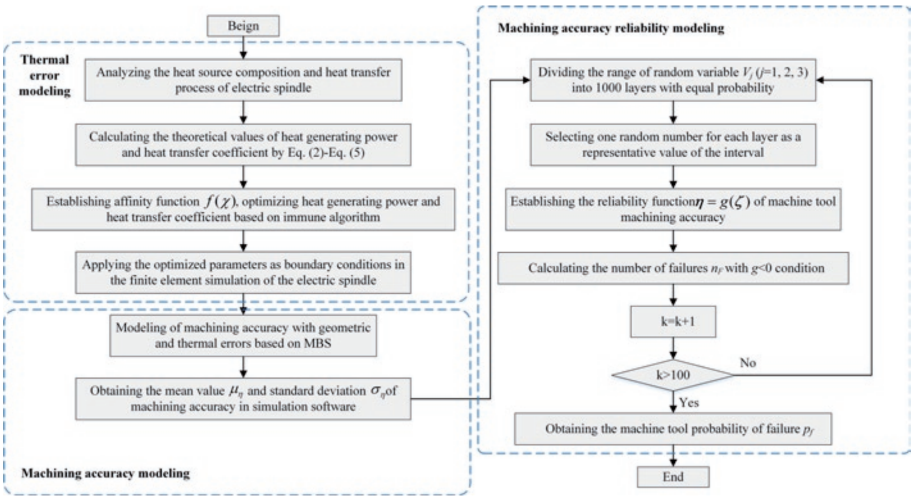

Fig. 4. Flow chart for machining accuracy reliability analysis of the four-axis machine tool

a)

b)

c)

d)

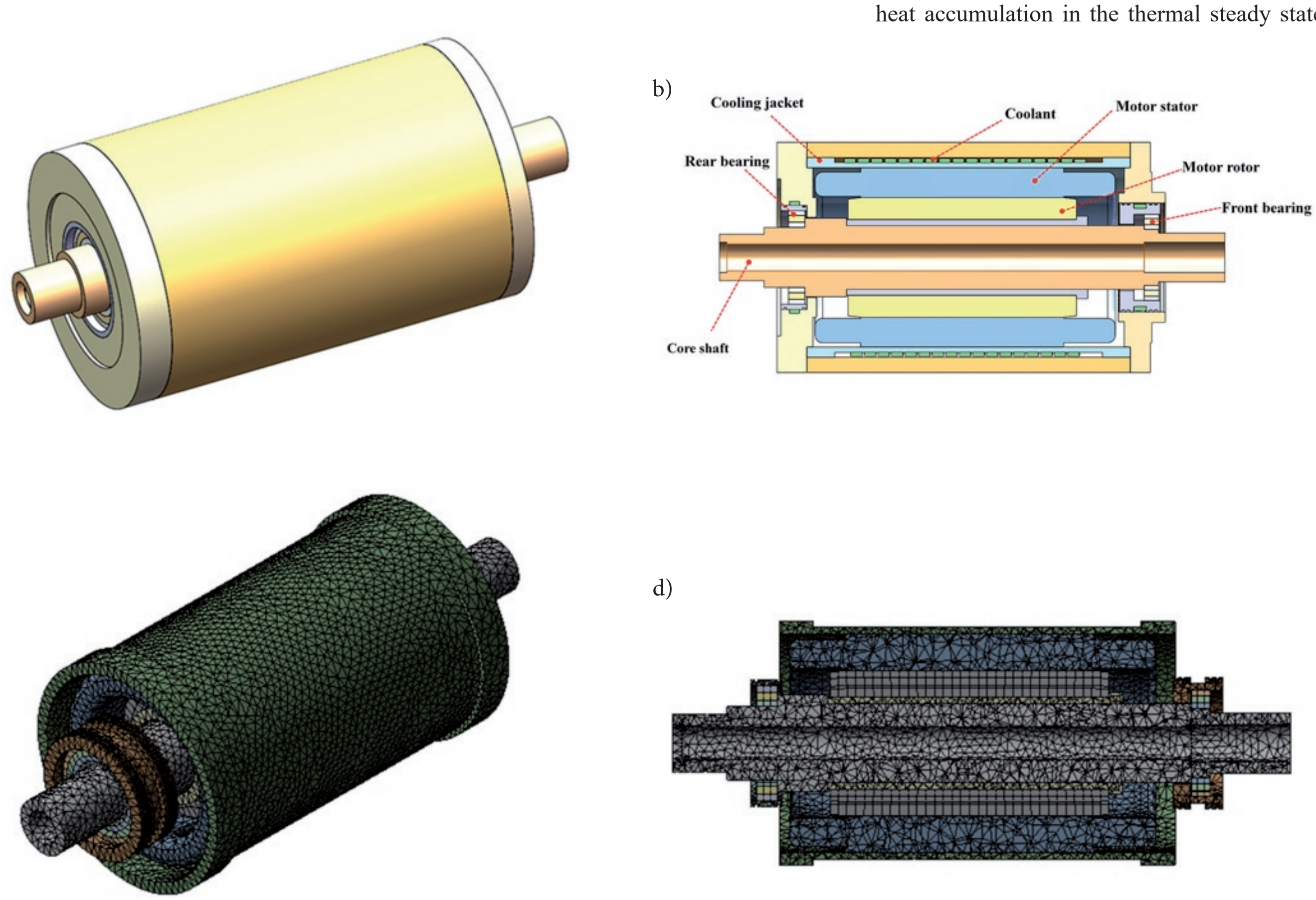

Fig. 5. The finite element model of the spindle unit: a) the overall structure of the electric spindle, b) the half-section structure of the electric spindle, c) the finite element mesh model of main components, d) the section view of finite element mesh model of main components

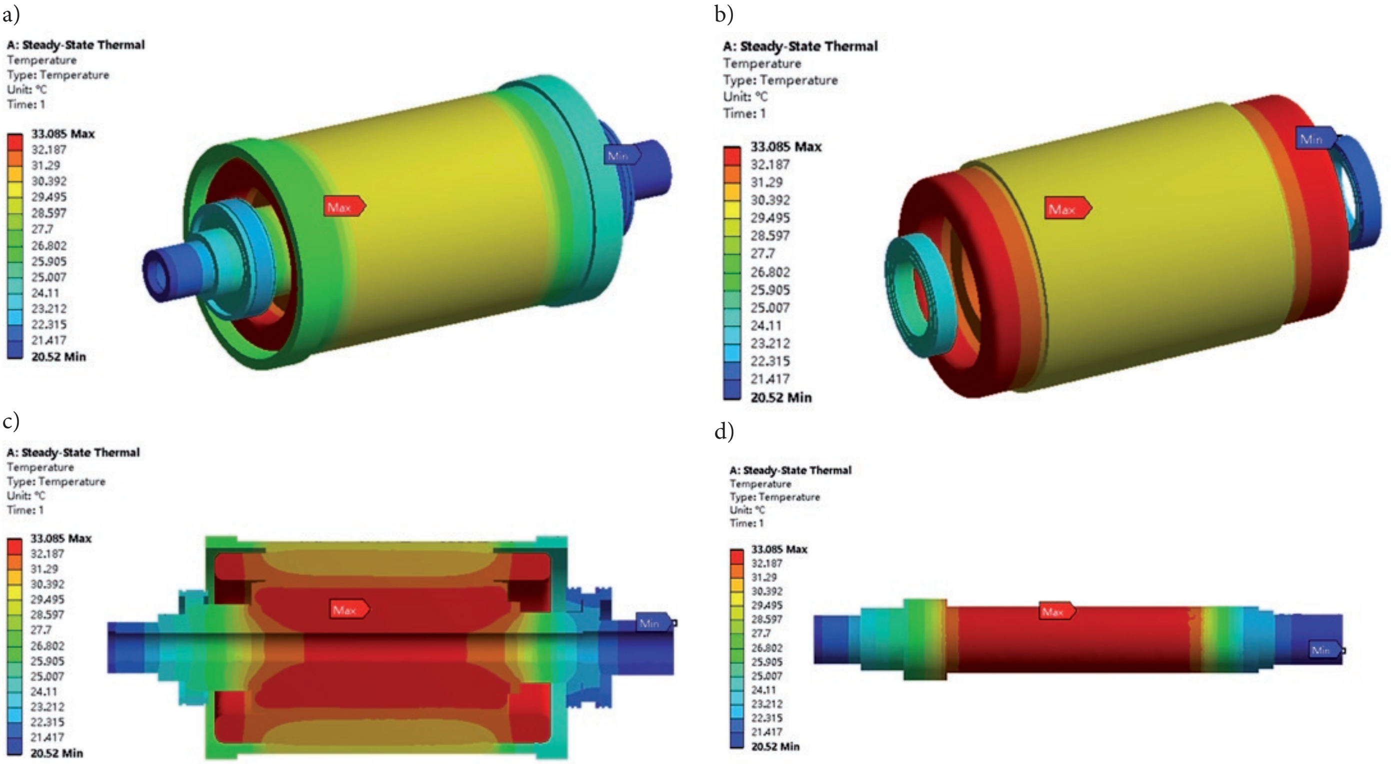

Fig. 6. Temperature distribution of the spindle unit in thermal steady state: a) the temperature field of main components, b) the temperature field of heat generating components, c) the internal temperature field of the electric spindle, d) the temperature field of the core shaft

Fig. 6(d) shows the temperature distribution and characteristic of the core shaft, the highest temperature (33.09°C) occurs in the middle part of the core shaft.

The temperature prediction values and the experimental values based on Particle swarm optimization algorithm (PSO) and IA are given in Table 4. The two methods are both used to optimize the characteristic parameters.

Table 4 indicates that the temperature rise of different components of the spindle unit was predicted based on IA with less error than PSO, which explains the thermal error modeling based on IA has better prediction effect.

Table 4. The comparison between predicted temperature and experimental temperature

Location	Experimental value (°C)	Prediction value based on IA (°C)	Error%	Prediction value based on PSO (°C)	Error%
Front bearing	22.9	24.8	7.66	26.1	12.26
Rear bearing	21.5	23.6	8.90	24.6	12.60
Motor	27.5	29.5	6.78	30.8	10.71

The temperature field model was imported into the finite element mechanics analysis module, and the fixed constraints were configured. The deformation of the electric spindle unit was obtained as shown in Fig. 7 and Fig. 8.

Fig. 7(a) shows the total deformation distribution of the spindle unit, and the maximum deformation is 1.7446e-5m. The max deformation along the X-, Y- and Z-directions are 1.6799e-5m, 6.5465e-6m and 6.6051e-6m, as shown in Fig. 7(b)-(d). Fig. 8 shows the axial deformation of the core shaft is 1.3078e-5m.

4.2. Validation of machining accuracy

The machining accuracy model comprising the geometric and thermal errors was developed in the paper. To validate the model, the thermal deformation of the core shaft was extracted directly from the finite element simulation results as the thermal error. 30 geometric errors of the machine tool were measured by the relevant measuring instruments. Fig. 9 shows the platform and workpiece of the four-axis CNC machine tool. 30 measuring points are selected from the workpiece coordinate system, and their coordinates are:

$$(x, y, 1)(x = 50, 150, 250, 350, 450, 550, y = 100, 200, 300, 400, 500).$$

The machining accuracy of each point is calculated based on MBS, and the results are shown in Fig. 10.

Fig. 10 describes the predicted and measured values of the machining accuracy in the X-, Y- and Z-directions, respectively, which illustrates that the machining accuracy with thermal error exhibits less deviations from the measured machining accuracy. Hence, the thermal error model established in the paper is verified.

4.3. Validation of machining accuracy reliability

The distribution characteristics of errors need to be determined before discussing the machine tools reliability. Normally, the geometric errors are regarded as Gaussian distribution [26]. These 30 measuring points are employed to predict the machining accuracy reliability.

To predict the machining accuracy reliability at different coordinates, the Monte Carlo method was used as the simulation standard. The LHSMC and the AFOSM methods were used as the prediction methods, and the deviation of their reliability prediction values from Monte Carlo was shown in Fig. 11.

Fig. 11 demonstrates that the prediction value of machining accuracy reliability obtained by LHSMC, AFOSM and Monte Carlo, respectively. It can be noted that the reliability prediction value of LHSMC is closer to Monte Carlo than AFOSM. The results illustrate that the LHSMC method in predicting the machining accuracy reliability has a higher accuracy compared with AFOSM.

To verify the machining accuracy reliability analysis method proposed in this paper, the coordinates covering the entire workpieces are selected according to the dimensions of the workpieces. A total of 300 workpieces are machined, as shown in Fig. 12. The failure possibility

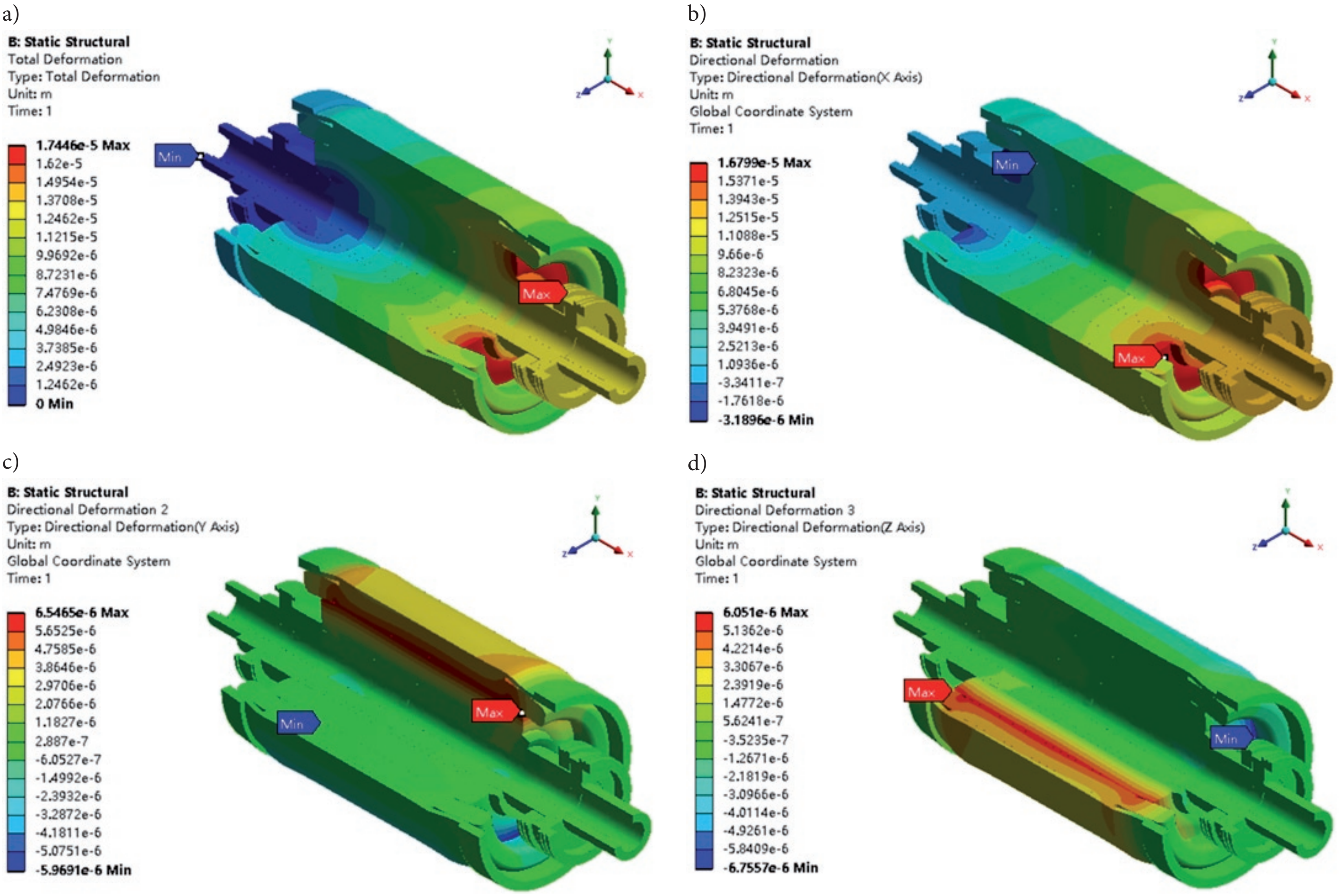

Fig. 7. Thermal deformation nephogram of the spindle unit, a) the total deformation, b) the deformation in X-direction, c) the deformation in Y-direction, d) the deformation in Z-direction

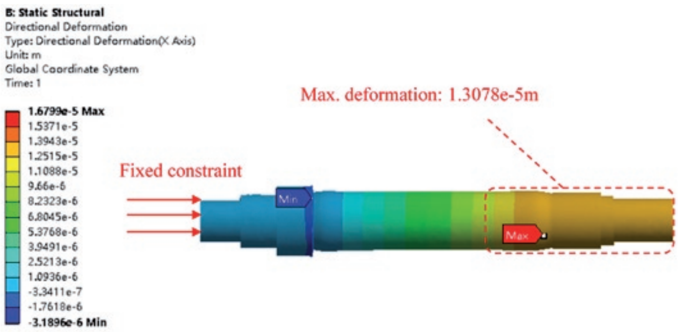

Fig. 8. Axial deformation of the core shaft

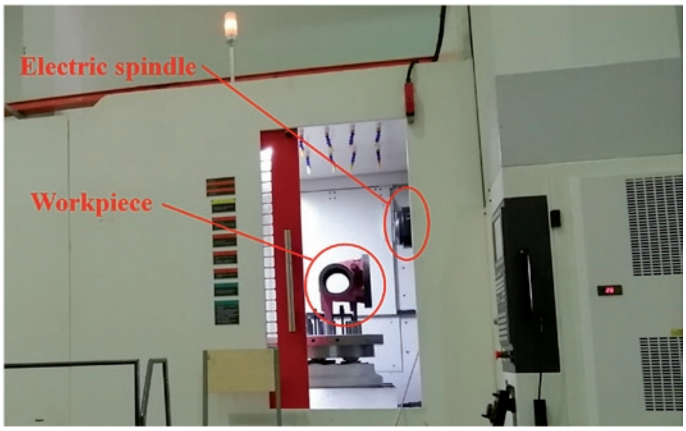

Fig. 9. Four-axis CNC machining tool platform

is calculated as the experimental data of machining accuracy reliability. The results are shown in Table 5.

Table 5 shows the predicted values of machining accuracy reliability based on different methods, and the comparison with the experimental values verifies that the machining accuracy reliability analysis method proposed in the paper has a higher accuracy than AFOSM.

5. Conclusion

CNC machine tools are high continuity equipment, and their machining accuracy reliability mainly is affected by the geometric and thermal errors. Therefore, a thermal error modeling and machining accuracy reliability analysis method is presented, and the detailed conclusions comprise as following:

1. Based on the heat generation mechanism and IA, a thermal error model was established, which was used to estimate the thermal error in the actual machining process of machine tools;
2. Applying the MBS theory, a machining accuracy model including both geometric and thermal errors was established to derive the machining accuracy of machine tools;
3. A machine accuracy reliability prediction method was put forward considering the spindle thermal error. The effectiveness and superiority of the method were experimentally demonstrated. It can provide the methodological support for spindle unit thermal error modeling and dynamic machining accuracy reliability prediction of machine tools.

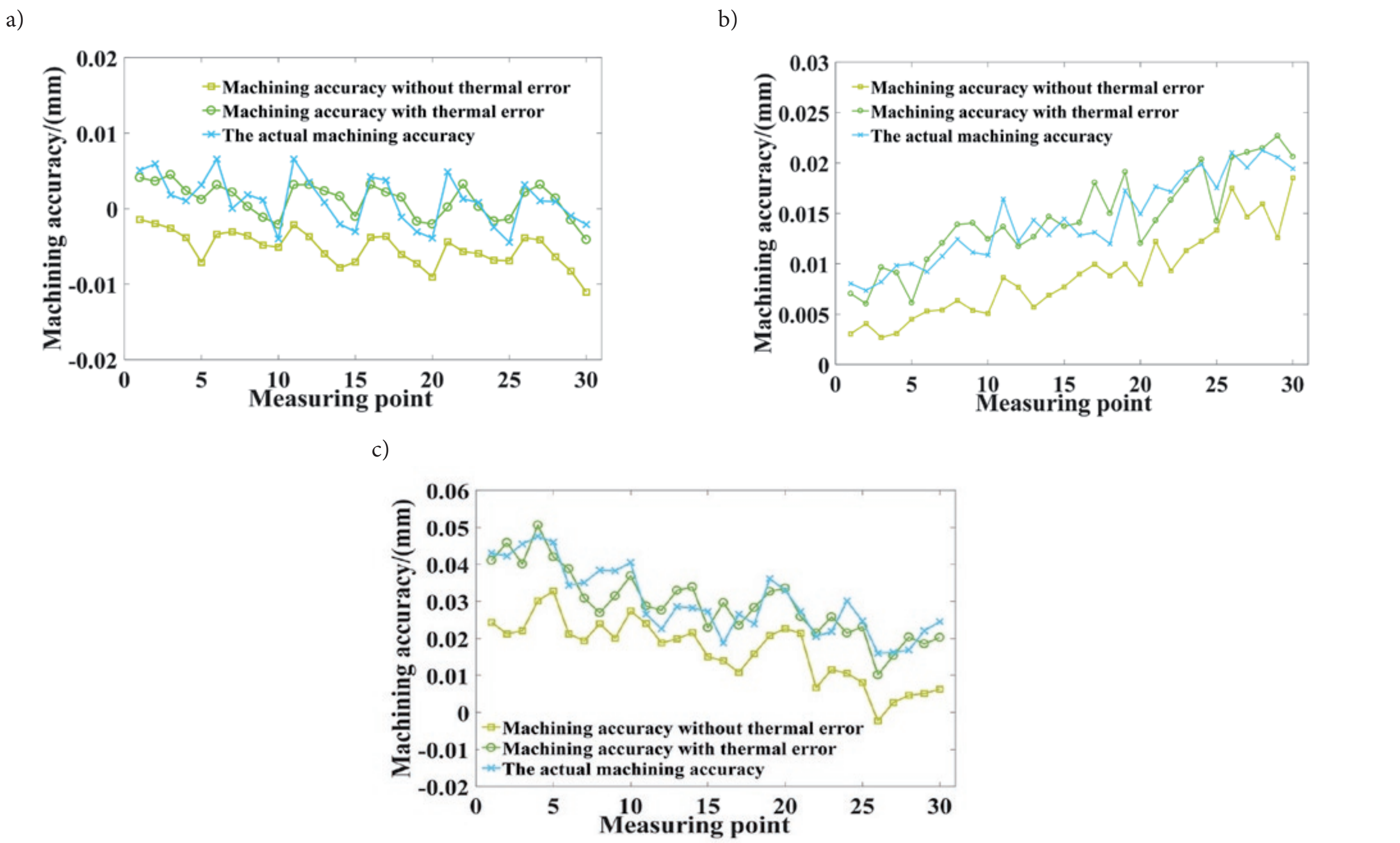

Fig. 10. Machining accuracy of 30 measuring points: a) machining accuracy in X-direction, b) machining accuracy in Y-direction, c) machining accuracy in Z-direction

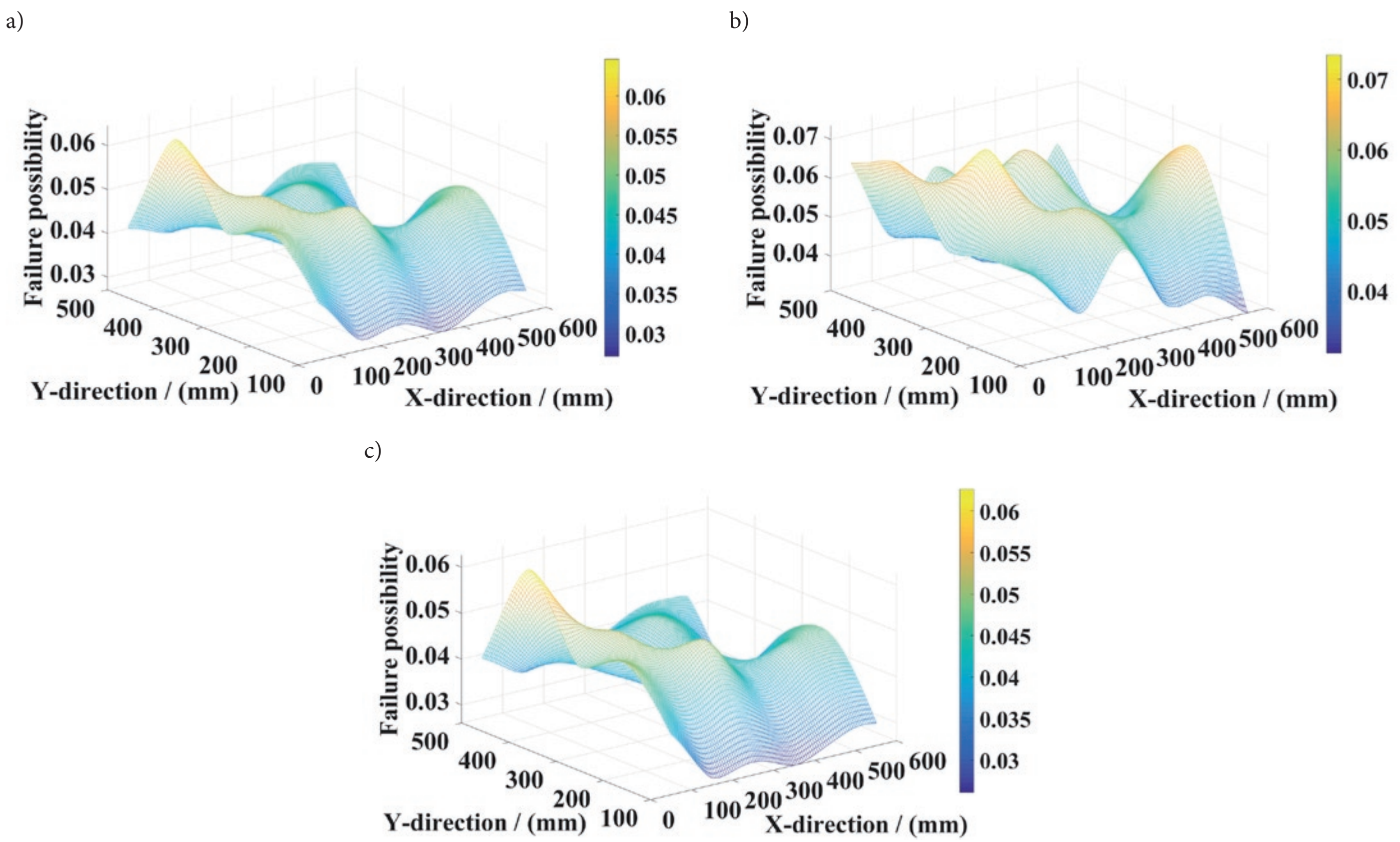

Fig. 11. Machining accuracy reliability of 30 measuring points: a) failure possibility based on LHSMC, b) failure possibility based on AFOSM, c) failure possibility based on Monte Carlo

a)

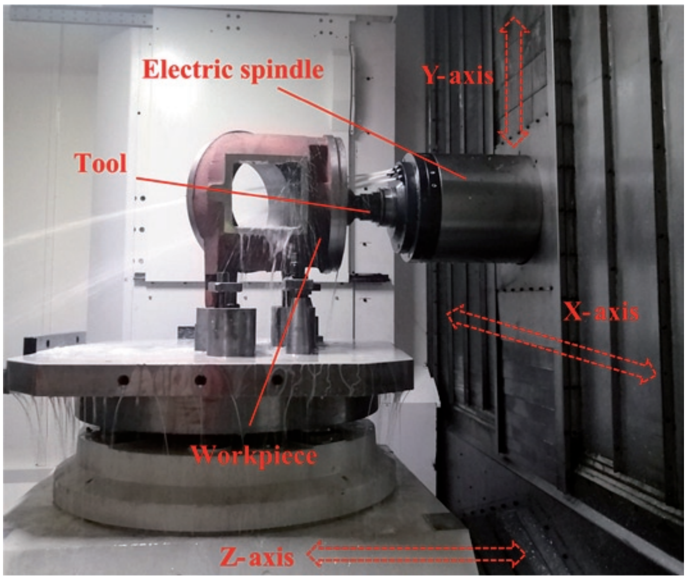

b)

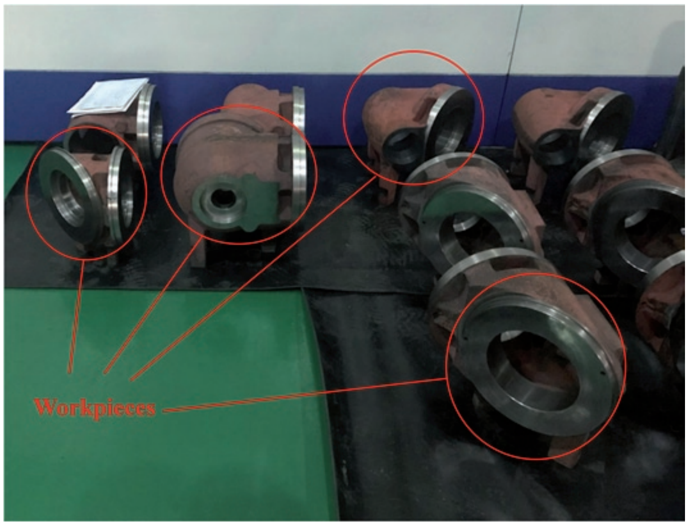

Fig. 12. The machining process of the workpieces: a) the machining process of a workpiece, b) various workpieces

Table 5. Failure possibility of measuring points obtained based on different methods

Coordinate of point (x, y)	Total number of workpieces	Number of failed workpieces	The failure possibility			
			Experimental value	Monte Carlo	LHSMC	AFOSM
(300,30)	300	9	3.00%	3.11%	3.25%	3.96%
(570,300)	300	11	3.67%	3.68%	3.84%	4.35%
(300,570)	300	13	4.33%	4.01%	4.32%	5.03%
(30,300)	300	10	3.33%	3.39%	3.58%	3.97%
(110,110)	300	8	2.67%	2.68%	2.53%	3.31%
(490,110)	300	9	3.00%	3.12%	3.05%	3.28%
(110,490)	300	10	3.33%	3.38%	3.46%	3.36%
(490,490)	300	14	4.67%	4.58%	4.72%	5.03%

Acknowledgements

The research was sponsored by the National Natural Science Foundation of China (grant no.51905334, grant no.51975012 and grant no.12002186), Shanghai Sailing Program (grant no.19YF1418600), Beijing Nova Programmer Interdisciplinary Cooperation Project (grant no. Z191100001119010), and the National Science and Technology Major Project (grant no.2018ZX04033001-003).

Appendix

Parameter	Equation	Value
M_{v1} (N • mm) (Front bearing)	$M_{v1,v2} = 10^{-7} f^{*}(vn')^{2/3} d_{m1,m2}^{3}$ f^{*} denotes the coefficient related to bearing lubrication, and f^{*} =4; v denotes the lubricant kinematic viscosity, and v =45 (mm^2/s);	1811.1
M_{v2} (N • mm) (Rear bearing)	n' denotes the bearing speed, and n' =8000 (r/min); d_{m1} is the front bearing mean diameter, and d_{m1} =95(mm); d_{m2} is the rear bearing mean diameter, and d_{m2} =100.25 (mm)	2128.3

M_{e1} (N • mm) (Front bearing)	$$M_{e1,e2} = f_{1,2}P_{1,2}d_{m1,m2}$$ $f_{1,2}$ denotes the coefficient related to bearing type, and f_1 =0.0012, f_2 =0.001;	7501.2
M_{e2} (N • mm) (Rear bearing)	$P_{1,2}$ denotes the bearing equivalent dynamic load, and P_1 =65.8 (KN), P_2 =81.5 (KN)	8987.4
Q_1 (w) (Rotor)	$$Q_{1,2} = (1-\eta)K_{1,2}W_{\mathrm{M}}$$ η is the power conversion efficiency of the motor, and η =0.85;	1155
Q_2 (w) (Stator)	$K_{1,2}$ is the heat production proportion of rotor and stator, and K_1 =0.35, K_2 =0.65; W_{M} is the rated power of the motor, and W_{M} =22 (kW)	2145
V_1 (m^3) (Rotor)	$$V_{1,2} = \pi(r_{o1,o2} - r_{i1,i2})^2 h_{1,2}$$ $r_{o1,o2}$ is the outer diameter of the rotor and stator, and r_{o1} =0.08 (m), r_{o2} =0.12 (m);	0.000876
V_2 (m^3) (Stator)	$r_{i1,i2}$ is the inner diameter of the rotor and stator, and r_{i1} =0.05 (m), r_{i2} =0.08 (m); $h_{1,2}$ is the length of the rotor and stator, and h_1 =0.31 (m), h_2 =0.41 (m)	0.0021
$\bar{\theta}$ (W/(m·°C))	$\bar{\theta}$ is the thermal conductivity of the spindle unit, and $\bar{\theta}$ =45.	45
l_a (m)	l_a is the cross-sectional circumference of the motor cooling jacket, and l_a =0.7536.	0.7536
Re	$$Re = \frac{u'd'}{v'}$$ u' is the coolant average flow rate, and u' =0.99 (m/s) d' is the cooling pipe diameter, and d' =0.006 (m) v' is the coolant kinematic viscosity, and v' =0.0008737/1000 (m^2/s)	6798
Pr	$$Pr = \frac{\mu C_p}{k}$$ μ is the dynamic viscosity of the coolant, and μ =0.8937/1000 (kg/s·m) C_p is the specific heat at constant pressure of coolant, and C_p =4.18 (kJ/kg·K) k is the thermal conductivity of the coolant, and k =0.61 (W/m·K)	6.12

References

1. Cai LG, Zhang ZL, Cheng Q, Liu ZF, Gu PH. A geometric accuracy design method of multi-axis NC machine tool for improving machining accuracy reliability. Eksploatacja i Niezawodnosc - Maintenance and Reliability 2014; 17(1): 143–155, https://doi.org/10.17531/ein.2015.1.19.
2. Cheng Q, Zhao HW, Zhao YS, Sun BW, Gu PH. Machining accuracy reliability analysis of multi-axis machine tool based on Monte Carlo simulation. Journal of Intelligent Manufacturing 2018; 29(1): 191–209, https://doi.org/10.1007/s10845-015-1101-1.
3. Chen JX, Lin SW, Zhou XL. A comprehensive error analysis method for the geometric error of multi-axis machine tool. International Journal of Machine Tools and Manufacture 2016; 106: 56–66, https://doi.org/10.1016/j.ijmachtools.2016.04.001.
4. Cheng Q, Sun BW, Zhao YS, Gu PH. A method to analyze the machining accuracy reliability sensitivity of machine tools based on Fast Markov Chain simulation. Eksploatacja i Niezawodnosc - Maintenance and Reliability 2016; 18(4): 552–564, https://doi.org/10.17531/ein.2016.4.10.
5. Fu GQ, Fu JZ, Xu YT, Chen ZC, Lai JT. Accuracy enhancement of five-axis machine tool based on differential motion matrix: Geometric error modeling, identification and compensation. International Journal of Machine Tools and Manufacture 2015; 89: 170–181, https://doi.org/10.1016/j.ijmachtools.2014.11.005.
6. Hou RS, Yan ZZ, Du HY, Chen T, Tao T, Mei XS. The Application of Multi-objective Genetic Algorithm in the Modeling of Thermal Error of NC Lathe. Procedia CIRP 2018; 67: 332–337, https://doi.org/10.1016/j.procir.2017.12.222.
7. Huang YB, Fan KC, Lou ZF, Sun W. A novel modeling of volumetric errors of three-axis machine tools based on Abbe and Bryan principles. International Journal of Machine Tools and Manufacture 2020; 151: 103527, https://doi.org/10.1016/j.ijmachtools.2020.103527.
8. Jiang ZY, Huang XZ, Chang MX, Li C, Ge Y. Thermal error prediction and reliability sensitivity analysis of motorized spindle based on

Kriging model. Engineering Failure Analysis 2021; 127: 105558, https://doi.org/10.1016/j.engfailanal.2021.105558.
9. Kiridena V, Ferreira PM. Mapping the effects of positioning errors on the volumetric accuracy of five-axis CNC machine tools. International Journal of Machine Tools and Manufacture 1993; 33(3): 417–437, https://doi.org/10.1016/0890-6955(93)90049-Z.
10. Kwintarini W, Wibowo A, Martawirya YY. Mathematical approach for geometric error modeling of three axis CNC vertical milling machine. Applied Mechanics and Materials 2016; 842: 303–310, https://doi.org/10.4028/www.scientific.net/AMM.842.303.
11. Li B, Tian XT, Zhang M. Thermal error modeling of machine tool spindle based on the improved algorithm optimized BP neural network. The International Journal of Advanced Manufacturing Technology 2019; 105(1–4): 1497–1505, https://doi.org/10.1007/s00170-019-04375-w.
12. Li HZ, Yang ZJ, Xu BB, Chen CH, Kan YN, Liu GF. Reliability Evaluation of NC Machine Tools considering Working Conditions. Mathematical Problems in Engineering 2016; 2016: 1–11, https://doi.org/10.1155/2016/9842607.
13. Li YF, Zhang YJ, Zhao YQ, Shi XJ. Thermal-mechanical coupling calculation method for deformation error of motorized spindle of machine tool. Engineering Failure Analysis 2021; 128: 105597, https://doi.org/10.1016/j.engfailanal.2021.105597.
14. Liu K, Sun MJ, Zhu TJ, Wu YL, Liu Y. Modeling and compensation for spindle's radial thermal drift error on a vertical machining center. International Journal of Machine Tools and Manufacture 2016; 105: 58–67, https://doi.org/10.1016/j.ijmachtools.2016.03.006.
15. Liu K, Wu JK, Liu HB, Sun MJ, Wang YQ. Reliability analysis of thermal error model based on DBN and Monte Carlo method. Mechanical Systems and Signal Processing 2021; 146: 107020, https://doi.org/10.1016/j.ymssp.2020.107020.
16. Liu T. Thermal error modeling and active control method of electric spindle unit. Tianjin: Tianjin University 2016.
17. Luo X, Xie FG, Liu XJ, Li J. Error modeling and sensitivity analysis of a novel 5-degree-of-freedom parallel kinematic machine tool. Proceedings of the Institution of Mechanical Engineers, Part B: Journal of Engineering Manufacture 2019; 233(6): 1637–1652, https://doi.org/10.1177/0954405418782283.
18. Ma C, Yang J, Zhao L, Mei XS, Shi, H. Simulation and experimental study on the thermally induced deformations of high-speed spindle system. Applied Thermal Engineering 2015; 86: 251–268, https://doi.org/10.1016/j.applthermaleng.2015.04.064.
19. Mohamed R, Fethi S, Abdelmadjid C. Study and Modeling of Machining Errors on the NC Machine Tool. International Journal of Mechanical Engineering and Robotics Research 2017; 6(1): 54–57, https://doi.org/10.18178/ijmerr.6.1.54-57.
20. Shi H, Jiang CP, Yan ZZ, Tao T, Mei XS. Bayesian neural network–based thermal error modeling of feed drive system of CNC machine tool. International Journal of Advanced Manufacturing Technology 2020; 108(9–10): 3031–3044, https://doi.org/10.1007/s00170-020-05541-1.
21. Srivastava AK, Veldhuis SC, Elbestawit MA. Modelling geometric and thermal errors in a five-axis CNC machine tool. International Journal of Machine Tools and Manufacture 1995; 35(9): 1321–1337, https://doi.org/10.1016/0890-6955(94)00048-O.
22. Uhlmann E, Hu J. Thermal Modelling of a High-Speed Motor Spindle. Procedia CIRP 2012; 1(1): 313–318, https://doi.org/10.1016/j.procir.2012.04.056.
23. Wang ZM, Yuan H. Enhancing machining accuracy reliability of multi-axis CNC machine tools using an advanced importance sampling method. Eksploatacja i Niezawodnosc - Maintenance and Reliability 2021; 23(3): 559–568, https://doi.org/10.17531/ein.2021.3.17.
24. Xiang ST, Yao XD, Du ZC, Yang JG. Dynamic linearization modeling approach for spindle thermal errors of machine tools. Mechatronics 2018; 53: 215–228, https://doi.org/10.1016/j.mechatronics.2018.06.018.
25. Yang AS, Yu XH, Zhuang JR, Lee CY, Hsieh WH. DOE-FEM based design improvement to minimize thermal errors of a high-speed spindle system. Thermal Science and Engineering Progress 2018; 8: 525–536, https://doi.org/10.1016/j.tsep.2018.10.011.
26. Zhang ZL, Cai LG, Cheng Q, Lui ZF, Gu PH. A geometric error budget method to improve machining accuracy reliability of multi-axis machine tools. Journal of Intelligent Manufacturing 2019; 30(2): 495–519, https://doi.org/10.1007/s10845-016-1260-8.
27. Zhang ZL, Cheng Q, Qi BB, Tao ZQ. A general approach for the machining quality evaluation of S-shaped specimen based on POS-SQP algorithm and Monte Carlo method. Journal of Manufacturing Systems, 2021, 60: 553-568, https://doi.org/10.1016/j.jmsy.2021.07.020.
28. Zhang ZL, Qi Y, Cheng Q, Liu ZF, Tao ZQ, Cai LG. Machining accuracy reliability during the peripheral milling process of thin-walled components. Robotics and Computer-Integrated Manufacturing 2019; 59: 222–234, https://doi.org/10.1016/j.rcim.2019.04.002.
29. Zhang ZS. Mechanism research of the contact thermal resistance and its application in thermal analysis of motorized spindles. Beijing: Beijing University of Technology 2018.
30. Zhao CL, Guan XS. Thermal Analysis and Experimental Study on the Spindle of the High-Speed Machining Center. AASRI Procedia 2012; 1: 207–212, https://doi.org/10.1016/j.aasri.2012.06.032.
31. Zhao HT, Yang JG, Shen JH. Simulation of thermal behavior of a CNC machine tool spindle. International Journal of Machine Tools and Manufacture 2007; 47(6): 1003–1010, https://doi.org/10.1016/j.ijmachtools.2006.06.018.
32. Zhao Y, Lin TM, Tang XQ. Geometric Error Modeling of Machine Tools Based on Screw Theory. Procedia Engineering 2011; 24: 845–849, https://doi.org/10.1016/j.proeng.2011.11.2748.
33. Zheng DX, Chen WF. Effect of structure and assembly constraints on temperature of high-speed angular contact ball bearings with thermal network method. Mechanical Systems and Signal Processing 2020; 145: 106929, https://doi.org/10.1016/j.ymssp.2020.106929.
34. Zhu SW, Ding GF, Qin SF, Lei J, Zhuang L, Yan KY. Integrated geometric error modeling, identification and compensation of CNC machine tools. International Journal of Machine Tools and Manufacture 2012; 52(1): 24–29, https://doi.org/10.1016/j.ijmachtools.2011.08.011.

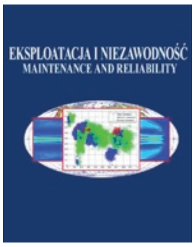

Eksploatacja i Niezawodnosc – Maintenance and Reliability

Volume 24 (2022), Issue 1

journal homepage: http://www.ein.org.pl

Article citation info:
Loska A, Paszkowski W. Geometric approach to machine exploitation efficiency: modelling and assessment. Eksploatacja i Niezawodnosc – Maintenance and Reliability 2022; 24 (1): 114–122, http://doi.org/10.17531/ein.2022.1.13.

Indexed by: Web of Science Group

Geometric approach to machine exploitation efficiency: modelling and assessment

Andrzej Loska[a], Waldemar Paszkowski[a]

[a]Silesian University of Technology, Faculty Organization and Management, ul. Roosevelta 26, 41-800 Zabrze, Poland

Highlights

- The analysis of selected exploitation measures in discrete production processes is presented.
- A new approach to OEE modelling is proposed, based on a geometric interpretation of the time dependent components.
- The verification of this developed model is carried out with the use of analytical and simulation tools.
- The proposed method allows for the real-time mapping of the variability of the exploitation efficiency.
- There is a significant difference to the classical static approach of such an assessment

Abstract

This article presents a new approach to the exploitation assessment of machines and devices. A key aspect of this approach is the construction of the assessment model based on the geometric representation of measures associated with each other, which covers the full specifics of the exploitation process. This approach is successfully implemented by the Overall Equipment Effectiveness (OEE) model, which is fully susceptible to the geometric modelling process due to the three-way system of assessed exploitation aspects. The result of this approach is the vectored OEE model and its interpretation in terms of time series of changes in values of components. Methods of determining vector calculus measures were developed, including the second-order tensor and gradient. This is the subject of the variability of the reliability conditions of machines or production processes. It allows for the realisation of an exploitation assessment based on dynamic changes in the values of their components in the time domain. This is a significant difference to the classical static approach to such an assessment. The developed new geometric OEE model was confirmed by verification tests using the LabView software, based on two parallel data sets obtained with analytical and simulation methods using the FlexSim software.

Keywords

exploitation process, time series, exploitation efficiency, OEE, gradient, tensor, vectored model, maintenance.

1. Introduction

Exploitation decision-making problems relate to the search for ways to extend the periods of use (operate) and shorten non-use (maintenance) times with the assumed quality level of the performed work. The choices cover both technical and non-technical aspects (economic, organizational). In the exploitation assessment process, the operation of technical objects in specific environmental conditions is also taken into account. Such an approach means that the specificity of the undertaken exploitation decision problems is influenced by those factors which are related to the variability of both determinate and random features.

The need to achieve and maintain high exploitation efficiency in industrial practice applies not only to individual machines and devices, but above all to complex technical systems (e.g., industrial installations, process lines, network technical systems) [11]. For this reason, in the operational decision-making process, it is necessary to jointly consider the systems of machines and devices operating in the system. The increasing complexity of such systems may result in a potential deterioration of the values of reliability features. Different durability and diagnostic susceptibility of components of complex technical systems frequently make rational exploitation decisions and activities difficult to use [35]. However, the summary value of such systems (e.g., replacement cost) often significantly exceeds the amounts that are currently available to maintain their efficiency. These factors necessitate systematic exploitation (maintenance and repair) actions in order to achieve the desired effect over the long term.

The basis for undertaking, and consequently implementing, preventive and intervention maintenance actions is an appropriate exploitation assessment system. Such a system consists of models, methods, and tools that allow for:

- obtaining and collecting data directly describing the exploited machines,
- processing data into exploitation measures,
- interpretation of the results of measures in relation to machines and the exploitation context,
- possible feedback on the analysed operational decision-making process on the analysed exploitation decision-making process realised in the industrial environment.

One of the most important aspects of developing the exploitation assessment is the identification and verification of the measure model. Such a model, which is a set of deliberately selected indicators, must take into account, on the one hand, the specificity of the exploitation

E-mail addresses: A. Loska (ORCID: 0000-0003-0041-795X): Andrzej.Loska@polsl.pl, W. Paszkowski (ORCID: 0000-0001-5739-7449): Waldemar.Paszkowski@polsl.pl

process, including the required direction of its analysis and interpretation, and, on the other hand, the availability of an appropriate resource of input data.

Various operational evaluation systems are most often built on the basis of a set of averaged measures clustered within the Overall Equipment Effectiveness (OEE) indicator. The popularity of this model stems primarily from the simplicity of its construction of measures (low mathematical complexity), easy accessibility of input data, and mutual comparability between different technical systems. The area and scope of the interpretation of the measurement values is also significant. It can be related not only to the analysed machines, but also to their environment and the functioning of the maintenance department.

However, the popularity of the OEE model also causes ambiguity due to its many variants. This results from both the high flexibility of the construction of individual measures and the ways of interpreting the results of the assessment. Therefore, in the latter part of this article, the use of vector calculus and simulation methods for the construction of the exploitation assessment model and the method of calculating and distributing measures within the new OEE model are discussed.

2. Analysis of the possibility and need of using OEE for the exploitation assessment of machines in discrete production processes

The effectiveness of the exploited technical systems is defined ambiguously. This is indicated by the ongoing scientific debate about the effects of working machines and devices. In the classical approach, technical and/or economic efficiency can be distinguished [4]. More complex interpretations assume the possibility of building a model of efficiency as a resultant value of features of different importance. The problem of assessing effectiveness is addressed in a wide range of research works, the majority of which are concerned with attempts to develop mathematical models of measures and the implementation of organisational procedures. Contemporary publications describing the results of research on the efficiency of exploitation cover a wide range of issues concerning Total Productive Maintenance (TPM) strategy, including methodological assumptions, among others [21, 34], and application solutions [16, 29, 30]. Attempts to build computational models and their industrial verification are also widely undertaken, based on the measures focused on the OEE model [9, 28], or operational measures concentrated in a set of KPI (Key Performance Indicators) [22, 27, 31], often associated with the issue of benchmarking [26, 37].

The efficiency measures most often express the level of key exploitation features in a comprehensive and aggregated manner. Mathematical models are resultant values in relation to the applied simple measures, describing selected aspects of the exploitation of technical systems. In this area, it can be distinguished [23, 28]:

- The exploitation availability indicator is described by the following relationship:

$$A = \frac{MTBF}{(MTBF + MFOT)} \tag{1}$$

where: MTBF - Mean Time Between Failures, MFOT - Mean Force Outage Time.

This expression represents the relationship between broadly understood reliability and maintainability. The expected availability assumes the maximisation of MTBF while minimising the MFOT.

The exploitation efficiency indicator is described by the following relationship:

$$E = \frac{MTBF}{(MTBF + MTTR)} \tag{2}$$

where: MTTR - Mean Time to Repair.

This expression, similar to (1), represents the relationship between reliability and maintainability. However, in this case, maintainability has a different interpretation as it more closely reflects efficiency and responsiveness in the organisational context. This method of determining efficiency shows its importance in the assessment of a company's maintenance department.

The OEE model is the most important part of the quantitative assessment of the TPM strategy. This indicator expresses the overall exploitation efficiency using three main factors: availability, efficiency, and quality (Tab. 1).

Table 1. Components of the OEE indicator [21, 28, 34]

Availability		**Efficiency**		**Quality**	
$D = \frac{t_d - t_p}{t_d}$	(3)	$E = \frac{t_c \cdot n}{t_o}$	(4)	$J = \frac{n - d}{n}$	(5)
t_d - worktime, t_p - downtime.		t_c - theoretical cycle time, n - processed quantity, t_0 - operational runtime.		n - quantity of produced products, d - quantity of incorrect products (defects).	
		$\boldsymbol{OEE = D \cdot E \cdot J}$			(6)

The OEE model is characterised by high flexibility in terms of the possible structure of data sets as the basis for determining the particular measures. This causes the goal of obtaining the values of these measures to become dominant. However, less attention is paid to the realisation of the assessment, including its representation and the selection of input data sets. The exploitation assessment of technical systems, based on the OEE model, is the result of the simultaneous observation of two related processes:

- the exploitation process describes the time course of operation of production machines and devices, expressed in the form of a set of events, which may be subjected to a technical object, with a change between possible technical states,
- in the production process, in this context, the effect of the operation of production machines and devices is in the form of products or services.

The implementation of production processes requires maintenance and repair work of machines and devices (planned and random), considered as part of exploitation processes. On the other hand, the analysis of the exploitation process as a sequence of time-period series of observations of events approximates the mapping of the work of technical systems.

The shaping and interpretation of the OEE model has for years been the subject of many concepts and solutions and, consequently, the resulting publications. These publications can be organised into the following thematic groups:

- the fundamental principles of building the OEE model in its original form, and research on the ways and scope of its application, besides user experiences and opinions, are considered. This includes proposals for interpretation at various points of reference (e.g., taking into account the specifics of various branches of industry) [3, 5, 12, 14],
- the ways to shape measures concerning the concepts of valuation and weighting of the component measures of the OEE model (D, E, J), as well as research on the impact and interpretation of input factors on the form of the OEE model, especially in terms of meaning, taking into account the specificity of the environment of the operated machines and the implemented production/exploitation process [2, 13, 32, 33],

ways of interpreting the OEE model, taking into account the context of the object and the production/exploitation process, and the effects of which may be an element of the decision-making process [7, 8, 15, 25].

Research on the construction of the exploitation assessment models, as well as the interpretation of their results, allowed for the identification of the research gap. The authors assumed that the research gap lies in the imperfection of the classical mathematical OEE model, which can be expressed with the following arguments:

- multiple complexity is manifested by the fact that the result of OEE calculation is a simple product of partial measures (components), which themselves are measures of relative values based on the input data; a product constructed in this manner is extremely sensitive to minor value changes in any of its factors,
- the internal linearity of partial measures (components) consists of the fact that the OEE model does not take into account the differences in the impact of individual partial measures on the final result,
- the mutual dependence of input factors of partial measures implies the possibility of multiple inclusion of the same features in the final computational result of the OEE model,
- the limited domain-specificity of the OEE model consists of the possibility of calculating and interpreting measures regardless of time, which is of key importance in the assessment of the exploitation events and processes due to the nature of the functioning of machines.

The identified and described research gap is the starting point for the formulation and solution of the research problem, i.e. the development of an OEE evaluation model that would be free from the limitations described above.

The research problem being solved is of a modeled-mathematical nature, but its effects are observed in the industrial environment, in the practical area of machinery and devices exploitation. In this context, the machine can be treated as a dynamic object, the features of which change over time and depend on their values in previous moments of time [6]. The dynamic and continuous nature of the machine operation influences the choice of its observation. Based on the assessment of the variability features of the machine, it is possible to infer not only the variability of its technical condition but also that of its interaction with the environment [24]. In the assessment of machines with the use of the OEE model, there are considered long-term input data sets continuous in time, which in many cases do not reflect the specifics of real production processes and, above all, real exploitation processes. These processes are characterised by interruptions directly related to the course of the technological process or breaks/downtimes resulting from the exploitation of machines. Thus, the realisation of production and exploitation processes and the specificity of their direct linkage justify the discrete assessment. This introduces a fundamental change in the approach to the exploitation assessment method in relation to the classic OEE model. This change consists of the use of the discrete form of time in the description of production and exploitation events identified at equally defined unit time intervals. The result of this approach is the consideration of data sets describing the discussed processes in the form of time series. The analysis of the time series in relation to the OEE model, apart from the assessment process itself, offers possibilities of:

- identifying changes in the discussed processes represented by the sequence of observations. That is, determining a trend (development tendency) and distinguishing cyclical and seasonal fluctuations,
- predicting and simulating future values of the component measures of the OEE model.

In summary, the main goals of the research described in the article include:

- development of a geometric model of the exploitatation assessment based on the OEE structure,
- development of the assessment method with the use of time series of changes in selected features of production and exploitation processes,
- verification of the developed models in the context of data obtained in the discrete events simulation process.

The analysis of the existing solutions described in scientific publications shows that the methodproposed by the authors is original. It has not been undertaken so far in the exploitation area.

3. Geometric interpretation of the OEE model

It is assumed that the components of the OEE model can be analysed as discrete variables represented by vectors [1, 17, 20]. In this approach, OEE is a cumulative representation of three component vectors, the values of which are subject to change over time.

This means that the OEE model in a three-dimensional system can be expressed as a vector basis whose components are: availability ($\vec{D}$), efficiency ($\vec{E}$), and quality ($\vec{J}$). They are spread over planes of a rectangular coordinate system (Fig. 1). Each of the component vectors is respectively a projection of the OEE vector on the axes x, y, and z.

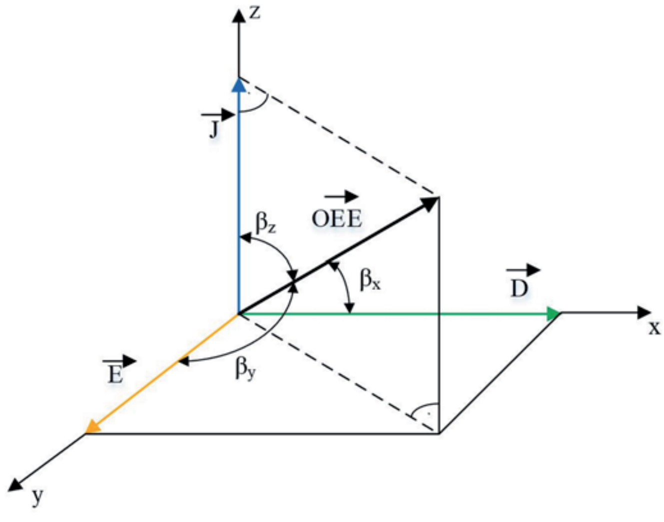

Fig. 1. Vector representation of the OEE model with projections of its components on the axes in a rectangular coordinate system

Based on Fig. 1 and (6), the OEE indicator can be represented as a vector:

$$\overrightarrow{OEE} = \left[\vec{D}, \vec{E}, \vec{J}\right] \tag{7}$$

Introducing the axis unit versors:

$$\vec{d} = [1,0,0], \vec{e} = [0,1,0], \vec{j} = [0,0,1] \tag{8}$$

then $\overrightarrow{OEE}$ takes the form:

$$\overrightarrow{OEE} = \vec{D} + \vec{E} + \vec{J} \tag{9}$$

The vector $\overrightarrow{OEE} = \left[\vec{D}, \vec{E}, \vec{J}\right]$, forms the angles $\beta_x, \beta_y, \beta_z$ β_x, β_y, β_z with the coordinate axes. For the coordinates of the vector $\overrightarrow{OEE}$ there are appropriate geometrical relationships:

$$\vec{D} = \overrightarrow{OEE} \cdot \cos\beta_x, \quad \vec{E} = \overrightarrow{OEE} \cdot \cos\beta_y, \quad \vec{J} = \overrightarrow{OEE} \cdot \cos\beta \tag{10}$$

$$\cos^2\beta_x+\cos^2\beta_y+\cos^2\beta_z=1$$

Assuming that the vectors $\vec{D},\vec{E},\vec{J}$ are non-coplanar, a parallelepiped can be stretched over them, by placing the beginnings of these vectors at a selected point *O* in the Euclidean space (Fig. 2).

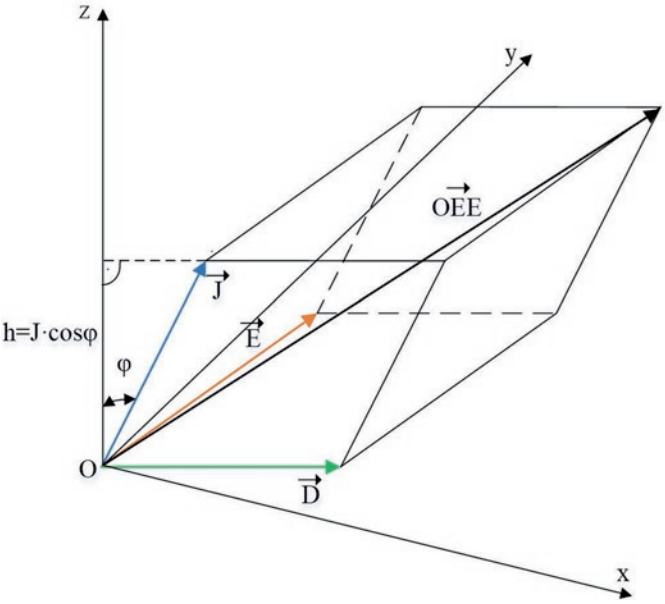

Fig. 2 Graphical representation of a parallelepiped stretched over the $\vec{D},\vec{E},\vec{J}$ vectors

Assuming, that the area of the parallelogram spanned by $\vec{D}$ and $\vec{E}$ is a vector product $\left|\vec{D}\times\vec{E}\right|$, and the height of the parallelepiped *h* is expressed through $\vec{J}\cdot\cos\phi$, then the resulting volume of the parallelepiped can be determined from the mixed product of the component vectors $\vec{D},\vec{E},\vec{J}$:

$$V=\left|\left(\vec{D}\times\vec{E}\right)\cdot\vec{J}\right| \tag{11}$$

Geometric representation of the vector $\overrightarrow{OEE}$, expressed by a mixed product of vectors $\vec{D},\vec{E},\vec{J}$, means that the same values of the parallelepipeds volumes (i.e., $V_1=V_2$) can correspond various features of these vectors in the form of their coordinates and angle φ (Fig. 2). This mixed product has all the properties of the determinant, including multi-lineage. In other words, you can get the same values of the vector $\overrightarrow{OEE}$ for different variants of combinations of the features of the component vectors $\vec{D},\vec{E},\vec{J}$. This means, that the same values of the determined volumes of the parallelepipeds will then correspond to these combinations (11).

The image of the vector $\overrightarrow{OEE}$ and the component vectors $\vec{D},\vec{E},\vec{J}$ corresponds to the geometric interpretation of the model in relation to the exploited technical systems and exploitation processes. Such an interpretation may include:

- the vector length $\left|\overrightarrow{OEE}\right|$ determined geometrically in the Euclidean space both in the entire time range and in individual periods,
- the tensor of second order,
- the directional vector of a scalar function (gradient).

Including projections of the vector $\overrightarrow{OEE}$ on the individual coordinate axes (Fig. 1), the modulus of this vector (length) can be determined by the geometrical relationship with its components (12).

$$\left|\overrightarrow{OEE}\right|=\sqrt{\left|\vec{D}\right|^2+\left|\vec{E}\right|^2+\left|\vec{J}\right|^2} \tag{12}$$

The length of the vector $\left|\overrightarrow{OEE}\right|$ may be a new measure of exploitation assessment, Its interpretation in the context of vector calculus takes into account the variability and specificity of the exploitation and production process.

For the purposes of mapping the exploitation process, in particular taking into account the change in time of the values of its features, based on (12), the vector length $\left|\overrightarrow{OEE}\right|$ can be described by a formula (13):

$$\begin{gathered}\left|\overrightarrow{OEE}\right|(\delta t)=\sqrt{\left|\vec{D}\right|^2(\delta t)+\left|\vec{E}\right|^2(\delta t)+\left|\vec{J}\right|^2(\delta t)}\\ \delta t=t_i-t_{i-1}\end{gathered} \tag{13}$$

Generalizing the formula (12) to vector form, model OEE can take the special form of a tensor of second order (as a square matrix 3x3) $\vec{D},\vec{E},\vec{J}$:

$$OEE=\begin{bmatrix}D & 0 & 0\\ 0 & E & 0\\ 0 & 0 & J\end{bmatrix} \tag{14}$$

where the components are the vectors $\vec{D},\vec{E},\vec{J}$ in the Cartesian coordinate system.

In the Cartesian coordinate system the quadric equation of the OEE tensor takes the following form:

$$\begin{gathered}D_i x^2+E_i x^2+J_i x^2=1\\ D_i>0;E_i>0;J_i>0\end{gathered} \tag{15}$$

The surface resulting from the equation (15) is an ellipsoid, and the lengths of its semi-axes represented respectively by:

$$\frac{1}{\sqrt{D_i}};\frac{1}{\sqrt{E_i}};\frac{1}{\sqrt{J_i}} \tag{16}$$

The form of the second-order tensor of the OEE model, as a linear representation, corresponds to the operations of the tensor calculus. The representation of the OEE model in the form of a tensor can be used in the description of the variability of the exploitation conditions. The components are calculated for values of i in order to compare the exploitation conditions corresponding to each moment in time D_i,E_i,J_i. On this basis, the exploitation tensor OEE_i can be determined. The obtained values of the exploitation tensor OEE_i, can be compared with each other and thus assessed for various time points.

The time distribution of OEE depends on the variables that can be described by a differentiable function. Expressing OEE as a vector of n partial derivatives of this function allows one to determine the direction of its greatest increase and the magnitude of this increase at a given point. Examination of the OEE with the use of the directional vector of a scalar function (gradient) [10] allows determining its variability, taking into account the importance and impact of its individual components for the assessment of the analysed exploitation process. Assuming the gradient in the Cartesian coordinate system for the needs of the exploitation assessment, there is also included the differentiability of the functions such that they express availability (D), efficiency (E) and quality (J):

$$\begin{gathered}\nabla OEE(D,E,J)=\left(\frac{\partial OEE}{\partial D},\frac{\partial OEE}{\partial E},\frac{\partial OEE}{\partial J}\right)\\ \partial D\neq 0,\ \partial E\neq 0,\ \partial J\neq 0\end{gathered} \tag{17}$$

The gradient of OEE for the versors of the individual axes: e_D, e_E, e_J of the Cartesian coordinate system can be written as:

$$\nabla OEE = \frac{\partial OEE}{\partial D} \cdot e_D + \frac{\partial OEE}{\partial E} \cdot e_E + \frac{\partial OEE}{\partial J} \cdot e_J \tag{18}$$

If the formula (18) is related to a given time t_i, it becomes reasonable to determine the gradient of OEE for the discrete representation of data sets:

$$\nabla OEE(t_i) = \frac{\partial OEE(t_i)}{\partial D(t_i)} + \frac{\partial OEE(t_i)}{\partial E(t_i)} + \frac{\partial OEE(t_i)}{\partial J(t_i)} \tag{19}$$

The use of a gradient for the purpose of determining measures of the OEE model allows for the exploitation assessment on the basis of dynamic changes in the time domain of the values of its components. This is a significant difference to the classical static approach of realisation of such an assessment.

4. Development of verification data sets

The proposed geometrical form of the OEE model has been verified. In order to obtain interpretative results, a procedure for acquiring and adjusting the input data is proposed and will be implemented. This procedure is shown in Fig. 3.

In the first step, an inventory of the components of the technical system involved in the production process was made. First, the authors relied on the serial production of plastic components, carried out with the use of an injection moulding machine. Then, based on the identified and pre-interpreted technical system, a model of the production and exploitation processes was developed using the Flexsim software (Fig. 4) [19, 36].

The developed simulation model includes:

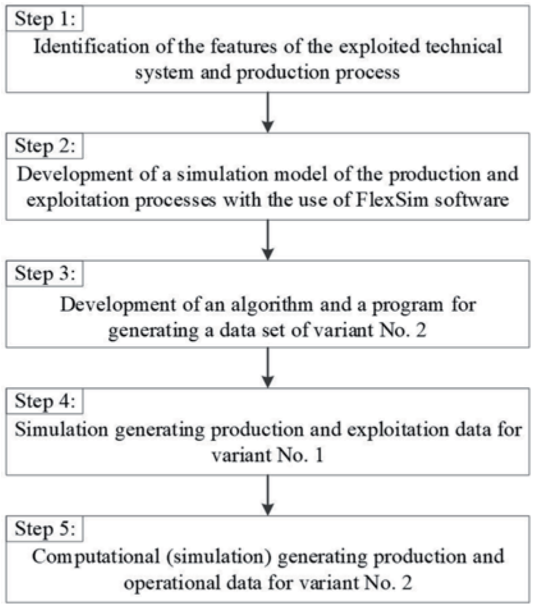

Fig. 3. The procedure for acquiring and positioning the input data

1. Source1 – token generator (logical element representing the product). The frequency of generating the next token was set at 5 minutes, i.e. an average of 12 tokens per hour according to a normal distribution with a standard deviation of 2 (*normal(12, 2, getstream(current)*)).
2. Queue1 – buffer for generated tokens waiting to be processed in Processor1. The maximum queue capacity is assumed to be 1000 elements.
3. Processor1 – an object representing a production machine (in our case an injection machine). This object simulates a delay in relation to the maximum theoretical efficiency of the production process. The processing time for each product was set at 60

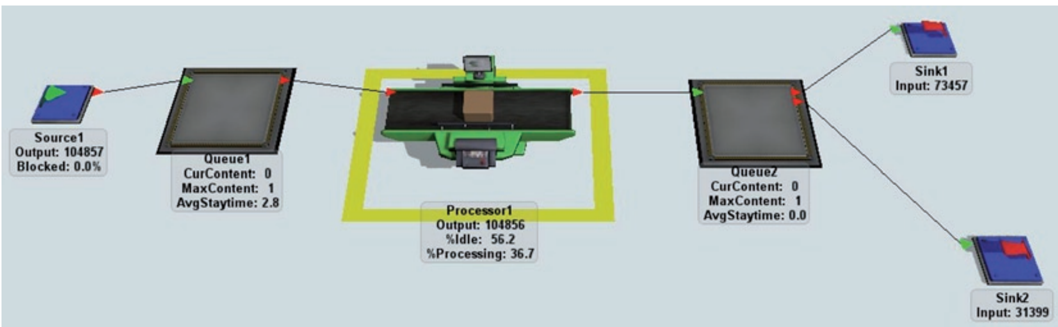

Fig. 4. The model of the production and exploitation processes developed with the use of the Flexsim software

Table 2. A part of the input data resources

Day No.	Variant No. 1				Variant No. 2			
	D_1	E_1	J_1	OEE_1	D_2	E_2	J_2	OEE_2
1	0,6963	0,7919	0,8475	**0,4673**	0,7913	0,6695	0,8822	**0,4673**
2	0,9963	0,5912	0,8623	**0,5079**	0,8119	0,9225	0,6781	**0,5079**
3	1,0000	0,8270	0,9825	**0,8126**	1,0000	1,0000	0,8126	**0,8126**
4	0,8894	0,8092	0,9231	**0,6644**	0,8608	0,8036	0,9604	**0,6644**
5	1,0000	0,4454	0,9449	**0,4209**	1,0000	0,4811	0,8748	**0,4209**
6	0,5181	0,4486	0,8443	**0,1963**	0,7138	0,3124	0,8801	**0,1963**
7	0,8406	0,5068	1,0000	**0,4260**	0,9281	0,5184	0,8853	**0,4260**
8	1,0000	0,6676	0,8893	**0,5937**	0,7300	0,8133	1,0000	**0,5937**
9	1,0000	0,8157	0,9822	**0,8012**	0,9388	0,8719	0,9789	**0,8012**
10	0,9256	0,6259	0,9320	**0,5400**	0,7781	0,8185	0,8478	**0,5400**

seconds, with a random delay described by the exponential distribution (*exponential(0.60, getstream (current)*). A simulation of the machine delay associated with downtime was described using the Weibull distribution with an average event frequency of 6 hours (*weibull(0.0, 11600, 4, getstream(current)*).
4. Sink1, Sink2 - process output. The model defines two outputs that separate the correct products from the defective products. This separation was made according to the discrete Bernoulli binomial distribution with an average probability of 0.9 (*bernoulli(70, 0, 1, getstream(current)*).

This enabled the generation of a complete set of input data for the OEE model. Based on the simulation model, the simulation process was launched. This allowed for the generation of a time series with a unit of one day of production and exploitation values. Finally, the values of the OEE model were calculated on the basis of the relationships (3) - (6).

In the third step, an algorithm and a programme generating the second set of input data were developed (using the Python and Pandas environments). For the needs of the latter set of input data, the same corresponding OEE result values were assumed for both data sets, at particular time points, with various values of their components. That is:

$$OEE_I(t) = OEE_{II}(t) \tag{20}$$

In practice, for each line, modifications of two component values were made in an iterative way, adjusting computationally the value of the third component in such a way that the resultant would not change.

The analyzed vectors: $\vec{D}, \vec{E}, \vec{J}, \overrightarrow{OEE}$, included the collected sets of input data represented in the discrete time points. For the purpose of simulation, equal cumulative OEE values for the tested variants were assumed. Every set contained 1810 data points for each of the vectors. A part of the input data resources for the two variants is shown in Tab. 2.

The differentiation of the components of the OEE model for individual variants and combinations of their pairs was tested using selected statistical evaluation measures, that is: skew, standard deviation, kurtosis and the coefficient of correlation (Spearman). The obtained values indicated significant differences in the input data sets of the time series of the components D, E, J, with the same forms of result sets of time series (OEE).

5. An example of the use of the developed model in the exploitation assessment

Based on the data prepared in accordance with the procedure and description presented in the previous section, verification calculations were carried out to confirm the mathematical correctness and industrial suitability of the developed method of exploitation assessment. For the purposes of this verification, calculations were carried out based on the models developed by the authors in the LabView environment. Examples of models with the results of calculations are presented in Fig. 5 - Fig. 8.

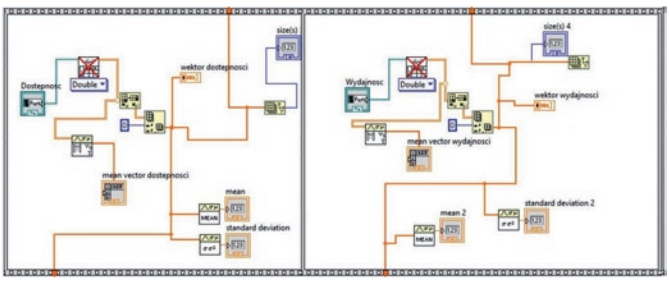

Fig. 5. A model for calculating the vector length $\left|\overrightarrow{OEE}\right|$

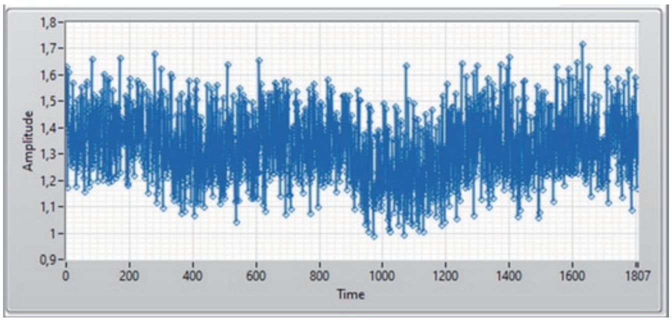

Fig. 6. A visualization of changes in length of the vector $\left|\overrightarrow{OEE}\right|$

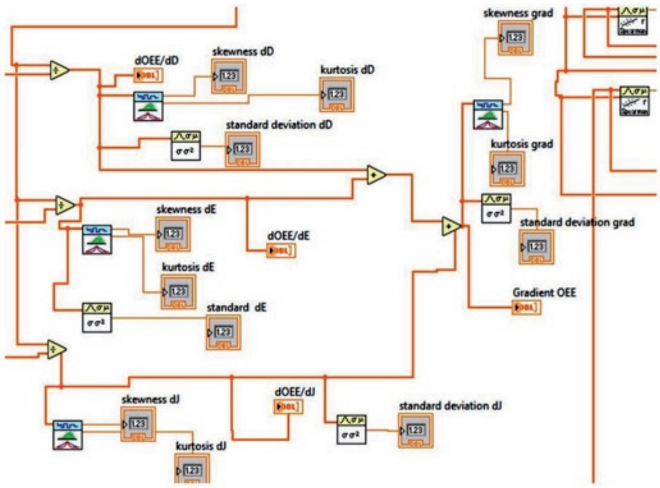

Fig. 7. A model for calculating the directional vector of the scalar function (gradient)

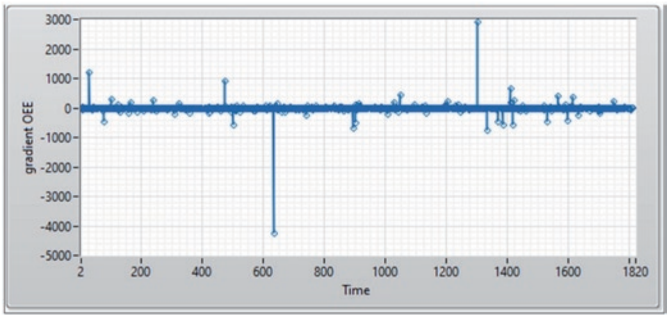

Fig. 8. A visualization of changes in the gradient ∇OEE

Based on a formula (12), the vector length values $\left|\overrightarrow{OEE}\right|$ for successive elements of the time series of the two considered variants were determined. Time changes of measures in classical and geometric versions are shown in Fig. 9. For greater readability, the set of results was limited to 50 observations.

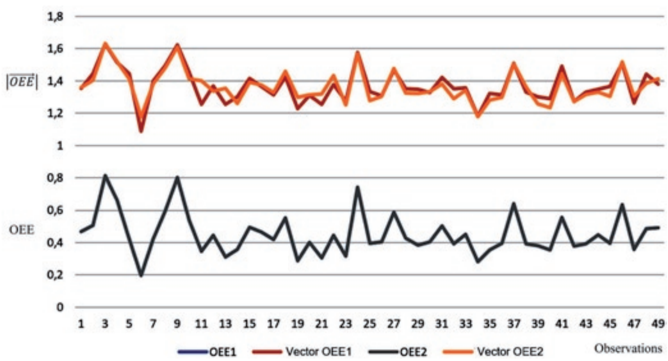

Fig. 9. Time changes of measures in classical and geometric versions for two variants of time series

Table 3. Values of selected statistical measures for two variants of time series

Statistical measure	Variant No. 1		Variant No. 2	
	OEE_1	$\left\|\overrightarrow{OEE}\right\|_1$	OEE_2	$\left\|\overrightarrow{OEE}\right\|_2$
Arithmetic mean	0,3931	1,3043	0,3931	1,3246
Median	0,3784	1,3026	0,3784	1,3211
St. deviation	0,1476	0,1427	0,1476	0,1241
Kurtosis	0,2059	-0,1102	0,2059	−0,2847

The results of the calculation indicate no differences in values of the statistical measures for variants of the OEE model for classic calculations (by the product of D, E, J), as well as significant differences in values and statistical measures for variants of the geometric OEE model (length of the $\left|\overrightarrow{OEE}\right|$ vector). This means a greater susceptibility (sensitivity) of the geometric model to the variability of the values of its components, and it has been shown, that:

- various component values (D, E, J) can lead to the same resultant values in the classic OEE model,
- various component values ($\vec{D},\vec{E},\vec{J}$) can lead to different resultant values in the geometric OEE model.

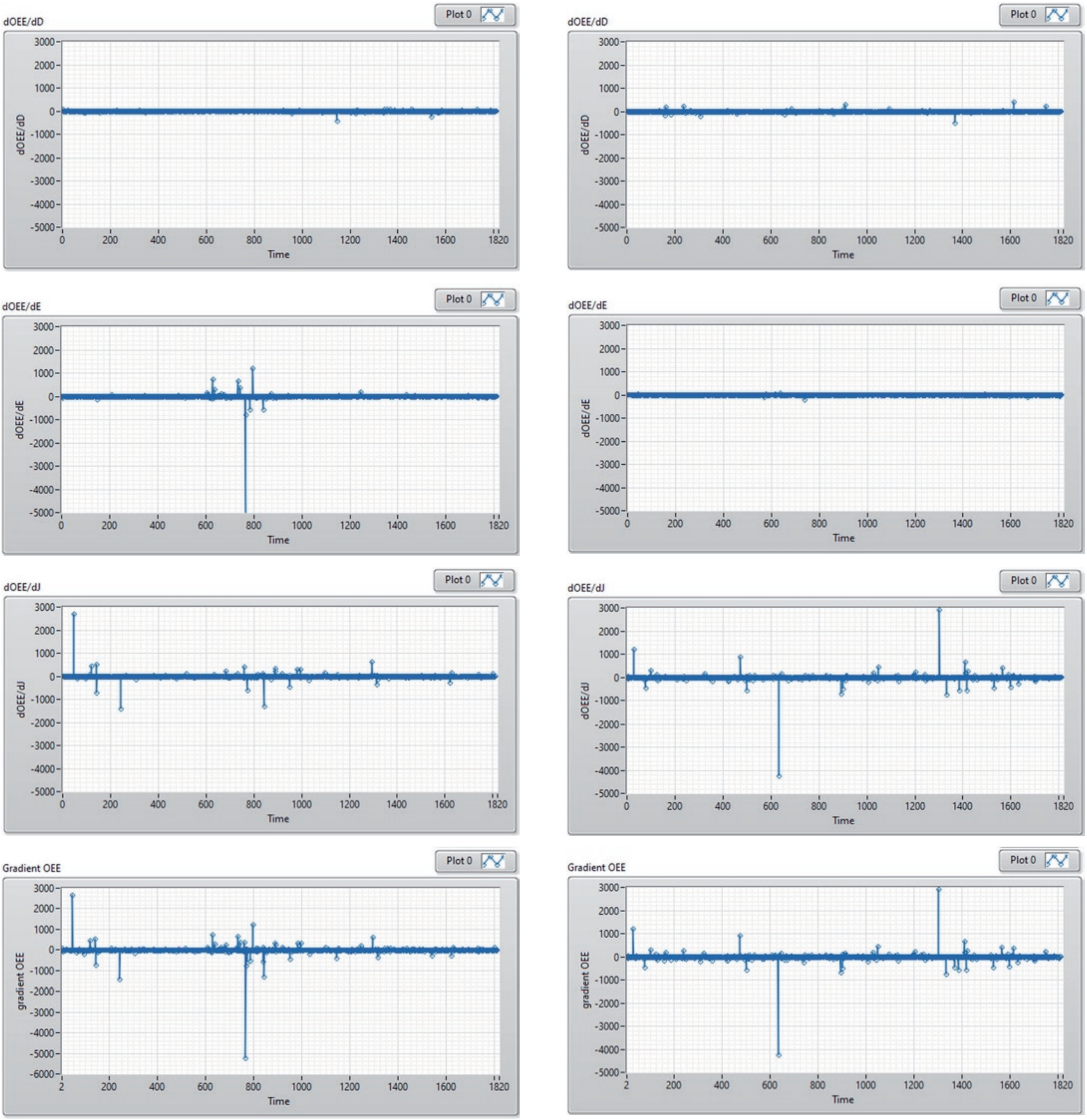

Fig. 10. Graphical interpretation of the gradient: a. the variant no. 1, b. the variant no. 2

Then, selected statistical measures were determined for all elements of the time series.

The above conclusions confirm the significance and practical usefulness of the geometric model for the evaluation of the implementation of the exploitation and production processes, because it takes into account individual components in the vector approach. This makes it possible to apply vector calculus operations to represent the components of the OEE model.

By analysing and interpreting the variability of vectors $\vec{D},\vec{E},\vec{J}$ in relation to the change in the vector $\overrightarrow{OEE}$, the gradient values ∇OEE, for the considered variants of time series, based on the formulas (17) - (19) were determined. The results are presented graphically in Fig. 10.

Based on the results obtained (Fig. 10), it can be concluded that the variability of the characteristics of vectors $\vec{D},\vec{E},\vec{J}$ in relation to the change in the vector $\overrightarrow{OEE}$ shows differentiation in a given time period. Thus, Thus, for the analysed variants, different gradient values, ∇OEE were obtained. Selected statistical measures presenting these differences are shown in Tab. 4.

value of OEE but also about the speed and level of change in a given direction. Furthermore, this may determine the dynamics of changes in selected features of exploitation and production processes.

The results obtained for the differences in the determination of OEE measures in a classical and geometric manner for the tested variants may be more significant for the analysis of a larger amount of data. However, this requires further simulation tests.

The advantage of the presented solution is the possibility of identifying anomalies in the exploitation conditions of machines based on the assessment of the variability of the particular vectors $\vec{D},\vec{E},\vec{J}$ and the $\overrightarrow{OEE}$ vector itself, in a given time period.

The inclusion of time series in the analysis of exploitation and production processes opens new possibilities for assessing the exploitation efficiency of machines. In particular, the analysis, evaluation, and interpretation of the variability of the vectors $\vec{D},\vec{E},\vec{J}$, permits the determination of the operational efficiency for any time point.

Table 4. Statistical evaluation of the variability of the examined vectors

Statistical measure	**Variant No. 1**				**Variant No. 2**			
	$\frac{\partial OEE}{\partial D}$	$\frac{\partial OEE}{\partial E}$	$\frac{\partial OEE}{\partial J}$	$\nabla \boldsymbol{OEE}$	$\frac{\partial OEE}{\partial D}$	$\frac{\partial OEE}{\partial E}$	$\frac{\partial OEE}{\partial J}$	$\nabla \boldsymbol{OEE}$
Skewness	13,20	−33,62	11,77	**−17,19**	0,15	−14,92	−10,73	**−10,26**
St. deviation	14,89	131,95	88,62	**159,23**	22,08	7,50	136,26	**137,95**
Kurtosis	363,26	1354,05	548,40	**688,51**	224,57	436,98	639,85	**606,16**

Simulation studies allow for detailed variability analyzes of the vectors $\vec{D},\vec{E},\vec{J}$, in relation to the change in the vector $\overrightarrow{OEE}$ and the assessment of their impact on the obtained values of the gradient ∇OEE.

6. Conclusions

In the course of exploitation processes, there are complex relationships of technical features, the change of which may cause an increase or decrease in the effectiveness of the use of machines.

According to the authors, in the method of calculating OEE (as a product of the values of partial indicators), the absolute value of this indicator is not so important as the information resulting from its time variability. Therefore, the mathematical interpretation of its variability should have the character of a dynamic assessment. Taking into account the components of the OEE indicator, machine efficiency can be analysed in three-dimensional space based on the geometric (vector) representation of the component features. In this context, by presenting the OEE model in a vector form in three-dimensional space, it is possible to formulate conclusions not only about the instantaneous

In the authors' opinion, the proposed method allows for the real mapping of the variability of the tested exploitation efficiency. The implementation of such a solution may consist in the collecting and processing data in real time, with the simultaneous evaluation of the realization of the process. For this purpose, there can be used real-time wireless data transmission devices between the exploited production system and the data analysis system. The proposed method can be used to monitor the effectiveness of production and exploitation processes with the use of industry 4.0 solutions. This is of particular importance for the technical and economic exploitation assessment of machines and devices, which undoubtedly contributes to the reduction of the costs of enterprises.

The approach to the method proposed in the article consists of not only taking into account the influence of its components and its time variability, but also giving the opportunity to generate development scenarios and forecast the future exploitation policy of the enterprise [18].

References

1. Agrawal OP, Xu YF. Generalized vector calculus on convex domain. Communications In Nonlinear Science And Numerical Simulation 2015; 23(1-3): 129-140, http://doi.org/10.1016/j.cnsns.2014.10.032.
2. Aratujo I.G, Gomes F.M, Pereira F.M. Application of Monte Carlo's method to predict the overall equipment effectiveness index of a cellulose machine. Sistemas & Gestao 2020; 15(1): 25-37, https://doi.org/10.20985/1980-5160.2020.v15n1.1608.
3. Bengtsson M. Using a game-based learning approach in teaching overall equipment effectiveness. Journal of Quality in Maintenance Engineering 2019; 26(3): 489-507, https://doi.org/10.1108/JQME-03-2019-0031.
4. Campbell J., Jardine A., McGlynn J. Asset Management Excellence. Optimizing Equipment Life-Cycle Decisions. CRC Press, Boca Raton: 2011.
5. Corrales NGL, Lambán MP, Korner MEH, Royo J. Overall equipment effectiveness: systematic literature review and overview of different approaches. Applied Sciences-Basel 2020, 10(18): 6469, https://doi.org/10.3390/app10186469.
6. Duda S, Kawlewski K, Gembalczyk G. Concept of the system for control over keeping up the movement of a crane. Solid State Phenomena 2015, 220-221: 339-344, https://doi.org/10.4028/www.scientific.net/SSP.220-221.339.
7. EL Mazgualdi C, Masrour T, El Hassani I, Khdoudi A. Machine learning for KPIs prediction: a case study of the overall equipment effectiveness within the automotive industry. Soft Computing 2021; 25: 2891-2909, https://doi.org/10.1007/s00500-020-05348-y.
8. Farahani Ameneh, Tohidi Hamid, Shoja Ahmad. Optimization of overall equipment effectiveness with integrated modeling of maintenance and quality. Engineering Letters 2020; 28(2): 400-405.
9. Gola A, Nioczym A. Application of OEE coefficient for manufacturing lines reliability improvement. Proceedings of the International

Conference on Management Science and Management Innovation (MSMI 2017), Book Series: Advances in Economics Business and Management Research 2017; 31: 189-194.
10. Hall P, Muller HG, Yao F. Estimation of functional derivatives. Annals of Statistics 2009; 37(6A): 3307-3329, https://doi.org/10.1214/09-AOS686.
11. Janik A, Ryszko A. Mapping the field of Industry 4.0 based on bibliometric analysis. VISION 2020: Sustainable Economic Development and Application of Innovation Management, Proceedings of the 32nd Conference of the International-Business-Information-Management-Association (IBIMA) 2018: 6316-6330.
12. Jaqin C, Rozak A, Purba HH. Case study in increasing overall equipment effectiveness on progressive press machine using plan-do-check-act cycle. International Journal of Engineering, 2020; 33(1): 2245-2251, https://doi.org/10.5829/ije.2020.33.11b.16.
13. Jasiulewicz-Kaczmarek M, Antosz K, Wyczolkowski R, Mazurkiewicz D, Sun B, Qian, C. Application of MICMAC, fuzzy AHP, and fuzzy TOPSIS for evaluation of the maintenance factors affecting sustainable manufacturing. Energies 2021; 14(5): 1436, http://doi.org/10.3390/en14051436.
14. Jasiulewicz–Kaczmarek M, Antosz K. Żywica P, Mazurkiewicz D, Sun B, Ren Y. Framework of machine criticality assessment with criteria interactions. Eksploatacja i Niezawodnosc – Maintenance and Reliability 2021; 23 (2): 207–220, http://doi.org/10.17531/ein.2021.2.1.
15. Kalisch M, Przystalka P, Timofiejczuk A. Genetic optimization of meta-learning schemes for context-based fault detection. Advances In Technical Diagnostics, Book Series: Applied Condition Monitoring 2018; 10: 287-297, http://doi.org/10.1007/978-3-319-62042-8_26.
16. Kozlowski E, Mazurkiewicz D, Zabinski T, Prucnal S, Sep J. Machining sensor data management for operation-level predictive model. Expert Systems with Applications 2020; 159: 113600, https://doi.org/10.1016/j.eswa.2020.113600.
17. Lohgheswary N, Nopiah ZM, Aziz AA, Zakaria E. Achievement of course outcome in vector calculus pre-test questions. Journal of Fundamental and Applied Sciences 2017; 9(5): 394-403, http://doi.org/10.4314/jfas.v9i5s.28.
18. Loska A.: Variant assessment of exploitation policy of selected companies managing technical network systems. Management Systems in Production Engineering 2015; 3(19): 179-188, http://doi.org/10.12914/MSPE-13-03-2015.
19. Luscinski S, Ivanov V. A simulation study of industry 4.0 factor on the ontology on flexibility with using FlexSim (R) software. Management and Production Engineering Review 2020; 11(3): 74-83, http://doi.org/10.24425/mper.2020.134934.
20. Mostyn V, Huczala D, Moczulski W, Timofiejczuk A. Dimensional optimization of the robotic arm to reduce energy consumption. MM Science Journal 2020: 3745-3753, https://doi.org/10.17973/MMSJ.2020_03_2020001.
21. Nakajima S.: Introduction to TPM. Total Productive Maintenance. Productivity Press, Portland: 1988.
22. Narayan V.: Effective Maintenance Management: Risk and Reliability Strategies for Optimizing Performance. Industrial Press Inc., New York: 2003.
23. Niebel W.B.: Engineering Maintenance Management, second edition. Marcel Dekker Inc., New York: 1994.
24. Paszkowski W.: The assessment of acoustic effects of exploited road vehicles with the use of subjective features of sound. Eksploatacja i Niezawodność – Maintenance and Reliability 2019; 21(3): 522-529, 9, http://dx.doi.org/10.17531/ein.2019.3.19.
25. Pater J, Basara D, Stadnicka D. Influence of temperature based process parameter compensation on process efficiency and productivity. Technologia i Automatyzacja Montażu 2021; 2(7): 44-51, http://doi.org/10.15199/160.2021.2.7.
26. Peters R.W.: Maintenance Benchmarking and Best Practices: A Profit - and Customer - Centered Approach, McGraw-Hill, New York: 2006.
27. PN-EN 15341:2019 - Maintenance - Maintenance Key Performance Indicators.
28. Productivity Press Development Team: OEE for Operators. Productivity Press Inc., New York: 1999.
29. Shehzad A, Zahoor S, Sarfraz S, Shehab E. Implementation of TPM in a process industry: a case study from Pakistan. Advances in Manufacturing Technology XXXII, Book Series: Advances in Transdisciplinary Engineering 2018; 8: 511-516, http://doi.org/10.3233/978-1-61499-902-7-511.
30. Singh J, Singh H, Sharma V. Success of TPM concept in a manufacturing unit - a case study. International Journal of Productivity and Performance Management 2018; 67(3): 536-549, https://doi.org/10.1108/IJPPM-01-2017-0003.
31. Smith J.: The KPI Book. Insight Training & Development Limited, Stoubridge: 2001.
32. Stecula K, Brodny J, Palka D. Analysis of reasons for unplanned stoppages of machines in the example of the longwall shearer. Innovations In Science And Education, CBU International Conference Proceedings 2017; 5: 1210-1214, http://doi.org/10.12955/cbup.v5.1098.
33. Supriatna A, Singgih ML, Widodo E, Kurniati N. Overall equipment effectiveness evaluation of maintenance strategies for rented equipment. International Journal of Technology 2020; 11(3): 619-630, https://doi.org/10.14716/ijtech.v11i3.3579.
34. Suzuki T. (ed.): TPM in Process Industries. Productivity Press, Portland: 1994.
35. Swiderski A, Borucka A, Grzelak M, Gil L. Evaluation of machinery readiness using semi-Markov processes. Applied Sciences-Basel 2020; 10(4): 1541, http://doi.org/ 10.3390/app10041541.
36. Wang YR, Chen AN. Production logistics simulation and optimization of industrial enterprise based on FlexSim. International Journal of Simulation Modelling 2016; 15(4): 732-741, http://doi.org/10.2507/IJSIMM15(4)CO18.
37. Wiremann T. Developing performance indicators for managing maintenance (second edition). Industrial Press, New York: 2005.

Eksploatacja i Niezawodnosc – Maintenance and Reliability

Volume 24 (2022), Issue 1

journal homepage: http://www.ein.org.pl

Article citation info:
Wan L, Jiang K, Zeng Q, Gao K. Dynamic response and reliability analysis of shearer drum cutting performance in coal mining process. Eksploatacja i Niezawodnosc – Maintenance and Reliability 2022; 24 (1): 123–129, http://doi.org/10.17531/ein.2022.1.14.

Indexed by: Web of Science Group

Dynamic response and reliability analysis of shearer drum cutting performance in coal mining process

Lirong Wan[a], Kao Jiang[a], Qingliang Zeng[a,b], Kuidong Gao[a,*]

[a] Shandong University of Science and Technology, College of Mechanical and Electrical Engineering, Qingdao 266590, China
[b] Shandong Normal University, College of Information Science and Engineering, Jinan 250358, China

Highlights

- Measures to improve shearer stability are proposed from vibration reduction points;
- Shearer hydraulic system is more vulnerable to shocks in the height adjustment stages;
- Proper height adjustment speeds would reduce severe load fluctuations in the process.

Abstract

Vibration is an inevitable phenomenon in the coal cutting process and severe vibration leads to efficiency loss for cutting equipment. To understand the impact of vibration on cutting equipment and explore the measures to improve the stability, the dynamic response of cutting equipment is analyzed. The shearer drum, which always undertakes coal cutting task and is the vibration source in working process, is established with finite element method and the relations between cutting performance and vibration characteristics are analyzed. Hydraulic system, vulnerable to external shocks, is also established and the dynamic responses of hydraulic piston under different working stages are analyzed. In the frequency domain analysis on cutting load, results show that a vibration signal with higher amplitude appears, which is consistent with the drum vibration frequency. It demonstrates that drum vibration happens under impact load, especially during height adjustment stages. The research provides the methods for vibration reduction and would be helpful for improvement of shearer reliability.

Keywords

shearer drum; drum vibration; cutting performance; hydraulic system; operation reliability.

1. Introduction

Shearer, as shown in Fig. 1, is one of the important fully mechanized mining equipment underground, which mainly undertakes the task of coal cutting. During coal cutting process, vibration is an inevitable phenomenon, especially rock fracture happens during working process [1, 22]. There are many components on shearer, such as transmission gears and conical cutters are vulnerable to failure under shock and vibration as shown in Fig. 2. Meanwhile, failure on those components results in too much difficulty of cutting process and affects the reliability of shearer in return [14, 18]. Therefore, study on the vibration characteristics of shearer drum and the influence of vibration on cutting performance is meaningful for improve the working performance and reliability of shearer.

To improve the cutting performance and working reliability of shearer, many approaches have been proposed recently and most are related with installation angles and arrangement of cutter on shearer drum. In addition, Bołoz [10] found that cutting performance was also related with cutting directions and provided a new way to improve cutting performance. During those research, ground test is one of the

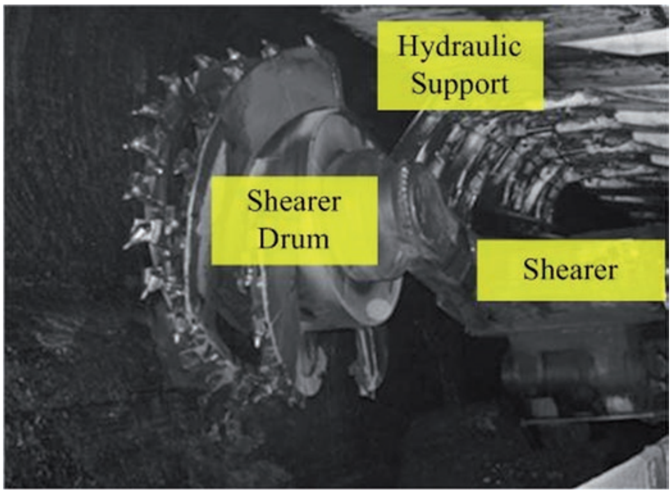

Fig. 1. Coal cutting equipment, named shearer in this paper

(*) Corresponding author.

E-mail addresses: L. Wan (ORCID: 0000-0002-4279-1598): lirong.wan@sdust.edu.cn, K. Jiang (ORCID: 0000-0002-4915-2748): JiangKao93@126.com, Q. Zeng (ORCID: 0000-0002-3842-9107): qlzeng@sdust.edu.cn, K. Gao (ORCID: 0000-0002-8303-5991): gaokuidong22@163.com

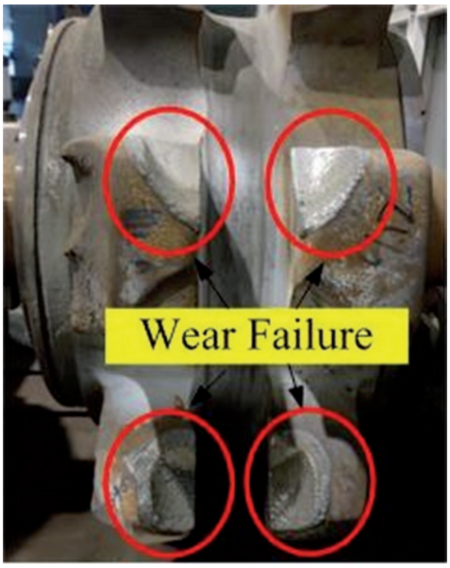

Fig. 2. Component failure on shearer

most common approaches to study cutting performance of the drum [13, 17]. However, sometimes the requirements of ground test can not be fully guaranteed and some researchers began to pay attention to simulation method. In this process, results comparison between simulation and experiment methods were made and the accuracy of the results by simulation method was proved by lots of researchers [5, 16, 23]. Mat_105 in material library is used to simulate the coal and rock cutting process and it is found that the simulation results are in good agreement with the experimental results [12]. Then, results gotten from simulation began to getting recognized and the working performance of cutting equipment under all kinds of possible conditions were explored with simulation method [3, 6, 11, 15]. Chen [2] studied the pore elastic effect in rock cutting process, and gave the influence of rock pore spreading coefficient and cutting speed on rock pore pressure response. Liu [7] innovatively put forward a non-planar tool, triangular diamond tool, and analyzed the influence of caster angle, cutting depth and rotation angle on rock crushing effect. These simulation studies provide reference in the material parameter choice and the contact information between cutter and coal, providing the basis for our simulation research. In fact, shearer drum is indirectly connected with hydraulic cylinder through rocker arm as shown in Fig. 3. Apart from the structural parameters mentioned in the above reference, vibration on cutters and the influence of vibration on cutting performance is rarely studied in those research. Considering the compressibility of fluid in hydraulic cylinder, drum vibration is an inevitable phenomenon during working process. Therefore, it is necessary to conduct the research on drum vibration and its influence on cutting performance.

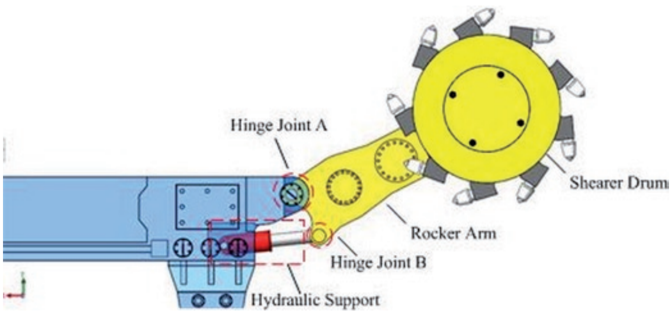

Fig. 3. Diagram of shearer cutting system

To get the vibration characteristics of shearer drum, the hydraulic system for shearer is essential. The dynamic response of hydraulic system has been studied by many researchers under impact load [19, 20, 24]. Zhang [25] got the response characteristics of shearer height adjustment system under constant heavy load condition, and studied the tracking trajectory and its error under the condition of sudden speed and load. Gao [4, 26] applied the cutting force on the free end of the rocker arm and got the dynamic response of hydraulic piston and other components. According to the recent researches, AMESim software has been recognized by researchers and widely used for analysis of hydraulic system.

In order to improve the reliability of shearer operation, this paper analyzed the dynamic response of cutting system and hydraulic system during working process. Firstly, the simulation model of hydraulic system for height adjustment was established. Cutting forces, which were obtained from the finite element model, served as the input signal of hydraulic system and the dynamic characteristics of cylinder piston were obtained. Further, according to the dynamic characteristics of cylinder piston, the cutting load on shearer drum under different dynamic characteristics of piston were simulated with the help of finite element model. Finally, the methods and measures to reduce the impact of cutting load on the shearer reliability were proposed. The research provides measures for vibration reduction and would be helpful for improvement of shearer reliability.

2. Method and Numerical Model

2.1. AMESim-based simulation model of shearer rocker arm and hydraulic system

According to Fig. 3, the cutting system of shearer mainly consists of hydraulic system, rocker arm and drum. Fig. 4 shows the simplified diagram of cutting system and force analysis could be made with the diagram.

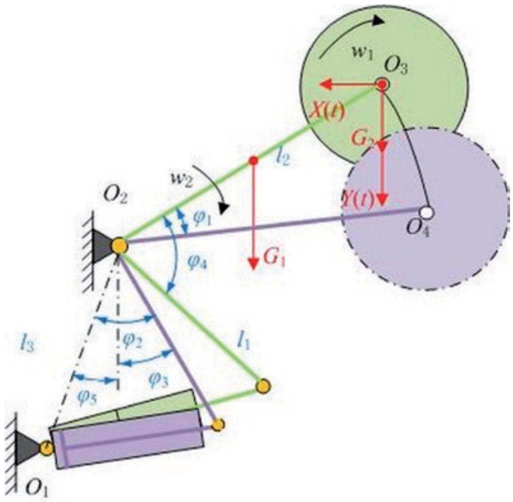

Fig. 4. Schematic diagram of cutting system

Taking the hydraulic piston in hydraulic system as the analysis object and according to force balance equation, the force on hydraulic piston can be gotten:

$$F_e = f(G_1, G_2, X(t)\; Y(t), M(t)) \tag{1}$$

where, G_1, G_2 are the gravity of rocker arm and shearer drum, kN; $X(t)$ and $Y(t)$ are the cutting load on shearer drum in X and Y directions,kN; $M(t)$ is random moment on shearer drum, kN·mm.

To study the dynamic characteristics of hydraulic system of shearer, AMESim-based simulation model of shearer rocker arm and hydraulic system was established and it consisted of hydraulic and mechanical system as shown in Fig. 5. In the figure, the hydraulic system consists of motor (1), pump (2), hydraulic relief valve (3), control signal (4), direction valve (5), bidirectional hydraulic lock (6) and hydraulic chamber (7). The mechanical system consists of the hinge joint (9), (11) and rocker arm (10). Besides, the hinge joint (9) is responsible for connection of rocker arm and haulage unit of shearer like the hinge joint A shown in Fig. 3. The hinge joint (11) is responsible for connection of rocker arm and hydraulic cylinder like the hinge joint B shown in Fig. 3. The relevant parameters about hydraulic system and rocker arm are shown in Table.1. In addition, according to Eq.1, cutting loads on shearer drum in X and Y directions, which will be gotten with finite element method shown in the Fig. 6, should be input into the system as well.

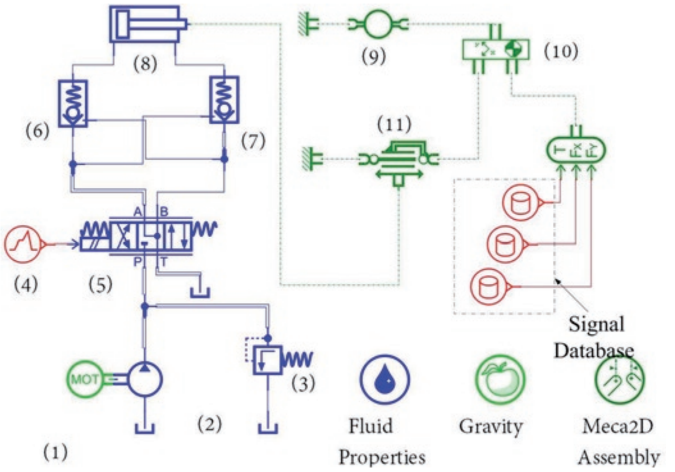

Fig. 5. Mechanism-hydraulics coupling model of drum height adjustment system

Table 1. Structural parameters of mechanism-hydraulics coupling simulation model

Variables	Values	Variables	Values
Pump speed	1470r/min	Length of rocker arm	2620mm
Pump displacement	57L/min	Length of piston stroke	740mm
Relief valve cracking pressure	18MPa	Mass of rocker arm	13295kg
Piston diameter	278mm	Mass of shearer drum	5330kg
Rod diameter	150mm		

2.2. Finite element model of drum cutting coal

To study cutting performance of shearer drum in different working stages and get the dynamic response under influence of vibration, the finite element method was applied and the drum cutting coal model was established, as shown in Fig. 6 to simulate coal cutting process. The diameter of shearer drum shown in the figure is 2.2m and it works at the rotation speed of 28 r/min and haulage speed of 2.5 m/min. In the finite element model, the drum finite element model, including blades and cutters, is set as a rigid body, and the coal body is set as brittle damage material. The tensile strength of coal material used in the paper is 2.0 MPa and the uniaxial compressive strength of rock material is 5.0 MPa. In order to make the coal body separated from the working face under the action of cutters, the failure model "ADD_ EROSION" is introduced into coal material model and it is able to simulate different failure modes, such as stress failure, strain failure et al. Meanwhile, elements which attain to its maximum values will be deleted from the finite element model and it is suitable for simulation of coal cutting process. In addition, the moving degree of freedom in Y directions of shearer drum is released in this paper to enable to simulate the vibration characteristics of shearer drum during cutting process.

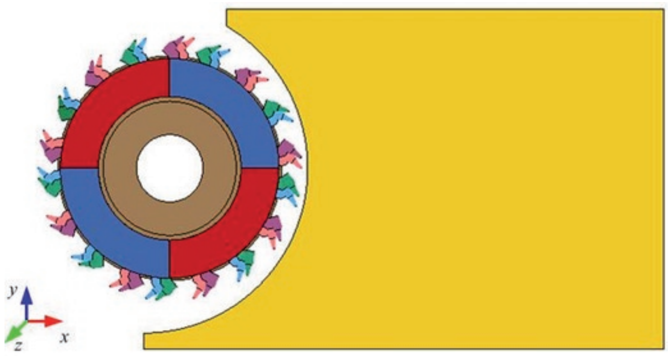

Fig. 6. Finite element model of drum cutting coal

3. Numerical simulation for dynamic response of hydraulic system under cutting loads

3.1. Possible working conditions during hydraulic system working process

From the equation, the piston in hydraulic cylinder is not only forced by gravity, but also forced by the cutting force in *X* and *Y* directions and the random moment on shearer drum $M(t)$. In the previous research, the load input into hydraulic system was mostly step signal. The step signal could simulate the characteristics of sudden load, but the frequency characteristics of load were difficult to be comprehensively reflected by step signal. Therefore, the cutting loads shown in Fig. 7, coming from the simulation results with the finite element method shown in Section 2.2, were adopted in this paper as the input signals of hydraulic system and served as the load signals input into the signal database as shown in Fig. 5. In addition, the random moment $M(t)$ which results from other factors not related with cutting load is not considered and $M(t)$=0 kN·mm in this paper.

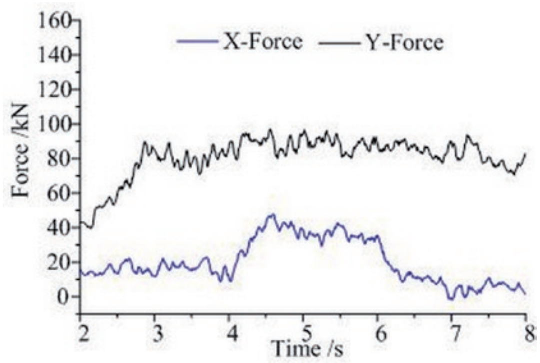

Fig. 7. Cutting load input into hydraulic system

3.2. Velocity analysis of piston under different working conditions

Most of the time, shearer drum works at the fixed heights like the working process from t_1 to t_2, from t_3 to t_4 shown in Fig. 8 and marked with T_1 and T_3. When roof cutting happens in cutting process, shearer drum might descend its working height like the working process from t_2 to t_3 shown in Fig. 8 and marked with T_2 to avoid rock cutting condition [8, 9, 21]. To get the comprehensive understanding of dynamic response of hydraulic system, the two mentioned working process are discussed and in the paper. In the paper, t_1=2s, t_2=4s, t_3=6s, t_4=8s.

From 4~8 seconds, the control current attains to −40 mA, the direction valve (5) works in the left position. During this period, hydraulic oil enters the hydraulic cylinder from pump to push piston to work and shearer drum begins to work at rising or falling height. From the figure, the piston velocity fluctuates largely at the beginning of valve opening. Therefore, the piston velocity varies in a large range at the

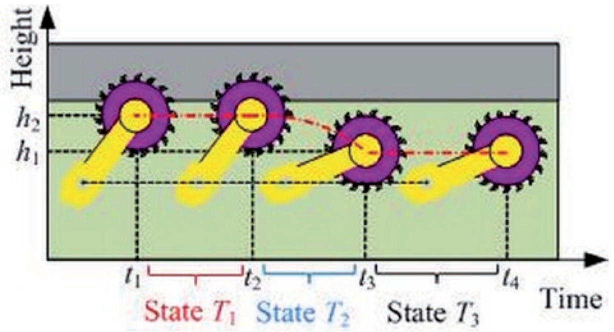

Fig. 8. Possible cutting states of shearer drum in working process

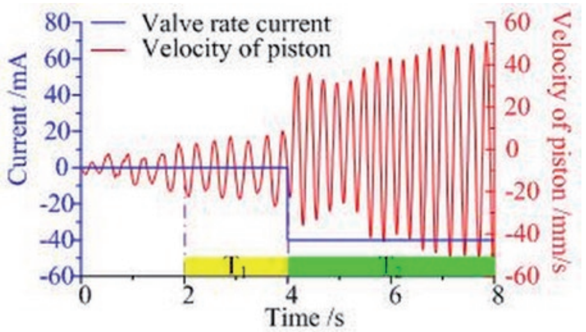

Fig. 9. Piston velocity during different working process

beginning of height adjustment and severe oscillation might happen in this process.

3.3. Displacement characteristics of piston and drum under different working conditions

Fig. 10 shows drum and piston displacement characteristics under different cutting load. From the figure, drum and piston displacement is a constant at the first four seconds and drum works without height adjustment. From the fourth seconds, drum begins to work with height adjustment. From the figure, during height adjustment process, the ratio between piston and drum displacement changes and is not a linear any more. To study the displacement characteristics of piston, however, it is difficult to observe the oscillation of piston and shearer drum in Fig. 10 directly, because the amplitude of piston oscillation is not obvious. To get a better view of that, the frequency domain analysis is used in this paper. The drum vibration in different cutting stages (T_1 and T_2) are studied with frequency analysis method and the results are shown in Fig. 11.

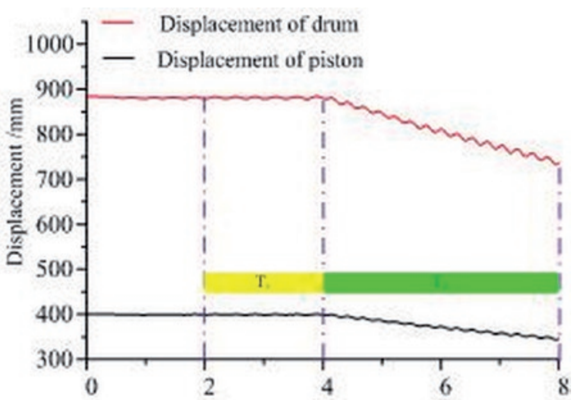

Fig. 10. Displacement characteristics of shearer drum

From Fig. 11, the vibration amplitude of drum is smaller and it is smaller than 2 mm when drum is working without height adjustment. When drum is in the process of height adjustment, the vibration amplitude enlarges and the maximum amplitude of shearer drum is close to 4 mm. Therefore, drum vibration during height adjustment process is obvious and the influence of drum vibration on cutting load needs to be studied further.

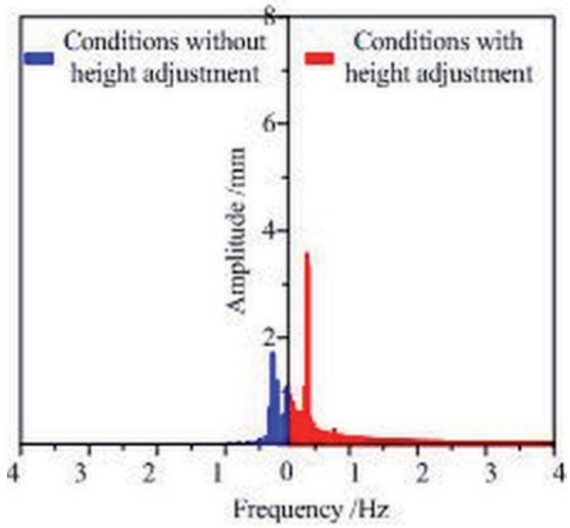

Fig. 11. Amplitude-frequency characteristics of drum vibration

4. Numerical simulation of drum cutting performance under different vibration characteristics

4.1. Dynamic cutting performance of shearer drum under different speeds of height adjustment

It is mentioned that drum vibration is much more obvious during height adjustment process in the last part and attention should be paid on the height adjustment to study the dynamic response of shearer drum. The dynamic response of shearer drum under different speeds of height adjustment and the vibration characteristics are studied in the following parts.

(1) Drum height adjustment speed of 200 mm/s

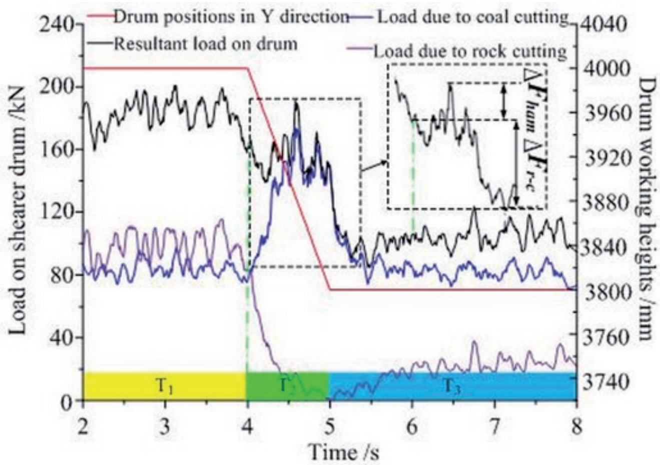

Fig. 12. Cutting load under drum descending speed of 200 mm/s

From the figure, when the drum height adjustment speed reaches 200 mm/s, the cutting load due to coal is about 70 ~ 100 kN before the drum height adjustment; When the drum descends its working height during 4~5 s, the cutting load on drum due to coal rises sharply to 180 kN, the cutting load on drum due to rock decreases about 70 kN and the total force finally increases to 250 kN. Height adjustment increases the total cutting load, instead of decreasing the cutting load in this condition. Therefore, the improper height adjustment speed might increase the cutting load.

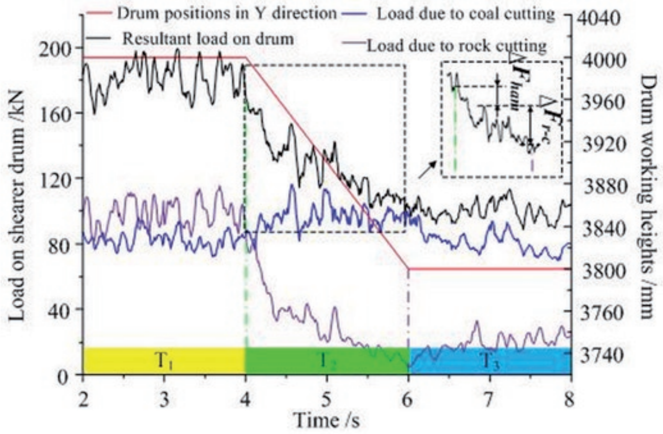

Fig. 13. Cutting load under drum descending speed of 100 mm/s

To evaluate the speed of height adjustment, two kinds of evaluation variables are provided and they are marked with ΔF_{ham} and $\Delta F_{r\text{-}c}$. The variable ΔF_{ham} as expressed in Eq. 2 and shown in Fig. 12, is the difference between the cutting load at the beginning of height adjustment and the maximum cutting load during height adjustment process. The variable $\Delta F_{r\text{-}c}$ as expressed in Eq. 3 and shown in Fig. 12, is the difference between the cutting load at the beginning of height adjustment and the cutting load at the end of height adjustment. The variable $\Delta F_{ham}<0$ illustrates the cutting load still increases even if rock cutting in the cutting ranges decreases and it also indicates that the speed of height adjustment is not suitable and should be slowed. When the variable $\Delta F_{ham}>0$, it means the cutting loads during height adjustment are less than that before height adjustment and the speed of height adjustment is reasonable. Besides, the larger ΔF_{ham} means the speed of height adjustment is suitable and the larger $\Delta F_{r\text{-}c}$ means the greater importance of height adjustment on decreasing the drum cutting loads.

$$\Delta F_{ham} = F_{start} - F_{med\_\max} \tag{2}$$

$$\Delta F_{r-c} = F_{start} - F_{final} \tag{3}$$

where F_{start} is the cutting load on shearer drum at the beginning of height adjustment, kN; $F_{med\_\max}$ is the maximum cutting load on shearer drum during height adjustment process, kN; F_{final} is the cutting load on shearer drum at the end of height adjustment, kN.

(2) Drum height adjustment speed of 100 and 50 mm/s

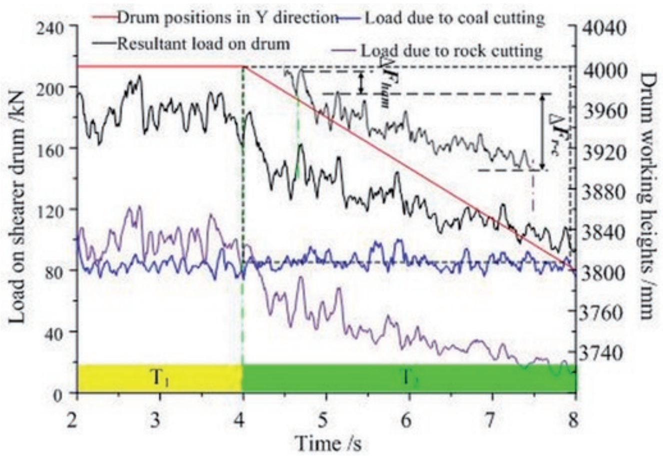

Fig. 14. Cutting load under drum descending speed of 50 mm/s

Similarly, when the speed of drum height adjustment duration descends to 100 mm/s and 50 mm/s, the total cutting load on shearer drum during height adjustment process is less than that before height adjustment, which are shown in Figs.13 and 14. According to Eqs. 2, 3 and Figs. 12~14, the influence of height adjustment speed on the cutting load can be gotten in Fig. 15. From the figure, when the speed of height adjustment exceeds 200 mm/s, $\Delta F_{ham}=-7<0$, it means the quick speed of height adjustment process increases the cutting load and it is supported to be slowed. From the figure, when the speeds of height adjustment are 50 and 100 mm/s, $\Delta F_{ham}>0$ and it means that those speeds of height adjustment are suitable for working. In addition, for the variable $\Delta F_{r\text{-}c}$, it varies from 92 kN to 83 kN and little differences on this variable exist under different speeds of height adjustment. It demonstrates that the differences of cutting loads at the beginning and end of height adjustment are less influenced by speed of height adjustment, but the cutting load during height adjustment process is prone to influence by the speed of height adjustment.

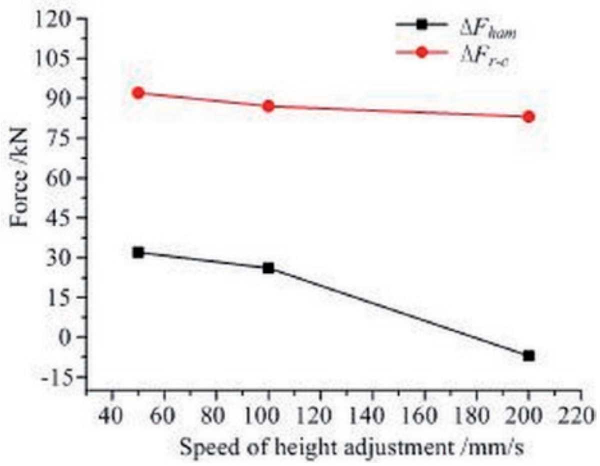

Fig. 15. ΔF_{ham} and $\Delta F_{r\text{-}c}$ under different drum descending speeds

4.2. Dynamic cutting performance under drum vibration

According to Fig. 11, it is found that the vibration of drum in Y direction always happens during drum height adjustment process. To study the influence of vibration in Y direction on the cutting performance, the cutting load on shearer drum is obtained under vibration frequency *f* and amplitude *A* as shown in Fig. 16.

Fig. 16 shows the cutting load on shearer drum and the frequency domain analysis of cutting load. Fig. 16(a) shows cutting load on shearer drum when drum works to cut coal and rock mixed seam at different heights. From 4th s, the shearer drum begins to work at the descending states, accompanied with vibration frequency of 4 Hz and amplitude of 6mm. From the figure, the cutting loads on shearer drum perform with regular fluctuation during 4~6 s. Then, frequency domain analysis is made on the cutting loads and the results can be seen in Fig. 16(b). From the figure, the large amplitude of cutting load on shearer drum is mostly on low frequency. Besides, in the frequency domain figure, a local peak occurs at the frequency of 3.98 Hz, which is closer to the vibration frequency of drum displacement in Y direction. The results show that the cutting performance on shearer drum might be influenced by drum vibration in Y direction. Therefore, it can be concluded that the cutting load on shearer drum can be influenced by drum vibration. In addition, the amplitude of cutting load at the frequency closer to the drum vibration frequency will increase obviously. It also can be concluded that drum vibration reduction in Y direction is helpful for decreasing the fluctuation range of cutting load.

5. Conclusion

The models of shearer drum used for coal cutting and the hydraulic system used for height adjustment are established in this paper. The dynamic response of hydraulic system under different working condi-

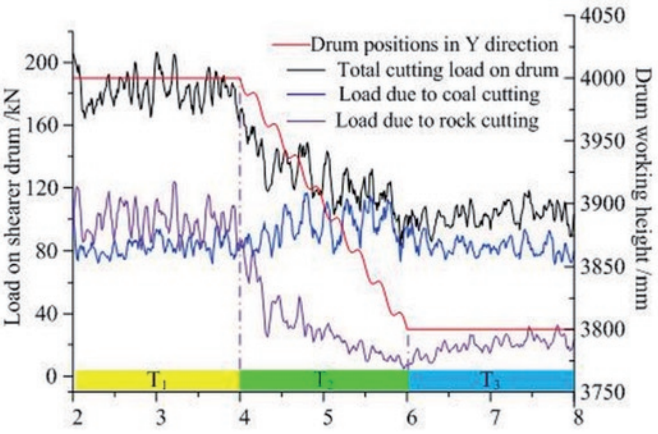

(a) Cutting load on shearer drum at different working heights

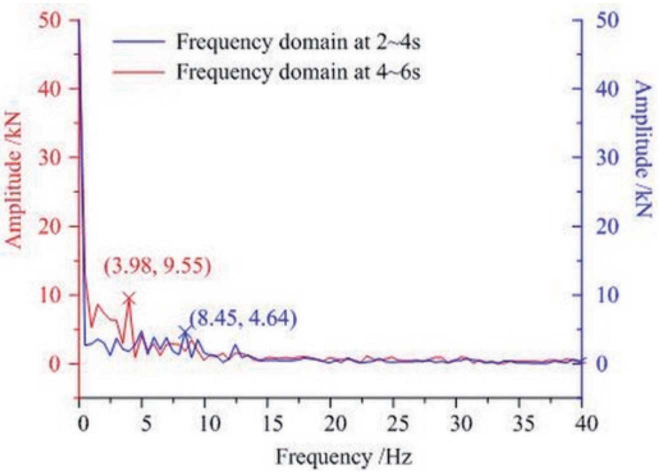

(b) Amplitude and frequency of drum cutting load

Fig. 16. Cutting load characteristics under drum vibration of f=4 Hz, A=4 mm

tions are studied and the influence of external loads on the piston velocity are also analyzed. Considering the dynamic response of piston in hydraulic cylinder, the cutting performance of shearer drum under vibration conditions is also obtained and the following conclusions can be gotten in the paper:

1. Under external shocks, the dynamic response of the hydraulic system, represented by the piston, performs with different characteristics. When drum works for coal cutting and without height adjustment, the piston velocity varies slightly around 0mm/s and the piston vibration is also slight in this working conditions. When drum works for cutting and is accompanied with height adjustment, large variation of piston velocity appears at the beginning of height adjustment and piston oscillation gets more serious in this process. The worse working conditions of hydraulic system in height adjustment process requires more attention during reliability design.
2. Under the cutting condition of coal and rock mixed strata, the height adjustment of drum is the most common operations. Generally, longer time spent on drum height adjustment process is helpful to decrease the cutting load, but it does not mean that the longer the spent time is, the more conducive it is to the decrease of the cutting load. In addition, the frequency of cutting load is influenced by the vibration frequency of shearer drum. Reducing the high-frequency vibration on shearer drum is an effective way to reduce fluctuation of cutting load and improve reliability in the process of height adjustment.

Acknowledgement

This work was supported by the National Natural Science Foundation of China [Grant No. 52174146], the National Natural Science Foundation of China [Grant No. 51674155], the Key Research and Development of Shandong Province (Exploration and Mining of Deep Resources) [Grant No.2019SDZY01].

Reference

1. Bilgin N, Demircin MA, Copur H, Balci C, Akcin AA. Dominant rock properties affecting the performance of conical picks and the comparison of some experimental and theoretical results. International Journal of Rock Mechanics & Mining Science 2006; 43(1): 139-156, https://doi.org/10.1016/j.ijrmms.2005.04.009.
2. Chen PJ, Meng M, Ren R, Miska S. Modeling of PDC single cutter – Poroelastic effects in rock cutting process. Journal of Petroleum ence and Engineering 2018; 183: e106389, https://doi.org/10.1016/j.petrol.2019.106389.
3. Gao MY, Zhang K, Zhou Q, Zhou HF, Liu BL, Zheng GJ. Numerical investigations on the effect of ultra-high cutting speed on the cutting heat and rock-breaking performance of a single cutter, Journal of Petroleum Science and Engineering 2020; 190 e107120. https://doi.org/10.1016/j.petrol.2020.107120.
4. Gao KD, Meng ZS, Jiang K, Zhang HZ, Zeng QL. Shearer height adjustment based on mechanical-electrical-hydraulic cosimulation. IEEE Access 2020; 8: 222064-222076, https://doi.org/10.1109/ACCESS.2020.3043516.
5. Jaime MC, Zhou Y, Lin JS. Finite element modeling of rock cutting and its fragmentation process. International Journal of Rock Mechanics & Mining Sciences 2015; 80: 137-146, https://doi.org/10.1016/j.ijrmms.2015.09.004.
6. Li GH, Wang WJ, Jing ZJ, Zuo LB, Wang FB, Wei Z. Mechanism and numerical analysis of cutting rock and soil by TBM cutting tools. Tunnelling and underground space technology 2018; 81: 428-437, https://doi.org/10.1016/j.tust.2018.08.015.
7. Liu JX, Zheng HL, Kuang YC, Xie H, Qin C. 3D Numerical Simulation of Rock Cutting of an Innovative Non-Planar Face PDC Cutter and Experimental Verification. Applied Sciences 2019; 9(20), e4372, https://doi.org/10.3390/app9204372.
8. Li W, Fan QG, Wang YQ, Yang X F. Adaptive height adjusting strategy research of shearer cutting drum. Acta Montanistica Slovaca 2011; 16: 114-122, https://doi.org/10.1111/j.1755-6724.2011.00389.x.
9. Li W, Luo CX, Hai Y, Fan QG. Memory cutting of adjacent coal seams based on a hidden markov model. Arabian Journal of Geosciences 2014; 7: 5051-5060, https://doi.org/10.1007/s12517- 013-1145-5.
10. Bołoz, L. Interpretation of the results of mechanical rock properties testing with respect to mining methods. Acta Montanistica Slovaca 2020; 25(1):81-93, https://doi.org/10.46544/AMS.v25i1.8.
11. Menezes PL, Lovell MR, Avdeev IV. Studies on the formation of discontinuous rock fragments during cutting operation. International Journal of Rock Mechanics & Mining Sciences 2014; 71 (2014): 131-142, https://doi.org/10.1016/j.ijrmms.2014.03.019.
12. Menezes PL. Influence of rock mechanical properties and rake angle on the formation of rock fragments during cutting operation. International Journal of Advanced Manufacturing Technology 2017; 90: 127-139, https://doi.org/10.1007/s00170-016-9342-5.
13. Pan YC, Liu QS, Peng XX, Liu Q. Full-Scale Linear Cutting Tests to Propose Some Empirical Formulas for TBM Disc Cutter Performance Prediction. Rock Mechanics & Rock Engineering 2019; 52: 4763–4783, https://doi.org/10.1007/s00603-019-01865-x.

14. Stachurski W, Midera S, Kruszyński B. Mathematical model describing the course of the process of wear of a hob cutter for various methods of cutting fluid supply. Eksploatacja i Niezawodnosc – Maintenance and Reliability 2016; 18 (1): 123–127, http://dx.doi.org/10.17531/ein.2016.1.16.
15. Samui P, Kumar R, Kurup P. Determination of Optimum Tool for Efficient Rock Cutting. Geotechnical and Geological Engineering 2016; 34: 1257-1265, https://doi.org/10.1007/s10706-016-0035-5.
16. Wyk G, Els DNJ, Akdogan G, Bradshaw SM, Sacks N. Discrete element simulation of tribological interactions in rock cutting. International Journal of Rock Mechanics & Mining Sciences 2014; 65: 8-19, https://doi.org/10.1016/j.ijrmms.2013.10.003.
17. Xiong C, Huang ZW, Yang RY, Sheng M, Shi HZ, Dai XW, Wu XG. Comparative analysis cutting characteristics of stinger PDC cutter and conventional PDC cutter. Journal of Petroleum Science and Engineering 2019; 189(1), e106792. https://doi.org/10.1016/j.petrol.2019.106792.
18. Yang XW, Zou XF, Zhang S, Chen HY, Wei YJ, Li PF. Dynamic behavior of coal shearer under the influence of multiple factor in slant-cutting conditions. Scientific Reports 2021; 11(1), e18447. https://doi.org/10.1038/s41589-021-98049-x.
19. Yang Y, Fan H, Ma PC. Research on dynamic characteristics for longwall shearer cutting transmission system with varying cutting speed. International Journal of Precision Engineering and Manufacturing 2017; 18: 1131–1138, https://doi.org/10.1007/s12541-017-0132-2.
20. Yang SY, Ou YB, Guo Y, Wu XM. Analysis and optimization of the working parameters of the impact mechanism of hydraulic rock drill based on a numerical simulation. International Journal of Precision Engineering & Manufacturing 2017; 18: 971-977, https://doi.org/10.1007/s12541-017-0114-4.
21. Yang DL, Li JP, Wang YX, Jiang HX. Analysis on vertical steering vibration of drum shearer cutting part. Journal of Central South University. 2018; 25: 2722-2732, https://doi.org/10.1007/s11771-018-3949-7.
22. Zhang ZH, Gao WL, Li KP, Li BJ. Numerical simulation of rock mass blasting using particle flow code and particle expansion loading algorithm. Simulation Modelling Practice and Theory 2020: 104(2), e102119. https://doi.org/10.1016/j.simpat.2020.102119.
23. Zhen C, Mao S, Li GS, Huang ZW, Wu XG, Zhu ZP. Imaging the formation process of cuttings: Characteristics of cuttings and mechanical specific energy in single PDC cutter tests. Journal of Petroleum Science and Engineering 2018; 171: 854-862, https://doi.org/10.1016/j.petrol.2018.07.083.
24. Zhou W. Simulation of Hydraulic System Faults for Marine Machinery Based on AMESim. Journal of Coastal Research 2019; 94(S1): 357-361, https://doi.org/10.2112/SI94-073.1.
25. Zhang YF. Research on trajectory tracking and its control strategies of drum shearer. Zhejiang University, 2014.03.19.
26. Zeng QL, Gao KD, Zhang HZ, Jiang SB, Jiang K. Vibration analysis of shearer cutting system using mechanical hydraulic collaboration simulation. Proceedings of the Institution of Mechanical Engineers Part K Journal of Multi-body Dynamics 2017: 231: 708-725, https://doi.org/10.1177/1464419317705986.

EKSPLOATACJA I NIEZAWODNOŚĆ
MAINTENANCE AND RELIABILITY

Eksploatacja i Niezawodnosc – Maintenance and Reliability

Volume 24 (2022), Issue 1

journal homepage: http://www.ein.org.pl

Article citation info:
Zdziebko P, Martowicz A, Uhl T. Multi-domain approach to modeling pantograph-catenary interaction. Eksploatacja i Niezawodnosc – Maintenance and Reliability 2022; 24 (1): 130–139, http://doi.org/10.17531/ein.2022.1.15.

Multi-domain approach to modeling pantograph-catenary interaction

Indexed by: Web of Science Group

Paweł Zdziebko[a,*], Adam Martowicz[a], Tadeusz Uhl[a]

[a]AGH University of Science and Technology, Faculty of Mechanical Engineering and Robotics, Department of Robotics and Mechatronics, al. A. Mickiewicza 30, 30-059 Krakow, Poland

Highlights

- Multi-domain simulation for a pantograph-catenary system has been proposed.
- Analysis of importance of physical domains included in the model has been performed.
- Aerodynamics has been identified as the most influential domain in the model.
- It has been shown that the electromagnetic induction force can be neglected.

Abstract

When a railway pantograph interacts with a catenary during the movement of a rail vehicle, several physical phenomena, both mechanical and electrical, occur in the system. These phenomena affect the quality of power supply of a train from traction devices. The unfavourable arcing occurring when there are disturbances of contact between the pantograph's slider and the catenary contact wire. In turn, it results in energy loss and increased wear of the components of the system. When designing new solutions, computational models are helpful to predict the quality of interaction between the components of the pantograph-contact line system already at the virtual prototyping stage. In this paper, the authors comprehensively present a multi-domain (multiphysics) model, which takes into account necessary conditions for interaction between pantograph elements and a catenary. Finally, the impact of the individual physical domains are analysed and the ones which have a significant impact on the simulation of the operation results are identified.

Keywords

pantograph-catenary system, dynamic interaction, multi-domain approach, numerical simulation, Finite Element Analysis, multibody dynamics, co-simulation.

1. Introduction

The pantograph mechanism is used for receiving electrical power from a catenary. It is used in trams, freight locomotives, and high-speed passenger trains. A typical 160ECT [10] pantograph is presented in Figure 1. When interacting with a catenary, a collector head with carbon strips is in a sliding contact with a catenary contact wire. The electrical power is transferred through the pantograph structural elements (arms, links and frame), and then to the electrical system of the rail vehicle.

Increases in trains speeds are observed for years and require improvements to the various components of the whole system, covering both vehicles and the entire infrastructure. Due to the proportional relationship between the train speed and the current consumed from the traction system, the mechanisms for collecting power from the catenary is one of the factors limiting the maximum speed of trains. Figure 2A presents the main components of the catenary system.

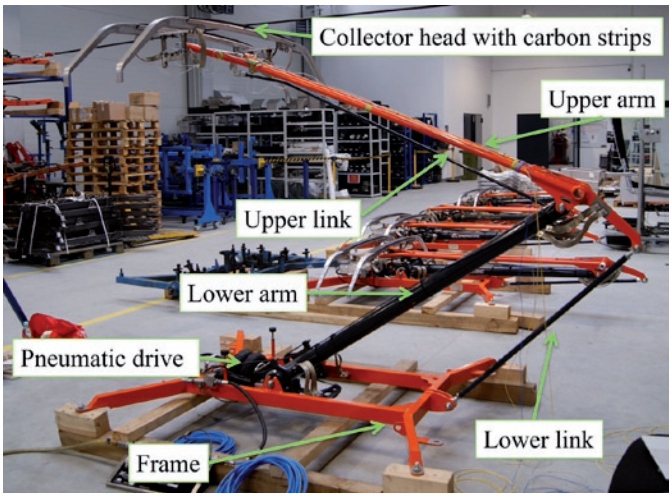

Fig. 1. Pantograph mechanism on a test stand

(*) Corresponding author.
E-mail addresses: P. Zdziebko (ORCID: 0000-0001-6845-033X): zdziebko@agh.edu.pl,
A. Martowicz (ORCID: 0000-0001-9630-0355): adam.martowicz@agh.edu.pl, T. Uhl (ORCID: 0000-0002-4332-3067): tuhl@agh.edu.pl

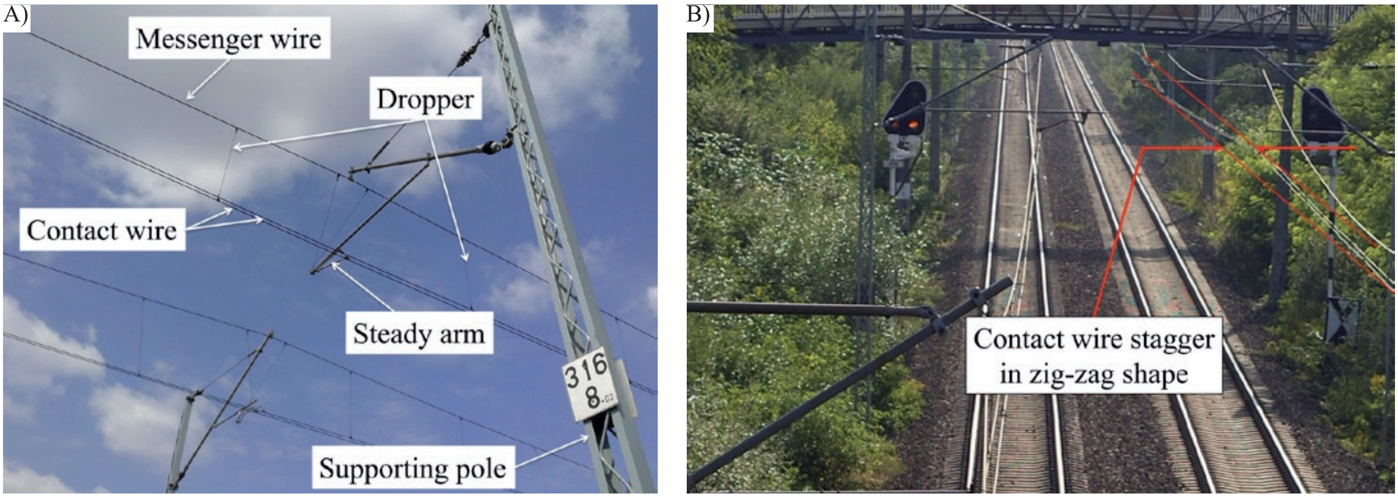

Fig. 2. Description of the catenary system: (A) components of the catenary system and (B) catenary staggering – photographs taken by Pawel Zdziebko

The catenary is a flexible, periodic structure which consists of a contact wire and a messenger wire. The messenger wire is suspended to the poles with supporting arms, while the contact wire is suspended to a messenger wire using droppers and steady arms. On straight track sections, the catenary is staggered as shown in Figure 2B. This makes the pantograph slider wear evenly when travelling over long straight sections, because the contact point keeps moving from side to side of slider. Contact and messenger wires are subjected to tension, which reduces the unevenness of the stiffness of the catenary. Railway power supply systems are considered to be critical in terms of reliability, it is also postulated that they should be treated as critical for safety [24]. At high speeds, fluctuations in contact force (CF) are observed. They may lead to a loss of contact between the pantograph head and the contact wire. Even small disturbances in contact, lasting a few milliseconds, may cause arcing in the contact area. This results in the increased wear on the components, that remain in contact, due to heating and melting the materials. Thermal wear is one of the important factors limiting the lifetime of the pantograph slider and reliability of the system [9]. Increased wear of contact strips increase the risk of fatal failure in pantograph-catenary interaction. In the recent paper [17] authors emphasize that very strict monitoring of contact strips is extremely important, because its timely replacement guarantees trouble-free operation and no need for costly and long-lasting repairs. The authors proposed an evaluation method of preventive renewal strategies of railway vehicles selected parts, which has been demonstrated for contact strips case study . The research on thermal and mechanical wear of the contact wire and pantograph head strip [3, 5, 23] shows that the increased uplift force between the pantograph and the traction reduces arcing, but at the same time, increased sliding friction force increases mechanical wear. Pombo et al. [27] concludes that the use of two pantographs on a single rail vehicle significantly influences fluctuations in CF. However, with appropriately adjusted pantograph spacing, such a configuration may improve dynamic interaction with the catenary[18]. The latest studies also indicate the significant impact of the rail vehicle on the resulting quality of the interaction between the pantograph and the catenary. The research conducted by Song et al. [30] shows that poor track quality reduces the quality of the pantograph's interaction with the catenary.

The numerical models of dynamic interaction between the catenary and pantograph are commonly used for designing the system components. Moreover, the Technical Specifications for Interoperability (TSIs) issued by the European Commission require the presentation of numerical results for positive certification process of the pantographs and overhead contact lines components. Those documents define the technical and operational standards which must be met by the pantograph-catenary system components in order to meet requirements and ensure the interoperability of the railway systems.

The simplest computational models for simulating the interaction between the pantograph and the catenary with the lumped parameters date back to the 1970s [13, 14]. Models with one [31, 32] or more [26, 28] degrees of freedom (DOFs) are based on a variable stiffness representing the catenary system. A small number of DOFs results in high computational performance for these models. Above mentioned elementary models provide an overall understanding of the interaction between the pantograph and the catenary, but they still exhibit several imperfections. The most important ones are the mechanical wave propagation in the overhead contact line being overlooked, followed by significant oversimplification of the pantograph model. These drawbacks result in a failure to properly validate these models according to the applicable EN 50318 standard [11]. Application of the Finite Element Method (FEM) in the catenary model allows one to account for propagation and reflection of the mechanical wave [15] on the overhead contact line and the nonlinear characteristics of the droppers. Such improvements allowed one to obtain a positive validation results against the EN 50318, as published by Carnicero et al. [4].

Simplified pantograph models with lumped parameters are being replaced by the Multibody Dynamics (MBD) models, as demonstrated, by Ambrosio et al.[2], Pappalardo et al. [25], and Song et al. [29]. In these models, rigid pantograph components, described by geometry, material, and inertial properties, are interconnected using rotating and sliding kinematic pairs. To enable simulations using the FEM model of the overhead contact line and the advanced MBD pantograph model, it is necessary to use the co-simulation procedure as shown in work by Massat et al. [20] and Ambrosio et al. [1]. This algorithm relies on exchanging data between the pantograph and catenary models during the simulation. This approach allows to simultaneously take advantage of the FEM model of the catenary and the MBD model of the pantograph. Simulations based on co-simulation procedure are currently the most advanced method for numerically testing the pantograph-catenary system.

Despite the computational models used being highly sophisticated, it should be highlighted that there is still a need to improve them. The model that would simultaneously take into account the effects of all relevant forces and torques which are affecting pantograph-catenary interaction is needed. The authors' review showed that the models reported in the literature usually ignore such phenomena as the effects of aerodynamic forces, electromagnetic forces, or rail vehicle dynamics. Moreover, it is not clearly defined which phenomena are necessary in modelling and which can be ignored due to the small influence on the obtained results of numerical simulations. In response to the imperfections of existing models, in this paper, we use a multi-domain approach for analysing the interaction of the pantograph and catenary. The purpose of the works presented herein is to build a multi-domain numerical model describing the behaviour of the overhead contact line and pantograph system including all potentially important factors. Another goal is to investigate effect of their omission in the multi-domain simulation model and propose guidelines for pantograph-catenary modelling process in this field.

This paper consists of the following parts: In Section 2, we present the proposed multi-domain model of the catenary-pantograph system. Section 3 describes the details of the FEM model of the catenary, including the shape-finding methodology and validation results for this model. Next, Section 4 presents the details of the MBD pantograph and rail vehicle model. Section 5 presents the simulation results for the tested 160ECT pantograph. This Section also investigates the influence of individual phenomena omission on the results of the multi-domain model simulation. Finally, conclusions are presented in Section 6.

2. Multi-domain simulation of a pantograph-catenary system

As already mentioned in the literature review in Section 1, there is still a need to develop computer modelling and simulation techniques for the pantograph-catenary system. Such a model should be considered as multi-domain system, because the resulting interaction between the pantograph with the catenary is affected by various phenomena. In the paper, we present the methodology for conducting computer simulations for a multi-domain model of pantograph and catenary. The system under consideration has been presented schematically in Figure 3.

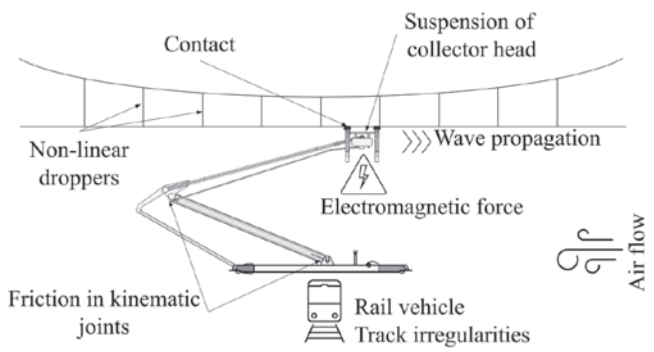

Fig. 3. Physical phenomena in the pantograph-catenary interface

Figure 3 shows schematically important phenomena that can have a key impact on the quality of the interaction between the pantograph and the overhead contact line. In the proposed numerical model, the following are taken into account:

- Three-dimensional pantograph model, which reflects a kinematic chain of the mechanism, with friction model in kinematic joints.
- Model of the rail vehicle together with track irregularities which causes vibration of the vehicle body, and then, vibration of the pantograph frame.
- Aerodynamic and electromagnetic forces, which acts on the pantograph components and influence the pantograph uplift force.
- Nonlinearities of the catenary system, resulting from the nonlinear stiffness of droppers and relatively large displacements of cables.
- The phenomenon of mechanical wave propagation in the overhead lines during the passage of the pantograph and rail vehicle.

For the studies presented in this paper, we assumed a straight-line section of a track and catenary. The pantograph mechanism is located on the roof of the rail vehicle. Due to the specificity of the modelled system, it is necessary to describe interactions between its components with significantly different stiffness properties. Therefore, we used the MBD approach for modelling the pantograph and the rail vehicle. The rail vehicle travels on tracks described using the vertical irregularities profile for each rail independently. The pantograph's kinematic joints are modelled with dry sliding friction. The proposed pantograph model also takes into account the impact of aerodynamic forces. They have a significant effect on the CF when travelling at high speed. The electromagnetic force, induced by the current conducted through the catenary and the pantograph head, has also been taken into account. We modelled the flexible catenary system using the FEM and took into account propagation and reflection of the mechanical wave in its structure. The catenary model accounts for the non-linear nature of the droppers which are made of a steel cable that remains stiff under tensile stress but is elastic in compression.

Figure 4 presents a diagram with computer simulations proposed herein. The proposed approach to simulating pantograph interaction with traction is based on integrated FEM-MBD model, and thus the model shall be treated as coupled. The data exchange between these partial models is carried out using the co-simulation procedure. First, sub-models are formulated to determine the pre-configuration of the catenary and calculate the electromagnetic and aerodynamic forces acting on the pantograph components. These models are later described in the paper. At the same time, other relevant parameters of the rail vehicle and pantograph model are defined, such as the speed of the rail vehicle, the profile of the vertical track irregularities, the coefficient of friction in the pantograph kinematic pairs, the nominal uplift torque of the pantograph (responsible for the static uplift force of the pantograph slider), and the suspension parameters of the pantograph slider. Next, the dynamic interaction between pantograph and catenary using co-simulation is lunched. The procedure is based on data exchange in subsequent calculation steps between FEM (catenary) and MBD (pantograph-rail vehicle assembly) models. In order to ensure high quality of the FEM and MBD models, validation of

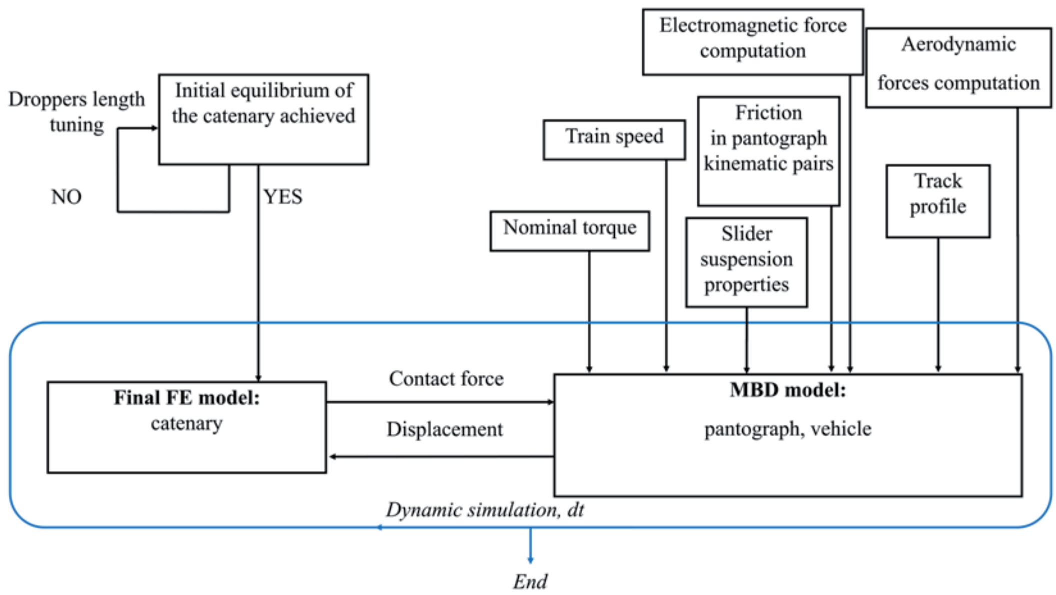

Fig. 4. The proposed multi-domain approach for pantograph-catenary simulation

selected sub-models is needed to be carried out (to the extent available to conduct). The catenary model is validated against the EN 50318, while the MBD pantograph model is formulated based on the technical data provided by the manufacturer, and therefore is assumed to be realistic. Collector head suspension properties, friction in kinematic joints and aerodynamic properties were identified experimentally, and thus reflects real working conditions. Rail vehicle and track irregularities model was not validated, but taken from the literature – as described later in text.

The proposed procedure for calculating the dynamic multi-domain co-simulation is as follows:

Step 1:

For the current input parameters and the adopted computational step, the MBD model of the pantograph and rail vehicle is solved. The equations of motion are solved using the Hilber -Hughes-Taylor integration scheme [21]. The calculations yield the current position of the pantograph slider head, which is then transferred to the FEM model of the catenary.

Step 2:

Then, for the same computational step, the FEM model of the catenary is solved by taking into account the current position of the pantograph slider head, as determined in the MBD model. The integration procedure used in the FE model is the Single-Step Houbolt scheme, which is unconditionally stable [21]. Next, number of iterations with frozen time are being computed to allow the two models (MBD and FEM) to agree on both force and displacement. Usually less than 10 iterations are needed for convergence. These calculations yield instantaneous CF acting on the contact wire of the catenary and the pantograph head.

Step 3:

The instantaneous value of the CF is then transmitted to the MBD model, which is solved for the next computational step, thus taking into consideration the subsequent positions of the rail vehicle and the pantograph resulting from the assumed vehicle speed and the size of the computational step.

Step 4:

Return to Step 2.

The steps for solving model equations described in points 2 and 3 are repeated in a loop for all the computational steps in the time interval used for analysis. In all the considerations presented in this work, the assumed simulation time corresponds to the travel of a rail vehicle along the 10 catenary spans (600 m), and the computational step is 0.001 s, similarly as proposed by Cho et al. [6].

3. Catenary FEM model

A very important phenomenon described in the literature, which influences the contact between the pantograph slider and the contact wire, is the propagation of the mechanical wave in the wires and its reflection from the rigid traction components. Therefore, the FEM is used for catenary model. The overhead contact line model used in the analysis corresponds to the model described in the EN 50318 [11]. The catenary has one contact wire and one messenger wire, nine droppers per span, and a single span length of 60 m. The height of the catenary is 1.2 m and the zig-zag stagger is ±0.2 m. The catenary model under consideration has been schematically represented in Figure 5.

The boundary conditions in the model reflect actual operating constrains that are present in real centenaries. The effect of gravity on traction components, the tensioning forces in the traction lines are considered as well. The wires in the catenary structure exhibit tensions of 16 kN (contact wire) and 20 kN (messenger wire). The linear density of cables is 1.07 kg/m and 1.35 kg/m respectively for the contact wire and the messenger wire. Due to the occurrence of staggering in zig-zag shape, the structure of the overhead contact line is modelled in

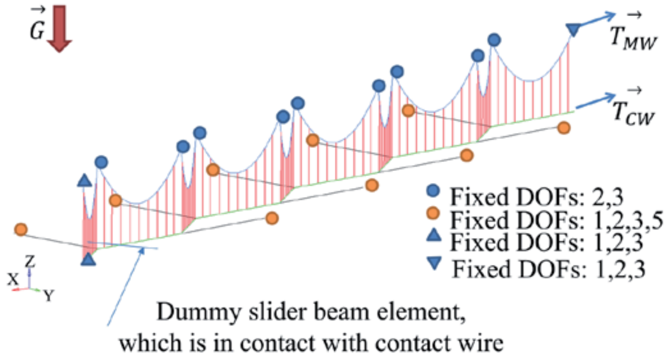

Fig. 5. The FEM model of a simple catenary system modelled as 3-D structure

three dimensions. According to the reference model description in the Standard, the catenary model does not take into account damping.

The diameter of wires is considerably smaller than their length, so the traction model uses 1D finite elements. These are type 98 elements (MSC.Marc solver) that take into account shear forces [22]. The model includes 100 elements per span for both the contact wire and the messenger wire. The assumed average length of the beam elements is 0.6 m. Such a size is considered small enough [28] and also allows to perform simulations efficiently.

The droppers exhibit nonlinear behaviour and they transmit tensile loads while remaining very loose during compression. To account for such bi-linear stiffness, elastic elements with nonlinear stiffness characteristics were used: 0 N/mm for compression and 100 N/mm for tension.

As shown in Figure 5, the rail vehicle and the pantograph move in a direction (-X). The position of the pantograph head, which is determined based on the MBD model, is related to the position of the dummy slider beam element modelled with the FEM model. This component is in contact with the contact wire. The contact algorithm used is the beam-to-beam contact which is available in MSC.Marc solver [21]. Contact is detected when the smallest distance between the dummy slider beam element and the contact wire is less than the assumed threshold value, i.e. 0.1 mm. The algorithm then automatically introduces a multipoint constraint equation to ensure that the elements do not interpenetrate. During the subsequent integration steps, the point of contact between the elements may change as the elements move relative to each other and stay in contact. In such a case, the multipoint constraint equation is automatically updated.

3.1. An initial configuration (pre-sag) of catenary

The pre-sag is an important parameter of the catenary which influences the dynamic interaction between the traction and the pantograph [7]. According to the adopted model of the catenary, the pre-sag is set to 0 mm. It is therefore necessary to adjust the length of the subsequent droppers to obtain zero pre-sag at the centre of the span under gravity and tension. The established procedure for determining the initial configuration of the catenary model has been schematically presented in Figure 6.

For the initially defined model (*Initial configuration, step 1*), we determine the difference between the required sag (0 mm) and the calculated sag value at the point of attaching droppers to the contact wire. Then, the model is reconfigured and the dropper lengths are corrected for the difference determined in the previous step (*initial configuration, step 2*). The procedure for static calculations and correction of droppers length is repeated until the sag value meets the requirements. To determine pre-sag, it was necessary to run nine iterations to adjust the droppers length, which were found as: 995.5; 813.8; 657.0; 563.0; 531.7 mm respectively for droppers counting from the end to the centre of a single span. Additionally, position of a fixed end of steady arms were found as translated from span ends by [0; 257.3; (+/-) 966.3] on X, Y and Z components respectively. Sign '+/-' for Z

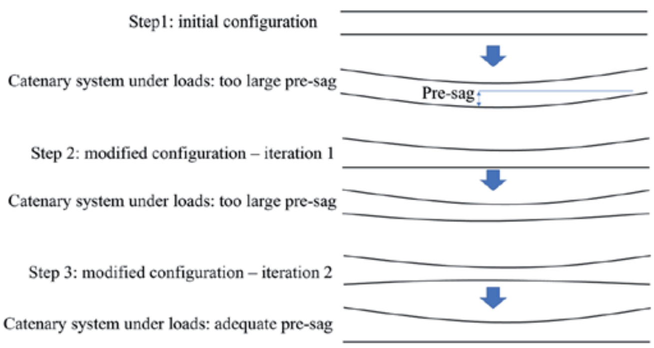

Fig. 6. Iterative procedure for determining catenary state under initial loads

translation corresponds to zig-zag shape for subsequent spans. Resulting pre-sag error for designed model of the catenary is less or equal 0.13 mm.

3.2. Catenary model validation

The subsequent step of the work included validation of the numerical model. The standard solution consists of performing experiments and comparing the results obtained for the CF course and the contact wire uplift with the numerical model. This can only be done by measuring CF indirectly, and is expensive and difficult. During our work, we validated the numerical model based on basic validation procedure described in the EN 50318. The process of validation of the numerical model consists of comparing statistical parameters describing the course of CF and contact wire lift with the tolerances given in this standard for precisely described catenary model. The standard utilizes basic pantograph model with lumped parameters and two degrees of freedom. Detailed information on the pantograph model can be found in the previously referenced standard. The validation procedure requires the statistical parameters of CF and contact wire uplift to be determined. The results are then compared with the allowable limits given by that standard. Simulation were performed for passage speed 250 km/h and 300 km/h. Please note that the computed statistical parameters are determined for a limited amount of data, i.e., for the two central spans of the catenary. Such an approach aims to exclude the impact of the boundary conditions on the results obtained. In case of CF results, they are filtered using a low-pass filter with a cut-off frequency of 20 Hz. Figure 7 presents results obtained in computer simulations for 250 km/h passage speed, but similar results were obtained also for passage speed 300 km/h. Results of uplift of contact wire at steady arms' location are presented in Figure 7A, while Figure 7B depict simulated CF in pantograph-catenary interface. Vertical lines in both figures depict section of two central spans of catenary. The integration time steps in both cases (250 and 300 km/h) were the same and set to 0.001 s.

Statistical parameters of the CF and wire uplift courses are computed next. The results are provided in Table 1. It can be noted that all parameters are within the acceptance ranges for both analysed passage speeds. Therefore, the obtained results successfully validated the numerical model according to the adopted methodology described in the Standard. It can be concluded that the formulated catenary model reflects the real dynamic behaviour of the catenary with deviations accepted by the standard.

4. Pantograph and rail vehicle model

The validity of the pantograph model is very important for the representation of the realistic interaction with catenary. Important factors affecting how the pantograph cooperates with the catenary, which are taken into account in the model developed here, include the vibrations of the railway vehicle that are transmitted to the pantograph frame, the influence of electromagnetic and aerodynamic forces on the pantograph components, energy dissipation through friction in the kinematic joints of the pantograph, and the actual spatial structure of the pantograph kinematic chain.

The model of the pantograph mechanism was formulated using the MBD method. With this method the number of degrees of freedom can be reduced compared to the FEM model, making the MBD model computationally efficient. At the same time, this modelling method allows for the implementation of forces resulting from all the relevant phenomena that affect the pantograph components. The model was formulated using the MSC.Adams package. For the formulation of the MBD model, it is necessary to define spatial configuration of the pantograph components and joints between them. The developed pantograph model is shown in Figure 8.

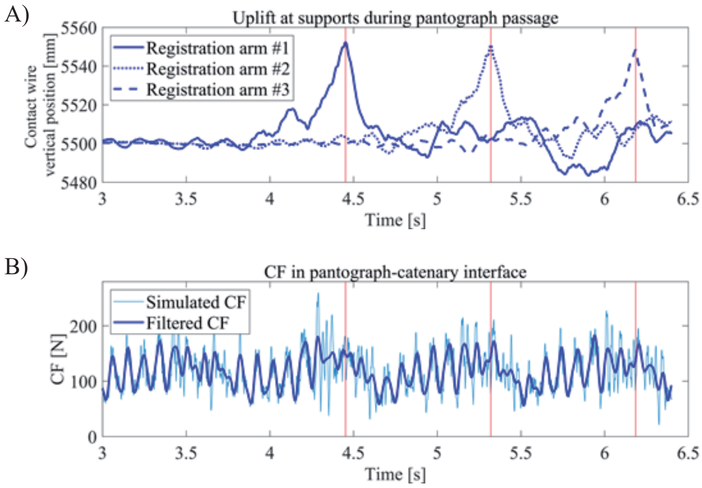

Fig. 7. Results of computed contact wire uplift (A) and CF (B) in case of 250 km/h train speed

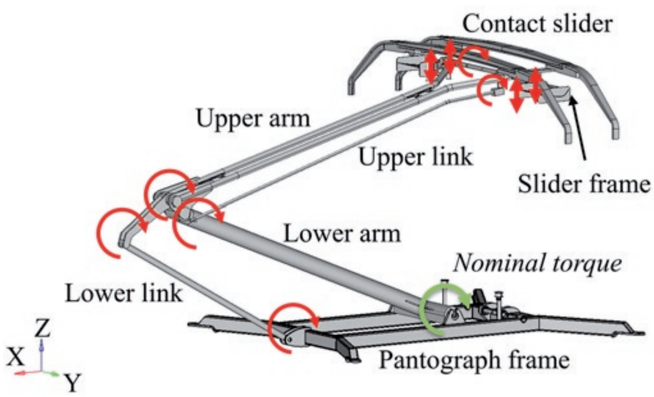

Fig. 8. Scheme of pantograph MBD model

All the modelled pantograph components are marked in the scheme. Their mass and moment of inertia parameters are taken from the manufacturer's technical documentation. There are rotational kinematic pairs between the components marked with circular arrows. In addition, in the place where the revolute joint is found between *the pantograph frame* and *lower arm* components torque forcing applies from the pantograph pneumatic drive (*Nominal torque*). Linear arrows show the locations of the pantograph head suspension springs in the model. The stiffness and damping parameters of the slider suspension are fundamental in determining the quality of cooperating with the catenary. Thus, experimental testing was necessary to identify the characteristics of the slider suspension for the utilized 160ECT pantograph. The results of performed experiments are presented in our recent paper [34]. Experimentally determined stiffness and damp-

Table 1. Catenary model validation results

Parameters		Simulation results	Accepted ranges	Simulation results	Accepted ranges
Speed [km/h]		250	250	300	300
Mean CF [N] F_M		117.7	110-120	117.9	110-120
Standard deviation of CF [N] σ		28.17	26-31	36.3	32-40
Statistical maximum of CF: $F_M + 3\sigma$		202.21	190-210	226.8	210-230
Statistical minimum of CF: $F_M - 3\sigma$		33.19	20-40	9	(–5)-20
Actual maximum of CF [N]		182.5	175-210	205.5	190-225
Actual minimum of CF [N]		56.63	50-75	33.6	30-55
Maximum uplift at supports [mm]	Support 1	52.4	48-55	57.2	55-65
	Support 2	51		60.1	
	Support 3	48.4		60.7	
Percentage contact loss [%]		0	0	0	0

ing properties of slider suspension are implemented next in the numerical model as lumped parameters elements (K=3.93 N/mm and C=0.0005 Ns/mm).

The pantograph system dissipates some amount of energy thanks to the friction torque that is present in kinematic pairs. Our recently presented study [35] made it possible to fine-tune the dry friction coefficients in the revolute joints to reflect the experimentally determined characteristics of energy dissipation by friction in joints of the pantograph.

The dynamics of the rail vehicle is also an important factor influencing the interaction of the pantograph with the catenary. A rail vehicle with two-level suspension with two bogies and eight wheels was taken into account in our model. The scheme of the model has been presented in Figure 9.

The parameters of the rail vehicle model are taken from the work by Zboiński et al. [33]. The rail vehicle moves in the negative direc-

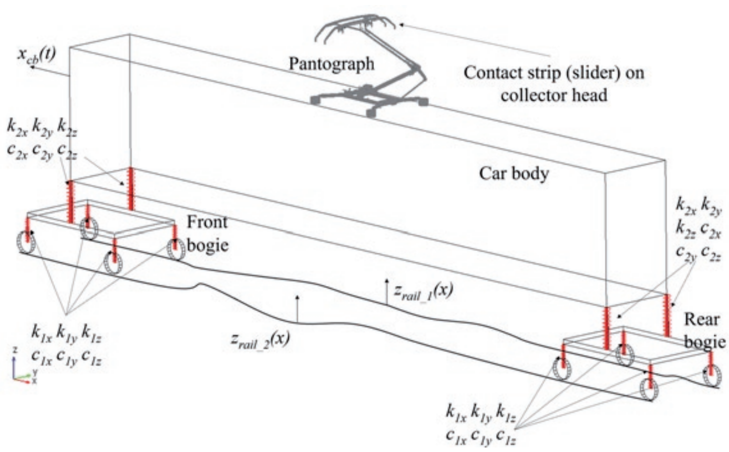

Fig. 9. Scheme for a rail vehicle model

tion relative to the global X direction at a pre-defined speed. During the run, the vehicle wheels are subjected to vertical track irregularities. With a model formulated in this way, it is possible to take into account vibrations of the rail vehicle body. In turn, those vibrations affect the pantograph frame, and therefore influence the current collection quality.

In reality, there are also lateral track's profile irregularities, but in this study we consider only vertical ones, since they are of the greatest importance when driving on straight-line sections of tracks (and such a section is simulated). The track vertical irregularities profile has been generated based on the methodology published in the work by Karttunen et al. [16]. The authors presented formula that allows to describe irregularities as a random data characterized by the following expression for the power spectral density (PSD) in spatial form:

$$S_A(\lambda) = 2\pi \frac{A_A \cdot \Omega_c^2}{\left(\left(\frac{2\pi}{\lambda}\right)^2 + \Omega_r^2\right) \cdot \left(\left(\frac{2\pi}{\lambda}\right)^2 + \Omega_c^2\right)} \tag{1}$$

where $\Omega_c = 0.82$ rad/m, $\Omega_r = 0.02$ rad/m are pre-set cut-off frequencies and λ is the wavelength in [m], wavelengths are taken in range of 3-150 m, and a number of 500 waveforms were used to generate realistic profiles. The parameter A_A [m·rad] corresponds to the amplitude of irregularities and the utilized value of $4.1 \cdot 10^{-7}$ represents a medium quality track. To obtain the track irregularities profile in sense of a distance function, the PSD formula is retransformed using the inverse Fourier transform with random phases. Importantly, the courses obtained are characterized by randomness, while their statistical parameters meet the criteria for the middle class of track quality.

In the considerations presented in this work, we have computed the individual track profiles for the right and left rails separately. The vertical irregularities generated using above mentioned procedure and implemented in the multi-domain model are shown in Figure 10.

4.1. Aerodynamic and electromagnetic induction forces

Aerodynamic forces are one of the external forces loading pantograph components. Especially at high speeds they influence the dynamic interaction between pantograph and catenary. The current standard for railway applications describes acceptable average CF ranges for different train speeds, including the aerodynamic effects on pantograph [12]. Dai et al. [8] in their recent research investigated the influence of additional baffles application in the pantograph head. The goal was to tune the aerodynamic lift force on the pantograph components, which influences the CF mean value. Thanks to the great influence of aerodynamic forces, the multi-domain model

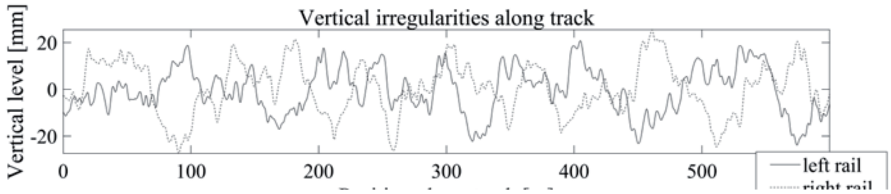

Fig. 10. Utilized vertical tracks' profile

its segments, with an assumed finite length, is calculated. The resultant electromagnetic force acting on is calculated as the sum of the forces acting on all segments in each direction. Based on the simulations conducted, we demonstrated that, depending on the working height of the pantograph, electromagnetic force influence may results in an increase of the static uplift force by 2N (Figure 12).

utilised in this paper has to include this phenomenon. Aerodynamic properties for the adopted pantograph model were investigated in our recent paper [36]. In general, the numerical model which employs the Fluid-Structure-Interaction method has been formulated first. Individual aerodynamic forces which load all components of the pantograph were computed then using Altair AcuSolve solver. Next, forces were implemented into the MBD pantograph model, and then the resulting uplift force exerted by the pantograph head on the contact wire was computed. Experimental tests were performed in the wind tunnel as well, for numerical model validation. The key results of this research are presented in Table 2.

The results obtained for the numerical model and in the experiment showed a high agreement (relative error up to 2%),

Table 2. Uplift force under aerodynamic forces

Uplift force	Air flow speed [km/h]		
	120	140	160
Experiment [N]	124.2	129.4	135.4
Numerical model [N]	122.2	128.9	135.4
Relative error	2%	0.4%	0.4%

which prove positive numerical model validation. It should be noted that, in fact, the pantograph moves at a certain speed and thus makes the surrounding air to flow around it. In the conducted numerical analyses and tests in the wind tunnel, the opposite situation was assumed: the stationary pantograph interacted with a forced stream of air at a given velocity. Such a simplification is used in practice, such as in ref. [8], in order to limit the number of factors influencing the uplift force. Indeed, the aim of the research was to determine only the influence of aerodynamics - with omission of other factors, which is impossible during the actual journey of the vehicle. In order to best reflect the operating conditions of the pantograph, the experimental tests were carried out in a wind tunnel with an open measurement space. Thanks to it the impact of disturbed flow in the boundary layer of wind tunnel was minimized. In the numerical analysis, care was taken to ensure that the model reflects the pantograph on the wind tunnel test stand as accurately as possible.

The electromagnetic force is another potentially important phenomenon taken into account in the multi-domain model of the dynamic interaction between the pantograph and the catenary. According to Liu et al. [19] inclusion of electromagnetic force is one of the directions of the pantograph-catenary models development. In fact the pantograph head through which electric current flows, is located in the magnetic field inducted around the contact wire, as shown schematically in Figure 11.

Considering the above presented assumptions, the pantograph head is affected by the electromagnetic force. The computational model proposed was presented in the work by Zdziebko et al. [37]. For the assumed current load scenario of the contact wire |PRC"ST| the computation rule is as follows. Using Biot-Savart law, the magnetic induction vector is determined at the subsequent points of the pantograph slider head |AB| from individual contact wire pieces |PR|, |RC"|, |C"S|, and |ST|. Then, for the assumed current flow distribution in slider head segments |AC| and |CB|, the electromagnetic force acting on each of

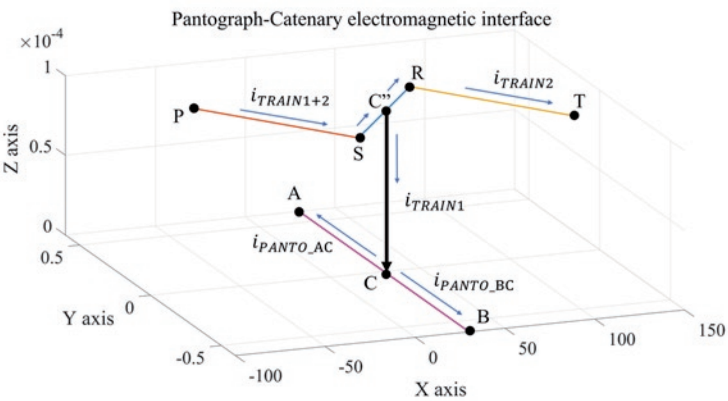

Fig. 11. Scheme of electricity flow in adopted scenario (axis units in [m])

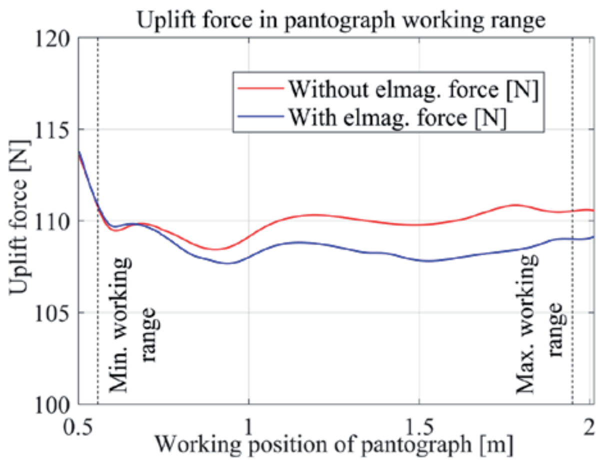

Fig. 12. Influence of electromagnetic force on uplift force for various pantograph working heights

The received results show, that the influence of electromagnetic force on uplift force depends on working height of the pantograph, but is significantly lower than influence of aerodynamic forces.

5. Results of multi-domain simulations

Hereafter we present the results of numerical simulations employing the multi-domain model described in Sections 2 to 4. The computation time for simulating the interaction between the pantograph and the catenary over a 600 m-long section is about 70 minutes. Simulations were performed using an available workstation with the following configuration: CPU Intel R Core^{TM} i7-2600K 3.4GHz x64, 32GB RAM, 1TB HDD.

Results of computed CF for driving speed of 160 km/h is shown in Figure 13A. The analysis of statistical parameters describing variations in the course of the CF was limited to two central spans and was filtered as described in Section 3.2 (Figure 13B). The 160ECT pantograph is certified to a maximum speed of 160 km/h, but for testing purposes, numerical simulations were performed in an extended speed range of 120–200 km/h. The statistical parameters usually em-

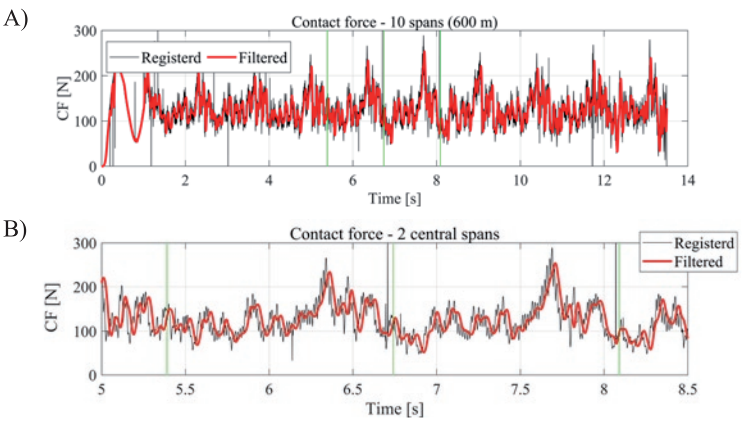

Fig. 13. CF time history computed for 600 m distance (A) and close-up view for the two central spans (B) – vertical lines depict two central spans

ployed to determine the pantograph-catenary interaction quality are shown in Table 3.

Table 3. The results of pantograph-catenary dynamic interaction computed with complex multi-domain model, after low-pass filtration

Rail vehicle speed [km/h]:	120	160	200
Mean CF [N]:	118.4	131.7	132.9
STD of CF [N]:	17.3	38.6	59.6
Min. of CF[N]	82.3	37.2	-3.7 (0N)
Max. of CF[N]	173.2	260.3	290.9
Peak-to-Peak of CF [N]:	90.9	223.1	294.5

The results obtained show that for a train speed of 120 km/h the mean uplift force is much lower than the corresponding value obtained for the higher driving speeds. This is due to aerodynamic forces being significantly reduced when driving at low speed. For higher speeds, the CF exhibits more varied behaviour expressed by relatively higher STD and peak-to-peak CF parameters. At a speed of 200 km/h, detachments of contact strip from the contact wire were observed. In the originally computed CF time history, the value of 0N was recorded while detachments. Nevertheless, the course of CF after filtration was statistically analysed (Table 3), therefore the presented value of Min. of CF is below zero - it is caused by the effect of low-pass filtration.

At a subsequent stage of our work, we investigated the CF in the pantograph-catenary system as well as its change resulting from the choice on the analysed physical phenomena distorting the force interaction in the mentioned system. The analysis consisted of observing selected statistical parameters of the CF in different computational cases where the presence of individual sub-models related to a given physical phenomenon was either ignored or taken into account. The results are presented in Figure 14. The case in which all phenomena described earlier and the corresponding computational models were taken into account was considered as a reference – this case is marked with 'X'. The calculation for the full model resulted in the CF course described by the following statistical parameters: Mean CF of 131.7 N and CF STD of 38.6 N. The analysis was limited only to these statistical parameters and to a single-speed value of 160 km/h.

The simulation results show that the inclusion of aerodynamic forces has the greatest impact on the change in mean CF. The aerodynamic forces exclusion causes the mean CF to decrease approximately by 25 N. On the other hand, small effects of the presence of electromagnetic force on the results obtained have also been noticed. Its omission does not significantly change the results obtained (change in CF STD of 0.6 N and change in mean CF of 1.9 N). If the multi-domain model ignores phenomena associated with the non-linear behaviour of the droppers or friction in kinematic pairs, the STD of CF increases by 7.5 N and 8.4 N respectively. In addition, excluding the track irregularities from the model results in lowering the STD of CF by 4 N compared to the comprehensive multi-domain model, while the mean CF remains at a similar level. Our analysis shows that aerodynamic forces must be included in the model of dynamic interaction between the pantograph and the catenary. Moreover, it is recommended to include a model of non-linear droppers, friction in the pantograph joints, and the dynamics of the rail vehicle and track irregularities. These factors have a significant effect on the change in CF STD, but their impact on the mean CF is negligible. However, electrodynamic forces may be omitted from modelling as they only negligibly affect the results obtained. This applies to the mean CF and CF STD alike.

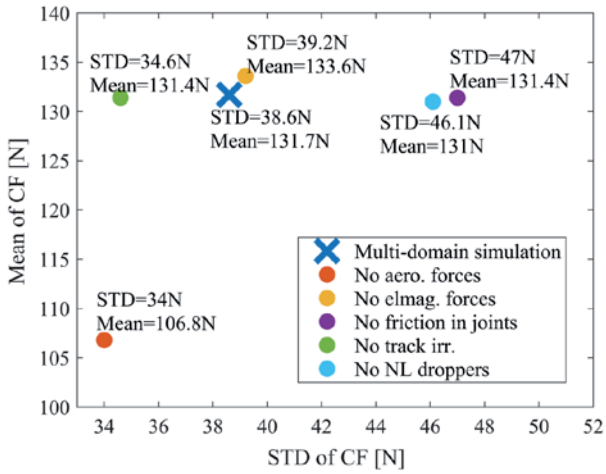

Fig. 14. Influence of physical phenomena exclusion in model on the obtained CF results

6. Summary and concluding remarks

The development of computer simulation techniques dedicated to the pantograph-catenary system is still open to discussion. This system is subjected to several physical phenomena which significantly affect the resulting interaction of the pantograph with the catenary. Computer-aided numerical tools are very helpful when designing new system components and it is necessary to develop them to reflect as accurately as possible the actual operating conditions of the system under analysis. The computational methodology presented in this work allows for the formulation of a multi-domain model, which in turn allows for the analysis of the effects of these phenomena on the dynamics of the pantograph-overhead contact line system. From the literature review presented in the introduction, it can be concluded that such a comprehensive multi-domain model for simulating the dynamic interaction between the pantograph and the catenary has not yet been published. The numerical model proposed hereby states a comprehensive methodology for pantograph-catenary simulations. Together with the inclusion of such phenomena as vibrations from the rail vehicle, the effects of electromagnetic and aerodynamic forces, the propagation of the mechanical wave in the catenary, the actual kinematic chain of the pantograph, together with the friction model in joints and the suspension model of the pantograph (3D) makes the approach to be innovative. The model accounts for strong non-linearity: the contact of the slider and the catenary and the non-linear characteristics of droppers.

The analysis of physical phenomena accounted for in the multi-domain model shows that the model of aerodynamic influence is very significant as it greatly affects the change in the mean CF and CF STD compared to the nominal case. It is also recommended to take into account the model of non-linear droppers, friction in the pantograph joints, the dynamics of the rail vehicle, and track irregularities. Omission of these factors cause the CF STD to change significantly, but no significant change in the mean CF is observed. The impact of electromagnetic force has negligible effect on the results of pantograph-catenary dynamic interaction and thus may be omitted in the modelling process.

Further directions of work are related to development of the computational model with the friction between the slider and the contact wire of the catenary. So far it has not been included in the model and it is potentially an important factor, which may influence the interaction of the pantograph with the catenary. Moreover, development of other traction system (DC/AC) models might be an interesting challenge for multi-system pantographs simulations.

Acknowledgements

First and third co-authors, Paweł Zdziebko and Tadeusz Uhl, declare that the research have been conducted within the scope of the project no. INNOTECH K3/IN3/5/225857/NCBR/14. Moreover, the second co-author, Adam Martowicz, would like to gratefully acknowledge the Department of Robotics and Mechatronics at the AGH University of Science and Technology, Krakow, Poland, for the research subsidy. Finally, all the authors appreciate the company EC Engineering, Poland, for granted access to the investigated pantographs as well as for sharing the technical data and results of experiments.

References

1. Ambrósio J, Rauter F, Pombo J, Pereira M. Co-Simulation Procedure for the Finite Element and Flexible Multibody Dynamic Analysis. 11th Pan-American Congress of Applied Mechanics, January 04-08, 2010, Foz do Iguacu, PR Brasil, 2010.
2. Ambrósio J, Rauter F, Pombo J, Pereira MS. A Flexible Multibody Pantograph Model for the Analysis of the Catenary-Pantograph Contact. In Arczewski K, Blajer W, Frączek J, Wojtyra M (eds): Multibody Dynamics Computational Methods and Applications, Springer: 2011; 23: 1-27, https://doi.org/10.1007/978-90-481-9971-6_1.
3. Bucca G, Collina A. A procedure for the wear prediction of collector strip and contact wire in pantograph-catenary system. Wear 2009; 266(1-2): 46-59, https://doi.org/10.1016/j.wear.2008.05.006.
4. Carnicero A, Jimenez-Octavio JR, Such M et al. Influence of static and dynamics on high performance catenary designs. International Conference on Pantograph Catenary Interaction Framework for Intelligent Control - PACIFIC 2011. Amiens, Francia. 8 Diciembre 2011, 2011.
5. Chen GX, Yang HJ, Zhang WH et al. Experimental study on arc ablation occurring in a contact strip rubbing against a contact wire with electrical current. Tribology International 2013; 61: 88-94, https://doi.org/10.1016/j.triboint.2012.11.020.
6. Cho YH. Numerical simulation of the dynamic responses of railway overhead contact lines to a moving pantograph, considering a nonlinear dropper. Journal of Sound and Vibration 2008; 315(3): 433-454, https://doi.org/10.1016/j.jsv.2008.02.024.
7. Cho YH, Lee K, Park Y et al. Influence of contact wire pre-sag on the dynamics of pantograph-railway catenary. International Journal of Mechanical Sciences 2010; 52(11): 1471-1490, https://doi.org/10.1016/j.ijmecsci.2010.04.002.
8. Dai Z, Li T, Zhou N et al. Numerical simulation and optimization of aerodynamic uplift force of a high-speed pantograph. Railway Engineering Science 2021, https://doi.org/10.1007/s40534-021-00258-7.
9. Ding T, Chen GX, Bu J, Zhang WH. Effect of temperature and arc discharge on friction and wear behaviours of carbon strip/copper contact wire in pantograph-catenary systems. Wear 2011; 271(9): 1629-1636, https://doi.org/10.1016/j.wear.2010.12.031.
10. EC Engineering. Internal report: Pantograph 160ECT. 2016.
11. European Committee for Electrotechnical Standardization EN-50318:2002. Railway applications - Current collection systems. Validation of simulation of the dynamic interaction between pantograph and overhead contact line. 2002.
12. European Committee for Electrotechnical Standardization EN-50367:2012. Railway applications - Current collection systems - Technical criteria for the interaction between pantograph and overhead line). 2012.
13. Grajnert J. Zastosowanie tłumienia w odbieraku prądu. Pojazdy Szynowe 1977.
14. Grajnert J, Marcinkowski J. Zwis wstępny przewodu jezdnego jako czynnik eksploatacyjny kształtowania dynamiki współpracy odbieraka prądu z siecią trakcyjną. Trakcja i Wagony 1982.
15. Jiménez-Octavio JR, Such M, Carnicero A, Lopez-Garcia O. Validation of Simulation Approaches for Catenary-Pantograph Dynamics. Civil-Comp Proceedings 2008; 88: 1-11.
16. Karttunen K, Kabo E, Ekberg A. The influence of track geometry irregularities on rolling contact fatigue. Wear 2014; 314(1-2): 78-86, https://doi.org/10.1016/j.wear.2013.11.039.
17. Lewandowski J, Młynarski S, Pilch R et al. An evaluation method of preventive renewal strategies of railway vehicles selected parts. Eksploatacja i Niezawodnosc – Maintenance and Reliability 2021; 23(4): 678-684, https://doi.org/10.17531/ein.2021.4.10.
18. Liu Z, Jönsson PA, Stichel S, Rønnquist A. Implications of the operation of multiple pantographs on the soft catenary systems in Sweden. Proceedings of the Institution of Mechanical Engineers, Part F: Journal of Rail and Rapid Transit 2016; 230(3): 971-983, https://doi.org/10.1177/0954409714559317.
19. Liu Z, Song Y, Han Y et al. Advances of research on high-speed railway catenary. Journal of Modern Transportation 2018; 26(1): 1-23, https://doi.org/10.1007/s40534-017-0148-4.
20. Massat JP, Laurent C, Bianchi JP, Balmès E. Pantograph catenary dynamic optimisation based on advanced multibody and finite element co-simulation tools. Vehicle System Dynamics 2014; 52(SUPPL. 1): 338-354, https://doi.org/10.1080/00423114.2014.898780.
21. MSC.Software. Marc Volume A: Theory and User information. 2016.
22. MSC.Software. Marc Volume B: Element library. 2016.
23. Nagasawa H, Kato K. Wear mechanism of copper alloy wire sliding against iron-base strip under electric current. Wear 1998; 216(2): 179-183, https://doi.org/10.1016/S0043-1648(97)00162-2.
24. Oz MA, Kaymakcı OT, Koyun A. A safety related perspective for the power supply systems in railway industry. Eksploatacja i Niezawodnosc – Maintenance and Reliability 2017; 19(1): 114-120, https://doi.org/10.17531/ein.2017.1.16.
25. Pappalardo CM, Patel MD, Tinsley B, Shabana AA. Contact force control In multibody pantograph/catenary systems. Proceedings of the Institution of Mechanical Engineers, Part K: Journal of Multi-body Dynamics 2016; 230(4): 307-328, https://doi.org/10.1177/1464419315604756.
26. Park TJ, Han CS, Jang JH. Dynamic sensitivity analysis for the pantograph of a high-speed rail vehicle. Journal of Sound and Vibration 2003; 266(2): 235-260, https://doi.org/10.1016/S0022-460X(02)01280-4.

27. Pombo J, Ambrósio J, Ambrosio J. Environmental and track perturbations on multiple pantograph interaction with catenaries in high-speed trains. Computers and Structures 2013; 124: 88-101, https://doi.org/10.1016/j.compstruc.2013.01.015.
28. Sanchez-Rebollo C, Jimenez-Octavio JR, Carnicero A. Active control strategy on a catenary-pantograph validated model. Vehicle System Dynamics 2013; 51(4): 554-569, https://doi.org/10.1080/00423114.2013.764455.
29. Song Y, Ouyang H, Liu Z et al. Active control of contact force for high-speed railway pantograph-catenary based on multi-body pantograph model. Mechanism and Machine Theory 2017; 115: 35-59, https://doi.org/10.1016/j.mechmachtheory.2017.04.014.
30. Song Y, Wang Z, Liu Z, Wang R. A spatial coupling model to study dynamic performance of pantograph-catenary with vehicle-track excitation. Mechanical Systems and Signal Processing 2021; 151: 107336, https://doi.org/10.1016/j.ymssp.2020.107336.
31. Wu TX, Brennan MJ. Dynamic stiffness of a railway overhead wire system and its effect on pantograph-catenary system dynamics. Journal of Sound and Vibration 1999; 219(3): 483-502, https://doi.org/10.1006/jsvi.1998.1869.
32. Wu TX, Brennan MJ. Basic analytical study of pantograph-catenary system dynamics. Vehicle System Dynamics 1998; 30(6): 443-456, https://doi.org/10.1080/00423119808969460.
33. Zboiński K, Dusza M. Bifurcation analysis of 4-axle rail vehicle models in a curved track. Nonlinear Dynamics 2017; 89: 863-885, https://doi.org/10.1007/s11071-017-3489-y.
34. Zdziebko P, Martowicz A, Uhl T. Experimental and numerical investigation on the components of a pantograph slider suspension. MATEC Web Conf. 2019, https://doi.org/10.1051/matecconf/201925205003.
35. Zdziebko P, Martowicz A, Uhl T. An investigation on the influence of pantograph friction on its interaction with a catenary using co-simulations. Proceedings of ISMA 2018 - International Conference on Noise and Vibration Engineering and USD 2018 - International Conference on Uncertainty in Structural Dynamics, Katholieke Univ Leuven, Dept Werktuigkunde: 2018: 3283-3294.
36. Zdziebko P, Martowicz A, Uhl T. An investigation on the active control strategy for a high-speed pantograph using co-simulations. Proceedings of the Institution of Mechanical Engineers, Part I: Journal of Systems and Control Engineering 2018: 095965181878364, https://doi.org/10.1177/0959651818783645.
37. Zdziebko P, Martowicz A, Uhl T. An investigation into multi-domain simulation for a pantograph-catenary system. ITM Web of Conferences 2017; 15: 03001, https://doi.org/10.1051/itmconf/20171503001.

Eksploatacja i Niezawodnosc – Maintenance and Reliability
Volume 24 (2022), Issue 1
journal homepage: http://www.ein.org.pl
Article citation info:
Semenov I, Jacyna M. The synthesis model as a planning tool for effective supply chains resistant to adverse events. Eksploatacja i Niezawodnosc – Maintenance and Reliability 2022; 24 (1): 140–152, http://doi.org/10.17531/ein.2022.1.16.

The synthesis model as a planning tool for effective supply chains resistant to adverse events

Indexed by: Web of Science Group

Iouri Semenov[a], Marianna Jacyna[b,*]

[a]WSB University in Poznań, 5 Powstańców Wielkopolskich, 61-895 Poznań, Poland
[b]Warsaw University of Technology Faculty of Transport, 75 Koszykowa str. Warsaw, Poland

Highlights

- Planning modular supply chains enables them to be adapted to flexible innovative transformation.
- The method of synthesis is the basic tool for creating an effective and reliable sequence of modules.
- The modular supply chain synthesis should be a continuous and uniform process.
- The synergy effect can measure the effectiveness of designing modular, reliable supply chains.

Abstract

The article presents the problem of planning effective modular supply chains to resist adverse events. The lack of effective models for planning such supply chains based on the synergy of individual links widens the knowledge gap in this area. The analyses confirm the legitimacy of forming effective and reliable supply chains ready for fitting supplies to specific orders, adaptation to flexible and innovative transformations, and minimization of time losses and costs of restoring supply capacity in case of a threat. The authors provide a theoretical analysis of the problem and present a proprietary approach to constructing reliable modular supply chains in the automotive industry. It has been shown that the synergy effect can measure the effectiveness of the design of such chains. A proprietary synthesis model was presented. The model can serve as a tool to support the planning of modular supply chains that are resistant to adverse events.

Keywords

synthesis model, structural-functional module, supply chains effectiveness, process reliability.

1. Introduction

Since the beginning of the customer era, logistics operators or service companies operating in different areas or regions have to be more and more flexible in adapting to the requirements of customers and the changing market requirements [9, 46, 66]. The most visible changes relate to the modern automotive economy. They include increasingly differentiated rules for the operation of the new car production industry and the after-sales service of end-of-life vehicles for maintenance and repair [25].

This requires companies to offer an extended range of services, complicating the process of constructing supply chains, increasing costs, and determining the emergence of new threats to the smooth supply of spare parts and accessories, particularly in the automotive aftermarket [27]. As many studies show, the possibility of undesirable events in supply chains is associated with vulnerability to threats, disruptions or uncertainty, and in some cases, with the security of the supply chain [1, 16, 17].

In response to these challenges, networks of cooperating carriers, logistic centres, warehouses and loading points [26, 57, 30] are being created. On the European transport services market, more than 60% of participants in such networks are classified in the segment of small and medium-sized enterprises - SMEs [5]. This is because big market players can provide the supplies of the ordered goods on their own. At the same time, smaller enterprises are forced to look for orders supplementing the regular activities to increase their profitability [2], including services related to fleet management [54]. For these companies, cooperation in the service market becomes a strategic necessity to obtain financial flow through.

Research [20] shows that SMEs manage many different and interconnected relationships throughout the supply chain. Whereas [13] Faisal et al., by researching three Indian clusters of SMEs, indicated that managing risk in the supply chain requires a large exchange of information, close relationships and partners, and the adjustment of incentives and knowledge about the risk.

This article highlights the fundamental difference in procurement processes in the automotive market in the case of:

- fulfilment of procurement as an integral part of the production process; to mitigate the effects of a collapse in the supply chain, the use of factory stocks of auto parts is planned,
- realization of supplies in the service segment of the automotive market; with this approach, neither service centres nor car workshops create significant stocks of spare parts, which forces service companies to become highly flexible in the supply of parts and to quickly restore the supply capacity of chains in the event of a breakdown in supply.

According to the authors, meeting the requirements of flexibility and quick restoration of the supply chain's capacity is possible when

(*) Corresponding author.
E-mail addresses: I. Semenov (ORCID: 000-0002-2250-9591): iouri.semenov@wsb.szczecin.pl, M. Jacyna (ORCID: 0000-0002-7582-4536): marianna.jacyna@pw.edu.pl

adopting a modular approach to create such a structure of supply chains. It allows contractors to:

- quick design of effective and reliable supply chains of spare parts and accessories tailored to specific orders,
- adaptation of supply chains to their flexible innovative transformations,
- minimizing the loss of time and costs of restoring the supply chain's resourcing capacity in emergencies.

Such an approach requires the development of unified modules both in the organizational and communication sphere and information interfaces of individual participants of the entire process. Considering the above, this article presents the concept model of planning effective and reliable modular supply chains resistant to adverse events and indicates the most important applications. The proposed approach combines many aspects: constructing the supply chains of spare parts and accessories adapted to specific orders, adapting supply chains to their flexible innovative transformations, and minimizing the loss of time and costs of restoring supply capacity in the event of a threat. The results obtained from the model can be used to support decision-making in planning modular supply chains resistant to adverse events based on various goals, such as lowering the cost of completing tasks, risk of fulfilling orders, etc.

Following the presented research methodology, the article's structure was planned as follows. Section 2 presents the theoretical background of the analysed problem and a literature review in the field of risk-based supply chain design. It also indicated a proprietary approach to constructing supply chains in the automotive industry. Section 3 describes the decision problems involved in designing supply chains for spare parts and accessories. The general mathematical formulation of the model and the procedure are presented in section 4. Section 5 describes the results of the case study of modular supply chain planning. In contrast, section 6 of the article discusses the challenges and possibilities of using the proposed approach in economic practice.

2. Literature review

The analysis of the literature on the subject allows us to state that the construction of supply chains can be carried out using both the integration approach [67] and the modular approach [7, 10]. The difference between these approaches is that the constructing process is based on maximum integrity in the first case. The second case is based on the rational selection of modules as components of supply chains. As shown in Figure 1, an unreliable supplier can be replaced at the request of the customer to reverse the supply chain's capacity quickly.

According to Clark and Baldwin [7], modularity should be seen as a concept based on interdependence between modules included in the supply chain and independence between modules not included in this chain. In addition, it was emphasized that when using a modular approach, attention should be paid to the fact that:

- isolating business activity as a certain structure-function module is a kind of abstraction because full business independence is not possible,
- there is a phenomenon of hiding information, which is defined in the literature as information asymmetry, which makes it difficult to select appropriate modules,
- the unification of interfaces should be carried out to connect modules while constructing the supply chains quickly.

As Jacyna-Gołda I. [31] points out, all elements (links) v, v' belonging to the ld-th ($v, v' \in V(ld)$, $ld \in \boldsymbol{LD}$) of the chain must meet their separate performance expectations. This means that its components can be treated as a reliability system for the entire series. The failure of one or more elements means a failure of the entire chain. Conversely, the reliability of individual elements of the supply chain means that it can meet performance expectations in all markets around it. Hence,

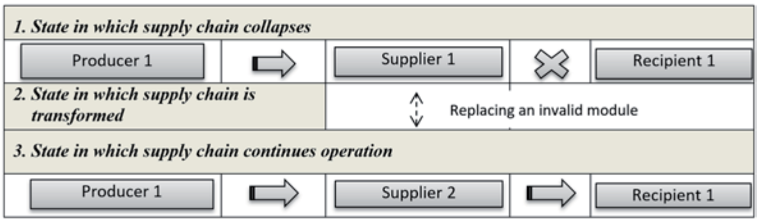

Fig. 1. Restoration of the supply chain's resupply capacity following an adverse event

for the entire supply chain, assuming that it has a serial structure, its *VNS*(*ld*) reliability in a structural sense can be determined as follows [29], [31]:

$$\forall ld \in \boldsymbol{LD} \quad WNS(ld) = x(ld) \cdot \prod_{(v,v') \in \mathbf{L}(ld)} nl(ld,(v,v')) \cdot \prod_{v \in \mathbf{V}(ld)} nv(ld,v)) \tag{1}$$

The most important factor determining effective supply chain management is credibility and trust in the relationships between the partners. Therefore, the key factors in achieving the sustainable success of enterprises and the development of each supply chain are increasing trust among partners and creating effective and reliable connections in the implementation of logistic tasks [34].

The authors of the paper argue that the only way to manage complex systems is to break them down into smaller pieces, then hide the complexity of each part behind an abstraction depicted as a module and introduce the links between modules - interfaces. In other words, modularization is the process of „... *creating a complex product or service from smaller subsystems that can be designed independently but work together as a whole*" [10]. Modularization is based on the concepts of "modular system" and "design using a modular approach."

The modular system is a set of activities:

- related to the development of databases of discrete unified units to be used in the designs of various chains,
- related to the development of standard interfaces, and
- used to create a sequence of selected modules by connecting their interfaces to achieve the intended result.

Thus, designing using a modular approach constructs supply chains by selecting their components from a set of unified units with interfaces, hereinafter called modules, which can be independently created, modified, or exchanged between the designed chains.

An important problem in designing supply chains of spare parts and accessories is the right choice of connections between cooperating modules [50]. Much attention to this problem was devoted in publication [8]. On the other hand, Spring and Santos [56] categorize such connections, noting the difference between structural and procedural interfaces. Structured interfaces refer to the physical dimension of service modules, while procedural interfaces refer to the service provided by this module. Procedural interfaces focus on integrating the offer of services and relating to the service provider and the customer [45].

Another categorization was proposed in Van der Laan [60], who noticed the difference between functional and organizational interfaces. Functional interfaces combine modules' functions and affect the procurement task results. Organizational interfaces connect partners during delivery, including customers. Although many researchers point out that capturing the multidimensional and interdependent risk [17] and its dynamic nature [51] is necessary for designing supply chains. The individual modules are sensitive, vulnerable to threats and various disruptions and safety. Aspects related to the design of internal and external processes should also be taken into account [42].

Moreover, when designing supply chains in a modular approach, not only the risk assessment, the probability factor and the level of impact are important aspects [63] but also the dependencies of the weak links that are related to:

- time, e.g. time delays, delivery time and delivery schedule [22, 48],
- functionally, e.g. stocks, production, products, transport [24, 64],
- relational, e.g. knowledge, social aspects, communication, suppliers and customers [3, 41].

For example, Nooraie and Parast [48] emphasized that identifying and eliminating many undesirable situations is possible long before reaching a critical state by modelling various scenarios. On the other hand, Heckmann I. in [22] presented a model built using the FTA (*Fault Tree Analyzes*) to analyse the symptoms of single threats in terms of timely deliveries.

Importantly, understanding supply chain risks promotes internal integration and strengthens alert capacities [53]. As the author points out, this enables enterprises to identify the risk associated with the supply chain in advance and shorten the obvious consequences or eliminate them.

Consumer perceptions of the risks associated with remanufactured products have been analysed by Wang et al. [61] using structural equation modelling on the example of the Chinese automotive spare parts industry. In the research, 288 respondents were tested to show that the perceived total risk was influenced by partial risks, such as physical risk, financial risk, time risk, resource risk, etc. As Ganguly [15] notes, the inability to integrate all relevant risks into the model can be problematic and potentially limits its effectiveness in categorizing supply chain risk and creating the risk assessment portfolio.

Similar studies with structural equation modelling were carried out by Yeh [63] and involved 851 suppliers of raw materials and spare parts for the Taiwanese automotive industry. In this case, the research results indicated a positive relationship between resources, trust, and commitment to supplier relationships and the electronic supply chain and a negative attitude to risk in case of electronic collaborative relationships. Similar studies were carried out by Wieland and Wallenburg [62] based on data collected from 270 respondents from three countries: Germany, Austria and Switzerland.

Identifying the risk in the supply chain is an ongoing process that may change over time. The potential risk may not be a future risk due to the development of new products or processes [67]. Therefore, we should strive to create system integration that will increase the visibility and transparency of risk throughout the entire supply chain [6, [33, 58].

Many studies in the last decade indicate the need to take into account the risk associated with the supply chain at the stage of its designing ([28, 37] or [44]) or the physical design of the supply chain [38]. The authors of the works [32, 35] discussed the relationship between contractors of tasks in the supply chain and the risk associated with it, e.g., the supplier-buyer relationship.

Frazzon E. M. et al. [14] drew attention to the fact that risk is related to costs. They use simulation and model oriented to minimize unplanned interruptions in the supply chain of car service stations and maintain their operating costs at an optimal level. They performed the simulations to improve procurement by optimizing logistic tasks in terms of economic and environmental efficiency.

Similarly, Ho C. et al. [23] built a model to assess the procurement cost depending on the effectiveness of the supply chain, which is implemented in the conditions of cooperation of various companies within the three-tier ERP (*Enterprise Resource Planning*) system. Deloitte Consulting approached the problem a bit differently [9]. They developed a model which uses information gathered through expert interviews, the experience of managers gained from organizing previous deliveries, and/or information collected through condition monitoring and historical databases. It was found that applied assumption causes a lack of flexibility in the information flows and the incompleteness of the obtained results. Thus, it limits the proper assessment of the resilience of supply chains to risks.

On the other hand, Luksch S., [43] uses a model that considers the uncertainty resulting from the lack of complete and reliable information about inbound suppliers. However, it does not take into account random threats to individual links in the supply chain. He W. [21] approached the issue differently by using the model to develop forecasts ensuring safe goods stocks.

The analysis of the literature revealed several substantive gaps regarding:

- failure to take into account the various effects that arise during cooperation within supply chains,
- omitting the use of synthesis methods when constructing supply chains,
- no justification for the design of unique supply chains beyond the claim that such chains can be “perfectly” matched to specific procurement tasks. However, it should be emphasized that achieving ideal solutions is impossible because chains function in a changing environment.

When supplementing the above-mentioned substantive gaps, the authors focus, in particular, on the specificity of horizontal cooperation of suppliers. Particular attention has been paid to the SME segment due to its major share of the delivery services market in the economy of various regions. In the changing environment, service companies must develop such strategies for the performance of procurement that would correspond to their expanding scope. According to the authors, in most cases, such strategies enable avoiding adverse events. Therefore, the article proposes the use of:

- a modular approach taking into account the synergetic effects that arise during the cooperation of modules,
- synthesis methods as the basic tool for creating a sequence of modules,
- a multi-criteria evaluation model that considers the availability of a given module to resources and techniques reducing the manifestations of threats, the speed of its response to emergencies, and the minimization of costs for the performance of delivery tasks.

2. Knowledge acquisition as a stage of synthesis of the supply chains structures

2.1. Knowledge Mining

The effectiveness of the subcontractors’ selection depends on the completeness of both the list of companies offering transport and logistics services and the information on their servicing capabilities. The analyses show that such information is not always consistent and reliable. To supplement the necessary information, it is proposed to use data exploration techniques (i.e., data mining) [49, 59], which were used for:

1. Anomaly detection,
2. Association rules,
3. Sorting of the search result.

The Apriori algorithm [4, 36] was chosen as the basic technique of knowledge mining. It detects combinations of logical events in data subgroups based on an “*if-then*” procedure, the application of which is based on the fact that:

- analysed information is sufficient because it brings together the basic number of companies offering their transport and logistics services,
- it is possible to divide the collected information into a small group of clusters.

For information processing, the authors adopted the following assumptions:

1. The database contains all the information on the most important transport and logistics market players.

2. The information space topology in the database is discrete. The values of the data parameters only take discrete values, which creates the basis for the decision to lock them into certain combinations of modules useful for achieving goals by the supply chain.
3. The gathered information is arranged as a square matrix and sufficient for successfully selecting 1st generation modules.
4. The selection process is carried out by referencing the combination of functional parameters of each module to the best values of such combinations characterizing the early selected modules.
5. The parameter sets of each of the selected 1st-generation modules can be used as the coordinates of the information space grid nodes of the structure of the designed supply chain. Such a mapping makes it possible to limit the number of further analysed module combinations.
6. Each selected 1st generation module should meet all requirements to create conditions for synergy effects during interaction with other modules.
7. The number of modules selected for subsequent analyses should be minimal but sufficient for implementing the transport and logistics task.

The recommendations regarding the advisability of using the analysed 1st-generation modules in the structure of the designed supply chain were developed during the research. Information instability creates gaps in the knowledge of decision-makers, increases their uncertainty and, consequently, becomes the cause of wrong decisions. This situation worsens due to the lack of certainty in the accuracy of the mathematical representation of transport and logistics activities, which creates premises for a low assessment of their credibility.

Supply chain activities are typically unique and cannot be accurately described by incomplete information gathered from past experiences. Various approaches to knowledge gathering are used to solve this problem, both with traditional planning methods (e.g., flexible planning, lean planning) and synthesis methods (in the sets of modules or in databases). To alleviate the above-mentioned difficulties, the authors introduced a two-stage procedure of knowledge mining useful in practical decision-making during for construction of supply chains (Figure 2).

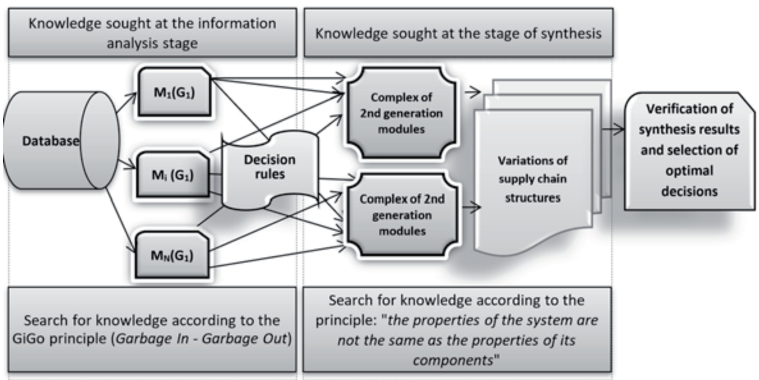

Fig. 2. The concept of a two-step search for knowledge in supply chain synthesis models

In line with this idea, the concepts of 2-generation modules have been introduced. Modules can be combined into stable two or three-module complexes to detect information about the chances of synergy effects in the case of their permanent cooperation.

2.2. Knowledge mining algorithm

A procedure for identifying 1st generation modules and their formation into a uniform complex was developed. The sequence of steps in selecting modules to be included in the chain structure is shown in Figure 3, and its practical implementation was carried out using the Apriori algorithm [4, 36, 65].

At the first stage, the process of acquiring new knowledge is aimed at acquiring a set of 1st generation modules. The information collected in database is structured, and the participants of the service market (0-generation modules) are selected as hypothetically useful to perform tasks within the chain (set $D\left[M\left(G_0\right)\right]$). Decisions about the capabilities of each 0-generation module (*Candidate Counting*) are based on the analysis of the parameters $P_z = \left(p_0, \ldots, p_n\right)$, their efficiency $\left(P_{iw}\right)$ and resistance $\left(P_{iod}\right)$, Figure 3.

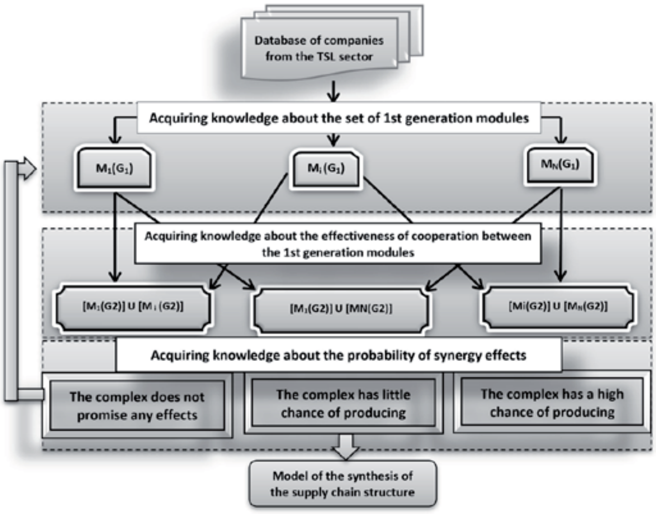

Fig. 3. Concept of the process of acquiring new knowledge in the supply chain synthesis model

A comparative assessment of the values of structural and functional parameters of modules with the minimum permissible values is performed. Then the set of 1st generation modules can be presented in the form:

$$\left[M_i(G_0)\right] \rightarrow D\left[M_i(G_1)\right], \text{if} \left\{\forall M_i\left(G_0\right)\left[\left(\Sigma P_{iw} \geq P_{wmin}\right) \& \left(\Sigma P_{iod} \geq P_{min}\right)\right]\right\} \quad (2)$$

where:

$\left(P_{iw}\right)$ – parameters of the *i*-modules of the 1st generation characterizing their performance,

$\left(P_{iod}\right)$ – parameters of *i*-modules of the 1st generation resistant to threats.

The module selection process continues until the following condition is met:

$$D\left[M_i\left(G_1\right)\right] \geq N_s \quad (3)$$

where:

$M_i\left(G_0\right)$ – set of „Mi" modules with retrieved parameters, $\left[M_i\left(G_0\right)\right] \in D\left[M_i\left(G_1\right)\right]$,

N_s – number of executive modules included in the structure of the supply chain, $s = 1 - S$.

Modules selected for the 1st generation are sorted according to their performance and resilience levels. For this purpose, the weight value function is used (Table 1):

$$Wi = \frac{1}{2^{i-1}} \quad (4)$$

Unselected market participants are collected in the set $D\left[M_j\left(G_0\right)\right]$:

$$D\left[M_j\left(G_0\right)\right] \notin D\left[M_i\left(G_1\right)\right] \quad [5]$$

The acquired knowledge is subjected to assessing the accuracy of decisions made with Boolean algebras. If the module parameters $M\left(G_0\right)\left[\left(P_{iw}\right),\left(P_{iod}\right)\right]$ are below accepted level, then its inclusion in the next generation is a wrong decision:

$$M\left(G_0\right)\left[\left(P_{iw}\right),\left(P_{iod}\right)\right] \rightarrow M_i\left(G_1\right) \subseteq \text{[set of wrong decisions]} \quad (6)$$

If the analysed module parameters $M\left(G_0\right)\left[\left(P_{iw}\right),\left(P_{iod}\right)\right]$ are above the accepted level, its inclusion in the next generation is the right decision:

$$M\left(G_0\right)\left[\left(P_{iw}\right),\left(P_{iod}\right)\right] \rightarrow M_i\left(G_1\right) \subseteq \text{[set of good decisions]} \quad (7)$$

The condition for the completion of the decision validity process is to analyse all tested modules stored in the database:

$$D\left[M\left(G_0\right)\right] \supseteq \left\{D\left[M_j\left(G_0\right)\right] + D\left[M_i\left(G_1\right)\right]\right\} \quad [8]$$

At the second stage of the process of acquiring new knowledge, modules with indicator values at an acceptable level are included in the set of 2nd generation candidate modules. The rest of the modules are not considered further and remain in the database as candidates. The step is carried out using Boolean algebras and consists of the alternative:

Case 1: The required compatibility level $\left(P_{ik}\right)$ of the module $\left[M_i\left(G_1\right)\right]$ is achieved:

$$\left[M_i\left(G_1\right)\right] \in D\left[M\left(G_2\right)\right], \quad if \quad \left\{\forall M_i\left(G_1\right)\left[\sum P_{ik} \geq P_{kmin}\right]\right\} \quad (9)$$

Case 2: The required compatibility level $\left(P_{ik}\right)$ modułu $\left[M_j\left(G_1\right)\right]$ is not achieved:

$$\left[M_j\left(G_1\right)\right] \notin D\left[M\left(G_2\right)\right], \quad if \quad \left\{\forall M_i\left(G_1\right)\left[\sum P_{ik} \geq P_{kmin}\right]\right\} \quad (10)$$

The module files included and not included in the 2nd generation set include all or most of the 1st generation modules collected in the database:

$$D\left[M\left(G_1\right)\right] \supseteq \left\{\left[M_j\left(G_1\right)\right] \& D\left[M_i\left(G_2\right)\right]\right\} \quad [11]$$

At the third stage of acquiring knowledge, the sufficiency of the acquired modules is assessed. The sufficiency condition is the basic task in the synthesis of the supply chain structure. The lack of even one 2-generation module makes it impossible to build an integrated structure as incapable of providing the required transport and logistics services:

$$D\left[M_i\left(G_1\right)\right] \geq LM_{min} \quad (12)$$

where:

$M_i\left(G_1\right)$ – set of 1st generation modules, $\left[M_i\left(G_1\right)\right] \in D\left[M_i\left(G_0\right)\right]$

LM_{min} – the minimum number of modules needed to complete the tasks.

At the fourth stage of knowledge acquisition, the 1st generation modules, ordered according to performance and resistance parameters, are assessed according to the ability to cooperate (compatibility level P_k).

$$P_k = \begin{vmatrix} 0, \textit{ in case of incompatibility}; \\ \in [0;1], \textit{ in case of partial compatibility (e.g. geometric)}; \\ 1, \textit{ in case of full compatibility (ideal situation)}. \end{vmatrix} \quad (13)$$

Table 1. Weight index values

Analysed 0-generation modules		Absolute value	Relative value	Recommended decision
1	$\left[M_{i1}\left(G_0\right)\right]$	1,00	0,25	module is accepted into the basic list of 1st generation modules
2	$\left[M_{i2}\left(G_0\right)\right]$	1,00	0,25	module is accepted into the basic list of 1st generation modules
3	$\left[M_{i3}\left(G_0\right)\right]$	0,750	0,189	module is accepted into the additional list of 1st generation modules
4	$\left[M_{i4}\left(G_0\right)\right]$	0,500	0,126	module is accepted into the additional list of 1st generation modules
5	$\left[M_{i5}\left(G_0\right)\right]$	0,310	0,078	module is accepted conditionally
6	$\left[M_{i6}\left(G_0\right)\right]$	0,187	0,047	module is accepted conditionally
7	$\left[M_{i7}\left(G_0\right)\right]$	0,110	0,028	module is accepted conditionally
8	$\left[M_{i8}\left(G_0\right)\right]$	0,062	0,016	module is not accepted
9	$\left[M_{i9}\left(G_0\right)\right]$	0,035	0,009	module is not accepted
10	$\left[M_{i10}\left(G_0\right)\right]$	0,0195	0,005	module is not accepted

As most of the connections correspond to a situation of partial compatibility, all modules from the set $D\left[M_i\left(G_1\right)\right]$, are analysed, and the evaluation procedure is based on their compatibility indicators $\left(WK\right)$, which can be assessed as follows:

$$WK = 1 - \frac{N\left(L_k\right)}{\sum_s N_s} \tag{14}$$

where:

$N\left(L_k\right)$ –the number of links needed for the module to provide the required level of compatibility;

N_s – the total number of links needed by the module to complete the assigned tasks.

The value of the compatibility index is variable within limits [0; 1]:

$$\begin{cases} WK = 0 \text{, in case of } N\left(L_k\right) = \sum_i N_i \\ WK = 1 \text{, in case of } N\left(L_k\right) = 0 \end{cases} \qquad [15]$$

The analysis shows that the greater the ability of a module to co-operate, the smaller number of links ensures their compatibility with other modules belonging to the supply chain structure. In addition to the links ensuring required compatibility, each module needs links to perform planned tasks. At this stage, the essence of the knowledge mining procedure is the analysis of events in which the module under consideration may take an active part while performing planned tasks. This ability is defined as „Support" by the analysed module of providing transport and logistics services in the supply chain.

The „Confidence" procedure verifies declared ability of the module to participate in the planned executive tasks actively. The procedure consists in assessing the probability that the module $\left[M_i\left(G_2\right)\right]$ will be able to jointly perform the intended tasks together with the module $\left[M_k\left(G_2\right)\right]$ already included in the supply chain structure. If the probability is above the required level, then the analysed module is included in the 2-generation set $D\left[M_i\left(G_2\right)\right]$.

The above analyses show that a given module $\left[M_i\left(G_1\right)\right]$ has the support of W_s, if its cooperation with the module $\left[M_k\left(G_2\right)\right]$ is effective in 95% of events predicted in the analysed period. Then:

$$SUPPORT\left[M_i\left(G_1\right)\right] \cup \left[M_k\left(G_2\right)\right] = \left(W_s\right)\left[M_i\left(G_1\right)\right] \cup \left[M_k\left(G_2\right)\right] \; for\; ZT \geq 0{,}95 - 0{,}97 \qquad [16]$$

$$CONFIDENCE\left[M_i\left(G_1\right)\right] \cup \left[M_k\left(G_2\right)\right] = P\left(W_s\right)\left[M_i\left(G_1\right)\right] \cup \left[M_k\left(G_2\right)\right] \qquad [17]$$

At the fifth stage of acquiring new knowledge, a decision is made to use the procedure of supplementing the set of 2-generation modules (in case of a shortage of modules for the implementation of the chain tasks as a whole) or to proceed with the implementation of synthesis procedures (combining selected 2-generation modules into complexes containing two or three components).

Acquiring the knowledge gathered on the list of 1st-generation modules triggers acquiring knowledge about 2nd-generation modules, which, when cooperate, can be:

- combined into interlocked complexes, creating more efficient supply chains,
- excluded from the structure of the supply chain (lean supply chains),
- shifted in structure to increase the chain's resistance to environmental changes.

3. Model of supply chain synthesis

3.1. Model assumptions

The ability of the constructed supply chain to provide services depends on the number of subcontractors in its structure. The achievement of the appropriate size can be determined by the parameter CMI (*Critical Mass Index*). In our case, CMI indicates the minimum number of modules included in the chain so that the tasks included in the order are fulfilled and the costs incurred by subcontractors do not exceed the acceptable limits.

The authors of the article propose to focus on creating conditions for synergy effects after meeting these primary conditions. One of these conditions is the inclusion of technologically advanced subcontractors in the list of 2nd generation modules. The fulfilment of this condition is possible assuming that:

- any situation requiring changes in the supply chain structure is an opportunity to increase the quality of services by achieving the maximum level of synergy effects,
- in a situation of increased competition and new, unprecedented early requirements, the use of high-quality supply chains in logistics practice costs less than maintaining and repairing unreliable low-performance chains,
- the model of the synthesis of effective supply chains should include the morphological and structural-functional areas of the modelling of transport and logistics processes,
- the synthesis model is built based on the IDEF3 method, the main purpose of which is to visualize the sequence of processes performed on a set of selected 1st generation modules. The applied procedure is based on the assumed service provision scenario, where the supply chain is an ordered sequence of actions in the context of the performance of a service [39, 40],
- the solution to the problem of synthesis will be reliable if and only when, apart from solving the problems of morphological synthesis and structural synthesis, the third problem is solved - a combination of 1-generation modules in the structure of the supply chain that creates the basis for synergy effects as a result of their interaction.

3.2. The concept of a synthesis model based on defined assumptions

For years, supply chain planning has been carried out using the method of sequential analysis of all possible solutions under a deterministic algorithm [55]. In practice, the number of options that must be analysed is so large, and the knowledge gaps are so deep that the continued use of such methods may fail in the entire process, and the credibility of the solutions becomes diminished.

If an effective variant of the supply chain structure is indicated, there is still a risk of low efficiency. High efficiency of the integrated supply chain is possible in the case of synergy effects (Figure 4).

Such effects result from the intra-chain cooperation of modules on the condition of their full structural and functional compatibility. The synergy effects are possible due to the right decisions during the supply chain synthesis forward and backward.

The fulfilment of this condition, reinforced by possessing at least one of the cooperating modules of innovative technologies, promises an increase in their efficiency and/or resistance to the manifestations of threats. According to the presented model, the knowledge about the supply chain structure becomes complete with the sequential introduction of new executive modules to this structure. Their implementation is based on information about relations between single modules arranged in a matrix, which creates the basis for completing multi-module complexes as links in the supply chain.

Each complex performs tasks on a specific supply chain section representing individual transport and logistics technologies. Therefore, in the process of synthesis, decisions result from answering the

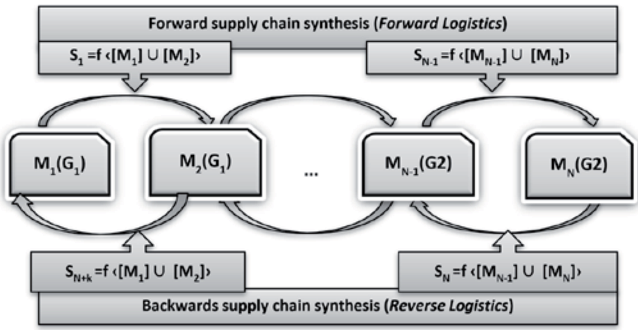

Fig. 4. The sequence of procedures for the synthesis of the supply chain structure in a closed-loop

questions "*how*" and "*to whom and when*" tangible goods mixed within the supply chain will be transferred.

3.3. Conceptual problems of the synthesis model

The analysis of information sources indicates a number of difficulties in the formalization of the synthesis model of technical and logistic systems based on a set of components distinguished by local goals and local modes of operation [34], [52]. In the opinion of the authors, there are three difficulties arising from:

- Incompatibility of single models included in the supply chain structure. The authors' analysis confirms that the compatibility is not a permanent feature of the modules, as the interoperability of the modules involved in different supply chains differ significantly. This is the result of different requirements for the services provided.
- Low credibility of the assumption that emergencies due to past threats are highly probable and future.
- Lack of certainty that the constructed supply chain will be as efficient and resilient as it was assumed during its design.

To alleviate the difficulties mentioned above, it was proposed to use the "Management and Coordination" subsystem (Figure 5). It eliminates the premises for the emergence of internal and external threats. Elimination of internal threats takes place by unifying the standards of links used by subcontractors. Elimination of external threats occurs by enhancing the overall resistance of the chain to threats as a result of the accumulation of individual resistances of each subcontractor involved.

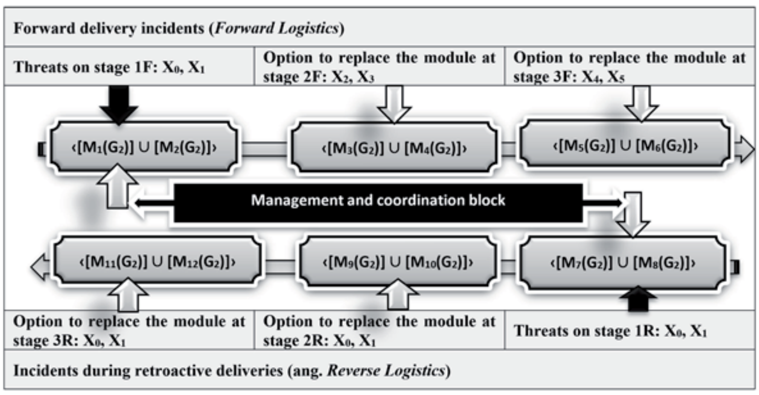

Fig. 5. The sequence of mechanisms for changing the executive modules

Secondly, to avoid difficulties resulting from the lack of reliable information on the effectiveness of cooperation of individual subcontractors in the future, the authors propose to use tools from the theory of probabilities in these studies. These tools allow for conclusions about the possible synergy effects in terms of potential opportunities.

3.4. Rules of structure synthesis vs set of events

The supply chain structure's synthesis should be based on a set of 1st generation executive modules capable of cooperation within this chain and a set of links between these modules. To be successful in the synthesis process, the rules concerning a selection of appropriate modules and their combinations must be applied, i.e.:

R1: The decision to include the executive module $\left[M_i\right]$ in the supply chain structure is made if this module can generate synergy effects. This ability is checked at each subsequent stage of synthesis.
R2: During the implementation of the executive modules, 4 procedures are used:

a. *Duress*, according to which previously selected module $\left[M_i\right]$ requires the selection of the module $\left[M_{i+1}\right]$.
b. *Double duress*, whereby modules $\left[M_i\right]$ and $\left[M_{i+1}\right]$ are implemented together as a combined complex, creating a single link in the supply chain structure.
c. *Need*, according to which the selection condition for the module $\left[M_{i+1}\right]$ is the selection of the module $\left[M_i\right]$.
d. *Prohibition of binary choices*, according to which two modules $\left[M_i\right]$ and $\left[M_{i+1}\right]$. cannot be implemented in parallel for one free position in the chain structure.

R3: If none of the 1st generation modules meets the requirements, the knowledge acquisition procedure should be restarted to search for the correct module on the list of 0th generation units.
R4: The choice of the interface of two cooperating modules must ensure their operation in which the probability of unplanned interruptions will be at an acceptable level.

In the proposed synthesis model, an event is understood as a set of input information $\left(ZS_z\right)$ and information about situations inside the chain $\left(ZS_w\right)$. Thus, the set of events can be represented as:

$$ZS = ZS_z\left(ZW + \Delta ZW, EZ + \Delta EZ\right) + ZS_w\left(WM + \Delta WM\right) \quad (18)$$

- The set of information on external events combines information about executive tasks $\left(ZW\right)$ and changes in these tasks $\left(\Delta ZW\right)$ and information about expected threats $\left(EZ\right)$ from the environment and unexpected threats $\left(\Delta EZ\right)$. These setes reflect various events outside the chain, including unplanned events causing rescheduling of tasks, delivery delays, etc.
- The set of internal events is a collection of information about activities planned during the cooperation of modules $\left(WM\right)$ and unplanned activities $\left(\Delta WM\right)$ caused by unexpected environmental threats. They have a decisive impact on changes in the states $\left[SL_i\right]$ of the supply chain as a result of, for example, the formation of „bottlenecks" and can take place in the following manner:

a. *slow transformation processes* (refer to changes in the structures of modules):

$$ST_1\left[M_i^*\left(G_2\right)\right] \cong ST_0\left[M_i\left(G_2\right)\right] + \Delta ST\left[M_i\left(G_2\right)\right]\Delta t\,,\ \Delta t \to T \quad (19)$$

where:

ST_0 – structural parameter of the module $\left[M_i\left(G_2\right)\right]$ in the $\left[SL_0\right]$ state of supply chain,

ST_1 – structural parameter of the module $\left[M_i^*\left(G_2\right)\right]$ in the $\left[SL_1\right]$ state of supply chain,

T – supply chain life cycle period

b. *fast nonlinear processes* (refer to step changes during the cooperation of modules under the influence of changes in their environment):

$$x_1(t) \cong x_0(t) + \Delta x(\Delta t), \quad \Delta t \to 0 \tag{20}$$

where:

x_0 – parameter of cooperation of modules in the state $[SL_0]$ of the supply chain,

x_1 – parameter of cooperation of modules in the state $[SL_1]$ of the supply chain.

3.5. Selection of executive modules

The supply chain synthesis model is based on information organized according to the square matrix principles DSM (*Design Structure Matrix*) [12]. Individual cells correspond to the 2-generation modules needed to perform the designed supply chain tasks. Single modules are analysed as components of particular chain links in which specific activities will be performed during the delivery. If the module is not needed for these steps, its value is zero. Only those modules necessary for the performance of appropriate activities in the implementation of a specific procurement task are activated, and their interfaces, as part of the planned activity, are in interaction with at least one other module (Table 2).

In the DSM matrix, the executive module is treated as a component of the supply chain structure. Its exclusion from the structure can be quickly replaced with another module with the same or better functional parameters than the previous version's modules. The module selection procedure is carried out in the following order:

Step 1: *Module's suitability analysis* based on an ordered square matrix; the decision to include new modules in the chain structure is made to meet the requirements of their efficiency, resistance and compatibility. Both basic (obligatory) and supplementary modules can be used, each of which should be appropriately selected to perform specific functions;
Step 2: *Assess the number of modules selected*. Only as many modules as needed for the transport and logistics task should be chosen;
Step 3: *Shaping the sequence of the selected modules*. Laying the structure of supply chains should be carried out, considering the possibility of quick modernization consisting of the efficient replacement of passive modules.

After finalizing the shaping of the sequence of modules, the chain structure should be arranged into one, two, or three module complexes (links). The interactions between links occur according to the logic of unconditional realization of the transport task.

Unplanned changes to the modes of executive processes (rapid changes) lead to bottlenecks and an increased risk of losing the chain's integrity as a whole. Failure to take this into account in the traditional approach causes neglect of the meticulous selection of interfaces and reduces the possibility of using the resistance of individual modules. As an effective tool to meet this requirement, it is proposed to use the "module + interface" combination in the synthesis process, arranged in the ISM (Interface Structure Matrix) presented in Table 3.

Table 2. Ordered matrix of 1st generation modules

Modules	**Ordered set of modules**									**Examination of the supply chain link**
	Module $M_1(G_1)$	Module $M_2(G_1)$	Module $M_3(G_1)$	Module $M_4(G_1)$	Module $M_5(G_1)$	Module $M_6(G_1)$	Module $M_7(G_1)$	Module $M_8(G_1)$	Module $M_9(G_1)$	
Module $M_1(G_1)$		1	1	x	x	x	x	x	x	Supply module cells
Module $M_2(G_1)$	0		1	x	x	x	x	x	x	
Module $M_3(G_1)$	1	1		x	x	x	x	x	x	
Module $M_4(G_1)$	x	x	x		1	1	x	x	x	Technology module cells
Module $M_5(G_1)$	x	x	x	1		0	x	x	x	
Module $M_6(G_1)$	x	x	x	1	1		x	x	x	
Module $M_7(G_1)$	x	x	x	x	x	x		0	1	Distribution module cells
Module $M_8(G_1)$	x	x	x	x	x	x	1		0	
Module $M_9(G_1)$	x	x	x	x	x	x	0	1		

Source: own work based on [18]

Table 3. Ordered matrix of inter-module interfaces

Moved goods	**Inter-module interfaces**									**Types of activity**
	Module $M_1(G_1)$	**Module $M_2(G_1)$**	**Module $M_3(G_1)$**	**Module $M_4(G_1)$**	**Module $M_5(G_1)$**	**Module $M_6(G_1)$**	**Module $M_7(G_1)$**	**Module $M_8(G_1)$**	**Module $M_9(G_1)$**	
Materials, car parts		IWY	IWE	x	x	x	x	x	x	Negotiations, purchase, delivery
	0		0	x	x	x	x	x	x	
	IWY	IWE		x	x	x	x	x	x	
Stocks of auto parts, new cars	x	x	x		IWE	IWY	x	x	x	Sorting, storage and picking
	x	x	x	IWY		0	x	x	x	
	x	x	x	IWE	IWY		x	x	x	
New cars	x	x	x	x	x	x		IWE	IWY	Planning, packing, delivery
	x	x	x	x	x	x	IWE		0	
	x	x	x	x	x	x	0	IWY		

Source: own work based on [18]

To select the appropriate link, the following approaches are used:
- in the case of similar efficiency and resistance to threats of the analysed interfaces - the selection is made on a discretionary basis;
- in the case of using the assumption of the need for frequent changes of executive modules - an interface with a high degree of universality is selected, which will not require replacement in the case of replacing the executive modules with new ones;
- in the case of a high probability of the manifestation of threats - a selection is made by searching for an interface capable of eliminating negative influences from previous interfaces.

4. Case study for the synthesis model taking into account weak synergy effects

4.1. Selection of executive modules

In line with market practice, there are two possible approaches to transforming the structures of supply chains:

1. Division of the functions of the withdrawn module between the remaining modules; in this case, there is a depletion of the Lean Supply Chain, justified not by the pursuit of increasing resilience but by the intention to reduce costs,
2. Without dividing the functions of the withdrawn module between the others and selecting modules that would create conditions for the synergy effects, radically increasing the chain's resistance.

The above means that the synthesis process must be based on selecting modules and using inter-module interfaces, which maximize the probability of positive synergy effects, thus increasing the chain's resistance to adverse events. Therefore, the modelling of synergy effects can be used to measure the effectiveness of cooperation of the supply chain participants.

Accurately selected interfaces ensure the horizontal and vertical fusion of a supply chain designed on the principle of modularity of its components. Such a merger in terms of synchronization has three possible consequences for the bidding companies.

The first one is the possibility of achieving the market position strengthening effect, which is the subject of several studies [11, 19, 47]. On the other hand, the second is the possibility of achieving the multiplier effect, increasing the resistance to adverse events of the connected modules. The multiplier effect is the result of the correct selection of modules, the combination of which in the supply chain generates a synergy of resistance of individual modules interacting within the chain, which can be written:

$$\sum ODs = k_W\left(OD_1 + OD_2 + \cdots + OD_n\right) \tag{21}$$

$k_W > 1.0$ –measure of the effectiveness of combining modules (positive synergy effect),

$k_W = 1.0$ – measure of the effectiveness of combining modules (the synergy effect does not arise - the combination of modules is aggregated),

$k_W < 1.0$ – measure of the effectiveness of combining modules (negative synergy effect - asynergy).

The third effect is the possibility of achieving a multiplier effect of lowering overhead costs KO :

$$\sum KO_s = k_Z\left(KO_1 + KO_2 + \cdots + KO_n\right) \quad [22]$$

$k_Z > 1.0$ – measure of the effectiveness of combining modules (negative synergy effect - asynergy);

$k_Z = 1.0$ – measure of the effectiveness of combining modules (the synergy effect does not arise - the combination of modules is aggregated);

$k_Z < 1.0$ – measure of the effectiveness of combining modules (positive synergy effect).

4.2. Synergy effects during the cooperation of executive modules

It is assumed that the supply chain structure is in a stable state $\left[SL_0\right]$ and consists of active and passive modules. At some point, under the influence of events, the regular functioning of the chain becomes unstable, and the structure changes to the state $\left[SL'_0\right]$. Wherein:

1. The $\left[SL_{n+1}\right]$ state was considered at the design stage (all modules are resistant).
2. The state $\left[SL_{n+1}\right]$ was not considered at the design stage and requires the transformation of the chain structure by replacing the passive module with an innovative module.

In case of a decision to replace modules, the structure of the supply chain is transformed into its new state $\left[SL_{n+2}\right]$, creating conditions for the synergy effects that are:

- short-term (*weak effects*) lasting in the period of inter-module cooperation, in the conditions of a stable structure of the supply chain,

Table 4. Dimensions of the synergy effects during the cooperation of executive modules

Dimensions of the manifestation of effects		Types of synergy effects
1	Effects in the demand dimension	• positive, increasing efficiency and resistance to threats; • negative; reducing as efficiency as resistance to threats;
2	Effects in the supply dimension	• possibility to participate in more deliveries; • possibility to access new reliable information; • possibility of access to new technologies;
3	Effects in the operational dimension	• possibility to use partners' resources temporarily; • team resistance to possible threats; • positive image on the demand market
4	Effects in the structural dimension	• binary (as a result of the union of two partners); • general (as a result of joining all partners).
5	Effects in the time dimension	• slow, long-term • quick, short-term
6	Effects in the economic dimension	• possibility to reduce accumulated stocks; • joint responsibility for possible risks of financial losses; • diversification of delivery costs to a larger number of subcontractors.

Table 5. Input information for comparative analysis of synergy effects

Cooperation mode	Graphical representation	Calculation formula
1. Parallel mode	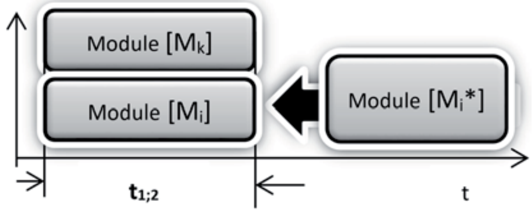	1) $P(t)=1-\prod\{1-p_z[M_z(t)]\}$ 2) $P^*(t)=1-\prod\{1-p_z^*[M_z(t)]\}$ 3) $\Delta ES=\frac{P^*(t)-P(t)}{P^*(t)}$
2. Serial mode	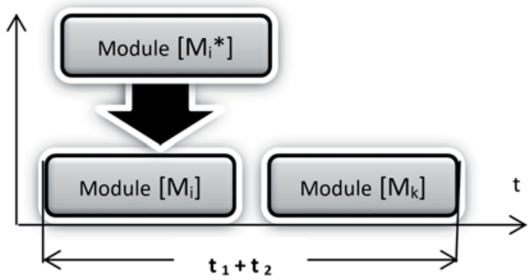	1) $P(t)=p_i[M_i(t)]\times p_k[M_k(t)]$ 2) $P^*(t)=p_i[M_i^*(t)]\times p_k[M_k(t)]$ 3) $\Delta ES=\frac{P^*(t)-P(t)}{P^*(t)}$

- long-term (*strong effects*) generating changes in the structures of cooperating modules, in the conditions of modernization changes in the supply chain structure.

It is proposed to apply three steps to the study of weak synergy effects:

Stage 1. Integrated two- or three-module complexes are created from the 2nd generation modules. For example, the complex $[M_i(G_2)]\cup[M_kG_2]$ combines the module $[M_i(G_2)]$ presenting the transport company and the module $[M_k(G_2)]$ presenting the Regional Logistics Center. The research at this stage concerns methods of collecting and analyzing information and techniques for detecting missing information.

Stage 2. Single complexes are combined in an integrated structure of the supply chain. In this case, the research concerns development of a rational chain structure (continuous, efficient and sufficient) and the impact of events on the ability of the supply chain to perform the task. The power of the chain depends on the performance and resilience of each module $[M_i]$, both properties being independent.

Stage 3. After completing the task, the chain structure is decomposed. By examining the effects during intermodal cooperation and when the reversibility condition is met (according to which modules $[M_i(G_2)]$ and $[M_k(G_2)]$ are disconnected), it maintains the original internal structure.

The highest capacity of the supply chain to perform task occurs when events ZD_1 and ZD_2 occur during the cooperation of modules $[M_1(G_2)]$ and $[M_2(G_2)]$. Such synergy effects can occur in various dimensions (Table 4).

The emergence of synergy effects is three-dimensional and consists of indicating the value of such effects, assessing the pace of their formation, and assessing the impact on the transport and logistics capacity of the entire chain (positive or negative).

4.3. Example of a comparative analysis of synergy effects

A comparative analysis of the synergy effects for the cooperation of two modules in parallel and serial mode will be performed (Table 5). It is assumed that within the analysed complex two modules were connected - $[M_i(G_2)]$ and $[M_k(G_2)]$. During the transport and logistics activities, the module $[M_i(G_2)]$ lost its resistance to threats to a large extent. A decision was made to replace this module with the innovative $[M_i^*(G_2)]$.

The possible effect of such an exchange will be assessed. The following parameters were used as part of the analysis:

- $P(t)$ – probability of resilience of an unreliable complex of modules $[M_i(G_2)]$ and $[M_k(G_2)]$;
- $P^*(t)$ – probability of resilience of modernized complex of modules $[M_i^*(G_2)]$ i $[M_k(G_2)]$;
- $p_k(t)$ – probability of resilience of the active module $[M_k(G_2)]$;
- $p_i(t)$ – probability of resilience of a passive module $[M_i(G_2)]$;
- $p_i^*(t)$ – probability of resilience of a innovative module $[M_i^*(G_2)]$;
- ΔES – synergy effect from cooperation of modules $[M_i^*(G_2)]$ and $[M_k(G_2)]$.

To conduct a comparative analysis, the following assumptions are made:

1. The service life of [$[M_i(G_2)]$ and $[M_k(G_2)]$ modules within a single complex are 5 years.
2. The loss of the complex's resilience to threats occurs when this property is lost by at least one module connected in series with the second module.
3. The loss of resilience of each module occurs irrespective of the state of the other module.
4. The dynamics of the loss of resilience to threats by both modules is linear.
5. The module $[M_i(G_2)]$ has an accelerated dynamics of the loss of resilience in relation to $[M_k(G_2)]$.
6. The innovative module $[M_i^*(G_2)]$ has the resilience P = 0,99.
7. Inter-module interfaces are considered to be absolutely reliable.

The results of the simulation are presented in Table 6. The comparative analysis shows that:

Table 6. Test results for weak synergy effects

Parameters	Passive period before module replacement				
	1 year	2 years	3 years	4 years	5 years
$p_i(t)/\ p_i^*\ (t)$ parallel mode	0,952/0,990	0,893/0,990	0,851/0,990	0,782/0,990	0,721/0,990
$p_k(t)$ parallel mode	0,981	0,963	0,942	0,926	0,901
$P(t)\ /\ P^*(t)$ parallel mode	0,9991	0,9962	0,9914	0,9840	0,974
	0,9981	0,9963	0,9942	0,9926	0,9912
ΔES parallel mode of cooperation	Synergy effect in a complex with the parallel mode of modules cooperation				
	-0,011 %	0,0%	0,28%	0,86%	1,73%
$p_i(t)/\ p_i^*\ (t)$ serial cooperation mode	0,952/0,990	0,893/0,990	0,751/0,990	0,652/0,990	0,550/0,990
$p_k(t)$ serial cooperation mode	0,981	0,963	0,942	0,926	0,901
$P(t)\ /\ P^*(t)$ of serial modules	0,935	0,821	0,707	0,604	0,496
	0,971	0,953	0,934	0,907	0,892
ΔES serial cooperation mode	Synergy effect in a complex with the serial mode of modules cooperation				
	3,71 %	4,56%	7,07%	6,05%	4,96%

- replacement of passive modules with active ones is advisable in the case of complexes with a serial mode of their cooperation. The values of these effects range from 3,5-7,1%;
- the most effective is a replacement in the 2-4 years of operation of the supply chain,
- it is less effective to replace passive modules with active ones in the case of complexes with a parallel mode of cooperation. However, such a replacement for a 1-year operation may be contraindicated, as it may cause adverse synergy effects,
- after the second year of operation, synergy effects with 0,5% positive dynamics can be observed.

5. Conclusions

Transport and logistics companies are rational in their economic activities by engaging only in projects maximizing their financial liquidity. The disadvantages of the traditional approach are:

- no desire to integrate with other companies on a "win-win" basis,
- too much space for possible solutions, lack of transparency and stability of knowledge about opportunities to strengthen the market position.

As the analysis has shown, it is possible to build effective supply chain structures if a modular approach. It requires the identification of executive modules as components of the structure being constructed and the interfaces connecting these modules. This involves identifying the number of modules needed and the rules for combining them.

The assumption about the possibility of searching for the intended result (achieving the maximum synergy effects as a result of the cooperation of executive modules) is not acceptable in the structural and functional model of the supply chain synthesis. This is because selecting any module to include in the chain structure may change the initial conditions for selecting other modules. This leads to the conclusion that the process of synthesizing a modular supply chain should be a continuous and uniform process.

The results of research on the effectiveness of the modular approach showed significant benefits for the design of supply chain structures, including openness to the use of new methods of making design decisions, high flexibility and adaptability, transparency and compliance with the practice used in the TSL market.

References

1. Autry C W, Bobbitt LM. Supply chain security orientation: conceptual development and a proposed framework. The International Journal of Logistics Management 2008; 19(1): 42-64, https://doi.org/10.1108/09574090810872596.
2. Aylward D, Clements M. Crafting a local-global nexus in the Australian wine industry. Journal of Enterprising communities: People and Places in the Global Economy 2008; 2(1): 73-87, https://doi.org/10.1108/17506200810861267.
3. Barchański A, Żochowska R. Estimation of critical gaps and follow-up times at median uncontrolled T-intersection. Archives of Transport 2021; 60(4): 105-124, https://doi.org/10.5604/01.3001.0015.6030.
4. Bayardo R Jr, Efficiently Mining Long Patterns from Databases. Proceeding of the ACM-SIGMOD International Conference on Management of Data, 1998; 85-93, https://doi.org/10.1145/276305.276313.
5. Berger S, Bierwirth C. Solutions to the request reassignment problem in collaborative carrier networks Transportation Research Part E 2010; 46: 627-638, https://doi.org/10.1016/j.tre.2009.12.006.
6. Christopher M, Holweg M. Supply Chain 2.0: managing supply chains in the era of turbulence. International Journal of Physical Distribution and Logistics Management 2011; 41(1): 63-82, https://doi.org/10.1108/09600031111101439.
7. Clark KB, Baldwin CY. Design Rules: The Power of Modularity. Cambridge MIT Press 1999, https://doi.org/10.7551/mitpress/2366.001.0001.
8. De Blok C, Meijboom B, Luijkx K, Schols J, Schroeder R. Interfaces in Service Modularity: A Typology Developed in Modular Healthcare Provision. Journal of Operations Management 2014; 32 (4): 175-189, https://doi.org/10.1016/j.jom.2014.03.001.
9. Deloitte Consulting. The Deloitte Automotive Value Chain Industry Model 2017; https://www2.deloitte.com/content/dam/Deloitte/us/Documents/consumer-business/us-cb-future-of-the-automotive-supplier-industry-outlook.pdf.12/2017.

10. Doran D. Rethinking the supply chain: an automotive perspective. Supply Chain Management: An International Journal 2004; 9(1): 102-109, https://doi.org/10.1108/13598540410517610.
11. Eckbo E. Horizontal Mergers, Collusion, and Stockholder Wealth, Journal of Financial Economics 1983; 11: 241-273, https://doi.org/10.1016/0304-405X(83)90013-2.
12. Eppinger S, Browning, T. Design Structure Matrix Methods and Applications (Engineering Systems), MIT Press 2016.
13. Faisal MN, Banwet DK, Shankar R. Supply Chain Risk mitigation: modelling the enablers. Business Process Management Journal 2006; 12(4): 535-552, https://doi.org/10.1108/14637150610678113.
14. Frazzon EM. et al.: Spare parts supply chains' operational planning using technical condition information from intelligent maintenance systems Annual Reviews in Control 2014, https://doi.org/10.1016/j.arcontrol.2014.03.014.
15. Ganguly K. Integration of analytic hierarchy process and Dempster-Shafer theory for supplier performance measurement considering risk. International Journal of Productivity and Performance Management 2014; 63(1): 85-102, https://doi.org/10.1108/IJPPM-10-2012-0117.
16. Ghadge A, Dahi S, and Kalawsky R. Supply Chain Risk Management: present and future scope. International Journal of Logistics Management 2012; 23(3): 313-339, https://doi.org/10.1108/09574091211289200.
17. Ghadge A, Dan S, Chester M, Kalawsky R. A systems approach for modelling supply chain risks. Supply chain management: An International Journal 2013; 18(5): 523-538, https://doi.org/10.1108/SCM-11-2012-0366.
18. Göhlich D, Hildebrand S, Schellert D. Augmented DSM sequencing to support product development planning. International Design Conference - DESIGN 2018; 1139-1148, https://doi.org/10.21278/idc.2018.0434.
19. Gupta S. Mergers and acquisitions for enhancing supply chain competitiveness. Journal of Marketing and Operations Management Research; Hauppauge Tom 2, 2012; 3: 129-147.
20. He P, Li J. Vehicle routing problem with partly simultaneous pickup and delivery for the cluster of small and medium enterprises. Archives of Transport 2018; 45(1): 35-42, https://doi.org/10.5604/01.3001.0012.0940.
21. He W. An Inventory Controlled Supply Chain Model Based on Improved BP Neural Network. Discrete Dynamics in Supply Chain Management 2013; 5: 1-7, https://doi.org/10.1155/2013/537675.
22. Heckmann I. Towards Supply Chain Risk Analytics: Fundamentals, Simulation Optimization. Springer, 2016, https://doi.org/10.1007/978-3-658-14870-6.
23. Ho C. et al.: Measuring system performance of an ERP-based supply chain. International Journal of Production Research 2006; 45 (6): 1255-1277, https://doi.org/10.1080/00207540600635235.
24. Izdebski M, Jacyna-Gołda I, Markowska K, Murawski J. Heuristic algorithms applied to the problems of servicing actors in supply chains. Archives of Transport 2017; 44(4): 25-34, https://doi.org/10.5604/01.3001.0010.6159.
25. Jacyna M, Izdebski M, Szczepański E, Gołda P. The task assignment of vehicles for a production company, Symmetry-Basel 2018; 11(10): 1-19, https://doi.org/10.3390/sym10110551.
26. Jacyna M, Jachimowski R, Szczepański E, Izdebski M. Road vehicle sequencing problem in a railroad intermodal terminal - simulation research. Bulletin of the Polish Academy of Sciences, Technical Sciences 2020; 68(5): 1135-1148.
27. Jacyna M, Semenov I. Models of vehicle service system supply under information uncertainty. Eksploatacja i Niezawodnosc - Maintenance and Reliability 2020; 22(4): 694-704, https://doi.org/10.17531/ein.2020.4.13.
28. Jacyna M, Wasiak M, Lewczuk K, Chamier-Gliszczyński N, Dąbrowski T. Decision problems in developing proecological transport system. Annual Set The Environment Protection 2018; 20: 1007-1025.
29. Jacyna-Gołda I, Lewczuk K. The method of estimating dependability of supply chain elements on the base of technical and organizational redundancy of process. Eksploatacja i Niezawodnosc - Maintenance and Reliability 2017;19(3): 382-392, https://doi.org/10.17531/ein.2017.3.9.
30. Jacyna-Golda I, Wasiak M, Izdebski M, Lewczuk K, Jachimowski R, Pyza D. The Evaluation of the Efficiency of Supply Chain Configuration. Proceedings of the 20th international scientific conference Transport Means 2016, Kaunas Univ Technol, 953-957.
31. Jacyna-Gołda I. Evaluation of operational reliability of the supply chain in terms of the control and management of logistics processes, [in:] Safety and Reliability: Methodology and Applications/ Nowakowski T. [i in.] (ed.), CRC Press Taylor & Francis Group, 2015: 549-558.
32. Jia F, Rutherford C. Mitigation of supply chain relational risk caused by cultural differences between China and the West. The International Journal of Logistics Management 2010; 21(2): 251-270, https://doi.org/10.1108/09574091011071942.
33. Jing Zhu et al. Effects of upstream and downstream mergers on supply chain profitability. European Journal of Operational Research 2016; 249(1): 131-143. https://doi.org/10.1016/j.ejor.2015.08.030
34. Jixin Zhao J, Meng Ji Bo Feng. Smarter supply chain: a literature review and practices. Journal of Data, Information and Management 2020; 2: 95-110. https://doi.org/10.1007/s42488-020-00025-z
35. Johnson N, Elliott D, Drake P. Exploring the role of social capital in facilitating supply chain resilience. Supply Chain Management: An International Journal 2013; 18(3): 324-336, https://doi.org/10.1108/SCM-06-2012-0203.
36. Jufang Li, Yuan T, Xiao X, Yu G. Applied Research of an improved Apriori algorithm in the logistics industry. 5th International Conference on Measurement, Instrumentation and Automation ICMIA 2016; 356-360.
37. Khan O, Christopher M, Burnes B. The impact of product design on supply chain risk: a case study. International Journal of Physical Distribution & Logistics Management 2008; 38(5): 412-432, https://doi.org/10.1108/09600030810882834.
38. Khan O, Christopher M, Creazza A. Aligning product design with the supply chain: a case study. Supply Chain Management: An International Journal 2012; 17(3): 323-336, https://doi.org/10.1108/13598541211227144.
39. Kim CH, Weston RH, Hodgson A, Lee KH. The complementary use of IDEF and UML Modelling approaches. Computers in Industry 2003; 50(1): 35-56, https://doi.org/10.1016/S0166-3615(02)00145-8.
40. Kunlin Z, Gang R. Study of supply chain monitoring system based on IDEF method. International Conference on Logistics Systems and Intelligent Management (ICLSIM) 2010; 278 - 281.
41. Li G, Fan H, Lee PK, Cheng TCE. Joint supply chain risk management: An agency and collaboration perspective. International Journal of Production Economics 2015; 164: 83-94, https://doi.org/10.1016/j.ijpe.2015.02.021.
42. Lin Y, Zhou L. The impacts of product design changes on supply chain risk: a case study. International Journal of Physical Distribution & Logistics Management 2011; 41(2):162-186, https://doi.org/10.1108/09600031111118549.
43. Luksch, S. After sales supply chain risk management. University of Louisville 2014; (5): 137.

44. Manuj I, Esper TL, Stank TP. Supply chain risk management approaches under different conditions of risk. Journal of Business Logistics 2014; 35(3): 241-258, https://doi.org/10.1111/jbl.12051.
45. Michlowicz E, Wojciechowski J. A method for evaluating and upgrading systems with parallel structures with forced redundancy. Eksploatacja i Niezawodnosc - Maintenance and Reliability 2021; 23 (4): 770-776, http://doi.org/10.17531/ein.2021.4.19.
46. Mitchell M. et al. The impact of industry shocks on takeover and restructuring activity. Journal of Financial Economics June 1996; 41(2): 193-229, https://doi.org/10.1016/0304-405X(95)00860-H.
47. Moufad I, Jawab F. Mixed applied survey methodology for planning/enforcement of urban logistics delivery bays- An application to the Moroccan context. Archives of Transport 2020; 55(3): 95-110, https://doi.org/10.5604/01.3001.0014.4237.
48. Nooraie SV, Parast MM. A multi-objective approach to supply chain risk management: Integrating visibility with supply and demand risk. International Journal of Production Economics 2015; 161: 192-200, https://doi.org/10.1016/j.ijpe.2014.12.024.
49. Olson DL. A review of supply chain data mining publications. Archives, January 2020 - June 2020; 1(1-2).
50. Peters VJT. et. Al. Interfaces in service modularity: a scoping review. International Journal of Production Research 2018; 56(20): 6591-6606, https://doi.org/10.1080/00207543.2018.1461270.
51. Qazi A, Quigley J, Dickson A, Ekici ŞÖ. Exploring dependency based probabilistic supply chain risk measures for prioritising interdependent risks and strategies. European Journal of Operational Research 2017; 259(1): 189-204, https://doi.org/10.1016/j.ejor.2016.10.023.
52. Reisig W. The Synthesis Problem. In: Jensen K., van der Aalst W.M.P., Balbo G., Koutny M., Wolf K. (ed.) Transactions on Petri Nets and Other Models of Concurrency VII. Lecture Notes in Computer Science, Springer 2013; 7480, https://doi.org/10.1007/978-3-642-38143-0_8.
53. Riley JM, Klein R, Miller J, Sridharan V. How internal integration, information sharing, and training affect supply chain risk management capabilities. International Journal of Physical Distribution & Logistics Management 2016; 46(10): 953-980, https://doi.org/10.1108/IJPDLM-10-2015-0246.
54. Rudyk T, Szczepański E, Jacyna M. Safety factor in the sustainable fleet management model. Archives of Transport 2019; 49(1): 103-114, https://doi.org/10.5604/01.3001.0013.2780.
55. Sawik T. Stochastic versus Deterministic Approach to Coordinated Supply Chain Scheduling. Mathematical Problems in Engineering 2017, https://doi.org/10.1155/2017/3460721.
56. Spring M, Santos J. Interfaces in Service and Process Modularity. Paper presented at the 5th International Seminar on ervice Architecture and Modularity, Copenhagen, January 16-17, 2014.
57. Szczepański E, Jachimowski R, Izdebski M, Jacyna-Gołda I. Warehouse location problem in supply chain designing: a simulation analysis. Archives of Transport 2019; 50(2): 101-110. https://doi.org/10.5604/01.3001.0013.5752.
58. Tse Y K, Chung SH, Lim MK. Quality Risk in Global Supply Network. Journal of Manufacturing Technology Management 2011; 22(8): 1002-1013, https://doi.org/10.1108/17410381111177458.
59. Valverde R. Data Mining: A Tool to Increase Productivity in Supply Chain Management. Electronic Journal 2015, https://doi.org/10.2139/ssrn.2642145.
60. Van der Laan MR. The Feasibility of Modularity in Professional Service Design: Towards Low Cost Person-centred Care. PhD diss., University of Groningen 2015, https://doi.org/10.1108/IJOPM-06-2015-0370.
61 Wang Y, Wiegerinck V, Krikke H, Zhang H. Understanding the purchase intention towards remanufactured product in closed-loop supply chains: An empirical study in China. International Journal of Physical Distribution & Logistics Management 2013; 43(10): 866-888, https://doi.org/10.1108/IJPDLM-01-2013-0011.
62. Wieland A, Marcus Wallenburg C. The influence of relational competencies on supply chain resilience: a relational view. International Journal of Physical Distribution & Logistics Management 2013; 43(4): 300-320, https://doi.org/10.1108/IJPDLM-08-2012-0243.
63. Yeh YP. Identification of factors affecting continuity of cooperative electronic supply chain relationships: empirical case of the Taiwanese motor industry. Supply Chain Management: An International Journal 2005; 10(4): 327-335, https://doi.org/10.1108/13598540510612802.
64. Zepeda ED, Nyaga GN, Young G J. Supply chain risk management and hospital inventory: Effects of system affiliation. Journal of Operations Management 2016; 44: 30-47, https://doi.org/10.1016/j.jom.2016.04.002.
65. Zhenhong Lang. The Improved Apriori Algorithm based on Matrix Pruning and Weight Analysis. AIP Conference Proceedings 2018; 040113, https://doi.org/10.1063/1.5033777.
66. Żochowska R, Soczówka P. Method for identifying hazardous road locations at the intersection of tramlines and road traffic. Scientific Journal of Silesian University of Technology. Series Transport. 2017; 97: 201-213, https://doi.org/10.20858/sjsutst.2017.97.18.
67. Zsidisin GA, Ellram LM, Carter JR, Cavinato JL. An analysis of supply risk assessment techniques. International Journal of Physical Distribution & Logistics Management 2014; 34(5): 397-413, https://doi.org/10.1108/09600030410545445.

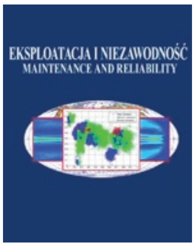

Eksploatacja i Niezawodnosc – Maintenance and Reliability

Volume 24 (2022), Issue 1

journal homepage: http://www.ein.org.pl

Article citation info:
Chen X, Przystupa K, Ye Z, Chen F, Wang C, Liu J, Gao R, Wei M, Kochan O. Forecasting short-term electric load using extreme learning machine with improved tree seed algorithm based on Lévy flight. Eksploatacja i Niezawodnosc – Maintenance and Reliability 2022; 24 (1): 153–162, http://doi.org/10.17531/ein.2022.1.17.

Forecasting short-term electric load using extreme learning machine with improved tree seed algorithm based on Lévy flight

Indexed by: Web of Science Group

Xuan Chen[a], Krzysztof Przystupa[b,*], Zhiwei Ye[a], Feng Chen[a], Chunzhi Wang[a], Jinhang Liu[a], Rong Gao[a], Ming Wei[c,d], Orest Kochan[a,d]

[a] Hubei University of Technology, School of Computer Science, Wuhan, Hubei, 430068, PR China
[b] Lublin University of Technology, Department of Automation, ul. Nadbystrzycka 36, 20-618 Lublin, Poland
[c] Wuhan Fiberhome Technical Services Co., Ltd., Wuhan, Hubei, 430074, PR China
[d] Wuhan FiberHome Telecommunication Technologies Co., Ltd., Wuhan, Hubei, 430074, PR China
[e] Lviv Polytechnic National University, Bandery 12, 79013 Lviv, Ukraine

Highlights

- Forecasting Short-term Electric Load using Extreme Learning Machine is considered.
- Improved Tree Seed Algorithm based on Lévy flight is proposed.
- This method has better convergence, prediction accuracy and stability than similar ones.

Abstract

In recent years, forecasting has received increasing attention since it provides an important basis for the effective operation of power systems. In this paper, a hybrid method, composed of kernel principal component analysis (KPCA), tree seed algorithm based on Lévy flight (LTSA) and extreme learning machine (ELM), is proposed for short-term load forecasting. Specifically, the randomly generated weights and biases of ELM have a significant impact on the stability of prediction results. Therefore, in order to solve this problem, LTSA is utilized to obtain the optimal parameters before the prediction process is executed by ELM, which is called LTSA-ELM. Meanwhile, the input data is extracted by KPCA considering the sparseness of the electric load data and used as the input of LTSA-ELM model. The proposed method is tested on the data from European network on intelligent technologies (EUNITE) and experimental results demonstrate the superiority of the proposed approaches compared to the other methods involved in the paper.

Keywords

short-term electric load forecast; extreme learning machine; Lévy flight; tree-seed algorithm; Kernel principal component analysis.

1. Introduction

High quality and uninterrupted power supply are indispensable today [25, 40], because many processes and systems are integrated into a global network using Internet of Things (IoT) concept [15, 48]. They need a reliable power supply for proper operation [1, 42]. Improper operation, failures and accidents in the power supply network not only directly affect the operation of devices and systems, but also can indirectly affect the modes of their operation [34, 49]. In general, reliability in technology and industry is very important [41], as a consequence, a lot of attention is paid to the development of methods of preventing equipment failure [14], its diagnostics and early failure detection [12, 22, 51].

However, the development of science and technology needs more research, especially in the estimation of equipment lifespan, the forecast of different modes of its operation [27, 28, 35] and process control methods [7, 24]. Regression analysis is traditionally used for prediction [26, 60], however, the methods of artificial intelligence have been actively used recently in this area [13, 44]. This paper is devoted to the use of such methods.

Short-term electric load forecasting generally refers to forecasts within a year and in units of months, weeks, days or hours, including ultra-short-term load forecasts with a period of one hour or even a few minutes. The accuracy of forecasting is directly related to the normal use of electricity by customers. The improvement of electric load forecasting technology not only improves the safety and reliability of grid operation but also reduces the cost of power generation and maximizes the benefits [39]. Major methods for short-term electric load forecasting are broadly classified into traditional forecasting methods and neural network methods [18, 32]. Traditional forecast-

(*) Corresponding author.

E-mail addresses: X. Chen (ORCID:0000-0003-1343-7132): xuan927@hbut.edu.cn, K. Przystupa (ORCID: 0000-0003-4361-2763): k.przystupa@pollub.pl, Z. Ye (ORCID: 0000-0001-6668-4634): hgcsyzw@mail.hbut.edu.cn, F. Chen (ORCID: 0000-0001-9517-1301): chenfeng4179@fiberhome.com, C. Wang (ORCID: 0000-0002-6742-3644): chunzhiwang@mail.hbut.edu.cn, J. Liu (ORCID:0000-0002-5509-0846): liujinhang@hbut.edu.cn, R. Gao (ORCID:0000-0001-7935-7173): gaorong@hbut.edu.cn, M. Wei (ORCID: 0000-0003-4695-5657): mwei@fiberhome.com, O. Kochan (ORCID: 0000-0002-3164-3821): orest.v.kochan@lpnu.ua

ing methods include regression analysis [33] and expert systems [37]. These methods are difficult to build effective mathematical models and fit highly nonlinear multi-factor electric loads. Neural network methods contain regression trees [57], grey prediction [65], support vector machines [38] and artificial neural networks. Artificial neural network has satisfied fault tolerance rate, nonlinear mapping ability, adaptive learning ability and efficiency compared with other forecasting methods. As a result, artificial neural network is widely used in the field of electric load forecasting for solving complex nonlinear practical problems [29].

Extreme learning machine (ELM) has been widely used in the field of electric load forecasting as one of artificial neural networks [4, 9]. Chen [3] proposed a hybrid intelligent optimization algorithm to optimize the parameters of ELM. The method achieves high accuracy for short-term electric load forecasting. ELM is feed-forward neural network with a single hidden layer [20] and has the advantages of simple structure, fast training speed, fewer adjustment parameters, strong generalization and nonlinear approximation ability. However, there are some defects of ELM in practical applications [54]. Impact on prediction results as the setting of relevant parameters in ELM includes three aspects according to the literature [21]. Firstly, the choice of activation function in different instances influences the prediction results. The second is the predefined number of hidden layer nodes in ELM increases the subjectivity of the process of determining the hidden layer nodes in the network. Finally, the randomly defined input weight matrix and hidden layer thresholds in ELM lead to the failure of partially hidden layer nodes, less specific sample learning and unstable performance.

Some evolutionary algorithms have been used to solve these problems. For instance, particle swarm optimization algorithm (PSO) [61], grey wolf optimizer algorithm (GWO) [10], moth flame optimization algorithm (MFO) [56], differential evolution algorithm (DE) [19], cuckoo search algorithm (CS) [63] and harmony search algorithm (HS) [43] were used to optimize ELM. For parameter optimization of ELM, Wei [52] presented a prediction method based on MFO optimizing the parameters of random forest and ELM to forecast CO2 emissions. Yang [58] proposed a differential evolution-based feature selection and parameter optimization for ELM in tool wear estimation. Wang [55] proposed a hybrid model based on CS algorithm to forecast solar radiation. These works achieved good results. Nonetheless, some evolutionary algorithms have complicatedly operators and constantly adjusted parameters, which results in ineffective convergence to the global optimum. Therefore, trying more new algorithms to deal with this problem is necessary. The tree seed algorithm (TSA) [5] is one of the newest heuristic algorithms. Compared with other heuristic algorithms, TSA is easy to implement, has fewer tuning parameters and takes less time to compute. This method was successfully used to solve different engineering optimization problems. Ali [8] adopted TSA to solve the optimal power flow problem in large-scale power systems. Zhao [64] utilized residual vectors and TSA to identify the structural damage. Muneeswaran [36] developed a performance evaluation method for the radial basis function neural network based on TSA. However, TSA is affected by the search trend (ST) which leads to the update falling into local optimum. TSA with the Lévy flight is proposed for balancing the global and local search capabilities to obtain a better prediction effect [2].

In the paper, LTSA is introduced to optimize initialization parameters to improve the prediction performance of ELM. This method reduces the training time of network and improves the stability and accuracy. The method of ELM combined with LTSA (LTSA-ELM) is used to predict the electric load data processed by kernel principal component analysis (KPCA). The experimental results show that the hybrid method of KPCA, LTSA and ELM (KPCA-LTSA-ELM) proposed in this paper achieves better prediction results.

The rest of the paper is structured as follows. The basic principle of TSA and ELM is illustrated in section 2. The proposed KPCA-LTSA-ELM is explained in section 3. The experimental results and discussion are demonstrated in section 4. Finally, the paper is concluded in section 5.

2. Preliminary

2.1. Extreme learning machine

ELM is a three-layer network composed of the input layer, hidden layer and output layer. Each layer is connected by neurons. The structure diagram of ELM is depicted in Figure 1.

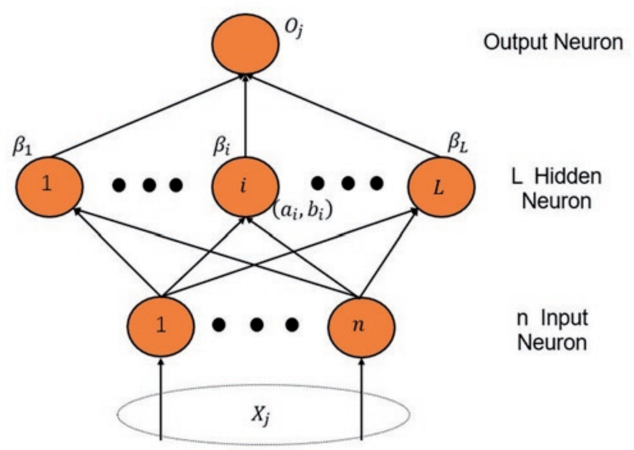

Fig. 1. The structure diagram of ELM

Let us assume the amount of neurons in the hidden layer is L .
The standard form of the model is expressed in equations (1-3):

$$t_i = \sum_{j=1}^{L} \beta_j g(w_j x_i + b_j)(i = 1,2,...,N) \tag{1}$$

where L is a number of hidden layer, N is a number of training samples, $g(x)$ is the activation function, w_j is the input weight, β_j is the output weight, b_j is the bias of the j_{th} hidden layer unit, and $w_j x_i$ is the inner product of w_j and x_i .

When the output error is the minimum, it can be calculated by equation (2):

$$\sum_{i}^{N} \| t_i - y_i \| = 0 \tag{2}$$

Thus, there exists β_j , w_j and b_j such that:

$$y_i = \sum_{j=1}^{L} \beta_j g(w_j x_i + b_j)(i = 1,2,...,N) \tag{3}$$

The matrix form of the model is expressed in equations (4-7):

$$H\beta = Y \tag{4}$$

where H is the output matrix of the hidden layer of the neural network, β is the weight output matrix, Y is the target output matrix:

$$H = \begin{bmatrix} g(\omega_1 \cdot x_1 + b_1) & g(\omega_2 \cdot x_1 + b_2) & \cdots & g(\omega_L \cdot x_1 + b_L) \\ g(\omega_1 \cdot x_2 + b_1) & g(\omega_2 \cdot x_2 + b_2) & \cdots & g(\omega_L \cdot x_2 + b_L) \\ \vdots & \vdots & \ddots & \vdots \\ g(\omega_1 \cdot x_N + b_1) & g(\omega_2 \cdot x_N + b_2) & \cdots & g(\omega_L \cdot x_N + b_L) \end{bmatrix}_{N \times L} \tag{5}$$

$$\beta = \left[\beta_1^{\mathrm{T}} \beta_2^{\mathrm{T}} \cdots \beta_{\mathrm{L}}^{\mathrm{T}} \right]_{L \times m} \tag{6}$$

$$Y = \left[Y_1^T Y_2^T \cdots Y_L^T \right]_{N \times m} \tag{7}$$

To forecast a single hidden layer neural network, it can be defined as follows:

$$\left\| H\left(\hat{w}_j, \hat{b}_j\right) \hat{\beta}_j - Y \right\| = \min_{w,b,\beta} \left\| H\left(w_j, b_j\right) \beta_j - Y \right\| \tag{8}$$

where $j = 1, 2, ..., L$, this is equivalent to minimizing the loss function. It can be defined in equations (9-10):

$$E = \sum_{i=1}^{N} \left(\sum_{j=1}^{L} \beta_j g(w_j x_i + b_j) - y_i \right)^2 \tag{9}$$

$$\hat{\beta} = H^{+} Y \tag{10}$$

where H^{+} is the Moore-Penrose generalized inverse matrix of the output matrix of the hidden layer H. When the activation function is infinitely differentiable, the connection weight w_j of the input layer to the hidden layer and the threshold b_j of the hidden layer can be randomly assigned before training and remain unchanged during the training. Then the output matrix of the hidden layer H is determined, that is, the connection weight matrix $\hat{\beta}$ of the hidden layer to the output layer can be determined by equation (10).

2.2. Tree seed algorithm

TSA is a new intelligent optimizer proposed by M.S. Kiran in 2015 to solve the continuous optimization problems. In nature, trees spread their seeds to the surfaces. If these surfaces are considered as the search space for the optimization problem, the location of the tree and seeds are the possible solutions to the optimization problem. Therefore, the search for seeds location is an important step in TSA to solve the optimization problem. In the primary TSA, each tree simulates the solution of the optimization problem in the search space. The fitness value of the tree is usually calculated by the objective function or the optimization problem.

Before the algorithm starts searching, equation (11) is used to generate the latest initial tree positions for subsequent iterations of the search. The initial tree positions are the feasible solutions of TSA:

$$T_{i,j} = Low_j + r_{i,j}(High_j - Low_j) \tag{11}$$

where $T_{i,j}$ represents the corresponding value of the j_{th} dimension of the i_{th} tree randomly generated in search space. Low_j and $High_j$ are the lower and upper bounds of the j_{th} dimension, respectively.

The trees generate new seed locations and the number of seeds depends on the size of the population, therefore the number of seeds can exceed one. In the analysis of the influence of controlled variables on the performance of TSA, the minimum quantity of tree seeds is 10% of the population size and the maximum quantity is 25% of the population size. The amount of seeds produced is completely random in TSA.

Then equation (12) is used to optimize the feasible solution for the population obtained in the first batch to select the trees with strong capability for seed production and the optimal location:

$$Best = \min \left\{ f\left(\vec{T}_i\right) \right\} i = 1, 2, ..., N \tag{12}$$

where N is the population size of trees in TSA.

The selected trees will continue to update their positions and produce new seeds. There are two search modes for seeds, one of which focuses on the global search and the other on the local one.

Two ideal conditions are usually assumed for the search:

(1) The first update of the new seed location is determined by the position of the tree and the position of the optimal tree in the tree population. This search enhances the local search capability of the algorithm. It can be updated by equation (13).

(2) The second update of the new seed location is determined by two randomly selected trees with different locations. It can be updated by equation (14):

$$S_{i,j} = T_{i,j} + \alpha_{i,j} \times \left(Best_j - T_{r,j} \right) \tag{13}$$

$$S_{i,j} = T_{i,j} + \alpha_{i,j} \times \left(T_{i,j} - T_{r,j} \right) \tag{14}$$

where $S_{i,j}$ is the j_{th} dimension of the i_{th} seed which generated by the i_{th} tree, $T_{i,j}$ is the j_{th} dimension of the i_{th} tree, $Best_j$ is the best tree currently obtained, $T_{r,j}$ is the j_{th} dimension of the r_{th} tree randomly selected from the population, and $\alpha_{i,j}$ is a scale factor randomly generated within the range of [-1, 1].

The choice of the specific update mode of the seed is regulated by the search tendency (ST) parameter within the scope of [0,1]. A larger ST value provides powerful local search capability and faster convergence speed. A smaller ST value results in slower convergence but strong global search capabilities. According to previous experiments [23], when the value of ST is 0.1, most functions can get the optimal solution. If the ST generated randomly within the range of [0, 1] is less than 0.1, then equation (13) is selected to update each dimension of the seed produced by each tree, otherwise equation (14) is used. The procedure of TSA is described in Algorithm 1.

Algorithm 1 Procedure of TSA

Input: The parameters and the termination condition of TSA.
Output: The best solution obtained by TSA.
Step1: The initialization of the algorithm
    Randomly generate tree locations in the D-dimensional search space.
    Evaluate the tree location by the fitness function.
    Select the best solution.
Step2: Search with seeds
    FOR all trees
      Decide the number of seeds produced for this tree.
      FOR all seeds
        FOR all dimensions
          IF (rand < ST)
            Update this dimension using equation **(13)**
          ELSE
            Update this dimension using equation **(14)**
          END IF
        END FOR
      END FOR
      Select the best seed and compare it with the tree.
      If the seed location is better than the tree location, the seed substitutes for this tree.
    END FOR
Step3: Selection of the best solution
    Select the best solution of the population.
    If the new best solution is better than the previous best solution, new best solution substitutes for the previous best solution.
Step4: Testing termination condition

If the termination condition is not met, go to **Step 2.**
If the termination condition is met, output the best solution**.**

3. The proposed method

3.1. Kernel principal component analysis

In order to ease the training of the model to learn the correct load variation law for short-term electric load forecasting, we perform feature extraction on data processed by LTSA-ELM. These re-extracted indicators can reflect the information of the original data as much as possible, simplifying the network structure and improving the training rate of the network.

Since the relationship between the short-term electric load indicators is usually non-linear, the use of linear principal component analysis (PCA) [50, 62] tends to cause the contribution rate of each principal component to be too dispersed to find a component with comprehensive capabilities. KPCA [45] circumvents the unascertained nonlinear transformation in nonlinear principal component analysis (NLPCA) [6] by using the kernel techniques. Therefore, the principal components can be obtained in a more concentrated manner, and the evaluation results are more consistent with objective facts. KPCA is applied to improve the input of LTSA-ELM, which can effectively reduce the input dimension while retaining most of the original information. Therefore, we can predict and analyze load data in the actual power grid and improve the efficiency and precision of the forecast.

In the process of the kernel principal component analysis, the analysis results are related to the choice of kernel function. The proper selection of kernel functions and parameters can effectively improve the overall performance of KPCA. There are two common kernel functions:

The Polynomial kernel can be expressed by equation (15):

$$K(x,y)=\left[s(x,y)+c\right]^{d} \tag{15}$$

The Gaussian kernel can be expressed by equation (16):

$$K(x,y)=\exp\left(-\frac{\|x-y\|}{2e^{2}}\right) \tag{16}$$

In the paper, these two functions are selected for calculations. The kernel parameter in the polynomial kernel is $\mathrm{var}=sign=2$, and the kernel parameter in the Gaussian kernel is $\mathrm{var}=281, sign=1$. The selection of kernel functions is explained in section 4.3.

3.2. Lévy flight distribution introduced to TSA

Lévy flight (LF) [30] is a random walk mode between short-range search and occasional long-range search. Similarly, researchers found that the Lévy flight can also improve the performance of nature-inspired algorithms [46, 47].

The LF distribution generates new solutions by randomly selecting short or long steps. At present, the LF distribution is widely utilized in many fields for improving the exploration ability, because it can increase the variety of species and expand the search range. For example, CS algorithm uses the LF for updating position [59], bat algorithm uses the LF strategy to mimic the predation behavior of bats instead of the speed and position of the original algorithm [31], PSO uses the LF to update particle position after iterating multiple times [16] etc.

The position of LF is updated by equations (17-19):

$$x_i^{(t+1)}=x_i^{(t)}+\alpha\oplus Levy(\lambda) \qquad i=1,2,\ldots,n \tag{17}$$

$$Levy(\lambda)\sim u=t^{-\lambda} \qquad 1<\lambda\le 3 \tag{18}$$

$$Levy(\lambda)\sim\frac{\phi*\mu}{|\upsilon|^{\frac{1}{\beta}}} \tag{19}$$

where, μ,υ follow the standard normal distribution β=1.5. The mathematical definition formula of ϕ can be expressed by equation (20):

$$\phi=\left(\frac{\Gamma(1+\beta)*\sin(\pi\times\frac{\beta}{2})}{\Gamma\left(\left(\frac{1+\beta}{2}\right)*\beta*2^{\frac{(\beta-1)}{2}}\right)}\right)^{\frac{1}{\beta}} \tag{20}$$

where Γ is the standard Gamma function.

To improve the global and local search capabilities of TSA, LTSA combines the advantages of the LF distribution with TSA for overcoming the problem of trapping into a local optimum. In the case of rand<ST, the LF random walk strategy is introduced when the seed is updated. The seed update rule is changed from equation (13) to equation (21):

$$S_{i,j}=T_{i,j}+\alpha_{i,j}\oplus Levy(\lambda)\times\left(Best_j-T_{r,j}\right) \tag{21}$$

where $Levy(\lambda)$ represents a random search vector whose jump step obeys the Lévy distribution, $\lambda(1<\lambda\le 3)$ is a scale parameter.

The choice of the fitness function directly affects the rate of convergence of the tree algorithm and whether the best solution can be found. In the evolutionary search, the algorithm calculates the individual fitness values according to the fitness function, and fitness value is used to evaluate the pros and cons of the individual tree.

The tree individual $\vec{T}_i$ in the population corresponds to the arrangement of the weights and thresholds of ELM network.

The value of the fitness function can be calculated by equation (22):

$$fitness(\vec{T}_i)=E(\vec{T}_i)=\frac{1}{2}\sum_{k=1}^{m}\left(y_k-o_k\right)^2 \tag{22}$$

where: o_k is the actual output of the output layer neurons, y_k is the expected output of the output layer neurons, and m is the number of output layer neurons. According to the error function, the weight and threshold between each neuron are continuously adjusted to train the neural network to achieve the optimal solution.

The procedure of LTSA-ELM is described in Algorithm 2.

Algorithm2 Procedure of LTSA-ELM

Input: The best solution obtained by LTSA
Output: The predicted results obtained by LTSA-ELM
Step 1: Set the best solution
The best solution is the connection weight for the input layer and hidden one and the neuron threshold of the hidden layer.
Step 2: Select an activation function to calculate the output matrix H of the hidden layer neurons.

Step 3: Calculate a connection weight matrix $\hat{\beta}$ of the hidden layer to the output layer.

Step 4: Predict the results by the output weight matrix and activation function.

The flowchart of KPCA-LTSA-ELM model is shown in Figure 2.

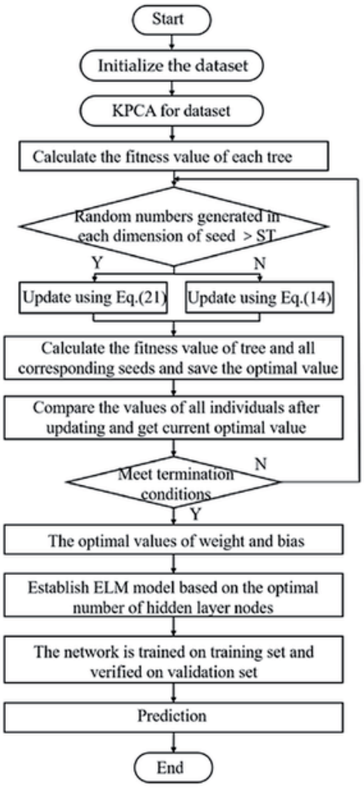

Fig. 2. The flowchart of KPCA-LTSA-ELM model

4. Experiments and Discussions

The experiment verifies the model proposed in the paper from three aspects. First, the stability and accuracy of LTSA-ELM prediction were verified by experiments on six UCI public datasets using five common methods (section 4.1). Second, KPCA-LTSA-ELM is applied to data provided by EUNITE (section 4.2). Third, the relevant parameters of LTSA-ELM are selected. Then PCA, KPCA based on the Polynomial kernel and KPCA based on the Gaussian kernel are applied to evaluate eleven characteristic attributes in data provided by EUNITE. The experimental results indicate that KPCA based on the Gaussian kernel should be used preferentially in dimensionality reduction of short-term electric load data (section 4.3).

Table 1. Parameters of different algorithms

Parameters	Value
Population size	100
Dimension	Number of bands
Hidden layer nodes	10
Number of runs for each technique	30
c1,c2 Acceleration coefficient in the PSO algorithm	c1 = 2.1, c2 = 1.6
A Convergence factor in the GWO algorithm	2
B Parameter in the MFO algorithm	1
The ST Search trend in TSA algorithm	0.1
The Nvar Parameter in LTSA algorithm	1
The β Parameter in LTSA algorithm	1.5

Table 2. Statistics of the data set

Data set	Instances	Attributes	Forecast number
Combined Cycle Power Plant(CCPP)	9568	4	1
Airfoil Self-Noise(ASN)	1503	5	1
Concrete Compressive Strength(CCS)	1030	8	1
Yacht Hydrodynamics(YH)	308	6	1
Wine quality-red(WR)	1599	11	1
Wine quality-white(WW)	4898	11	1

4.1. Experiments of LTSA-ELM on UCI datasets

To verify the effectiveness of LTSA-ELM, the proposed method is compared with some commonly used algorithms: PSO, GWO, MFO, and parameters of these algorithms are shown in Table 1. In this paper, six UCI standard datasets are used to test the model, as shown in Table 2. All experimental data sets are mapped to the [-1, 1] by the maximum and minimum normalization method [17]. Using 5-fold cross-validation technique [11], each data set is divided into five parts, four of which are selected as training sets and one as a testing set. The ELM adopts S-type activation function, the selection of activation functions is explained in section 4.3. The results of the prediction accuracy (ACC) and the mean square error (MSE) on six UCI public datasets are shown in Table 3.

Table 3. Prediction results of five methods on the UCI datasets

Data set	ELM		PSO-ELM		GWO-ELM		MFO-ELM		TSA-ELM		LTSA-ELM	
	ACC /%	MSE	ACC /%	MSE	ACC/%	MSE	ACC /%	MSE	ACC /%	MSE	ACC /%	MSE
ASN	98.77	1.51e-16	99.15	7.23e-17	99.15	7.28e-17	99.15	7.29e-17	99.15	7.22e-17	**99.45**	7.30e-18
CCS	98.99	1.03e-12	99.01	9.72e-13	99.02	9.54e-13	99.02	9.52e-13	99.02	9.66e-13	**99.87**	9.52e-13
YH	91.61	7.03e-7	98.56	2.08e-8	98.51	2.21e-8	98.35	2.73e-8	98.56	2.07e-8	**99.51**	2.02e-8
WR	97.50	7.22e-5	99.22	6.03e-9	98.40	2.56e-8	98.89	1.22e-8	98.92	1.17e-8	**99.77**	5.12e-10
WW	98.50	2.47e-9	99.43	3.28e-11	99.46	2.91e-11	99.41	3.44e-11	99.40	3.61e-11	**99.96**	4.12e-12
CCPP	99.13	7.48e-19	99.17	6.80e-19	99.65	1.20e-17	99.88	1.38e-18	99.85	7.12e-19	**99.99**	1.29e-19

As can be seen from Table 3, LTSA-ELM outperforms other competing algorithms on all test data sets. The accuracy of LTSA-ELM on the six data sets has reached more than 99%. In addition, LTSA-ELM achieves better accuracy especially on YH which is higher than ELM without LTSA about 8.6%. Moreover, the comparison between the results of TSA-ELM and LTSA-ELM demonstrates that the combination of Lévy flight and TSA further improve the probability of getting the optimal parameters. Meanwhile, LTSA-ELM has better stability compared with other algorithms as it gets the minimum results on MSE for most datasets. It is proved that the predefined parameters optimized by LTSA effectively improve the performance of ELM.

4.2. Experiments of KPCA-LTSA-ELM for electric load datasets

The proposed method in this paper is applied to predict short-term electric load based on EUNITE competition data [53].

KPCA is used to perform the principal component analysis of sample data. The electric load data extracted by KPCA is used as the input sample of LTSA-ELM model. Among them, 6880 samples are randomly selected as the training data and 1719 samples are used as the test data. In order to compare the prediction advantages of each model, the mean absolute error (MAE), the average absolute percentage error (MAPE), the predicted root mean square error (MSE), the coefficient of determination (R^2), the test accuracy rate (accuracy) and the test time (T) are used as evaluation indicators. Then, the evaluation values corresponding to the respective prediction models are calculated. The results are shown in Table 4 and Figures 3 and 4.

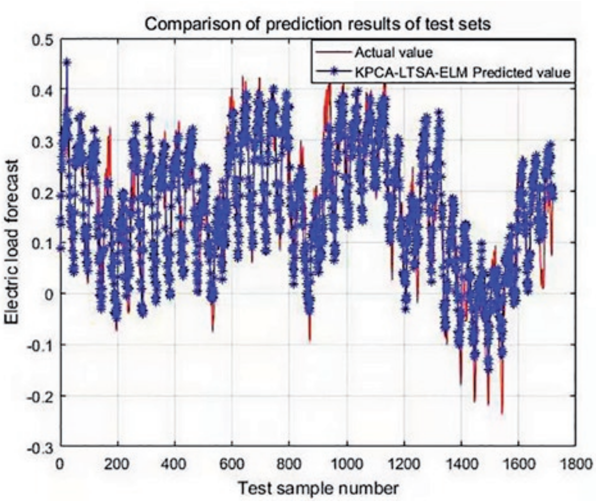

Fig. 3. Electric load prediction of KPCA-LTSA-ELM

As can be seen from Table 4, the predicted values of KPCA-LTSA-ELM has the highest prediction accuracy. The mean square error of prediction is the minimum compared with the other models. Compared with LTSA-ELM, the prediction accuracy of KPCA-LTSA-ELM is improved by 1.84%, the mean square error is reduced by 0.00051, and the test determination coefficient is increased by 0.01855. This shows that the sample data processed based on KPCA eliminates the related redundancy between influencing factors. From the stability of the model, KPCA-LTSA-ELM outperforms ELM, PSO-ELM, GWO-ELM, MFO-ELM, TSA-ELM, LTSA-ELM and SVM models. In terms of model convergence, the convergence time of LTSA-ELM and KPCA-LTSA-ELM are shorter and more efficient than most other models.

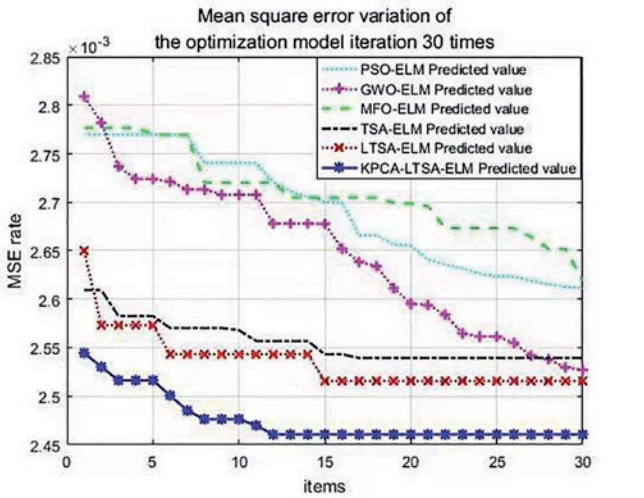

Fig. 4. The root mean square error (MSE) curve of each model versus the number of iteration

As shown in Figure 3, the red line represents the true value, and the blue line represents the predicted value of KPCA-LTSA-ELM. The predicted value curve and the true value curve can fit well. This indicates that KPCA-LTSA-ELM has a high prediction accuracy. According to Figure 4, the mean square error predicted by each model decreases as the number of iterations increases. The convergence curve shows that KPCA-LTSA-ELM has smaller training errors and faster convergence speed than other models. The model can fully exploit the internal implicit laws of the prominent samples and effectively interpret the nonlinear relationship between short-term electrical load and other influencing factors. Therefore, this model can be applied to the field of short-term electric load forecasting to provide a theoretical guarantee for users to use normal electricity and reduce generation costs.

4.3. Sensitivity analysis of parameters

4.3.1. Determination of hidden nodes and the type of activation function for ELM

In order to determine the optimal activation function and the number of nodes in the hidden layer, the trial and error method is used in this paper. The number of hidden layer nodes is determined as 13 based on the empirical formula.

Table 4. Analysis of results of each prediction model

Model category	MAE	MAPE	MSE	R^2	Accuracy(%)	T(s)
ELM	0.04448	1.17311	0.00334	0.7902	92.20	0.0468
PSO-ELM	0.04128	0.87613	0.00253	0.8468	95.08	0.0468
GWO-ELM	0.04092	0.89789	0.00272	0.83549	92.90	0.1248
MFO-ELM	0.04113	0.94533	0.00295	0.82159	93.75	0.0312
TSA-ELM	0.03995	0.84463	0.00274	0.83412	93.76	0.0312
LTSA-ELM	0.03892	0.81437	0.00263	0.84077	94.76	0.0312
KPCA-LTSA-ELM	0.03800	0.76717	0.00212	0.85932	96.60	0.0312
SVM	0.05572	1.27575	0.00506	0.69640	92.88	5.7849

ELM has three kinds of activation functions: S-type (Sigmoid type), sine function (Sine type), and the hard-threshold type transfer function (Hardlim type). The generalization ability of each activation function has different prediction effects in different instances. The expressions of these three activation functions correspond to equations (23-25) respectively as below:

$$f(x_1) = \frac{1}{1+e^{-x_1}} \tag{23}$$

$$f(x_2) = \sin(x_2) \tag{24}$$

$$f(x_3) = \begin{cases} 1 & x_3 > 0 \\ -1 & x_3 < 0 \end{cases} \tag{25}$$

The prediction result of the above three different activation functions is calculated to determine the optimal activation function. The results are shown in Table 5:

Table 5. Prediction results of different activation functions

Type of activation function	Number of hidden layer nodes	Mean square error (MSE%)
Sigmoid type	13	0.21398
Sine type	13	0.21848
Hardlim type	13	0.22056

The Sigmoid activation function has the best prediction effect, followed by the Hardlim and Sine activation functions. Therefore, the activation function of ELM can be determined as the Sigmoid function.

Then, the number of hidden layer nodes is calculated with a test interval of [3, 13] to determine the optimal number of nodes in the hidden layer. In the paper, the same data sample set is selected. Under the same conditions in all aspects, the quantity of neurons in the hidden layer is determined by comparing the mean square error. Multiple network trainings are conducted on different hidden layer neurons, and the mean square error is shown in Table 6.

From the comparison of the distributions in Table 6, it can be seen that the mean square error tends to be minimized when the number of neurons in the hidden layer is 13. Therefore, the number of nodes in the hidden layer is set as 13.

4.3.2. Feature extraction based on KPCA

The eleven characteristic attributes in the short-term electric load data of Europe are processed by PCA, KPCA based on the polynomial

Table 6. Mean Square Errors for different number of neurons in the hidden layer

Number of hidden layer neurons	Number of training	Mean square error (MSE%)	Decision coefficient (R^2)
3	50	0.27461	0.83014
4	50	0.26966	0.84129
5	50	0.25291	0.85116
6	50	0.24351	0.85668
7	50	0.23656	0.86077
8	50	0.22557	0.86195
9	50	0.21156	0.86385
10	50	0.20934	0.86724
11	50	0.20861	0.87075
12	50	0.20852	0.87143
13	50	0.20845	0.87679

kernel and KPCA based on the Gaussian kernel extract the first six principal components.

The eigenvalue (Eig), the Variance contribution rate (Vcr), and the cumulative contribution rate (Ccr) are calculated. In this paper, the cumulative contribution rate of principal component is greater than 96% as the standard. When using KPCA (Gaussian kernel) to select features, the cumulative contribution rate of the variance of the first six principal components reaches 96.05%, which can replace the original eleven indicators. The experimental results are shown in Table 7:

As can be seen from the above table, the methods using PCA and KPCA reduce the features of training samples inputs, and retains most of information. However, there are some differences in the effectiveness of these three methods. The short-term electric load feature extraction method based on PCA has the advantages of dimension reduction and feature extraction. But its first principal component contribution rate is only 29.23%, which is 15.96% lower than KPCA based on linear kernel function and 14.3% lower than KPCA based on Gaussian kernel function. KPCA expands the research range of data characteristics from linear to nonlinear, therefore it can reduce the dimensionality and obtain better performance than PCA. KPCA based on linear kernel function has the similar principal component contribution rate as KPCA based on Gaussian kernel function. However, KPCA based on Gaussian kernel function extracts fewer features than the linear kernel function extraction, consequently, it is better to choose the Gaussian radial kernel function.

Table 7. Comparison table of three analytical methods

Number	PCA			KPCA (Linear kernel)			KPCA(Gaussian kernel)		
	Eig	Vcr(%)	Ccr(%)	Eig	Vcr(%)	Ccr(%)	Eig	Vcr(%)	Ccr(%)
1	3.2150	29.23	29.23	3702.5	45.19	45.19	0.0034	43.53	43.53
2	2.4834	22.58	51.80	2351.2	28.70	73.89	0.0023	29.98	73.51
3	1.9021	17.29	69.10	628.9	7.68	81.57	6.65e-04	8.62	82.13
4	1.0194	9.27	78.36	473.6	5.78	87.35	4.67e-04	6.06	88.19
5	0.9343	8.49	86.86	373.3	4.56	91.90	3.60e-04	4.67	92.85
6	0.5030	4.57	91.43	259.5	3.17	95.08	2.46e-04	3.19	96.05
7	0.3899	3.54	94.97	122.6	1.50	96.57	1.26e-04	1.63	97.68
8	0.2386	2.17	97.14	76.6	0.94	97.51	7.65e-05	0.99	98.67
9	0.1531	1.39	98.53	58.9	0.72	98.23	4.43e-05	0.57	99.25
10	0.0971	0.88	99.42	38.1	0.47	98.69	3.78e-05	0.49	99.25
11	0.0641	0.58	100	27.2	0.33	99.03	2.04e-05	0.26	99.74

5. Conclusion

In general, a method for short-term electric load forecasting based on ELM and the improved TSA is put forward. The performance of LTSA-ELM is evaluated on six different dimensional datasets. It is demonstrated that LTSA is more suitable for learning the optimal parameters of ELM in terms of convergence speed, prediction accuracy and stability among experimental results. Moreover, KPCA is used to extract the features in the experiment for forecasting short-term electric load in Europe. Experimental results of the test load data show that KPCA-LTSA-ELM successfully forecasts the required load at a certain time of the day. In conclusion, the combination of ELM and LTSA achieves higher accuracy in less time and maintains a better balance between prediction efficiency and accuracy. In recent years, the scale of electricity consumption continually increases and the power system faces greater challenges. This research only focuses on short-term electric load forecasting, whereas middle-term and long-term load forecasting is more valuable to the energy market than short-term electric load forecasting. We will explore these issues in future research.

Acknowledgement

This research was funded by the National Natural Science Foundation of China under Grant No.61502155, 61772180, and the technological innovation project of Hubei Province 2019 No.2019AAA04, also funded by Fujian Provincial Key Laboratory of Data Intensive Computing and Key Laboratory of Intelligent Computing and Information Processing, Fujian No.BD201801.

This work was financed in the framework of the project Lublin University of Technology - Regional Excellence Initiative, funded by the Polish Ministry of Science and Higher Education (contract no. 030/RID/2018/19).

References

1. Čepin M. Evaluation of the importance factors of the power plants within the power system reliability evaluation. Eksploatacja i Niezawodnosc - Maintenance and Reliability 2019; 21(4): 631-637, https://doi.org/10.17531/ein.2019.4.12.
2. Barshandeh S, Haghzadeh M. A new hybrid chaotic atom search optimization based on tree-seed algorithm and Levy flight for solving optimization problems. Engineering with Computers 2020: 1-44, https://doi.org/10.1007/s00366-020-00994-0.
3. Chen F. Research on Short-term Power Load Forecasting Based on Hybrid Intelligent Optimization Algorithm. Master thesis, Hubei University of Technology, 2020.
4. Chen Y, Kloft M, Yang Y et al. Mixed kernel based extreme learning machine for electric load forecasting. Neurocomputing 2018; 312: 90-106, https://doi.org/10.1016/j.neucom.2018.05.068.
5. Dash R, Dash PK, Bisoi R. A self adaptive differential harmony search based optimized extreme learning machine for financial time series prediction. Swarm and Evolutionary Computation 2014; 19: 25-42, https://doi.org/10.1016/j.swevo.2014.07.003.
6. Dong H, Li M, Zhang S et al. Short-term power load forecasting based on kernel principal component analysis and extreme learning machine. J. Electron. Meas. Instrum 2018; 32: 188-193.
7. Dukalski P, Będkowski B, Parczewski K et al. Dynamics of the vehicle rear suspension system with electric motors mounted in wheels. Eksploatacja i Niezawodnosc - Maintenance and Reliability 2019; 21(1): 125-136, https://doi.org/10.17531/ein.2019.1.14.
8. El-Fergany AA, Hasanien HM. Tree-Seed Algorithm for Solving Optimal Power Flow Problem in Large-Scale Power Systems Incorporating Validations and Comparisons. Applied Soft Computing 2018; 64: 307-316, https://doi.org/10.1016/j.asoc.2017.12.026.
9. Ertugrul ÖF. Forecasting electricity load by a novel recurrent extreme learning machines approach. International Journal of Electrical Power & Energy Systems 2016; 78: 429-435, https://doi.org/10.1016/j.ijepes.2015.12.006.
10. Faris H, Mirjalili S, Aljarah I. Automatic selection of hidden neurons and weights in neural networks using grey wolf optimizer based on a hybrid encoding scheme. International Journal of Machine Learning and Cybernetics 2019; 10(10): 2901-2920, https://doi.org/10.1007/s13042-018-00913-2.
11. Fushiki T. Estimation of prediction error by using K-fold cross-validation. Statistics and Computing 2011; 21(2): 137-146, https://doi.org/10.1007/s11222-009-9153-8.
12. Glowacz A, Tadeusiewicz R, Legutko S et al. Fault diagnosis of angle grinders and electric impact drills using acoustic signals. Applied Acoustics 2021; 179: 108070, https://doi.org/10.1016/j.apacoust.2021.108070.
13. Glowacz A. Fault diagnosis of electric impact drills using thermal imaging. Measurement 2021; 171: 108815, https://doi.org/10.1016/j.measurement.2020.108815.
14. Glowacz A. Ventilation diagnosis of angle grinder using thermal imaging. Sensors 2021; 21(8): 2853, https://doi.org/10.3390/s21082853.
15. Greengard S. The internet of things. MIT press: 2021, https://doi.org/10.7551/mitpress/13937.001.0001.
16. Haklı H, Uğuz H. A novel particle swarm optimization algorithm with Levy flight. Applied Soft Computing 2014; 23: 333-345, https://doi.org/10.1016/j.asoc.2014.06.034.
17. Han J, Pei J, Kamber M. Data mining: concepts and techniques. Elsevier: 2011.
18. Houimli R, Zmami M, Ben-Salha O. Short-term electric load forecasting in Tunisia using artificial neural networks. Energy Systems 2020; 11(2): 357-375, https://doi.org/10.1007/s12667-019-00324-4.
19. Hu J, Wu M, Chen X et al. A multilevel prediction model of carbon efficiency based on the differential evolution algorithm for the iron ore sintering process. IEEE Transactions on Industrial Electronics 2018; 65(11): 8778-8787, https://doi.org/10.1109/TIE.2018.2811371.
20. Huang G, Zhu Q, Siew CK. Extreme learning machine: Theory and applications. Neurocomputing 2006; 70(1): 489-501, https://doi.org/10.1016/j.neucom.2005.12.126.
21. Kang F, Liu J, Li J, Li S. Concrete dam deformation prediction model for health monitoring based on extreme learning machine. Structural Control and Health Monitoring 2017; 24(10): e1997, https://doi.org/10.1002/stc.1997.
22. Kapłonek W, Nadolny K, Królczyk GM. The use of focus-variation microscopy for the assessment of active surfaces of a new generation of coated abrasive tools. Meas. Sci. Rev 2016; 16(2): 42-53, https://doi.org/10.1515/msr-2016-0007.
23. Kiran MS. TSA: Tree-seed algorithm for continuous optimization. Expert Systems with Applications 2015; 42(19): 6686-6698, https://doi.org/10.1016/j.eswa.2015.04.055.
24. Kochan O, Sapojnyk H, Kochan R. Temperature field control method based on neural network. 2013 IEEE 7th International Conference on Intelligent Data Acquisition and Advanced Computing Systems (IDAACS), IEEE: 2013; 1: 21-24, https://doi.org/10.1109/IDAACS.2013.6662632.
25. Kozieł J, Przystupa K. Using the FTA method to analyze the quality of an uninterruptible power supply unitreparation UPS. Przeglad

Elektrotechniczny 2019; 95(3): 37-40, https://doi.org/10.15199/48.2019.01.20.
26. Kozłowski E, Mazurkiewicz D, Sęp J, Żabiński T. The Use of Principal Component Analysis and Logistic Regression for Cutter State Identification. International Conference Innovation in Engineering, Springer: 2021: 396-405, https://doi.org/10.1007/978-3-030-78170-5_34.
27. Kozłowski E, Mazurkiewicz D, Żabiński T et al. Assessment model of cutting tool condition for real-time supervision system. Eksploatacja i Niezawodnosc - Maintenance and Reliability 2019; 21(4): 679-685, https://doi.org/10.17531/ein.2019.4.18.
28. Krolczyk G, Gajek M, Legutko S. Predicting the tool life in the dry machining of duplex stainless steel. Eksploatacja i Niezawodnosc - Maintenance and Reliability 2013; 15: 62-65.
29. Kyriakides E, Polycarpou M. Short Term Electric Load Forecasting: A Tutorial. In Chen K, Wang L (eds): Trends in Neural Computation, Berlin, Heidelberg, Springer Berlin Heidelberg: 2007: 391-418, https://doi.org/10.1007/978-3-540-36122-0_16.
30. Li H, Zhang S, Zhang C et al. A novel unsupervised Levy flight particle swarm optimization (ULPSO) method for multispectral remote-sensing image classification. International Journal of Remote Sensing 2017; 38(23): 6970-6992, https://doi.org/10.1080/01431161.2017.1368102.
31. Liu C, Ye C. Bat algorithm with Levy flight characteristics. CAAI Trans Intell Syst 2013; 3: 240-246.
32. Liu T, Chen R, Xiao Y, Yang J. Stream-Based Short-Term Demand Forecasting Model Using ARIMA. Applied Mechanics and Materials 2012; 220-223: 315-318, https://doi.org/10.4028/www.scientific.net/AMM.220-223.315.
33. Mao L, Jiang Y. Medium-and long-term load forecasting based on partial least squares regression analysis. Power System Technology 2008; 32(19): 71-77.
34. Mazurek PA, Michałowska J, Koziel J et al. The intensity of electromagnetic fields in the range of GSM 900, GSM 1800 DECT, UMTS, WLAN in built-up areas. Przeglad Elektrotechniczny 2018; 94(12): 202-205, https://doi.org/10.15199/48.2018.12.45.
35. Michałowska J, Józwik J. Prediction of the parameters of magnetic field of CNC machine tools. Przeglad Elektrotechniczny, 95 (1): 134-136, https://doi.org/10.15199/48.2019.01.34.
36. Muneeswaran V, Rajasekaran MP. Performance evaluation of radial basis function networks based on tree seed algorithm. 2016 International Conference on Circuit, Power and Computing Technologies (ICCPCT), 2016: 1-4, https://doi.org/10.1109/ICCPCT.2016.7530267.
37. Niu D, Ji L, Tian J. Wavelet neural network embedded expert system used in short-term load forecasting. 2011 2nd IEEE International Conference on Emergency Management and Management Sciences, IEEE: 2011: 190-193.
38. Pai P, Hong W. Support vector machines with simulated annealing algorithms in electricity load forecasting. Energy Conversion and Management 2005; 46(17): 2669-2688, https://doi.org/10.1016/j.enconman.2005.02.004.
39. Pedregal DJ, Young PC. Development of improved adaptive approaches to electricity demand forecasting. Journal of the Operational Research Society 2008; 59(8): 1066-1076, https://doi.org/10.1057/palgrave.jors.2602447.
40. Przystupa K, Koziel J. Analysis of the quality of uninterruptible power supply using a UPS. 2018 Applications of Electromagnetics in Modern Techniques and Medicine (PTZE), IEEE: 2018: 191-194, https://doi.org/10.1109/PTZE.2018.8503204.
41. Przystupa K. An attempt to use FMEA method for an approximate reliability assessment of machinery. ITM Web of conferences, EDP Sciences: 2017; 15: 05001, https://doi.org/10.1051/itmconf/20171505001.
42. Przystupa K. Selected methods for improving power reliability. Przegląd Elektrotechniczny 2018; 94(12): 270-273, https://doi.org/10.15199/48.2018.12.62.
43. Razfar MR, Farshbaf ZR, Haghshenas M. Optimum surface roughness prediction in face milling by using neural network and harmony search algorithm. The International Journal of Advanced Manufacturing Technology 2011; 52(5): 487-495, https://doi.org/10.1007/s00170-010-2757-5.
44. Sachenko A, Kochan V, Turchenko V, Golovko V, Savitsky Y, Laopoulos T. Method of construction of training set for neural network that predicts drift of data acquisition module. Patent of Ukraine 50380. G06F15/18.
45. Schölkopf B, Smola A, Müller KR. Kernel principal component analysis. In Gerstner W, Germond A, Hasler M, Nicoud J-D (eds): Artificial Neural Networks - ICANN'97, Berlin, Heidelberg, Springer: 1997: 583-588, https://doi.org/10.1007/BFb0020217.
46. Senthilnath J, Das V, Omkar SN, Mani V. Clustering Using Levy Flight Cuckoo Search. Proceedings of Seventh International Conference on Bio-Inspired Computing: Theories and Applications (BIC-TA 2012), India, Springer: 2013: 65-75, https://doi.org/10.1007/978-81-322-1041-2_6.
47. Senthilnath J, Kulkarni S, Raghuram Dr. et al. A novel harmony search-based approach for clustering problems. International Journal of Swarm Intelligence 2016; 2(1): 66-86, https://doi.org/10.1504/IJSI.2016.077434.
48. Song W, Beshley M, Przystupa K et al. A software deep packet inspection system for network traffic analysis and anomaly detection. Sensors 2020; 20(6): 1637, https://doi.org/10.3390/s20061637.
49. Su J, Kochan O. Common mode noise rejection in measuring channels. Instruments and Experimental Techniques 2015; 58(1): 86-89, https://doi.org/10.1134/S0020441215010091.
50. Sultoni S, Abdullah AG. Real Time Facial Recognition Using Principal Component Analysis (PCA) And EmguCV. IOP Conference Series: Materials Science and Engineering 2018; 384: 012079, https://doi.org/10.1088/1757-899X/384/1/012079.
51. Sun S, Przystupa K, Wei M et al. Fast bearing fault diagnosis of rolling element using Lévy Moth-Flame optimization algorithm and Naive Bayes. Eksploatacja i Niezawodnosc - Maintenance and Reliability 2020; 22: 730-740, https://doi.org/10.17531/ein.2020.4.17.
52. Sun W, Wang Y, Zhang C. Forecasting CO2 emissions in Hebei, China, through moth-flame optimization based on the random forest and extreme learning machine. Environmental Science and Pollution Research 2018; 25(29): 28985-28997, https://doi.org/10.1007/s11356-018-2738-z.
53. Wang B, Zhao S, Zhang S. A distributed load forecasting algorithm based on cloud computing and extreme learning machine. Power System Technology 2014; 38(2): 526-531.
54. Wang G, Lu M, Dong Y, Zhao X. Self-adaptive extreme learning machine. Neural Computing and Applications 2016; 27(2): 291-303, https://doi.org/10.1007/s00521-015-1874-3.
55. Wang J, Jiang H, Wu Y, Dong Y. Forecasting solar radiation using an optimized hybrid model by Cuckoo Search algorithm. Energy 2015; 81: 627-644, https://doi.org/10.1016/j.energy.2015.01.006.
56. Yamany W, Fawzy M, Tharwat A, Hassanien A E. Moth-flame optimization for training Multi-Layer Perceptrons. 2015 11th International Computer Engineering Conference (ICENCO), 2015: 267-272, https://doi.org/10.1109/ICENCO.2015.7416360.

57. Yang J, Stenzel J. Short-term load forecasting with increment regression tree. Electric Power Systems Research 2006; 76(9-10): 880-888, https://doi.org/10.1016/j.epsr.2005.11.007.
58. Yang W, Zhou Q, Tsui KL. Differential evolution-based feature selection and parameter optimisation for extreme learning machine in tool wear estimation. International Journal of Production Research 2016; 54(15): 4703-4721, https://doi.org/10.1080/00207543.2015.1111534.
59. Yang X, Deb S. Engineering optimisation by cuckoo search. International Journal of Mathematical Modelling and Numerical Optimisation 2010; 1(4): 330-343, https://doi.org/10.1504/IJMMNO.2010.035430.
60. Yeromenko V, Kochan O. The conditional least squares method for thermocouples error modeling. 2013 IEEE 7th International Conference on Intelligent Data Acquisition and Advanced Computing Systems (IDAACS), IEEE: 2013; 1: 157-162, https://doi.org/10.1109/IDAACS.2013.6662661.
61. Yu Z, Xiao L, Li H et al. Model Parameter Identification for Lithium Batteries Using the Coevolutionary Particle Swarm Optimization Method. IEEE Transactions on Industrial Electronics 2017; 64(7): 5690-5700, https://doi.org/10.1109/TIE.2017.2677319.
62. Zhang S, Ren S, Chen R et al. Short-term Power Load Forecast Based on Big Data Reduction and PCA-improved RBF Network. Acta Metrologica Sinica 2018; 39(3): 392-396.
63. Zhang Y, Yang S, Guo Z et al. Wind speed forecasting based on wavelet decomposition and wavelet neural networks optimized by the Cuckoo search algorithm. Atmospheric and Oceanic Science Letters 2019; 12(2): 107-115, https://doi.org/10.1080/16742834.2019.1569455.
64. Zhao Y, Liu J, Lyu Z, Ding Z. Structural damage identification based on residual vectors and Tree-seed algorithm. Acta Scientiarum Naturalium Universitatis Sunyatseni 2017; 56(4): 46-50.
65. Zhou P, Ang B, Poh KL. A trigonometric grey prediction approach to forecasting electricity demand. Energy 2006; 31(14): 2839-2847, https://doi.org/10.1016/j.energy.2005.12.002.

EKSPLOATACJA I NIEZAWODNOŚĆ
MAINTENANCE AND RELIABILITY

Eksploatacja i Niezawodnosc – Maintenance and Reliability

Volume 24 (2022), Issue 1

journal homepage: http://www.ein.org.pl

Article citation info:
Mysior M, Pietrucha G, Koziołek S. Strength testing of a modular trailer with a sandwich platform. Eksploatacja i Niezawodnosc – Maintenance and Reliability 2022; 24 (1): 163–169, http://doi.org/10.17531/ein.2022.1.18.

Strength testing of a modular trailer with a sandwich platform

Indexed by: Web of Science Group

Marek Mysior[a,*], Grzegorz Pietrucha[b,*], Sebastian Koziołek[a]

[a]Wroclaw University of Science and Technology, Faculty of Mechanical Engineering, Department of Machine and Vehicle Design and Research, ul. Łukasiewicza 7/9, 50-371 Wroclaw, Poland
[b]HONEYtech Sp. z o.o., Huta 58, 98-360 Lututów

Highlights

- The work describes the experimental testing process of light trailers.
- The test was conducted on trailers equipped with a sandwich panel and a plywood.
- Performed bench test made it possible to evaluate operational parameters of trailers.
- The described method represents experimental testing on a special testing track.
- A trailer equipped with a sandwich panel has higher stiffness and durability.

Abstract

The article presents the experimental strength evaluation of modular car trailers with a maximum permissible total mass of up to 3500 kg and its application to assess the mechanical strength of box-type car trailers. Tests were carried out using an original test bench dedicated to fatigue testing. They aimed to compare a trailer made in traditional technology with a trailer equipped with a load-carrying structure containing a sandwich panel. As a result of the conducted work, the displacement values of the measurement points were measured. The deformation form of the trailer made in the traditional technology was compared with the trailer containing the sandwich panel. The proposed method of experimental strength evaluation of modular car trailers enables a quantitative assessment of the mechanical strength of the load-carrying structures of trailers. This results in improved safety of trailer operation in road traffic by identifying the critical elements of the load-carrying structure at the early design phase before the trailer is allowed to run on the road.

Keywords

fatigue life, light trailer, road testing, sandwich panel, honeycomb.

1. Introduction

The issue of reliability and durability of machines, devices, and vehicles is widely discussed worldwide. An essential element of the conducted research in the field is concerned with predicting and modeling the durability of mechanical objects [3, 4] and assessing their service life [10]. Mathematical and statistical methods are of particular interest in determining useful features of a mechanical object [12]. Apart from this, the growing diversity of useful functions of products leads to the increased variety of design features of designed mechanical objects. This represents an increasing number of design variants that should be durable and reliable. As a consequence, there is an urgent need to develop a novel design and testing methods dedicated to ordered design families.

In conceptual and detailed design, product modularity is currently getting more attention. It is defined as the ability to create functional variants out of a set of modules, which form a future technical object [18]. In modular products, implementation of design changes requires lower usage of time, information, material, energy, and space resources than integral products, and the later the change is implemented, the more resources it requires [17]. As vehicles are concerned, high implementation costs also result from obtaining an official certification, which is costly and time-consuming. It means that all the issues in design identified during vehicle exploitation may require a complete redesign, which significantly increases the total investment cost to implement a product on the market.

The issues mentioned above make it necessary to look for novel methods to evaluate the mechanical strength and durability of machines and vehicles that can be implemented at an early design stage, when the cost to implement a change is the lowest. For those changes to be effective, knowledge of quantitative criteria describing useful functions of a designed system is necessary. Durability, defined as a time in which an object keeps operational parameters valuable to users, is regarded as one of them. It directly impacts both safety and usefulness of a product.

Current vehicle testing is connected mainly with active and passive safety assessment [19] and mechanical strength evaluation for static and fatigue loads. Criteria used for this evaluation can result from formal standards [6, 13] or researchers' experience. A widely used method for mechanical strength evaluation is the Finite Elements Method. It is commonly used to assess the durability of vehicle frames [1, 5] and load transferring parts [2] in static [1], fatigue [25], impact [16], and mixed loading [20]. The advantage of numerical testing is the

(*) Corresponding author.
E-mail addresses: M. Mysior (ORCID: 0000-0002-9973-704X): marek.mysior@pwr.edu.pl, G. Pietrucha (ORCID: 0000-0002-6635-4069): grzegorz.pietrucha@innovento.pl, S. Koziołek (ORCID: 0000-0002-5440-8146): sebastian.koziolek@pwr.edu.pl

possibility to assess mechanical strength without needing a physical prototype, which reduces design costs [15]. On the other hand, numerous simplifications and uncertainty of relevance of applied boundary conditions is a drawback of this method. Because of that, experimental testing methods are still used that can be divided into bench testing and empirical evaluation on a test track. Both types aim to evaluate strength and durability of individual components as well as entire vehicles. In this paper, authors concentrate on experimental strength evaluation of light trailers.

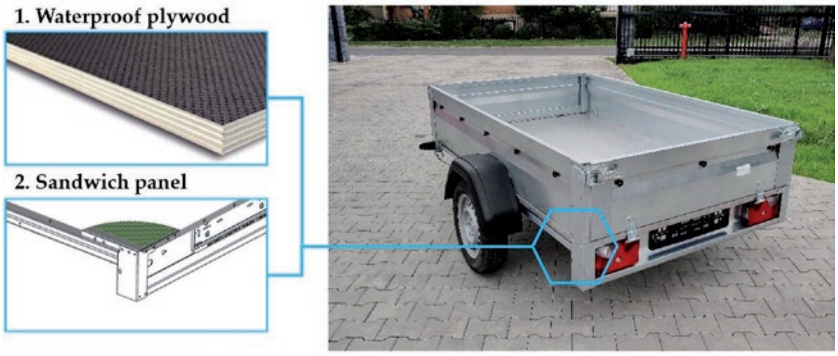

Fig. 1. Picture of the examined trailer

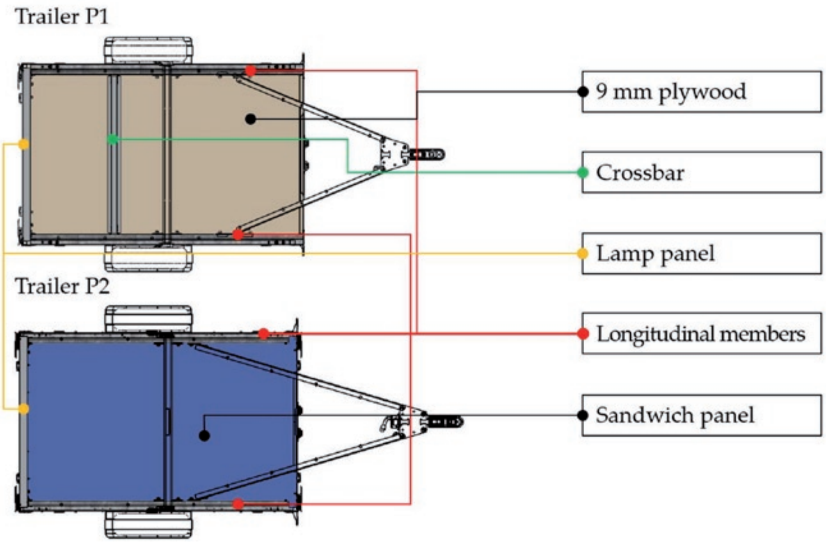

Fig. 2. Comparison of load carrying structures of the type 1 (top) and type 2 (bottom)

Experimental testing conducted on dedicated testing tracks is used to assess durability in operational conditions, although it is not formally required by the certifying authority [9, 14]. During testing, a vehicle is subjected to a specified load cycle that simulates extreme operational conditions in road exploitation. This cycle comprises passage through several types of pavements that induce loads on the structure of a vehicle. The quantitative characteristic of a testing cycle is determined by the type of vehicle and its planned exploitation. It is established that the total distance covered by a vehicle on a testing track represents an operational distance increased by the factor of 10. This means that a distance of 400 km traveled on a test track represents 4 000 km in road exploitation [14]. Experimental testing on special tracks reduces the amount of time needed to assess the safety of a vehicle in the scope of cyclic loads. However, this type of evaluation is time-consuming and costly due to the necessity of transporting uncertified vehicles to a test track to perform long-lasting trials.

An alternative form of experimental testing is connected with bench testing, in which individual vehicle components [7] or assemblies [21] are being evaluated on dedicated test platforms. Parts usually subjected to this type of testing are mechanical coupling devices, load-carrying frames, drawbars, and others [23]. Research apparatus typically consists of a test platform, actuators, fixing systems, and data acquiring units. Often, the analysis outcome is the identification of cracks and deflection measurement [22].

The above-described bench testing methods of vehicle strength, including light trailers, consider the limited variety of the load cycles; thus some of the load cycles existing in operational conditions are skipped. Moreover, such tests require specialized data acquiring units that make it possible to evaluate the fatigue life of the analyzed object.

In this paper, the authors present a novel method of experimental strength evaluation of trailers, equivalent to a full-scale assessment on a special test track. The work done consisted of empirical testing of two types of a light trailer on a special testing track and comparing the obtained results with the outcome of the bench testing of the same trailer types. The application of test loads and their duration were adjusted to represent the conditions existing during testing on a track. As a result, both trailer types were compared from an operational point of view.

2. Research method and object

In this paper, two types of light trailers were examined that differed in the manufacturing technology. Each trailer was characterized by a TPLM (Total Permissible Laden Mass) of 750 kg, corresponding to vehicle category O1. Both types were equipped with a single unbraked axle and V-shaped drawbar having a B50-X coupling head. Dimensions of the loading box were 129 cm x 204 cm. Fig. 1 presents a photograph of one of the examined trailers with a floor description.

First examined trailer (P1) was characterized by a floor made of a 9 mm thick waterproof, antislip plywood attached to the frame comprising two steel longitudinal members and one crossbar. The second trailer (P2) was manufactured using HONEYtech technology, characterized by a honeycomb plate used to strengthen the load-carrying structure. Like the first type, the floor plate was supported by two longitudinal members but without any crossbar. The comparison of load-carrying structures of both trailer types is shown in Fig. 2.

A scheme of the applied experimental strength evaluation method of trailers is shown in Fig. 3.

The presented method involves a bench test of trailers with a TPLM of 750 kg. It consists of four steps. In the first step, a trailer is assessed to verify its dimensional conformity to the trailer types tested on a test track. Those dimensions are related to the loading box, coupling point, and axle positioning. Next, a trailer is prepared for a bench test by attaching a loading frame to the lashing eyes of the trailer using transport belts. The remaining mass is supplemented with an evenly distributed loose material. The bench test is conducted continuously, with an excitation frequency of 22 to 26 Hz.

Every trailer subjected to testing is analyzed based on loading box diagonals and floor deformation measurements. The result of the bench test is considered positive if both diagonals are within their tolerance range and floor deformation is not bigger than 5%. The method presented in Fig. 3 was applied to assess the strength of both trailer types and is described in detail in chapter 4. The upcoming chapter describes validation studies of trailers on a test track.

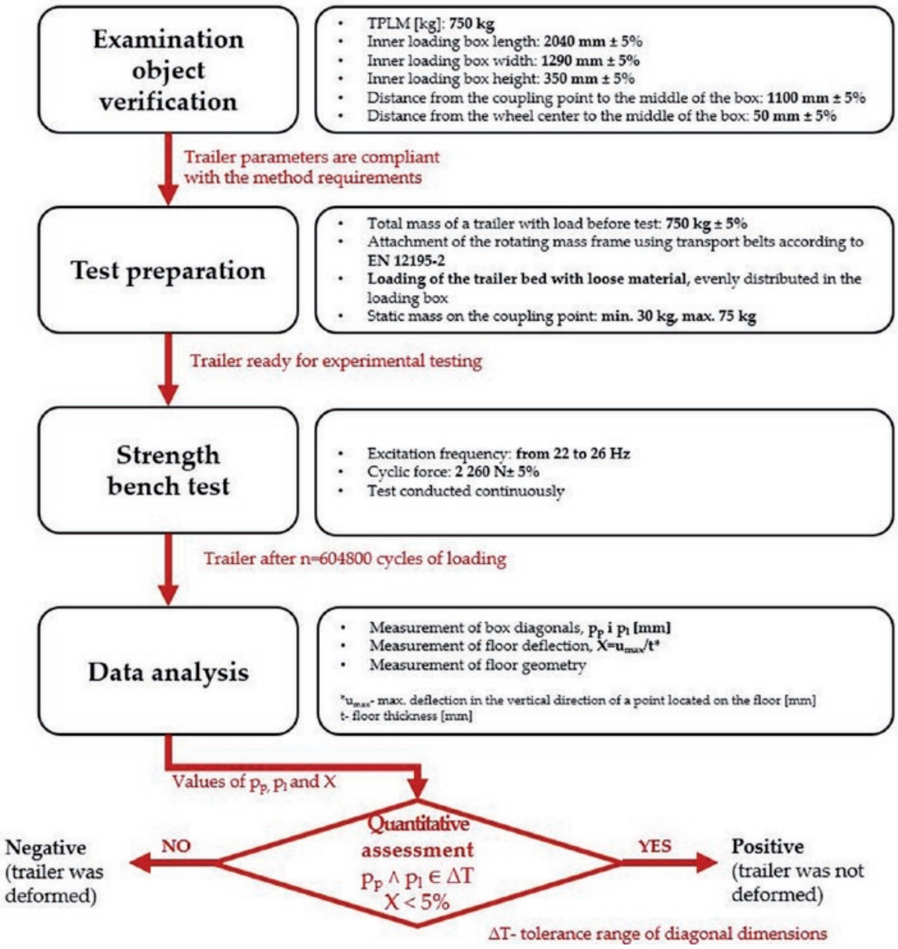

Fig 3. Diagram showing an original method of experimental strength bench test

3. Experimental evaluation of trailers on a testing track

Both trailer types (P1 and P2) were examined on a test track with the same loading cycle, traveling through resonance, rocky, and winding trails with a total distance of 20 km. Fig. 4 shows a picture of a test track with each of the used trails. Parametric description of test trails is shown in Table 1.

Evaluation of a plywood trailer (P1) on a test track resulted in a permanent change in the geometry of the loading box. This phenomenon was not observed for the trailer equipped with a sandwich panel (P2). Comparison of geometric forms of both trailers after testing on the track is shown in Fig. 5. Both trailers survived 100% of the test.

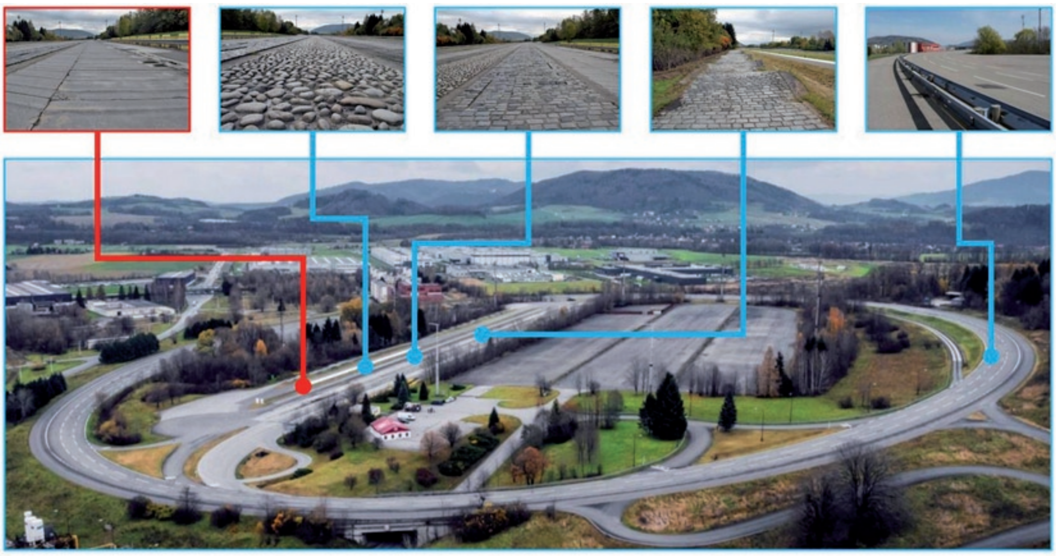

Fig 4. Picture of the TATRA Testing Grounds showing test trails used in experiment. Kopřivnice, CZ [24]

Table 1. Parametric description of test trails

	**Length**: 400 m **Obstacle height**: 0,02 m, **Obstacle spacing**: 0,770 m. **Max. velocity**: 60 km/h Made of concrete plates. Used for generation of cyclic dynamic loads for functional testing of vibrating elements and durability of vehicles.
	**Length**: 400 m **Dist. between rocks**: from 0,1 to 0,3 m. **Placement density**: od 20 do 30 pcs/m^2. **Effective height of obstacles**: 0,015 m. **Max. velocity**: 60 km/h Pavement made of 15-30 centimeters high granite stones, embedded from ½ to ¾ in flat concrete.

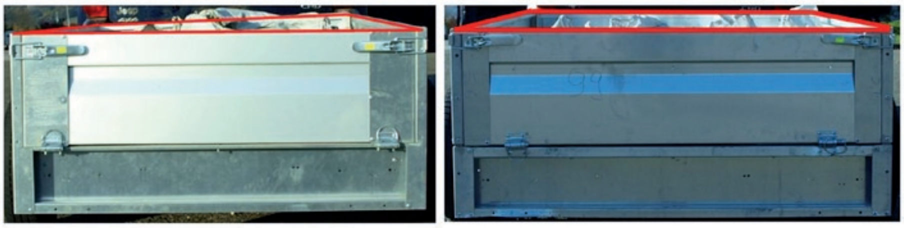

Fig. 5. Deformation form of evaluated trailers. A plywood trailer (P1) on the left and a trailer equipped with a sandwich panel (P2) on the right

4. Bench testing of trailers

After experimental evaluation of both trailer types on a test track, authors focused on creating a bench testing method that resembles the conditions met on the track. To meet this assumption, the proposed method had to fulfill a set of requirements that were defined in the literature [9]:

1. A method should make it possible to evaluate a complete trailer in the same configuration as during testing on a test track, **completeness condition,**
2. A method should lead to a similar deformation form as during testing on a test track, **analogy condition** and
3. A degree of that deformation should resemble the one observed during experimental evaluation on a test track, **proportionality condition**.

For this method to be effective, it is vital to determine how loads are imposed on the trailer. During testing on track, forces result from an evenly distributed load attached to the trailer structure by transport belts, which secure it to 4 corners of the box. On a test bench, a trailer is repeatedly loaded in the vertical and horizontal directions, simulating forces coming from various test trails acting on a trailer. The testing setup consisted of a coupling ball connected with a coupling head during an examination, wherein two trailer wheels supported the remaining load. A mass mount non-axially on a rotating shaft created a cyclic force acting on a trailer. Additionally, a loose material was distributed in the loading box to provide the static load. A scheme showing how forces act on a trailer during bench testing is shown in Fig. 6.

A cargo during bench testing was secured to the trailer frame by transport belts in the same way as during testing on track. Total reaction force on wheels and a coupling point corresponded to the weight of a TPLM of a trailer, i.e., 750 kg ± 5%. A cyclic load was obtained with an electric motor switched on, as shown in Fig. 7. The value of the cyclic force was selected such that the load amplitude was equal to 40% of the weight of the trailer load, i.e., 2 260 N. A change of variable force vector within a single loading cycle is shown in Fig. 8.

For a rotating mass-selected, the required value of the cyclic force was achieved with the excitation frequency of 24 Hz. This corresponds to the excitement frequency when traveling on a resonance trail with a velocity of 67 km/h. Table 2 summarizes parameters used for bench testing.

Test duration was selected based on the fulfillment of completeness, analogy, and proportionality conditions. Based on the experimental testing of trailers on a test track, the total number of cycles used in bench testing was determined to be equal to 604 800 cycles.

After bench testing of a plywood trailer, a change in the geometry of a loading box was observed. Measured values of box diagonals have shown a significant difference between right (p_p=2492 mm) and left (p_l=2509) mm diagonal, which exceeded the tolerance range for the reference dimension p=2499 ± 2 mm according to the ISO 2768-1 standard. From the operational point of view, visible damage to the trailer floor resulted from an influence of sand and a vibrating frame on the floor. This led to the formation of visible scratch marks and fissures, impacting the waterproof properties of the plywood.

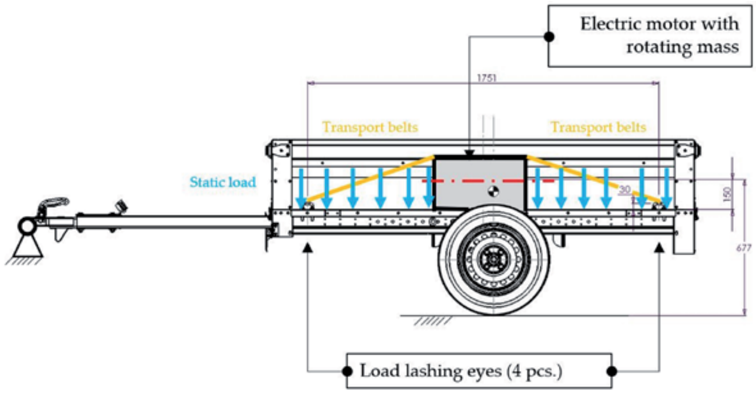

Fig 6. A loading scheme of a trailer on a test bench

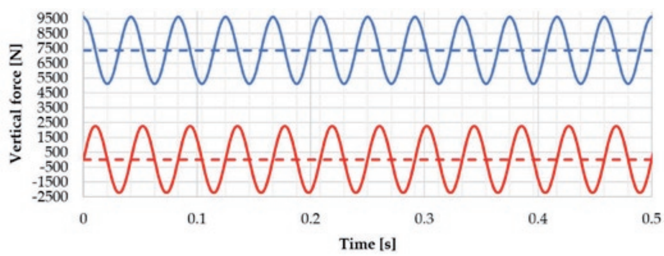

Fig. 7. The course of a cyclic load during bench testing

Analyzing the second type of trailer (P2), there was no visible deformation of a loading box, as observed with the first trailer type (Fig. 9). Additionally, the trailer kept all operational abilities of sideboards,

Table 2. Quantitative parameters describing bench testing of trailers

	Horizontal load	Vertical load
$\mathbf{F_A}$ [N] (*amplitude*)	2260	2260
$\mathbf{F_M}$ [N] (*mean value*)	7358	0
$\mathbf{F_{max}}$ [N] (*max. value*)	9618	2260
$\mathbf{F_{min}}$ [N] (*min. value*)	5098	-2260
f [Hz] (*excitation frequency*)	24	

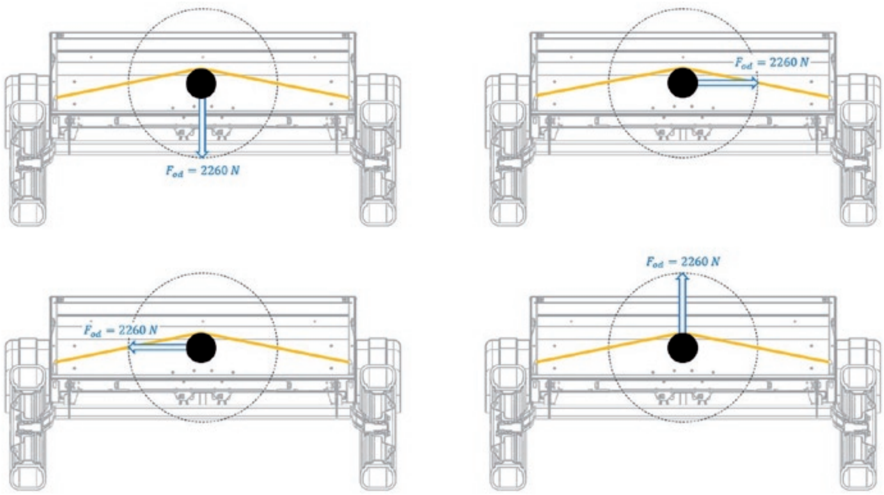

Fig. 8. Change of a loading force within a cycle

Fig. 9. Comparison of geometric forms of a plywood trailer (on the left) and a trailer equipped with a sandwich panel (on the right)

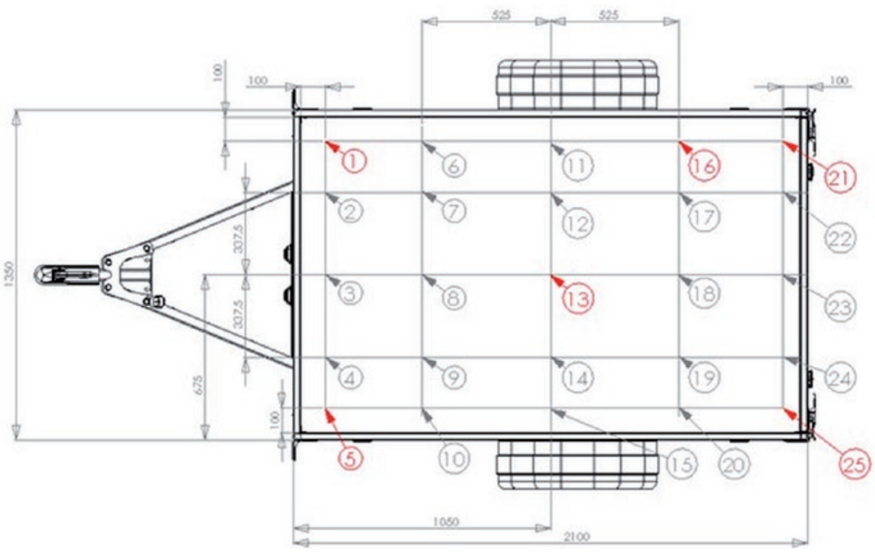

Fig. 10. Measurement points located on a trailer floor

locks, and hinges, together with the proper operation of a tilt feature. Measured values of box diagonals showed no difference between left (p_l=2498 mm) and right diagonal (p_p=2498 mm), remaining in the tolerance range for the reference dimension p=2499 ± 2 mm according to the ISO 2768-1 standard.

To confirm that the trailer type P2 was not deformed during bench testing, additional measurements were conducted for a given set of measurement points located on the top of the trailer floor, as shown in Fig. 10.

Measurements were made vertically with respect to a leveled base using an analog sensor. During measurements, a trailer was supported on longitudinal members of the frame, eliminating the influence of the suspension and tires deflection on the measurement results. Fig. 11. shows measured values of the vertical position of measurement points before (blue) and after bench testing (green), with respect to the same measurement base.

Measured differences between vertical position of measurement points before and after bench testing for P2 type trailer is shown in Fig. 12. The maximum difference was equal to 1.91 mm. Only four points (13, 14, 18, 19) had a difference of more than 1 mm.

5. Discussion and conclusions

An original method of experimental strength evaluation of trailers was used to examine two types of trailers having different load-carrying structures. The dimensions of their loading box and method of load lashing for both trailers were the same. Results obtained from experimental testing of trailers on a track were compared with those from bench testing. In Fig. 13, a comparison between deformations for both trailer types are shown for bench and track testing.

The track and bench testing results in similar deformation forms and degrees for two kinds of trailers. This concludes that analogy and proportionality conditions were met during bench tests for both analyzed trailer types, i.e., deformation forms for a corresponding trailer type match for two examination methods. Since complete trailers were analyzed in both track and bench tests, the condition of completeness is also satisfied, and the proposed bench testing method represents experimental testing on a track. It means that the loading cycle comprises traveling through resonance, rocky, and winding trails with a total distance of 20 km is equivalent to 604 800 cycles of loading on a test bench.

Based on the results of experimental testing of a modular trailer having a load-carrying structure equipped with a sandwich panel (type P2), neither permanent deformation was observed nor any damages, scratches, or breaks that could negatively impact the operational features of the said trailer. The difference in both diagonal lengths of the loading box was smaller than 1%. In the other trailer (type P1), a visible deformation of a loading box was observed, impacting the vehicle's operational values, including aesthetics and appearance of a trailer. Furthermore, the deformed shape of the trailer box has a negative impact on the positioning of accessories, i.e., the cover stand attached to four corner posts. If a trailer is deformed, the assembly process of the said stand will be more complex and will require additional force.

Also, after the assembly, residual stresses will exist in the structure of the cover stand. Observed deformation form and extent is a typical

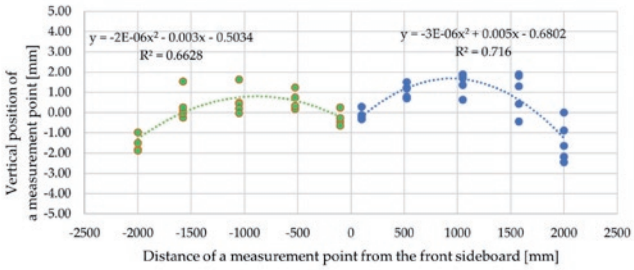

Fig. 11. Measured values of the vertical position of measurement points before (blue) and after bench testing (green)

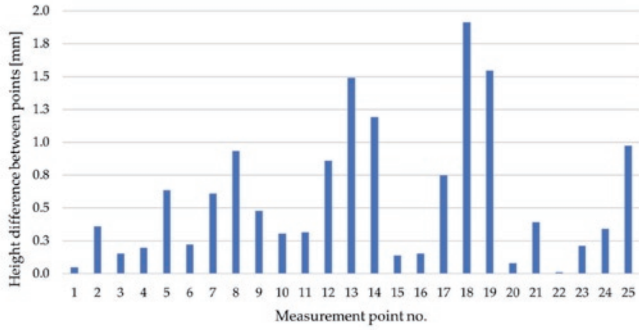

Fig. 12. Measured differences between vertical position of measurement points before and after bench testing for P2 type trailer.

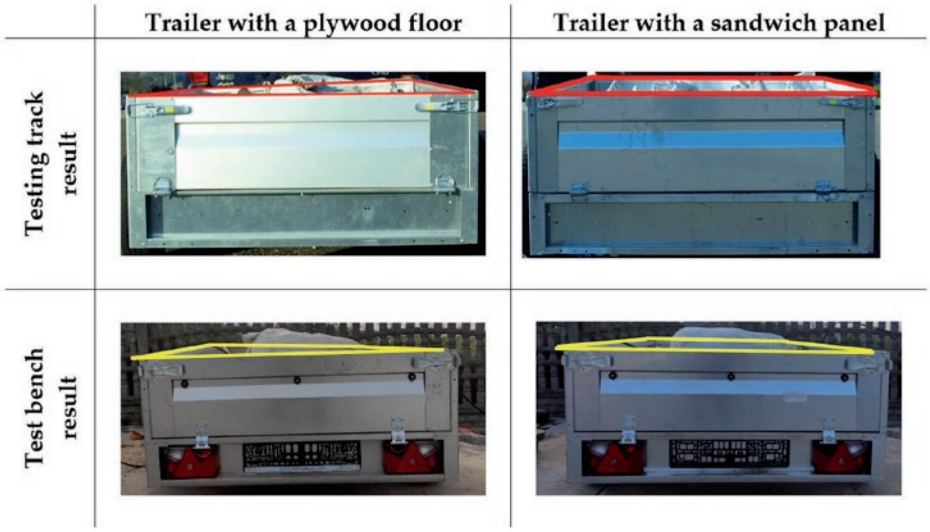

Fig. 13. Comparison of track and bench testing results of both trailer types

phenomenon in exploiting trailers currently available on the market. Recently, a standard thickness of a plywood floor was equal to 12 mm. Nowadays, in pursuit of manufacturing cost reduction, producers tend to reduce the price of a trailer by substituting it with thinner plywood. This leads to reduced stiffness of the trailer and, as a result, to its deformation in operation.

The lack of loading box deformation of trailer P2 makes it possible to conclude that the stiffness of the load-carrying structure of said trailer increases compared to already existing solutions because of an application of a sandwich panel. This finding confirms current research in the field [8, 11]. This stiffness is vital for trailer behavior on the road, influencing motion stability and certainty of driving. From the operational point of view, sandwich panels make it possible to use metallic materials on the top of the floor, including stainless steel. This is a desired feature in exploitation, connected with increased corrosion resistance and ease of cleaning. Furthermore, as compared to regular plywood, no damage in the form of scratches or fissures was observed for this type of floor panel. Also, due to the increased stiffness of the sandwich panel, there is no need to use additional strengthening elements, i.e., crossbars, which simplifies the trailer's assembly process.

The presented method of experimental strength evaluation of trailers is an original and effective way to determine the durability of trailers with a TPLM of 750 kg and can be used to assess the operational values of designed vehicles. It represents the expensive and time-consuming track testing meaning, that for trailers having defined dimensions and TPLM, it is possible to limit a research agenda to bench testing. If a change in TPLM or trailer sizes occurs, it is necessary to validate the proposed method for a broader range of initial parameters. It is connected with a different loading cycle on a test track, depending on the designed trailer having other operational parameters. The proposed method of bench testing makes it possible to examine a full-scale prototype without special preparation of the test specimen. It proves the versatility of the proposed method, unlike already existing solutions in bench testing. Furthermore, the approach fits broad research agendas, including but not limited to quality control of the full-scale prototypes of a trailer and verification of conformity with official requirements. This represents an evolutionary approach in vehicle design that increases the design process's effectiveness by identifying those areas that should be improved before vehicle certification and exploitation in road traffic.

The article presents results of a project:"Modular, multifunctional and ultralight trailer manuafactured in a flexible production system" project no.: POIR.01.01.01-00-0563/17 and „Flexible production system (ESPP) of modular car trailers with GW up to 3500kg manufactured in HoneyTech technology", project no.: POIR.01.01.01-00-0589/19, realized within Measure 1.1 „R&D projects of enterprises", Sub-measure 1.1.1 „Industrial research and development work implemented by enterprises", Project co-financed by the European Union from the European Regional Development Fund under the Smart Growth Operational Programme 2014-2020. Data used for analysis and conducted research together with its results are the sole property of above project beneficiaries.

References

1. Caban J, Nieoczym A, Gardyński L. Strength analysis of a container semi-truck frame. Engineering Failure Analysis 2021; 127(February): 105487, https://doi.org/10.1016/j.engfailanal.2021.105487.
2. Chudzik A, Warda B. Fatigue life prediction of a radial cylindrical roller bearing subjected to a combined load using FEM. Eksploatacja i Niezawodnosc - Maintenance and Reliability 2020; 22(2): 212-220, https://doi.org/10.17531/ein.2020.2.4.
3. Chybowska D, Chybowski L, Guze S, Wilczyński P. A method for determining critical events during large disasters of production platforms. Journal of Loss Prevention in the Process Industries 2021; 72: 104528, https://doi.org/10.1016/j.jlp.2021.104528.
4. Chybowska D, Guze S. A Multiphase Process Approach to the Analysis of the Reliability and Safety in Maritime Transport Systems.

TransNav, the International Journal on Marine Navigation and Safety of Sea Transportation 2020; 14(4): 985-990, https://doi.org/10.12716/1001.14.04.25.
5. Dębski H, Koszałka G, Ferdynus M. Wykorzystanie mes w analizie struktury nośnej ramy naczepy o zmiennych parametrach eksploatacyjnych. Eksploatacja i Niezawodnosc - Maintenance and Reliability 2012; 14(2): 107-114.
6. Działak P, Karliński J. Comparative examination of the trailer frame in accordance with UIC 596-5. Materials Today: Proceedings 2019; 12: 416-422, https://doi.org/10.1016/j.matpr.2019.03.144.
7. Kozłowski E, Borucka A, Szymczak E, et al. Predicting the Fatigue Life of a Ball Joint. Transport and Telecommunication Journal 2021; 22(4): 453-460. https://doi.org/10.2478/ttj-2021-0035
8. Giglio M, Gilioli A, Manes A. Numerical investigation of a three point bending test on sandwich panels with aluminum skins and NomexTM honeycomb core. Computational Materials Science 2012; 56: 69-78, https://doi.org/10.1016/j.commatsci.2012.01.007.
9. Halfpenny A. Methods for accelerating dynamic durability tests. 9th International Conference on Recent Advances in Structural Dynamics 2006: 1-19.
10. Han Y, Lin Y, Zhang C, Wang D F. Customer-related durability test of semi-trailer engine based on failure mode. Engineering Failure Analysis 2021; 120(September 2020): 105095, https://doi.org/10.1016/j.engfailanal.2020.105095.
11. He M, Hu W. A study on composite honeycomb sandwich panel structure. Materials & Design 2008; 29(3): 709-713, https://doi.org/10.1016/j.matdes.2007.03.003.
12. Kamiński Z, Kulikowski K. Determination of the functional and service characteristics of the pneumatic system of an agricultural tractor with mechanical brakes using simulation methods. Eksploatacja i Niezawodnosc - Maintenance and Reliability 2015; 17(3): 355-364, https://doi.org/10.17531/ein.2015.3.5.
13. Karlinski J, Ptak M, Chybowski L. A Numerical Analysis of the Working Machine Tyre Inflation Process to Ensure Operator Safety. Energies 2019, https://doi.org/10.3390/en12152971.
14. Kepka M, Kepka M, Václavík J, Chvojan J. Fatigue life of a bus structure in normal operation and in accelerated testing on special tracks. Procedia Structural Integrity 2019; 17: 44-50, https://doi.org/10.1016/j.prostr.2019.08.007.
15. Koziołek S. Inżynieria Wynalazczości. Metodologia projektowania innowacyjnych systemów technicznych. Wrocław, Oficyna Wydawnicza Politechniki Wrocławskiej: 2019.
16. Mackiewicz A, Pyka D, Pach J et al. Comparison of Numerical Modelling Methods of Innovative Materials for Ballistic Shields. 2020: 119-127, https://doi.org/10.1007/978-3-030-34123-7_13.
17. Mysior M, Hnat W, Koziołek S. Method of Identification of Useful Functions in the Scope of Technical System Development. 2019, https://doi.org/10.1007/978-3-030-32497-1_17.
18. Mysior M. Metoda projektowania maszyn oraz urządzeń w aspekcie modułowości. 2021.
19. Ptak M. Method to Assess and Enhance Vulnerable Road User Safety during Impact Loading. Applied Sciences 2019; 9(5): 1000, https://doi.org/10.3390/app9051000.
20. Rusiński E. Zasady projektowania konstrukcji nośnych pojazdów samochodowych. Wrocław, Oficyna Wydawnicza Politechniki Wrocławskiej: 2002.
21. Szymczak T, Brodecki A, Kowalewski Z L, Makowska K. Tow truck frame made of high strength steel under cyclic loading. Materials Today: Proceedings 2019; 12: 207-212, https://doi.org/10.1016/j.matpr.2019.03.115.
22. Szymczak T, Brodecki A, Sobolewski T. Laboratoryjna ocena stanu technicznego komponentów do pojazdów samochodowych. Przegląd Techniczny 2021.
23. Szymczak T, Cholewiński S, Sobolewski T. Badania wytrzymałościowe i stanowiskowe - jako narzędzie do oceny jakości technicznej materiałów i komponentów konstrukcyjnych związanych z bezpieczeństwem ruchu drogowego. Bezpieczeństwo Ruchu Drogowego 2020; 3-4: 21-24.
24. Tello L, Castejon L, Malon H et al. Development of a fatigue life prediction methodology for welded steel semi-trailer components based on a new criterion. Engineering Failure Analysis 2020; 108(January 2019): 104268, https://doi.org/10.1016/j.engfailanal.2019.104268.

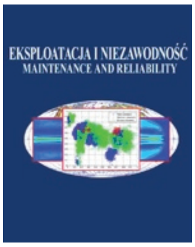

Eksploatacja i Niezawodnosc – Maintenance and Reliability

Volume 24 (2022), Issue 1

journal homepage: http://www.ein.org.pl

Article citation info:
Kruczyński SW, Orliński P, Ślęzak M. The comparative analysis of catalytic properties of Group 11 elements in NO_x reduction by hydrocarbons in the presence of oxygen. Eksploatacja i Niezawodnosc – Maintenance and Reliability 2022; 24 (1): 170–176, http://doi.org/10.17531/ein.2022.1.19.

The comparative analysis of catalytic properties of Group 11 elements in NO_x reduction by hydrocarbons in the presence of oxygen

Indexed by: Web of Science Group

Stanisław W. Kruczyński[a], Piotr Orliński[b], Marcin Ślęzak[a]

[a] Motor Transport Institute, ul. Jagiellońska 80, 03-301 Warsaw, Poland
[b] Warsaw University of Technology, Faculty of Automotive and Construction Machinery Engineering, Institute of Vehicles and Construction Machinery Engineering, ul. Narbutta 84, 02-524 Warsaw, Poland

Highlights

- The structure of metal monolith models coated with the Al_2O_3-SiO_2 carrier was discussed.
- The surface topography of the Al_2O_3-SiO_2 carrier was assessed based on SEM images and acidity tests of its surface using the ammonia desorption method, including measurements of the specific surface using the BET method and porosity of the catalytic carrier using the BJH method.
- The results of NO_2, NO, and C_3H_6 conversion tests as well as CO and N_2O formation were analysed and assessed in the developed reactors located in an electric tubular furnace, depending on the NO_x conversion temperature at a constant dose of the reducing agent (C_3H_6).

Abstract

NO_x emission reduction in diesel engines can be achieved by using catalytic reactors reducing nitrogen oxides, including NH_3-SCR and possibly also HC-SCR reactors. Reactors using ammonia achieve large conversion rates but cause a lot of operational problems. For this reason, the interest in reactors using hydrocarbons and their derivatives to reduce NO_x has increased. Such reactors are the ones using metals from Group 11 (coinage metals) such as Cu, Ag and Au placed on an Al_2O_3-SiO_2 carrier as active materials. The article characterizes the porosity and acidity of the carrier surface. Conversion of NO_2, NO and propene as well as the formation of CO and N_2O depending on the temperature at constant dosing of propene on a carrier covered with Cu, Ag and Au with a metal content of 4 g/dm^3 were evaluated. The results of the tests showed that the tested Group 11 elements can be the basis for further experiments related to the development of this exhaust fumes cleaning technology for diesel engines.

Keywords

Diesel engine, NO_x reduction, conversion testing, Group 11 elements.

1. Introduction

Based on the analysis of the test results of diesel engines manufactured so far and the possibilities of development of their injection systems, it may be concluded that they meet the standards limiting the emission of carbon monoxide and hydrocarbons, while it is much more difficult to meet the requirements limiting the emission of particulate matter and nitrogen oxides [10, 11, 19]. The emission of nitrogen oxides, due to their toxic properties and large amounts emitted into the atmosphere, has become one of the main problems that need to be solved in future designs of these engines. The implementation of Euro 6 standard provisions in Europe since 2014 significantly reducing CO, THC, NO_x, PM and PN emissions in the LDV and HDV vehicle type-approval tests has forced vehicle manufacturers to significantly reduce emissions of harmful substances, including in particular NO_x emissions. Therefore, research is being carried out on the creation, under laboratory conditions, of running cycles corresponding to the actual operation of vehicles so that actual emissions of harmful components into the environment, including in particular nitrogen oxides, could be assessed quickly and accurately [22].

The reduction of the NO_x emissions of diesel engines can be achieved [11]:

- by methods applied inside the engine. These methods consist in conducting the processes occurring during the preparation and subsequent combustion of the mixture in such a way that the concentration of NO_X in the exhaust gases of the engine could be as low as possible [24]. This process involves finding an optimum between engine power, specific fuel consumption and emissions of harmful substances,
- by using selective catalytic reduction reactors for nitrogen oxides, such as NH_3-SCR or possibly HC-SCR reactors,
- by using LNT reactors that selectively reduce nitrogen oxides, being NO_x traps [11].

Exhaust fumes recirculation, when applied to an extent that does not significantly increase fuel consumption and PM emission, reduces the NO_x emission to a small extent and is not sufficient to meet the requirements of Euro 6 and Euro VI standards. However, its application contributes to the reduction of NO_x concentration upstream of the SCR reactors, thus facilitating their operation. Therefore, it is necessary to use the reactors for selective catalytic reduction of NO_x.

Nitrogen oxides in the presence of oxygen can be removed by selective chemical reduction, which can be divided into two groups, depending on the properties of the reducing agent:

E-mail addresses: S.W. Kruczyński (ORCID: 0000-0001-8607-186X): stanislaw.kruczynski@its.waw.pl, P. Orliński (ORCID: 0000-0002-1433-5202): piotr.orlinski@pw.edu.pl, M. Ślęzak (ORCID: 0000-0001-6059-8110): marcin.slezak@its.waw.pl

- ammonia reduction (NH_3-SCR)
- In the NH_3-SCR systems, gaseous ammonia can be released from ammonia sorbents or by ammonium salt decomposition and can be introduced into the exhaust gases at any temperature, especially at low loads of the combustion engine [9].
- In the case of SCR reactors active at a low temperature, NO_x emissions can be reduced at a temperature well below 200°C. $MgCl_2$ composites with various carbon materials, such as graphite or graphene can be used as ammonia sorbents [5].
- The commonly used method of ammonia supply to the NH_3-SCR reactor is the injection of an aqueous urea solution (AdBlue liquid), from which gaseous ammonia is obtained in hydrolysis and thermolysis processes [16]. The dimensions of sprayed AdBlue droplets have a fundamental impact on the efficiency of the selective catalytic reduction of NO_x [16].
- The hydrolysis of the aqueous urea solution may lead to the formation of poisonous sediments that may be problematic during the operation. Several combinations of urea decomposition reactions and sediment formation mechanisms are presented in the paper [2]. An important problem of effective NO_x reduction is the proper control of AdBlue fluid injection in an open loop or more precisely in a closed loop, taking into account the phenomenon of gaseous ammonia storage [23]. The most frequently used catalytically active materials are V_2O_5/TiO_2 or $V_2O_5/WO_3/TiO_2$ oxides. [25, 26]. Zeolites are also used as catalytically active materials in modern solutions. The problems with unburned hydrocarbons stored in large-pore zeolites have been an incentive to search for small-pore materials. Chabazite reactors were developed [4], containing Cu or Fe ions marked as Cu/SSZ-13 or Fe/SSZ-13, for NH_3-SCR catalysis applications. Despite these drawbacks and due to the high NO_x to N_2 conversion, these reactors are commonly used in LDV and HDV vehicles.
- the reduction with hydrocarbons (HC-SCR) or their derivatives containing oxygen, most often light alcohols. These reactors feature the following properties:
  - they achieve a relatively smaller conversion of NO_x not exceeding 80% [12],
  - NO_X conversion is achieved in a narrow range of high temperatures of 400–500°C [12],
  - they require high hydrocarbon doses due to their low selectivity and thus contribute to the heating of the reactor [7, 12]. It is often observed that the higher the dose of the injected hydrocarbons, the broader the range of the NO_x reduction temperature. A large dose of the injected hydrocarbons may increase the reactor temperature to values not encountered in oxidizing reactors used in diesel engines. The injection of 3% of the fuel dose upstream the HC-SCR reactor increases the temperature of the reactor bed by 30°C, and the injection of 6% of the fuel increases the temperature by 50°C.

Group 11 elements were considered catalytically active materials. Papers [15, 18] present the results of research on the use of copper ions placed in zeolites impacting their activity, depending on the oxygen content in exhaust fumes and the acidity of the reactor active surface.

Paper [17] compares the activity of the bimetal Ag-Au system on Al_2O_3, as compared to the activity of Ag on Al_2O_3, demonstrating that the activity of the Ag-Au bimetal is higher than either Ag or Au. On the other hand, the authors of the paper [3] found a promotional effect of hydrogen addition to propene in the Au/Al_2O_3 reactor. Paper [12] describes the preparation for obtaining the Ag/Al_2O_3 reactor and characterizes the porosity and acidity of its surface. The silver dispersion was assessed based on oxygen adsorption tests on silver crystallites and based on TEM images of silver crystallites. NO_2, NO and propane conversion was evaluated depending on the temperature. The conversion of NO_2, NO and propane at 500°C was also evaluated, depending on the added reducing agent and the selectivity of propane in the NO reduction.

Papers [7, 20] present the results of research concerning NO_x reduction with hydrocarbons and light alcohols on silver reactors. In order to increase the activity of the silver catalyst, the admixtures of MgO and CeO_2 oxides were added to the interlayer with Al_2O_3 [21]. Metal ion substituted zeolites are often used as active materials in HC-SC technology [15]. It was concluded that the most active HC-SCR catalysts should have strong acid locations, an active phase such as copper or cobalt, or element activity such as silver or a mixture of metals for the broader scope of activity. To reduce deactivation, materials should contain noble metals such as platinum or rhodium. Tests of the impact of hydrogen addition to different hydrocarbon reducing agents on the NO_x reduction efficiency were conducted both under laboratory experiments and in the engine dynamometer at a temperature below 315°C on the Ag/Al_2O_3 reactor with a 2.5% silver weight content [6]. Hydrogen increased the NO_x reduction efficiency at low temperatures (245–315°C).

The catalytic reduction of NO_x on the Ag/Al_2O_3 catalyst was also tested using such reactants as liquid hydrocarbons (GTL) and butanol [8]. It was proved that the effects obtained result from high reactivity, polarity and diffusivity of butanol in the catalyst, increasing the NO_x conversion.

In research works on increasing NO_x reduction activity, especially at low temperatures, the phenomenon of cold plasma was used. Thus, the efficiency of NO_x reduction using HC SCR technology with Pt- and Ag-based catalysts on an Al_2O_3 carrier at different temperature values was assessed using hydrogen and hydrocarbons as reducing agents supplied directly or generated on an engine station by plasma reforming [14]. The cold plasma produced in the corona discharge reactor was used to reform the diesel fuel for the selective catalytic reduction (HC-SCR) of NO_x on the Ag/Al_2O_3 catalysts [1].

2. Objective and scope of the works

The literature on the subject does not include the results of the tests of NO_x selective catalytic reduction with hydrocarbons using Group 11 elements applied on a carrier with high surface acidity. However, the acidity of the surface of the carrier [12] is specified in the literature as a factor contributing to the catalytic reduction of NO_x.

The objective of the paper is to assess and compare the catalytic activity of copper, silver and gold applied onto a carrier with high acidity in the selective catalytic reduction of NO and NO_2 with propene and additionally to compare the formation understood as the formation of undesired emission of N_2O and CO in actual exhaust fumes of a diesel engine containing large amounts of oxygen.

The work was carried out in the following stages:

- The structure of metal monolith models covered with the Al_2O_3-SiO_2 carrier.
- The assessment of surface topography of the Al_2O_3-SiO_2 carrier based on SEM images and acidity tests of its surface using the ammonia desorption method, including measurements of the specific surface using the BET method and porosity of the catalytic carrier using the BJH method.
- Impregnation of the carrier with selected Group 11 metals.
- The tests of NO_2, NO, and C_3H_6 conversion as well as CO and N_2O formation in the developed reactors located in an electric tubular furnace, depending on the NO_x conversion temperature at constant reducing agent dose (C_3H_6).
- Analysis of test results.

3. The structure of metal monolith models covered with the Al_2O_3-SiO_2 carrier

The monolith models were made of heat-resistant steel with a diameter Φ = 30 mm, a length L = 80 mm and with 400 cpsi cells, covered with aluminium polyphosphate. The carrier in the form of aluminosilicate with a content of 70% of Al_2O_3 and 30% of SiO_2 was then applied onto them using the sol-gel method.

Unfavourable transformation of active forms ofγ-Al_2O_3 with a large surface to α-Al_2O_3 can be prevented by introducing elements or compounds thermally stabilizing aluminium oxides varieties into the carrier. Such a compound is SiO_2, which is formed by $Si(OC_2H_5)_4$ hydrolysis process [12]. An additional positive effect of the introduction of SiO_2 into the carrier layer may be an increase in the acidity of the carrier surface. The ceramic base layer, i.e. aluminium polyphosphate layer, is covered with a silver carrier layer consisting of aluminium hydroxide with an addition of silicon hydroxide. During baking, Al_2O_3 and SiO_2 are obtained, which form an appropriate layer of the catalytic carrier. This layer is applied using the sol-gel method with a hydrolysed solution of $Al(OC_4H_9)_3$ and $Si(OC_2H_5)_4$ subject to hydrolysis.

4. The assessment of surface topography of the Al_2O_3-SiO_2 carrier

The visualization of the surface topography of the Al_2O_3-SiO_2 carrier was performed using the LEO 1530 microscope equipped with the EDX microanalysis system. For microscopic tests, carrier samples were prepared on 5×10 mm plates, the surface of which was covered with a layer of carbon with the thickness of ~ 25 nm in the PVD machine at a pressure of 10^{-5} TR. 500× magnified and 5,000×magnified surface images were obtained, as presented in Figure 1.

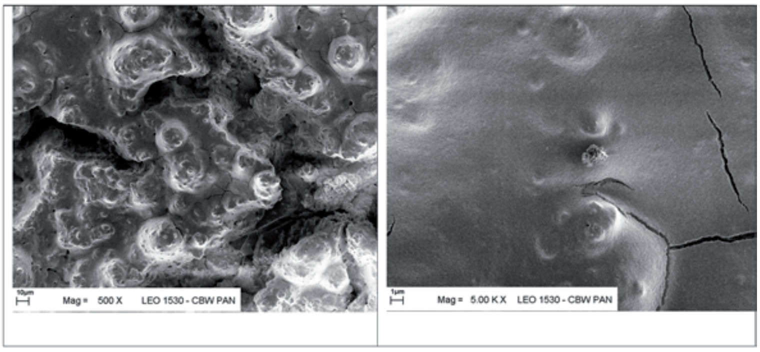

Fig. 1. SEM images of a fragment of the catalytic carrier surface Al_2O_3-SIO_2 magnified 500× and 5,000× prepared for copper impregnation

5. Acidity tests of the surface of the Al_2O_3-SiO_2 carrier

Literature review suggests a direct link between the catalytic activity in the reduction of nitrogen oxides and the acidic properties of the active catalyst carrier surface [12]. Since the results of tests of the Al_2O_3-SiO_2 carrier clearly indicate its activity in the conversion of nitrogen oxides, tests were performed to determine the acidity of the surface of the Al_2O_3-SiO_2 carrier used for the construction of Cu/Al_2O_3-SiO_2, Ag/Al_2O_3-SiO_2 and Au/Al_2O_3-SiO_2 reactors.

The acidity of the catalyst carrier surface in the form of powder isolated from the plate of the reactor model was determined using Shimadzu GCMS-QP2020 gas chromatograph equipped with a TCD concentration detector. Argon was used as carrier gas. Ammonia vapours were dosed until the ammonia peak appeared, then the sample was heated at a temperature of approx. 100°C until the signal coming from ammonia disappeared and the ammonia desorption was started:

- 3 minutes at a temperature of approx. 100°C (373K),
- sample heating at a rate of 12 degrees/min. to approx. 420°C (693K),
- sample warm-up for 30 minutes until the ammonia signal disappeared.

The surface area between the desorption peak curve and the zero line was calculated and compared with the surface area of the test, where 4 cm^3 of ammonia became fully adsorbed on the strong centres of the carrier.

The calculation of the amount of adsorbed ammonia and surface area of the NH_3-covered carrier calculated according to the BET model (one particle may be adsorbed on one acidic centre of the catalyst), which may be a measure of the acidity of its surface, has been presented in Table 1. These calculations were performed for two temperature ranges: 373K–693K, and 600K–693K.

The results of the determinations included in Table 1 show that the developed carrier features high surface acidity. The concentrations of acid centres for aluminosilicates amount to approx. 1.012–1.014 centres per 1 cm^2, which corresponds from 0.2 to 20% of the catalyst surface occupation. The developed carrier, within the range of temperature relevant for the conversion of NO_x, has a surface covered with NH_3 which is approximately 8% greater than the acid surface present in aluminosilicates [12].

6. Tests of the specific surface and porosity of the Al_2O_3-SiO_2 carrier

The measurements of the BET specific surface of the Al_2O_3-SiO_2 catalytic carrier in the form of powder isolated from the metal plate of the reactor model were performed based on the nitrogen adsorption isotherm equation using an ASAP 2420 Micromeritics Inc. USA apparatus. The measured surface value was 195.4 m^2/g.

The volume and surface tests of mesopores in the range of their dimensions from 1.7 to 23 nm were carried out using the method developed by Barrett, Joyner and Halenda (BJH) [11].

The relationship between the steam pressure above the curved surface with the radius of curvature r_k and the steam pressure above the flat surface p_o is described by the Thomson-Kelvin equation used in the BJH method:

$$\ln\frac{p}{p_o} = \left(\frac{-2V_m}{r_k RT}\right)\cdot \cos \qquad (1)$$

where:

p – steam pressure above the flat surface [Pa],
p_o – steam pressure above the curved (cylindrical) surface [Pa],
δ – liquid surface tension [N/m],
V_m – molar volume [m^3/mol],
φ – liquid meniscus wetting angle in relation to the capillary walls [°],
R – universal gas constant [J/(mol · K)],
T – absolute temperature [K].

The phenomenon of capillary condensation is used to quantify mesoporous solids. This phenomenon occurs in transition pores (mes-

Table 1. Results of acidity determinations of the catalyst carrier surface

NH_3 desorption temperature range [K]	Dose of ammonia [mmol NH_3/g]	Number of particles [NH_3/g]	Number of particles of the [NH_3/cm^2]	Surface catalyst coated with NH_3 [%]
372–692 K	0.56	3.373×10^{20}	1.449×10^{14}	27.7
600–692 K	0.28	1.687×10^{20}	0.7245×10^{14}	13.85

opores), the diameter of which according to IUPAC classification ranges from 2 to 50 nm.

The results of the measurements of nitrogen adsorption and desorption of the total area of the mesopores and their increment using the BJH method have been presented in Figure 2, whereas the total volume and volume increment of the mesopores have been presented in Figure 3.

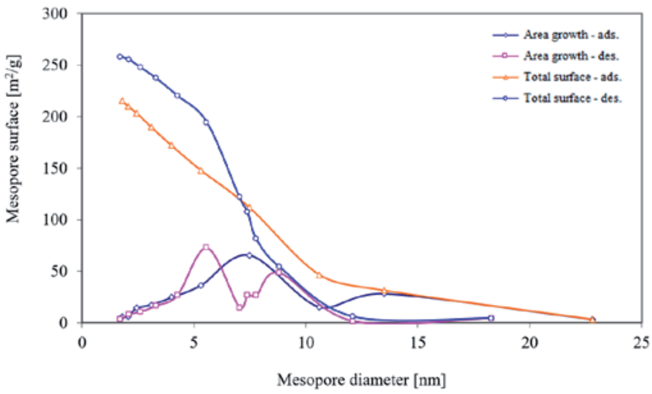

Fig. 2. The total surface area of mesopores and the increment of the mesopore surface area as a function of their diameters calculated using the BJH method with nitrogen adsorption and desorption isotherms

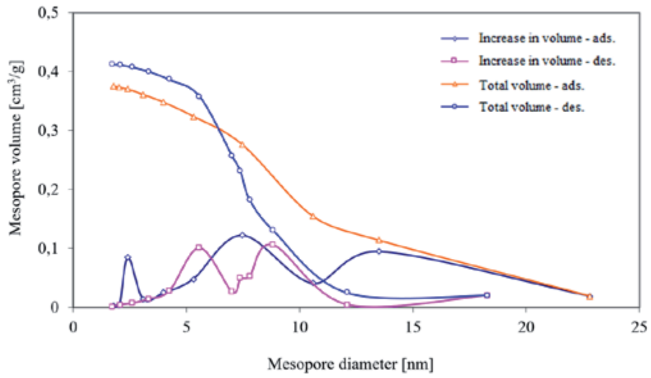

Fig. 3. The total volume of mesopores and the increment of mesopore volume as a function of their diameters calculated using the BJH method with nitrogen adsorption and desorption isotherms

7. Impregnation of the carrier with selected Group 11 elements

After drying and baking, the monoliths were covered with copper, silver and gold using the carrier impregnation materials listed in Table 2. As a result, research reactors were obtained, which were characterized in Table 2.

Table 2. Reactor characteristics

Reactor	Metal content [g/dm^3]	Materials used for carrier impregnation
Cu/Al_2O_3-SiO_2	4	Copper nitrate $[Cu(NO_3)_2 \cdot 3H_2O]$
Ag/Al_2O_3-SiO_2	4	Silver nitrate, formic acid
Au/Al_2O_3-SiO_2	4	Chloroauric acid

8. Tests of NO_2, NO, and C_3H_6 conversion as well as CO and N_2O formation

The research catalytic reactors were placed in an electric furnace and the actual exhaust fumes from a diesel engine with direct injection were passed through them at a constant relative volume flow rate SV = 30,000 h^{-1}. Directly downstream the engine outlet header, propylene was added to the exhaust fumes at a constant dose of approx. 800 ppm. The reducing agent dose was measured using a rotameter. The engine was supplied with commercial diesel fuel manufactured by PKN Orlen with a sulphur content of up to 10 ppm. The exhaust fumes temperature was measured upstream and downstream of the catalytic reactor, and the average value of the measured temperature was adopted as the catalytic reaction temperature. Gas concentration was measured using the AVL CEB2 analyser using the following techniques. The concentrations of NO and NO_2 were measured using the CL method, the concentrations of C_3H_6 were measured using the FID method, the concentrations of N_2O, CO and CO_2 were measured using the IR method, and the concentrations of O_2 were measured using the paramagnetic method. The measurements were performed until reaching the average exhaust fumes temperature $T_s \sim 600$ C°. Based on the results of the measurements, the following parameters of changes of exhaust fumes components in the reactor models were determined:

$$\text{Conversion of } NO_2\text{, NO and } C_3H_6 \quad k_i = \frac{C_{ip} - C_{iz}}{C_{iz}} \cdot 100\% \tag{2}$$

$$\text{Formation of } N_2O \text{ and CO} \quad p_i = \frac{C_{iz} - C_{ip}}{C_{iz}} \cdot 100\% \tag{3}$$

where:
C_{ip} – concentration of the i-th component upstream the reactor,
C_{iz} – concentration of the i-th component downstream the reactor.

A comparison of test results for the developed models of reactors depending on the catalytic reaction temperature with the constant addition of propylene has been presented in figures 4–8.

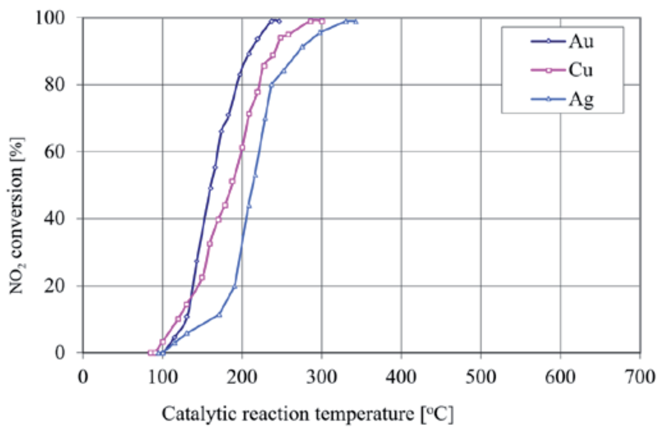

Fig. 4. The conversion of nitrogen dioxide depending on the temperature of catalytic processes for researched models of reactors upon NO_X reduction with propylene upon mixture combustion with the composition λ = 4.1. Initial concentrations of exhaust fumes components were as follows: NO_2 = 70÷100 ppm, NO = 365÷420 ppm, N_2O = 85÷100 ppm, C_3H_6 = 810÷830 ppm, CO = 0.04%, CO_2 = 5%, O_2 = 13.7÷13.9%. Relative volumetric exhaust fumes flow rate SV = 30,000 h^{-}

9. Analysis of test results

The properties of developed models of reactors were evaluated based on the determined conversion parameters and the formation of exhaust fumes components. The basic criterion was the conversion of nitric oxide, nitrogen dioxide and hydrocarbons. The reactor evaluation also took into account the secondary effects of the selective reduction of nitrogen oxides, such as the formation of additional amounts of nitrous oxide and carbon monoxide.

Conversion of NO and NO_2 and C_3H_6

The parameters of gas conversion in the tested reactor models, such as k_{max} – the maximum achieved conversion, and T_{50} – 50% conversion temperature have been presented in Table 3.

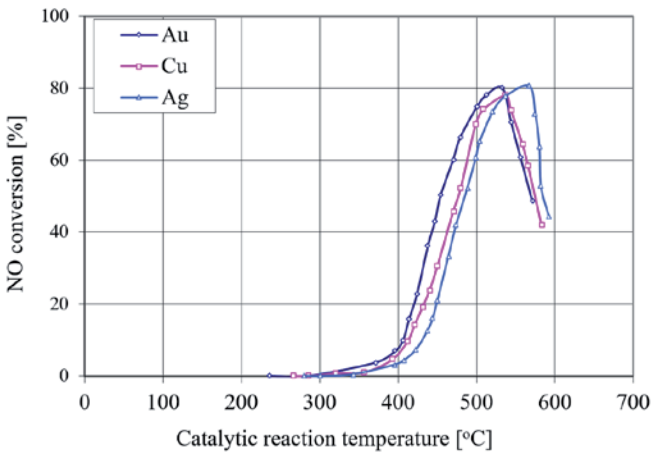

Fig. 5. The conversion of nitric oxide depending on the temperature of catalytic processes for researched models of reactors upon NO_X reduction with propylene. Initial concentrations of exhaust fumes components as shown in Fig. 4

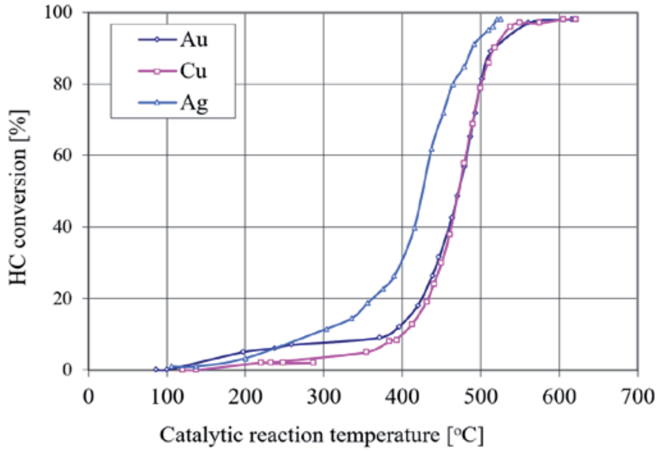

Fig. 6. The conversion of hydrocarbons depending on the temperature of catalytic processes for researched models of reactors with NO_X reduction with propylene. Initial concentrations of exhaust fumes components were as shown in Fig. 4

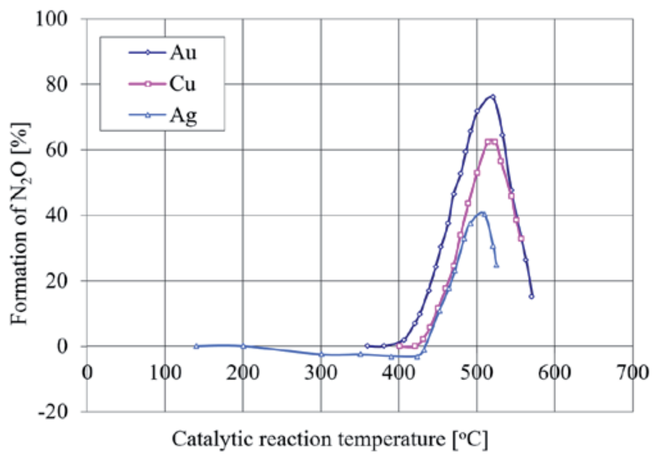

Fig. 7. The formation of nitrous oxide depending on the temperature of catalytic processes for tested reactor models upon NO_X reduction with propylene. Initial concentrations of exhaust fumes components as shown in Fig. 4

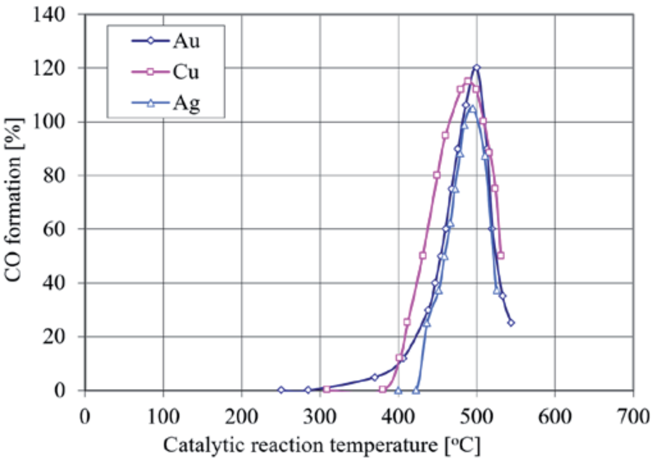

Fig. 8. The formation of carbon monoxide depending on the catalytic process temperature for the tested reactor models upon NO_X reduction with propylene. Initial concentrations of exhaust fumes components were as shown in Fig. 4

Table 3. Conversion parameters of NO, NO_2 and C_3H_6

Reactor	Conversion parameters					
	NO_2		NO		C_3H_6	
	k_{max} [%]	T_{50} [°C]	k_{max} [%]	T_{50} [°C]	k_{max} [%]	T_{50} [°C]
Au	99	160	80	455	98	
Cu	99	180	78	475	98	
Ag	99	210	81	480	98	

The developed reactors have similar NO, NO_2 and C_3H_6 conversion properties. They achieve almost 100% NO_2 conversion at a relatively low temperature (160–210°C) and NO conversion of up to 80% at relatively high temperature (455–480°C) as well as C_3H_6 conversion of approximately 98%.

The most prospective was the A reactor, obtaining relatively large NO conversion at the lowest temperature.

Formation of N_2O and CO

Parameters of gas formation in the tested catalysts, such as p_{max} – maximum formation and T_{50} – temperature of formation of 50% have been presented in Table 4.

A characteristic feature of the developed reactor models is the formation of nitrous oxide as an intermediate product of NO reduction, reaching 80% for Au and Cu catalysts. In this case, the Ag reactor displays the best properties, forming only approximately 40% of N_2O. The developed reactors also generate large amounts of carbon monoxide (above 100%) as an intermediate product of hydrocarbon oxidation.

Table 4. Parameters of N_2O and CO formation

Reactor	Formation parameters			
	N_2O		CO	
	p_{max} [%]	T_{50} [°C]	p_{max} [%]	T_{50} [°C]
Au	76	475	120	455
Cu	62	495	115	430
Ag	41	-	105	460

10. Conclusions

The developed models of reactors using Group 11 elements (Au, Cu and Ag) do not meet the conditions enabling their use in NOx reduction with hydrocarbons as independent reactors in the actual combustion engine. They achieve high NO conversion at temperatures above 450°C, reaching 80% at 550°C. Unfortunately, they do not achieve sufficiently high NO_X conversion over the full exhaust fumes temperature range (200–500°C) of the diesel engine and will result in high hydrocarbon emissions (below 500°C) and high carbon monoxide emissions (around 500°C) as well as nitrous oxide. An analysis of available literature on the use of silver in the amount of 4% by weight of the Al_2O_3 carrier in the HC-SCR catalyst indicates that the use of light alcohols (ethanol) as a reducing agent has a positive impact [7] on increasing the conversion to 98% and reducing the T_{50} temperature to 260°C. On the other hand, a bimetal reactor with a content of 1% AG and 11% of Au in Al_2O_3 achieves [17] NO_x conversion of almost 100%. Research on the impact of copper in the form of its ions placed in ZSM5 zeolite [13] confirmed the possibility of achieving a conversion of 90% at a T_{50} temperature of 300°C. Therefore, it is necessary to conduct further research of catalytic materials, in particular systems of catalytic materials (with the use of Group 11 elements, possibly with the addition of noble metals) while reducing NO_x with alcohols which may better meet the requirements occurring in the process of catalytic exhaust fumes treatment of the diesel engine.

References

1. Bao X, Malik M A, Norton D G, Neculaes V B, Schoenbach K H, Heller R, Conway K R. Shielded sliding discharge-assisted hydrocarbon selective catalytic reduction of NO_x over Ag/Al2O3 catalysts using diesel as a reductant. Plasma Chemistry and Plasma Processing 2014; 34(4): 825-836, https://doi.org/10.1007/s11090-014-9551-3.
2. Bernhard A M, Peitz D, Elsener M, Schildhauer T, Kröcher O. Catalytic urea hydrolysis in the selective catalytic reduction of NO_x: catalyst screening and kinetics on anatase TiO2 and ZrO2. Catalysis Science & Technology 2013; 3(4): 942-951, https://doi.org/10.1039/C2CY20668D.
3. Chaieb T. et al. Selective Catalytic Reduction of NO_x over Au/Al2O3: Influence of the Gold Loading on the Promoting Effect of H2 in H2-Assisted C_3H_6-SCR of NO_x. Catalysis Letters, 2018, 148(2): 539-546, https://doi.org/10.1007/s10562-017-2276-1.
4. Gao F. et al. Understanding ammonia selective catalytic reduction kinetics over Cu/SSZ-13 from motion of the Cu ions. Journal of Catalysis, 2014, 319: 1-14, https://doi.org/10.1016/j.jcat.2014.08.010.
5. Grimaldos O N. Novel Ammonia Storage Materials for SCR Systems: Carbon Materials - Salt Composites. 2019, p. 61 Independent thesis. Advanced level degree of Master.
6. Gu H, Chyn K M, Song S. The effects of hydrogen on the efficiency of NO_x reduction via hydrocarbon-selective catalytic reduction (HC-SCR) at low temperature using various reductants. International journal of hydrogen energy, 2015, 40(30): 9602-9610, https://doi.org/10.1016/j.ijhydene.2015.05.070.
7. He H, Yu Y. Selective catalytic reduction of NO_x over Ag/Al2O3 catalyst: from reaction mechanism to diesel engine test. Catalysis Today 2005; 100(1-2): 37-47.
8. Herreros J M, George P, Umar M, Tsolakis A. Enhancing selective catalytic reduction of NO_x with alternative reactants/promoters. Chemical Engineering Journal 2014; 252: 47-54, https://doi.org/10.1016/j.cej.2014.04.095.
9. Karkamkar A, Deshmane C. Next Generation SCR-Dosing System Investigation 2016, Annual Merit Review (Report).
10. Knefel T, Nowakowski J. Model-based analysis of injection process parameters in a common rail fuel supply system. Eksploatacja i Niezawodnosc - Maintenance and Reliability 2020; 22 (1): 94-101, http://dx.doi.org/10.17531/ein.2020.1.11.
11. Kruczyński S W, Merkisz J, Ślęzak M. Zanieczyszczenia powietrza spalinami przez transport samochodowy [Air pollution by exhaust fumes from motorised transport], Wydawnictwo WKiŁ, Warsaw 2019.
12. Kruczyński S, Orliński P, Ślęzak M. NO_x Reduction in Ag/Al2O3-SiO2 Converters in the Exhaust of a Compression-Ignition Engine. Energies 2021; 14(1): 20, https://doi.org/10.3390/en14010020.
13. Kyungseok L. et al. NO_x Reduction with the HC-SCR System over Cu/Zeolite Based Catalysts. SAE Technical Paper, 2015, https://doi.org/10.4271/2015-01-2012.
14. Lee D H, Lee J O, Kim K T, Song Y H, Kim E, Han H. S. Hydrogen in plasma-assisted hydrocarbon selective catalytic reduction. International Journal of Hydrogen Energy 2012; 37(4): 3225-3233, https://doi.org/10.1016/j.ijhydene.2011.11.070.
15. Lee K, Ogita Y, Sato S, Kosaka H. NO_x Reduction with the HC-SCR System over Cu/Zeolite Based Catalysts, SAE Technical Paper, 2015, https://doi.org/10.4271/2015-01-2012.
16. Liao Y, Eggenschwiler P D, Spiteri A, Nocivelli L, Montenegro G, Boulouchos K. Fluid dynamic comparison of AdBlue injectors for SCR applications. SAE International Journal of Engines 2015; 8(5): 2303-2311, https://www.jstor.org/stable/26278121.
17. More P. M. et al. Activation by pretreatment of Ag–Au/Al2O3 bimetallic catalyst to improve low temperature HC-SCR of NO_x for lean burn engine exhaust. Applied Catalysis B: Environmental, 2015, 174: 145-156, https://doi.org/10.1016/j.apcatb.2015.02.035.
18. Mrad R. et al. Catalysts for NO_x selective catalytic reduction by hydrocarbons (HC-SCR). Applied Catalysis A: General, 2015, 504: 542-548, https://doi.org/10.1016/j.apcata.2014.10.021.
19. Rymaniak Ł, Merkisz J, Szymlet N, Kamińska M, Weymann S. Use of emission indicators related to CO2 emissions in the ecological

assessment of an agricultural tractor. Eksploatacja i Niezawodnosc - Maintenance and Reliability 2021; 23 (4): 605-611, http://doi.org/10.17531/ein.2021.4.2.
20. Thomas J F, Lewis S A, Bunting B G, Storey J M, Graves R L, Park P W. Hydrocarbon selective catalytic reduction using a silver-alumina catalyst with light alcohols and other reductants (No. 2005-01-1082). SAE Technical Paper 2005.
21. Valanidou L, Theologides C, Zorpas A A, Savva P G, Costa C N. A novel highly selective and stable Ag/MgO-CeO2-Al2O3 catalyst for the low-temperature ethanol-SCR of NO. Applied Catalysis B: Environmental 2011; 107(1-2): 164-176, https://doi.org/10.1016/j.apcatb.2011.07.010
22. Wiśniowski P, Ślęzak M, Niewczas A, Szczepański T. Method for synthesizing the laboratory exhaust emission test from car engines based on road tests. IOP Conference Series: Materials Science and Engineering 2018; 421/4: 042080.
23. Yuan X, Liu H, Gao Y. Diesel engine SCR control: current development and future challenges. Emission Control Science and Technology 2015; 1(2): 121-133, https://doi.org/10.1007/s40825-015-0013-z.
24. Zamboni G, Moggia S, Capobianco M. Effects of a dual-loop exhaust gas recirculation system and variable nozzle turbine control on the operating parameters of an automotive diesel engine. Energies 2017; 10(1): 47, https://doi.org/10.3390/en10010047.
25. Zhang W, Qi, S, Pantaleo G, Liotta L. WO3–V2O5 Active Oxides for NO_x SCR by NH3: Preparation Methods, Catalysts Composition, and Deactivation Mechanism - A Review. Catalysts 2019; 9 (6): 527, https://doi.org/10.3390/catal9060527.
26. Zhao W, Li Z, Wang Y, Fan R, Zhang C, Wang Y, Zhang S. Ce and Zr Modified WO3-TiO2 Catalysts for Selective Catalytic Reduction of NOx by NH3. Catalysts 2018; 8(9): 375, ttps://doi.org/10.3390/catal8090375.

Eksploatacja i Niezawodnosc – Maintenance and Reliability

Volume 24 (2022), Issue 1

journal homepage: http://www.ein.org.pl

Article citation info:
BreńkaczŁ, Bagiński P, Adamowicz M, Giziewski S. Failure analysis of a high-speed induction machine driven by a SiC-inverter and operating on a common shaft with a high-speed generator. Eksploatacja i Niezawodnosc – Maintenance and Reliability 2022; 24 (1): 177–185, http://doi.org/10.17531/ein.2022.1.20.

Failure analysis of a high-speed induction machine driven by a SiC-inverter and operating on a common shaft with a high-speed generator

Indexed by: Web of Science Group

Łukasz Breńkacz[a,*], Paweł Bagiński[a], Marek Adamowicz[b], Sebastian Giziewski[c]

[a] Polish Academy of Sciences, Institute of Fluid Flow Machinery, ul. Fiszera 14, 80-231 Gdańsk, Poland
[b] Gdańsk University of Technology, Faculty of Electrical and Control Engineering, Gabriela Narutowicza 11/12, 80-233, Gdańsk, Poland
[c] SGI Engineering, MMB Drives Sp. z o.o., Maszynowa 26, 80-298 Gdańsk, Poland

Highlights

- A numerical analysis of the failure of a high-speed turbomachine was performed.
- Run-out analysis was carried out after the failure was performed.
- Modifications to the design of a test rig for high-speed generators were analysed.
- Rolling bearings and their influence on rotor dynamics were analysed.

Abstract

Due to ongoing research work, a prototype test rig for testing high speed motors/generators has been developed. Its design is quite unique as the two high speed machines share a single shaft with no support bearings between them. A very high maximum operating speed, up to 80,000 rpm, was required. Because of the need to minimise vibration during operation at very high rotational speeds, rolling bearings were used. To eliminate the influence of higher harmonics of supply voltage and current on the formation of torque oscillations on the shaft and excessive losses in the form of heat, a voltage source inverter with high switching silicon carbide (SiC) power transistors characterizing high precision of the output voltage generation with a fundamental harmonic frequency of several kilohertz has been used. During the first start-ups, it turned out that the system was not stable, and a failure occurred. The paper presents the consequences that may arise when a machine operating at a speed of about 70,000 rpm fails. The article contains pictures of a generator failure that occurred at a high rotational speed.

Keywords

high-speed generator, failure analysis, rotor dynamics, rolling bearing.

1. Introduction

The last decade has seen a rapid development of high-speed electric drives, especially as regards their use in air turbo compressors for fuel cell systems [3], variable frequency drives for LNG pumps, vacuum pumps, machine tools, turning centres or specialised medical equipment. The same applies to power generation systems with high-speed electric generators and gas microturbines used in distributed generation [16, 17, 36].

The development of high-speed drives has been made possible by, among others: (i) the development of new-generation power electronic converters with fast silicon carbide (SiC) and gallium nitride (GaN) semiconductor devices that enable precise generation of sinusoidal voltages with fundamental harmonic frequencies of several kilohertz—while reducing the production cost of power electronic converters [8, 13, 23]; (ii) the improved efficiency of high-speed motors and generators [11, 16], which operate at speeds above 100,000 rpm [3, 17, 36]; (iii) improvements in bearing technology [36] and (iv) the development of high-speed digital signal processors (DSPs) for industrial applications—which enables the use of advanced control algorithms at high rotational speeds [12, 33]. The development of these technologies affects both high-speed induction motors/generators that are valued in the industry for their reliability, simple rotor design, low inertia, and ability to operate in high temperatures, as well high-speed permanent magnet motors/generators with high torque density and power density. The stator and rotor of a 3.4 kW generator and a 6-kW generator, which were used on the test rig analysed, are shown in Fig. 1.

The research and development of electric generators is the subject of interest in numerous scientific works. Basic information on permanent-magnet synchronous generators operating at high rotational speeds has been already presented by Arkkio et al. [4]. Design and analysis technologies of high-speed permanent magnet machines have been recently reviewed by Ismagilov et al. [14] and Liu et al. [21]. The mechanical characteristics of high-speed permanent-magnet synchronous generators with different shaft material with taking into account the overhang effect have been analyzed by Lee et al. [19]. A comprehensive sensitivity analysis of the rotor parameters on Multiphysics performance of the high-speed permanent magnet syn-

(*) Corresponding author.

E-mail addresses: Ł. Breńkacz (ORCID: 0000-0001-7480-9636): lukasz.brenkacz@imp.gda.pl, P. Bagiński (ORCID: 0000-0003-3753-7525): pbaginski@imp.gda.pl, M. Adamowicz (ORCID: 0000-0003-0561-8697): marek.adamowicz@pg.edu.pl, S. Giziewski (ORCID: 0000-0003-1197-0291): s.giziewski@gmail.com

Fig. 1. Stator and rotor of a 3.4 kW induction motor/generator (left) and a 6-kW permanent magnet synchronous motor/generator (right) designed to operate at speeds above 80,000 rpm and voltage frequency above 1.3 kHz.

chronous machine, including the electromagnetic properties, losses, rotor stress, rotor dynamics, and the temperature has been presented by Du et al. [10]. The influence of different rectifier topologies on a high-speed permanent magnet generator used in a micro-gas turbine distributed generation system has been studied by Qiu et al. [27]. The design criteria, assembly practices and experimental analysis of the whole low-cost micro generation system with a high-power density microturbine has been discussed by Pottie et al. [25] The investigation of dynamic properties of the microturbine with a maximum rotational speed of 120 krpm was shown by Żywica et al. [37]. The dynamic analysis of 1 kW, 30 kW, and 700 kW turbines were presented by Breńkacz et al. [5–7].

A summary of the current evolution of electric generators and their development trends are presented, for example, in the work by Antipov and Danilevich [2]. The authors examined high-speed electric generators in the speed range of 10,000 to 50,000 rpm. Generally, high speed generators have been the subject of a considerable number of studies, mainly of those dealing with their electrical properties. However, studies that focus on two generators simultaneously are far less common. An example of this is the work by Kuznetsov et al. devoted to the study of two generators [18]. In this study, the authors analysed the synchronisation of two generators.

Studies that focus on the diagnostics of generators can be found in the literature. An example of such a study can be found in the article by Skowronek and Woźniak [31]. To generator diagnostics, the authors proposed a new classification method used for failure analysis. They presented the characteristics of the method based on the alternator diode failures. This method was compared with other diagnostic methods. An analysis of the evolution of the online diagnostic method was presented by Rubanenko et al. [28]. The authors focused on synchronous generators. They created a fault tree of various components of synchronous generators. Identification of wear and failure of brake system components during the warranty service was presented by Sliż and Wycinka [32]. Monitoring and predicting bearing failure was presented by Castilla-Gutiérrez et al. [9]. An example of a computer analysis of disc brakes was presented by Pranta et al. [26]. The effect of rotor eccentricity on radial bearings was presented by Abdou and Saber [1]. The effect of rotor eccentricity on electrical and mechanical characteristics of different types of high-speed machines has been discussed by Lee and Hong [20]. Another approach, which is an online estimation of stator current harmonics for status monitoring and diagnosis of high-speed permanent magnet synchronous machines has been proposed by Lu et al. [24]. As stated in [24], obtaining the harmonic distribution and magnitudes can also provide a reliable reference for optimization in the motor design stage.

In power systems with gas microturbines, the microturbine disk and the high-speed generator rotor generally share a common shaft. The turbine is attached to the free end of the shaft and the rotor of the high-speed generator is in the central part of the shaft, between the two bearings. To achieve the highest possible torque density and power density, the generator stator is embedded in a steel casing with O-ring seals fitted at each end and then placed inside the outer casing of the cooling jacket. Cooling air flows through the air gap between the rotor and the stator to help cool the rotor and shaft, while a mixture of water and glycol is pumped through the cooling jacket to remove heat from the stator [16]. Two bearing hubs are located on the same shaft where the turbine disk and generator rotor are mounted.

At specific dimensions and speed of a high-speed generator, the power density obtained depends on the induction in the air gap and the current system provided by the flow of stator currents. When designing or selecting high-speed electric generators, the specifications for the air gap stresses obtained due to the magnetic field, as well as the restrictions on the cooling system, which provide the maximum values for the machine current system, must be observed. A particular challenge for maximising the heat removal capacity of the cooling system is to avoid or minimise heat losses other than those associated with current flow in the copper-plated stator winding.

In high-speed machines, the most important aspect is to ensure stable operation of the rotor over a wide range of rotational speeds. It is also particularly important to accurately predict the natural frequencies of the rotor during the design phase to minimise the likelihood of failure. Improper rotor design can lead to excessive acoustic noise emissions, accelerated wear, or even bearing damage. At high rotational speeds, the movement of rotating elements can cause mechanical resonance resulting in potential rotor failure or catastrophic contact with the stator.

There is currently no scientific article available that would present the dynamic properties of two generators mounted on a single shaft. There is also a lack of articles available that would show the damage of small high-speed generators. It is this gap that this article aims to fill.

2. Research object

A diagram of the test rig used for high-speed generators testing is shown in Fig. 2. The diagram shows the positions of the bearings, the generators, and the structure on which the stators of the two generators are placed. Generator 1 is an asynchronous motor (IM-mW5,4/6-2-52c/52cr9) [38]. Generator 2 is a synchronous motor (PMSM-mSpW 5.5/4.5 – 4 – a1) [39]. The length of the entire test rig is 288 mm, and its diameter is 130 mm. The O-ring seals and screws used to secure the various components of the casing are also visible on the structure. The radial clearance between the rotor and the stator of the first generator was 300 µm. This is the shortest distance between the rotating rotor and the structure. No strength or dynamic analysis were performed prior to designing and constructing this test rig.

Fig. 3 shows a model of the rotor with the generators, bearings and nuts providing pressure to the bearings. The bearing system comprises four rolling bearings. Two pairs of bearings are positioned at both ends of the rotor. The distance between the bearing pairs was 200 mm.

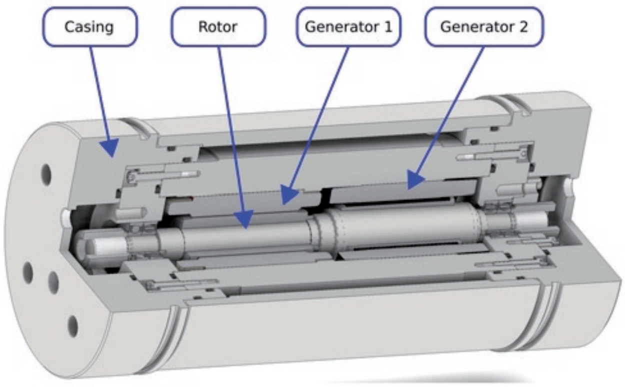

Fig. 2. Diagram of the test rig used for testing high-speed generators

The back-to-back arrangement, also known as the "O arrangement", was used for both pairs of bearings. To exert pressure on the bearings, two nuts were used at both ends of the shaft. High pressure was applied on the bearings (in compliance with the bearing manufacturer's catalogue [29]).

Four bearings marked with the designation HCB7001-C-2RSD-T-P4S were used in the design [29]. The acronym HCB indicates that these are hybrid bearings with ceramic balls. The meaning of individual bearing designation symbols used is as follows:

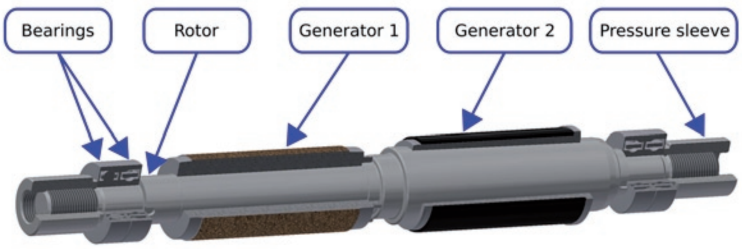

Fig. 3. 3D model of the rotor

- "70" indicates that it is an average series
- "01" indicates that the inner diameter is 12 mm
- "P4S" is the standard FAG designation, which is higher than P4 according to the standard accuracies defined by DIN 620
- "T" indicates a laminated version with guidance on the outer ring
- "2RSD" indicates that the bearing is sealed on both sides and lubricated with grease
- "C" indicates that the bearing angle is 15 degrees.

The maximum speed permitted by the manufacturer for a single bearing is 85,000 rpm. The outer diameter of the bearing was 28 mm and its length was 8 mm.

To verify the performance of the high-speed generator system with a power electronic converter, it is advantageous to analyse the functioning of the generator on an experimental test rig using an additional high-speed motor that simulates the microturbine before mounting it on the target generation system with a gas microturbine [36].

On such a test rig, two high-speed machines are placed on a common shaft. While one acts as a drive motor modelling the changes in the shaft torque generated by the microturbine, the other is analysed at selected dynamic states and performance levels when generating electrical power.

The major challenges encountered when designing an advanced test rig for testing high-speed generators include meeting the test rig specifications, selecting bearings, and integrating them with the shaft of a high-speed generator and a high-speed motor that simulates the performance of a gas microturbine, designing and constructing a cooling system for the generator and motor, as well as designing and constructing a power electronic converter with a control system. It is also of major importance to comprehensively develop testing instruments, tools, and strategies to ensure testing on a component, subsystem and system level aimed at reducing the complexity and risk level when designing the target power system with a gas microturbine.

To run two high-speed machines with rotors embedded on a common shaft, it is necessary to examine the natural frequencies of the shaft by means of a simulation using the finite element method before operating the test rig [36]. In this analysis, the elasticity constant of the bearing system, which affects the rotational speed at which resonant vibrations occur, is considered. The length of the shaft is then adjusted so that the nominal speed remains between the second and third flexural vibration modes of the shaft [36].

When designing a power electronic converter feeding a motor in traditional industrial drives with voltage inverters, motor stator inductance is used to filter out higher-order harmonics from the inverter's output current. This helps to create a relatively smooth motor current waveform. Higher-order harmonics visible in the stator current waveforms result from the switching of the inverter transistors. Except for the first harmonic, the so-called "current ripples" appear in the motor current waveform, and their period corresponds to the switching period of the inverter transistors. The ripples that occur in the inverter current waveform do not affect torque generation; however, they cause hysteresis losses and losses due to eddy currents released as heat in the rotor and stator of the motor. The current components associated with high-frequency current ripples cause higher-order harmonics to appear in the magnetic flux waveform, which in turn induce voltages resulting in the flow of eddy currents in the rotor core and the stator core [35]. In synchronous motors with permanent magnets mounted on the surface of the rotor, the flow of eddy currents in the permanent magnets is also caused by the current ripples in the stator and the arrangement of the grooves. In particular, the increase in temperature of permanent magnets, which can lead to a deterioration of their magnetic properties, is a major problem. The existence of eddy currents requires the motor core to be made of thin sheet metal plates (25 µm thick), insulated on one side. Amorphous alloy sheets, for example, exhibit this property. Hysteresis losses, on the other hand, can be reduced by adding various additives to the ferromagnetic material, resulting in the smallest possible hysteresis loop width. Power losses due to hysteresis are proportional to frequency, and power losses due to eddy currents are proportional to the square of the frequency. In general, the losses associated with supplying the inverter using the voltage pulse-width modulation method increase exponentially with the switching frequency of the transistors and can be very large, even if the pulsed current does not appear to be large in relation to the amplitude of the fundamental harmonic [16].

High-speed motors, especially permanent magnet synchronous motors, are characterised by significantly lower inductance values of the stator winding compared to motors used in typical industrial applications. To reduce the losses of the power supply of the PWM (Pulse Width Modulation) inverter, especially in drives with permanent magnet synchronous motors/generators, it is necessary to use a sinusoidal filter, which must be placed between the inverter and the motor to ensure further reduction of current ripple beyond the damping capacity of the motor stator inductance. The resonant frequency of the sinusoidal filter must be significantly higher than the frequency of the fundamental harmonic of the motor voltage to avoid excessive losses in the drive, but also much lower than the switching frequency of the converter transistors to ensure sufficient filtering efficiency of ripple currents. The use of a sinusoidal filter mounted between the motor/generator and a typical two-level inverter causes a drop in the supply voltage of the high-speed motor and power losses in the filter itself. It also increases the price and the weight of the drive by the cost and the weight of the filter. Since voltage and current resonances can occur in an inverter system with a filter and a high-speed motor, resonance damping resistors are needed in addition to the sinusoidal filter.

The power losses in these components can be significant and this can reduce the efficiency of the inverter and the entire drive system by up to several per cent.

3. Methodology

In this study, we conducted experiments in laboratory conditions based on a specialized testbed with a digitally controlled power electronic converter and two investigated high-speed machines: high-speed induction motor and high-speed permanent magnet generator mounted on a common shaft. It was assumed that the high-speed induction motor driving the generator is supplied with sinusoidal voltage from a voltage inverter with SiC MOSFETs (Metal Oxide Semiconductor Field Effect Transistors).

Since the inverter itself is characterized by a square-wave output voltage with modulated square-wave pulse width, we used an LC filter to obtain a sinusoidal voltage at the output. Thus, the research assumed ideal conditions for supplying the generator with sinusoidal current, so that there was no significant influence of current harmonics on, for example, torque oscillations on the common shaft. Similarly, the research assumed ideal conditions for supplying the high-speed induction motor with sinusoidal voltage, so that there was no significant influence of the harmonics of the supply voltage on the excessive formation of losses and excessive heating of the investigated machine. The test stand prepared in such a way makes it possible to carry out tests of start-ups, speed changes and steady operation of the investigated high-speed machines while concentrating all efforts on examining the mechanical properties of machines in the conducted experiments.

Fig. 4 shows pictures of the designed power electronic converter with SiC transistors and an output sinusoidal filter feeding the high-speed motor that simulates the dynamic states of the gas microturbine on the test rig. To build the power electronic converter, the authors used silicon carbide semiconductor power devices such as SiC MOSFETs and SiC Schottky diodes. Commercially available SiC power devices can be used to increase both the efficiency and the control precision of power electronic converters suitable for use in the renewable energy applications, such as grid-connected photovoltaic (PV) generation systems, and in adjustable-speed electric drives, including high-speed drives with speeds above 100,000 rpm.

SiC MOSFETs have low conduction losses due to the low channel resistance between the drain and the source ($R_{DS(ON)}$) during conduction. For example, in the case of SiC MOSFETs (model C3M0021120K) used in the investigated test rig, the channel resistance $R_{DS(ON)}$ at a rated current of 74 A and at a temperature of 100°C amounts to 21 mΩ. SiC MOSFETs are controlled by a higher gate voltage (from –5 V to +20 V) than their silicon counterparts. They can be switched on and off much faster than IGBT (Insulated-Gate Bipolar Transistors) and have a higher operating frequency. Thanks to significantly lower switching losses, they enable the energy-efficient operation of PWM inverters at switching frequencies above 50 kHz.

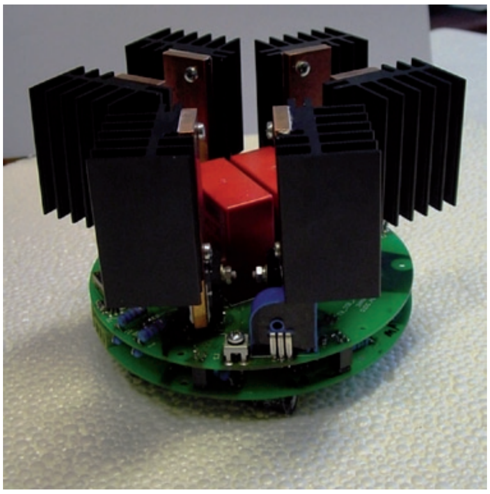

Fig. 4. Pictures of the designed power electronic converter with SiC MOSFETs and sinusoidal output filter used to control the high-speed motor that simulates the dynamic states of the gas microturbine on the test rig

The high switching frequency of SiC transistors, which allows voltage modulation frequencies higher than 50 kHz to be achieved, makes it possible to properly generate a voltage with a fundamental harmonic frequency significantly higher than that obtained in inverters with silicon IGBTs. According to [34], the voltage modulation factor is defined as follows:

$$m_f = f_{sw}/f_{1h} \tag{1}$$

where f_{sw} stands for the voltage modulation frequency of the inverter and f_{1h} stands for the frequency of the fundamental harmonic of the generated voltage; its value should be not less than 21. Therefore, to generate a voltage of 1,500 Hz, the inverter should operate with a modulation frequency of not less than $f_{sw} = 21 \cdot f_{1h} = 31.5\,\mathrm{kHz}$.

When switching voltages and currents within a very short time (in the range of nanoseconds), undesirable voltage and current oscillations may occur due to the existence of parasitic inductances and capacitances in high-current transistor switching circuits, as well as in transistor gate control circuits. High-frequency and high-amplitude oscillations can be a source of electromagnetic interference (EMI) and can cause serious problems with electromagnetic compatibility (EMC) [22]. As shown in Fig. 4, the voltage source inverter with SiC MOSFETs uses a circular main board with the DC-link capacitors located in the centre. This design was used to ensure that the distances between the SiC MOSFETs and the DC circuit terminals, which determine the parasitic inductance of the high-current circuit, are minimised and are the same for all six inverter transistors.

4. Results of experimental studies of a SiC inverter

Fig. 5 shows the voltage switching waveform of the C3M0021120K SiC MOSFET in the tested inverter. Due to the special design of the power circuit of the inverter and the SiC MOSFET gate driver, a very high voltage switching rate of 60 kV/µs has been achieved, reducing the duration of the switching process to tens of nanoseconds, which reduced switching losses. As can be seen from the waveform shown in Fig. 5, at a DC voltage of 670 V, the maximum value of the voltage oscillation of the SiC MOSFET transistor, which was obtained during the transient state of the voltage switching process, did not exceed 850 V, which is an acceptable value for a nominal transistor voltage of 1,200 V.

The parameters of the sinusoidal inductive – capacitive (LC) filter shown in Fig. 5 were selected assuming that the power electronic converter will be used to feed a 3.4 kW high-speed induction motor. The inductance of the filter (L) was calculated assuming that the permissible voltage drop (ΔU) of the inductor reactance is 10 V at a motor current (I_n) of 7 A and a frequency of the fundamental harmonic of the inverter voltage (f_{1h}) of 1,500 Hz, according to the following relation:

$$L = \frac{\Delta U}{2\pi f_{1h} I_n} \tag{2}$$

The capacitance (C) of the sinusoidal filter was chosen based on (3) and (4) so that the resonance frequency f_{res} (f_{res} – resonance frequency) of the filter would be 10 kHz:

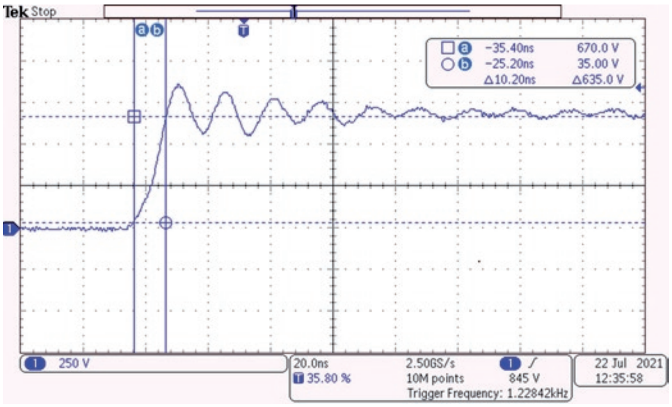

Fig. 5. Voltage switching waveform of the SiC MOSFET transistor in the tested inverter

$$f_{res} = \frac{1}{2\pi\sqrt{LC}} \tag{3}$$

$$C = \frac{1}{2\pi^2 f_{res}^2 L} \tag{4}$$

The modulation frequency f_{sw} = 60 kHz has been selected. The inductance and capacitance values chosen for the sinusoidal filter are respectively 150 µH and 3 µF.

Fig. 6 shows the current and voltage oscillogram obtained at the output of the inverter. The high-frequency ripple currents visible on the current waveform have very high values (like the amplitude of the fundamental harmonic of the current) due to the very low inductance (about several millihenries) of the stator winding. Fig. 7 shows the current and voltage oscillogram obtained at the output of the sinusoidal filter in the tested system with a silicon carbide inverter.

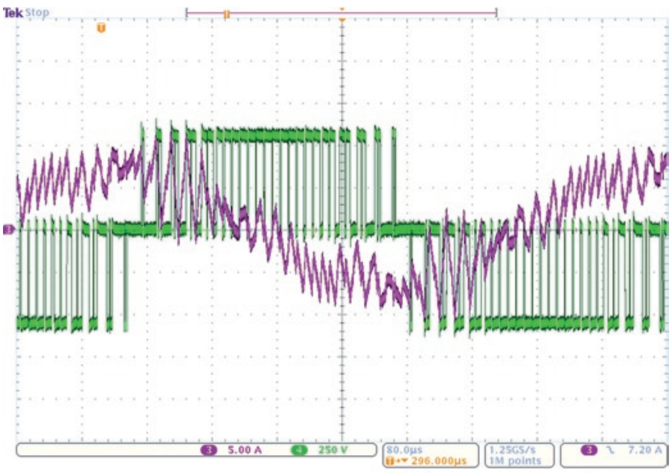

Fig. 6. Voltage and current waveforms of the stator of a 3.4 kW induction motor installed in the tested system with a silicon carbide inverter at voltage frequency of 1.5 kHz measured before the sinusoidal filter

Fig. 8 shows a comparison of the temperature increments of the stator of a 3.4 kW high-speed induction motor. The tests were performed at a motor load of 70% with the power supply at a voltage frequency of 1 kHz. Temperature measurements were carried out by measuring the resistance of a 4.7 kΩ negative temperature coefficient (NTC) thermistor mounted in the bearing disk of the high-speed induction motor. As shown in Fig. 8, the absence of a sinusoidal filter at the output of the inverter leads to an abrupt and very large increase in the temperature of the stator due to thermal losses caused by eddy currents and hysteresis losses in the stator core. The use of the LC

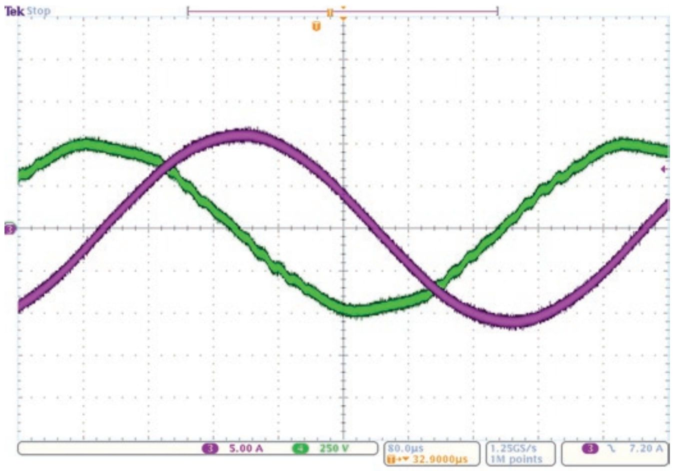

Fig. 7. Voltage and current waveforms of the stator of a 3.4 kW induction motor installed in the tested system with a silicon carbide inverter measured after the sinusoidal filter at a voltage frequency of 1.5 kHz

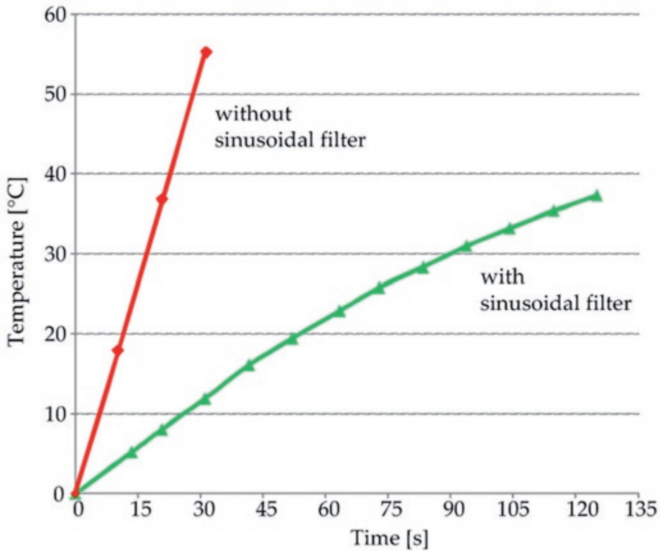

Fig. 8. Temperature increments of the stator of a 3.4 kW high-speed induction motor powered by a SiC inverter with and without a sinusoidal filter

sinusoidal filter results in a significant reduction of thermal losses and allows the high-speed motor to run for a long time.

4. Failure analysis

After the construction of the test rig, its operation was stable at low speeds of several tens of thousands of revolutions per minute. However, when approaching the nominal speed (after reaching a speed of about 60,000 rpm), it suffered damage visible in Fig. 9. In the first generator, located on the left, the distance between the rotor and the stator was only 300 µm. Due to the increased vibration amplitude, there was contact between the rotor and the stator. There is a scratch at the point of contact occupying a good portion of the generator.

Fig. 10 shows a zoom-in on the damaged rotor. The upper part of this figure, a), shows the generator attached to the shaft and the lower part, b), shows the generator removed from the shaft. The damage caused by the failure does not occupy the entire circumference of the generator; it is only local damage. Cavities of about 0.3 mm in depth are visible. This damage occupies approximately 1/3 of the circumference of the generator and 1/2 of its length. Dark discolourations can be seen around the cavities, which occurred due to the increase in temperature caused by friction and an electrical short circuit.

Fig. 9. Damaged rotor

Fig. 9. Damaged rotor

a)

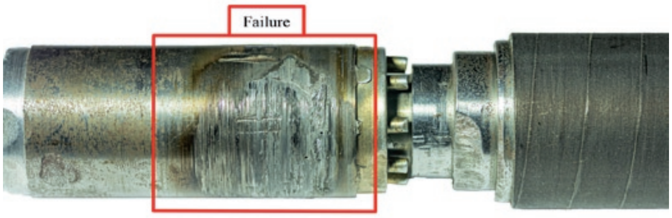

b)

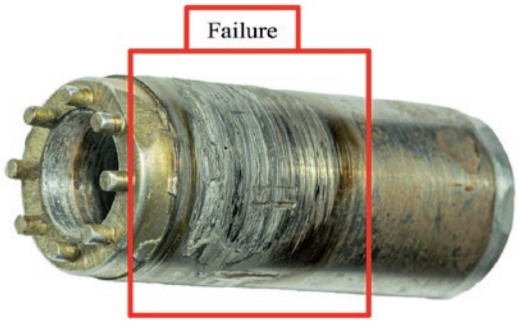

Fig. 10. Pictures showing a) a zoom-in on the damaged generator attached to the shaft, b) damaged generator. The damage is inside red rectangles

Table 1. Summary of run-out measurements measured in seven planes

Angle	Plane 1	Plane 2	Plane 3	Plane 4	Plane 5	Plane 6	Plane 7
0	0.000	0.005	0.006	0.010	0.032	0.019	0.000
45	0.000	-0.004	0.034	0.015	0.031	0.019	0.000
90	0.000	0.018	0.035	0.020	0.032	0.020	0.000
135	0.000	0.059	0.094	0.021	0.034	0.022	0.000
180	0.000	0.093	0.133	0.021	0.035	0.031	0.000
225	0.000	0.116	1.135	0.013	0.036	0.026	0.000
270	0.000	0.100	0.070	0.000	0.036	0.023	0.000
315	0.000	0.056	0.029	0.004	0.036	0.022	0.000
360	0.000	0.005	0.019	0.010	0.036	0.019	0.000

As part of the analysis of the damaged rotor, run-out measurements were carried out using a dial gauge with a measurement accuracy of one hundredth of a millimetre. These measurements are summarised in Table 1. A graphical representation of the shaft geometry is shown in Fig. 11. Some planes are not visible because they are too small in comparison with the planes with the highest displacements.

5. Numerical model

A numerical model was created using MADYN 2000 software to analyse the strength and dynamic properties [30]. A graphical representation of the beam model, with its dimensions and bearing positions, is shown in Fig. 12. This model consisted of 34 beam elements. The rotor mass was 0.987 kg, and the total length of the shaft was 261 mm. These values are the same as those of the manufactured rotor. The bearings were placed at nodes 6, 8, 28 and 30. The axial stiffness of each bearing was 31.1 N/μm and the radial stiffness was 186.6 N/μm. The damping was assumed to be 100 N·s/m for each bearing direction. Steel having the following parameters was selected as the material for the rotor:

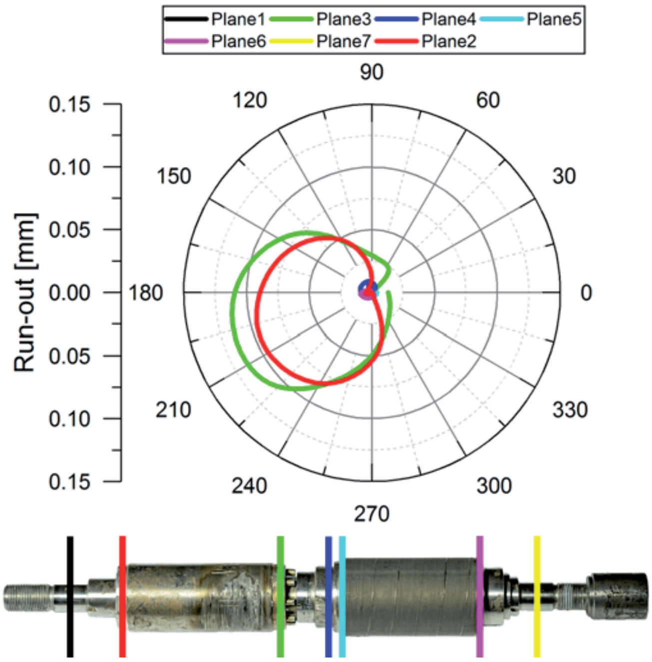

Fig. 11. Shaft run-out analysis

- Young's modulus – 205,900 MPa,
- Poisson ratio – 0.3,
- Density – 7,850 kg/m^3.

The generators were modelled as disks with an inner diameter equal to the diameter of the rotor. The inner diameter of the first and second generator was 29.4 mm and 31 mm, respectively. The generators were modelled using copper with the following parameters:

- Young's modulus – 100,000 MPa,
- Poisson ratio – 0.3,
- Density – 7,000 kg/m^3.

The unbalance is shown schematically in Fig. 13. For a balance quality grade of G2.5, a rotor mass of 0.912 kg and a speed of 80,000 rpm, the

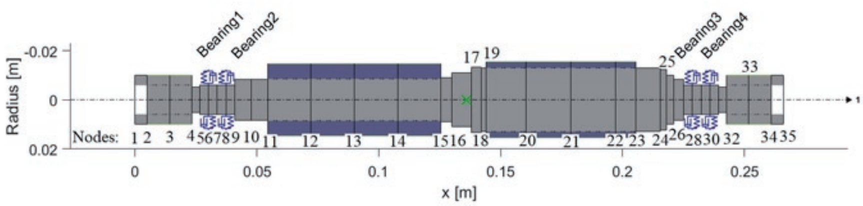

Fig. 12. Beam model

unbalance permitted according to the ISO 1940 standard [15] is 0.294 g·mm. It was placed at node 17.

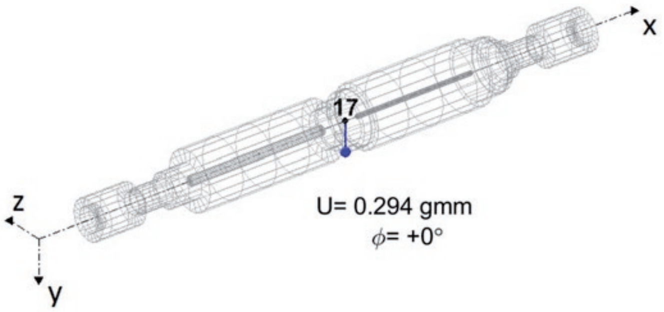

Fig. 13. Rotor unbalance

6. Results of numerical analyses

For the static analyses, the only force acting on the rotor was assumed to be the gravity of 9.81 m/s^2 acting along Y-axis. The displacement results are shown in Fig. 14. The static deflection of the rotor has the highest value in its central part, where it amounts to approximately 0.3 µm.

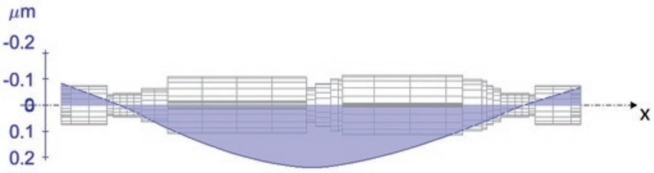

Fig. 14. Displacements due to gravity

The results of the reduced stresses due to the gravitational force are shown in Fig. 15. The maximum reduced stress did not exceed 0.5 MPa. The forces in the bearings are about 5 N and the bending moment reaches a maximum value of 0.2 Nm in the central part of the rotor. All the values of displacements, forces, moments, and stresses were found to be significantly lower than those allowed for this type of design.

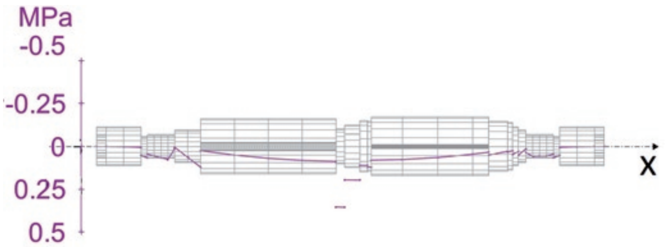

Fig. 15. Reduced stresses

When a rotor is in operation, one of the greatest risks is the occurrence of resonances at nominal speeds or when starting the machine. It is also important that the sub synchronous and super synchronous vibrations (induced for example by a clutch) do not coincide with the resonant frequencies. After the modal analysis, the first bending mode of natural vibrations (shown in Fig. 16) was found to occur at a frequency of 1,127.23 Hz, which corresponds to a speed of 67,633.6 rpm. The first bending mode of natural vibrations occurs at a speed dangerously close to the originally planned nominal speed.

To check whether the unbalance can induce natural vibration of the structure, a harmonic analysis must be performed. The results of the forced vibration analysis are shown in Fig. 17. The green line on the graph represents the vibration amplitude of the journal of the first bearing as a function of speed from 0 to 160,000 rpm. The red line, on the other hand, represents the vibration amplitude of node No. 15 in the central part of the rotor. This is the last node of the first generator and thus the part of the rotor that is most vulnerable to abrasion. For

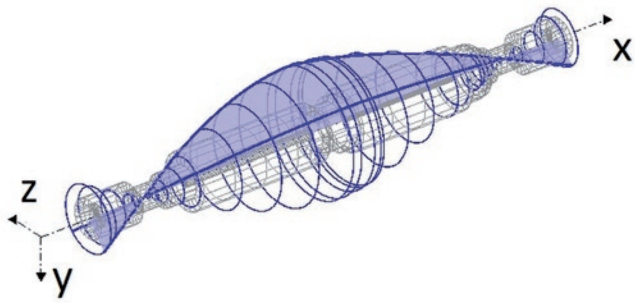

Fig. 16. The first form of natural vibrations of the rotor

design reasons, the distance between the rotor and the stator in this area, measured radially, is only 300 µm. In the numerical model, the global damping was assumed to be 1%. The blue vertical line indicates the nominal rotational speed. The maximum vibration amplitude occurred at a speed of 67,277 rpm and was 0.56 µm at the bearing journal and 26.33 µm at the central part of the rotor.

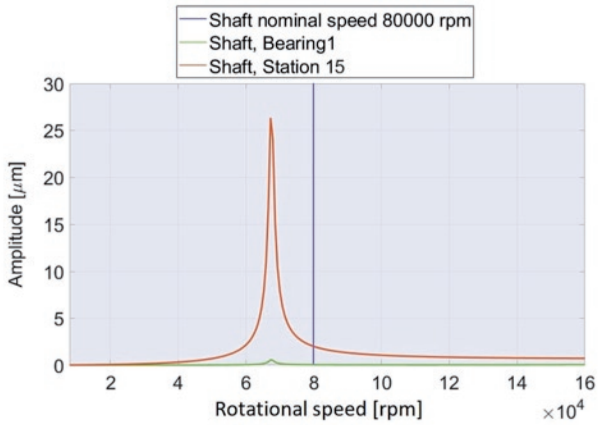

Fig. 17. Forced vibration analysis

7. Analysis of the causes of failure and proposals for changes

After carrying out several preliminary analyses, it became apparent that several factors contributed to the damage to the test rig analysed. Most importantly, the rotor was designed in such a way that the first bending mode of natural vibrations was in the expected speed range. This bending mode occurred at a speed of 67,277 rpm, whilst the nominal speed was designed to be equal to 80,000 rpm. The second very important factor was the presence of whipping between the rotor and the first generator (which occurred even before the rotor was damaged). The third and final factor was the selection of bearings that could operate at speeds of up to 85,000 rpm for a single bearing (according to the manufacturer's catalogue). However, no consideration was given to the fact that when a set of four bearings is in operation and the preload is high, the maximum speed should be reduced by a factor of 0.57, meaning that the bearings can only operate safely up to a speed of 48,450 rpm. Since the structure is not able to sustain large forces and moments, a set of four bearings is also not necessary. As part of the study, the geometry of the rotor was suggested to be changed so that the first bending mode of natural vibrations could be present at a higher rotational speed. A proposal was also made to change the type of bearings used. By changing the type of bearings, the permitted speed would be increased.

To increase the resonant speed of the rotor, a change in geometry was proposed which would increase the stiffness of the rotor. The new geometry is shown in Fig. 18. The updated model comprised 26 beam elements (8 fewer elements). The central beam element was shortened by 5 mm. After the modification, the model's weight was 0.897 kg, i.e., 15 grams lighter. The shaft had an overall length of 223 mm, making it 38 millimetres shorter. The bearings were placed at nodes 5 and 23.

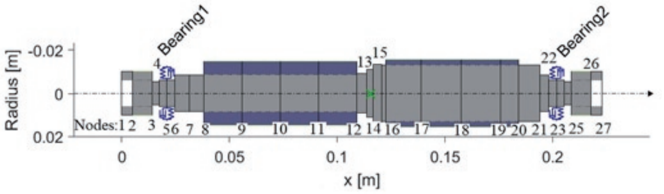

Fig. 18. Beam model

A different type of hybrid bearing with ceramic balls, designated HCB7000-C-2RSD-T-P4S, was used than before. The meaning of individual bearing designation symbols used is as follows:

- "70" indicates that it is an average series,
- "00" indicates that the inner diameter is 10 mm,
- "P4S" is the standard FAG designation, which is higher than P4 according to the standard accuracies defined by DIN 620,
- "T" indicates a laminated version with guidance on the outer ring,
- "C" indicates that the bearing angle is 15 degrees,
- "2RSD" indicates that the bearing is sealed on both sides and lubricated with grease.

The maximum speed permitted by the manufacturer for a single bearing is 95,000 rpm. A speed ratio of 0.75 must also be considered when using a two-bearing system with average tension. The maximum speed permitted by the manufacturer for these bearings is 71,250 rpm. This is lower than the previously assumed speed of 80,000 rpm. However, such a high speed is impossible to achieve anyway due to the resonant speed (as confirmed by the analyses below). The outer diameter of the bearing was 26 mm, and its length was 8 mm. At average bearing tension, the axial stiffness of each bearing was 18.5 N/µm, while the radial stiffness was 111 N/µm.

The unbalance was placed at node 14. As the shaft mass was changed to 0.912 kg, the permissible unbalance value, according to the ISO 1940 standard and a balance quality grade of G2.5, was now equal to 0.272 g·mm and the unbalance was placed at the centre of the rotor, i.e., at node 14.

The forced vibration analysis shows (Fig. 19) that the maximum displacement of the bearing journal (node 5 – green line) and of the part of the rotor which is most exposed to stator rubbing (node 12 – red line) was respectively 3.97 µm and 26.76 µm at a speed of 72,130 rpm. Compared to the reference case, the vibration amplitude has hardly changed. What has changed is the speed at which the resonant vibration occurred; it changed by 4,853 rpm. This indicates an increase in the maximum permissible speed of almost 5,000 rpm. However, for safety reasons, a speed of 6,000 rpm should not be exceeded.

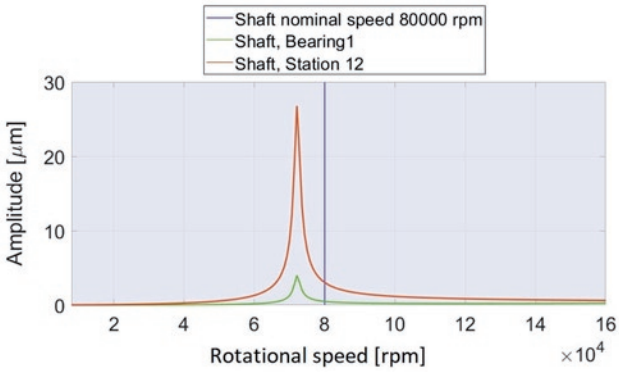

Fig. 19. Forced vibration analysis

9. Summary and conclusions

In this study, the dynamic properties of a test rig used to examine two generators were analysed. After it was designed and built, it was found to have failed. The paper presents the causes and consequences of such a failure. Several reasons contributed to its appearance. It turned out that the required speed of 80,000 rpm could not be achieved due to a resonance occurring at a speed of 67,277 rpm. The bearings were poorly selected, preventing them from operating at the higher speeds expected; and safe operation was only possible up to a speed of 48,450 rpm. There were also manufacturing errors encountered associated with whipping. Although the machine was balanced using an appropriate balance quality grade (G2.5), a failure occurred at a speed of about 60,000 rpm. This failure was most likely caused by the bearings operating at a speed greater than the maximum speed allowed by the manufacturer.

After the design was analysed, a change in the geometry of the rotating system was suggested to ensure that the first bending mode of natural vibrations does not occur until a speed of 72,130 rpm is reached. After the modifications, the first bending mode of natural vibrations will be excited at a speed that is 4,853 rpm higher than in the original design. After analysis, it became clear that without an additional support bearing located in the central part of the rotor—which, for design reasons, would involve two additional bearings and a coupling—operation at the originally planned speed of 80,000 rpm would not be possible. The maximum permissible speed after modifications would be equal to 60,000 rpm. The other way to increase the rotational speed is to use different types of bearings for example gas bearings, gas-foil bearings, or active foil bearings.

Acknowledgements

This paper was created within the framework of the ACTIVERING project entitled "Active foil bearings with variable dynamic properties", agreement no. LIDER/51/0200/L9/17/NCBR/2018, which is being implemented as part of the research and development programme called "LEADER".
The research was conducted using equipment from the KEZO research centre in Jablonna.
The calculations were performed using computers from the IT Centre of the Tri-city Academic Computer Network.

References

1. Abdou KM, Saber E. Effect of rotor misalignment on stability of journal bearings with finite width. Alexandria Engineering Journal 2020; 59(5): 3407–3417, https://doi.org/10.1016/j.aej.2020.05.020.
2. Antipov VN, Danilevich YB. High-speed electrical machines for power engineering: Current state and development trends. Russian Electrical Engineering 2007; 78(6): 277–279, https://doi.org/10.3103/S1068371207060016.
3. Antivachis M, Dietz F, Zwyssig C et al. Novel high-speed turbo compressor with integrated inverter for fuel cell air supply. Frontiers in Mechanical Engineering 2021; 6(February): 1–13, https://doi.org/10.3389/fmech.2020.612301.
4. Arkkio A, Jokinen T, Lantto E. Induction and permanent-magnet synchronous machines for high-speed applications. 2005 International Conference on Electrical Machines and Systems, IEEE: 2005: 871–876, https://doi.org/10.1109/ICEMS.2005.202668.
5. Breńkacz Ł, Żywica G, Bogulicz M. Selection of the Bearing System for a 1 kW ORC Microturbine. Mechanisms and Machine Science, 2019; 60: 223–235, https://doi.org/10.1007/978-3-319-99262-4_16.

6. Breńkacz Ł, Żywica G, Bogulicz M. Numerical Analysis of the Rotor of a 30 kW ORC Microturbine Considering Properties of Aerodynamic Gas Bearings. Mechanics and Mechanical Engineering 2018; 22(2): 425–436, https://doi.org/10.2478/mme-2018-0034.
7. Breńkacz Ł, Żywica G, Bogulicz M. Analysis of dynamical properties of a 700 kW turbine rotor designed to operate in an ORC installation. Diagnostyka 2016; 17(2): 17–23.
8. Carpenter AL, Beechner TL, Tews BE, Yelvington PE. Hybrid-electric turbocharger and high-speed SiC variable-frequency drive using sensorless control algorithm. Journal of Engineering for Gas Turbines and Power 2018; 140(12): 1–8, https://doi.org/10.1115/1.4040012.
9. Castilla-Gutiérrez J, Fortes Garrido JC, Davila Martín JM, Grande Gil JA. Evaluation procedure for blowing machine monitoring and predicting bearing skfnu6322 failure by power spectral density. Eksploatacja i Niezawodnosc - Maintenance and Reliability 2021; 23(3): 522–529, https://doi.org/10.17531/ein.2021.3.13.
10. Du G, Huang N, Zhao Y et al. Comprehensive Sensitivity Analysis and Multiphysics Optimization of the Rotor for a High Speed Permanent Magnet Machine. IEEE Transactions on Energy Conversion 2021; 36(1): 358–367, https://doi.org/10.1109/TEC.2020.3005568.
11. Gerlach ME, Zajonc M, Ponick B. Mechanical stress and deformation in the rotors of a high-speed PMSM and IM. Elektrotechnik und Informationstechnik 2021; 138(2): 96–109, https://doi.org/10.1007/s00502-021-00866-5.
12. Giziewski S. Trójfazowy falownik napięcia z tranzystorami SiC JFET. Przegląd Elektrotechniczny 2012; 88(4b): 76–79.
13. He J, Li C, Jassal A et al. Multi-domain design optimization of dv/dt filter for SiC-based three-phase inverters in high-frequency motor-drive applications. IEEE Transactions on Industry Applications 2019; 55(5): 5214–5222, https://doi.org/10.1109/TIA.2019.2922306.
14. Ismagilov FR, Uzhegov N, Vavilov VE et al. Multidisciplinary Design of Ultra-High-Speed Electrical Machines. IEEE Transactions on Energy Conversion 2018; 33(3): 1203–1212, https://doi.org/10.1109/TEC.2018.2803146.
15. iso.org. ISO 1940-1:2003 Mechanical vibration - balance quality requirements for rotors in a constant (rigid) state. Part 1: Specification and verification of balance tolerances. 2003: 1–28.
16. Kim D, O'Connor J, Schwenne F, Drumm M. Design and test of an advanced system for energy generation. 2020.
17. Krähenbühl D, Zwyssig C, Bitterli K et al. Evaluation of ultra-compact rectifiers for low power, high-speed, permanent-magnet generators. IECON Proceedings Industrial Electronics Conference 2009; (Cm): 448–455, https://doi.org/10.1109/IECON.2009.5414964.
18. Kuznetsov AP, Stankevich NV, Shchegoleva NA. Synchronization of coupled generators of quasi-periodic oscillations upon destruction of invariant curve. Izvestiya Vysshikh Uchebnykh Zavedeniy. Prikladnaya Nelineynaya Dinamika 2021; 29(1): 136–159, https://doi.org/10.18500/0869-6632-2021-29-1-136-159.
19. Lee J I, Bang TK, Lee HK et al. Design of the high-speed pmsg with two different shaft material considering overhang effect and mechanical characteristics. Applied Sciences (Switzerland) 2021; 11(16): 0–8, https://doi.org/10.3390/app11167670.
20. Lee TW, Hong DK. Electrical and mechanical characteristics of a high-speed motor for electric turbochargers in relation to eccentricity. Energies 2021. doi:10.3390/en14113340, https://doi.org/10.3390/en14113340.
21. Liu L, Guo Y, Lei G, Zhu J. Design and Analysis Technologies of High Speed Permanent Magnet Machines. 2021 31st Australasian Universities Power Engineering Conference (AUPEC), 2021: 1–6, https://doi.org/10.1109/AUPEC52110.2021.9597696.
22. Liu T, Wong TTY, Shen ZJ. A survey on switching oscillations in power converters. IEEE Journal of Emerging and Selected Topics in Power Electronics 2020; 8(1): 893–908, https://doi.org/10.1109/JESTPE.2019.2897764.
23. Loncarski J, Monopoli VG, Leuzzi R et al. Analytical and simulation fair comparison of three level Si IGBT based NPC topologies and two level SiC MOSFET based topology for high speed drives. Energies 2019; 12(23): 1–16, https://doi.org/10.3390/en12234571.
24. Lu Y, Zhang X, Zhu C et al. On-line Estimation of Current Harmonics for Status Monitoring and Diagnosis of High-Speed Permanent Magnet Synchronous Motors. 2021 IEEE International Conference on Mechatronics (ICM), 2021: 1–6, https://doi.org/10.1109/ICM46511.2021.9385654.
25. Pottie DLF, Mendonça GA, Faria OA et al. Some aspects of the electromechanical design of high-speed microturbines for power generation. International Journal of Applied Electromagnetics and Mechanics 2020; 63(4): 621–644, https://doi.org/10.3233/JAE-190166.
26. Pranta MH, Rabbi MS, Banik SC et al. A computational study on structural and thermal behavior of modified disk brake rotors. Alexandria Engineering Journal 2021, https://doi.org/10.1016/j.aej.2021.07.013.
27. Qiu H, Zhao X, Wei Y et al. Comparative analysis of super high-speed permanent magnet generator electromagnetic and temperature fields with the PWM and uncontrolled rectifiers. EPE Journal 2020; 30(4): 181–191, https://doi.org/10.1080/09398368.2020.1776494.
28. Rubanenko O, Gundebommu S L, Hunko I, Peroutka Z. Analysis of development directions of online diagnostics of synchronous generator. Przegląd Elektrotechniczny 2021; 1(4): 22–28, https://doi.org/10.15199/48.2021.04.04.
29. Schaeffler. Super precision bearings. 2019: 262.
30. Schmied J, Perucchi M, Pradetto J C. Application of madyn 2000 to rotordynamic problems of industrial machinery. Proceedings of the ASME Turbo Expo 2007; 5(November): 799–810, https://doi.org/10.1115/GT2007-27302.
31. Skowronek K. FFT-PCA-LDA classifier in A.C . generator diagnostics. Eksploatacja i Niezawodnosc – Maintenance and Reliability 2013; 15(2): 140–146.
32. Sliż P, Wycinka E. Identification of factors that differentiate motor vehicles that have experienced wear or failure of brake system components during the warranty service period. Eksploatacja i Niezawodnosc 2021; 23(3): 430–442, https://doi.org/10.17531/EIN.2021.3.4.
33. Stumpf P, Bara I. Model predictive torque control with synchronized sampling frequency for high frequency induction machine drives. IEEE International Symposium on Industrial Electronics 2020; 2020-June: 332–338, https://doi.org/10.1109/ISIE45063.2020.9152245.
34. Stumpf P, Varga Z, Bartal P et al. Effect of subharmonics on the operation of ultrahigh speed induction machines. IECON Proceedings Industrial Electronics Conference 2009: 426–431, https://doi.org/10.1109/IECON.2009.5414960.
35. Zhang C, Chen L, Wang X, Tang R. Loss calculation and thermal analysis for high-speed permanent magnet synchronous machines. IEEE Access 2020; 8: 92627–92636, https://doi.org/10.1109/ACCESS.2020.2994754.
36. Zwyssig C, Kolar J W, Thaler W, Vohrer M. Design of a 100 W, 500000 rpm permanent-magnet generator for mesoscale gas turbines. Conference Record - IAS Annual Meeting IEEE Industry Applications Society 2005; 1(Im): 253–260, https://doi.org/10.1109/IAS.2005.1518318.
37. Żywica G, Kaczmarczyk T Z, Breńkacz Ł et al. Investigation of dynamic properties of the microturbine with a maximum rotational speed of 120 krpm – predictions and experimental tests. Journal of Vibroengineering 2020; 22(2): 298–312, https://doi.org/10.21595/jve.2019.20816.
38. Asynchronous motor mW 5.4/6-2-52c/52cr9 data sheet. e+a Elektromaschinen und Antriebe AG, 2010.
39. Synchronous motor mSpW 5.5/ 4.5-4-a1 ENCA data sheet. e+a Elektromaschinen und Antriebe AG, 2010.

INFORMATION FOR AUTHORS

Terms and Conditions of Publication

1. The quarterly „Eksploatacja i Niezawodnosc - Maintenance and Reliability" publishes original papers written in English. Authors are strongly recommended to have their manuscripts checked by a native English speaker or a professional language editing service before submission, in order to ensure that the language is acceptable. Submissions may be rejected due to low quality of the translation.
2. The Quarterly welcomes all original submissions of articles that comply with its Aims and Scope. If a paper contains any material that has already been published (e.g. figures), then this must be declared by referencing the source in the manuscript, and authors are responsible for obtaining relevant permissions to republish. Evidence of permission granted must be available upon request.
3. All submissions should be made online via the peer-review system. Authors can use the „Articles" button to make a new submission or check the status of their manuscript. New users will need to create an account.
4. Submissions are made on the understanding that the manuscript has not been published elsewhere and is not currently under consideration by another journal published by any other publisher.
5. The submitting author is responsible for ensuring that the submission has been approved for publication by all co-authors. Submitting authors' responsibilities include especially the following issues: plagiarism, authorship, conflict of interest and misleading or misreporting of findings. In all cases, the Editorial Office reserves the rights to contact the authors' institutions if serious misconduct has been identified, and to retract any articles in which serious misconduct has been identified.
6. Each submission is checked for suitability when received by the Editorial Office, and may be rejected without review if it is outside the scope of the journal, is obviously of insufficient quality, or is missing important sections. This ends the assessment procedure. Re-submission of a rejected manuscript is not possible.
7. Reviewers are selected in accordance with the principle of avoiding conflict of interest (examples of conflicts of interest include a personal relationship between reviewer and author, occupational subordination, direct scientific cooperation over the last two years prior to the review). The journal operates a single-blind peer review system.
8. The review is provided in written form and concludes with an explicit recommendation to accept, revise or reject the paper for publication. If a negative review is given, the submission is rejected, which ends the assessment procedure. Re-submission of a rejected manuscript is not possible.
9. The Editor-in-Chief makes the publication decision after receiving at least two external reviewer reports with recommendations. On receiving the required number of reviews, the Editors pass them immediately to authors. The Editors require that authors prepare answers to reviewers' comments, which are then sent to the referees. The Editor-in-Chief will make a decision to accept, accept with minor revisions, accept with major revisions, or reject the paper for publication. The reasons for the decision will be communicated to the authors. When the decision of minor/major revisions is made, and the authors do not revise their articles satisfactorily after receiving reviewer reports, then the Editor-in-Chief reserves the right to reject the article. When revised articles are received, they will either be sent out for further review or the Editor-in-Chief will make a decision depending on the level of revision requested.
10. The time required for reviewing a manuscript and making a publication decision may vary a lot from one submission to the next since it is sometimes difficult to find suitable reviewers, and there may be delays in receiving reviewer reports. The Editor-in-Chief and the Editorial Office try their best to minimize the time from submission to first decision. The journal aims to make the first decision within 7 days after the Editorial Office check and the second decision within 30 days after the review, but no guarantees can be made in this regard.
11. Submissions with positive reviews are subjected to an originality check. Only those articles that have successfully passed the anti-plagiarism test are finally accepted for publication.
12. All accepted articles are published as open-access and distributed under the terms of the Creative Commons Attribution 4.0 International License, which permits unrestricted use, distribution, and reproduction in any medium, provided the original author and source are credited. Full texts of all printed articles are available on the website of the Quarterly.

Fees

The publication fee for one text is 410 EUR (1700 PLN for submissions from Polish institutions).

Technical requirements

1. All papers must be submitted in a Microsoft Word document format. Drawings and photos should be submitted as separate graphic files in *.tif, *.jpg or *.cdr format.
2. A manuscript should include:

   Names of authors, **title**, **abstract**, and **keywords** that should complement the title and abstract. **The corresponding author** should be indicated. Abstract should not exceed 1100 characters (including spaces) and **must be divided into the following sections**: Objectives, Methods, Results, and Conclusions.

   Highlights (a short collection of bullet points that convey the core findings and provide researchers with a quick overview of the article in text form) - three to five bullet points should describe the essence of the study (e.g. results or conclusions) and highlight what is distinctive about it. Highlights should not exceed 90 characters (including spaces) in each bullet point.

   The text in English with a clear division into sections (please, do not divide words in the text).

   Tables, drawings, graphs, and photos included in the text should have descriptive English-language captions.

   If this can be avoided, **no formulae and symbols should be inserted into text paragraphs by means of a formula editor**.

   References (written in accordance with the enclosed reference format). Authors using the Mendeley and the Zotero citation plugins and styles support may download the required format file from the repository.

   Author data should include first names and surnames along with scientific titles, affiliation, detailed postal address and official e-mail address.

Wydawca:
Polskie Naukowo Techniczne
Towarzystwo Eksploatacyjne
Warszawa

Publisher:
Polish Maintenance Society
Warsaw

Członek:
Europejskiej Federacji
Narodowych Towarzystw
Eksploatacyjnych

Member of:
European Federation of National
Maintenance Societies

Patronat naukowy:
Polska Akademia Nauk
Oddział Lublin

Scientific Supervision:
Polish Academy of Sciences
Branch in Lublin